THE UNIVERSITY OF CHICAGO

DESIGN AND DEVELOPMENT OF METAL-ORGANIC FRAMEWORKS FOR SUSTAINABLE CATALYSIS

A DISSERTATION SUBMITTED TO

THE FACULTY OF THE DIVISION OF THE PHYSICAL SCIENCES

IN CANDIDACY FOR THE DEGREE OF

DOCTOR OF PHILOSOPHY

DEPARTMENT OF CHEMISTRY

BY

XUANYU FENG

CHICAGO, ILLINOIS

MARCH 2022

Table of Contents

List of Figures

List of Tables

List of Schemes

List of Abbreviations

1D, 2D, 3D	1-dimensional, 2-dimensional, 3-dimensional
°C	degree Celsius
Å	angstrom
ΔE	energy splitting
ΔG	Gibbs free energy change
ΔR	change in scattering half-path length
σ^2	mean standard relative deviation of a scatter
λ_{max}	emission maximum
abz	4-aminobenzoate
Ac_2O	acetic anhydride
AcOH	acetic acid
AFM	atomic force microscopy
APCI	atmospheric pressure chemical ionization
B3LYP	Becke 3-parameter, Lee-Yang-Parr (hybrid DFT functional)
BDC	1,4-benzenecarboxylate
BET	Brunauer-Emmett-Teller
BMPO	5-tert-butoxycarbonyl-5-methyl-1-pyrroline-*N*-oxide
BNA	1-benzyl-1,4-dihydronicotinamide
BNAH	*N*-benzyl-1,4-dihydronicotinamide
BPDC	biphenyl-4,4'-dicarboxylate
bpy	2,2'-bipyridine

BTB	1,3,5-benzenetribenzoate
BTC	1,3,5-benzenetricarboxylic acid
BIH	1,3-dimethyl-2-phenyl-2,3-dihydro-1*H*-benzo[*d*]imidazole
CCDC	Cambridge crystallographic data centre
CO_2RR	carbon dioxide reduction reaction
CT	charge transfer
CV	cyclic voltammogram
dcbpy	2,2'-bipyridine-5,5'-dicarboxylate
DCE	1,2-dichloroethane
DCM	dichloromethane
DDQ	2,3-dichloro-5,6-dicyano-1,4-benzoquinone
def2TZVP	valence triple-zeta with two sets of polarization functions
DFT	density functional theory
DMA	*N*,*N*-dimethylacetamide
DME	dimethoxyethane
DMF	*N*,*N*-dimethylformamide
DMSO	dimethyl sulfoxide
dppe	1,2-bis(diphenylphosphino)ethane
DRIFTS	diffuse reflectance infrared fourier transform spectroscopy
DUT	Dresden University of Technology
E_0	energy shift of the photoelectron
EAM	earth-abundant metal
EPR	electron paramagnetic resonance

ESI	electrospray ionization
ESI-MS	electrospray ionization-mass spectroscopy
EXAFS	extended X-ray absorption fine structure
FID	flame ionization detector
FT-IR	Fourier-transform infrared spectroscopy
GC	gas chromatography
GC-MS	gas chromatography-mass spectroscopy
H_2bpydc	2,2'-bipyridine-5,5'-dicarboxylic acid
HAA	hydrogen atom abstraction
HAT	hydrogen atom transfer
HBpin	pinacolborane
HER	hydrogen evolution reaction
HKUST	Hongkong University of Science and Technology
HMTS	1,1,1,3,5,5,5-heptamethyltrisiloxane
HOTf	triflic acid
HR-TEM	high resolution transmission electron microscopy
HR-MS	high resolution mass spectroscopy
HOMO	highest occupied molecular orbital
HPLS	high power light source
ICP-MS	inductively coupled plasma mass spectroscopy
I_0	incident beam density
I_t	transmitted beam density
I_{ref}	reference beam intensity

IFEFFIT	software used for fitting EXAFS spectra
^{i}Pr	isopropyl
IR	infrared spectroscopy
IRC	intrinsic reaction coordinate
K_{sv}	Stern-Völmer constant
LanL2DZ	Los Alamos national laboratory 2-double-zeta
LUMO	lowest occupied molecular orbital
Mc	methacrylate
MCR	multicomponent reaction
MeCN	acetonitrile
MeOH	methanol
MIL	Matériaux de l′Institut Lavoisier
MLCT	metal-to-ligand charge transfer
MOF	metal-organic framework
NADH	nicotinamide adenine dinucleotide
NADPH	nicotinamide adenine dinucleotide phosphate
NBO	natural bond orbital
NHE	normal hydrogen electrode
NL-DFT	nonlinear density functional theory
NMA	*N*-methylacridone
NMR	nuclear magnetic resonance
NP	nanoparticle
NPA	natural population analysis

NU	Northwestern University
PBE	Perdew-Burke-Ernzerhof functional
pdac	1,4-benzenediacrylate
PDB	protein data bank
PEG	polyethylene glycol
phen	phenanthroline
PLATON	a crystallographic program
POM	polyoxometalate
POP	bis(2-diphenylphosphino)phenyl ether
PS	photosensitizer
PSM	post-synthetic modification
PT	phenanthroline dibenzoate
PXRD	powder X-ray diffraction
QE	quantum yield
R^2	goodness-of-fit metric
ROS	reactive oxygen species
r.t.	room temperature
S_0^2	passive electron reduction factor
SBU	secondary building unit
SEM	scanning electron microscopy
SET	single electron transfer
SMD	solvation model based on density
SXRD	single crystal X-ray diffraction

^{t}Bu	tert-butyl
TCD	thermal conductivity detector
TEA	triethylamine
TEM	transmission electron microscopy
TEMPO	2,2,6,6-tetramethyl-1-piperidinyloxy
TFA	trifluoroacetic acid
TGA	thermogravimetric analysis
THF	tetrahydrofuran
THQL	tetrahydroquinoline
TLC	thin-layer chromatography
TMSOTf	trimethylsilyl triflate
TOF	turnover frequency
TOFMS	time-of-flight mass spectrometry
TON	turnover number
TPHN	2''-nitro-[1,1':4',1'':4'',1'''-quaterphenyl]-4,4'''-dicarboxylate
UiO	University of Oslo
UV-vis	ultraviolet and visible
XANES	X-ray absorption near-edge structure
XantP	dimethyl-4,5-bis(diphenylphosphino)xanthene
XAS	X-ray absorption spectroscopy
XPS	X-ray photoelectron spectroscopy
ZIF	zeolitic imidazolate framework

Abstract

Xuanyu Feng: Design and Development of Metal-Organic Frameworks for Sustainable Catalysis

Under Direction of Professor Wenbin Lin

As an emerging class of hybrid organic-inorganic materials, metal-organic frameworks (MOFs) provide a desirable and versatile platform to develop sustainable catalysts with high efficiency, low costs, and environmental friendliness. With both material property and intrinsic molecular nature, MOFs have demonstrated great potential in novel catalyst design and practical synthesis while eliminating the gap between traditional homogeneous and heterogeneous catalysts. My PhD research aimed at developing novel sustainable catalysts in the confined space of MOF materials, with efforts on both rational catalyst design and development of novel synthetic protocols and characterization methods, to advance MOF catalysis from conceptual demonstration to synthetically useful and practically advantageous catalytic processes.

To introduce the topic, Chapter 1 of this thesis discusses general concepts and challenges in transition metal catalysis, and briefly describe MOFs as well as design strategies for and applications of MOF catalysts. MOFs provide an irreplaceable platform to develop single-site heterogeneous catalysts for sustainable synthesis.

The first part of this thesis, including Chapters 2, 3, and 4, focuses on the sustainability of catalytic centers. These chapters describe a novel metalation strategy to anchor structurally uniform and solution-inaccessible Earth-abundant metal complexes, including Co, Fe, and Cu, on hydroxide-containing nodes in MOFs, and the application of these MOF catalysts in hydrofunctionalization and oxidative reactions. The highly reactive organometallic species and/or

intermediates were isolated and stabilized by rigid MOF frameworks, leading to long catalyst lifetimes and excellent catalytic activities.

The second part of this thesis, including Chapter 5, 6, and 7, focuses on the sustainability of catalytic processes. A triflation protocol was developed to quantitatively transform coordinatively unsaturated MOF nodes into super strong Lewis acidic metal triflate sites (M-OTf, M = Zr, Al). This triflation strategy was further combined with sustainable synthetic techniques including continuous flow process, multicomponent reaction, and tandem catalysis, to enhance process-, atom-, and step-economy.

The third part of this thesis, including Chapters 8, 9, and 10, addresses the sustainability of both energy sources and metal centers. By replacing precious and toxic Ru-, Ir-, Pt-containing photosensitizers with cost-effective and environmentally-friendly counterparts, a series of multifunctional MOFs were designed and constructed to hierarchically integrate Earth-abundant cuprous photosensitizers and catalytic metal centers for photocatalytic hydrogen evolution, photocatalytic CO_2 reduction, and photocatalytic aerobic oxidation. These systems showed improved stability of both photosensitizers and catalytic centers and more efficient electron transfer between them to promote energy conversion from abundant solar energy to chemical energy.

Acknowledgement

To me, graduation means another parting.

It is still well within the memories that when I first stood on this unfamiliar land, I was filled by ambition and enthusiasm, could not wait to start my new life as a PhD student. Yet five years have passed so quickly and I am now standing at another crossroad on my life-long journey.

I would say that it is never an easy task to pursue a PhD degree, especially at the University of Chicago. Once I was confused. Once I was lost. And once I wandered. Fortunately, I survived and I succeeded because of being surrounded by the most supportive, most intelligent, and kindest people that I can possibly imagine, without whom I would not have been able to reach here. Just like every journey has an end, I know here comes another time to say goodbye.

I would like to express my first and deepest thankness to my supervisor, Professor Wenbin Lin, who is not only my research advisor but also a life mentor. With his profound erudition of chemistry and beyond and endless spirit of learning and exploration, Wenbin really guided me into fantastic areas from inorganic chemistry to organic synthesis, from materials to medicines, and from fundamental science to practical applications. Without his encouragements and supports, and more important, the countless discussions from experimental details to big pictures, I cannot imagine that I would have the opportunities to get involved and succeed in so many exciting projects covering catalysis, energy, and nanomedicine. Besides the tremendous help on scientific problems, his seriousness for work, his rigorous treatment of science, his critical way of thinking, and his aspiration to knowledge, all left great impacts on my own behaviors and will continuously encourage me to keep forging ahead to purse my next goals.

I am so grateful to be surrounded by so many knowledgeable and supportive faculties during my PhD. Especially, I would like to thank Professor Guangbin Dong and Professor John

Anderson, for not only being my dissertation committee members, but also their inspiring teaching and patient guidance during the graduate-level courses I took. I would also like to thank Professor Bozhi Tian, who was once my candidacy exam committee member, for his friendly and helpful discussion through all these years.

I am so lucky to come across several experienced and warmhearted senior lab members, especially in the catalysis subgroup, as both my friends and mentors, who provided me with great help in accommodating the research and life in UChicago. I would like to truly thank Dr. Pengfei Ji, who was a great mentor in teaching me how to conduct experiments, a talent collaborator in sharing ideas and discussions, and a close friend for hanging out, travelling, and dinning. Pengfei also set me with a great model as a PhD researcher, with active learning, hardwork, and enthusiasm in science. I would also like to thank Dr. Kuntal Manna, who taught me a lot when I initially joined the Lin Lab as a summer intern. That period really gave me the faith to make my decision to go further and pursue my PhD here.

I am so fortunate to have the chance to work with some of the most fantastic collaborators, without whom none of my projects could have been accomplished and none of my assumptions could have been realized. I would like to first thank Dr. Yang Song, as we worked together on more than 6 published projects along with numerous discussions and trials on MOF catalysis. As Yang and I spent more than 4 years together in the Lin lab and in Chicago, we not only cooperated tacitly during scientific research, but also became great friends who shared happiness and hardships in daily lives. I would like to express my great thanks to Dr. Yunhong Pi, a former visiting student in the Lin Lab. With her abundant experience in the field of energy conversion, Yunhong provided me with great help in several photocatalytic projects. I would also like to thank

Dr. Zhe Li, another visiting student, for his significant effort and contributions on the computational part of the methane borylation project.

I am so glad to meet, work with, and learn from so many talented and helpful colleagues in the Lin Lab during these years. Dr. Takahiro Sawano and Dr. Zekai Lin taught me how to use the glove box and the high pressure parr reactor. Dr. Wenbo Han and Xiaomin Jiang walked me through the operation of HPLC and LC-MS instruments. Dr. Yingying Li shared with me so many valuable knowledge and experience in oncology and immunology. I also want to thank (by the order of joining the group) Dr. Kaiyuan Ni, Dr. Guangxu Lan, Dr. Yuanyuan Zhu, Theint Aung, Ziwan Xu, Taokun Luo, Geoffrey Nash, Dr. Deyan Gong, Dr. Yangjian Quan, Yingjie Fan, Youyou Li, Dr. Haifeng Zheng, Zitong Wang, and other current and former group members for their support and help on my research and life here in Chicago. I am also glad to work with quite a few energetic undergraduate students during my PhD, who really helped me a lot in several different projects. They are (by the order of joining the group) Emily Chen, Carter Brzezinski, Soren Dunn, and Pierce Yeary.

I have met so many kind and earnest people outside the lab during these years. Dr. Yu-Sheng Chen and Dr. Yujia Ding at Argonne National Lab provided me with great help to support my research and experiments. Dr. Vera Dragisich as the academic program director, Ms Melinda Moore as the student services administrator, and Mr John Philips as the GCIS building manager, all directly and significantly supported my daily study and life here at UChicago. I also want to thank my peers in the same program and the same boat, Zeyu Qiao, Pei Qu, Yibin Xue, and Yang Cao, either as my roommates or great friends, for their continuous help and friendship.

Finally, I would like to reserve my most sincere gratitude to my family, as my consistent support no matter how much I achieved, and as my eternal harbor no matter how far I sailed. I

went to a boarding high school at 15, during which time I went home once a week. I left my hometown and went to Beijing for college education three years later, when my distance from home became 4 hours of flight. When I made my first step on this unfamiliar land 5 years ago, I suddenly realized that, from that moment on, to me, home meant 14 time zones away and on the other side of the planet. As the luckiest child with the most supportive and understanding parents, no matter from where I depart and to where I go, my family always occupy the highest position in my heart.

To me, graduation means another departure.

Just like every seed of a dandelion has its own path, I will depart again in a short period of time. As I always mentioned, I am so lucky and glad to be always surrounded by some of the most outstanding and talented young peers of my age. Although we have different destinations, I would like to share with you one of my favorite poetries and wish you all the best:

“长风破浪会有时，直挂云帆济沧海。” —— 李白「行路难・其一」

“A time will come to ride the wind and cleave the waves,

We'll set our cloud-white sail and cross the sea which raves.”

Xuanyu Feng

New Year’s Eve 2021

At Hyde Park, Chicago

Chapter 1. Introduction

1.1 Catalytic Processes and Transition Metal Catalysis

As one of the most important concepts in modern chemistry, catalysis or catalytic process is widely applied in chemical and pharmaceutical industries to efficiently transform chemical feedstocks into valuable products.[1-4] At the center of the catalytic process, a catalyst is involved in the reaction pathway by reducing the activation barrier of the desired reaction while suppressing unwanted side reactions. The extensive utilization of catalysis has greatly benefited the humankind and advanced our civilization. A notable example is the Haber process, in which the finely divided iron bound to an iron oxide carrier containing other metal oxide promoters serves as a catalyst for the synthesis of ammonia directly from nitrogen and hydrogen gases. Ammonia is used mainly as a nitrogen fertilizer in the forms of ammonia itself, ammonium nitrate, or urea. The use of fertilizers in the past century has significantly increased the productivity of agricultural land to sustain the explosive growth of global population.[5-6] Catalysis has also played an important role in modern pharmaceutical industry, with successful examples including but not restricted to chirally catalyzed hydrogenation and oxidation (2001 Nobel Prize),[7-10] olefin metathesis in organic synthesis (2005 Nobel Prize),[11-13] pallidum-catalyzed carbon-carbon cross-coupling reactions (2010 Nobel Prize),[14-16] and asymmetric organocatalysis (2021 Nobel Prize).[17-18]

Among all catalytic systems, transition metal catalysis has distinguished itself with wide applications in the production of pharmaceuticals, agrochemicals, and chemical feedstocks. Catalysts are generally divided into homogeneous and heterogeneous catalysts depending on whether the catalysts stay in the same phase as the reactants. Homogeneous transition metal catalysts feature well-defined molecule structures and can be precisely designed through optimizing the chemical structures of supporting organic ligands around the active metal centers.

By fine-tuning the electronic and steric properties of metal centers, homogeneous transition metal catalysts can achieve high catalytic activity and selectivity while suppressing catalyst decomposition.[19-21] A well-known example is the development of Grubbs catalyst series (**Figure 1-1a**). First reported in 1995, the first-generation Grubbs catalyst was a ruthenium alkylidene dichloride complex with two phosphine supporting ligands and displayed high metathesis reactivity.[13] The same research group developed the second-generation Grubbs catalyst using an N-heterocyclic carbene (NHC) to replace one of the phosphine ligands in 1999.[22] Due to the electronic properties and steric bulkiness of NHC, the second-generation Grubbs catalyst featured higher activity as well as much better stability towards moisture and air. By further replacing the phosphine ligand with more labile pyridine ligands, i.e., 3-bromopyridine, the third-generation Grubbs catalyst increased the initiation rate in metathesis by more than a million-fold.[23] However, most supporting ligands require laborious and costly synthesis and homogeneous catalysts cannot be easily separated from reaction mixtures. As a result, homogeneous transition metal catalysts tend to be costly and many of them have low process efficiency.

In contrast to homogeneous catalysts, most heterogeneous catalysts are based on inorganic materials, such as metal oxides and zeolites. Heterogeneous catalysts are usually cost-effective, easily separated, and thermally robust, typically with a much longer catalyst lifetime. Heterogeneous catalysts are widely applied in large-scale industrial process and our daily activities, for example, the use of vanadium oxides in sulfuric acid synthesis and the use of evenly dispersed precious metals on alumina or/and ceria in automobile catalytic converters to suppress the generation of toxic gases and pollutants in exhaust gases. However, the non-uniform and complicated structures of active sites in traditional heterogeneous catalysts present significant challenges to charactering the active sites, increasing the densities of active sites, fine-tuning the

active sites for selective catalysis, and elucidating the mechanistic details of catalytic reactions (**Figure 1-1b**).[24-26]

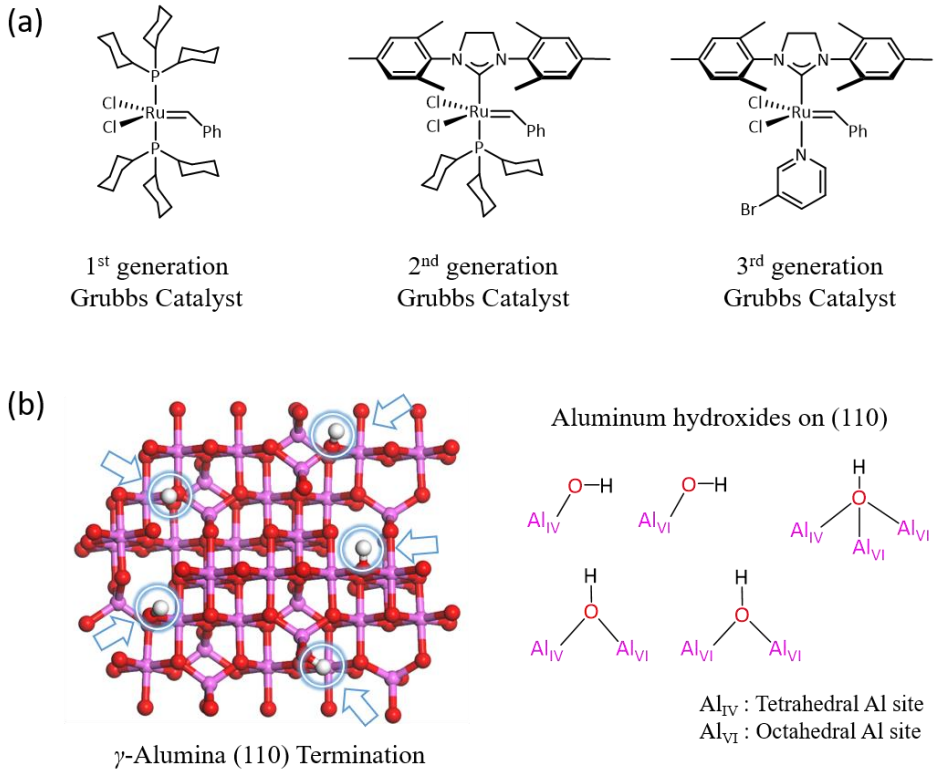

Figure 1-1. Representative examples of homogeneous and heterogeneous catalysts. (a) Chemical structures of 1st, 2nd, and 3rd generation Grubbs catalysts. (b) Non-uniform aluminum hydroxide species on the (110) surface of γ-alumina.

1.2 Metal-Organic Frameworks and Catalytic Applications

Porous materials have drawn significant attention due to their unique structures and potential applications in many areas.[27-31] As an emerging class of porous materials, metal-organic frameworks (MOFs), or porous coordination polymers (PCPs), have undoubtedly become one of the hottest research topics among scientists and engineers in past two decades (**Figure 1-2**). Omar M. Yaghi and coworkers reported that a zinc-based MOF (MOF-5) could reversibly store hydrogen at room temperature in 2003.[32] MOFs are crystalline organic-inorganic hybrid materials built from inorganic metal/metal cluster nodes (also called secondary building unites, SBUs) and exo-

multidentate organic linkers in a highly ordered manner.[33-39] Typically, the organic linkers contain N- or O-based lone pairs that can coordinate with metal ions in the SBUs to form 3D, 2D, or in rare cases, 1D networks. With the ability to choose from numerous inorganic nodes and organic linkers, MOFs can have distinct topologies and structures, and uniform pores or channels ranging from several Årmstrong to several nanometers in dimensions.[40] Besides, molecular tunability of MOF materials, including nodes, ligands, and pores, further expands the diversity of MOF libraries for a wide range of applications including gas adsorption and separation,[41-43] chemical sensing,[44] proton conductivity,[45] nanomedicine,[46-47] catalysis,[48-54] and others.[55-56]

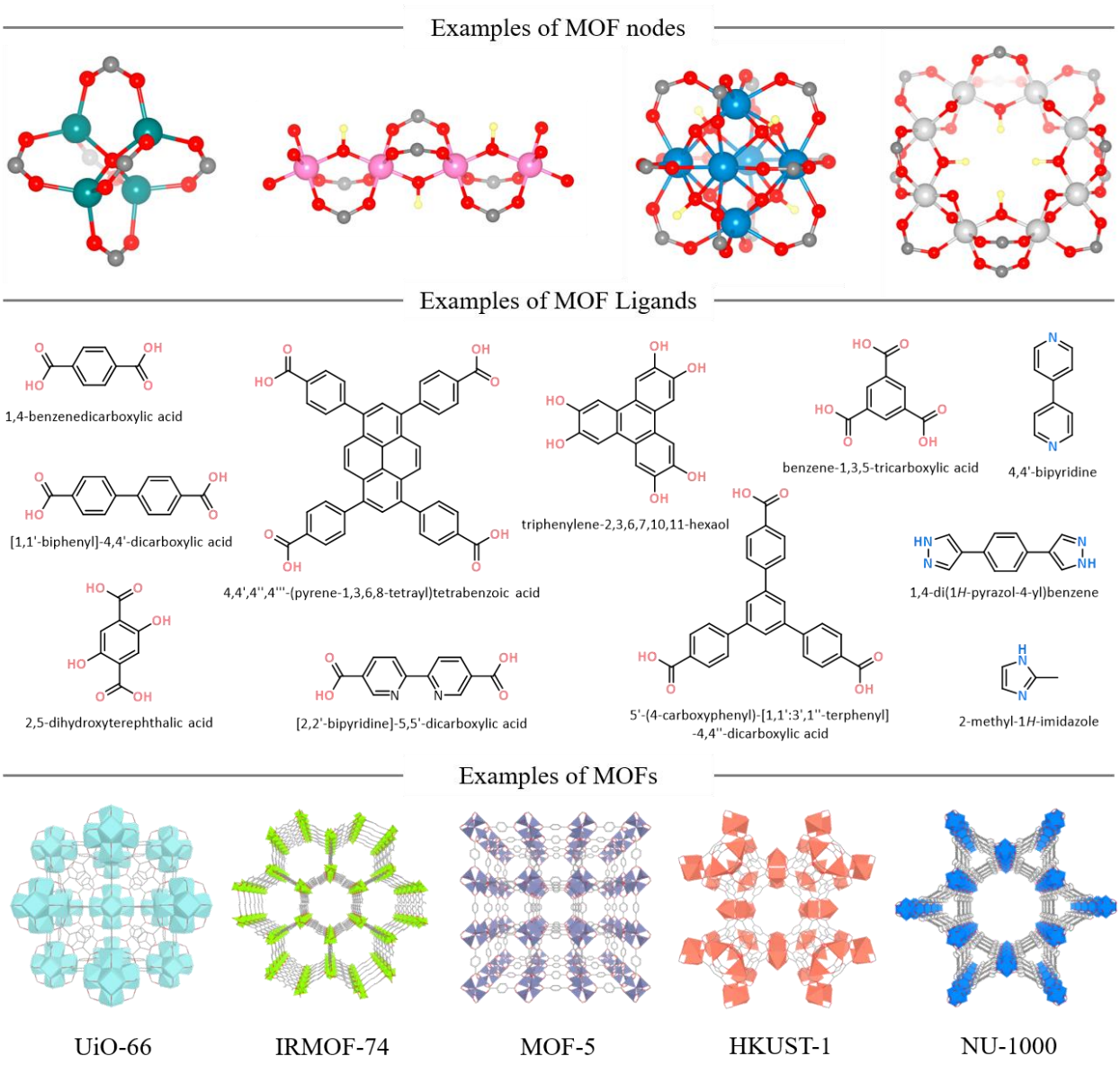

Figure 1-2. Representative examples of MOF nodes, ligands, and MOF structures.

With its high porosity and structural diversity, MOFs have been explored for their catalytic applications from the outset. In 1994, almost 10 years before the term of "Metal-Organic Framework" was coined, Fujita and coworkers reported a 2D $Cd(bpy)(NO_3)_2$ coordination polymer and used the Cd^{II} metal centers with two weakly coordinated nitrates in the axial positions as a Lewis acid to catalyze cyanosilylation of aldehydes.[57] After two decades of development, MOFs have proven as a unique hybrid porous material platform for the design of single-site solid

catalysts that bridge the gap between homogeneous and heterogeneous catalysts.[58-59] With crystalline frameworks, MOFs provide well-defined scaffolds at the molecular level for the installation of uniform catalytic active species whose electronic properties and surrounding environments can be precisely controlled as in homogeneous catalysts.[60-61] The heterogeneous (solid) nature of MOF catalysts allows for recycle and reuse via simple filtration, which reduces wastes and improves efficiency. The rigid MOF backbones separate the active site from each other to minimize undesired multicenter decomposition processes that are commonly observed in homogeneous transition metal catalysts. Lastly, different periodic components of MOF structures, i.e., the organic linkers, the SBUs, and the pores/channels, provide additional opportunities to immobilize active sites for catalytic applications.[62-68]

1.3 Catalyst Design and Site-isolation Effect in MOFs

One of the main chanllenges in catalyst design is to prevent catalyst deactivation during the reaction process. For transition metal catalysts, metal leaching, in which the metallic species go through de-coordination from the supporting sites, and multicentered process, through which the metal centers of the catalyst form unreactive multinuclear complexes or nanoparticles, contribute significantly to catalyst deactivation.[20, 69] A common and widely-used strategy to prevent the catalyst deactivation in homogeneous catalysts is the introduction of bulky and chelating ligands to provide steric hinderance around the metal centers and strong coordination,[70-72] which can largely suppress the multimetallic processes and metal leaching (**Figure 1-3**). However, such bulky multidentate ligands typically require lengthy and expensive synthetic routes. In addition, this stretagy also hinders a substrate approaching the catalytic metal centers, and thus often attenuates catalytic activities. In nature, enzymes typically use an elaborate protein scaffold to isolate active sites from each other to prevent deactivation. Proteins create a unique environment

to surround metal centers in well protected pockets, usually composed of amino acid residues (**Figure 1-3**).[73-74] For traditional heterogeneous catalysts, site-isolation can be achieved by templating the surface with barriers and/or by grafting catalytic species on functional surfaces, which prevents agglomeration and decomposition. Unfortunately, the nonuniform distribution of catalytic sites on most solid catalysts makes it difficult to characterize the catalytic species and to study the reaction mechanism.

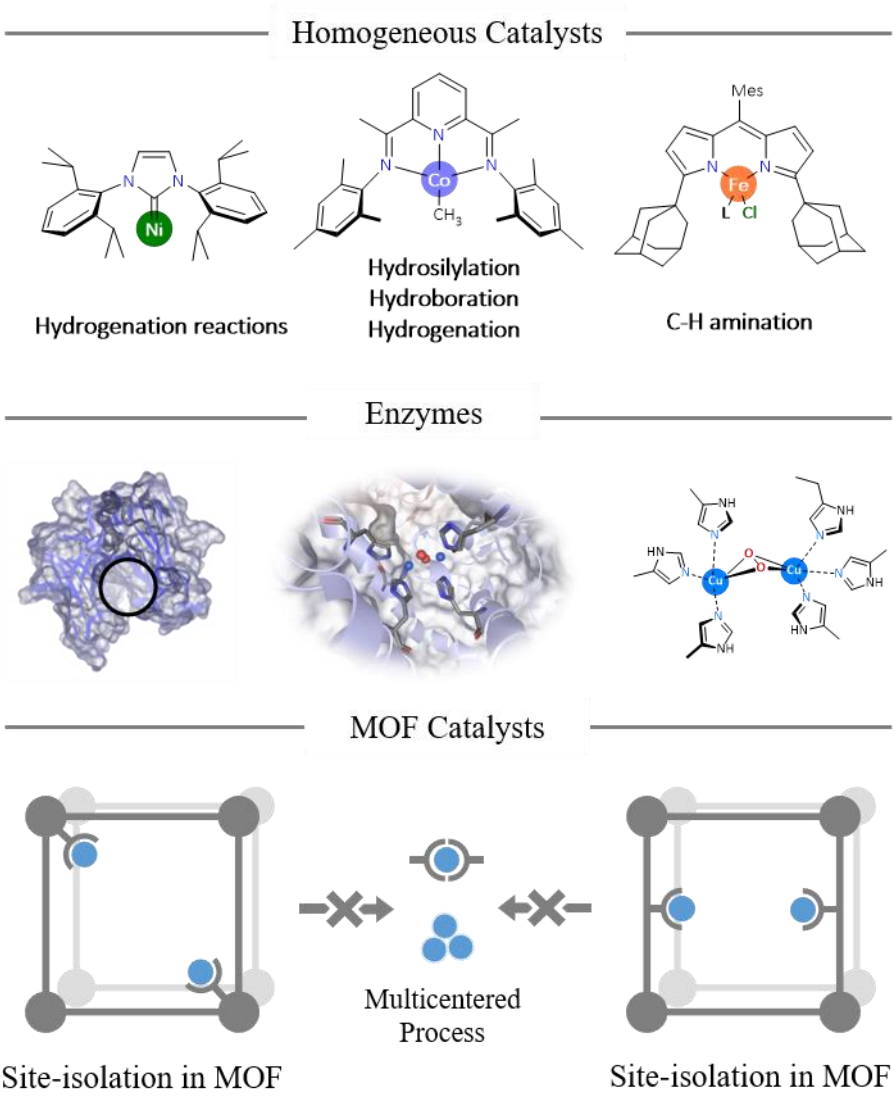

Figure 1-3. Strategies to suppress catalytic center deactivation in homogeneous catalysts, enzymes, and MOFs.

With rigid frameworks and well-defined molecular structures, MOF catalysts enjoy unique site-isolation effect in which the MOF matrix can immobilize the catalytic centers and prevent them from aggregation, thus significantly suppressing multicentered catalyst deactivaton processes (**Figure 1-3**). The site-isolation effect significantly suppresses catalyst deactivation in MOFs, leading to much extended catalyst lifetimes. The field of MOF catalysis has witnessed significant progress in the past two decades. The initial efforts on MOF catalysis focused on the use of coordinatively unsaturated sites around metal ions or clusters as Lewis acidic sites and modifications of organic linkers to install Brönsted acid sites (such as sulfonic acids)[75] and basic sites (such as amino groups).[76] The reaction scopes of such simple acid/base catalysis by MOFs are, however, rather limited. To unleash the potential of MOF catalysis, a number of novel synthetic strategies have been developed in the past 15 years to construct efficient MOF catalysts. These synthetic strategies can be broadly classified into three categories: (a) functionalization at MOF linkers/ligands; (b) functionalization at MOF SBUs; (c) entrapment of catalytically active species (e.g., metal nanoparticles, metal complexes, and organic molecules) in MOF pores, channels, and cavities (**Figure 1-4**). These synthetic strategies can be implemented via either direct incorporation[77] or post-synthetic modification (PSM).[78] Different synthetic strategies have also been combined to afford MOF catalysts with synergistic active sites.[79]

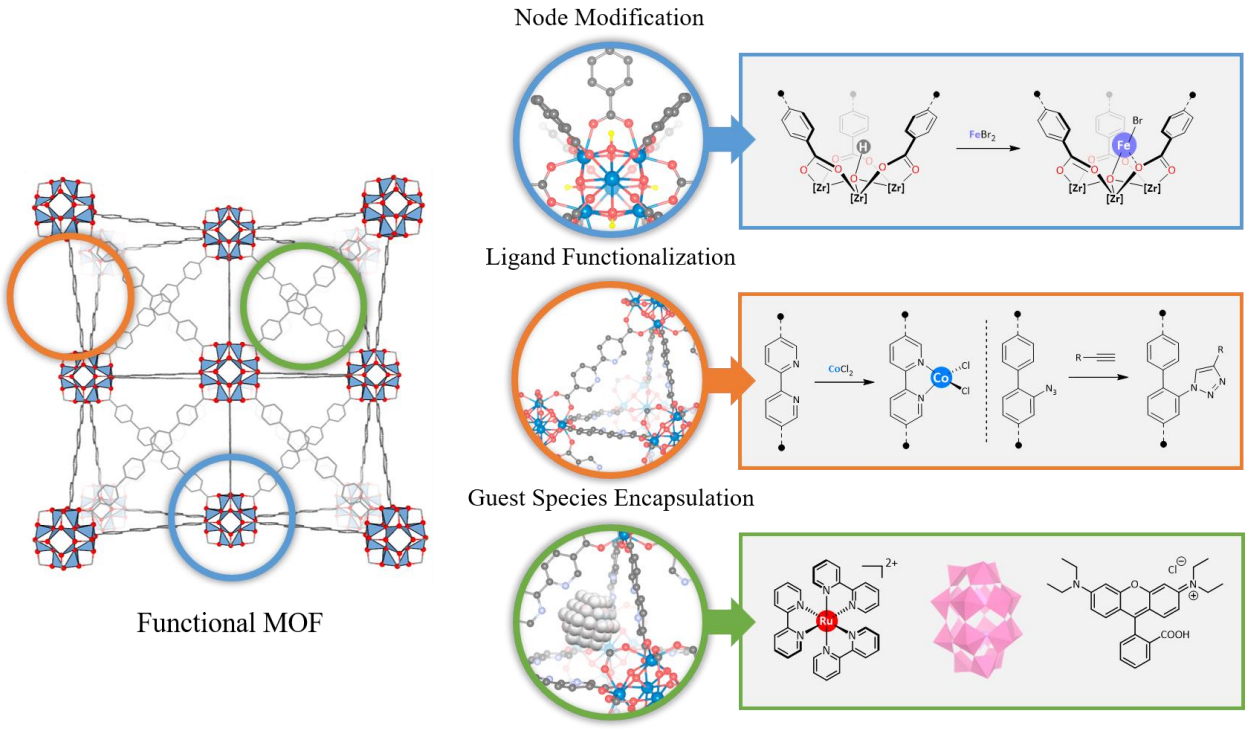

Figure 1-4. Catalyst design strategies in functional MOFs: node modification, ligand functionalization, and guest species incorporation.

1.4 MOF for Sustainable Catalysis: the Scope of This Dissertation

Despite tremendous contribution of catalytic processes to chemical and pharmaceutical industries, traditional transition metal catalysis faces several significant challenges, including the reliance on high-cost and low-abundance precious metals, generation of waste with low atom and step economy, and tedious reaction workup and product purification. The concept of green chemistry or sustainable chemistry, which was originally proposed in 1990s, focused on the design of chemical products and processes that reduce or eliminate the use or generation of hazardous substances.[80] It is not only the rising environmental burden but also the need to reduce the cost of catalytic processes that drives the discovery of new methodologies and catalytic platforms towards sustainability.

Built on the significant efforts and achievements on using the MOF platform for catalyst development, my PhD research aimed at developing novel sustainable catalysts in the confined spaces of MOF materials, with efforts on both rational catalyst design and development of novel synthetic protocols and characterization methods, to advance MOF catalysis from conceptual demonstration to synthetically useful and practically advantageous catalytic processes. This dissertation can be divided into three distinct parts based on their thematic differences.

The first part, including Chapters 2, 3, and 4, focuses on the sustainability of catalytic centers. These chapters describe a novel metalation strategy to anchor structurally uniform and solution-inaccessible Earth-abundant metal complexes on the hydroxide-containing nodes in MOFs. As the majority of metal-catalyzed transformations that are utilized in practical chemical synthesis still involve second- and third-row transition metals, there is an urgent need to find their substitutes based on abundant and sustainable first-row metals. In Chapter 2, we successfully installed Co and Fe complexes on the nodes of MIL-53(Al), an Al-MOF constructed from Al-oxo chain SBUs and 1,4-benzenedicarboxylated (BDC) ligands. The highly reactive organometallic species and/or intermediates were isolated and stabilized by the rigid MOF frameworks, leading to extended catalyst lifetimes and long-term catalytic activities. MIL-53(Al)-Co displayed high activity in catalyzing hydroboration of alkynes and nitriles as well as hydrosilyation of esters, while MIL-53(Al)-Fe promoted the oxidative sp3 C-H amination and Wacker-type oxidation reactions. In Chapter 3, we synthesized a Ti-MOF with anchored Co-hydride sites between the neighboring SBUs for direct reduction of pyridines and quinolines via a step-economical cascade hydroboration-hydrogenation pathway. The catalyst Ti_3-BPDC-Co was found to be highly active towards the cascade reduction of a wide scope of pyridines to piperidines and quinolines to 1,2,3,4-tetrahydroquinolines selectively. In Chapter 4, we further designed and constructed a binuclear Cu

catalyst on the SBUs of MIL-125(Ti) to mimic binuclear Cu enzymes. The MOF-based binuclear Cu catalyst acted as an artificial enzyme to efficiently promote the monooxygenation of a wide scope of organic substrates using dioxygen as oxidant.

The second part, including Chapter 5, 6, and 7, focuses on the sustainability of catalytic processes. In Chapter 5, we report the discovery of a triflation protocol which can quantitatively transform coordinatively unsaturated MOF nodes into super strong Lewis acidic metal triflate sites. We subsequently combined this triflation strategy with sustainable synthetic techniques including continuous flow process, multicomponent reaction, and tandem catalysis, to enhance process-, atom-, and step-economy. In Chapter 5, we developed a triflation strategy to significantly enhance the Lewis acidity of MOF SBUs, which is comparable with homogeneous benchmark $Sc(OTf)_3$, and then applied this MOF catalyst in continuous flow reactions by formulating a MOF@silica composite. These flow reactions significantly outperformed batch reactions with much higher turnover numbers (TONs), turnover frequencies (TOFs), and productivity. In Chapter 6, we designed and synthesized a 2D MOF with strong Lewis acidity and systematically studied the effects of the MOF topology on multicomponent reactions. The 2D MOF, Zr_6OTf-BTB, with fully exposed Lewis acidic MOF nodes, demonstrated excellent catalytic activity towards multicomponent reactions to construct a series of substituted tetrahydroquinolines and aziridines, including several bioactive compounds and drug candidates. In Chapter 7, we combined triflated MOF nodes with entrapped Pd nanoparticles in a single bifunctional framework to promote a tandem process. With the cooperation between Al-OTf sites and Pd-nanoparticles, this MOF catalyst catalyzed tandem dehydroalkoxylation-hydrogenation of a wide scope of oxygen-containing compounds, including alcohols, ethers, and esters, under relatively mild conditions to afford saturated alkanes as fuel stocks.

The third part, including Chapters 8, 9, and 10, addresses the sustainability of both energy source and metal centers. We designed and constructed a series of multifunctional and photosensitizing MOFs, which hierarchically integrated Earth-abundant cuprous photosensitizers (PSs) and catalytic metal centers. These MOF systems demonstrated much improved stability of both PSs and catalytic centers and more efficient electron transfer between them to promote the conversion of abundant solar energy to chemical energy. In Chapter 8, we successfully introduced cuprous diimmine-diphosphine photosensitizing complex into the bridging ligands of MOF materials. These photosensitizing MOFs were further metalated with catalytic centers on the same framework and exploited for highly efficient photocatalytic hydrogen evolution reaction (HER) and photocatalytic CO_2 reduction, with TONs of up to 18,700 and 1,328, respectively. In Chapter 9, we constructed a series of Fe^{SBU}@Zr_6-Cu by integrating MOF ligand-based Cu-PSs and MOF SBU-supported Fe^{II} sites for photocatalytic HER. By decreasing the coordination strength of the counter anions in Fe-based HER catalysts (i.e., from OAc^-, Cl^-, Br^-, to BF_4^-), Fe^{SBU}@Zr_6-Cu with BF_4^- showed extremely high photocatalytic HER TONs of up to 33,700 and TOFs of up to 880 h^{-1}. In Chapter 10, we developed another multifunctional MOF, Zr_6-Cu/Fe, containing Cu-PS and bipyridine-Fe^{II} centers with close proximity in the MOF structures, for organic photoredox aerobic oxidation reactions. This system displayed excellent reactivity and broad substrate scopes towards aerobic photooxidation of alcohols and benzyl compounds to afford corresponding carbonyl products, with TONs of up to 500.

1.5 References

1. Cornils, B.; Herrmann, W. A., Concepts in homogeneous catalysis: the industrial view. *Journal of Catalysis* **2003,** *216* (1), 23-31.

2. Cabri, W., Catalysis: The pharmaceutical perspective. *Catalysis Today* **2009,** *140* (1), 2-10.

3. Armor, J. N., A history of industrial catalysis. *Catalysis Today* **2011,** *163* (1), 3-9.

4. Hayler, J. D.; Leahy, D. K.; Simmons, E. M., A Pharmaceutical Industry Perspective on Sustainable Metal Catalysis. *Organometallics* **2019,** *38* (1), 36-46.

5. Russel, D. A.; Williams, G. G., History of Chemical Fertilizer Development. *Soil Science Society of America Journal* **1977,** *41* (2), 260-265.

6. Appl, M. D. In *The Haber-Bosch Process and the Development of Chemical Engineering*, 1982.

7. Knowles, W. S.; Sabacky, M. J., Catalytic asymmetric hydrogenation employing a soluble, optically active, rhodium complex. *Chemical Communications (London)* **1968,** (22), 1445-1446.

8. Miyashita, A.; Yasuda, A.; Takaya, H.; Toriumi, K.; Ito, T.; Souchi, T.; Noyori, R., Synthesis of 2,2'-bis(diphenylphosphino)-1,1'-binaphthyl (BINAP), an atropisomeric chiral bis(triaryl)phosphine, and its use in the rhodium(I)-catalyzed asymmetric hydrogenation of .alpha.-(acylamino)acrylic acids. *Journal of the American Chemical Society* **1980,** *102* (27), 7932-7934.

9. Katsuki, T.; Sharpless, K. B., The first practical method for asymmetric epoxidation. *Journal of the American Chemical Society* **1980,** *102* (18), 5974-5976.

10. Knowles, W. S., Asymmetric hydrogenation. *Accounts of Chemical Research* **1983,** *16* (3), 106-112.

11. Jean-Louis Hérisson, P.; Chauvin, Y., Catalyse de transformation des oléfines par les complexes du tungstène. II. Télomérisation des oléfines cycliques en présence d'oléfines acycliques. *Die Makromolekulare Chemie* **1971,** *141* (1), 161-176.

12. Schrock, R. R., Alkylcarbene complex of tantalum by intramolecular .alpha.-hydrogen abstraction. *Journal of the American Chemical Society* **1974,** *96* (21), 6796-6797.

13. Schwab, P.; France, M. B.; Ziller, J. W.; Grubbs, R. H., A Series of Well-Defined Metathesis Catalysts–Synthesis of [RuCl2(CHR′)(PR3)2] and Its Reactions. *Angewandte Chemie International Edition in English* **1995,** *34* (18), 2039-2041.

14. Heck, R. F., Acylation, methylation, and carboxyalkylation of olefins by Group VIII metal derivatives. *Journal of the American Chemical Society* **1968,** *90* (20), 5518-5526.

15. Negishi, E.-i.; Baba, S., Novel stereoselective alkenyl–aryl coupling via nickel-catalysed reaction of alkenylanes with aryl halides. *Journal of the Chemical Society, Chemical Communications* **1976,** (15), 596b-597b.

16. Miyaura, N.; Yamada, K.; Suzuki, A., A new stereospecific cross-coupling by the palladium-catalyzed reaction of 1-alkenylboranes with 1-alkenyl or 1-alkynyl halides. *Tetrahedron Letters* **1979,** *20* (36), 3437-3440.

17. List, B.; Lerner, R. A.; Barbas, C. F., Proline-Catalyzed Direct Asymmetric Aldol Reactions. *Journal of the American Chemical Society* **2000,** *122* (10), 2395-2396.

18. Ahrendt, K. A.; Borths, C. J.; MacMillan, D. W. C., New Strategies for Organic Catalysis: The First Highly Enantioselective Organocatalytic Diels−Alder Reaction. *Journal of the American Chemical Society* **2000,** *122* (17), 4243-4244.

19. Crabtree, R. H., Multifunctional ligands in transition metal catalysis. *New Journal of Chemistry* **2011,** *35* (1), 18-23.

20. Crabtree, R. H., Deactivation in Homogeneous Transition Metal Catalysis: Causes, Avoidance, and Cure. *Chemical Reviews* **2015,** *115* (1), 127-150.

21. Billow, B. S.; McDaniel, T. J.; Odom, A. L., Quantifying ligand effects in high-oxidation-state metal catalysis. *Nature Chemistry* **2017,** *9* (9), 837-842.

22. Scholl, M.; Ding, S.; Lee, C. W.; Grubbs, R. H., Synthesis and Activity of a New Generation of Ruthenium-Based Olefin Metathesis Catalysts Coordinated with 1,3-Dimesityl-4,5-dihydroimidazol-2-ylidene Ligands. *Organic Letters* **1999,** *1* (6), 953-956.

23. Love, J. A.; Morgan, J. P.; Trnka, T. M.; Grubbs, R. H., A Practical and Highly Active Ruthenium-Based Catalyst that Effects the Cross Metathesis of Acrylonitrile. *Angewandte Chemie International Edition* **2002,** *41* (21), 4035-4037.

24. Friend, C. M.; Xu, B., Heterogeneous Catalysis: A Central Science for a Sustainable Future. *Accounts of Chemical Research* **2017,** *50* (3), 517-521.

25. Liu, L.; Corma, A., Metal Catalysts for Heterogeneous Catalysis: From Single Atoms to Nanoclusters and Nanoparticles. *Chemical Reviews* **2018,** *118* (10), 4981-5079.

26. Hülsey, M. J.; Lim, C. W.; Yan, N., Promoting heterogeneous catalysis beyond catalyst design. *Chemical Science* **2020,** *11* (6), 1456-1468.

27. Makal, T. A.; Li, J.-R.; Lu, W.; Zhou, H.-C., Methane storage in advanced porous materials. *Chemical Society Reviews* **2012,** *41* (23), 7761-7779.

28. Perego, C.; Millini, R., Porous materials in catalysis: challenges for mesoporous materials. *Chemical Society Reviews* **2013,** *42* (9), 3956-3976.

29. Slater Anna, G.; Cooper Andrew, I., Function-led design of new porous materials. *Science* **2015,** *348* (6238), aaa8075.

30. Yang, X.-Y.; Chen, L.-H.; Li, Y.; Rooke, J. C.; Sanchez, C.; Su, B.-L., Hierarchically porous materials: synthesis strategies and structure design. *Chemical Society Reviews* **2017,** *46* (2), 481-558.

31. Huang, H.; Shi, H.; Das, P.; Qin, J.; Li, Y.; Wang, X.; Su, F.; Wen, P.; Li, S.; Lu, P.; Liu, F.; Li, Y.; Zhang, Y.; Wang, Y.; Wu, Z.-S.; Cheng, H.-M., The Chemistry and Promising Applications of Graphene and Porous Graphene Materials. *Advanced Functional Materials* **2020,** *30* (41), 1909035.

32. Rosi Nathaniel, L.; Eckert, J.; Eddaoudi, M.; Vodak David, T.; Kim, J.; O'Keeffe, M.; Yaghi Omar, M., Hydrogen Storage in Microporous Metal-Organic Frameworks. *Science* **2003,** *300* (5622), 1127-1129.

33. Li, H.; Eddaoudi, M.; O'Keeffe, M.; Yaghi, O. M., Design and synthesis of an exceptionally stable and highly porous metal-organic framework. *Nature* **1999,** *402* (6759), 276-279.

34. Tranchemontagne, D. J.; Mendoza-Cortés, J. L.; O'Keeffe, M.; Yaghi, O. M., Secondary building units, nets and bonding in the chemistry of metal–organic frameworks. *Chemical Society Reviews* **2009,** *38* (5), 1257-1283.

35. Férey, G., Hybrid porous solids: past, present, future. *Chemical Society Reviews* **2008,** *37* (1), 191-214.

36. Kitagawa, S.; Kitaura, R.; Noro, S.-i., Functional Porous Coordination Polymers. *Angewandte Chemie International Edition* **2004,** *43* (18), 2334-2375.

37. Zhou, H.-C.; Long, J. R.; Yaghi, O. M., Introduction to Metal–Organic Frameworks. *Chemical Reviews* **2012,** *112* (2), 673-674.

38. Mellot-Draznieks, C.; Dutour, J.; Férey, G., Hybrid Organic–Inorganic Frameworks: Routes for Computational Design and Structure Prediction. *Angewandte Chemie International Edition* **2004,** *43* (46), 6290-6296.

39. Zhou, H.-C. J.; Kitagawa, S., Metal–Organic Frameworks (MOFs). *Chemical Society Reviews* **2014,** *43* (16), 5415-5418.

40. Zhang, X.; Chen, Z.; Liu, X.; Hanna, S. L.; Wang, X.; Taheri-Ledari, R.; Maleki, A.; Li, P.; Farha, O. K., A historical overview of the activation and porosity of metal–organic frameworks. *Chemical Society Reviews* **2020,** *49* (20), 7406-7427.

41. Li, J.-R.; Sculley, J.; Zhou, H.-C., Metal–Organic Frameworks for Separations. *Chemical Reviews* **2012,** *112* (2), 869-932.

42. Sumida, K.; Rogow, D. L.; Mason, J. A.; McDonald, T. M.; Bloch, E. D.; Herm, Z. R.; Bae, T.-H.; Long, J. R., Carbon Dioxide Capture in Metal–Organic Frameworks. *Chemical Reviews* **2012,** *112* (2), 724-781.

43. Murray, L. J.; Dincă, M.; Long, J. R., Hydrogen storage in metal–organic frameworks. *Chemical Society Reviews* **2009,** *38* (5), 1294-1314.

44. Hu, Z.; Deibert, B. J.; Li, J., Luminescent metal–organic frameworks for chemical sensing and explosive detection. *Chemical Society Reviews* **2014,** *43* (16), 5815-5840.

45. Fujie, K.; Kitagawa, H., Ionic liquid transported into metal–organic frameworks. *Coordination Chemistry Reviews* **2016,** *307*, 382-390.

46. Giménez-Marqués, M.; Hidalgo, T.; Serre, C.; Horcajada, P., Nanostructured metal–organic frameworks and their bio-related applications. *Coordination Chemistry Reviews* **2016,** *307*, 342-360.

47. Della Rocca, J.; Liu, D.; Lin, W., Nanoscale Metal–Organic Frameworks for Biomedical Imaging and Drug Delivery. *Accounts of Chemical Research* **2011,** *44* (10), 957-968.

48. Liu, J.; Chen, L.; Cui, H.; Zhang, J.; Zhang, L.; Su, C.-Y., Applications of metal–organic frameworks in heterogeneous supramolecular catalysis. *Chemical Society Reviews* **2014,** *43* (16), 6011-6061.

49. Dhakshinamoorthy, A.; Asiri, A. M.; Garcia, H., Metal–organic frameworks catalyzed C–C and C–heteroatom coupling reactions. *Chemical Society Reviews* **2015,** *44* (7), 1922-1947.

50. Zhang, T.; Lin, W., Metal–organic frameworks for artificial photosynthesis and photocatalysis. *Chemical Society Reviews* **2014,** *43* (16), 5982-5993.

51. Chughtai, A. H.; Ahmad, N.; Younus, H. A.; Laypkov, A.; Verpoort, F., Metal–organic frameworks: versatile heterogeneous catalysts for efficient catalytic organic transformations. *Chemical Society Reviews* **2015,** *44* (19), 6804-6849.

52. Ma, L.; Abney, C.; Lin, W., Enantioselective catalysis with homochiral metal–organic frameworks. *Chemical Society Reviews* **2009,** *38* (5), 1248-1256.

53. Ji, P.; Drake, T.; Murakami, A.; Oliveres, P.; Skone, J. H.; Lin, W., Tuning Lewis Acidity of Metal–Organic Frameworks via Perfluorination of Bridging Ligands: Spectroscopic, Theoretical, and Catalytic Studies. *Journal of the American Chemical Society* **2018,** *140* (33), 10553-10561.

54. Ji, P.; Feng, X.; Oliveres, P.; Li, Z.; Murakami, A.; Wang, C.; Lin, W., Strongly Lewis Acidic Metal–Organic Frameworks for Continuous Flow Catalysis. *Journal of the American Chemical Society* **2019,** *141* (37), 14878-14888.

55. Cui, Y.; Yue, Y.; Qian, G.; Chen, B., Luminescent Functional Metal–Organic Frameworks. *Chemical Reviews* **2012,** *112* (2), 1126-1162.

56. Mínguez Espallargas, G.; Coronado, E., Magnetic functionalities in MOFs: from the framework to the pore. *Chemical Society Reviews* **2018,** *47* (2), 533-557.

57. Fujita, M.; Kwon, Y. J.; Washizu, S.; Ogura, K., Preparation, Clathration Ability, and Catalysis of a Two-Dimensional Square Network Material Composed of Cadmium(II) and 4,4'-Bipyridine. *Journal of the American Chemical Society* **1994,** *116* (3), 1151-1152.

58. Thomas, J. M.; Raja, R.; Lewis, D. W., Single-Site Heterogeneous Catalysts. *Angewandte Chemie International Edition* **2005,** *44* (40), 6456-6482.

59. Cui, X.; Li, W.; Ryabchuk, P.; Junge, K.; Beller, M., Bridging homogeneous and heterogeneous catalysis by heterogeneous single-metal-site catalysts. *Nature Catalysis* **2018,** *1* (6), 385-397.

60. Furukawa, H.; Cordova, K. E.; O'Keeffe, M.; Yaghi, O. M., The Chemistry and Applications of Metal-Organic Frameworks. *Science* **2013,** *341* (6149), 1230444.

61. Yuan, S.; Feng, L.; Wang, K.; Pang, J.; Bosch, M.; Lollar, C.; Sun, Y.; Qin, J.; Yang, X.; Zhang, P.; Wang, Q.; Zou, L.; Zhang, Y.; Zhang, L.; Fang, Y.; Li, J.; Zhou, H.-C., Stable Metal–Organic Frameworks: Design, Synthesis, and Applications. *Advanced Materials* **2018,** *30* (37), 1704303.

62. Wasson, M. C.; Buru, C. T.; Chen, Z.; Islamoglu, T.; Farha, O. K., Metal–organic frameworks: A tunable platform to access single-site heterogeneous catalysts. *Applied Catalysis A: General* **2019,** *586*, 117214.

63. Wei, Y.-S.; Zhang, M.; Zou, R.; Xu, Q., Metal–Organic Framework-Based Catalysts with Single Metal Sites. *Chemical Reviews* **2020**.

64. Yang, D.; Gates, B. C., Catalysis by Metal Organic Frameworks: Perspective and Suggestions for Future Research. *ACS Catalysis* **2019,** *9* (3), 1779-1798.

65. Rogge, S. M. J.; Bavykina, A.; Hajek, J.; Garcia, H.; Olivos-Suarez, A. I.; Sepúlveda-Escribano, A.; Vimont, A.; Clet, G.; Bazin, P.; Kapteijn, F.; Daturi, M.; Ramos-Fernandez, E. V.; Llabrés i Xamena, F. X.; Van Speybroeck, V.; Gascon, J., Metal–organic and covalent organic frameworks as single-site catalysts. *Chemical Society Reviews* **2017,** *46* (11), 3134-3184.

66. Drake, T.; Ji, P.; Lin, W., Site Isolation in Metal–Organic Frameworks Enables Novel Transition Metal Catalysis. *Accounts of Chemical Research* **2018,** *51* (9), 2129-2138.

67. Dhakshinamoorthy, A.; Asiri, A. M.; García, H., Metal–Organic Frameworks as Multifunctional Solid Catalysts. *Trends in Chemistry* **2020,** *2* (5), 454-466.

68. Zhao, W.; Li, G.; Tang, Z., Metal-organic frameworks as emerging platform for supporting isolated single-site catalysts. *Nano Today* **2019,** *27*, 178-197.

69. Moulijn, J. A.; van Diepen, A. E.; Kapteijn, F., Catalyst deactivation: is it predictable?: What to do? *Applied Catalysis A: General* **2001,** *212* (1), 3-16.

70. Ogoshi, S.; Hoshimoto, Y.; Ohashi, M., Nickel-catalyzed Tishchenko reaction via hetero-nickelacycles by oxidative cyclization of aldehydes with nickel(0) complex. *Chemical Communications* **2010,** *46* (19), 3354-3356.

71. Tondreau, A. M.; Atienza, C. C. H.; Weller, K. J.; Nye, S. A.; Lewis, K. M.; Delis, J. G. P.; Chirik, P. J., Iron Catalysts for Selective Anti-Markovnikov Alkene Hydrosilylation Using Tertiary Silanes. *Science* **2012,** *335* (6068), 567-570.

72. Hennessy, E. T.; Betley, T. A., Complex N-Heterocycle Synthesis via Iron-Catalyzed, Direct C–H Bond Amination. *Science* **2013,** *340* (6132), 591-595.

73. Matoba, Y.; Kumagai, T.; Yamamoto, A.; Yoshitsu, H.; Sugiyama, M., Crystallographic evidence that the dinuclear copper center of tyrosinase is flexible during catalysis. *Journal of Biological Chemistry* **2006,** *281* (13), 8981-8990.

74. Ramsden, C. A.; Riley, P. A., Tyrosinase: The four oxidation states of the active site and their relevance to enzymatic activation, oxidation and inactivation. *Bioorganic & Medicinal Chemistry* **2014,** *22* (8), 2388-2395.

75. Jiang, J.; Yaghi, O. M., Brønsted Acidity in Metal–Organic Frameworks. *Chemical Reviews* **2015,** *115* (14), 6966-6997.

76. Zhu, L.; Liu, X.-Q.; Jiang, H.-L.; Sun, L.-B., Metal–Organic Frameworks for Heterogeneous Basic Catalysis. *Chemical Reviews* **2017,** *117* (12), 8129-8176.

77. Deng, H.; Doonan, C. J.; Furukawa, H.; Ferreira, R. B.; Towne, J.; Knobler, C. B.; Wang, B.; Yaghi, O. M., Multiple Functional Groups of Varying Ratios in Metal-Organic Frameworks. *Science* **2010,** *327* (5967), 846.

78. Cohen, S. M., The Postsynthetic Renaissance in Porous Solids. *Journal of the American Chemical Society* **2017,** *139* (8), 2855-2863.

79. Huang, Y.-B.; Liang, J.; Wang, X.-S.; Cao, R., Multifunctional metal–organic framework catalysts: synergistic catalysis and tandem reactions. *Chemical Society Reviews* **2017,** *46* (1), 126-157.

80. Anastas, P. T.; Warner, J. C., Principles of green chemistry. *Green chemistry: Theory and practice* **1998,** *29*.

Chapter 2. Aluminum Hydroxide SBUs Support Cobalt/Iron Catalysts for Broad-Scope Organic Transformations

2.1 Introduction

As one of the most abundant, widely used, and thoroughly studied metal oxide supports, alumina (Al_2O_3), especially γ-Al_2O_3, has drawn great interest in industrial research, due to its high surface area (80-250 m^2/g), acid/base chemistry, thermal and chemical stability, and abundance of surface hydroxy (OH) groups.[1-3] Previous studies have demonstrated the ability of γ-Al_2O_3 in supporting either metallic nanoparticles for catalytic methanation[4-5] and dehydrogenation reactions[6] or organometallic species for olefin polymerization,[7] C-H activation,[8] and metathesis reactions.[9-10] However, unlike the thermodynamically stable phase α-Al_2O_3, which has a compact and crystalline structure, γ-Al_2O_3 features different aluminum (Al) coordination numbers (Al_{IV} and Al_{VI}) and varied surface OH coordination modes (terminal-, μ_2-, and μ_3-) to the Al centers (**Figure 2-1a**).[3, 11] This intrinsic heterogeneity of γ-Al_2O_3 surface presents a challenge for the uniform modification of catalytically active species, the characterization of these active species, and the elucidation of reaction mechanisms.[12] Furthermore, non-uniform OH groups and defect surface Al sites cause undesired reforming and hydration/dehydration processes at elevated temperatures,[2] leading to insufficient binding strength between active species and oxide support and consequently decreased catalytic activity. Thus, new Al-based materials with uniform OH groups are highly desired for mimicking γ-Al_2O_3 in supporting single-site catalysts and providing better understanding of γ-Al_2O_3-supported commercial catalytic systems.

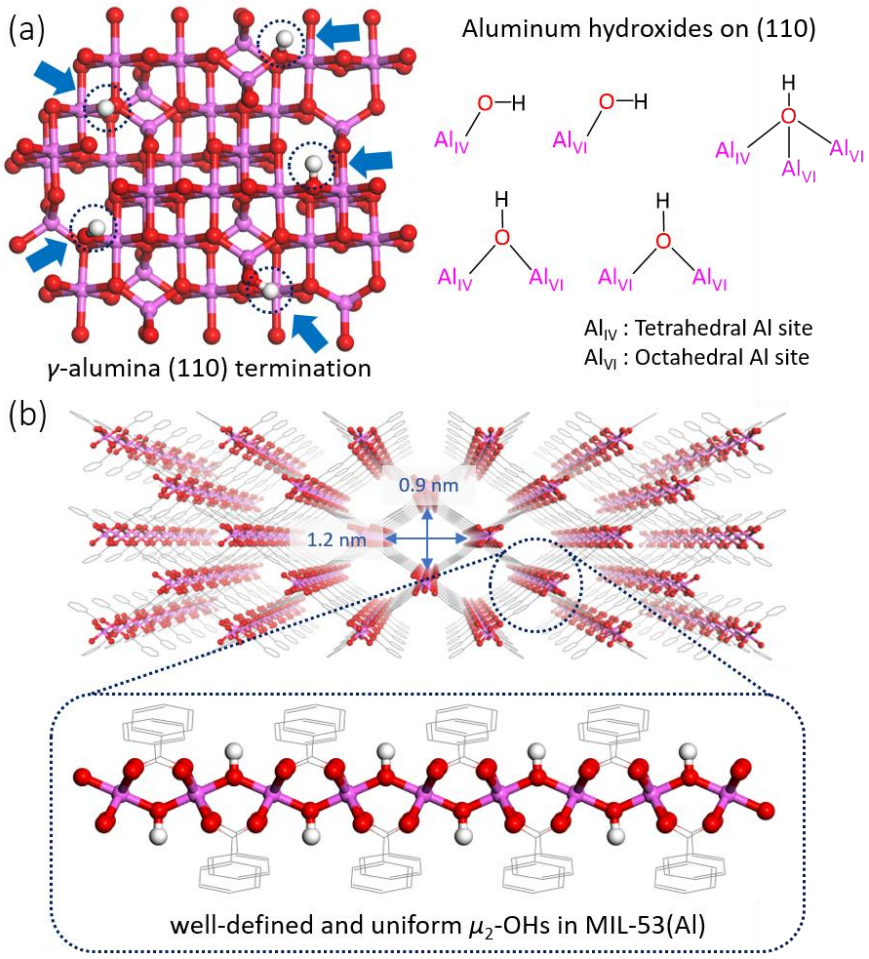

Figure 2-1. (a) The presence of five main types of OH groups on the (110) surface of γ-Al_2O_3. (b) The structure of MIL-53(Al) features large one-dimensional channels (1.2 × 0.9 nm^2) and a high density of uniform μ_2-OH groups. Copyright 2019 American Chemical Society.

In this chapter, we report the use of MIL-53(Al), which is composed of one-dimensional Al-hydroxo chains linked together by 1,4-benzenedicarboxylate (BDC) bridging ligands,[13] as a mimic for the alumina surface to anchor Co and Fe complexes for a broad range of organic transformations (**Scheme 2-1**). The isolated μ_2-OH groups were first deprotonated to give μ_2-O^- and then metalated with Co and Fe complexes to afford MIL-53(Al)-supported precatalysts. Following activation with a hydride source, the resultant MIL-53(Al)-CoH effectively catalyzed hydroboration of alkynes and nitriles as well as hydrosilylation of esters. MIL-53(Al)-FeCl efficiently catalyzed oxidative C-H amination and Wacker-type alkene oxidation reactions. MIL-

53(Al) possesses several advantages over traditional alumina supports including a higher Al to OH ratio (1:1) and uniform and structurally defined μ_2-OH groups (**Figure 2-1b**), allowing for a greater density of functionalization with metal complexes and easier investigation of catalytically active sites and reaction mechanisms. The perforated structure of uniform 1-D channels in MIL-53(Al) allows for facile substrate diffusion to access the catalytic sites to effect reduction and oxidation reactions with diverse mechanisms. Moreover, compared to the well-studied Zr_3-OH sites, Al_2-OH moieties are expected to be more electron donating after deprotonation. MIL-53(Al)-supported Earth-abundant metal catalysts thus represent a versatile and cost-effective alternative to traditional metal oxide heterogeneous catalysts.

Scheme 2-1. Aluminum hydroxide SBUs support cobalt/iron catalysts for broad-scope organic transformations. Copyright 2019 American Chemical Society.

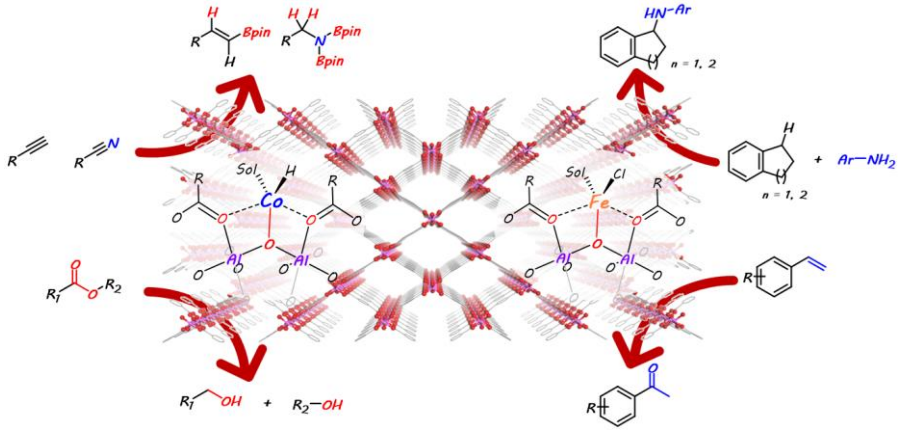

2.2 Results and Discussion

2.2.1 Synthesis and characterization of MIL-53(Al)-CoCl and MIL-53(Al)-FeCl

MIL-53(Al) of the formula Al(OH)(BDC) was synthesized in 85% yield through a solvothermal reaction between $AlCl_3 \cdot 6H_2O$ and H_2BDC in *N*,*N*-dimethylformamide (DMF) in 18 h. MIL-53(Al) was first treated with $LiCH_2Si(CH_3)_3$ to generate Al(OLi)(BDC) via deprotonation, and then metalated with 1 equiv. of $CoCl_2$ or $FeCl_2$. (**Figure 2-2**) After removing unreacted metal

salts via extensive washing with tetrahydrofuran (THF), MIL-53(Al)-CoCl and MIL-53(Al)-FeCl were obtained as light blue and light brown solids, respectively. Powder X-ray diffraction (PXRD) patterns of the metalated MOFs remained unchanged from that of as-synthesized MIL-53(Al), indicating the maintenance of crystallinity after metalation with Co and Fe (**Figure 2-2b**). The Co and Fe contents in the metalated MOFs were determined to be 0.15 Co per Al and 0.23 Fe per Al, respectively, by inductively coupled plasma-mass spectrometry (ICP-MS) analysis of digested samples. Nitrogen sorption isotherms of MIL-53(Al)-CoCl and MIL-53(Al)-FeCl indicated highly porous structures with Brunauer-Emmett-Teller (BET) surface areas 2066 and 2001 m^2/g, respectively (**Figure 2-2d**). Pore size distribution analyses by density functional theory (DFT) showed a pore size of 8 Å for both metalated MOFs, matching well with that expected from the crystal structure (**Figure 2-2e**).

We performed DFT calculations using the B3LYP level of theory to optimize the coordination environments of Co and Fe in the metalated MOFs. The Co coordination converged at a distorted square pyramidal geometry with one anionic bridging oxo (from the deprotonation of the μ_2-OH group), two carboxylate oxygen, one chloride, and one THF molecule to afford the [(μ_2-O^-)(carboxylate-O)$_2$CoCl(THF)] species. The Co-(μ_2-O^-) distance is 1.91 Å, while the Co-(carboxylate-O) distances are longer at 2.21 Å and 2.58 Å, respectively. The Co-Cl distance is 2.33 Å and the Co-(THF-O) distance is 2.06 Å. The calculated model fitted well to the Co K-edge absorption of the extended X-ray fine structure spectroscopy (EXAFS) data of MIL-53(Al)-CoCl with a R factor of 0.0045 (**Figure 2-2f**). EXAFS fitting gave a Co-(μ_2-O^-) distance of 1.87 Å, and Co-(carboxylate-O) distances of 1.96 Å and 2.32 Å, a Co-Cl distance of 2.28 Å, and a Co-(THF-O) distance of 2.02 Å. DFT calculations indicated a similar distorted square pyrimidal geometry for Fe centers in MIL-53(Al)-FeCl. The calculated Fe-(μ_2-O^-) distance of 1.91 Å, Fe-(carboxylate-

O) distances of 2.32 and 2.41 Å, Fe-Cl distance of 2.31 Å, and Fe-(THF-O) distance of 2.14 Å, match well with those determined by EXAFS fitting (1.91, 2.39, 2.48, 2.13, and 2.11 Å, respectively). The R-factor of the EXAFS fitting is 0.015 (**Figure 2-2g**).

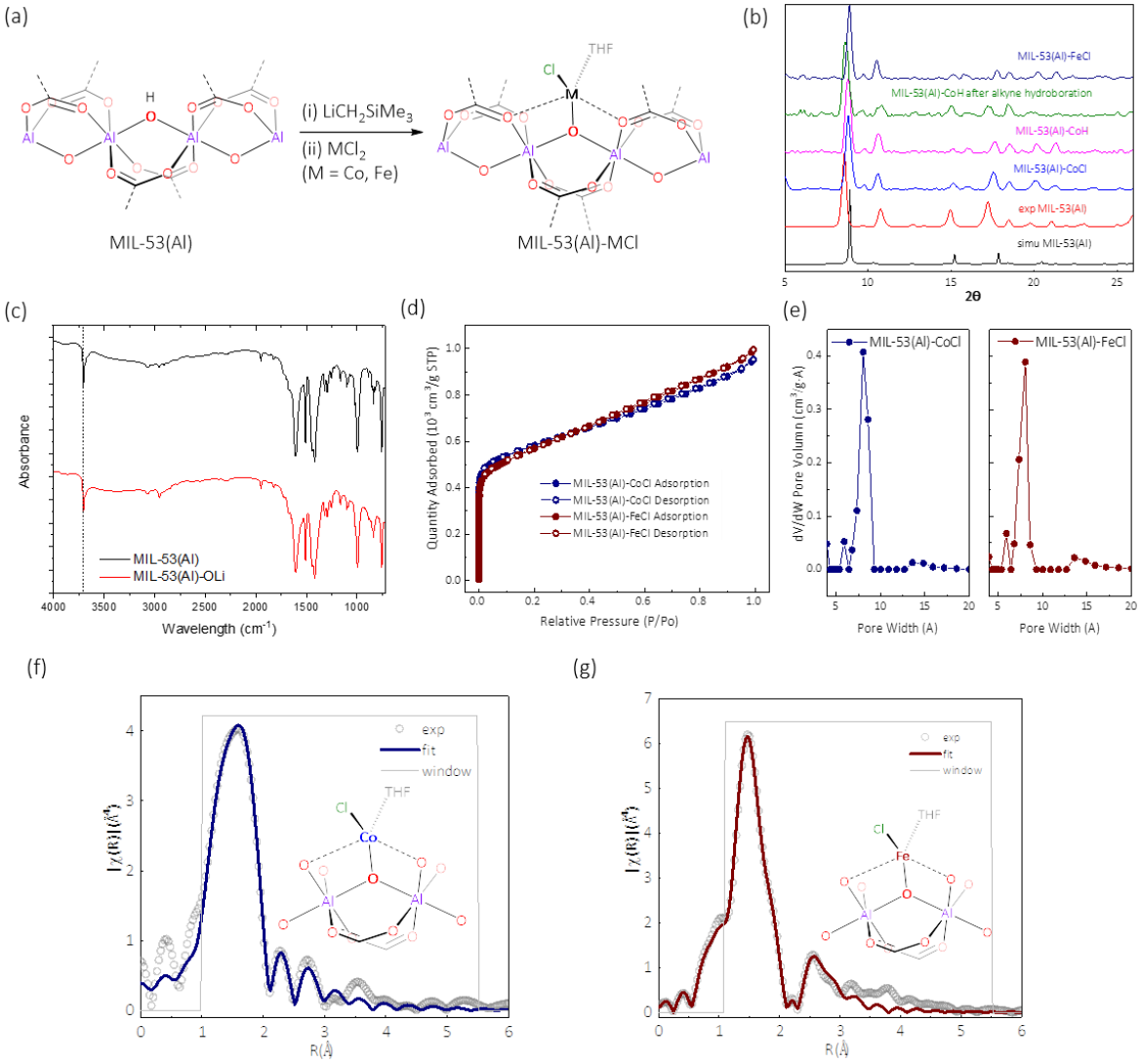

Figure 2-2. Synthesis and structural characterization of MIL-53(Al)-Co and MIL-53(Al)-Fe. (a) The preparation of MIL-53(Al)-CoCl from MIL-53(Al) via sequential deprotonation and metalation. (b) PXRD patterns of as-synthesized MIL-53(Al) (red), MIL-53(Al)-CoCl (blue), MIL-53(Al)-FeCl (navy), MIL-53(Al)-CoH (magenta) and after catalytic alkyne hydroboration. (c) DRIFTS spectra of MIL-53(Al) and MIL-53(Al)-OLi (after deprotonation). (d) N_2 sorption isotherms of MIL-53(Al)-CoCl (navy) and MIL-53(Al)-FeCl (wine). (e) Pore size distributions of MIL-53(Al)-CoCl (navy) and MIL-53(Al)-FeCl (wine). (f) EXAFS spectra (gray circles) and fits (navy solid line) in R-space at the Co K-edge adsorption of MIL-53(Al)-CoCl. (g) EXAFS spectra (gray circles) and fits (navy solid line) in R-space at the Fe K-edge adsorption of MIL-53(Al)-FeCl. Copyright 2019 American Chemical Society.

2.2.2 Structure and electronic properties of MIL-53(Al)-CoH

Upon treatment with $NaBEt_3H$, the color of MIL-53(Al)-CoCl changed from light blue to black, suggesting the formation of MIL-53(Al)-CoH via chloride/hydride exchange. The MOF crystallinity was maintained after chloride/hydride exchange based on the similarity of PXRD patterns. X-ray photoelectron spectroscopy (XPS) was used to determine the oxidation states of Al and Co centers in MIL-53(Al)-CoH. MIL-53(Al)-CoH displayed strong $2p_{3/2}$ and $2p_{1/2}$ peaks at 778.3 and 794.3 eV along with strong $2p_{3/2}$ and $2p_{1/2}$ shake-up peaks at 783.0 and 800.2 eV for Co centers, indicating typical Co^{II} species (**Figure 2-3d**). MIL-53(Al)-CoH showed one set of strong $2p_{3/2}$ and $2p_{1/2}$ peaks at 71.5 and 71.0 eV for Al centers, which are characteristic of Al^{III} species (**Figure 2-3e**). These results indicate that neither Al^{III} or Co^{II} species were reduced by $NaBEt_3H$ during the chloride/hydride exchange process.

X-ray absorption near-edge spectroscopy (XANES) analysis supported the Co oxidation state assignment by XPS. The pre-K edge features of MIL-53(Al)-CoCl and MIL-53(Al)-CoH are identical to that of $CoCl_2$, indicating the Co^{II} centers before and after chloride/hydride exchange (**Figure 2-3c**). The presence of only Co^{II} centers in MIL-53(Al)-CoH ruled out the possibility of forming Co nanoparticle during the $NaBEt_3H$ treatment. Treatment of MIL-53(Al)-CoH with excess amount of trifluoroacetic acid (TFA) generated 1.10±0.03 equiv. of H_2 w.r.t. Co, indicating the presence of Co-H species in the MOF. EXAFS fitting was also performed at the Co K-edge for MIL-53(Al)-CoH. The EXAFS spectrum was well fitted with a Co coordination environment calculated by DFT, indicating the formation of (μ_2-O)(O-carboxylate)$_2$CoH(THF) species in MIL-53(Al)-CoH (**Figure 2-3b**).

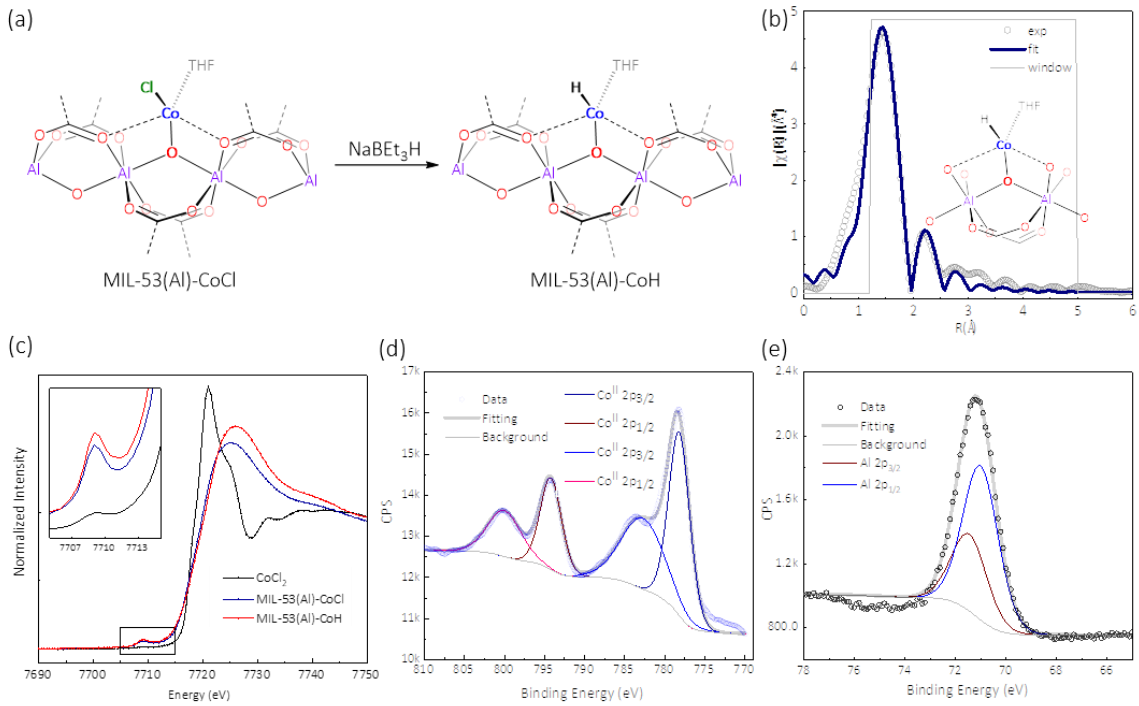

Figure 2-3. Synthesis and characterization of MIL-53(Al)-CoH. (a) Activation of MIL-53(Al)-CoCl to form MIL-53(Al)-CoH with $NaBEt_3H$ in THF. (b) EXAFS fitting of MIL-53(Al)-CoH shows the Co coordination environment as (μ_2-O)(O-carboxylate)$_2$CoH(THF). (c) XANES pre-edge features of MIL-53(Al)-CoCl (navy) and MIL-53(Al)-CoH (red) as compared to that of $CoCl_2$ (black), indicating the Co^{II} oxidation state before and after $NaBEt_3H$ treatment. (d) Co 2p XPS spectra of MIL-53(Al)-CoH (blue circle) and the fitting result (gray solid line) indicate the Co^{II} oxidation state after $NaBEt_3H$ treatment. (e) Al 2p XPS spectra of MIL-53(Al)-CoH (black circle) and fitting result (gray solid line) indicate the Al^{III} oxidation state after $NaBEt_3H$ treatment. Copyright 2019 American Chemical Society.

2.2.3 MIL-53(Al)-CoH catalyzed hydroboration of alkynes

As important starting materials for the synthesis of a wide range of organic compounds via cross-coupling reactions, transition metal catalyzed hydroboration of alkynes provides the simplest and most atom-efficient synthetic route to alkenylboronate esters.[14-15] MIL-53(Al)-CoH was found to be a highly effective catalyst for hydroboration of alkynes. Screening of reaction conditions revealed that, at 0.2 mol% of catalyst loading, MIL-53(Al)-CoH catalyzed the solvent-free reaction of phenylacetylene with 1.2 equiv pinacolborane (HBpin) at 90 °C for 22 h to give the *E*-alkenylboronate in 85% yield, with a turnover number (TON) of 425. No conversion was found in

the control experiment without adding the MOF. Addition of 2 equiv. HBpin did not lead to further hydroboration of the alkenylboronate ester. A TON of 1428 was achieved when the reaction was carried out with 0.035 mol % MIL-53(Al)-CoH at 90 °C. PXRD pattern of MIL-53(Al)-CoH recovered from the hydroboration reaction was similar to that of as-synthesized MIL-53(Al)-CoH (**Figure 2-2b**), indicating the stability of MOF framework during hydroboration reaction.

Table 2-1. MIL-53(Al)-CoH catalyzed hydroboration of alkynes.[a]

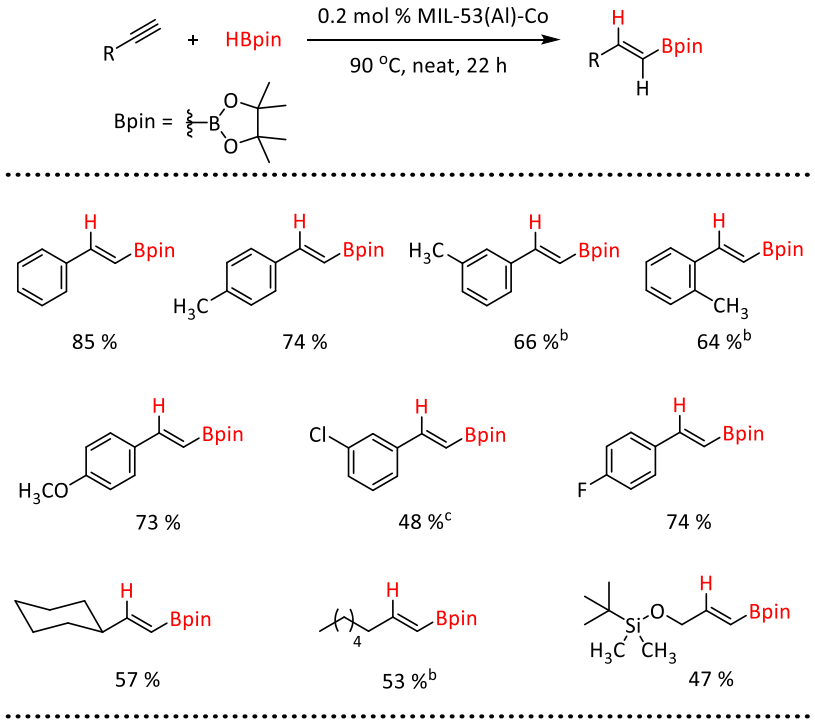

[a]Standard condition: 1.00 mmol alkyne substrate, 1.20 mmol HBpin, 0.2 mol% Co, 90 °C, 22 h; Yield was determined by ^{1}H NMR using mesitylene as internal standard. [b]0.4 mol% Co. [c]1.0 mol% Co.

MIL-53(Al)-CoH-catalyzed hydroboration had a broad substrate scope and exhibited good functional group tolerance (**Table 2-1**). Both electron donating group (*i.e.*, CH_3, OCH_3) and electron withdrawing group *(i.e.*, F) worked well under standard reaction conditions. The methyl group on the *para* position did not impact the reactivity, but the substrates with the methyl group in *ortho* and *meta* positions required twice the catalyst loading. Halogen atoms did not interfere

with the hydroboration reaction. Under un-optimized conditions, MIL-53(Al)-CoH catalyzed hydroboration of aliphatic alkynes to give exclusively *E*-alkenylboronate esters in 47-57% of yields.

As a solid catalyst, MIL-53(Al)-CoH was readily recycled and re-used for hydroboration of phenylacetylene. At a 1.0 mol% Co loading, MIL-53(Al)-Co catalyzed five consecutive runs of phenylacetylene hydroboration without a significant drop in yields (Yield in 1^{st} to 5^{th} run: 81%, 77%, 82%, 73%, 75%). The leaching of Co and Al into the supernatant after the hydroboration was determined to be 0.3% and 0.8%, respectively, by ICP-MS analysis. Moreover, control experiments using Co nanoparticles with the same amount of Co gave only 7% of yields of the products, further confirming single site supported Co-H complex as the true catalytic species.

We also conducted deuterium labeling experiments to gain further insight into MIL-53(Al)-Co catalyzed hydroboration of alkynes. After hydroboration of phenylacetylene-d_1 with HBpin, ^{1}H NMR analysis of the product (53% yield) revealed exclusive deuterium labeling at the 1-position of trans-2-phenylvinylboronic acid pinacol ester, indicating no H/D exchange between the alkyne and Co centers.[16] Based on the deuterium labeling result and the Co^{II} oxidation state in 53(Al)-CoH, we propose a reaction pathway involving σ-bond metathesis as a key step for the hydroboration of terminal alkynes. The coordination of an alkyne to the Co center of the active catalyst MIL-53(Al)-CoH is followed by migratory insertion of the hydride to the triple bond to form the Co-alkenyl intermediate, which undergoes σ-bond metathesis with HBpin to give the alkenylboronate ester product and regenerate the Co-H catalyst (**Figure 2-4b**).

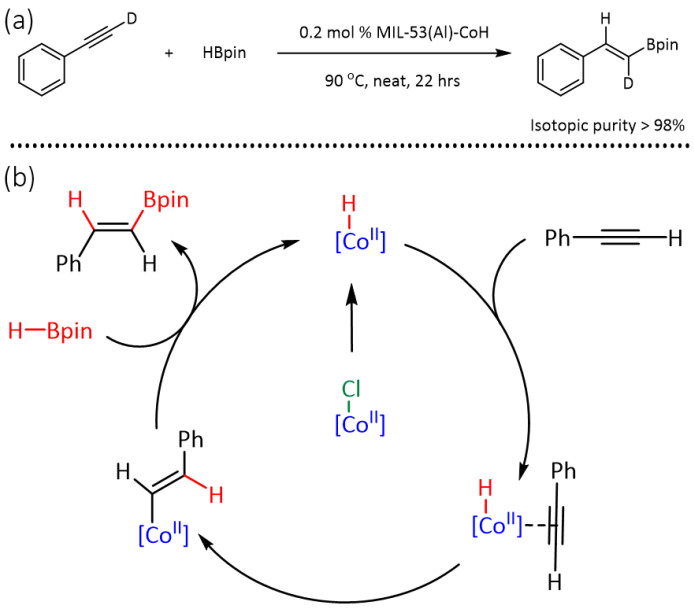

Figure 2-4. (a) Deuterium labeling experiment and (b) proposed mechanism of MIL-53(Al)-CoH catalyzed hydroboration of alkynes.

2.2.4 MIL-53(Al)-CoH catalyzed hydroboration of nitriles

Encouraged by the success in hydroboration of alkynes, we tested MIL-53(Al)-CoH in hydroboration of nitriles. Reduction of nitriles to amines with high activity and selectivity is important for the production of many dyes, agrochemicals, and pharmaceutical compounds.[17] Hydroboration of nitriles also provides a route to protected amines for further functionalization.[18-19] Treatment of benzonitrile with 2.1 equiv. of HBpin in the presence of 1.0 mol% MIL-53(Al)-CoH at 90 °C for 2 days afforded the fully hydroborated product in 73% yield. No semi-hydroborated or other by-products were observed. Under this un-optimized condition, a wide range of nitriles were hydroborated with HBpin to afford fully hydroborated products in 58% to 91% yields (**Table 2-2**). The hydroboration reaction works for aromatic nitriles containing electron-withdrawing groups, electron-donating groups, and halogens as well as aliphatic nitriles.

Table 2-2. MIL-53(Al)-CoH catalyzed hydroboration of nitriles.[a]

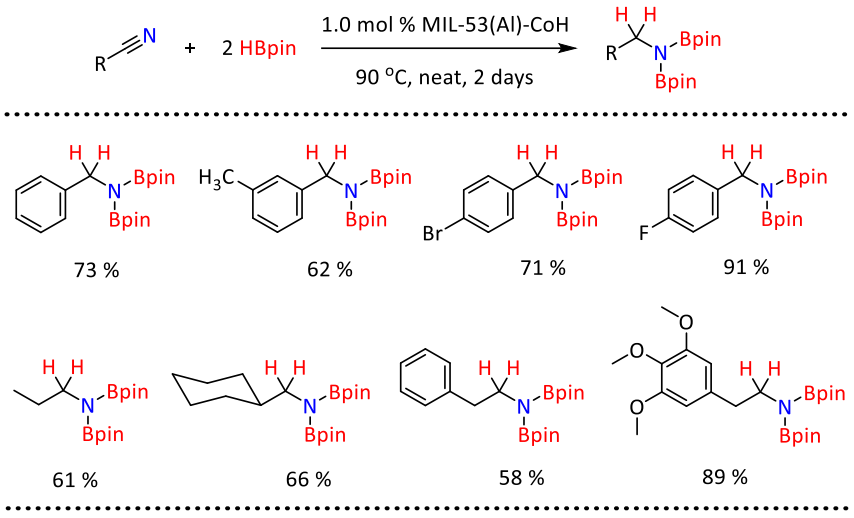

[a]Standard condition: 0.60 mmol nitrile, 1.26 mmol HBpin, 1.0 mol% Co, 90 °C, 2 days; Yield was determined by ^{1}H NMR using mesitylene as internal standard.

2.2.5 MIL-53(Al)-CoH catalyzed hydrosilylation of esters

Beside hydroboration reactions, hydrosilylation provides another reductive pathway to introduce silyl groups into unsaturated bonds for further functionalization.[20] In contrast to extensively studied hydrosilylation of ketones and aldehydes,[21-22] hydrosilylation of less reactive substrates such as amides and esters remains a challenge, especially for EAM catalysts.[23-24] We investigated hydrosilylation of esters using MIL-53(Al)-CoH as catalyst. Impressively, at 0.1 mol % loading of the MOF catalyst, simply stirring an equimolar mixture of methyl benzoate and phenylsilane ($PhSiH_3$) at room temperature over 18 h afforded the hydrosilylation products with complete conversion. ^{1}H NMR spectroscopy identified the hydrosilylation products as a mixture of $PhSi(OCH_3)_2(OCH_2C_6H_5)$ (42 %), $PhSi(OCH_3)(OCH_2C_6H_5)_2$ (45 %), and $PhSi(OCH_2C_6H_5)_3$ (13 %) in addition to the by-product $PhSi(OCH_3)_3$. Treatment of this mixture with 2 M NaOH in 1:1 MeOH/H_2O (*v*/*v*) afforded benzyl alcohol in 92% isolated yield. No conversion was observed in the background reaction without the MOF catalyst.

MIL-53(Al)-CoH catalyzed hydrosilylation of esters exhibited a broad substrate scope (**Table 2-3**). Substituted benzoates, dibenzoates, and acetate esters were readily hydrosilylated in the presence of 0.1 mol% MIL-53(Al)-CoH. For less reactive aliphatic esters, such as methyl octanoate and methyl phenylacetate, quantitative hydrosilylation was achieved in the presence of 1.0 mol% MIL-53(Al)-CoH. Due to the mild reaction conditions, MIL-53(Al)-CoH catalyzed hydrosilylation showed good functional group tolerance to esters containing reducible groups such as alkynyl and bromo groups. More importantly, MIL-53(Al)-CoH catalyzed hydrosilylation of esters containing a pyridyl or thiophenyl moiety, which usually poisons catalysts due to strong coordination to the metal centers. Upon basic workup, corresponding alcohols were obtained in 71% and 93% yield.

Table 2-3. MIL-53(Al)-CoH catalyzed hydrosilylation of esters.[a]

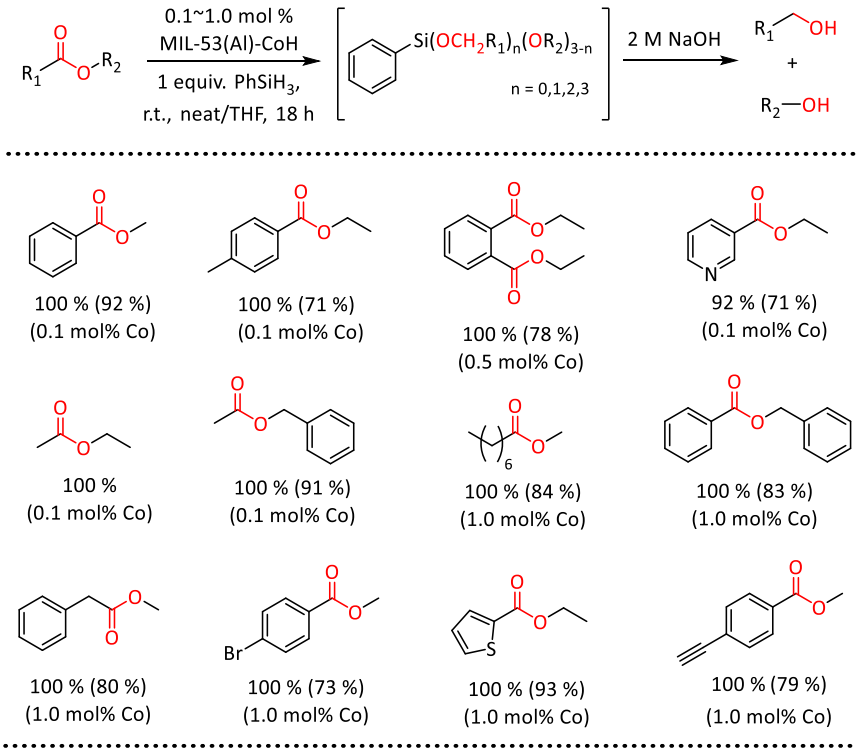

[a]Standard condition: 1.0 mmol ester, 1.0 mmol $PhSiH_3$, 0.1-1.0 mol% Co, r.t., 18 h; For solid substrates, 0.3 mL THF was added as solvent; Hydrosilylation yields are based on ^1H NMR integration with isolated yields of alcohols in parenthesis.

2.2.6 MIL-53(Al)-FeCl catalyzed C-H amination

To further explore the potential of MIL-53(Al) hydroxyl groups as a support for base metal catalysts, we introduced Fe centers into this MOF. MIL-53(Al)-FeCl was similarly prepared as a pale-yellow solid through deprotonation of μ_2-OH sites in MIL-53(Al) with $LiCH_2SiMe_3$ followed by metalation with $FeCl_2$. We hypothesized that the Fe^{II} centers can undergo the Fe^{II}/Fe^{III} redox process to enable the application of MIL-53(Al)-FeCl in catalyzing challenging reactions through single electron transfer (SET) processes.

Catalytic formation of C-N bonds through Csp^3-H amination using Earth-abundant and environmental-friendly first-row transition metals (*e.g.*, Fe, Cu) has attracted significant research interest.[25-26] We tested the catalytic performance of MIL-53(Al)-FeCl in Csp^3-H amination using aniline as the nitrogen source. At 5.0 mol% loading of MIL-53(Al)-Fe, heating a mixture of aniline and indane in the presence of 1.5 equiv. of $(^tBuO)_2$ at 105 °C gave the desired amination product, N-phenyl-2,3-dihydro-1H-inden-1-amine, in 63% yield. The protocol converted tetralin to the Csp^3-H amination product in 70% yield. Indane and tetralin were also aminated with different aniline derivatives containing 2,4,6-substitutents and 4-substituent to afford desired products in moderate to good yields (15-70% yields for 5 mol% catalyst loading, **Table 2-4**). Lower yields of desired Csp^3-H amination products were obtained for bulky anilines such as 2,4,6-trimethylaniline and 2,4,6-trichloroaniline, likely because of steric hindrance around the Fe centers. Higher yields of amination products were generally obtained for *para*-substituted anilines with electron-withdrawing groups (Cl and Br) in comparison with those with electron-donating groups (CH_3).

Table 2-4. MIL-53(Al)-FeCl catalyzed C-H amination.[a]

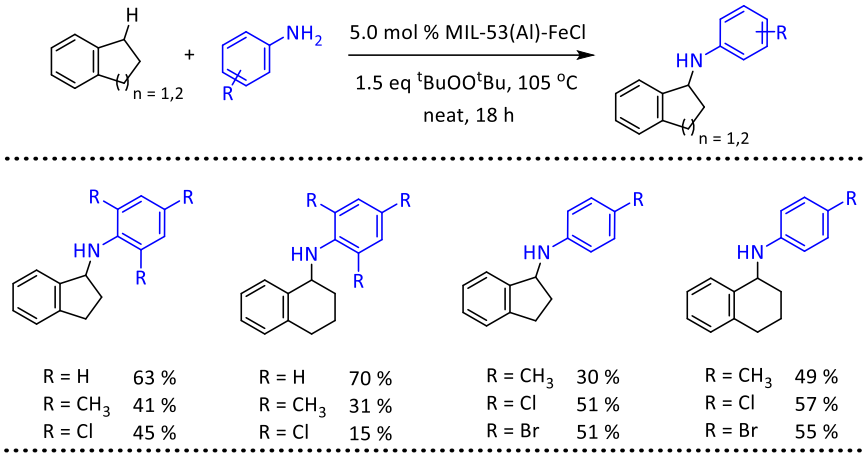

[a]Standard condition: 0.32 mmol anilines substrate, 6.4 mmol indane or tetralin, 5 mol% Fe, 105 °C, 18 h; Yield was determined by ^{1}H NMR or GC-MS analysis using mesitylene as internal standard.

MIL-53(Al)-FeCl catalyzed Csp^3-H amination was proposed to proceed through radical-mediated C-H activation followed by C-N cross coupling between the alkyl radical and Fe^{III}-anilide, analogous to the mechanism proposed in the literature for Cu^I-catalyzed C-H amination reactions.[27-28] XANES analysis was carried out to identify the oxidation state of Fe centers in the activated MIL-53(Al)-FeCl catalyst (**Figure 2-5a**). As-prepared MIL-53(Al)-FeCl exhibited similar pre-edge features to $FeCl_2$. After treatment with $(^tBuO)_2$, the MOF showed similar pre-edge features to $FeCl_3$, indicating the formation of Fe^{III}–O^{t}Bu species via SET between Fe^{II} centers in MIL-53(Al)-FeCl and $(^tBuO)_2$ with concomitant generation of one equiv of $^tBuO\cdot$ radical. The $^tBuO\cdot$ radical subsequently underwent C-H activation through hydrogen atom abstraction (HAT). Interestingly, Fe^{III} pre-edge features of MIL-53(Al)-Fe^{III}O^{t}Bu were maintained after its treatment with aniline, indicating a simple anion exchange with aniline to generate MIL-53(Al)-Fe^{III}-anilide. The final step of the reaction involved C-N coupling between the Fe^{III}-anilide and alkyl radical with concomitant SET to the anilide to the Fe^{III} center to regenerate the Fe^{II} catalyst (**Figure 2-5b**).

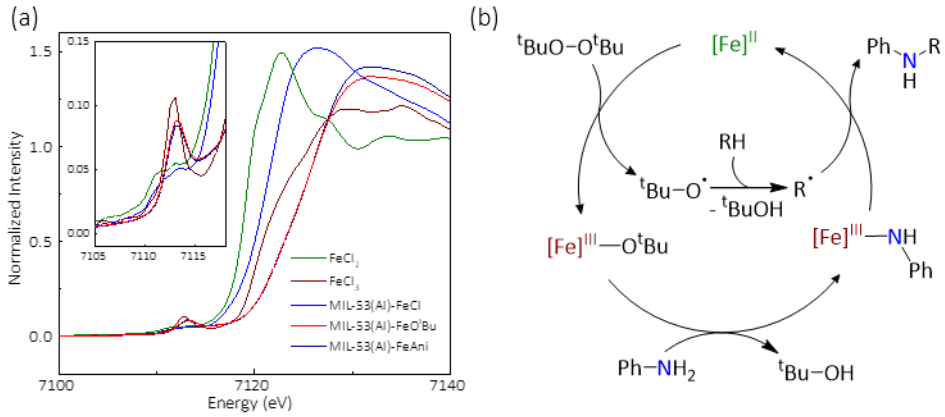

Figure 2-5. Mechanism studies of MIL-53(Al)-FeCl catalyzed oxidative C-H amination. (a) XANES pre-edge features of MIL-53(Al)-$Fe^{II}Cl$ (blue), MIL-53(Al)-$Fe^{III}O^tBu$ (red), and MIL-53(Al)-Fe^{III}-anilide (navy) as compared to those of $FeCl_2$ (green) and $FeCl_3$ (wine). (b) Proposed mechanism for MIL-53(Al)-FeCl catalyzed Csp^3-H amination involving the Fe^{II}/Fe^{III} cycle. Copyright 2019 American Chemical Society.

2.2.7 MIL-53(Al)-FeCl catalyzed Wacker-type alkene oxidation

MIL-53(Al)-FeCl is also highly effective in catalyzing Wacker-type alkene oxidation reactions. Wacker-Tsuji oxidation directly converts terminal alkenes into carbonyl-containing compounds using a wide range of oxidants.[29] However, precious metal catalysts (*e.g.*, $PdCl_2$) along with stoichiometric Cu salt[30-31] or "unusual" oxidants, such as hypervalent iodine[32] and 1,4-benzoquinoline,[33] are needed in Wacker oxidation reactions to achieve high chemo-selectivity, significantly restricting their broad applications. Recently, Han and co-workers[34] reported an Fe-based catalyst for Wacker-type oxidation under ambient air conditions. The reaction was believed to go through the Fe^{II}/Fe^{III} cycle. We hypothesized that MIL-53(Al) with isolated μ_2-OH sites could provide an excellent support for developing single-site solid catalyst for Wacker-type olefin oxidation.

We found that MIL-53(Al)-FeCl showed high catalytic activity for the oxidation of a wide range of styrene derivatives using ambient air as the oxidant and 1,1,1,3,5,5,5-

heptamethyltrisiloxane (HMTS) as the additive (**Table 2-5**). At 3.0 mol% loading of MIL-53(Al)-FeCl (w.r.t. Fe), acetophenone was obtained in 92% yield from the oxidation of styrene at 60 °C for 12 h. No reaction occurred in the absence of either the MOF, silanes, or the air. Substrate scope of this reaction was broad and extended to styrenes containing both electron-donating groups such as methyl, methoxyl (at either *para*- or *meta*-position), and t-butyl groups and electron-withdrawing groups such as fluoro, chloro, and bromo substituents. In all cases, acetophenone derivatives were obtained in very high yields (90-100%). MIL-53(Al)-FeCl was also readily recovered and used in three consecutive run of oxidation reactions with no significant drop in reaction yields (Yields of 1st to 3rd run: 92%, 92%, 73%). Only 0.3% of Fe leached into the supernatant as determined by ICP-MS, indicating the stability of the MOF catalyst.

Table 2-5. MIL-53(Al)-FeCl catalyzed Wacker-type alkene oxidation.[a]

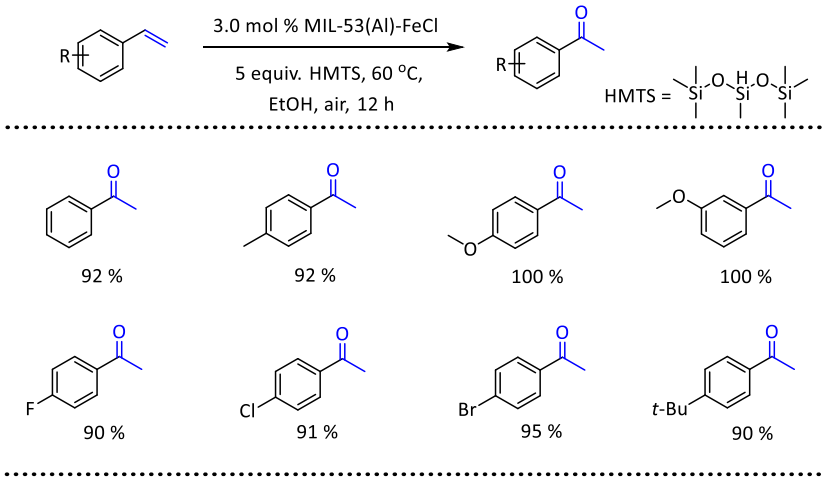

[a]Standard condition: 0.20 mmol alkenes substrate, 1.0 mmol HMTS, 3 mol% Fe, 1.0 mL dry EtOH, 60 °C, 12 h; Yield was determined by GC-MS analysis using mesitylene as internal standard.

2.2.8 Catalytic performance comparison between MIL-53(Al)-CoH and UiO-68-CoH

To further demonstrate the outstanding catalytic performance and the unique electronic property of EAM catalysts supported on Al-OH chain SBUs, several control reactions were conducted using the well-established UiO-68-Co MOF catalyst at the same Co loading.[35]

Significantly lower yields of hydroboration and hydrosilylation products were observed when UiO-68-CoH was used in place of MIL-53(Al)-CoH. For the hydroboration of alkynes, aromatic alkynes (phenylacetylene) and aliphatic alkynes (ethynylcyclohexane) achieved moderate to good yields at 0.2 mol% MIL-53(Al)-CoH loading, but the same loading of UiO-68-CoH afforded the aromatic and aliphatic products in 16% and 8% yields, respectively. Significant drops of catalytic activities were also observed in the hydroboration of aromatic and aliphatic nitriles. Moreover, UiO-68-CoH was completely inactive for the hydrosilylation of esters, with >99% of starting substrates recovered (**Figure 2-6**).

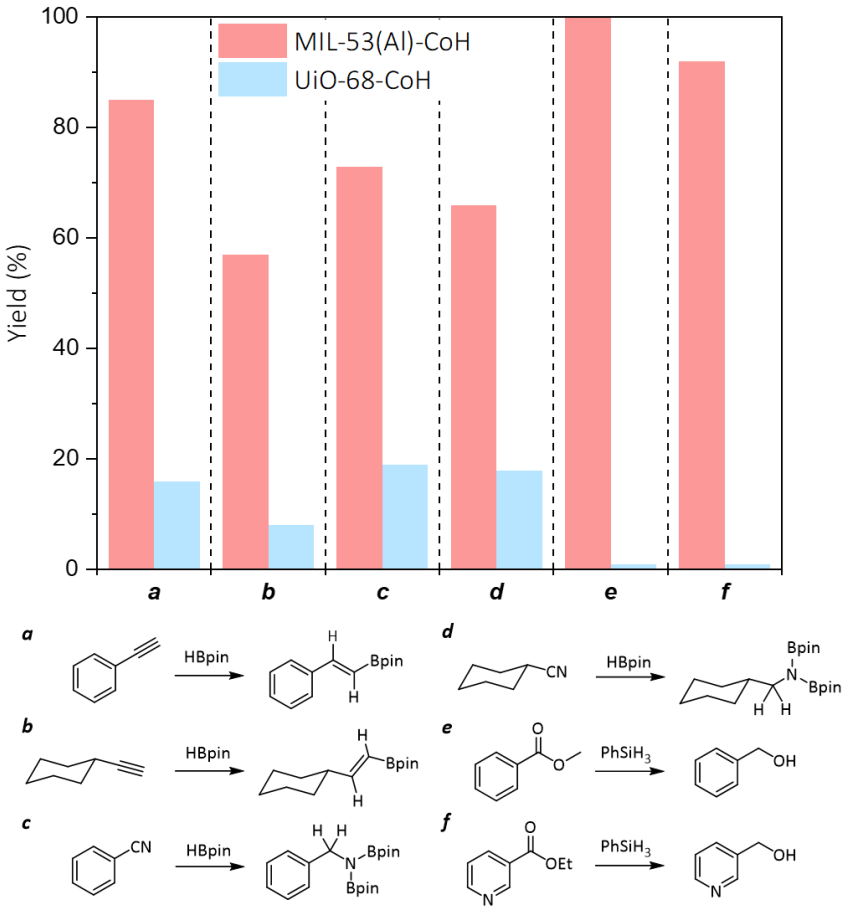

Figure 2-6. Hydroboration of alkynes and nitriles and hydrosilylation of esters with different MOF SBU supported Co-hydride catalysts. Reaction conditions: (**a**, **b**) 0.2 mol% of MOF-CoH catalyst, alkynes (1.0 mmol), HBpin (1.2 mmol), 90 °C, 22 h. (**c**, **d**) 1.0 mol% of MOF-CoH catalyst, nitriles (0.6 mmol), HBpin (1.26 mmol), 90 °C, 2 days. (**e**, **f**) 0.1 mol% of MOF-CoH catalyst, esters (1.0 mmol), $PhSiH_3$ (1.0 mmol), *r.t.*, 18 h. Copyright 2019 American Chemical Society.

To understand the reason for such drastic differences in hydrofunctionaliztion activities, DFT calculations were carried out on the two MOF SBU supported Co-hydride catalytic systems. With the same overall charge and Co^{II} spin state, MIL-53(Al)-CoH features a more electron-rich hydride site with a NBO charge of -0.441 on the hydride. In comparison, UiO-68-CoH has a NBO charge of -0.354 on the hydride (**Figure 2-7**). We believe that electron-rich oxo sites in MIL-53(Al)-CoH afford a reactive Co-hydride for insertion to the unsaturated bonds to lead to excellent catalytic performance in hydrofunctionalization reactions. Upon dissociation of THF, the Co centers in MIL-53(Al)-CoH also have more open coordination site for substrate binding to further facilitate hydrofunctionalization reactions.

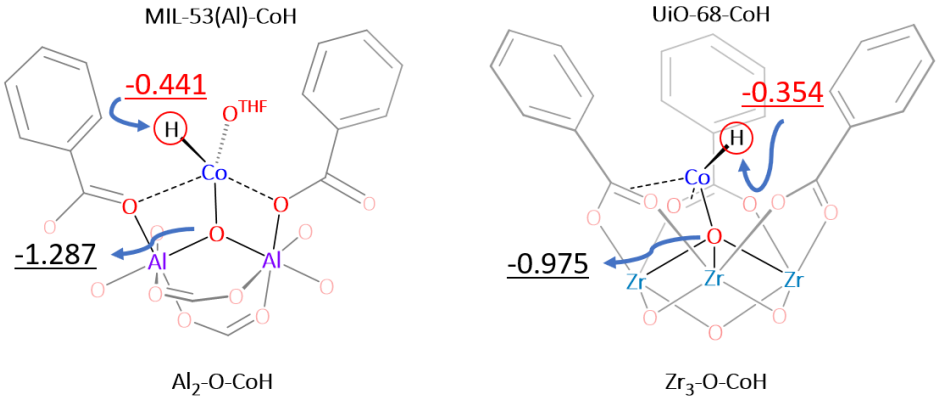

Figure 2-7. NBO charges of Co centers and hydride and bridging oxo groups in MIL-53(Al)-CoH and UiO-68-CoH.

2.3 Conclusion

MIL-53(Al) with one-dimensional Al-OH chain SBUs was used as a structural and functional mimic of γ-Al_2O_3 surface to support Earth-abundant Co and Fe catalysts. Deprotonation of the μ_2-OH groups in MIL-53(Al) followed by metalation with $CoCl_2$ and $FeCl_2$ afforded MIL-53(Al)-CoCl and MIL-53(Al)-FeCl precatalysts which showed impressive catalytic activities in distinct reductive addition and oxidative amination/alkene oxidation reactions. MIL-53(Al)-CoCl was activated by $NaBEt_3H$ to afford MIL-53(Al)-CoH for reductive hydrofunctionalization

reactions, including hydroboration of alkynes to generate *E*-alkenylboronates, hydroboration of nitriles to give *N*,*N*-difunctionalized amines, and hydrosilylation of esters followed by hydrolysis to afford corresponding alcohols. Due to the site-isolation effect and unique coordination environment, this highly stable and solution-inaccessible Co^{II} hydride species exhibits unprecedented catalytic activities in reductive hydrofunctionalization reactions. On the other hand, due to the Fe^{II}/Fe^{III} redox property, MIL-53(Al)-FeCl catalyzed interesting oxidative transformations, including Csp^3-H amination and Wacker-type alkene oxidation reactions. Spectroscopic studies indicated the involvement of the Fe^{II}/Fe^{III} redox process in oxidative transformations. Compared to traditional γ-Al_2O_3-supported metal catalysts, structurally-defined and single-site of MIL-53(Al)-M (M = Co, Fe) solid catalysts allow for molecular level understanding of coordination environments and electronic structures of the catalytically active site as well as the probing of reaction mechanisms in unprecedented details. Moreover, control experiments combined with computational studies showed that such Al_2-O^- sites provide electron-rich Co-H sites to facilitate hydrofuctionalization reactions. The establishment of structure/activity relationships in MOF-supported catalysts promises to facilitate their rational optimization to afford cost-effective and sustainable solid catalysts for the practical synthesis of commodity and fine chemicals.

2.4 Experimental Section

2.4.1 Materials and methods

All the reactions and manipulations were carried out under N_2 with the use of a glove box or Schlenk technique, unless otherwise indicated. Unless noted, solvents and chemicals were purchased from Fisher and Sigma-Aldrich and used as received. PXRD data was collected on Bruker D8 Venture diffractometer using Cu Kα radiation source (l = 1.54178 Å). N_2 sorption

experiments were performed on a Micromeritics TriStar II 3020 instrument. FT-IR spectra were collected using a Nexus 870 spectrometer (Thermo Nicolet) installed with Diffuse Reflectance Infrared Fourier Transform Spectroscopy (DRIFTS) system. XPS data was collected using an AXIS Nova spectrometer (Kratos Analytical) with monochromatic Al Kα X-ray source, and the binding energies were referenced to the C 1s peak at 284.8 eV. ICP-MS data was obtained with an Agilent 7700x ICP-MS and analyzed using ICP-MS MassHunter version B01.03.

^{1}H NMR spectra were recorded on a Bruker NMR 500 DRX spectrometer at 500 MHz and referenced to the proton resonance resulting from incomplete deuteration of $CDCl_3$ (δ 7.26) or C_6D_6 (δ 7.16). High-resolution mass spectra were obtained using an Agilent 6224 Accurate-Mass TOF spectrometer. The conversions of Wacker-type alkene oxidation reactions were determined by gas chromatography-mass spectroscopy (GC-MS) using a Shimadzu GCMS-QP2010 Ulta. Column: SH-Rxi-5Sil MS column, 30.0 m in length, 0.25 mm in diameter, 0.25 μm in thickness. GC conditions: Injection temperature, 220 °C; Column temperature program, 30 °C hold for 5 min, followed by a ramp of 5 °C/min to 60 °C then a ramp of 20 °C/min to 300 °C; Column flow, 1.21 mL/min.

2.4.2 Synthetic procedures of MOF catalysts

Synthesis of MIL-53(Al)- CoCl ($Al(\mu_2\text{-}OLi)_{0.85}(\mu_2\text{-}OCoCl)_{0.15}$): In a glovebox, MIL-53(Al) (200.0 mg, 0.674 mmol μ_2-OH) in 4 mL hexanes was treated with $LiCH_2SiMe_3$ (3.37 mL, 3.37 mmol, 1.0 M solution in pentane). The resultant mixture was stirred at 25 °C for 6 h. The light-yellow solid was collected after centrifugation and washed with hexanes 5 times. Then, the lithiated MIL-53(Al) was transferred to a vial containing 50 mL THF solution of $CoCl_2$ (130 mg, 1.5 equiv. to μ_2-OLi). The mixture was stirred for 12 h and the deep blue solid was then centrifuged and washed with THF 5 times. The metalated MOF was stored in THF in the glovebox for further

use. ICP-MS analysis indicated a Co/Al ratio of 0.15. PXRD showed the crystallinity of MOF was maintained after metalation.

Synthesis of MIL-53(Al)- FeCl ($Al(\mu_2\text{-}OLi)_{0.77}(\mu_2\text{-}OFeCl)_{0.23}$): In a glovebox, MIL-53(Al) (200.0 mg, 0.674 mmol μ_2-OH) was dispersed in 15 mL hexane, then $LiCH_2SiMe_3$ (3.37 mL, 3.37 mmol, 1.0 M solution in pentane) was added dropwise to the suspension. The resultant light-yellow mixture was stirred slowly overnight at room temperature. The light-yellow solid was centrifuged out and washed with hexane 5 times and THF 5 times over 6 h. Then, the lithiated MIL-53(Al) was transferred to a vial containing 100 mL THF solution of $FeCl_2$ (126.7 mg, 1 mmol). The mixture was stirred for 24 h before the light brown solid was centrifuged out and washed with THF 5 times to remove excess $LiCH_2SiMe_3$ and benzene 5 times for solvent exchange. The metalated MOF was then freeze-dried under vacuum and stored in the glovebox for further uses. ICP-MS analysis showed 23% Fe-loading with respect to μ_2-OH centers.

2.4.3 Catalytic reaction setup and product characterization

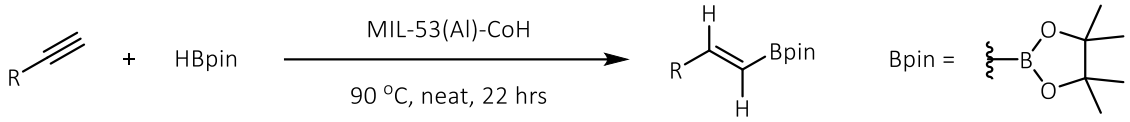

Typical procedures for MIL-53(Al)-CoH catalyzed hydroboration of alkynes: MIL-53(Al)-CoH (2.0 μmol Co) was prepared as described above. Phenylacetylene (110 μL, 1.00 mmol) was then added to a solution of MIL-53(Al)-CoH and pinacolborane (175 μL, 1.20 mmol). The reaction mixture was stirred under N_2 at 90 °C for 22 hrs. The MOF was removed from the solution by centrifugation. The supernatant was transferred to a vial, and the MOF was washed with toluene. The combined organic extracts were concentrated in vacuo to afford a crude product of (*E*)-4,4,5,5-tetramethyl-2-styryl-1,3,2-dioxaborolane (0.85 mmol, 85% NMR yield based on mesitylene as an

internal standard). 0.3% of Co leaching was determine by ICP-MS analysis of the organic extract, indicating minimal MOF decomposition during catalysis.

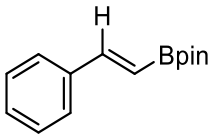

(CAS: 83947-56-2) ^{1}H NMR (500 MHz, $CDCl_3$): δ 1.32 (s, 12H), 6.18 (d, *J* = 18.4 Hz, 1H), 7.28-7.32 (m, 1H), 7.32-7.37 (m, 2H), 7.41 (d, *J* = 18.5 Hz, 1H), 7.47-7.51 (m, 2H). HRMS (ESI, positive mode): $(M+H)^+$ m/z calcd 231.1551, found 231.1537.

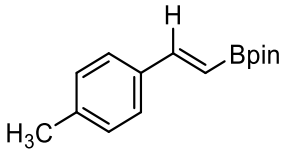

(CAS: 149777-84-4) ^{1}H NMR (500 MHz, $CDCl_3$): δ 1.32 (s, 12H), 2.35 (s, 3H), 6.12 (d, *J* = 18.4 Hz, 1H), 7.15 (d, *J* = 8.0 Hz, 2H), 7.38 (d, *J* = 17.8 Hz, 1H), 7.39 (d, *J* = 7.9 Hz, 2H). HRMS (ESI, positive mode): $(M+H)^+$ m/z calcd 245.1707, found 245.1694.

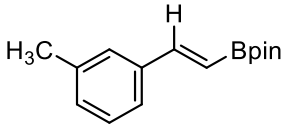

(CAS: 1421061-31-5) ^{1}H NMR (500 MHz, $CDCl_3$): δ 1.32 (s, 12H), 2.35 (s, 3H), 6.15 (d, *J* = 18.4 Hz, 1H), 7.10-7.15 (m, 1H), 7.16-7.20 (m, 1H), 7.21-7.25 (m, 1H), 7.28-7.31 (m, 1H), 7.38 (d, *J* = 18.5 Hz, 1H). HRMS (ESI, positive mode): $(M+H)^+$ m/z calcd 245.1707, found 245.1676.

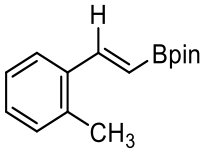

(CAS: 1294009-26-9) ^{1}H NMR (500 MHz, $CDCl_3$): δ 1.32 (s, 12H), 2.43 (s, 3H), 6.09 (d, *J* = 18.3 Hz, 1H), 7.14-7.16 (m, 1H), 7.18-7.20 (m, 2H), 7.54-7.58 (m, 1H), 7.65 (d, *J* = 18.3 Hz, 1H). HRMS (ESI, positive mode): $(M+H)^+$ m/z calcd 245.1707, found 245.1693.

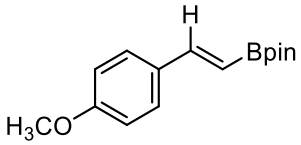

(CAS: 149777-83-3) ^{1}H NMR (500 MHz, $CDCl_3$): δ 1.31 (s, 12H), 3.81 (s, 3H), 6.02 (d, *J* = 18.4 Hz, 1H), 6.85-6.88 (m, 2H), 7.36 (d, *J* = 18.4 Hz, 1H), 7.43-7.46 (m, 2H). HRMS (ESI, positive mode): $(M+H)^+$ m/z calcd 261.1657, found 261.1633.

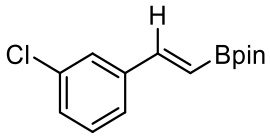

(CAS: 871125-84-7) ^{1}H NMR (500 MHz, $CDCl_3$): δ 1.32 (s, 12H), 6.17 (d, *J* = 18.3 Hz, 1H), 7.15-7.20 (m, 1H), 7.23-7.26 (m, 2H), 7.32 (d, *J* = 18.7 Hz, 1H), 7.45-7.47 (m, 1H). HRMS (ESI, positive mode): $(M+H)^+$ m/z calcd 265.1161 (^{35}Cl), found 265.1156.

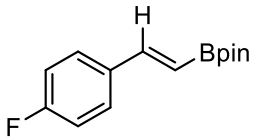

(CAS: 504433-86-7) ^{1}H NMR (500 MHz, $CDCl_3$): δ 1.31 (s, 12H), 3.81 (s, 3H), 6.08 (d, *J* = 18.4 Hz, 1H), 7.00-7.04 (m, 2H), 7.35 (d, *J* = 18.4 Hz, 1H), 7.44-7.48 (m, 2H). HRMS (ESI, positive mode): $(M+H)^+$ m/z calcd 249.1457, found 249.1447.

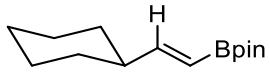

(CAS: 172512-85-5) ^{1}H NMR (500 MHz, $CDCl_3$): δ 1.03-1.14 (m, 4H), 1.26 (s, 12H), 1.68-1.77 (m, 6H), 1.97-2.05 (m, 1H), 5.37 (dd, *J* = 18.2, 1.5 Hz, 1H), 6.58 (d, *J* = 18.2, 6.2 Hz, 1H). HRMS (ESI, positive mode): $(M+H)^+$ m/z calcd 237.2020, found 237.2011.

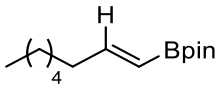

(CAS: 83947-55-1) ^{1}H NMR (500 MHz, $CDCl_3$): δ 0.84-0.89 (m, 3H), 1.27 (m, 18H), 1.37-1.44 (m, 2H), 2.11-2.15 (m, 2H), 5.42 (dt, *J* = 17.9, 1.6 Hz, 1H), 6.63 (d, *J* = 17.9, 6.4 Hz, 1H). HRMS (ESI, positive mode): $(M+H)^+$ m/z calcd 239.2177, found 239.2244.

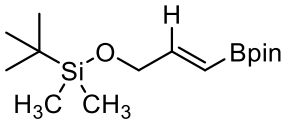

(CAS: 114653-19-9) ^{1}H NMR (500 MHz, $CDCl_3$): δ 0.06 (s, 6H), 0.91 (s, 9H), 1.26 (s, 12H), 4.24 (dd, *J* = 3.6, 2.1 Hz, 2H), 5.75 (dt, *J* = 17.9, 2.1 Hz, 1H), 6.67 (dt, *J* = 17.9, 3.6 Hz, 1H). HRMS (ESI, positive mode): $(M+H)^+$ m/z calcd 299.2208, found 299.2212.

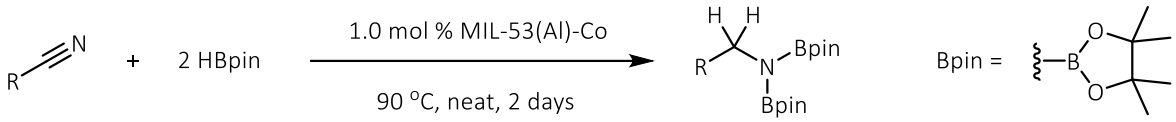

Typical procedure for MIL-53(Al)-CoH catalyzed hydroboration of nitriles: MIL-53(Al)-CoH (6.0 μmol Co) was prepared as described above. Benzonitrile (62 μL, 0.60 mmol) was added to a solution of MIL-53(Al)-CoH and pinacolborane (183 μL, 1.26 mmol). The reaction mixture was stirred under N_2 at 90 °C for 2 days. The MOF was removed from the solution by centrifugation. The supernatant was transferred to a vial, and the MOF was washed with toluene. The combined organic extracts were concentrated in vacuo to afford a crude dihydroboration product of *N*-benzyl-4,4,5,5-tetramethyl-*N*-(4,4,5,5-tetramethyl-1,3,2-dioxaborolan-2-yl)-1,3,2-dioxaborolan-2-amine (0.44 mmol, 73% NMR yield based on mesitylene as an internal standard) and unreacted nitriles. 0.6% of Co leaching was determine by ICP-MS analysis of the organic extract, indicating minimal MOF decomposition during catalysis.

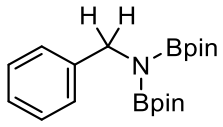

(CAS: 1812886-41-1) ^{1}H NMR (500 MHz, $CDCl_3$): δ 1.20 (s, 24H), 4.23 (s, 2H), 7.13-7.18 (m, 1H), 7.24 (m , 2H), 7.28-7.33 (m, 2H). HRMS (ESI, positive mode): $(M+H)^+$ m/z calcd 360.2512, found 360.2506.

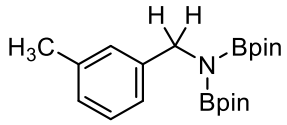

(CAS: 1858278-58-6) ^{1}H NMR (500 MHz, $CDCl_3$): δ 1.20 (s, 24H), 2.30 (s, 3H), 4.20 (s, 2H), 6.94-6.99 (m, 1H), 7.10 (s , 2H), 7.12-7.15 (m, 2H). HRMS (ESI, positive mode): $(M+H)^+$ m/z calcd 374.2668, found 374.2658.

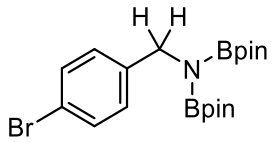

^{1}H NMR (500 MHz, $CDCl_3$): δ 1.19 (s, 24H), 4.16 (s, 2H), 7.15-7.21 (m, 2H), 7.34-7.39 (m, 2H). ^{13}C NMR (126 MHz, $CDCl_3$) δ = 131.40 (C-Br), 130.92 (CH), 129.39 (CH), 128.56 (C-CH_2), 82.53 (C-O), 46.77 (CH_2), 24.63 (CH_3). HRMS (ESI, positive mode): $(M+H)^+$ m/z calcd 438.1617 (^{79}Br), found 438.1625.

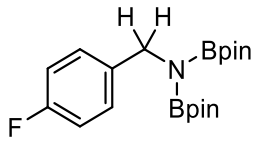

(CAS: 1812886-43-3) ^{1}H NMR (500 MHz, $CDCl_3$): δ 1.20 (s, 24H), 4.18 (s, 2H), 6.88-6.97 (m, 2H), 7.22-7.31 (m, 2H). HRMS (ESI, positive mode): $(M+H)^+$ m/z calcd 378.2418, found 378.2416.

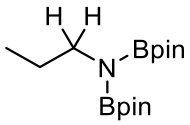

(CAS: 421556-96-9) ^{1}H NMR (500 MHz, $CDCl_3$): δ 0.83 (t, *J* = 7.4 Hz, 3H), 1.22 (s, 24H), 1.36-1.44 (m, 2H), 2.99 (t, *J* = 7.0 Hz, 2H). HRMS (ESI, positive mode): $(M+H)^+$ m/z calcd 312.2512, found 312.2518.

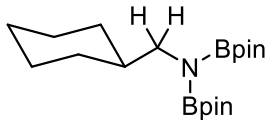

^{1}H NMR (500 MHz, $CDCl_3$): δ 0.79-0.92 (m, 2H), 1.07-1.17 (m, 4H), 1.21 (s, 24H), 1.59-1.63 (m, 1H), 1.64-1.74 (m, 4H), 2.87 (d, *J* = 7.0 Hz, 2H). ^{13}C NMR (126 MHz, $CDCl_3$): δ 24.47($OC(\underline{C}H_3)_2$), 26.17(Cy-C), 26.80(Cy-C), 30.55(Cy-C), 40.52($NCH_2\underline{C}H$), 49.70(NCH_2), 81.96($O\underline{C}(CH_3)_2$) HRMS (ESI, positive mode): $(M+H)^+$ m/z calcd 366.2981, found 366.2982.

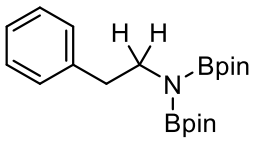

(CAS: 2030059-61-9) ^{1}H NMR (500 MHz, $CDCl_3$): δ 1.18 (s, 24H), 2.71 (t, *J* = 7.3 Hz, 2H), 3.30 (t, *J* = 7.2 Hz, 2H), 7.13-7.21 (m, 3H), 7.22-7.27 (m, 2H). HRMS (ESI, positive mode): $(M+H)^+$ m/z calcd 374.2668, found 374.2652.

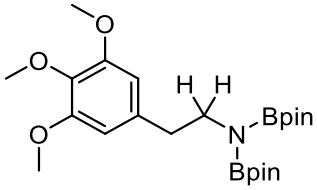

^{1}H NMR (500 MHz, $CDCl_3$): δ 1.17 (s, 24H), 2.66 (t, *J* = 6.9 Hz, 2H), 3.29 (t, *J* = 6.9 Hz, 2H), 3.79 (s, 3H), 3.85 (s, 6H), 6.39 (s, 2H). ^{13}C NMR (126 MHz, $CDCl_3$): δ 24.41($OC(\underline{C}H_3)_2$), 39.37($\underline{C}H_2CH_2N$), 44.97($CH_2\underline{C}H_2N$), 55.81(3,5-OCH_3), 60.56(4-OCH_3), 81.92($O\underline{C}(CH_3)_2$),

106.17(Ph-C), 125.44(Ph-C), 135.86(Ph-C), 162.65(Ph-C). HRMS (ESI, positive mode): $(M+H)^+$ m/z calcd 464.2985, found 464.2878.

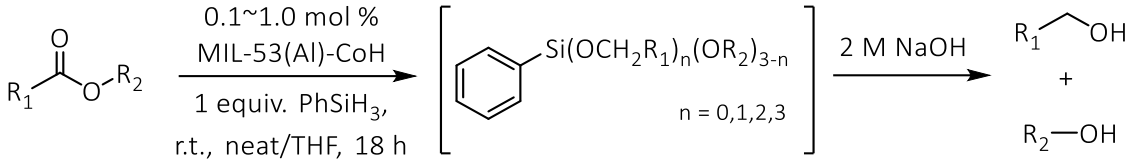

Typical procedure for MIL-53(Al)-CoH catalyzed hydrosilylation of esters: MIL-53(Al)-CoH (1.0 μmol Co) was prepared as described above. Methyl benzonate (126 μL, 1.00 mmol) was added to a solution of MIL-53(Al)-CoH and phenylsilane (123 μL, 1.00 mmol). The reaction mixture was stirred under N_2 at room temperature (~25 °C) for 18 hrs. The MOF was removed from the solution by centrifugation. The supernatant was transferred to a vial, and the MOF was washed with toluene. The combined organic extracts were concentrated in vacuo to afford an oil-like hydrosilylation product. Analysis by ^{1}H NMR spectroscopy showed the complete conversion of ester into a mixture of $PhSi(OCH_3)_2(OCH_2C_6H_5)$ (42%, mole ratio), $PhSi(OCH_3)(OCH_2C_6H_5)_2$ (45%), and $PhSi(OCH_2C_6H_5)_3$ (13%), with $PhSi(OCH_3)_3$ as by-product. The product ratio was determined based on the integration of the OCH_2 peaks. For the later hydrolysis procedure, the mixture of hydrosilylation product was then stirred in 2 M NaOH solution (10 mL, H_2O: MeOH = 1:1) overnight. Then 5 mL of H_2O was added to the system, and subsequently extracted with CH_2Cl_2 (3*5 mL). The combined organic layers were dried over Na_2SO_4 and the solvent was removed using rotavap to isolate the higher molecular weight alcohol, benzyl alcohol, in 92 % isolated yield.

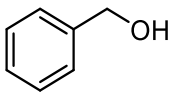

(CAS: 100-51-6) ^{1}H NMR (500 MHz, $CDCl_3$): δ 1.69 (s, 1H), 4.70 (s, 2H), 7.27-7.43 (m, 5H).

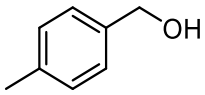

(CAS: 589-18-4) ^{1}H NMR (500 MHz, $CDCl_3$): δ 1.56 (t, *J* = 5.9 Hz, 1H), 2.35 (s, 3H), 4.65 (d, *J* = 5.8 Hz, 2H), 7.15-7.20 (m, 2H), 7.24-7.29 (m, 2H).

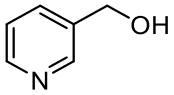

(CAS: 100-55-0) ^{1}H NMR (500 MHz, $CDCl_3$): δ 4.71 (s, 2H), 7.29 (ddd, *J* = 7.8, 4.9. 0.9 Hz, 1H), 7.72 (dt, *J* = 7.7, 1.9 Hz, 1H), 8.46 (dd, *J* = 5.0 Hz, 1.6H), 8.51-8.53 (m, 1H).

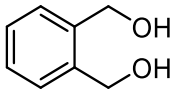

(CAS: 612-14-6) ^{1}H NMR (500 MHz, $CDCl_3$): δ 4.75 (s, 4H), 7.31-7.39 (m, 4H).

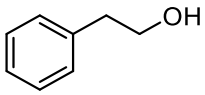

(CAS: 60-12-8) ^{1}H NMR (500 MHz, $CDCl_3$): δ 1.46 (s, 1H), 2.88 (t, *J* = 6.5 Hz, 2H), 3.87 (t, *J* = 6.6 Hz, 2H), 7.21-7.26 (m, 3H), 7.30-7.35 (m, 2H).

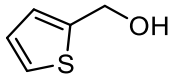

(CAS: 636-72-6) ^{1}H NMR (500 MHz, C_6D_6): δ 1.06 (s, 1H), 4.35 (s, 2H), 6.63-6.66 (m, 1H), 6.68 (dd, J = 5.1, 3.4 Hz, 1H), 6.85 (dd, J = 5.0, 1.3 Hz, 1H).

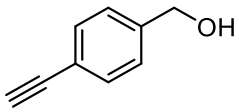

(CAS: 10602-04-7) ^{1}H NMR (500 MHz, $CDCl_3$): δ 1.72 (s, 1H), 3.07 (s, 1H), 4.70 (s, 2H), 7.30-7.35 (m, 2H), 7.47-7.51 (m, 2H).

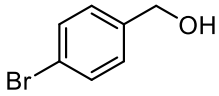

(CAS: 873-75-6) ^{1}H NMR (500 MHz, $CDCl_3$): δ 1.73 (t, *J* = 5.8 Hz, 1H), 4.65 (d, *J* = 5.5 Hz, 2H), 7.21-7.26 (m, 2H), 7.46-7.51 (m, 2H).

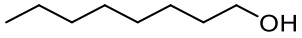

(CAS: 111-87-5) ^{1}H NMR (500 MHz, $CDCl_3$): δ 0.88-0.92 (m, 3H), 1.20-1.39 (m, 10H), 1.53-1.60 (m, 2H), 1.61 (s, 1H), 3.64 (t, *J* = 6.7 Hz, 2H).

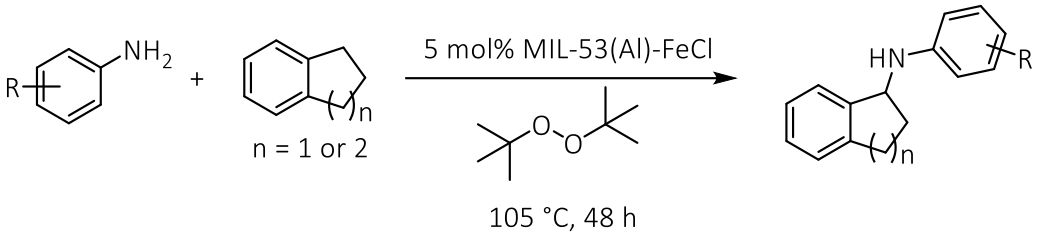

Typical procedure for MIL-53(Al)-FeCl Catalyzed C-H amination: MIL-53(Al)-FeCl was prepared as described above. In a glovebox, MIL-53(Al)-FeCl (16 μmol Fe) was weighed out on a balance and transferred into a Teflon-sealed tube with C–H substrate (6.4 mmol), then aniline (0.32 mmol) and ditertbutylperoxide (0.48 mmol) were directly added to the tube. The tube was sealed, transferred out of the glovebox and stirred at 105 °C for 48 h. Then, the solid was centrifuged out of suspension and washed with methanol twice, and the extract was concentrated under rotavap. Mesitylene (internal standard) was added to the reaction mixture, and the yield of the product was determined by ^{1}H NMR or GCMS. The leaching of Fe was analyzed by ICP-MS to be 4.5%.

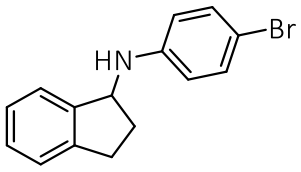

^{1}H NMR (500 MHz, $CDCl_3$) δ 7.36 (d, *J* = 7.4 Hz, 1H), 7.31 – 7.27 (m, 4H), 7.22 (ddd, *J* = 7.5, 6.3, 2.4 Hz, 1H), 6.61 (d, *J* = 8.8 Hz, 1H), 4.98 (t, *J* = 6.7 Hz, 1H), 3.03 (ddd, *J* = 16.0, 8.6, 4.4 Hz, 1H), 2.91 (dt, *J* = 15.9, 7.8 Hz, 1H), 2.58 (dddd, *J* = 12.7, 8.3, 7.0, 4.4 Hz, 1H), 1.91 (dddd, *J*

= 12.8, 8.7, 7.5, 6.4 Hz, 1H). ^{13}C NMR (126 MHz, $CDCl_3$) δ 146.54, 144.01, 143.61, 132.05, 128.12, 126.74, 124.98, 124.24, 114.91, 109.07, 58.76, 33.60, 30.25. HRMS (ESI, positive mode): $(M+H)^+$ m/z calcd 288.0388, found 288.0379.

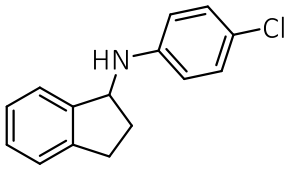

^{1}H NMR (500 MHz, $CDCl_3$) δ 7.36 (dd, *J* = 7.5, 1.1 Hz, 1H), 7.30 – 7.27 (m, 2H), 7.24 – 7.20 (m, 1H), 7.16 (d, *J* = 8.8 Hz, 2H), 6.65 (d, *J* = 8.9 Hz, 2H), 4.98 (t, *J* = 6.7 Hz, 1H), 3.03 (ddd, *J* = 16.0, 8.7, 4.4 Hz, 1H), 2.91 (dt, *J* = 15.9, 7.8 Hz, 1H), 2.58 (dddd, *J* = 12.7, 8.2, 7.0, 4.4 Hz, 1H), 1.91 (dddd, *J* = 12.8, 8.7, 7.5, 6.4 Hz, 1H). ^{13}C NMR (126 MHz, $CDCl_3$) δ 146.15, 144.04, 143.61, 129.18, 128.10, 126.72, 124.96, 124.23, 122.05, 114.38, 58.84, 33.63, 30.24. HRMS (ESI, positive mode): $(M+H)^+$ m/z calcd 244.0893, found 244.0888.

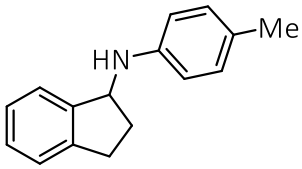

^{1}H NMR (500 MHz, $CDCl_3$) δ 7.42 (d, *J* = 7.4 Hz, 1H), 7.34 – 7.28 (m, 2H), 7.27 – 7.21 (m, 1H), 7.07 (d, *J* = 7.7 Hz, 2H), 6.70 (d, *J* = 8.4 Hz, 2H), 5.04 (t, *J* = 6.8 Hz, 1H), 3.88 (s, 1H), 3.06 (ddd, *J* = 16.0, 8.6, 4.3 Hz, 1H), 2.93 (dt, *J* = 15.9, 7.9 Hz, 1H), 2.62 (dddd, *J* = 12.7, 8.2, 7.0, 4.3 Hz, 1H), 2.31 (s, 3H), 1.95 (dddd, *J* = 12.8, 8.7, 7.7, 6.5 Hz, 1H). ^{13}C NMR (126 MHz, $CDCl_3$) δ 145.37, 144.70, 143.64, 129.86, 127.87, 126.79, 126.62, 124.86, 124.32, 113.50, 59.00, 33.89, 30.28, 20.45. HRMS (ESI, positive mode): $(M+H)^+$ m/z calcd 224.1439, found 224.1442.

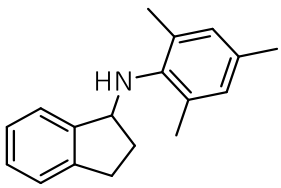

^{1}H NMR (500 MHz, $CDCl_3$) δ 7.33 (dd, *J* = 7.3, 1.3 Hz, 1H), 7.27 – 7.23 (m, 1H), 7.23 – 7.19 (m, 1H), 7.19 – 7.14 (m, 1H), 6.90 – 6.85 (m, 2H), 4.77 (t, *J* = 6.7 Hz, 1H), 3.20 (s, 1H), 3.05 (ddd, *J* = 15.9, 8.4, 4.6 Hz, 1H), 2.83 (dt, *J* = 15.8, 7.7 Hz, 1H), 2.44 (dddd, *J* = 12.7, 8.0, 7.0, 4.6 Hz, 1H), 2.28 (s, 3H), 2.26 (s, 6H), 1.89 (dddd, *J* = 12.7, 8.4, 7.4, 6.4 Hz, 1H). ^{13}C NMR (126 MHz, $CDCl_3$) δ 144.18, 143.57, 143.23, 129.61, 127.64, 126.43, 125.98, 124.79, 124.48, 124.38, 62.74, 32.89, 30.10, 20.61, 18.88. HRMS (ESI, positive mode): $(M+H)^+$ m/z calcd 252.1752, found 252.1745.

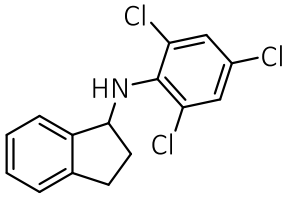

^{1}H NMR (500 MHz, $CDCl_3$) δ 7.42 – 7.36 (m, 1H), 7.30 (s, 2H), 7.30 – 7.20 (m, 3H), 5.34 (t, *J* = 6.9 Hz, 1H), 4.16 (s, 1H), 3.05 (ddd, *J* = 15.9, 8.5, 4.3 Hz, 1H), 2.85 (dt, *J* = 15.9, 7.9 Hz, 1H), 2.49 (dddd, *J* = 12.8, 8.1, 7.2, 4.3 Hz, 1H), 1.92 (dddd, *J* = 12.9, 8.5, 7.6, 6.6 Hz, 1H). ^{13}C NMR (126 MHz, $CDCl_3$) δ 144.34, 143.17, 141.14, 128.68, 127.99, 126.70, 125.98, 125.66, 124.86, 124.43, 62.05, 34.87, 30.01. HRMS (ESI, positive mode): $(M+Na)^+$ m/z calcd 333.9933, found 333.9921.

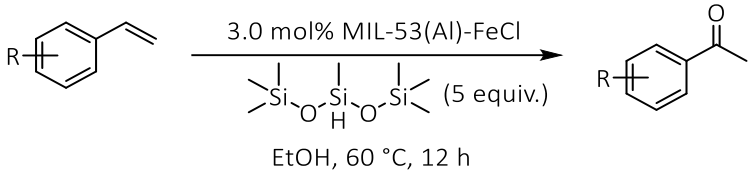

Typical procedure for MIL-53(Al)-FeCl catalyzed Wacker-type alkene oxidation: MIL-53(Al)-FeCl was prepared as described above. MIL-53(Al)-FeCl (6.0 μmol Fe) was transferred into a Schlenk tube, then alkene substrate (0.2 mmol), dry ethanol (1.0 mL) and 1,1,1,3,5,5,5-heptamethyltrisiloxane (1.0 mmol) were added. The Schlenk tube was attached with a condenser and stirred at 60 °C for 12 h. Then, KF (0.5 mmol) was added to quench excess silane for 1 h. The

solid was centrifuged and washed with methanol twice, and the extract was concentrated under rotavap. Mesitylene (internal standard) was added to the reaction mixture, and the yield of the product was determined by GCMS. The leaching of Fe was analyzed by ICP-MS to be 0.3%.

Table 2-6. The retention times of GC traces in MIL-53(Al)-FeCl catalyzed Wacker-type alkene oxidation.

Compound	Retention Time	Compound	Retention Time
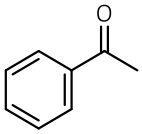	14.246 min	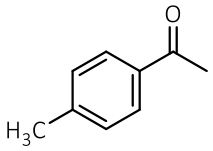	15.519 min
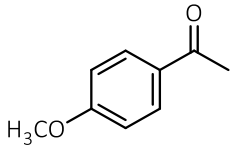	16.867 min	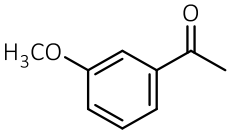	16.511 min
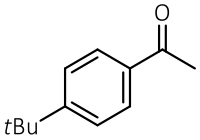	17.322 min	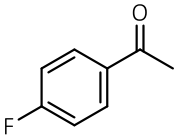	14.652 min
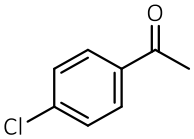	15.973 min	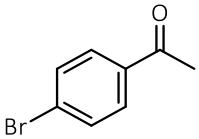	16.718 min

2.5 References

1. Euzen, P.; Raybaud, P.; Krokidis, X.; Toulhoat, H.; Le Loarer, J. L.; Jolivet, J. P.; Froidefond, C., Alumina. *Handbook of porous solids* **2002**, 1591-1677.

2. Trueba, M.; Trasatti, S. P., γ-Alumina as a support for catalysts: a review of fundamental aspects. *European journal of inorganic chemistry* **2005,** *2005* (17), 3393-3403.

3. Shirai, T.; Watanabe, H.; Fuji, M.; Takahashi, M., Structural properties and surface characteristics on aluminum oxide powders. **2010**.

4. Eckle, S.; Anfang, H.-G.; Behm, R. J., Reaction Intermediates and Side Products in the Methanation of CO and CO2 over Supported Ru Catalysts in H2-Rich Reformate Gases. *The Journal of Physical Chemistry C* **2011,** *115* (4), 1361-1367.

5. Zhen, W.; Li, B.; Lu, G.; Ma, J., Enhancing catalytic activity and stability for CO2 methanation on Ni-Ru/[gamma]-Al2O3 via modulating impregnation sequence and controlling surface active species. *RSC Advances* **2014,** *4* (32), 16472-16479.

6. Bocanegra, S. A.; Castro, A. A.; Guerrero-Ruíz, A.; Scelza, O. A.; de Miguel, S. R., Characteristics of the metallic phase of Pt/Al2O3 and Na-doped Pt/Al2O3 catalysts for light paraffins dehydrogenation. *Chemical Engineering Journal* **2006,** *118* (3), 161-166.

7. Williams, L. A.; Marks, T. J., Chemisorption Pathways and Catalytic Olefin Polymerization Properties of Group 4 Mono- and Binuclear Constrained Geometry Complexes on Highly Acidic Sulfated Alumina. *Organometallics* **2009,** *28* (7), 2053-2061.

8. Delley, M. F.; Silaghi, M.-C.; Nuñez-Zarur, F.; Kovtunov, K. V.; Salnikov, O. G.; Estes, D. P.; Koptyug, I. V.; Comas-Vives, A.; Copéret, C., X–H Bond Activation on Cr(III),O Sites (X = R, H): Key Steps in Dehydrogenation and Hydrogenation Processes. *Organometallics* **2017,** *36* (1), 234-244.

9. Mostafa, T.; Erwan, L. R.; Jean, T. C.; Jean-Marie, B., Direct Transformation of Ethylene into Propylene Catalyzed by a Tungsten Hydride Supported on Alumina: Trifunctional Single-Site Catalysis. *Angewandte Chemie International Edition* **2007,** *46* (38), 7202-7205.

10. Alain, S.; Anne, B.; Jean-Marie, B.; Christophe, C., Tuning the Selectivity of Alumina-Supported (CH3)ReO3 by Modifying the Surface Properties of the Support. *Angewandte Chemie International Edition* **2008,** *47* (11), 2117-2120.

11. Tsyganenko, A. A.; Mardilovich, P. P., Structure of alumina surfaces. *Journal of the Chemical Society, Faraday Transactions* **1996,** *92* (23), 4843-4852.

12. Rascón, F.; Wischert, R.; Copéret, C., Molecular nature of support effects in single-site heterogeneous catalysts: silica vs. alumina. *Chemical Science* **2011,** *2* (8), 1449-1456.

13. Thierry, L.; Christian, S.; Clarisse, H.; Gerhard, F.; Francis, T.; Marc, H.; Thierry, B.; Gé rard, F., A Rationale for the Large Breathing of the Porous Aluminum Terephthalate (MIL-53) Upon Hydration. *Chemistry- A European Journal* **2004,** *10* (6), 1373-1382.

14. Lee, T.; Baik, C.; Jung, I.; Song, K. H.; Kim, S.; Kim, D.; Kang, S. O.; Ko, J., Stereoselective Hydroboration of Diynes and Triyne to Give Products Containing Multiple Vinylene Bridges: A Versatile Application to Fluorescent Dyes and Light-Emitting Copolymers. *Organometallics* **2004,** *23* (20), 4569-4575.

15. Neilson, B. M.; Bielawski, C. W., Photoswitchable Metal-Mediated Catalysis: Remotely Tuned Alkene and Alkyne Hydroborations. *Organometallics* **2013,** *32* (10), 3121-3128.

16. Bew, S. P.; Hiatt-Gipson, G. D.; Lovell, J. A.; Poullain, C., Mild reaction conditions for the terminal deuteration of alkynes. *Organic letters* **2012,** *14* (2), 456-459.

17. Lawrence, S. A., *Amines: synthesis, properties and applications*. Cambridge University Press: 2004.

18. Weetman, C.; Anker, M. D.; Arrowsmith, M.; Hill, M. S.; Kociok-Köhn, G.; Liptrot, D. J.; Mahon, M. F., Magnesium-catalysed nitrile hydroboration. *Chemical Science* **2016,** *7* (1), 628-641.

19. Kaithal, A.; Chatterjee, B.; Gunanathan, C., Ruthenium-Catalyzed Selective Hydroboration of Nitriles and Imines. *The Journal of Organic Chemistry* **2016,** *81* (22), 11153-11161.

20. Marciniec, B., *Hydrosilylation: a comprehensive review on recent advances*. Springer Science & Business Media: 2008; Vol. 1.

21. Bhattacharya, P.; Krause, J. A.; Guan, H., Iron Hydride Complexes Bearing Phosphinite-Based Pincer Ligands: Synthesis, Reactivity, and Catalytic Application in Hydrosilylation Reactions. *Organometallics* **2011,** *30* (17), 4720-4729.

22. MacMillan, S. N.; Harman, W. H.; Peters, J. C., Facile Si–H bond activation and hydrosilylation catalysis mediated by a nickel–borane complex. *Chemical Science* **2014,** *5* (2), 590-597.

23. Bezier, D.; Venkanna, G. T.; Castro, L. C. M.; Zheng, J.; Roisnel, T.; Sortais, J. B.; Darcel, C., Iron‐Catalyzed Hydrosilylation of Esters. *Advanced Synthesis & Catalysis* **2012,** *354* (10), 1879-1884.

24. Kovalenko, O. O.; Adolfsson, H., Highly Efficient and Chemoselective Zinc‐Catalyzed Hydrosilylation of Esters under Mild Conditions. *Chemistry- A European Journal* **2015,** *21* (7), 2785-2788.

25. Gephart, R. T.; Warren, T. H., Copper-Catalyzed sp3 C–H Amination. *Organometallics* **2012,** *31* (22), 7728-7752.

26. Roizen, J. L.; Harvey, M. E.; Du Bois, J., Metal-Catalyzed Nitrogen-Atom Transfer Methods for the Oxidation of Aliphatic C–H Bonds. *Accounts of Chemical Research* **2012,** *45* (6), 911-922.

27. Jang, E. S.; McMullin, C. L.; Käß, M.; Meyer, K.; Cundari, T. R.; Warren, T. H., Copper(II) Anilides in sp3 C-H Amination. *Journal of the American Chemical Society* **2014,** *136* (31), 10930-10940.

28. Tran, B. L.; Li, B.; Driess, M.; Hartwig, J. F., Copper-Catalyzed Intermolecular Amidation and Imidation of Unactivated Alkanes. *Journal of the American Chemical Society* **2014,** *136* (6), 2555-2563.

29. Tsuji, J., Synthetic Applications of the Palladium-Catalyzed Oxidation of Olefins to Ketones. *Synthesis* **1984,** *1984* (05), 369-384.

30. Reinhard, J., Acetaldehyde from Ethylene—A Retrospective on the Discovery of the Wacker Process. *Angewandte Chemie International Edition* **2009,** *48* (48), 9034-9037.

31. Jia, D. J.; R., B. W.; L., F. B., Palladium - Catalyzed anti - Markovnikov Oxidation of Terminal Alkenes. *Angewandte Chemie International Edition* **2015,** *54* (3), 734-744.

32. Chaudhari, D. A.; Fernandes, R. A., Hypervalent Iodine as a Terminal Oxidant in Wacker-Type Oxidation of Terminal Olefins to Methyl Ketones. *The Journal of Organic Chemistry* **2016,** *81* (5), 2113-2121.

33. Bill, M.; K., W. Z.; H., G. R., Regioselective Wacker Oxidation of Internal Alkenes: Rapid Access to Functionalized Ketones Facilitated by Cross - Metathesis. *Angewandte Chemie* **2013,** *125* (37), 9933-9936.

34. Liu, B.; Jin, F.; Wang, T.; Yuan, X.; Han, W., Wacker - Type Oxidation Using an Iron Catalyst and Ambient Air: Application to Late - Stage Oxidation of Complex Molecules. *Angewandte Chemie International Edition* **2017,** *56* (41), 12712-12717.

35. Manna, K.; Ji, P.; Lin, Z.; Greene, F. X.; Urban, A.; Thacker, N. C.; Lin, W., Chemoselective single-site Earth-abundant metal catalysts at metal–organic framework nodes. *Nature Communications* **2016,** *7*, 12610.

Chapter 3. Cobalt-bridged SBUs in a Titanium MOF Catalyze Cascade Reduction of N-Heteroarenes

3.1 Introduction

The development and functionalization of Ti-oxo materials is a fertile research area due to their high crust abundance, low toxicity, excellent chemical and thermal stability, and unique photophysical properties. The introduction of permanent porosity into bulk TiO_2 allows efficient utilization of all surface functionalizable sites to ensure sustainable resource utilization.[1-2] For example, surface modifications of mesoporous titania have generated a series of Ti-OH anchored metal species displaying impressive catalytic or photocatalytic activities.[3-4]

Ti metal-organic frameworks (MOFs) provide a highly tuneable platform to realize molecular-level design and construction of single-crystalline and porous Ti-oxo materials that can be further functionalized for catalytic applications.[5-6] However, only a few Ti-carboxylate MOFs have been synthesized and characterized since the report of the first Ti-carboxylate MOF (MIL-125) with $Ti_8O_8(OH)_4$ secondary building units (SBUs) in 2009.[7-12] Ti MOFs with permanent porosity, large channels, and sterically open functionable sites are even rarer.

As one of the most important building blocks in drugs and bioactive alkaloids,[13-14] the synthesis of piperidines has drawn significant interest in the past few decades. Compared to traditional ring-closing pathways, catalytic hydrogenation of pyridines provides an atom-/step-efficient strategy to construct piperidines.[15] However, there has been only a few examples of hydrogenation of pyridines using homogeneous Rh[16] and Ir[17], heterogeneous Rh,[18] Pd,[19] and Co,[20] and metal-free systems,[21] as well as the semi-reduction of pyridines,[22] likely due to strong poisoning effect of pyridines on the catalytic sites. Inspired by our previous success in hydroboration and hydrogenation reactions catalyzed by SBU-supported Co-hydrides, we

envisaged a one-pot cascade reduction pathway to prepare piperidines from pyridines using Ti_3-BPDC-CoH. Pinacolborane (HBpin) was added to the reactions to first dearomatize N-heteroarenes via hydroboration, followed by the hydrogenation of the remaining unsaturated bonds of the hydroborated intermediates.

In this chapter, we report the rational synthesis of a novel porous Ti-carboxylate MOF, Ti_3-BPDC (BPDC = biphenyl-4,4'-dicarboxylate) with unprecedented $Ti_3(OH)_2$ SBUs. Two terminal Ti^{IV}-OH groups in the neighbouring SBUs of Ti_3-BPDC point at each other with a 2 Å distance and act as excellent bidentate ligands to complex Co^{II}-hydride species to provide a sterically open and electronically-rich earth-abundant metal catalyst for the cascade reduction of *N*-heteroarenes to piperidine and 1,2,3,4-tetrahydroquinoline derivatives (**Scheme 3-1**).

Scheme 3-1. Cobalt-bridged SBUs in a Titanium MOF catalyze cascade reduction of *N*-heteroarenes. Copyright 2019 Royal Society of Chemistry.

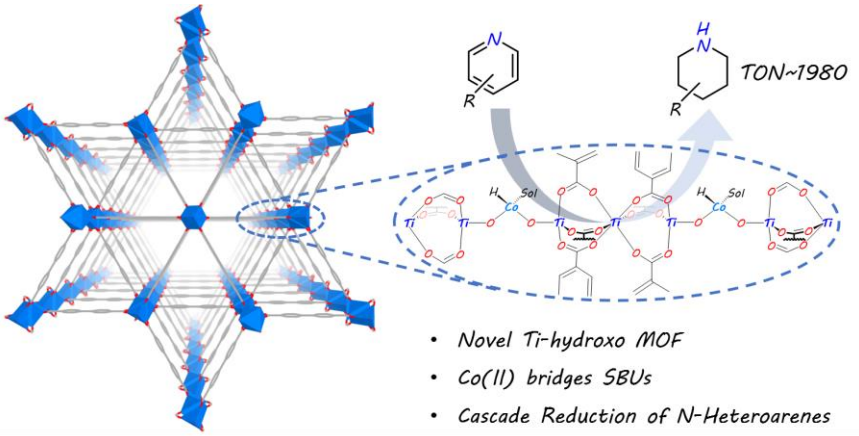

3.2 Results and Discussion

3.2.1 Synthesis and postsynthetic metalation of Ti_3-BPDC

To prevent the formation of amorphous TiO_2, we used $Ti_6O_6(OiPr)_6(abz)_6$ (abz = 4-aminobenzoate) cluster[23] as the Ti source for MOF growth. Colourless rhombic Ti_3-BPDC crystals were obtained in 31% yield via a solvothermal reaction between $Ti_6O_6(OiPr)_6(abz)_6$ and H_2BPDC

in *N*,*N*-dimethylformamide (DMF) at 120 °C for 3 days with acetic acid (HOAc) as modulator (**Figure 3-1b**). Single-crystal X-ray diffraction (SXRD) revealed that Ti_3-BPDC crystallized in the $R\bar{3}m$ space group (CCDC 1859034). Every three Ti atoms are linked by carboxylate groups to form $Ti_3(OH)_2$ SBUs, with the central Ti atom in octahedral coordination with six carboxylate groups and each of the two terminal Ti atoms in tetrahedral coordination with three carboxylate groups and one OH group (**Figure 3-1a**). $Ti_3(OH)_2$ SBUs are connected by six BPDC linkers to afford a 3D framework of *dia* topology with 1D triangle channel of 11 Å in length running along the c axis. The void space was calculated to be 71.9% by PLATON. Diffuse reflectance infrared Fourier transform spectroscopy (DRIFTS) revealed the presence of $\nu_{O\text{-}H}$ stretching band at 3678 cm^{-1} for the terminal Ti^{IV}-OH (**Figure 3-2c**).[24] ^1H NMR analysis of digested Ti_3-BPDC (in D_3PO_4/HF) showed the presence of 1.38 equiv. of HOAc *w.r.t.* H_2BPDC, affording a formula of $[Ti_3(BPDC)_3(OH)_2](OAc)_4$. Powder X-ray diffraction (PXRD) showed that bulk phase and single crystals of Ti_3-BPDC have identical structure (**Figure 3-2b**). Ti_3-BPDC exhibits a type I isotherm with a Brunauer-Emmett-Teller (BET) surface area of 636 m^2/g and a pore size of 11.8 Å (**Figures 3-1d, 3-1e**). To the best of our knowledge, Ti_3-BPDC is the first Ti-MOF based on the BPDC ligand, which provides a potential for further functionalization.[25]

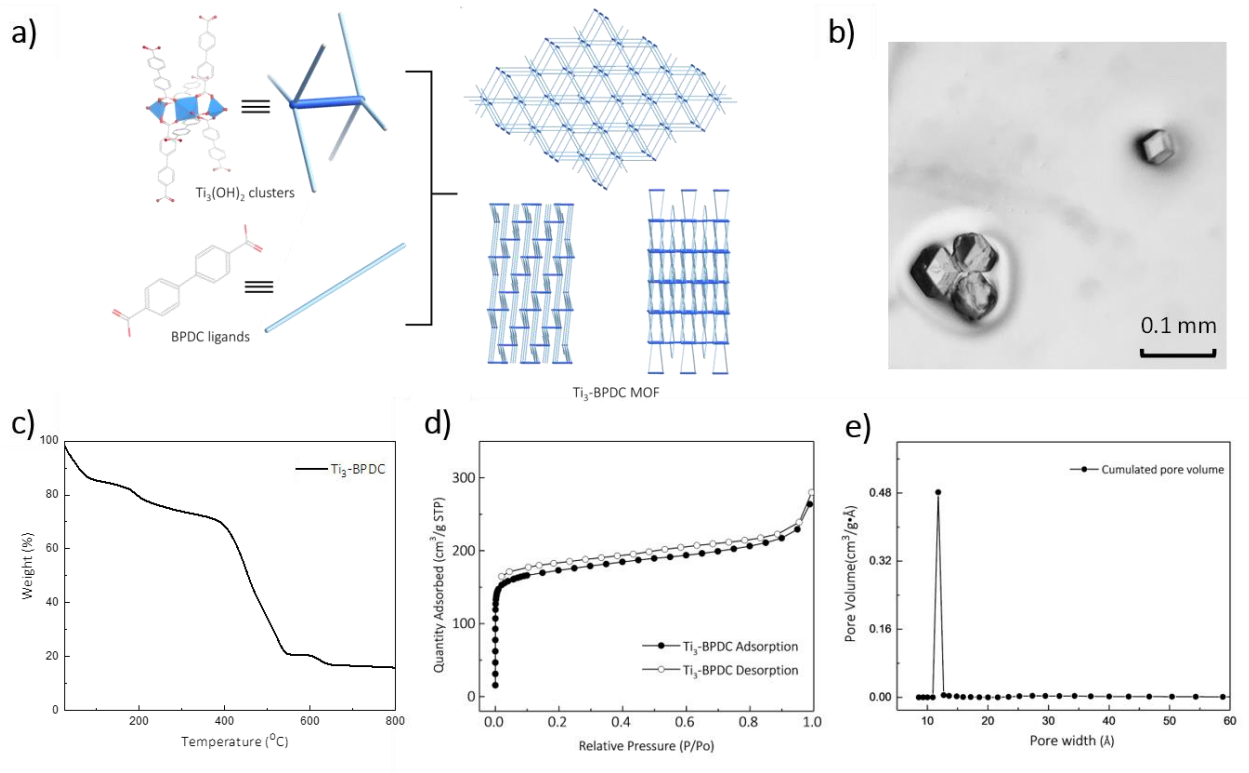

Figure 3-1. Structure and characterization of Ti_3-BPDC MOF. (a) Schematic representation of the 3D network of Ti_3-BPDC with *dia* topology. (b) Optical microscope photo of Ti_3-BPDC single crystals used for X-ray structure determination. (c) TGA weight loss curve of Ti_3-BPDC. (d) Nitrogen sorption isotherms of Ti_3-BPDC (77K) with a BET surface area of 636 m^2/g. (e) Pore size distributions of Ti_3-BPDC. Copyright 2019 Royal Society of Chemistry.

The unique structure of Ti_3-BPDC, particularly the proximity of the neighbouring Ti^{IV}-OH groups, inspired us to use the neighbouring SBUs as bidentate ligands to support Earth-abundant Metal catalysts. We posited that chelation by neighbouring SBUs affords several advantages including stronger coordination from two or more M-O^- groups, more electron-rich active metal site, and more sterically open coordination environment around catalytic centers. Ti_3-BPDC was deprotonated with 5 equiv. of $LiCH_2Si(CH_3)_3$ and then metalated with 1 equiv. of $CoCl_2$ in THF to afford Ti_3-BPDC-CoCl as the purple solid. Both the carboxylate groups and linkers remained intact during the lithiation and metalation process as evidenced by unchanged carbonyl stretching vibrations in the IR spectra. The disappearance of terminal OH groups stretching band (**Figure 3-**

2c) indicated complete deprotonation of Ti^{IV}-OH groups. Inductively coupled plasma-mass spectrometry (ICP-MS) analysis of digested Ti_3-BPDC-CoCl revealed the presence of 0.92 ± 0.04 Co per Ti_3 SBU, indicating nearly complete metalation of all Ti-OH pairs. Crystallinity was maintained after metalation as evidenced in the unchanged PXRD patterns, and SXRD of Ti_3-BPDC-CoCl displayed a nearly identical unit cell parameter to Ti_3-BPDC (**Figure 3-2b**). Extended X-ray absorption fine structure (EXAFS) spectroscopy and density functional theory (DFT) were used to determine the Co coordination environment in Ti_3-BPDC-CoCl. DFT calculation at the B3LYP level of theory converged at a distorted tetrahedral $[(Ti\text{-}O^-)_2CoCl(THF)]^-$ coordination with two oxo groups from the deprotonation of Ti-OH (Co-O^- distances of 1.89 and 1.95 Å), one chloride ion (Co-Cl distance of 2.33 Å), and one THF (Co-O^{THF} distance of 2.06 Å). The calculated model fitted well to the experimental EXAFS data of Ti_3-BPDC-CoCl, which gave Co-(O^{Ti}) distances of 1.86 and 1.93 Å, respectively, with a Co-Cl distance of 2.25 Å, and a Co-O^{THF} distance of 2.03 Å (**Figure 3-2d**).

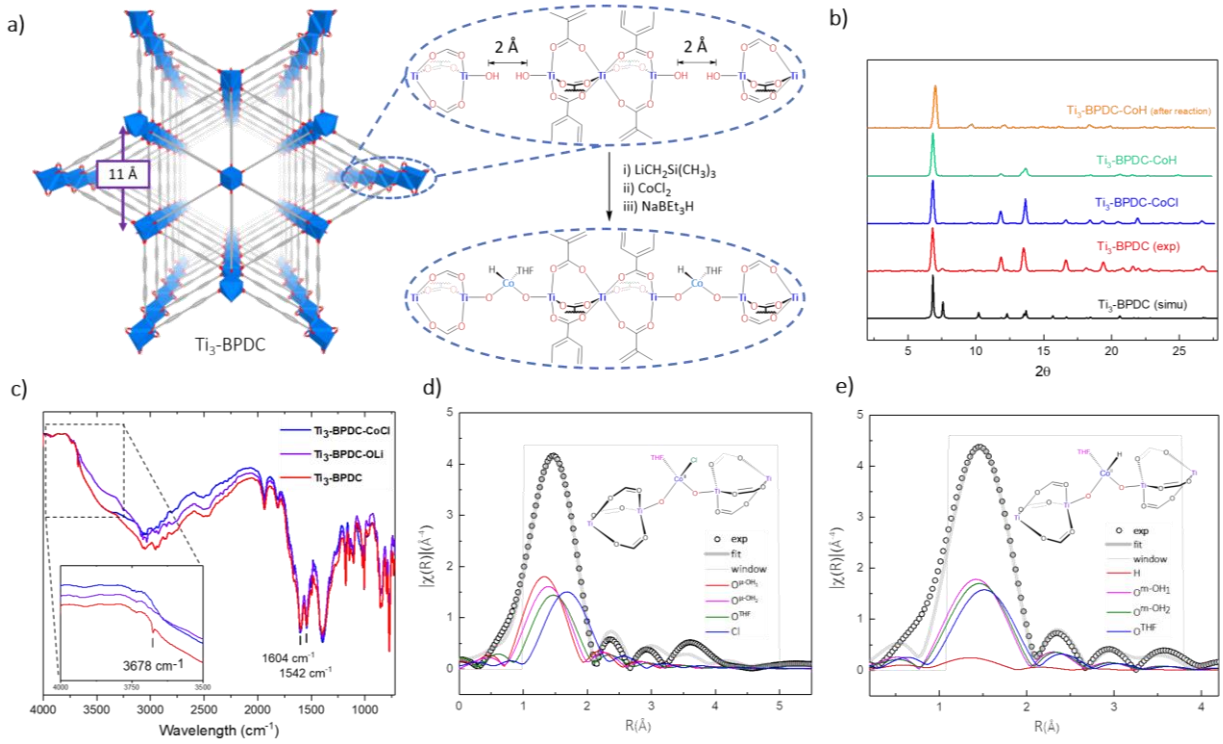

Figure 3-2. Synthesis and characterization of Ti_3-BPDC-Co. (a) Structure and SBU arrangement of Ti_3-BPDC and its conversion to Ti_3-BPDC-CoH. (b) PXRD patterns Ti_3-BPDC (red), Ti_3-BPDC-CoCl (navy), and Ti_3-BPDC-CoH (violet) and after-reaction (orange) along with simulated PXRD based on the SXRD structure (black). (c) DRIFT spectrum of Ti_3-BPDC showing stretching vibration of Ti-OH at 3678 cm^{-1} from $Ti_3(OH)_2$ SBUs. (d,e) EXAFS spectra (black circles) and fits (grey solid line) in R-space at the Co K-edge adsorption of (d) Ti_3-BPDC-CoCl and (e) Ti_3-BPDC-CoH. Copyright 2019 Royal Society of Chemistry.

Treatment of Ti_3-BPDC-CoCl with 10 equiv. of $NaBEt_3H$ in toluene generated Ti_3-BPDC-CoH as a dark blue solid through Cl/H exchange. MOF crystallinity was maintained based on similar PXRD patterns before and after $NaBEt_3H$ treatment (**Figure 3-2b**). X-ray photoelectron spectroscopy (XPS) and X-ray absorption near-edge spectroscopy (XANES) were used to determine the oxidation states of Ti and Co centers in Ti_3-BPDC-CoH. The Co centers exhibited strong $2p_{3/2}$ and $2p_{1/2}$ peaks at 781.1 and 796.8 eV along with $2p_{3/2}$ and $2p_{1/2}$ shake-up peaks at 785.9 and 802.6 eV, consistent with Co^{II} species (**Figure 3-3a**). Ti centers showed strong $2p_{3/2}$ and $2p_{1/2}$ peaks at 458.3 and 464.1 eV, which are characteristic of Ti^{IV} species (**Figure 3-3b**). The Co pre-edge features of Ti_3-BPDC-CoCl and Ti_3-BPDC-CoH are identical to that of $CoCl_2$ (**Figure**

3-3c), confirming the Co^{II} oxidation state before and after hydride activation. Similar Ti pre-edge features were observed for Ti_3-BPDC-CoCl and Ti_3-BPDC-CoH (**Figure 3-3d**), indicating the identical Ti oxidation states. Treatment of Ti_3-BPDC-CoH with excess formic acid generated 0.96 ± 0.04 equiv. of H_2 *w.r.t.* Co, indicating the presence of Co-H species. EXAFS fitting on Ti_3-BPDC-CoH showed that Co centers adopted $[(Ti\text{-}O^-)_2CoH(THF)]^-$ bridging mode with Co-(O^{Ti}) distances of 1.93 Å and 1.96 Å (**Figure 3-2e**) which are similar to those of Ti_3-BPDC-CoCl. Due to the unique site-isolation effect within the MOF structure, such monomeric Co-H species with oxo-based chelating ligands cannot be prepared in homogeneous systems as they have a tendency to oligomerize.

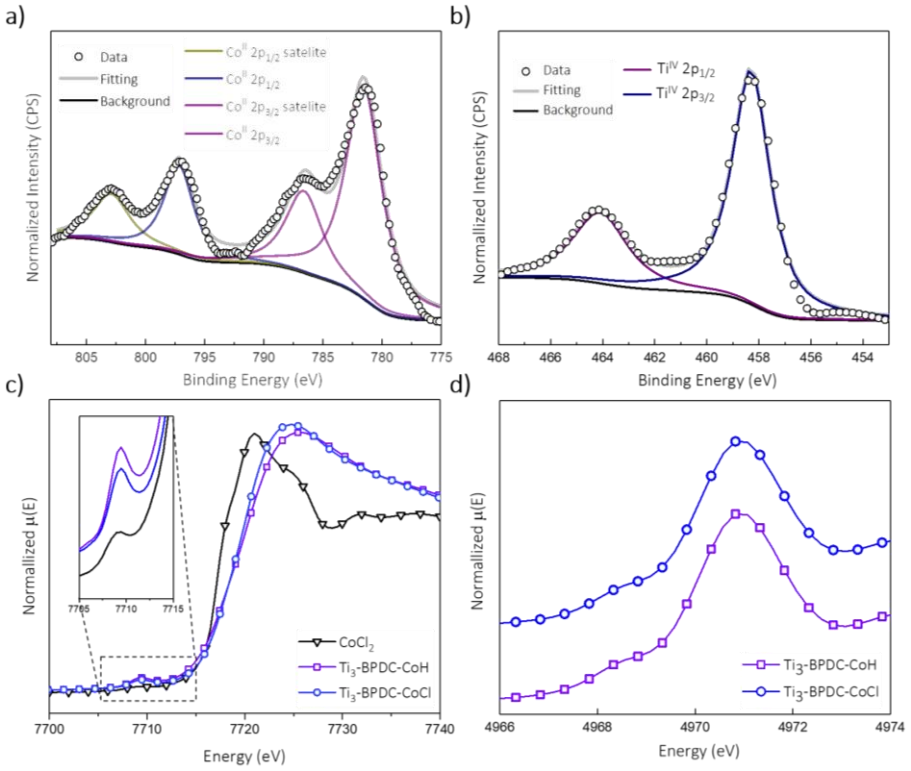

Figure 3-3. Electronic state characterization of Ti_3-BPDC-CoCl before and after the $NaBEt_3H$ treatment. (a) Co 2p XPS spectra of Ti_3-BPDC-CoH and the fitted result indicates the Co^{II} oxidation state after $NaBEt_3H$ treatment. (b) Ti 2p XPS spectra of Ti_3-BPDC-CoH and the fitted result indicates the Ti^{IV} oxidation state after $NaBEt_3H$ treatment. (c) Co pre-edge XANES features of Ti_3-BPDC-CoCl (navy) and Ti_3-BPDC-CoH (violet) in comparison to that of $CoCl_2$ (black). (d) Ti pre-edge XANES features of Ti_3-BPDC-CoCl (navy) and Ti_3-BPDC-CoH (violet). Copyright 2019 Royal Society of Chemistry.

3.2.2 Ti_3-BPDC-CoH catalyzed cascade reduction of pyridines

Table 3-1. Optimization of conditions for Ti_3-BPDC-CoH catalyzed cascade reduction using 3-picoline as substrate.[a]

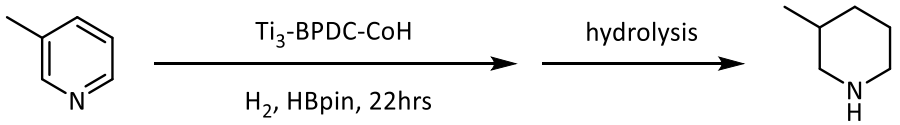

Entry	Cat. Loading / %	Solvent	HBpin equivalent	H_2 pressure / bar	Temp. / °C	Yield / %
1	0.5	Octane	3.00	50	100	>99
2	0.2	Octane	3.00	50	100	>99
3	0.2	Octane	1.05	20	100	97
4	0.2	Octane	0.30	50	100	26
5	0.05	Octane	1.05	20	100	65
6	0.05	Octane	1.05	5	100	2
7	0.2	THF	1.05	20	100	4
8	0.2	Toluene	1.05	20	100	10
9	0.2	Octane	1.05	20	80	0
10	0.2	Octane	1.05	20	120	>99
11[b]	0.05	Octane	1.05	20	100	99
12	0.01	neat	1.05	50	100	0

[a]Reaction conditions: Ti_3-BPDC-CoH (Loading *w.r.t.* Co), 0.5 mmol 3-picoline, 0-3.0 equiv. pinacolborane, 20-50 bar H_2, 1 mL Solvent; Yield was determined by GC-MS analysis, mesitylene as internal standard. [b]Reaction time: 3 days.

Ti_3-BPDC-CoH displayed high catalytic activities in the cascade reduction of pyridines to piperidine derivatives. At 0.2 mol% Ti_3-BPDC-CoH, treatment of 3-picoline with 1.05 equiv. of HBpin in *n*-octane under 20 bar H_2 at 100 °C for 22 h gave 3-methylpiperidine in 97% yield. No obvious change was observed in the PXRD pattern of the MOF recovered from catalytic recation (**Figure 3-2b**), indicating the stability of the MOF framework under reaction condition. Changing *n*-octane to coordinating solvents (*e.g.*, THF) or solvent-free condition led to a dramatic drop in

yields, suggesting the inhibition effect from coordination of the solvent or pyridine substrate (**Table 3-1**). No piperidine product was observed in the absence of MOF, HBpin, or H_2 (**Table 3-3**). An unprecedentedly high turnover number (TON) of 1980 was achieved at 0.05 mol% catalyst loading in 3 days.

Table 3-2. Ti_3-BPDC-CoH catalyzed cascade reduction of pyridines[a]

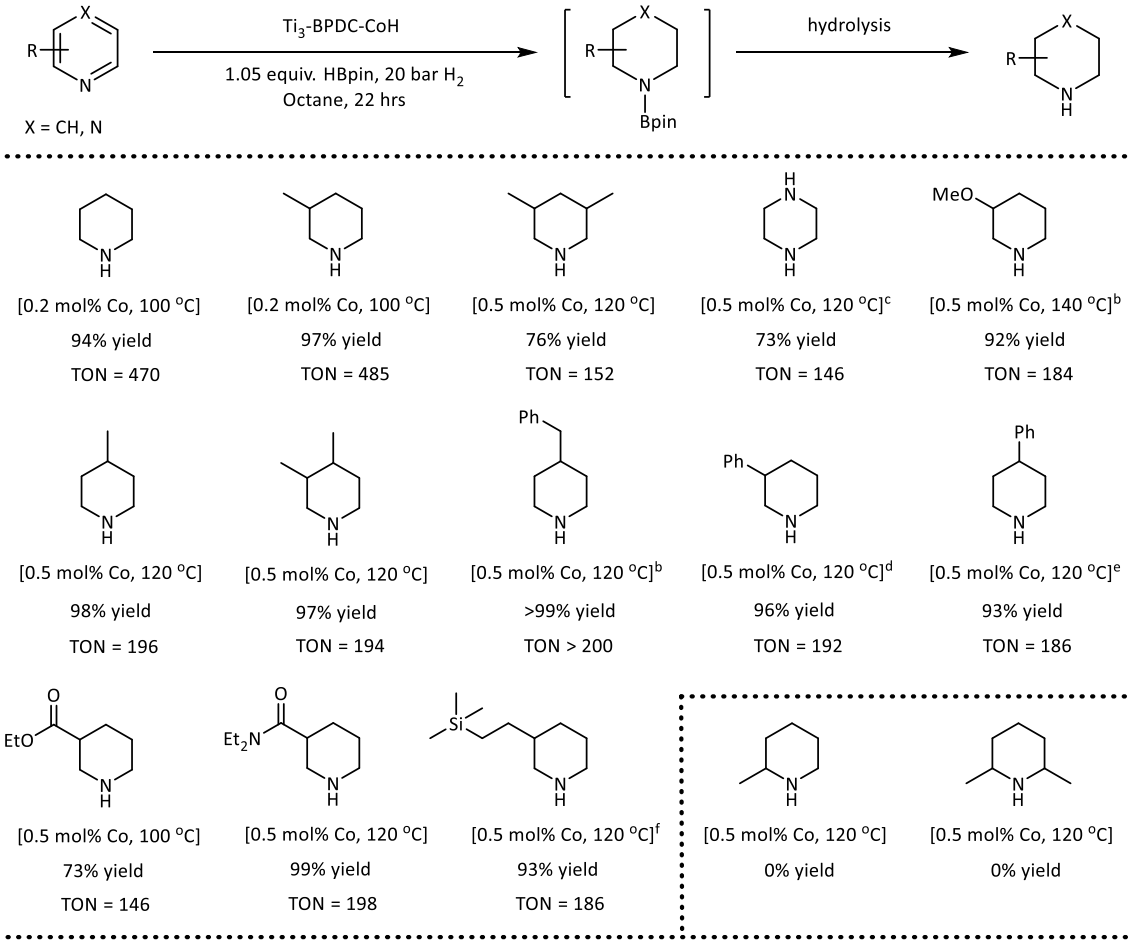

[a] 0.50 mmol pyridine, 0.525 mmol HBpin, 20 bar H_2, 0.2-0.5 mol% of Ti_3-BPDC-CoH, 100-140 °C, 22 h; Yield determined by GC-MS using mesitylene as internal standard. [b] Reaction time: 40 h. [c] 1.05 equiv. HBpin, 35 bar H_2. [d] 3 equiv. HBpin, 50 bar H_2. [e] 3 equiv. HBpin, 35 bar H_2. [f] 3-((Trimethylsilyl)ethynyl)pyridine as substrate, the triple bond was hydrogenated.

At 0.2-0.5 mol% of Co loading, a wide range of pyridines with electron donating or withdrawing groups on 3-, 4-, or 5-positions of the pyridine rings, were all reduced to piperidines

in high yields (73-100%). This cascade reduction reaction also exhibits good functional groups tolerance and outstanding product selectivity. Alkoxy, ester, dialkyl amide, and silyl groups all remained intact during the reduction process. For pyridine substrates containing aromatic rings, *e.g.*, 3/4-phenylpridines and 4-benzylpyridines, the pyridyl rings were selectively reduced without effecting the phenyl rings (**Table 3-2**).

Table 3-3. Background reactions and HBpin/H_2 control experiments for Ti_3-BPDC-CoH catalyzed cascade reduction using 3-picoline as substrate.[a]

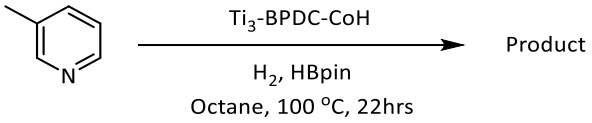

Entry	Cat. Loading / %	HBpin equivalent	H_2 pressure / bar	Product
1	0.5	0	50	>99% of 3-picoline recovered[a]  >99%
2	0	3.00	50	>99% of 3-picoline recovered[a]  >99%
3	2.0	1.50	0	15% of 1,4-hydroborated 3-picoline + 10% of 1,2-hydroborated 3-picoline[b] 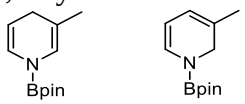 15% 10%

[a]Yield was determined by GC-MS analysis, mesitylene as internal standard. [b]Yield was determined by ^{1}H NMR analysis, mesitylene as internal standard.

Several lines of evidence support the cascade process. First, 2-picoline and 2,6-lutidine showed dramatic activity decrease compared to 3-picoline and 3,5-lutidine, respectively, likely due to the blocking of Co coordination by the methyl group(s) to inhibit the hydroboration step (**Table 3-2**). Second, we detected 25% hydroborated 3-picoline by Ti_3-BPDC-CoH in the absence of H_2, which demonstrates the Co centers could catalyze the hydroboration step (**Table 3-3**). Third, a mixture of 1-(4,4,5,5-tetramethyl-1,3,2-dioxaborolan-2-yl)-1,4-dihydropyridine and 1-(4,4,5,5-

tetramethyl-1,3,2-dioxaborolan-2-yl)-1,2-dihydropyridine[26] were quantitatively converted to piperidine at 0.5 mol% of Ti_3-BPDC-CoH under 20 bar H_2, while no piperidine was observed without the MOF catalyst. Cascade reduction was thus initiated by dearomative hydroboration of pyridines followed by hydrogenation of the remaining unsaturated bonds. Both steps are catalyzed by the Co-H species.

Table 3-4. Control experiments using different catalysts for cascade reduction of 3-picoline.[a]

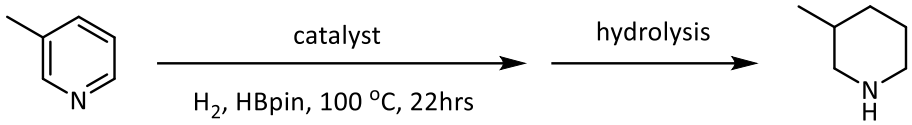

Entry	Cat. Loading / %	Solvent	HBpin equivalent	H_2 pressure / bar	Yield / %
1	0.2 mol% Ti_3-BPDC-CoH	Octane	1.05	20	97
2[b]	0.2 mol% Ti_3-BPDC-CoCl	Octane	1.05	20	0
3[c]	0.6 mol% Ti_3-BPDC	Octane	1.05	20	0
4[d]	0.2 mol% Co-NPs	Octane	1.05	20	0
5[e]	2 mol% $NaBEt_3H$	Octane	1.05	20	0

[a]Reaction conditions: Ti_3-BPDC-CoH (1 μmol Co) or other catalyst, 0.5 mmol 3-picoline, 0.525 mmol pinacolborane, 20 bar H_2, 1 mL Octane, 100 °C, 22 hrs; Yield was determined by GC-MS analysis, mesitylene as internal standard. [b]Ti_3-BPDC-CoCl (1 μmol Co), as prepared above, was used as catalyst without further treatment. [c]Ti_3-BPDC (3 μmol Ti), as prepared above, was used as catalyst without further treatment. [d]Co-NPs (1 μmol Co, black solid), generated by treating 1 μmol $CoCl_2$ (20 mM in THF) with 10 equiv. of $NaBEt_3H$ for 1 hour and washed 3 times with toluene, was used as catalyst. [c]$NaBEt_3H$ (10 μmol, 1.0 M in Hexane) was used as catalyst without further treatment.

Ti_3-BPDC-CoH was recovered and reused at least 6 times without significant decrease in yields (Yield of 1st to 6th run: 100%, 100%. 99%. 97%, 100%, 93%). ICP-MS showed minimal

leaching of Co and Ti (0.4% and 0.6%, respectively). Hot filtration experiment ruled out the possibility of leached Co species contributing to the cascade reduction reactivity. Additionally, neither Co nanoparticles nor $NaBEt_3H$ afforded any product to the cascade reduction of 3-picoline (**Table 3-4**).

3.2.3 Ti_3-BPDC-CoH catalyzed cascade reduction of quinolines

We then applied this cascade protocol to dearomatize other N-heteroarenes. Semi-hydrogenation of quinolines is the most straightforward and convenient way to synthesize 1,2,3,4-tetrahydroquinolines (1,2,3,4-THQLs), which have broad applications in pharmaceuticals and agrochemicals.[27] Although several catalysts have been reported for such semi-hydrogenation reactions[28-30], challenges still exist in terms of product selectivity and functional group tolerance. Ti_3-BPDC-CoH catalyzed semi-hydrogenation of quinolines to generate 1,2,3,4-THQLs with excellent selectivity and functional group tolerance via the cascade reduction process (**Table 3-5**). At 0.2 mol% catalyst loading and 100 °C, 1,2,3,4-THQL was generated in >99% yield with <1% of 5,6,7,8-THQL by-product. Quinolines with methyl groups on different positions (3-,4-,6-,7-) and with different functional groups (Cl, OMe, COOMe) as well as quinoxaline were all semi-hydrogenated to 1,2,3,4-THQLs in >84% yields and good selectivities. No conversion was detected for 2,6-dimethylquinoline due to the inhibition of substrate coordination to the Co center.

Table 3-5. Ti_3-BPDC-CoH catalyzed selective reduction of quinolines[a]

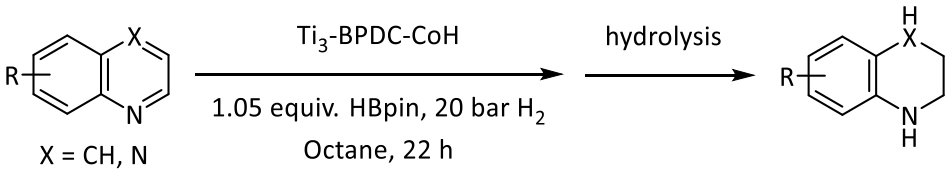

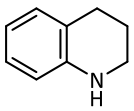	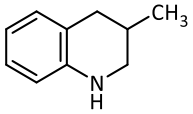	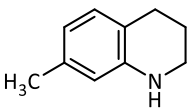	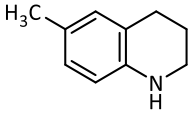	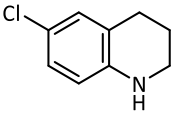
[0.2 mol% Co, 100 °C]	[0.2 mol% Co, 100 °C]	[0.5 mol% Co, 100 °C]	[0.5 mol% Co, 100 °C]	[0.2 mol% Co, 140 °C]
>99% yield	96% yield	>99% yield	98% yield	98% yield
(>100:1)	(24:1)	(pure 1,2,3,4-4HQL)	(pure 1,2,3,4-4HQL)	(pure 1,2,3,4-4HQL)
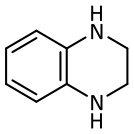	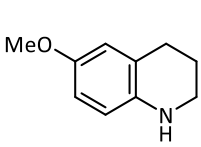	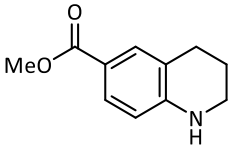	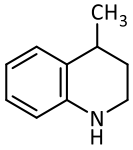	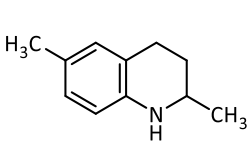
[0.5 mol% Co, 120 °C][b]	[0.5 mol% Co, 100 °C]	[0.5 mol% Co, 140 °C]	[0.5 mol% Co, 140 °C]	[0.5 mol% Co, 100 °C]
95% yield	92% yield	98% yield	84% yield	0% yield
(19:1)	(11:1)	(49:1)	(6:1)	(N.A.)

[a]0.50 mmol quinoline, 0.525 mmol HBpin, 20 bar H_2, 0.2-0.5 mol% of Ti_3-BPDC-CoH, 100-140 °C, 22 h; Yield determined by GC-MS using mesitylene as internal standard. [b]1.05 equiv. HBpin, 50 bar H_2. [c]3 equiv. HBpin, 20 bar H_2.

3.3 Conclusion

We have synthesized a novel single-crystalline Ti-carboxylate MOF with permanent porosity and large 1D channels based on unique $Ti_3(OH)_2$ SBUs and BPDC linkers. Each pair of closely spaced Ti^{IV}-OH groups from neighbouring SBUs are deprotonated and then chelate to Co^{II} centers. Such SBU-supported Co^{II}-hydride species is highly active for selective cascade reduction of *N*-heterocyclic rings of pyridines and quinolines: heteroarenes first undergo dearomative hydroboration followed by hydrogenation of the remaining unsaturated bonds to afford synthetically useful piperidines and 1,2,3,4-tetrahydroquinolines with excellent activity and chemoselectivity. This work expands the applications of MOFs in developing single-site solid

catalysts by using neighbouring SBUs to support Earth-abundant Metal complexes and highlights the great potential of MOF catalysts in fine chemical synthesis.

3.4 Experimental Section

3.4.1 Materials and methods

All the reactions and manipulations were carried out under N_2 with the use of a glovebox or Schlenk technique, unless otherwise indicated. Tetrahydrofuran and toluene were purified by passing through a neutral alumina column under N_2. Benzene, d_6-benzene, and *n*-octane were distilled over CaH_2. Pyridine and quinoline derivatives were purchased from Fisher or Aldrich, distilled, and then dried over 4Å molecular sieves prior to use. Pinacolborane was purchased from Sigma-Aldrich and distilled before use. Powder X-ray diffraction (PXRD) data was collected on Bruker D8 Venture diffractometer using Cu K radiation source (l = 1.54178 Å). N_2 sorption experiments were performed on a Micrometrics TriStar II 3020 instrument. Thermogravimetric analysis (TGA) was performed in air using a Shimazu TGA-50 equipped with a platinum pan and heated at a rate of 1.5 $^{\circ}$C per min. Fourier-transform infrared (FT-IR) spectra were collected using a Nexus 870 spectrometer (Thermo Nicolet) installed with Diffuse Reflectance Infrared Fourier Transform Spectroscopy (DRIFTS) system. X-ray Fluorescence (XRF) data was collected using a Rigaku NEX DE Energy Dispersive X-ray Fluorescence Spectrometer. X-ray photoelectron spectroscopy (XPS) data was collected using an AXIS Nova spectrometer (Kratos Analytical) with monochromatic Al Kα X-ray source; Al anode was powered at 10 mA and 15 kV, and the instrument work function was calibrated to give an Au $4f_{7/2}$ metallic gold binding energy (BE) of 83.95 eV. Instrument base pressure was ca. 1×10^{-9} Torr. The analysis area size was 0.3×0.7 mm^2. For calibration purposes, the binding energies were referenced to the C 1s peak at 284.8 eV. Survey spectra were collected with a step size of 1 eV and 160 eV pass energy. ICP-MS data was obtained

with an Agilent 7700x ICP-MS and analyzed using ICP-MS MassHunter version B01.03. Samples were diluted in a 2% HNO_3 matrix and analyzed with a ^{159}Tb internal standard against a 12-point standard curve over the range from 0.1 ppb to 500 ppb. The correlation was >0.9997 for all analyses of interest. Data collection was performed in Spectrum Mode with five replicates per sample and 100 sweeps per replicate.

^1H NMR spectra were recorded on a Bruker NMR 500 DRX spectrometer at 500 MHz and referenced to the proton resonance resulting from incomplete deuteration of $CDCl_3$ (δ 7.26) or C_6D_6 (δ 7.16). The following abbreviations are used herein: s: singlet, d: doublet, t: triplet, q: quartet, m: multiplet, br: broad, app: apparent. The conversions of reactions were determined by gas chromatography-mass spectrometry (GC-MS) using a Shimadzu GCMS-QP2010 Ulta equipped with SH-Rxi-5Sil MS 30 m × 0.5 mm × 0.25 μm column. GC conditions: Injection temperature, 220 °C; Column temperature program, 30 °C hold for 5 min, followed by a ramp of 5 °C/min to 60 °C then a ramp of 20 °C/min to 300 °C; Column flow, 1.21 mL/min.

3.4.2 Synthetic procedures of MOF catalysts

Synthesis of Ti_3-BPDC: $Ti_6O_6(O^iPr)_6(abz)_6$ cluster (1 mg), biphenyl-4,4'-dicarboxylic acid (3.74 mg), glacial acetic acid (15 μL), and DMF (1 mL) were charged in a 4 mL Pyrex vial. The mixture was heated in a 120 °C oven for 3 days. After cooling to room temperature, colorless transparent, rhombic crystals of the formula $Ti_3(BPDC)_3(OH)_2(CH_3COO)_4$ (Ti_3-BPDC) was harvested (0.5 mg, 31% yield). The PXRD pattern of the obtained MOF was compared to that of a simulated pattern based on the single-crystal structure to show the crystallinity and phase purity of the Ti_3-BPDC. No obvious TiO_2 peaks were observed.

Synthesis of Ti_3-BPDC-CoCl: In a N_2-filled glovebox, Ti_3-BPDC (200 mg) in 15 mL THF was cooled to -30 °C for 30 min. To the cold suspension, $LiCH_2SiMe_3$ (1.0 M in pentane, 2 ml, 5

equiv. to μ-OH) was added dropwise and the resultant light-yellow mixture was stirred at -30 °C for 3 h. The light-yellow solid was collected after centrifugation and washed with THF 5-6 times over 6 h. Then, the lithiated Ti_3-BPDC was transferred to a vial containing 20 mL THF solution of $CoCl_2$ (52 mg, 1 equiv. to μ-OLi). The mixture was stirred overnight, and the deep blue solid was then centrifuged and washed with THF 5-8 times. The metalated MOF was stored in THF in the glovebox for further use. ICP-MS analysis indicated a Ti/Co ratio of 3.1. PXRD showed the crystallinity of MOF was maintained after metalation.

Synthesis of Ti_3-BPDC-CoH: In a glovebox, Ti_3-BPDC-CoCl (5 μmol Co) in 1 mL toluene was dropwisely added $NaBEt_3H$ (1.0 M in toluene, 0.05 ml, 10 equiv. to μ-OCoCl). The color of the suspension immediately changed from deep blue to black. After stirring at room temperature for 3 h, a black solid was collected after centrifugation and washed with toluene three times.

3.4.3 Catalytic reaction setup and product characterization

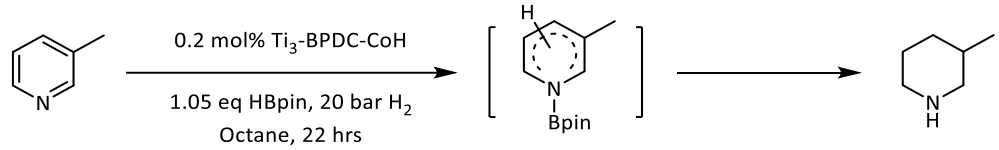

Typical procedure for Ti_3-BPDC-CoH catalyzed cascade reduction of pyridines: In a nitrogen-filled glovebox, Ti_3-BPDC-CoCl (2.0 mg, 1.0 μmol Co) in 1.0 mL toluene was charged into a glass vial. $NaBEt_3H$ (10 μL, 1.0 M in Toluene) was added to the vial and the mixture was stirred for 1 hour. The solid was then centrifuged, washed with toluene three times, and washed with octane twice, before being transferred into a Parr reactor with 1 mL octane. 3-Picoline (49 μL, 0.50 mmol) and pinacolborane (77 μL, 0.525 mmol) was then added to the solution. The Parr reactor was sealed under nitrogen and charged with hydrogen to 20 bars. After stirring at 100 °C for 22 hours, the pressure was released, and the MOF catalyst was removed from the reaction mixture via centrifugation. After being quenched with 2 drops of methanol, the supernatant was

analyzed by GC-MS to give 3-methylpiperidine in 97% yield. 0.4% of Co leaching was determine by ICP-MS analysis of the organic extract from the reaction mixture, indicating minimal MOF decomposition during catalysis.

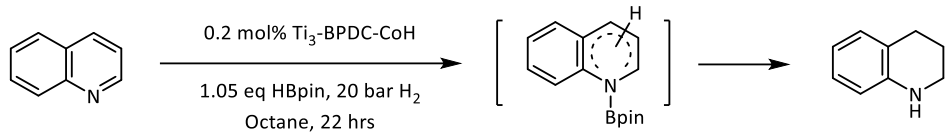

Typical procedure for Ti_3-BPDC-CoH catalyzed selective reduction of quinolines: In a nitrogen-filled glovebox, Ti_3-BPDC-CoCl (2.0 mg, 1.0 μmol Co) in 1.0 mL toluene was charged into a glass vial. $NaBEt_3H$ (10 μL, 1.0 M in toluene) was added to the vial and the mixture was stirred for 1 hour. The solid was then centrifuged, washed with toluene three times, and washed with octane twice, before being transferred into a Parr reactor with 1 mL octane. Quinoline (59 μL, 0.50 mmol) and pinacolborane (77 μL, 0.525 mmol) were then added to the solution. The Parr reactor was sealed under nitrogen and charged with hydrogen to 20 bars. After stirring at 100 °C for 22 hours, the pressure was released, and the MOF catalyst was removed from the reaction mixture via centrifugation. After being quenched with 2 drops of methanol, the supernatant was analyzed by GC-MS to selectively give 1,2,3,4-tetrahydroquinoline in 98% yield along with a trace amount (< 2%) of 5,6,7,8-tetrahydroquinoline and decahydroquinoline.

Table 3-6. The retention times of GC traces I (some compounds have multiple stereoisomers, thus showing more than one peak with the expected molecular mass).

Compound	Retention Time	Compound	Retention Time
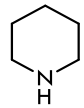	5.271 min	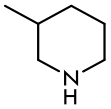	8.037 min
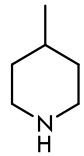	7.851 min	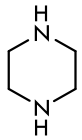	9.133 min
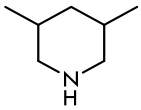	10.445 min; 10.755 min	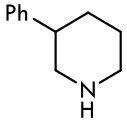	17.514 min
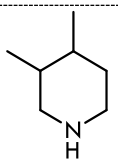	11.055 min; 11.700 min	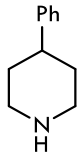	17.499 min
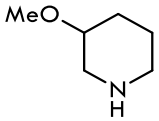	12.591 min	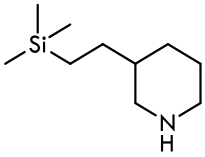	16.319 min
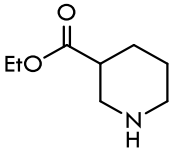	15.852 min	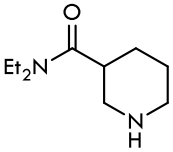	18.208 min
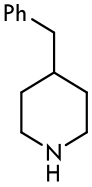	18.104 min	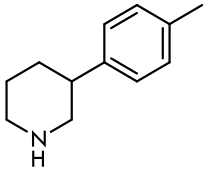	N.D.
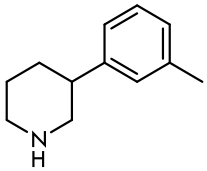	18.179 min	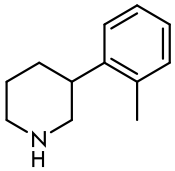	18.199 min

Table 3-7. The retention times of GC traces II.

Compound	Retention Time	Compound	Retention Time
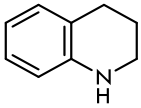	16.735 min	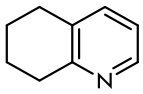	15.870 min
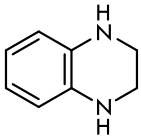	17.938 min	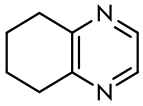	15.750 min
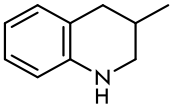	17.140 min	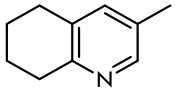	16.811 min
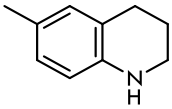	17.471 min	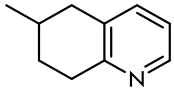	N.D.
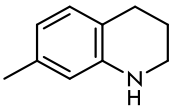	17.572 min	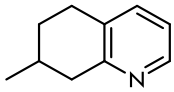	N.D.
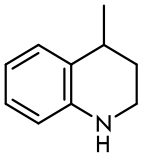	17.208 min	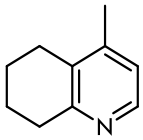	17.008 min
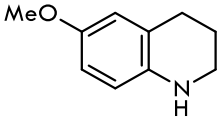	18.438 min	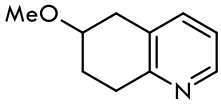	17.309 min
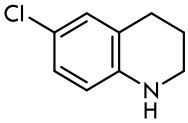	18.503 min	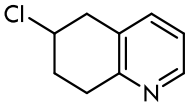	N.D.
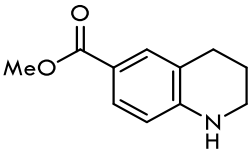	20.363 min	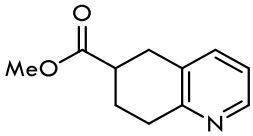	18.532 min
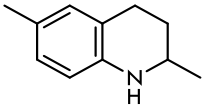	N.D.	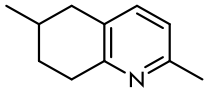	N.D.

3.5 References

1. Zhou, W.; Fu, H., Mesoporous TiO2: Preparation, Doping, and as a Composite for Photocatalysis. *ChemCatChem* **2013,** *5* (4), 885-894.

2. Li, W.; Wu, Z.; Wang, J.; Elzatahry, A. A.; Zhao, D., A Perspective on Mesoporous TiO2 Materials. *Chemistry of Materials* **2014,** *26* (1), 287-298.

3. Lakadamyali, F.; Reynal, A.; Kato, M.; Durrant, J. R.; Reisner, E., Electron Transfer in Dye-Sensitised Semiconductors Modified with Molecular Cobalt Catalysts: Photoreduction of Aqueous Protons. *Chemistry- A European Journal* **2012,** *18* (48), 15464-15475.

4. Kennedy, G.; Baker, L. R.; Somorjai, G. A., Selective Amplification of C O Bond Hydrogenation on Pt/TiO2: Catalytic Reaction and Sum-Frequency Generation Vibrational Spectroscopy Studies of Crotonaldehyde Hydrogenation. *Angewandte Chemie International Edition* **2014,** *53* (13), 3405-3408.

5. Nguyen, H. L., The chemistry of titanium-based metal–organic frameworks. *New Journal of Chemistry* **2017,** *41* (23), 14030-14043.

6. Yuan, S.; Qin, J.-S.; Lollar, C. T.; Zhou, H.-C., Stable Metal–Organic Frameworks with Group 4 Metals: Current Status and Trends. *ACS Central Science* **2018,** *4* (4), 440-450.

7. Dan-Hardi, M.; Serre, C.; Frot, T.; Rozes, L.; Maurin, G.; Sanchez, C.; Férey, G., A New Photoactive Crystalline Highly Porous Titanium(IV) Dicarboxylate. *Journal of the American Chemical Society* **2009,** *131* (31), 10857-10859.

8. Yuan, S.; Liu, T.-F.; Feng, D.; Tian, J.; Wang, K.; Qin, J.; Zhang, Q.; Chen, Y.-P.; Bosch, M.; Zou, L.; Teat, S. J.; Dalgarno, S. J.; Zhou, H.-C., A single crystalline porphyrinic titanium metal–organic framework. *Chemical Science* **2015,** *6* (7), 3926-3930.

9. Mason, J. A.; Darago, L. E.; Lukens, W. W.; Long, J. R., Synthesis and O2 Reactivity of a Titanium(III) Metal–Organic Framework. *Inorganic Chemistry* **2015,** *54* (20), 10096-10104.

10. Nguyen, H. L.; Gándara, F.; Furukawa, H.; Doan, T. L. H.; Cordova, K. E.; Yaghi, O. M., A Titanium–Organic Framework as an Exemplar of Combining the Chemistry of Metal– and Covalent–Organic Frameworks. *Journal of the American Chemical Society* **2016,** *138* (13), 4330-4333.

11. Nguyen, H. L.; Vu, T. T.; Le, D.; Doan, T. L. H.; Nguyen, V. Q.; Phan, N. T. S., A Titanium–Organic Framework: Engineering of the Band-Gap Energy for Photocatalytic Property Enhancement. *ACS Catalysis* **2017,** *7* (1), 338-342.

12. Wang, S.; Kitao, T.; Guillou, N.; Wahiduzzaman, M.; Martineau-Corcos, C.; Nouar, F.; Tissot, A.; Binet, L.; Ramsahye, N.; Devautour-Vinot, S.; Kitagawa, S.; Seki, S.; Tsutsui, Y.; Briois, V.; Steunou, N.; Maurin, G.; Uemura, T.; Serre, C., A phase transformable ultrastable titanium-carboxylate framework for photoconduction. *Nature Communications* **2018,** *9* (1), 1660.

13. Källström, S.; Leino, R., Synthesis of pharmaceutically active compounds containing a disubstituted piperidine framework. *Bioorganic & Medicinal Chemistry* **2008,** *16* (2), 601-635.

14. Vitaku, E.; Smith, D. T.; Njardarson, J. T., Analysis of the Structural Diversity, Substitution Patterns, and Frequency of Nitrogen Heterocycles among U.S. FDA Approved Pharmaceuticals. *Journal of Medicinal Chemistry* **2014,** *57* (24), 10257-10274.

15. Vardanyan, R., Chapter 1 - Introduction. In *Piperidine-Based Drug Discovery*, Vardanyan, R., Ed. Elsevier: 2017; pp 1-82.

16. Baralt, E.; Smith, S. J.; Hurwitz, J.; Horvath, I. T.; Fish, R. H., Homogeneous catalytic hydrogenation. 6. Synthetic and mechanistic aspects of the regioselective reductions of model coal nitrogen, sulfur, and oxygen heteroaromatic compounds using the (.eta.5-pentamethylcyclopentadienyl)rhodium tris(acetonitrile) dication complex as the catalyst precursor. *Journal of the American Chemical Society* **1992,** *114* (13), 5187-5196.

17. Wang, X.-B.; Zeng, W.; Zhou, Y.-G., Iridium-catalyzed asymmetric hydrogenation of pyridine derivatives, 7,8-dihydro-quinolin-5(6H)-ones. *Tetrahedron Letters* **2008,** *49* (33), 4922-4924.

18. Freifelder, M.; Robinson, R. M.; Stone, G. R., Hydrogenation of Substituted Pyridines with Rhodium on Carbon Catalyst1. *The Journal of Organic Chemistry* **1962,** *27* (1), 284-286.

19. Glorius, F.; Spielkamp, N.; Holle, S.; Goddard, R.; Lehmann, C. W., Efficient Asymmetric Hydrogenation of Pyridines. *Angewandte Chemie International Edition* **2004,** *43* (21), 2850-2852.

20. Chen, F.; Li, W.; Sahoo, B.; Kreyenschulte, C.; Agostini, G.; Lund, H.; Junge, K.; Beller, M., Hydrogenation of Pyridines using a Nitrogen-Modified Titania Supported Cobalt Catalyst. *Angewandte Chemie International Edition* **2018**, doi:10.1002/anie.201803426.

21. Liu, Z.-Y.; Wen, Z.-H.; Wang, X.-C., B(C6F5)3-Catalyzed Cascade Reduction of Pyridines. *Angewandte Chemie International Edition* **2017,** *56* (21), 5817-5820.

22. Dudnik, A. S.; Weidner, V. L.; Motta, A.; Delferro, M.; Marks, T. J., Atom-efficient regioselective 1,2-dearomatization of functionalized pyridines by an earth-abundant organolanthanide catalyst. *Nature Chemistry* **2014,** *6*, 1100.

23. Hong, K.; Chun, H., Nonporous Titanium–Oxo Molecular Clusters That Reversibly and Selectively Adsorb Carbon Dioxide. *Inorganic Chemistry* **2013,** *52* (17), 9705-9707.

24. Topsøe, N.-Y., Characterization of the nature of surface sites on vanadia-titania catalysts by FTIR. *Journal of Catalysis* **1991,** *128* (2), 499-511.

25. Song, Y.; Li, Z.; Zhu, Y.; Feng, X.; Chen, J. S.; Kaufmann, M.; Wang, C.; Lin, W., Titanium Hydroxide Secondary Building Units in Metal–Organic Frameworks Catalyze Hydrogen Evolution under Visible Light. *Journal of the American Chemical Society* **2019,** *141* (31), 12219-12223.

26. Ji, P.; Feng, X.; Veroneau, S. S.; Song, Y.; Lin, W., Trivalent Zirconium and Hafnium Metal–Organic Frameworks for Catalytic 1,4-Dearomative Additions of Pyridines and Quinolines. *Journal of the American Chemical Society* **2017,** *139* (44), 15600-15603.

27. Sridharan, V.; Suryavanshi, P. A.; Menéndez, J. C., Advances in the Chemistry of Tetrahydroquinolines. *Chemical Reviews* **2011,** *111* (11), 7157-7259.

28. Beckers, N. A.; Huynh, S.; Zhang, X.; Luber, E. J.; Buriak, J. M., Screening of Heterogeneous Multimetallic Nanoparticle Catalysts Supported on Metal Oxides for Mono-, Poly-, and Heteroaromatic Hydrogenation Activity. *ACS Catalysis* **2012,** *2* (8), 1524-1534.

29. Chen, F.; Surkus, A.-E.; He, L.; Pohl, M.-M.; Radnik, J.; Topf, C.; Junge, K.; Beller, M., Selective Catalytic Hydrogenation of Heteroarenes with N-Graphene-Modified Cobalt Nanoparticles (Co3O4–Co/NGr@α-Al2O3). *Journal of the American Chemical Society* **2015,** *137* (36), 11718-11724.

30. Sorribes, I.; Liu, L.; Doménech-Carbó, A.; Corma, A., Nanolayered Cobalt–Molybdenum Sulfides as Highly Chemo- and Regioselective Catalysts for the Hydrogenation of Quinoline Derivatives. *ACS Catalysis* **2018,** *8* (5), 4545-4557.

Chapter 4. Rational Construction of an Artificial Binuclear Copper Monooxygenase in MOF Secondary Building Unit

4.1 Introduction

Natural enzymes have evolved over millions of years to provide extremely powerful catalysts towards a variety of reactions with excellent activities under mild conditions and exquisite substrate specificity and product selectivity.[1-3] However, the practical use of natural enzymes in synthetic chemistry faces many challenges, including long-term stability, sensitivity to reaction conditions, and the difficulty in enzyme recovery and reuse.[4-5] Artificial enzymes with active metal or organic cofactors have been constructed to mimic the catalytic functions of natural enzymes,[6-10] showing promise in many catalytic transformations.[11-12] In-depth studies of these biomimetic artificial systems have in turn provided important insights into natural enzymes.

Among the diverse family of natural enzymes, monooxygenases (EC 1.13.x.x and EC 1.14.x.x) insert one oxygen atom from molecular oxygen (O_2) into organic substrates.[13-14] Monooxygenases with heme-, flavin-, copper-, non-heme iron-, or other cofactors efficiently catalyze a wide range of important oxidative processes, including hydroxylation, epoxidation, Baeyer-Villiger oxidation, sulfoxidation, and others.[15-17] In particular, natural monooxygenases with multi-centered cofactors such as soluble methane monooxygenase (Fe-Fe),[18] catechol oxidase (Cu-Cu),[19] and tyrosinase (Cu-Cu)[20] efficiently undergo multielectron processes through redox cooperativity to activate O_2 and oxidize organic substrates. Owing to the importance of direct activation of O_2 as a sustainable and cheap oxidant,[21-22] many artificial monooxygenases with heme- or flavin-derived cofactors have been developed but exhibit modest catalytic activity and substrate/product selectivity. In contrast, few artificial monooxygenases with binuclear cofactors have been studied and they exhibited limited catalytic activities.[22-26] We hypothesized that artificial

binuclear monooxygenases with well-defined active sites and high monooxygenation activities can be rationally designed based on crystalline and porous MOFs by taking advantage of recent advances in MOF biomimicry (**Figure 4-1**).[27-31]

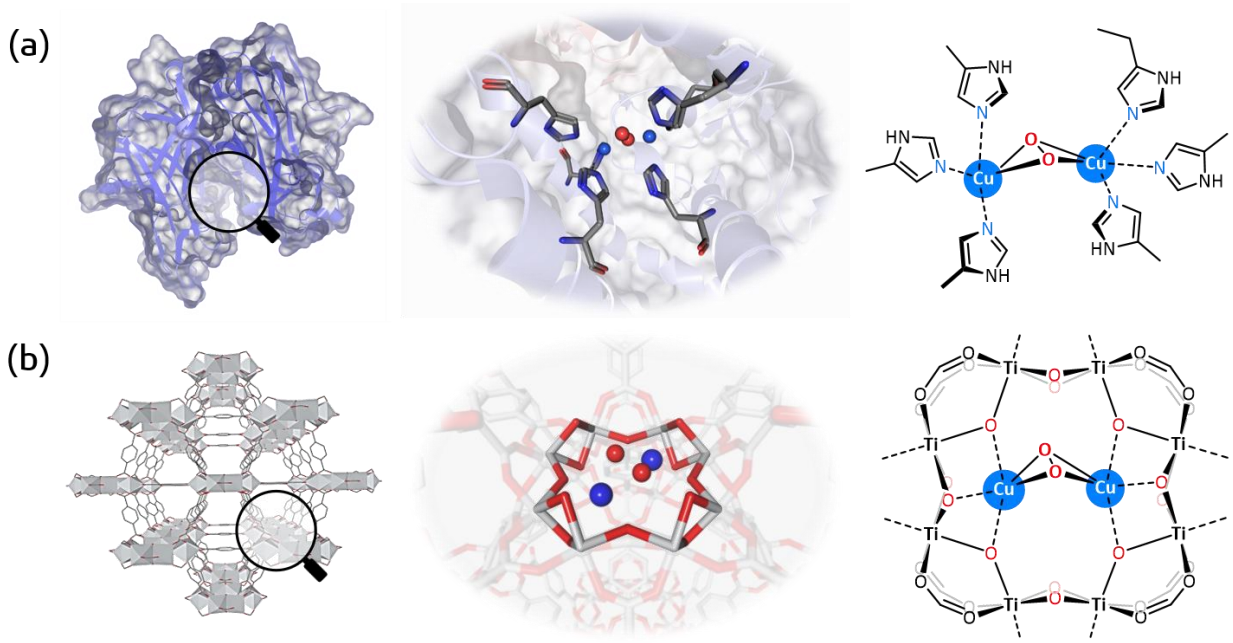

Figure 4-1. Schematic showing Cu_2 active sites with O_2 bonding in (a) the natural enzyme tyrosinase (PDB code: 1WX2) and (b) the MOF-based artificial enzyme **Ti_8-Cu_2** (this work). Copyright 2021 American Chemical Society.

Constructed from metal-oxo secondary building units (SBUs) and organic linkers, MOFs have been used to precisely install molecular functionalities with good spatial control.[32-36] The uniform SBUs of MOFs allow the installation of molecularly precise mono- or multi-metallic species as efficient cofactors,[37-41] while the uniform MOF pores and channels provide structurally-defined microenvironments to confer substrate/product selectivities.[42-44] In this chapter, we report the rational design of a binuclear copper cofactor in a Ti-MOF (MIL-125) as an efficient artificial monooxygenase for the first time (**Scheme 4-1**). The MOF-based artificial enzyme, **Ti_8-Cu_2**, displayed outstanding catalytic activity with turnover numbers (TONs) of up to 3450 towards a wide range of important monooxygenation processes, including epoxidation, hydroxylation,

Baeyer-Villiger oxidation, and sulfoxidation. **Ti_8-Cu_2** showed excellent stability and could be readily recycled and reused. Spectroscopic studies and computational results revealed the vital role of cooperativity between binuclear Cu centers in the O_2 activation process.

Scheme 4-1. Rational construction of an artificial binuclear copper monooxygenase in a MOF SBU. Copyright 2021 American Chemical Society.

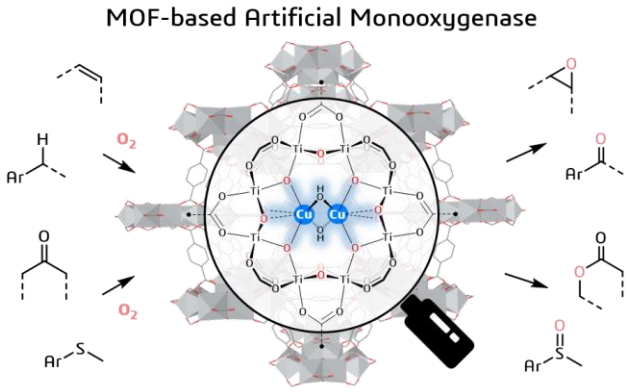

4.2 Results and Discussion

4.2.1 Synthesis and characterization of MOF-based artificial monooxygenases

We used the $Ti_8(\mu_2\text{-}O)_8(\mu_2\text{-}OH)_4$ SBUs of MIL-125(Ti), **Ti_8-OH**, to support mononuclear and binuclear Cu cofactors as artificial monooxygenases. Each SBU of **Ti_8-OH** features 4 bridging hydroxides pointing to the center, along with 8 adjacent bridging oxo groups. The precisely positioned bridging hydroxides were deprotonated to provide a hydrophilic binding pocket for reactive mononuclear or binuclear Cu species, while the small cavity in the SBU with a diameter of 5-6 Å brought the two Cu centers together via bridging hydroxide or oxo ligands to form redox-active cofactors for catalytic transformations.

Ti_8-OH was synthesized through solvothermal reactions between $Ti(O^iPr)_4$ (^{i}Pr = isopropyl) and H_2BDC based on a modified literature procedure.[45] Binuclear Cu species were installed on the SBUs of **Ti_8-OH** to afford the pre-catalyst **Ti_8-Cu_2-pre** through deprotonation of the hydroxides by $LiCH_2Si(CH_3)_3$ followed by metalation with excess $Cu(CH_3CN)_4(BF_4)$. **Ti_8-Cu_2-pre** was

oxidized by bubbling O_2 through a MOF suspension in CH_3CN to afford the binuclear artificial monooxygenase **Ti_8-Cu_2** with $[Cu^{II}_2(\mu_2\text{-}OH)_2]^{2+}$ cofactors (**Figure 4-2c**). Inductively coupled plasma-mass spectrometry (ICP-MS) analysis showed that **Ti_8-Cu_2-pre** and **Ti_8-Cu_2** had 2.0 and 1.95 Cu centers per SBU, suggesting complete metalation on all SBUs. By controlling the equivalent of Cu salts during the metalation process, **Ti_8-Cu_1** with mononuclear Cu site was also synthesized. ICP-MS analysis showed the presence of 0.3 Cu per Ti_8 node in **Ti_8-Cu_1** to ensure the formation of mononuclear Cu species only.

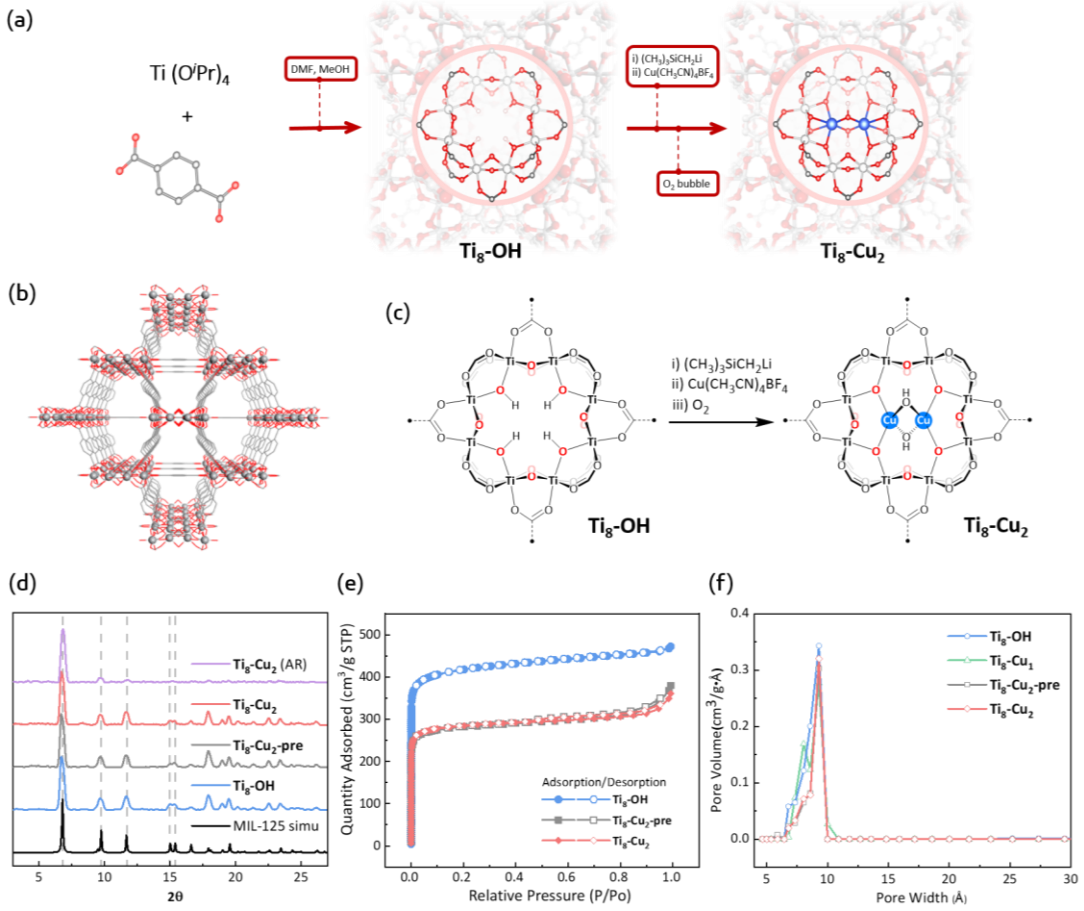

Figure 4-2. Synthesis and structural characterization of **Ti_8-OH**, **Ti_8-Cu_2-pre**, and **Ti_8-Cu_2**. (a) Synthetic scheme of the MOF-based artificial monooxygenase **Ti_8-Cu_2**. (b) SBU distribution and channel structure of the Ti MOF **Ti_8-OH**. (c) Installation of Cu^I centers and subsequent treatment with O_2 to afford **Ti_8-Cu_2**. (d) PXRD patterns of **Ti_8-OH** (blue), **Ti_8-Cu_2-pre** (grey), **Ti_8-Cu_2** (red), and the recovered **Ti_8-Cu_2** after reaction (AR, purple) along with the simulated pattern of MIL-125(Ti) (black). (e) Nitrogen sorption isotherms and (f) Pore size distributions of of **Ti_8-OH** (blue), **Ti_8-Cu_2-pre** (grey), and **Ti_8-Cu_2** (red). Copyright 2021 American Chemical Society.

Powdered X-ray diffraction (PXRD) studies showed that crystallinity of the MOF was retained throughout the metalation and oxidation processes (**Figure 4-2d**). Transmission electron microscopy (TEM) and scanning electron microscope (SEM) indicated that **Ti_8-Cu_2** maintained the disk-like morphology of **Ti_8-OH** of ~1 um in diameter and ~0.4 um in thickness (**Figures 4-3**, **4-4**). Installation of Cu centers reduced the Brunauer-Emmett-Teller (BET) surface area from 1520 m^2/g for **Ti_8-OH** to 1108 m^2/g and 1245 m^2/g for **Ti_8-Cu_2-pre** and **Ti_8-Cu_2**, respectively (**Figure 4-2e**), while the pore sizes and volumes remained similar (**Figure 4-2f**). Thermal gravimetric analysis (TGA) results supported the formulations of $Ti_8(\mu_2\text{-}O)_8[Cu(\mu_2\text{-}O)_2(CH_3CN)]_2(BDC)_6Li_2$ and $Ti_8(\mu_2\text{-}O)_8[Cu(\mu_2\text{-}O)_2(\mu_2\text{-}OH)]_2(BDC)_6Li_2$ for **Ti_8-Cu_2-pre** and **Ti_8-Cu_2**, respectively (**Figure 4-5**).

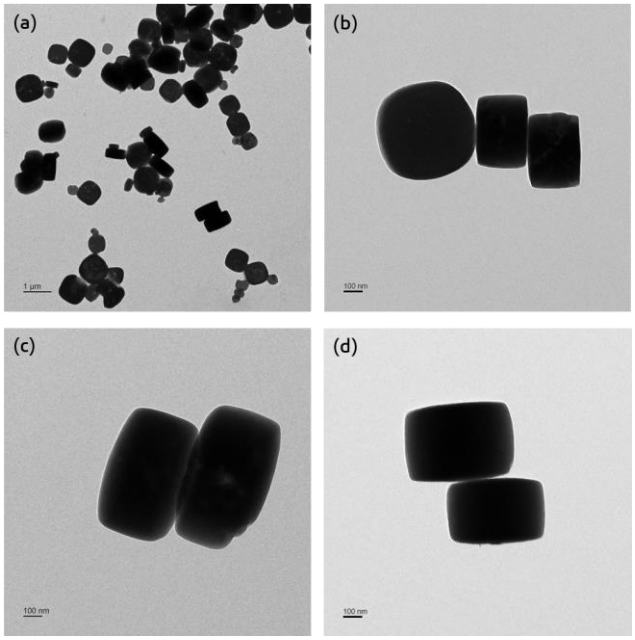

Figure 4-3. TEM images of MOFs. (a-b) TEM images of **Ti_8-OH** displaying plate-like morphologies with the scale bars of (a) 1 μm and (b) 100 nm. (c-d) TEM images of **Ti_8-Cu_2-pre** (c) and **Ti_8-Cu_2** (d) showing identical morphologies throughout Cu installation and O_2 treatment.

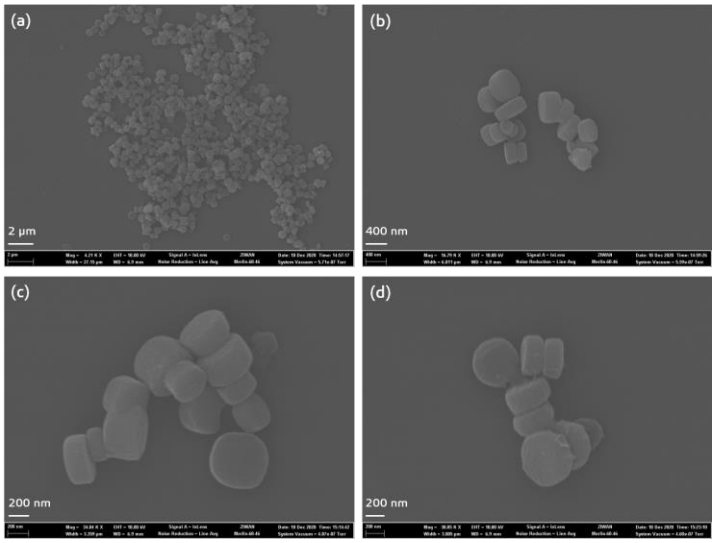

Figure 4-4. SEM images of MOFs (a-b) SEM images of **Ti_8-OH** displaying plate-like morphologies with the scale bars of (a) 2 μm and (b) 400 nm. (c-d) SEM images of **Ti_8-Cu_2-pre** (c) and **Ti_8-Cu_2** (d) showing identical morphologies throughout Cu installation and O_2 treatment.

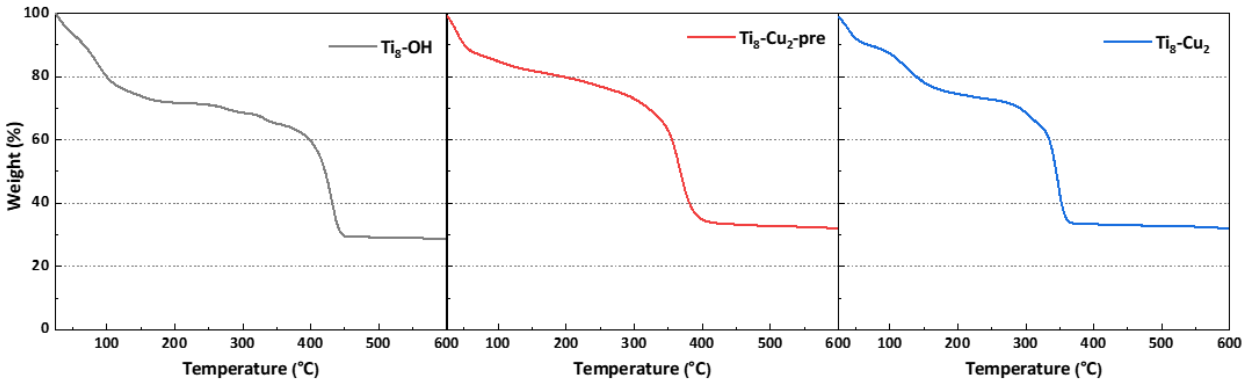

Figure 4-5. TGA curves of freshly prepared MOF matrix **Ti_8-OH** (grey), **Ti_8-Cu_2-pre** (red), and **Ti_8-Cu_2** (blue).

4.2.2 Olefin epoxidation catalyzed by MOF-based artificial monooxygenases

Natural monooxygenases efficiently transfer one oxygen from O_2 to form the mono-oxygenated product with concomitant oxidation of co-reductants such as NAD(P)H (NAD = nicotinamide adenine dinucleotide, NADP = nicotinamide adenine dinucleotide phosphate) and ascorbate in a 4-electron process.[46-47] With binuclear Cu cofactors, MOF-based artificial

monooxygenase **Ti_8-Cu_2** displayed excellent catalytic activity towards a broad range of monooxygenation reactions with O_2 as the oxygen source.

Table 4-1. Epoxidation of cyclohexene catalyzed by **Ti_8-Cu_2** and homogeneous controls.

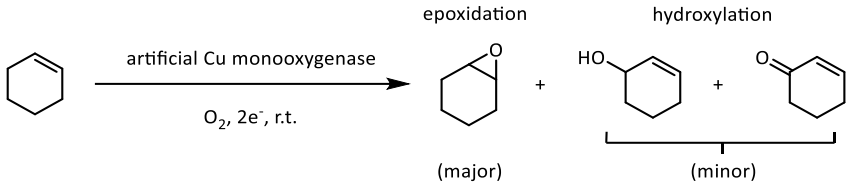

Entry	Catalyst	Reaction Condition	Conversion (Yield)	TON
1	0.2 mol% **Ti_8-Cu_2**	under O_2, with 2 eq. co-reductant, 24 h	97 (84)	485
2	0.02 mol% **Ti_8-Cu_2**	under O_2, with 2 eq co-reductant, 48 h	69 (56)	3450
3	0.2 mol% **Ti_8-Cu_2**	under air, with 2 eq. co-reductant, 24 h	92 (77)	460
4	0.2 mol% **Ti_8-Cu_2**	under N_2, with 2 eq. co-reductant, 24 h	0 (0)	-
5	0.2 mol% **Ti_8-Cu_2**	under O_2, without co-reductant, 24 h	0 (0)	-
6	-	under O_2, with 2 eq. co-reductant, 24 h	4 (4)	-
7	**Ti_8-OH**[b]	under O_2, with 2 eq. co-reductant, 24 h	6 (6)	-
8	0.2 mol% $CuCl_2$	under O_2, with 2 eq. co-reductant, 24 h	8 (7)	40
9	**Ti_8-OH**[b] + 0.2 mol% $CuCl_2$	under O_2, with 2 eq. co-reductant, 24 h	12 (11)	60
10	0.2 mol% **Ti_8-Cu_1**	under O_2, with 2 eq. co-reductant, 24 h	43 (35)	110

[a] Reactions were conducted with 0.25 mmol cyclohexene in 2.0 mL DCE. The reaction mixture was stirred at room temperature with a balloon of O_2, air, or N_2, and the conversions were determined by GC-MS analysis. Isobutyraldehyde was used as the co-reductant. [b] **Ti_8-OH** (1.0 mg) was used.

Ti_8-Cu_2 effectively catalyzed epoxidation of olefins to afford epoxides. We used cyclohexene as a model substrate to screen the conditions for epoxidation reactions. In the presence of 0.2 mol% **Ti_8-Cu_2**, treatment of cyclohexene and 2 equiv. of isobutyraldehyde as the co-reductant in 1,2-dichloroethane (DCE) under atmospheric O_2 at room temperature afforded cyclohexene oxide in 84% yield along with a small amount of hydroxylation products 2-cyclohexen-1-ol and 2-cyclohexen-1-one (13% in total). The reaction also proceeded under ambient air to afford cyclohexene oxide in 77% yield (Entry 3, **Table 4-1**). The absence of **Ti_8-**

Cu_2, O_2, or co-reductant shut down the monooxygenation reaction, affording no or negligible amount of cyclohexene oxide (Entries 4-6, **Table 4-1**). Replacement of **Ti_8-Cu_2** by homogeneous control, $CuCl_2$, afforded cyclohexene oxide in 7% yield (Entries 8-9, **Table 4-1**), demonstrating the important role of Cu coordination to the SBU in the monooxygenation activity.

The reaction conditions were further screened with **Ti_8-Cu_2**-catalyzed epoxidation of cyclohexene. First, polar solvents such as DCE, dichloromethane, and trifluorotoluene displayed better monooxygenation performance than non-polar solvents such as n-hexane. Notably, coordinating solvent, *e.g*, tetrahydrofuran (THF), led to poor monooxygenation result, probably due to the strong solvent coordination to the Cu sites. Second, the effects of co-reductants were also studied. Isobutyraldehyde, cyclohexanecarbaldehyde, and L-ascorbic acid showed 97%, 46%, and 5% conversions, respectively. Other electron donors such as 1,3-dimethyl-2-phenyl-2,3-dihydro-1H-benzo[*d*]imidazole (BIH), *N*-benzyl-1,4-dihydronicotinamide (BNAH), and tetrahydroxy-1,4-quinone did not work. Third, the effects of isobutyraldehyde concentration and equivalent on the epoxidation reaction were examined. When the amount of isobutyraldehyde increased from 1 to 10 equivalents, the selectivity of the epoxidation product over the hydroxylation products improved from 75% to >99%. However, the highest epoxidation yield was achieved when 2 equivalents of isobutyraldehyde were used (**Figure 4-6**). An excess amount of co-reductant likely accelerates the regeneration of $Cu_2(\mu\text{-}O)$ active species to suppress hydroxylation products, but co-reductant also competes with substrate oxidation to decrease the yield of monooxygenation products.

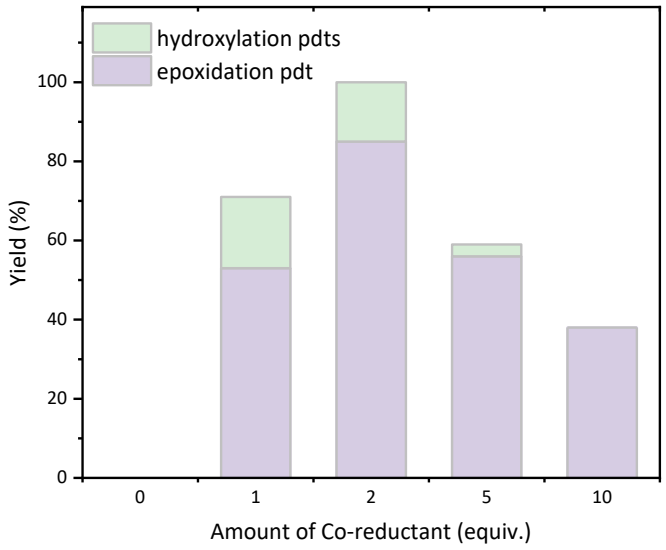

Figure 4-6. Screening of co-reductant amounts in **Ti_8-Cu_2**-catalyzed epoxidation of cyclohexene. Reactions were conducted with 0.2 mol% of **Ti_8-Cu_2**, 0.25 mmol cyclohexene, and co-reductant (isobutyraldehyde) in 2.0 mL DCE. The mixture was stirred at room temperature equipped with an O_2-filled balloon for 24h. The conversion was determined by GC-MS.

The reactivity difference between a binuclear Cu cofactor and a mononuclear Cu cofactor was studied using **Ti_8-Cu_2** and **Ti_8-Cu_1** as catalysts. As shown in **Figure 4-7a**, the time-dependent curves showed that **Ti_8-Cu_2** catalyzed cyclohexene monooxygenation efficiently within the first few hours with an initial turnover frequency (TOF) of 175 h^{-1} and a high conversion of 97% in 24 h. In contrast, **Ti_8-Cu_1** showed a much slower reaction rate with an initial TOF of 10 h^{-1} and a conversion of 43% in 24 h. This result shows the important role of binuclear Cu cofactors in the artificial monooxygenase.

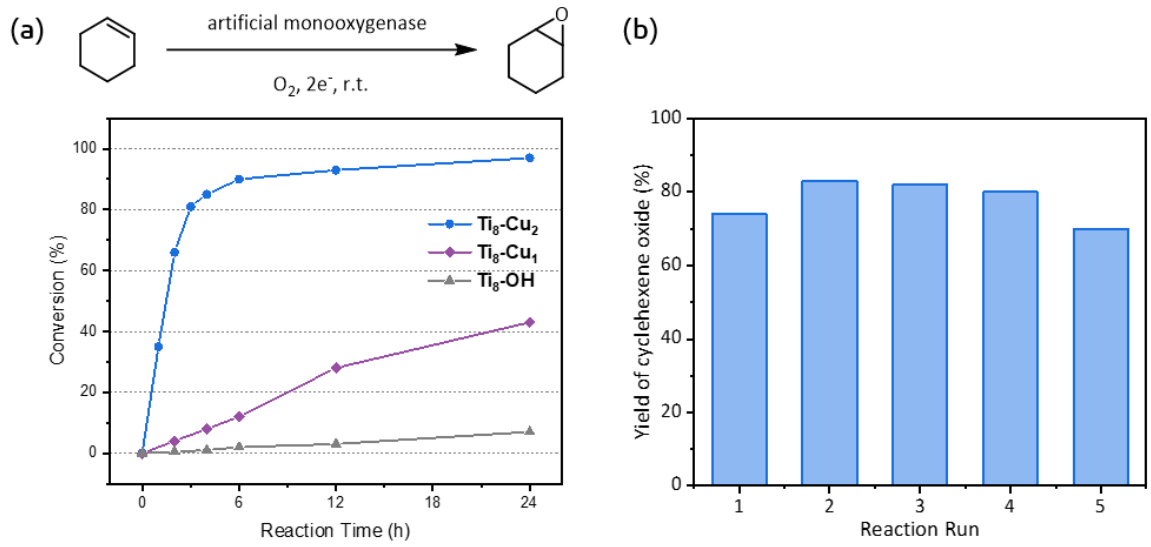

Figure 4-7. Time dependent curves and recycle experiments. (a) Time-dependent curves of cyclohexene epoxidation catalyzed by MOF-based artificial monooxygenases with a binuclear Cu cofactor (**Ti_8-Cu_2**) or a mononuclear Cu cofactor (**Ti_8-Cu_1**) and without a cofactor (**Ti_8-OH**). (b) Recycle and reuse of **Ti_8-Cu_2** catalyst in the epoxidation of cyclohexene.

We next examined the substrate scope for **Ti_8-Cu_2**-catalyzed olefin epoxidation reactions. At 0.2 mol% of **Ti_8-Cu_2**, various alkenes were smoothly converted to their corresponding epoxides in the presence of isobutyraldehyde under atmospheric O_2. Excellent yields of epoxides were obtained with cyclic alkenes bearing different substituents (Entries 1-4, **Table 4-2**). Exclusive epoxidation selectivity was observed for reactive cyclic olefinic bonds in limonene and 3-carene (Entries 5-6, **Table 4-2**). Non-cyclic alkenes, including styrene derivatives (Entries 7-8, **Table 4-2**) and linear-chain alkenes (Entries 9-10, **Table 4-2**), also underwent epoxidation to afford epoxides in good to excellent yields. Internal alkenes displayed higher reactivity than terminal alkenes, likely due to the more electron-rich nature of internal alkenes. As a heterogeneous catalyst, **Ti_8-Cu_2** was recycled by simple filtration from the reaction mixture and used in 5 consecutive runs of cyclohexene epoxidation. No significant reactivity drop was observed throughout the recycling experiments, demonstrating the stability of MOF-based artificial monooxygenase under oxygenation reaction conditions (**Figure 4-7b**).

Table 4-2. Ti_8-Cu_2-catalyzed monooxygenation reactions.

Entry	Substrate	Catalyst Loading	Product	Conv. (Yield)	TON	Entry	Substrate	Catalyst Loading	Product	Yield	TON
1		0.2 mol%		97% (84%)	420	10	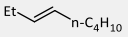	0.2 mol%	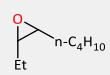	90% trans:cis 83:7	450
2		0.2 mol%		97% (92%)	460	11		0.5 mol%		87%	174
3		0.2 mol%		95% (92%)	460	12		0.2 mol%		86%	430
4		0.2 mol%		100% (81%)	405	13		0.5 mol%		94%	188
5	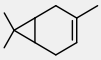	0.2 mol%	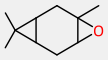	89% (89%)	445	14		0.5 mol%	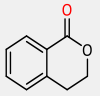	81%	162
6	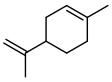	0.2 mol%	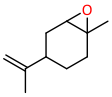	90% (90%)	450	15	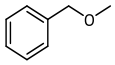	0.5 mol%	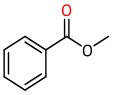	68%	136
7		0.2 mol%	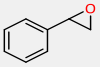	76% (70%)	350	16		0.5 mol%		46%	92
8	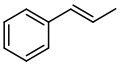	0.2 mol%	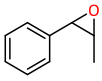	100% (88%)	440	17	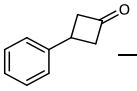	0.2 mol%	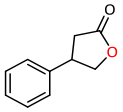	70%	350
9		0.2 mol%	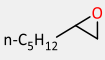	50% (50%)	250	18		0.2 mol%		95%	475

[a] Reactions were conducted with 0.25 mmol substrate in 2.0 mL DCE solvent. The reaction mixture was stirred at room temperature with an O_2 balloon. Isobutyraldehyde (2 equiv.) was applied as co-reductant. The conversions were determined by GC-MS analysis.

4.2.3 Other monooxygenation reactions catalyzed by MOF-based artificial monooxygenases

Encouraged by excellent epoxidation activities of **Ti_8-Cu_2**, we examined the use of **Ti_8-Cu_2** in other monooxygenation reactions. Direct hydroxylation of alkanes under mild conditions provides an attractive strategy to construct valuable alcoholic feedstocks which can also be further oxidized to carbonyl compounds.[48] **Ti_8-Cu_2** displayed excellent reactivity towards hydroxylation of benzylic substrates and further alcohol oxidation to carbonyl compounds. At 0.5 mol% of **Ti_8-**

Cu_2, indane was efficiently converted into 1-indanol (8%) and 1-indanone (61%) under atmospheric O_2 at room temperature in 24 h. Elongating the reaction time to 48 h increased 1-indanone yield to 87% while reducing the 1-indanol yield to <1%, which suggests sequential hydroxylation and oxidation to ketones (Entry 11, **Table 4-2**). Several other substrates bearing benzylic C-H bonds including tetralin, phthalane, isochromane, and (methoxymethyl)benzene were successfully converted to corresponding ketones, lactones, and esters in good to excellent yields (Entries 12-15, **Table 4-2**). The more difficult substrate ethylbenzene was oxidized to form acetophenone in 46% yield (Entry 16, **Table 4-2**).

Ti_8-Cu_2 also displayed high activities towards Baeyer-Villiger reaction and oxidation of thioethers. Specifically, **Ti_8-Cu_2** (0.2 mol%) catalyzed Baeyer-Villiger oxidation of 3-phenylcyclobutanone with O_2 as oxidant to afford 4-phenyloxolan-2-one in 70% yield within 48 h (Entry 17, **Table 4-2**). **Ti_8-Cu_2** catalyzed the oxidation of thioanisole to methyl phenyl sulfoxide in 95% yield under atmospheric O_2 in 72 h (Entry 18, **Table 4-2**). These results indicate the effectiveness of MOF-based artificial monooxygenases in producing valuable chemical feedstocks with O_2 as oxidant under mild reaction conditions.

4.2.4 Identification of the Cu cofactors

We used Cu K-edge X-ray absorption near-edge structure (XANES) and extended X-ray absorption fine structure (EXAFS) spectroscopies to study the Cu cofactors in MOF-based monooxygenases. The oxidation states of Cu centers in **Ti_8-Cu_2-pre** and **Ti_8-Cu_2** were determined by comparing the pre-edge features of their normalized XANES spectra to those of Cu_2O and CuO (**Figure 4-8a**). While **Ti_8-Cu_2-pre** showed a similar pre-edge peak corresponding to the spin-allowed 1s → 4p electronic transition at 8982-8984 eV to Cu^{I}_2O,[49] **Ti_8-Cu_2** exhibited a similar pre-edge peak attributed to the dipole-forbidden Cu^{II} 1s → 3d electronic transition at 8977-8979

eV to $Cu^{II}O$.[50] This pre-edge feature of **Ti_8-Cu_2** also suggests an octahedral symmetry for Cu^{II} centers.[51] Additionally, **Ti_8-Cu_2** showed a shoulder peak at 8989 eV which is assigned to Cu^{II} 1s → 4p + L shakedown transition.[52] The XANES studies thus indicate that the Cu centers in **Ti_8-Cu_2-pre** adopt +1 oxidation state while the Cu centers in **Ti_8-Cu_2** exhibit +2 oxidation state.

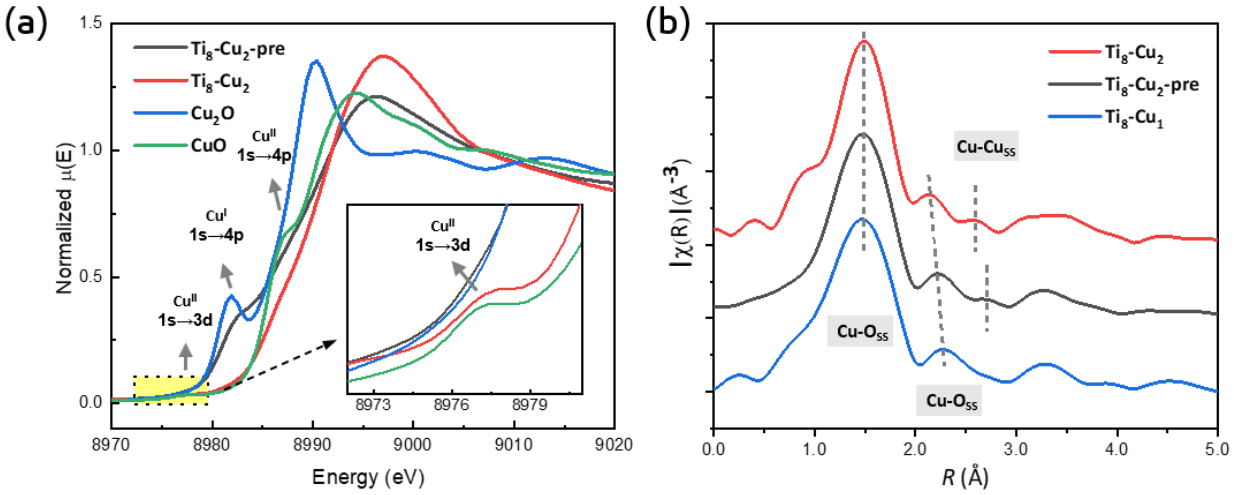

Figure 4-8. X-ray absorption fine structure (XAFS) characterization. (a) Normalized Cu-XANES spectra of **Ti_8-Cu_2-pre**, **Ti_8-Cu_2**, and reference compounds. The inset shows the pre-edge feature at 8973−8982 eV corresponding to the 1s → 3d electronic transition for Cu^{II}. (b) k^2-weighted Cu-EXAFS χ(R) spectra of **Ti_8-Cu_2-pre**, **Ti_8-Cu_2**, and **Ti_8-Cu_1**. SS = single scattering.

Density functional theory (DFT) calculations were performed using the B3LYP functional to determine Cu coordination environments in **Ti_8-Cu_2-pre** and **Ti_8-Cu_2**. DFT optimization of **Ti_8-Cu_2-pre** converged at a structure with two tetrahedral Cu^I centers slightly above and below the plane of the Ti_8 node. Each Cu^I center coordinates to two anionic bridging-oxo (μ_2-O^-) groups, one neutral bridging-oxo (μ_2-O) group, and one CH_3CN molecule in a distorted tetrahedral geometry. The distances of Cu-(μ_2-O^-), Cu-(μ_2-O), and Cu-N were 2.13/2.15. 2.23, and 1.95 Å, respectively. DFT optimization of **Ti_8-Cu_2** converged on a $Cu^{II}_2(\mu_2\text{-}OH)_2$ structure with two Cu^{II} centers in the plane of the Ti_8 node. Each Cu^{II} center adopted the octahedral geometry by coordinating to two anionic bridging-oxo (μ_2-O^-) groups in the axial positions as well as two neutral bridging-oxo (μ_2-

O) groups and two bridging μ_2-OH groups in the equatorial positions. The Cu-O distances were 2.12, 2.45, and 2.03 Å for the Cu(μ_2-O^-), Cu(μ_2-O), and Cu(μ_2-OH) moieties, respectively.

EXAFS analyses were performed to determine the local structures of Cu cofactors. We first compared the k^2-weighted χ(R) spectra of **Ti_8-Cu_2-pre**, **Ti_8-Cu_2**, and **Ti_8-Cu_1**. No signals attributable to Cu nanoparticle or CuO are present in these EXAFS spectra. **Ti_8-Cu_2** and **Ti_8-Cu_2-pre** showed characteristic Cu-Cu single scattering signals at R $\approx$ 2.58 and 2.73 Å, respectively (**Figure 4-8b**), consistent with the existence of Cu_2 species in both **Ti_8-Cu_2-pre** and **Ti_8-Cu_2**. In contrast, no Cu-Cu single scattering signal was present in the EXAFS spectrum of **Ti_8-Cu_1**, consistent with the mononuclear Cu species. Furthermore, **Ti_8-Cu_2** showed stronger Cu-Cu single scattering signal than **Ti_8-Cu_2-pre**, suggesting more intense interactions between two Cu^{II} centers in **Ti_8-Cu_2** due to the bridging of the Cu centers by two μ_2-OH groups after oxidation. This result matches the distance trend observed in DFT-optimized structures with Cu-Cu distances of 2.88 and 2.74 Å for **Ti_8-Cu_2-pre** and **Ti_8-Cu_2**, respectively.

We further fitted the Cu-EXAFS spectra using DFT-optimized structure models (**Figure 4-9**). For **Ti_8-Cu_2**, Cu-O single scattering pathways contributed most to the first and second peaks of the Cu K-edge EXAFS spectrum to afford Cu-O distances of 2.00, 2.20, and 1.91 Å for a Cu-(μ_2-O^-), Cu-(μ_2-O), and Cu-(μ_2-OH) species, respectively. The third peak came mainly from the contribution of Cu-Cu interaction with a Cu-Cu distance of 2.80 Å, which agrees well with the calculated distance of 2.74 Å. Similarly, the first and second peaks of **Ti_8-Cu_2-pre** were attributed to Cu-O interactions from (μ_2-O^-), (μ_2-O), and N, while the weak third peak was mainly assigned to Cu-Cu interactions. These EXAFS results are consistent with those reported in literature.[53-54]

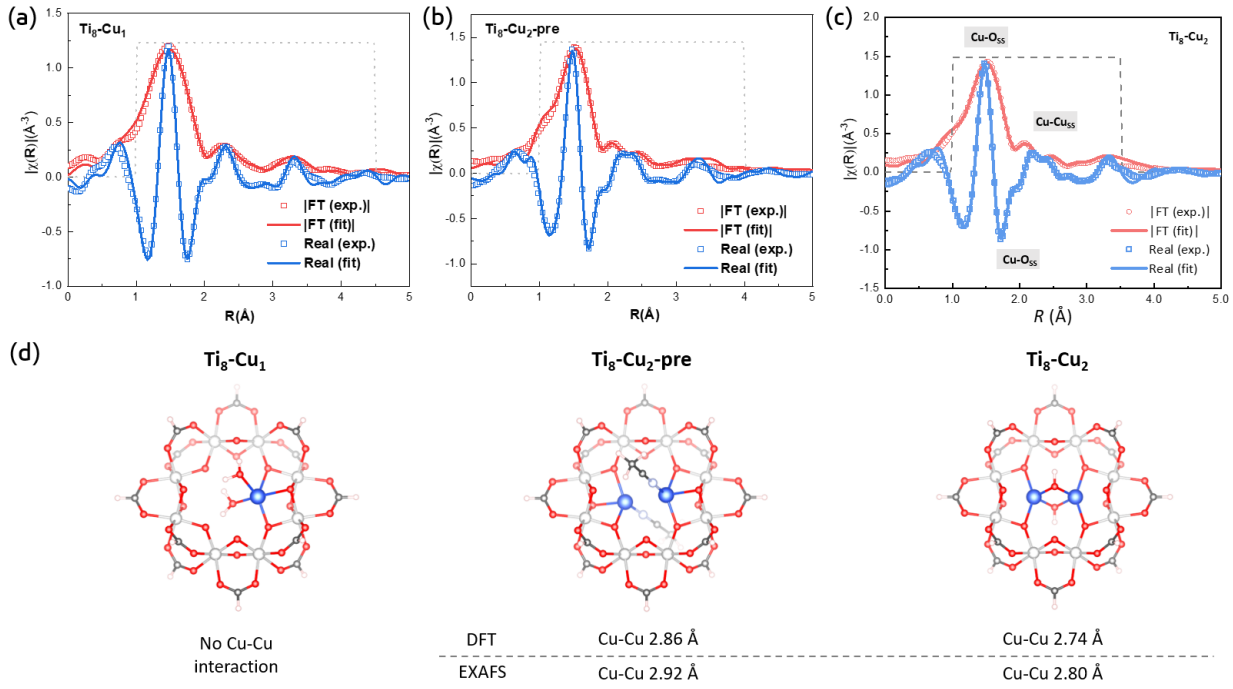

Figure 4-9. Determination of Cu local coordination in **Ti_8-Cu_1**, **Ti_8-Cu_2-pre**, and **Ti_8-Cu_2**. (a-c) EXAFS spectra and fits in R-space (within the grey lines) at the Cu K-edge of **Ti_8-Cu_1** (a), **Ti_8-Cu_2-pre** (b), and **Ti_8-Cu_2** (c) with the magnitude (open circles, red) and real components (open squares, blue) of the Fourier transforms (FT). (d) Structural models of **Ti_8-Cu_1** (left), **Ti_8-Cu_2-pre** (middle), and **Ti_8-Cu_2** (right) with the Cu-Cu distances from DFT optimization and EXAFS fitting. Copyright 2021 American Chemical Society.

Fourier-transform infrared (FT-IR) spectroscopy and UV-vis spectroscopy supported the generation of Cu cofactors in the MOFs. As shown in **Figure 4-10a**, **Ti_8-OH**, **Ti_8-Cu_2-pre**, and **Ti_8-Cu_2** displayed similar carbonyl stretching at ~1550 cm^{-1} and C_{sp2}-H stretching at~3000 cm^{-1}, but only **Ti_8-OH** showed a shoulder peak at 3645 cm^{-1} attributable to the O-H stretching of Ti(μ_2-OH)Ti species.[55] This peak disappeared after deprotonation and metalation with Cu in **Ti_8-Cu_2-pre** and **Ti_8-Cu_2**. Interestingly, a new sharp peak at 3670 cm^{-1} appeared in **Ti_8-Cu_2**, which is assigned to the O-H stretching of the Cu(μ_2-OH)Cu species.[56] UV-vis spectra were also taken on the MOF systems (**Figure 4-10b**). While **Ti_8-OH** displayed UV absorption at ~300 nm characteristic of Ti-O charge transfer (CT),[57] **Ti_8-Cu_2-pre** and **Ti_8-Cu_2** showed new bands at 330

and 355 nm, respectively. These bands are assigned to Cu^{I}-O and Cu^{II}-O CT absorptions, respectively.[58]

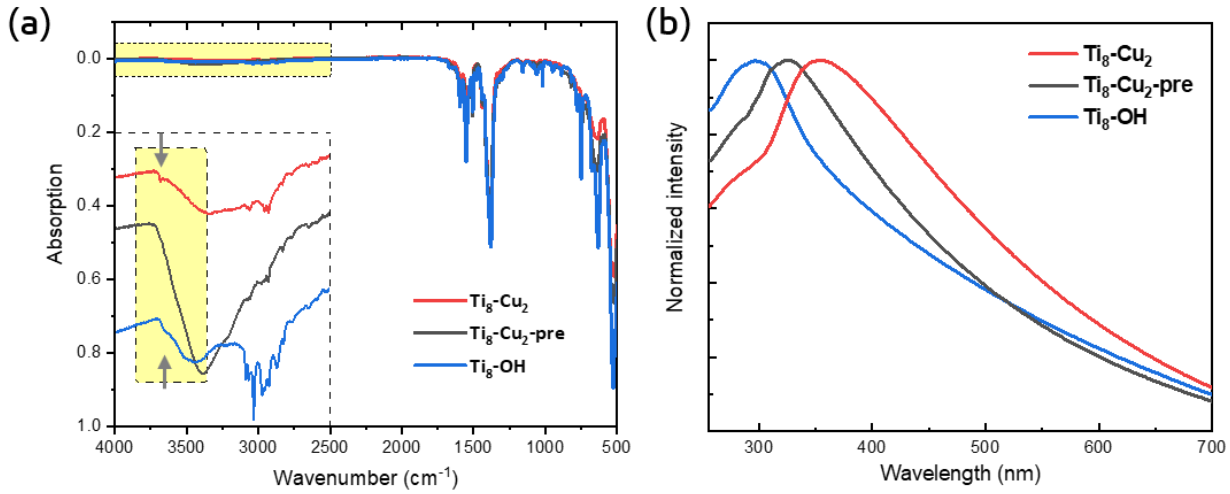

Figure 4-10. (a) FT-IR spectra of **Ti_8-OH** (blue), **Ti_8-Cu_2-pre** (black), and **Ti_8-Cu_2** (red). (b) UV-Vis absorption bands of **Ti_8-OH** (blue), **Ti_8-Cu_2-pre** (black), and **Ti_8-Cu_2** (red).

4.2.5 Energy profiles of monooxygenation processes

DFT calculations with the B3LYP functional were conducted on SBU-supported Cu cofactors to gain insight into dioxygen activation and substrate oxidation by the MOF-based monooxygenases and to understand the drastic reactivity difference between **Ti_8-Cu_2** and **Ti_8-Cu_1**. Significant efforts have been made to study O_2 activation and utilization by the active Cu centers in natural and artificial Cu-based monooxygenases. Spectroscopic and computational evidence strongly suggested Cu-oxo species as the key intermediates in the monooxygenation process.[59-61] We propose $Cu_2(\mu_2\text{-}O)_2$ and Cu-oxo species as the active catalysts for the monooxygenation processes catalyzed by **Ti_8-Cu_2** and **Ti_8-Cu_1**, respectively.

We first determined the energy profiles of O_2 activation processes on **Ti_8-Cu_2** and **Ti_8-Cu_1** (**Figure 4-11**). O_2 activation by **Ti_8-Cu_2** starts with the coordination of O_2 to the reduced $(Cu^{I})_2$ complex (IN-1) with an η^1-end-on mode to form a $Cu^{II}(\eta^1,\mu_2\text{-}O_2)Cu$ adduct (IN-2). IN-2 then transforms into a $Cu(\eta^2,\mu_2\text{-}O_2)Cu$ adduct (IN-3). The cleavage of the O-O bond affords the highly

active $Cu^{III}_2(\mu_2\text{-}O)_2$ intermediate (IN-4). For O_2 activation on **Ti_8-Cu_1**, O_2 first coordinates with Cu^I (IN-5) to form a η^1-O_2-adduct (IN-6), which is further activated via a one electron and one proton ($1e/1H^+$) process (provided by the co-reductant) to form a Cu^{II}-OOH intermediate (IN-7). IN-7 loses one H_2O to afford the active Cu^{III}=O species (IN-8) via another $1e/1H^+$ process. Calculations of the free energies of these key intermediates revealed total free energy increases of +47.7 kcal/mol for O_2 activation in **Ti_8-Cu_2** to access IN-4 and +54.3 kcal/mol for O_2 activation **Ti_8-Cu_1** to access IN-8. Although the cleavage of O-O bond in **Ti_8-Cu_1** features a lower barrier (IN-7 to IN-8, 23.6 kcal/mol) than in **Ti_8-Cu_2** (IN-3 to IN-4, 32.8 kcal/mol) with the assistance of the co-reductant, the significant stabilization of the dioxygen species by the Cu_2 species leads to a smaller free energy increase for the overall transformation by 6.6 kcal/mol. Such a difference indicates an easier O_2 activation process on the binuclear Cu site than the mononuclear Cu site.

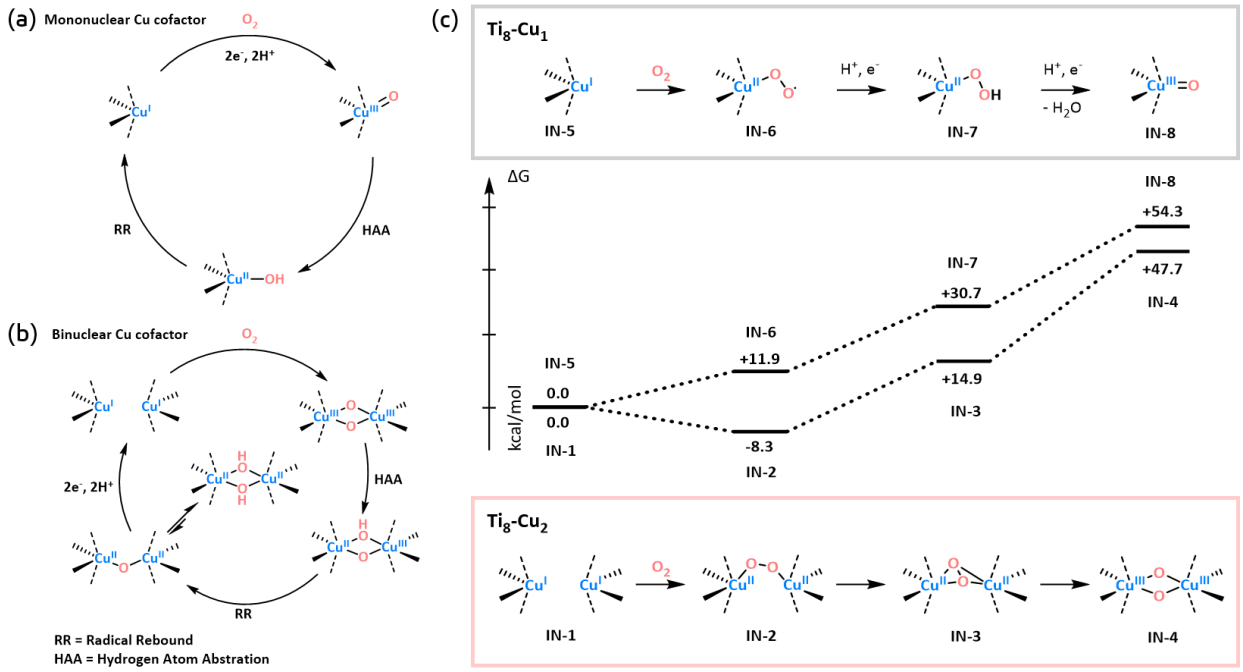

Figure 4-11. Energy profiles of O_2 activation processes on **Ti_8-Cu_2** and **Ti_8-Cu_1**. (a-b) Schematic of the monooxygenation process on (a) the mononuclear Cu cofactor in **Ti_8-Cu_1** and (b) the binuclear Cu cofactor in **Ti_8-Cu_2**. (c) Energy profiles of O_2 activation processes on **Ti_8-Cu_1** (top) and **Ti_8-Cu_2** (bottom). Copyright 2021 American Chemical Society.

DFT studies were also performed on the monooxygenation processes starting from the active Cu-oxo intermediates in **Ti_8-Cu_2** and **Ti_8-Cu_1** (**Figure 4-12**). The hydroxylation of toluene to afford benzyl alcohol was selected as a model reaction. Typically, hydroxylation of C-H bonds on Cu-oxo species is initiated by the hydrogen atom abstraction (HAA) from the substrate by the Cu-oxo species to form the Cu-hydroxo species and the carbon radical, followed by a radical rebound step to construct the C-O bond between the carbon radical and Cu-bounded hydroxide. **Figure 4-12** shows the key intermediates and transition states during the hydroxylation processes. The hydroxylation processes on both **Ti_8-Cu_2** and **Ti_8-Cu_1** are highly exothermic and spontaneous with small activation barriers. Specifically, the binuclear Cu cofactor featured a +4.2 kcal/mol activation barrier for the HAA step and a +1.9 kcal/mol barrier for the radical rebound to form the benzyl alcohol product. For the mononuclear Cu cofactor, a +2.6 kcal/mol activation barrier is calculated for the HAA step and a +9.2 kcal/mol barrier for the radical rebound step. Both processes are driven by the highly reactive nature of the Cu-oxo species (IN-4 and IN-8) and the formation of strong C-O bonds.

The DFT results suggest the O_2 activation as the rate-limiting step in the monooxygenation processes catalyzed by both **Ti_8-Cu_2** and **Ti_8-Cu_1**. Subsequent substrate oxidation processes by the active Cu-oxo species proceed spontaneously. Importantly, the Cu_2 sites in **Ti_8-Cu_2** cooperatively stabilize the Cu-dioxygen adduct for O-O bond cleavage, leading to a smaller free energy increase for the dioxygen activation than the mononuclear Cu sites in **Ti_8-Cu_1**. Although several factors, including substrate/product diffusions, MOF channels, and Cu co-factor concentrations, contributed to the monooxygenation reactivities, the 6.6 kcal/mol difference in ΔG values rationalized the significantly higher catalytic activity of **Ti_8-Cu_2** over **Ti_8-Cu_1**.

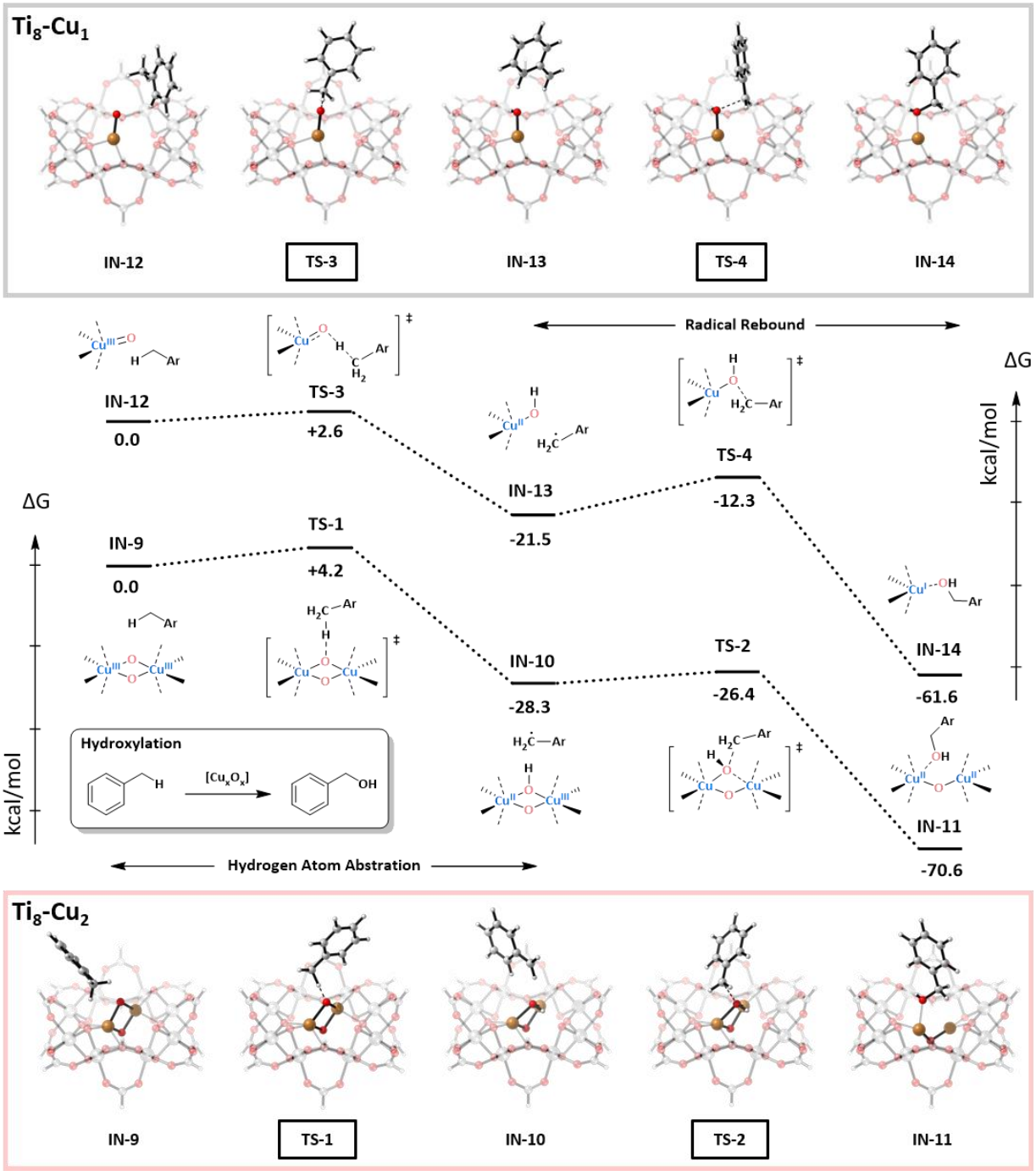

Figure 4-12. Energy profile of the hydroxylation process on **Ti_8-Cu_1** (up) and **Ti_8-Cu_2** (bottom). Copyright 2021 American Chemical Society.

4.3 Conclusion

In this work, we demonstrated a novel strategy to construct an artificial monooxygenase, **Ti_8-Cu_2**, starting from a Ti MOF following the blueprint of natural enzymes. The hydroxides of

the MOF SBUs were deprotonated to support a pair of Cu^{I} precursors, which were treated with O_2 to generate the $Cu^{II}_2(\mu_2\text{-}OH)_2$ cofactors in the artificial enzymes. The SBU provided a precise binding pocket for the installation of binuclear Cu cofactors to cooperatively activate O_2. The strong oxo ligating ligands and the reticular isolation of Cu_2 cofactors in the MOF led to a robust artificial enzyme for monooxygenation reactions. **Ti_8-Cu_2** catalyzed a wide scope of monooxygenation reactions, including epoxidation, hydroxylation, Baeyer-Villiger oxidation, and sulfoxidation, with atmospheric O_2 as the oxidant and isobutyraldehyde as the co-reductant. **Ti_8-Cu_2** efficiently catalyzed the epoxidation of alkenes with TONs as high as 3450 and an initial TOF of 175 h^{-1}, which was more than 17 times higher than the mononuclear analogue **Ti_8-Cu_1**. Computational studies revealed O_2 activation as the rate-limiting step in the monooxygenation processes catalyzed by both **Ti_8-Cu_2** and **Ti_8-Cu_1**. The Cu_2 sites in **Ti_8-Cu_2** cooperatively stabilize the Cu-dioxygen adduct for the O-O bond cleavage with 6.6 kcal/mol lower free energy increase than the mononuclear Cu sites in **Ti_8-Cu_1**, which accounts for the significantly higher catalytic activity of **Ti_8-Cu_2** over **Ti_8-Cu_1**. This work highlights the potential of MOFs in the construction of robust artificial enzymes with uniform and precise active sites and high catalytic activities.

4.4 Experimental Section

4.4.1 Materials and methods

All the reactions and manipulations were carried out under N_2 with the use of a glovebox or Schlenk technique, unless otherwise indicated. Tetrahydrofuran and toluene were purified by passing through a neutral alumina column under N_2. All starting materials were purchased from Sigma-Aldrich and Fisher (USA) unless otherwise noted and used without further purification. Powder X-ray diffraction (PXRD) data was collected on a Bruker D8 Venture diffractometer using Cu Kα radiation source (l = 1.54178 Å). N_2 sorption experiments were performed on a

Micrometrics TriStar II 3020 instrument. Thermogravimetric analysis (TGA) was performed in air using a Shimazu TGA-50 equipped with a platinum pan and heated at a rate of 1.5 °C per min. Fourier-transform infrared (FT-IR) spectra were collected using a Thermo NEXUS 670 Near-, Far-, and Mid-FTIR with attenuated total reflectance (ATR) accessory (for Powder Samples). UV-Vis spectra were collected on a Shimadzu UV-2600 UV-Vis spectrophotometer. Transmission electron microscopy (TEM) images were taken on a TECNAI F30 HRTEM. Scanning electron microscope (SEM) images were taken on the Carl Zeiss Merlin, with the detectors of In-Lens, EsB, AsB, & SE2. Inductively coupled plasma-mass spectrometry (ICP-MS) data was obtained with an Agilent 7700x ICP-MS and analyzed using ICP-MS MassHunter version B01.03.

The conversions of reactions were determined by gas chromatography-mass spectrometry (GC-MS) using a Shimadzu GCMS-QP2010 Ulta equipped with SH-Rxi-5Sil MS 30 m × 0.5 mm × 0.25 μm column.

4.4.2 Synthetic procedures of MOF catalysts

Synthesis of MOF matrix **Ti_8-OH** (MIL-125): $Ti_8(\mu_2\text{-}O)_8(\mu_2\text{-}OH)_4(BDC)_6$, **$Ti_8$-OH**, also known as MIL-125 (MIL = Matériauxs de l'Institut Lavoisier), was synthesized using a modified literature procedure.[45] 1,4-Benzenedicarboxylic acid (H_2BDC, 500 mg, 3.0 mmol) and titanium isopropoxide (0.6 ml, 2.0 mmol) were charged to a solvent mixture of 9.0 ml of anhydrous dimethylformamide and 1.0 ml of anhydrous methanol. The mixture was stirred gently for 5 min at room temperature and then transferred to a Teflon liner and put into a stainless-steel Parr bomb, which was heated at 150 °C for 24 h. After cooling to room temperature, the white solid was centrifuged out of the suspension and then sequentially washed with DMF three times, with THF three times, and with benzene three times. **Ti_8-OH** was obtained in 68% yield after freeze-drying

in benzene and stored in a N_2-filled glovebox for further usage. The PXRD pattern of the as-synthesized **Ti_8-OH** was identical to the simulated pattern of MIL-125.

Synthesis of **Ti_8-Cu_2-pre**: In a N_2-filled glovebox, $TMSCH_2Li$ (1.0 M in pentane, 0.2 mL, 10 equiv. w.r.t. Ti_8) was added dropwise to a cold suspension of **Ti_8-OH** (0.02 mmol Ti_8) in 20 mL hexanes, and the resultant milky-white mixture was stirred at room temperature for 6 h. The solid was collected through centrifugation and washed with hexanes six times to remove soluble residue. ICP-MS results showed a Ti/Li ratio of 1.98, indicating complete lithiation (99%) during the deprotonation process. The resultant **Ti_8-OLi** was then transferred to a vial containing 20 mL of $Cu(CH_3CN)_4BF_4$ solution (10 mM) in CH_3CN. After stirring at room temperature for 12 h, the yellow solid was centrifuged and washed with CH_3CN three times. The resultant **Ti_8-Cu_2-pre** with the composition of $Ti_8(\mu_2\text{-}O)_8[Cu(\mu_2\text{-}O)_2(CH_3CN)]_2(BDC)_6Li_2$ was soaked in CH_3CN for 1 day to completely remove Cu residues. The solvent was then exchanged with benzene and the slurry was freeze-dried. The resultant product was stored in a glovebox for further use. ICP-MS analysis gave a Ti/Cu ratio of 3.9, indicating 2.0 Cu per Ti_8 node.

Synthesis of artificial monooxygenase **Ti_8-Cu_2**: In a 20 mL vial, **Ti_8-Cu_2-pre** (50 mg) was dispersed in 10 mL MeCN with rigorous stirring. Oxygen was bubbled through overnight at room temperature. The color of the MOF turned from yellow to aquamarine blue, suggesting the oxidation of the Cu^I centers to the Cu^{II} centers. The resultant $Ti_8(\mu_2\text{-}O)_8[Cu(\mu_2\text{-}OH)_2]_2(BDC)_6Li_2$, **$Ti_8$-$Cu_2$**, was washed with CH_3CN three times, soaked in CH_3CN for 1 day, and then washed with CH_3CN three more times. The solvent was then exchanged to benzene and the slurry was freeze-dried to afford a blue powder (>95% recovery). ICP-MS analysis showed a Ti/Cu ratio of 4.1, indicating ~1.9 Cu per Ti_8 node with the proposed binuclear coordination. Similarly, **Ti_8-Cu_1** with mononuclear Cu cofactors was constructed with the same above procedure and lower

$Cu(CH_3CN)_4BF_4$ equivalence. ICP-MS analysis showed a Ti/Cu ratio of 27 in **Ti_8-Cu_1**, corresponding to 0.3 Cu per Ti_8 SBU.

4.4.3 Catalytic reaction setup and product characterization

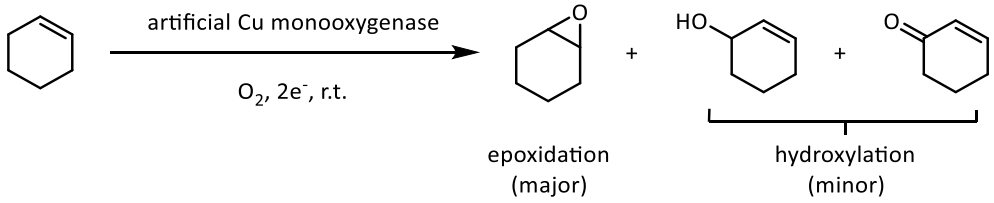

Typical procedure of epoxidation: Epoxidation catalyzed by MOF-based artificial monooxygenases was carried out in a 2-dram septum-sealed glass vial equipped with an O_2-filled balloon. In a standard reaction, Ti_8-Cu_2 (1.2 mg of MOF containing 0.5 μmol Cu_2 cofactor, 0.2 mol%), cyclohexene (0.25 mmol), isobutyraldehyde (0.50 mmol), and 2.0 mL of DCE were charged to a 2-dram septum-sealed glass vial. The reaction vial was capped and equipped with a O_2-filled balloon. After stirring for a preset reaction time (e.g., 24 h), the supernatant was analyzed by GC-MS to give cyclohexene oxide in 84% yield along with 13% of hydroxylation products (2-cyclohexen-1-ol and 2-cyclohexen-1-one). After one reaction run, ICP-MS analysis showed the leaching of 0.9% Cu and 0.1% Ti into the solution.

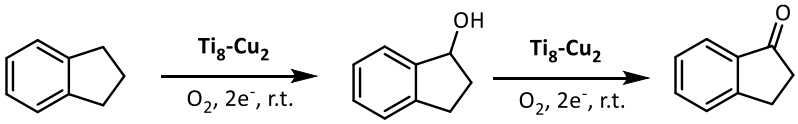

Typical procedure of C-H oxidation: Hydroxylation and subsequent alcohol oxidation catalyzed by **Ti_8-Cu_2** were carried out in a 2-dram septum-sealed glass vial equipped with an O_2-filled balloon. In a standard reaction, **Ti_8-Cu_2** (1.2 mg of MOF containing 0.5 μmol Cu_2 cofactor, 0.5 mol%), indane (0.10 mmol), isobutyraldehyde (0.50 mmol, added in five portions during the reaction), and 2.0 mL of DCE were charged to a 2-dram septum-sealed glass vial. The reaction vial was capped and equipped with an O_2-filled balloon. After stirring for a preset reaction time

(e.g., 48 h), the supernatant was analyzed by GC-MS to give 1-indanone in 87% yield along with <1% yield of 1-indanol. After one reaction run, ICP-MS analysis showed the leaching of 1.8% Cu and 0.3% Ti into the solution.

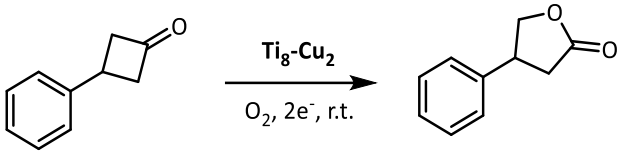

Typical procedure of Baeyer-Villiger oxidation: **Ti_8-Cu_2**-catalyzed Baeyer-Villiger oxidation reactions were carried out in a 2-dram septum-sealed glass vial equipped with an O_2-filled balloon. **Ti_8-Cu_2** (1.2 mg of MOF containing 0.5 μmol Cu_2 cofactor, 0.2 mol%), 3-phenylcyclobutan-1-one (0.25 mmol), isobutyraldehyde (0.50 mmol), and 2.0 mL of DCE were charged to a 2-dram septum-sealed glass vial. The reaction vial was capped and equipped with an O_2-filled balloon. After stirring for a preset reaction time (e.g., 48 h), the supernatant was analyzed by GC-MS to give 4-phenyloxolan-2-one in 70% yield. After one reaction run, ICP-MS analysis showed the leaching of 1.4% Cu and 0.3% Ti into the solution.

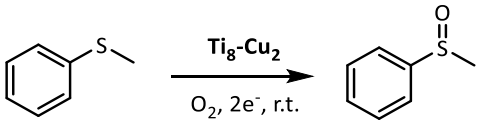

Typical procedure of sulfoxidation: **Ti_8-Cu_2**–catalyzed sulfoxidation reactions were carried out in a 2-dram septum-sealed glass vial equipped with an O_2-filled balloon. **Ti_8-Cu_2** (1.2 mg of MOF containing 0.5 μmol Cu_2 cofactor, 0.2 mol%), 3-phenylcyclobutan-1-one (0.25 mmol), isobutyraldehyde (0.50 mmol), and 2.0 mL of DCE were charged to a 2-dram septum-sealed glass vial. The reaction vial was capped and equipped with an O_2-filled balloon. After stirring for a preset reaction time (e.g., 48 h), the supernatant was analyzed by GC-MS to give 4-phenyloxolan-2-one in 70% yield. After one reaction run, ICP-MS analysis showed the leaching of 2.3% Cu and 0.6% Ti into the solution.

Table 4-3. Retention times of GC traces I (some compounds have multiple stereoisomers, thus showing more than one peak with the expected molecular mass).

Compound	Retention Time	Compound	Retention Time
	3.48 min		9.74 min
	6.90 min		13.19 min
	4.46 min		12.56, 13.18 min
	6.23 min		10.78 min
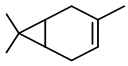	13.68 min	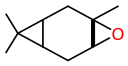	15.23 min
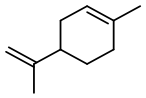	13.67 min	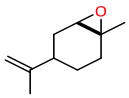	15.24 min
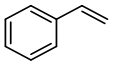	11.14 min	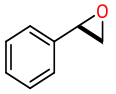	14.46 min
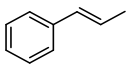	13.94 min	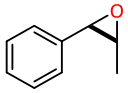	15.04, 15.15 min
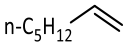	7.24 min	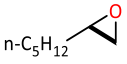	13.70 min
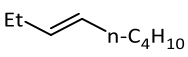	7.60 min	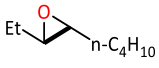	12.74, 13.10 min

Table 4-4. Retention times of GC traces II.

Compound	Retention Time	Compound	Retention Time
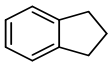	14.06 min	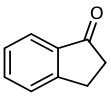	16.53 min
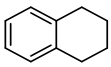	15.54 min	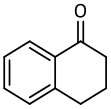	17.30 min
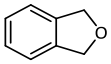	14.67 min	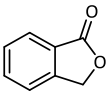	17.05 min
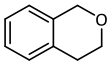	15.72 min	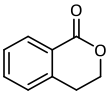	17.94 min
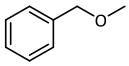	13.38 min	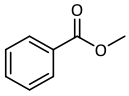	14.80 min
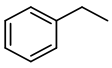	9.98 min	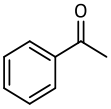	14.48 min
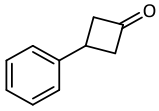	16.72 min	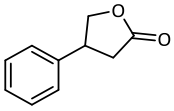	18.32 min
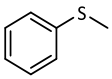	16.84 min	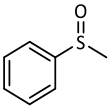	14.65 min

4.4.4 Computational analysis and reaction profiles

All density functional theory (DFT) calculations were carried out using Gaussian 16, Revision A.03.[62] The structures of intermediate (IN) species in solution-phase and gas-phase were fully optimized by using the B3LYP functional.[63-65] The 6-31+G(d) basis set was used for C, H, and O, and LanL2DZ (Lanl-2-double-zeta) was used for Ti and Cu. The single point energy

calculation was based on def2TZVP basis set to ensure accuracy and the corresponding thermal correction calculation was based on the 6-31+G(d) basis set. Solvation effect was accounted for by using the implicit solvation model, SMD.[66] The model contains a solvent molecule in a cavity surrounded by a continuous polarizable dielectric medium, which responds to the distributed solvent charges according to its dielectric constant. The $Ti_8O_8(O^-)_4$ SBU structure was modeled from the single crystal structure.[45] In the optimization process, $Ti_8O_8(O^-)_4$ SBUs were frozen to constrain the structures of the supported Cu sites on the SBUs. The transition states (TSs) during MOF catalyzed hydroxylation steps were found by using the TS method based on Berny algorithm[67] and further confirmed by the intrinsic reaction coordinate (IRC) method. All the TSs were validated by imaginary vibrational frequencies along the reaction coordinates and their reasonable geometries bridging the reactants and products.

The structures of MOF catalysts, **Ti_8-Cu_2-pre**, **Ti_8-Cu_2**, and **Ti_8-Cu_1**, were optimized by using B3LYP/6-31+G(d) for C, H, O, and N, and B3LYP/LanL2DZ for Ti and Cu. In the optimization process, $Ti_8O_8(O^-)_4$ SBUs were frozen to constrain the structures of the supported Cu sites on the SBUs. Charge distribution and spin density were also studied to make sure the structures are reasonable. Charge distributions were analyzed by natural population analysis (NPA).

Table 4-5. DFT optimized structure of **Ti_8-Cu_2-pre** and NBO charge distribution.

Optimized Structure	NBO Charge Distribution
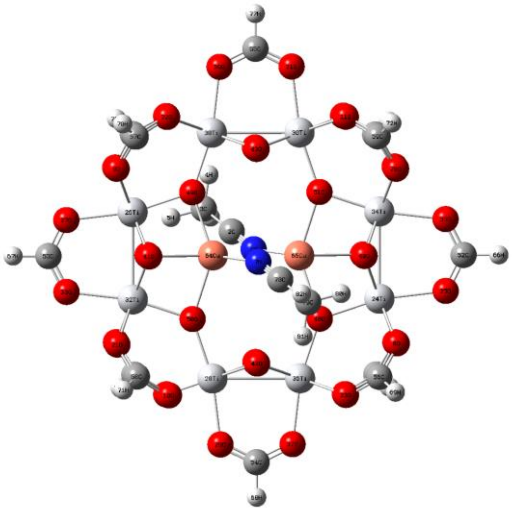	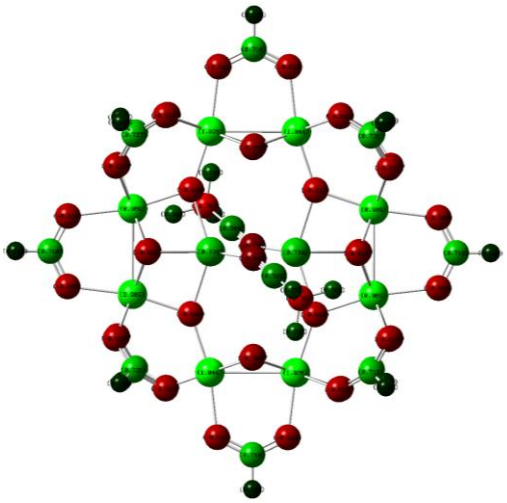
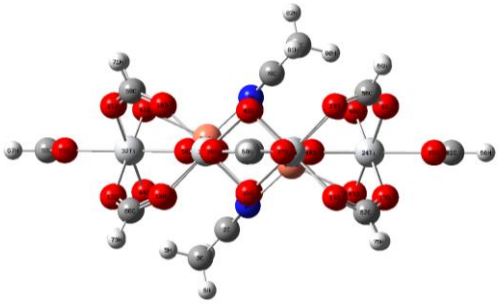	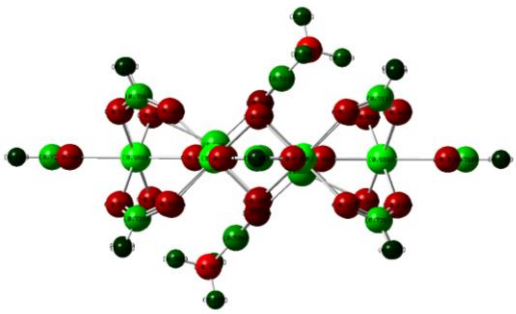

Table 4-6. Spin density and NBO charge of core atoms in **Ti_8-Cu_2-pre**.

Atom	Spin Density	NBO Charge
64Cu	0	0.728
65Cu	0	0.730
48O (μ_2-O^-)	0	-0.664
49O (μ_2-O^-)	0	-0.664
50O (μ_2-O^-)	0	-0.646
51O (μ_2-O^-)	0	-0.647
40O (μ_2-O)	0	-0.611
41O (μ_2-O)	0	-0.619
44O (μ_2-O)	0	-0.611
45O (μ_2-O)	0	-0.619
1N	0	-0.435
7N	0	-0.434
24Ti^{adjacent}	0	0.969
26Ti^{adjacent}	0	0.969
28Ti	0	1.044
30Ti	0	1.044
32Ti^{adjacent}	0	0.989
34Ti^{adjacent}	0	0.989
36Ti	0	1.026
38Ti	0	1.026

Table 4-7. DFT optimized structure of **Ti_8-Cu_2** and NBO charge distribution.

Optimized Structure	NBO Charge Distribution
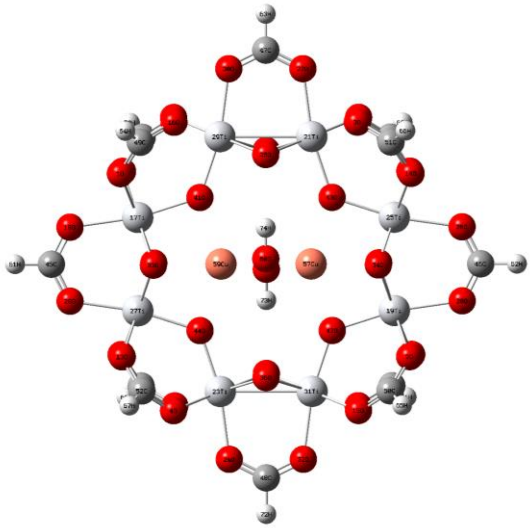	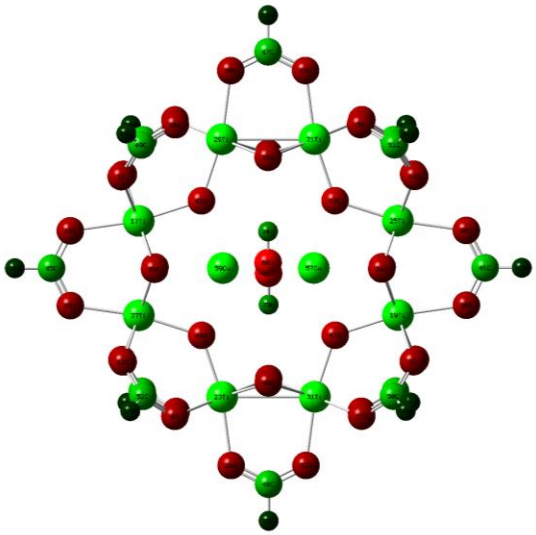
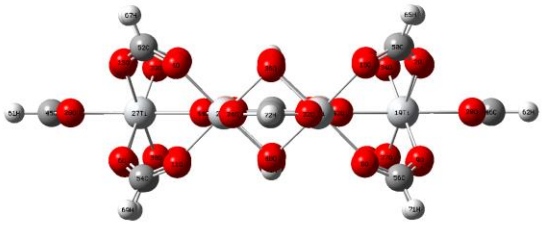	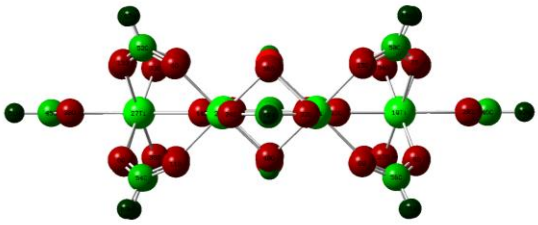

Table 4-8. Spin density and NBO charge of core atoms in **Ti_8-Cu_2**.

Atom	Spin Density	NBO Charge
57Cu	0.637884	1.103
59Cu	0.637884	1.103
41O (μ_2-O^-)	0.002944	-0.690
42O (μ_2-O^-)	0.002944	-0.690
43O (μ_2-O^-)	0.002944	-0.690
44O (μ_2-O^-)	0.002944	-0.690
33O (μ_2-O)	0.036996	-0.633
34O (μ_2-O)	0.036996	-0.633
37O (μ_2-O)	0.036996	-0.633
38O (μ_2-O)	0.036996	-0.633
58O (O^{OH})	0.303888	-0.914
60O (O^{OH})	0.303888	-0.914
73H (H^{OH})	-0.006115	0.519
74H (H^{OH})	-0.006115	0.519
17$Ti^{adjacent}$	-0.003901	0.986
19$Ti^{adjacent}$	-0.003901	0.986
21Ti	-0.004481	1.032
23Ti	-0.004481	1.032
25$Ti^{adjacent}$	-0.003901	0.986
27$Ti^{adjacent}$	-0.003901	0.986
29Ti	-0.004481	1.032
31Ti	-0.004481	1.032

Table 4-9. DFT optimized structure of **Ti_8-Cu_1** and NBO charge distribution.

Optimized Structure	NBO Charge Distribution
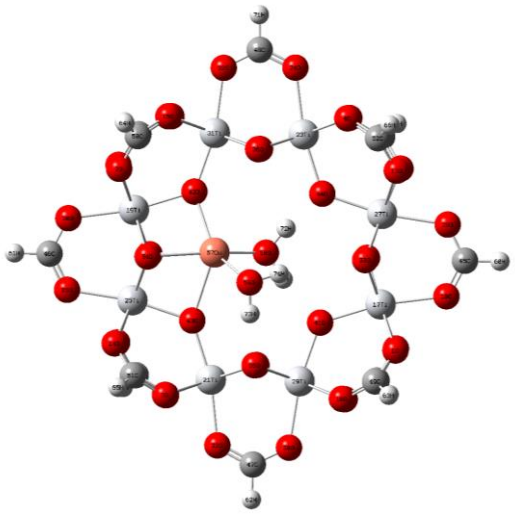	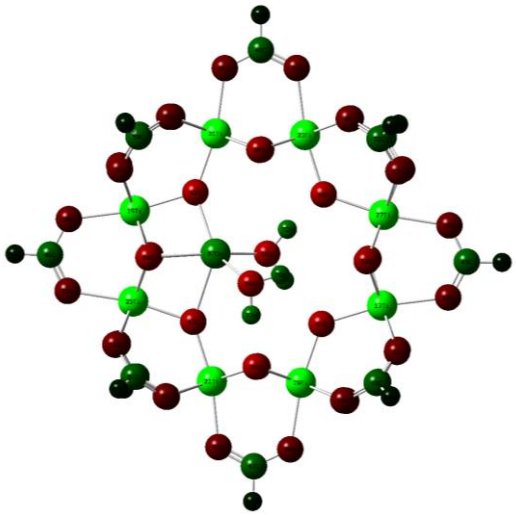
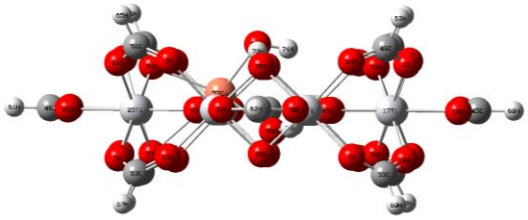	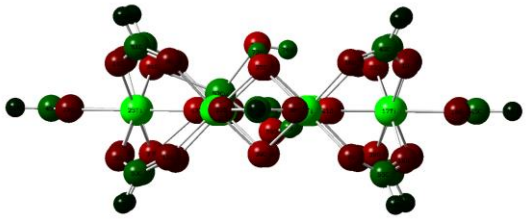

Table 4-10. Spin density and NBO charge of core atoms in **Ti_8-Cu_1**.

Atom	Spin Density	NBO Charge
57Cu	0.649223	1.195
41O (μ_2-O^-)	0.000972	-0.657
42O (μ_2-O^--Cu)	0.074692	-0.693
43O (μ_2-O^--Cu)	0.022826	-0.660
44O (μ_2-O^-)	0.001458	-0.670
33O (μ_2-O)	0.000034	-0.593
34O (μ_2-O)	0.101166	-0.654
37O (μ_2-O)	0.001327	-0.563
38O (μ_2-O)	-0.000051	-0.573
58O (O^{OH2})	0.125042	-0.921
59O (O^{OH2})	0.047551	-0.956
17Ti	0.000230	1.021
19$Ti^{adjacent}$	-0.018097	0.989
21Ti	-0.001496	1.038
23Ti	-0.001333	1.029
25$Ti^{adjacent}$	-0.010380	1.006
27Ti	0.000336	1.034
29Ti	-0.000814	1.028
31Ti	0.003099	1.036

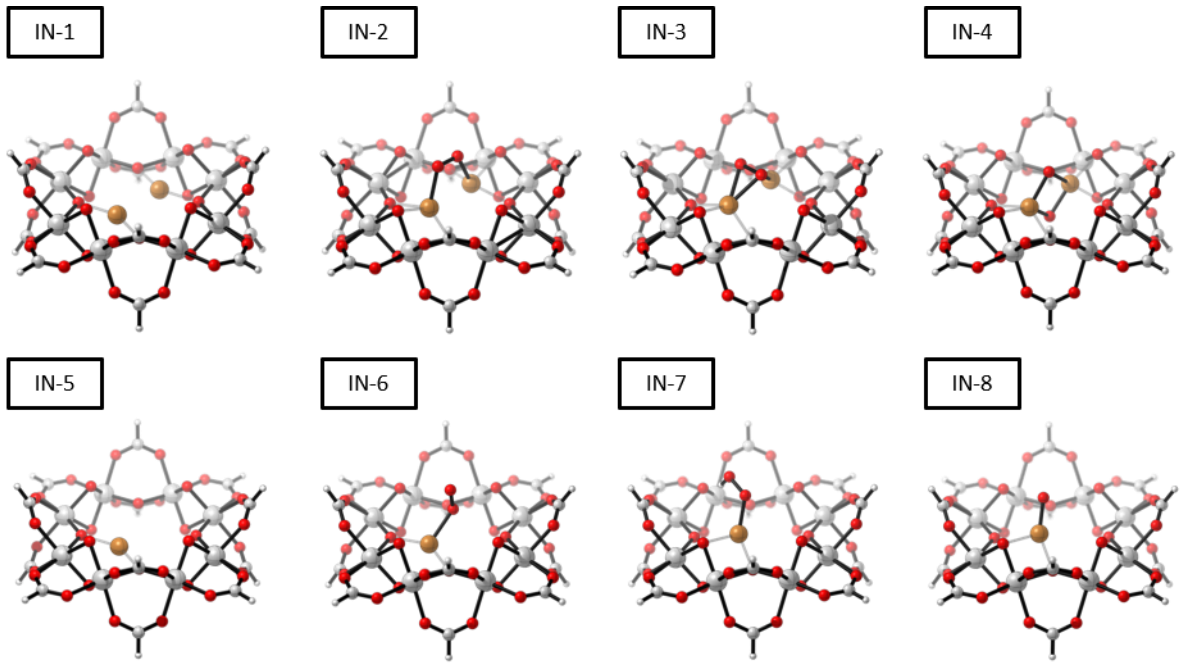

Figure 4-13. Structures of key intermediates during the dioxygen activation by **Ti_8-Cu_2** (top) and **Ti_8-Cu_1** (bottom).

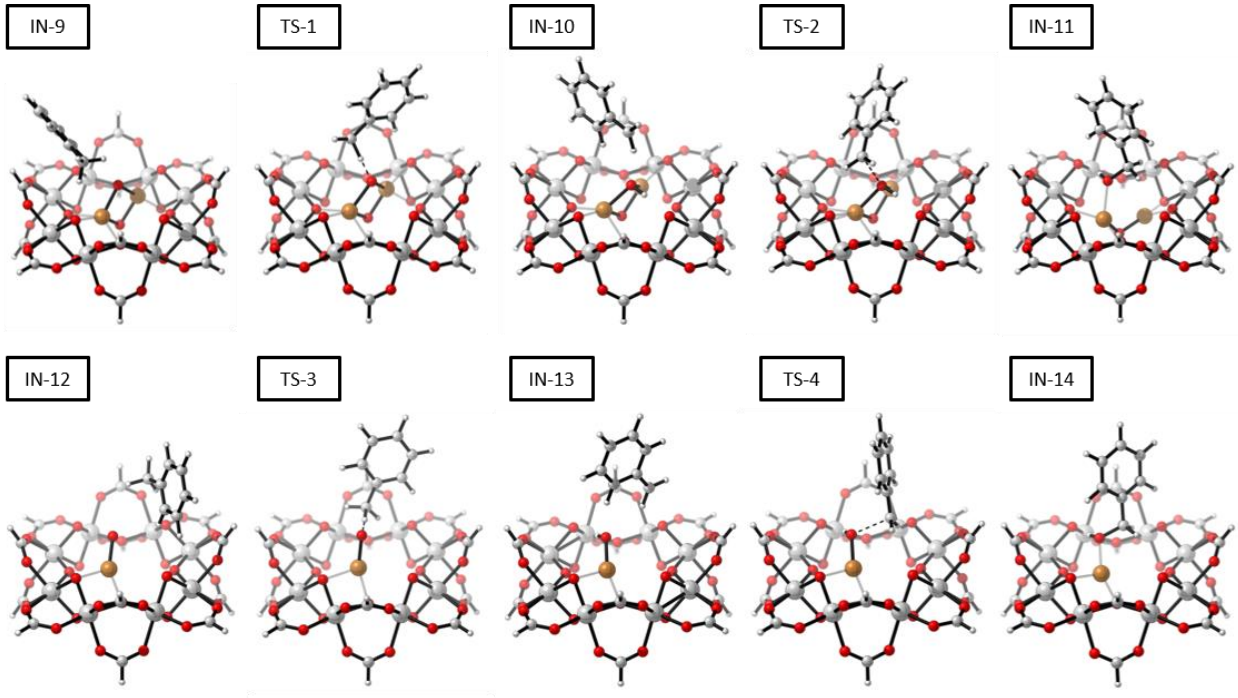

Figure 4-14. Structures of key intermediates and transition states during the hydroxylation by **Ti_8-Cu_2** (top) and **Ti_8-Cu_1** (bottom).

4.5 References

1. Benkovic, S. J.; Hammes-Schiffer, S., A Perspective on Enzyme Catalysis. *Science* **2003,** *301* (5637), 1196.

2. Bornscheuer, U. T.; Huisman, G. W.; Kazlauskas, R. J.; Lutz, S.; Moore, J. C.; Robins, K., Engineering the third wave of biocatalysis. *Nature* **2012,** *485* (7397), 185-194.

3. Sheldon, R. A.; Woodley, J. M., Role of Biocatalysis in Sustainable Chemistry. *Chemical Reviews* **2018,** *118* (2), 801-838.

4. Iyer, P. V.; Ananthanarayan, L., Enzyme stability and stabilization—Aqueous and non-aqueous environment. *Process Biochemistry* **2008,** *43* (10), 1019-1032.

5. DiCosimo, R.; McAuliffe, J.; Poulose, A. J.; Bohlmann, G., Industrial use of immobilized enzymes. *Chemical Society Reviews* **2013,** *42* (15), 6437-6474.

6. Breslow, R.; Overman, L. E., "Artificial enzyme" combining a metal catalytic group and a hydrophobic binding cavity. *Journal of the American Chemical Society* **1970,** *92* (4), 1075-1077.

7. Breslow, R., Artificial enzymes. *Science* **1982,** *218* (4572), 532.

8. Murakami, Y.; Kikuchi, J.-i.; Hisaeda, Y.; Hayashida, O., Artificial Enzymes. *Chemical Reviews* **1996,** *96* (2), 721-758.

9. Raynal, M.; Ballester, P.; Vidal-Ferran, A.; van Leeuwen, P. W. N. M., Supramolecular catalysis. Part 2: artificial enzyme mimics. *Chemical Society Reviews* **2014,** *43* (5), 1734-1787.

10. Wu, J.; Wang, X.; Wang, Q.; Lou, Z.; Li, S.; Zhu, Y.; Qin, L.; Wei, H., Nanomaterials with enzyme-like characteristics (nanozymes): next-generation artificial enzymes (II). *Chemical Society Reviews* **2019,** *48* (4), 1004-1076.

11. Bjerre, J.; Rousseau, C.; Marinescu, L.; Bols, M., Artificial enzymes, “Chemzymes”: current state and perspectives. *Applied Microbiology and Biotechnology* **2008,** *81* (1), 1-11.

12. Schwizer, F.; Okamoto, Y.; Heinisch, T.; Gu, Y.; Pellizzoni, M. M.; Lebrun, V.; Reuter, R.; Köhler, V.; Lewis, J. C.; Ward, T. R., Artificial Metalloenzymes: Reaction Scope and Optimization Strategies. *Chemical Reviews* **2018,** *118* (1), 142-231.

13. Torres Pazmiño, D. E.; Winkler, M.; Glieder, A.; Fraaije, M. W., Monooxygenases as biocatalysts: Classification, mechanistic aspects and biotechnological applications. *Journal of Biotechnology* **2010,** *146* (1), 9-24.

14. Dong, J.; Fernández-Fueyo, E.; Hollmann, F.; Paul, C. E.; Pesic, M.; Schmidt, S.; Wang, Y.; Younes, S.; Zhang, W., Biocatalytic Oxidation Reactions: A Chemist's Perspective. *Angewandte Chemie International Edition* **2018,** *57* (30), 9238-9261.

15. Bernhardt, R., Cytochromes P450 as versatile biocatalysts. *Journal of Biotechnology* **2006,** *124* (1), 128-145.

16. van Berkel, W. J. H.; Kamerbeek, N. M.; Fraaije, M. W., Flavoprotein monooxygenases, a diverse class of oxidative biocatalysts. *Journal of Biotechnology* **2006,** *124* (4), 670-689.

17. Solomon, E. I.; Heppner, D. E.; Johnston, E. M.; Ginsbach, J. W.; Cirera, J.; Qayyum, M.; Kieber-Emmons, M. T.; Kjaergaard, C. H.; Hadt, R. G.; Tian, L., Copper Active Sites in Biology. *Chemical Reviews* **2014,** *114* (7), 3659-3853.

18. Ross, M. O.; Rosenzweig, A. C., A tale of two methane monooxygenases. *JBIC Journal of Biological Inorganic Chemistry* **2017,** *22* (2), 307-319.

19. Eicken, C.; Krebs, B.; Sacchettini, J. C., Catechol oxidase — structure and activity. *Current Opinion in Structural Biology* **1999,** *9* (6), 677-683.

20. Ramsden, C. A.; Riley, P. A., Tyrosinase: The four oxidation states of the active site and their relevance to enzymatic activation, oxidation and inactivation. *Bioorganic & Medicinal Chemistry* **2014,** *22* (8), 2388-2395.

21. Fukuzumi, S.; Lee, Y.-M.; Jung, J.; Nam, W., Thermal and photocatalytic oxidation of organic substrates by dioxygen with water as an electron source. *Green Chemistry* **2018,** *20* (5), 948-963.

22. Jasniewski, A. J.; Que, L., Dioxygen Activation by Nonheme Diiron Enzymes: Diverse Dioxygen Adducts, High-Valent Intermediates, and Related Model Complexes. *Chemical Reviews* **2018,** *118* (5), 2554-2592.

23. Karlin, K. D.; Hayes, J. C.; Gultneh, Y.; Cruse, R. W.; McKown, J. W.; Hutchinson, J. P.; Zubieta, J., Copper-mediated hydroxylation of an arene: model system for the action of copper monooxygenases. Structures of a binuclear copper(I) complex and its oxygenated product. *Journal of the American Chemical Society* **1984,** *106* (7), 2121-2128.

24. Citek, C.; Lin, B.-L.; Phelps, T. E.; Wasinger, E. C.; Stack, T. D. P., Primary Amine Stabilization of a Dicopper(III) Bis(μ-oxo) Species: Modeling the Ligation in pMMO. *Journal of the American Chemical Society* **2014,** *136* (41), 14405-14408.

25. Cowley, R. E.; Tian, L.; Solomon, E. I., Mechanism of O2 activation and substrate hydroxylation in noncoupled binuclear copper monooxygenases. *Proceedings of the National Academy of Sciences* **2016,** *113* (43), 12035.

26. Ali, G.; VanNatta, P. E.; Ramirez, D. A.; Light, K. M.; Kieber-Emmons, M. T., Thermodynamics of a μ-oxo Dicopper(II) Complex for Hydrogen Atom Abstraction. *Journal of the American Chemical Society* **2017,** *139* (51), 18448-18451.

27. Meng, L.; Cheng, Q.; Kim, C.; Gao, W.-Y.; Wojtas, L.; Chen, Y.-S.; Zaworotko, M. J.; Zhang, X. P.; Ma, S., Crystal Engineering of a Microporous, Catalytically Active fcu Topology

MOF Using a Custom-Designed Metalloporphyrin Linker. *Angewandte Chemie International Edition* **2012,** *51* (40), 10082-10085.

28. Pullen, S.; Fei, H.; Orthaber, A.; Cohen, S. M.; Ott, S., Enhanced Photochemical Hydrogen Production by a Molecular Diiron Catalyst Incorporated into a Metal–Organic Framework. *Journal of the American Chemical Society* **2013,** *135* (45), 16997-17003.

29. Nath, I.; Chakraborty, J.; Verpoort, F., Metal organic frameworks mimicking natural enzymes: a structural and functional analogy. *Chemical Society Reviews* **2016,** *45* (15), 4127-4170.

30. Wright, A. M.; Wu, Z.; Zhang, G.; Mancuso, J. L.; Comito, R. J.; Day, R. W.; Hendon, C. H.; Miller, J. T.; Dincă, M., A Structural Mimic of Carbonic Anhydrase in a Metal-Organic Framework. *Chem* **2018,** *4* (12), 2894-2901.

31. Baek, J.; Rungtaweevoranit, B.; Pei, X.; Park, M.; Fakra, S. C.; Liu, Y.-S.; Matheu, R.; Alshmimri, S. A.; Alshehri, S.; Trickett, C. A.; Somorjai, G. A.; Yaghi, O. M., Bioinspired Metal–Organic Framework Catalysts for Selective Methane Oxidation to Methanol. *Journal of the American Chemical Society* **2018,** *140* (51), 18208-18216.

32. Cohen, S. M., Postsynthetic Methods for the Functionalization of Metal–Organic Frameworks. *Chemical Reviews* **2012,** *112* (2), 970-1000.

33. Cui, Y.; Li, B.; He, H.; Zhou, W.; Chen, B.; Qian, G., Metal–Organic Frameworks as Platforms for Functional Materials. *Accounts of Chemical Research* **2016,** *49* (3), 483-493.

34. Huang, Y.-B.; Liang, J.; Wang, X.-S.; Cao, R., Multifunctional metal–organic framework catalysts: synergistic catalysis and tandem reactions. *Chemical Society Reviews* **2017,** *46* (1), 126-157.

35. Xiao, J.-D.; Jiang, H.-L., Metal–Organic Frameworks for Photocatalysis and Photothermal Catalysis. *Accounts of Chemical Research* **2019,** *52* (2), 356-366.

36. Feng, L.; Wang, K.-Y.; Willman, J.; Zhou, H.-C., Hierarchy in Metal–Organic Frameworks. *ACS Central Science* **2020,** *6* (3), 359-367.

37. Nguyen, H. G. T.; Schweitzer, N. M.; Chang, C.-Y.; Drake, T. L.; So, M. C.; Stair, P. C.; Farha, O. K.; Hupp, J. T.; Nguyen, S. T., Vanadium-Node-Functionalized UiO-66: A Thermally Stable MOF-Supported Catalyst for the Gas-Phase Oxidative Dehydrogenation of Cyclohexene. *ACS Catalysis* **2014,** *4* (8), 2496-2500.

38. Manna, K.; Ji, P.; Lin, Z.; Greene, F. X.; Urban, A.; Thacker, N. C.; Lin, W., Chemoselective single-site Earth-abundant metal catalysts at metal–organic framework nodes. *Nat. Commun.* **2016,** *7* (1), 12610.

39. Feng, X.; Song, Y.; Lin, W., Transforming Hydroxide-Containing Metal–Organic Framework Nodes for Transition Metal Catalysis. *Trends in Chemistry* **2020,** *2* (11), 965-979.

40. Syed, Z. H.; Sha, F.; Zhang, X.; Kaphan, D. M.; Delferro, M.; Farha, O. K., Metal–Organic Framework Nodes as a Supporting Platform for Tailoring the Activity of Metal Catalysts. *ACS Catalysis* **2020,** *10* (19), 11556-11566.

41. Bour, J. R.; Wright, A. M.; He, X.; Dincă, M., Bioinspired chemistry at MOF secondary building units. *Chemical Science* **2020,** *11* (7), 1728-1737.

42. Liu, L.; Zhou, T.-Y.; Telfer, S. G., Modulating the Performance of an Asymmetric Organocatalyst by Tuning Its Spatial Environment in a Metal–Organic Framework. *Journal of the American Chemical Society* **2017,** *139* (39), 13936-13943.

43. Huxley, M. T.; Burgun, A.; Ghodrati, H.; Coghlan, C. J.; Lemieux, A.; Champness, N. R.; Huang, D. M.; Doonan, C. J.; Sumby, C. J., Protecting-Group-Free Site-Selective Reactions in a Metal–Organic Framework Reaction Vessel. *Journal of the American Chemical Society* **2018,** *140* (20), 6416-6425.

44. Liu, Y.; Shen, Y.; Zhang, W.; Weng, J.; Zhao, M.; Zhu, T.; Chi, Y. R.; Yang, Y.; Zhang, H.; Huo, F., Engineering channels of metal–organic frameworks to enhance catalytic selectivity. *Chemical Communications* **2019,** *55* (78), 11770-11773.

45. Dan-Hardi, M.; Serre, C.; Frot, T.; Rozes, L.; Maurin, G.; Sanchez, C.; Férey, G., A New Photoactive Crystalline Highly Porous Titanium(IV) Dicarboxylate. *Journal of the American Chemical Society* **2009,** *131* (31), 10857-10859.

46. Sono, M.; Roach, M. P.; Coulter, E. D.; Dawson, J. H., Heme-Containing Oxygenases. *Chemical Reviews* **1996,** *96* (7), 2841-2888.

47. Blain, I.; Slama, P.; Giorgi, M.; Tron, T.; Réglier, M., Copper-containing monooxygenases: enzymatic and biomimetic studies of the O-atom transfer catalysis. *Reviews in Molecular Biotechnology* **2002,** *90* (2), 95-112.

48. Parmeggiani, C.; Cardona, F., Transition metal based catalysts in the aerobic oxidation of alcohols. *Green Chemistry* **2012,** *14* (3), 547-564.

49. Groothaert, M. H.; van Bokhoven, J. A.; Battiston, A. A.; Weckhuysen, B. M.; Schoonheydt, R. A., Bis(μ-oxo)dicopper in Cu-ZSM-5 and Its Role in the Decomposition of NO: A Combined in Situ XAFS, UV−Vis−Near-IR, and Kinetic Study. *Journal of the American Chemical Society* **2003,** *125* (25), 7629-7640.

50. Deka, U.; Juhin, A.; Eilertsen, E. A.; Emerich, H.; Green, M. A.; Korhonen, S. T.; Weckhuysen, B. M.; Beale, A. M., Confirmation of Isolated Cu2+ Ions in SSZ-13 Zeolite as Active Sites in NH3-Selective Catalytic Reduction. *Journal of Physical Chemistry C* **2012,** *116* (7), 4809-4818.

51. Ikuno, T.; Zheng, J.; Vjunov, A.; Sanchez-Sanchez, M.; Ortuño, M. A.; Pahls, D. R.; Fulton, J. L.; Camaioni, D. M.; Li, Z.; Ray, D.; Mehdi, B. L.; Browning, N. D.; Farha, O. K.; Hupp, J. T.; Cramer, C. J.; Gagliardi, L.; Lercher, J. A., Methane Oxidation to Methanol Catalyzed by Cu-Oxo

Clusters Stabilized in NU-1000 Metal–Organic Framework. *Journal of the American Chemical Society* **2017,** *139* (30), 10294-10301.

52. Kau, L. S.; Hodgson, K. O.; Solomon, E. I., X-ray absorption edge and EXAFS study of the copper sites in zinc oxide methanol synthesis catalysts. *Journal of the American Chemical Society* **1989,** *111* (18), 7103-7109.

53. Handley, D. A.; Hitchcock, P. B.; Lee, T. H.; Leigh, G. J., Copper(II) adducts with N,N,N′,N′-tetramethylethane-1,2-diamine and attempts to prepare trinuclear derivatives. *Inorganica Chimica Acta* **2001,** *316* (1), 59-64.

54. Zheng, J.; Ye, J.; Ortuño, M. A.; Fulton, J. L.; Gutiérrez, O. Y.; Camaioni, D. M.; Motkuri, R. K.; Li, Z.; Webber, T. E.; Mehdi, B. L.; Browning, N. D.; Penn, R. L.; Farha, O. K.; Hupp, J. T.; Truhlar, D. G.; Cramer, C. J.; Lercher, J. A., Selective Methane Oxidation to Methanol on Cu-Oxo Dimers Stabilized by Zirconia Nodes of an NU-1000 Metal–Organic Framework. *Journal of the American Chemical Society* **2019,** *141* (23), 9292-9304.

55. Primet, M.; Pichat, P.; Mathieu, M. V., Infrared study of the surface of titanium dioxides. I. Hydroxyl groups. *Journal of Physical Chemistry* **1971,** *75* (9), 1216-1220.

56. Borfecchia, E.; Lomachenko, K. A.; Giordanino, F.; Falsig, H.; Beato, P.; Soldatov, A. V.; Bordiga, S.; Lamberti, C., Revisiting the nature of Cu sites in the activated Cu-SSZ-13 catalyst for SCR reaction. *Chemical Science* **2015,** *6* (1), 548-563.

57. Fu, Y.; Sun, D.; Chen, Y.; Huang, R.; Ding, Z.; Fu, X.; Li, Z., An Amine-Functionalized Titanium Metal–Organic Framework Photocatalyst with Visible-Light-Induced Activity for CO2 Reduction. *Angewandte Chemie International Edition* **2012,** *51* (14), 3364-3367.

58. Singh, L.; Rekha, P.; Chand, S., Cu-impregnated zeolite Y as highly active and stable heterogeneous Fenton-like catalyst for degradation of Congo red dye. *Separation and Purification Technology* **2016,** *170*, 321-336.

59. Mirica, L. M.; Ottenwaelder, X.; Stack, T. D. P., Structure and Spectroscopy of Copper−Dioxygen Complexes. *Chemical Reviews* **2004,** *104* (2), 1013-1046.

60. Rolff, M.; Schottenheim, J.; Decker, H.; Tuczek, F., Copper–O2 reactivity of tyrosinase models towards external monophenolic substrates: molecular mechanism and comparison with the enzyme. *Chemical Society Reviews* **2011,** *40* (7), 4077-4098.

61. Mahyuddin, M. H.; Shiota, Y.; Staykov, A.; Yoshizawa, K., Theoretical Overview of Methane Hydroxylation by Copper–Oxygen Species in Enzymatic and Zeolitic Catalysts. *Accounts of Chemical Research* **2018,** *51* (10), 2382-2390.

62. Frisch, M. J.; Trucks, G. W.; Schlegel, H. B.; Scuseria, G. E.; Robb, M. A.; Cheeseman, J. R.; Scalmani, G.; Barone, V.; Petersson, G. A.; Nakatsuji, H.; Li, X.; Caricato, M.; Marenich, A. V.; Bloino, J.; Janesko, B. G.; Gomperts, R.; Mennucci, B.; Hratchian, H. P.; Ortiz, J. V.; Izmaylov, A. F.; Sonnenberg, J. L.; Williams; Ding, F.; Lipparini, F.; Egidi, F.; Goings, J.; Peng, B.; Petrone, A.; Henderson, T.; Ranasinghe, D.; Zakrzewski, V. G.; Gao, J.; Rega, N.; Zheng, G.; Liang, W.;

Hada, M.; Ehara, M.; Toyota, K.; Fukuda, R.; Hasegawa, J.; Ishida, M.; Nakajima, T.; Honda, Y.; Kitao, O.; Nakai, H.; Vreven, T.; Throssell, K.; Montgomery Jr., J. A.; Peralta, J. E.; Ogliaro, F.; Bearpark, M. J.; Heyd, J. J.; Brothers, E. N.; Kudin, K. N.; Staroverov, V. N.; Keith, T. A.; Kobayashi, R.; Normand, J.; Raghavachari, K.; Rendell, A. P.; Burant, J. C.; Iyengar, S. S.; Tomasi, J.; Cossi, M.; Millam, J. M.; Klene, M.; Adamo, C.; Cammi, R.; Ochterski, J. W.; Martin, R. L.; Morokuma, K.; Farkas, O.; Foresman, J. B.; Fox, D. J. *Gaussian, Inc.*,, Wallingford, CT, 2016.

63. Becke, A. D., Density-functional exchange-energy approximation with correct asymptotic behavior. *Physical Review A* **1988,** *38* (6), 3098-3100.

64. Lee, C. T.; Yang, W. T.; Parr, R. G., DEVELOPMENT OF THE COLLE-SALVETTI CORRELATION-ENERGY FORMULA INTO A FUNCTIONAL OF THE ELECTRON-DENSITY. *Physical Review B* **1988,** *37* (2), 785-789.

65. Gupta, M.; da Silva, E. F.; Svendsen, H. F., Postcombustion CO2 Capture Solvent Characterization Employing the Explicit Solvation Shell Model and Continuum Solvation Models. *J. Phys. Chem., B* **2016,** *120* (34), 9034-9050.

66. Marenich, A. V.; Cramer, C. J.; Truhlar, D. G., Universal Solvation Model Based on Solute Electron Density and on a Continuum Model of the Solvent Defined by the Bulk Dielectric Constant and Atomic Surface Tensions. *The Journal of Physical Chemistry B* **2009,** *113* (18), 6378-6396.

67. Schlegel, H. B., Optimization of equilibrium geometries and transition structures. *Journal of Computational Chemistry* **1982,** *3* (2), 214-218.

Chapter 5. Strongly Lewis Acidic MOFs for Continuous Flow Catalysis

5.1 Introduction

Lewis acids efficiently catalyze many different types of organic reactions by withdrawing electron density from functional groups to make them susceptible to nucleophilic attacks.[1-2] In Diels-Alder reactions, for example, coordination of a dienophile to a Lewis acid significantly decreases its LUMO energy to facilitate its reaction with a diene.[3] Catalytic Diels-Alder reactions allow for efficient synthesis of functionalized cyclic compounds that have found widespread use as pharmaceutical ingredients, artificial flavors, fragrances, and agrochemicals.[4] Lewis acids are also used to catalyze the formation of epoxides and aromatic ketones and regioselective ring opening of epoxides to yield alcohols.

Early Lewis acid catalysts were typically based on main group or early transition metal halides. Lewis acidity of these metals increases when the halides are replaced with more electron-deficient and less coordinating anions, such as triflate ($^{-}$OTf) or bis(trifluoromethylsulfonyl)imide ($^{-}$NTf$_2$).[5-6] However, these Lewis acidic metal salts tend to have low solubility in nonpolar organic solvents, are sensitive to moisture, and have short lifetimes during catalysis. In order to overcome these drawbacks, researchers have devoted significant efforts to developing heterogeneous Lewis acid catalysts such as zeolites, metal oxides and resins over the past few decades. Solid acid catalysts can be readily separated from reaction mixtures for reuse and are compatible with flow catalysis, [7-8] but they have moderate Lewis acidity, low active site density, and non-uniform active sites.[9-10]

Metal-organic frameworks (MOFs) have recently emerged as a novel porous material platform for designing homogeneously inaccessible catalysts by taking advantage of their regular

framework structures and site isolation effects.[11-13] In particular, metal centers in MOF nodes have afforded outstanding single-site solid catalysts with unique electronic properties and steric environments that are not accessible via conventional homogeneous chemistry or heterogenization approaches. Although MOF nodes have been used as Lewis acidic sites to catalyze organic transformations, such as cyclization reactions,[14] C-H iodination,[15] hydrolysis,[16] and dehydration,[17] using activated substrates, Lewis acidity of these metal sites is significantly lower than the homogeneous benchmark $Sc(OTf)_3$.[18] Our group has previously developed two quantitative methods for measuring Lewis acidity of MOF through electron paramagnetic resonance (EPR) spectroscopy of MOF-bound superoxide ($O_2^{\bullet-}$) or fluorescence spectroscopy of MOF-bound *N*-methylacridone (NMA).[15] Such methods can potentially guide the discovery of highly Lewis acidic MOF catalysts for efficient organic synthesis through continuous flow catalysis.[15]

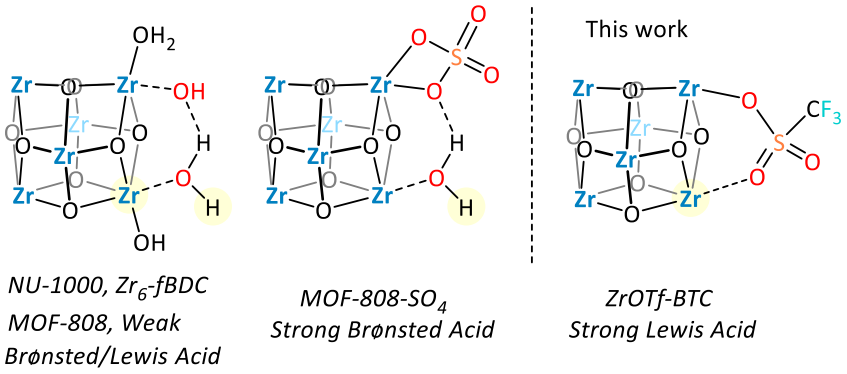

Figure 5-1. Chemical structures of reported acidic Zr MOFs and ZrOTf-BTC. Copyright 2019 American Chemical Society.

Several examples of Zr MOFs have recently been shown to possess relatively strong acidity (**Figure 5-1**).[14, 19-20] Notably, Yaghi and coworkers developed MOF-808-SO_4 as a strong Brönsted acid catalyst for alkene dimerization, in which the unsaturated Zr_6 nodes of MOF-808 were modified by sulfuric acid to display outstanding Brönsted acidity.[21] In this work, we aim to develop strongly Lewis acidic Zr MOF catalysts that work through different and complementary reaction

mechanisms. We synthesized Lewis acidic ZrOTf-BTC (BTC = 1,3,5-benzenetricarboxylic acid) MOF from Zr-BTC (MOF-808) through sequential post-synthetic formate removal and triflation of MOF nodes. ZrOTf-BTC is a highly active solid Lewis acid catalyst for a broad range of important organic transformations, including Diels-Alder reactions, epoxide ring-opening reactions, Friedel-Crafts acylation, and alkene hydroalkoxylation reactions. ZrOTf-BTC exhibits higher Lewis acidity than $Sc(OTf)_3$ and outperforms $Sc(OTf)_3$ in these reactions with higher catalytic activity and longer catalyst lifetime. We further supported ZrOTf-BTC on SiO_2 to afford a composite material as an efficient solid Lewis acid catalyst for continuous flow catalysis (**Scheme 5-1**).

Scheme 5-1. Strongly Lewis acidic MOFs for continuous flow catalysis. Copyright 2019 American Chemical Society.

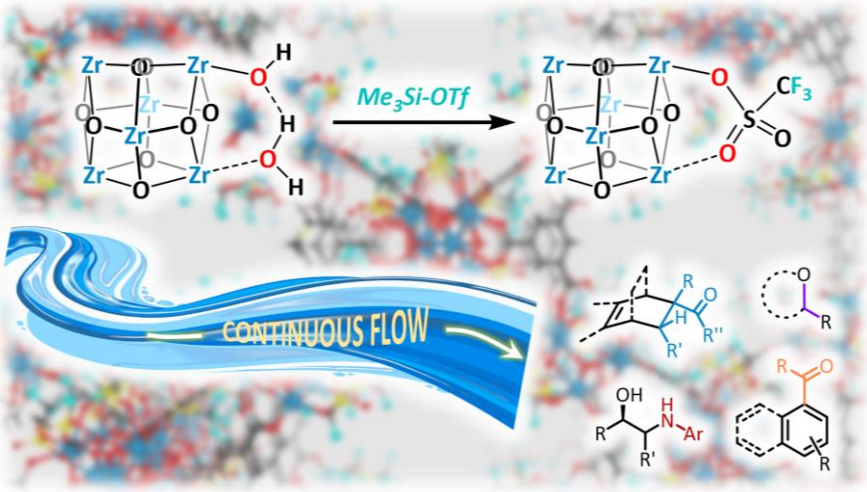

5.2 Results and Discussion

5.2.1 Synthesis and characterization of ZrOTf-BTC

Zr-BTC was synthesized following the literature procedure by a solvothermal reaction of trimesic acid and $ZrOCl_2 \cdot 8H_2O$ in a mixture of *N*,*N*-dimethylformamide (DMF) and formic acid.[22] The inorganic node of Zr-BTC has the composition of $Zr_6(\mu_3\text{-}O)_4(\mu_3\text{-}OH)_4(RCO_2)_6(HCO_2)_6$, where

six formate groups cap all the peripheral sites around the Zr_6 octahedron. Zr-BTC was subsequently activated with 1M aqueous HCl at 100 °C for 18 h to replace the formate groups with six pairs of Zr-coordinated hydroxide and water groups to afford ZrOH-BTC with the inorganic node composition of $Zr_6(\mu_3\text{-}O)_4(\mu_3\text{-}OH)_4(RCO_2)_6[(OH)(OH_2)]_6$. ZrOH-BTC was then treated with trimethylsilyl triflate (Me_3SiOTf) in benzene at 80 °C for 8 h to afford ZrOTf-BTC (**Figure 5-2a**). As the oxophilic Me_3Si group forms stronger bond with the ^{-}OH moiety than with the ^{-}OTf moiety, Me_3SiOTf readily removes OH^- from ZrOH-BTC to generate ZrOTf-BTC with the node composition of $Zr_6(\mu_3\text{-}O)_4(\mu_3\text{-}OH)_4(RCO_2)_6[OTf]_6$. The Me_3SiOH byproduct generated through this activation reacted with excess Me_3SiOTf to form $(Me_3Si)_2O$. The amount of $(Me_3Si)_2O$ was quantified to be 0.90 equiv. *w.r.t.* Zr by ^1H NMR, agreeing well with the proposed activation process.

Powder X-ray diffraction (PXRD) studies showed that ZrOTf-BTC remained crystalline and maintained the structure of ZrOH-BTC (**Figure 5-2b**). Transmission Electron Microscope (TEM) images of ZrOTf-BTC displayed highly crystalline octahedral particles of ~200nm in dimensions. (**Figure 5-2c**) The porosity of ZrOTf-BTC was confirmed by N_2 sorption isotherms, with a Brunauer-Emmett-Teller (BET) surface area of 779 m^2/g (**Figure 5-2d**). Pore size analysis by nonlinear density functional theory (NL-DFT) showed a uniform pore at ~16 Å that is attributable to the large hexagonal cages of the MOF. The pore size of ZrOTf-BTC is smaller than that of ZrOH-BTC (21 Å) due to the presence of six large triflate groups per SBU (**Figure 5-2e**).

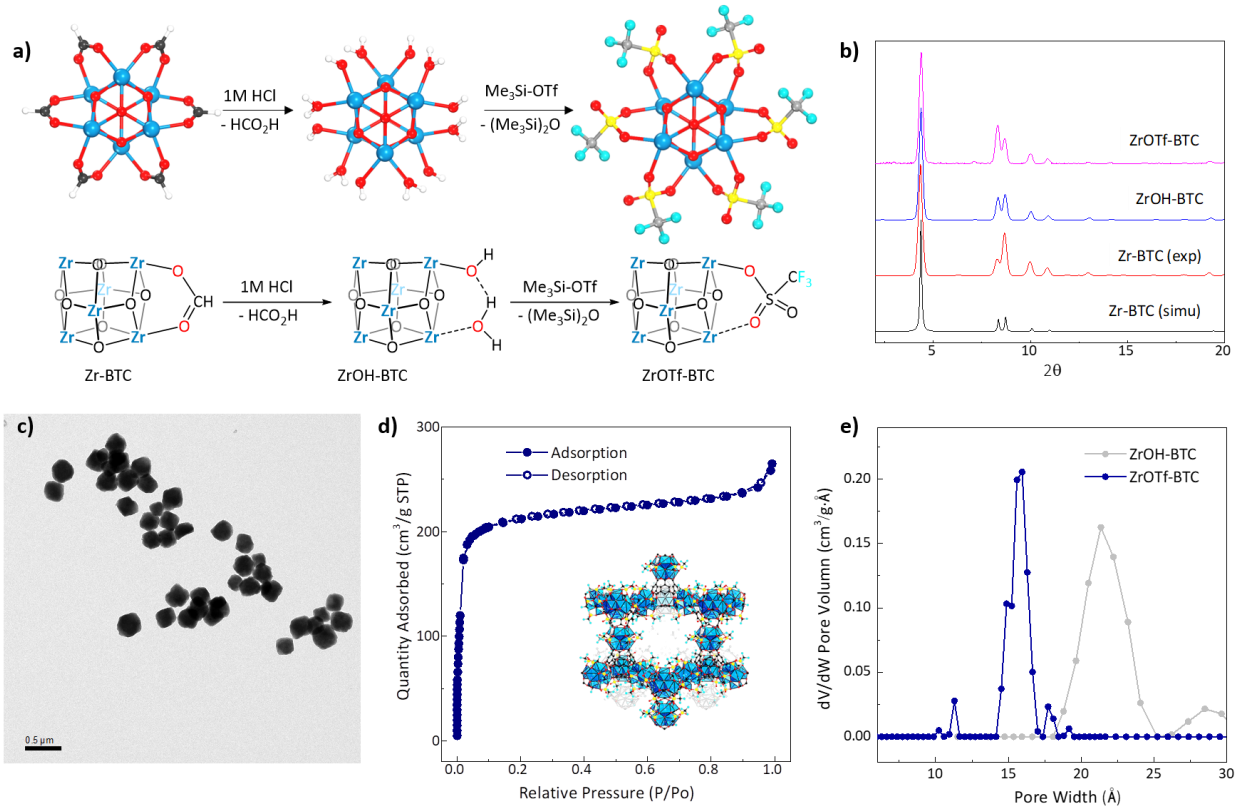

Figure 5-2. Synthesis and characterization of strongly Lewis acidic MOF ZrOTf-BTC. (a) Synthesis of ZrOTf-BTC through stepwise activation of Zr-BTC with 1M HCl and Me_3SiOTf. (b) Similarity between PXRD patterns of ZrOTf-BTC (magenta), Zr-BTC (red), and ZrOH-BTC (blue) indicates the maintenance of MOF crystallinity throughout post-synthetic treatments. (c) TEM image of ZrOTf-BTC showing octahedral morphology with an average diameter of 200 nm. (d) N_2 sorption isotherms of ZrOTf-BTC, with a calculated BET surface area of 779 m^2/g. (e) Pore size distribution of ZrOTf-BTC (blue) showing a uniform pore size of 16 Å that is smaller than that of ZrOH-BTC (21 Å, gray plot) due to the presence of six triflate groups per hexagonal pore in ZrOTf-BTC. Copyright 2019 American Chemical Society.

5.2.2 Computational and spectroscopic studies of Zr-OTf active sites

We used a range of computational and spectroscopic techniques, including density functional theory (DFT), extended X-ray absorption fine-structure (EXAFS) and X-ray near-edge spectroscopy (XANES), to elucidate the Zr coordination environment in ZrOTf-BTC. The first question we attempted to address was whether triflate groups were incorporated into the MOF. We performed sulfur K-edge XANES analysis to prove the presence of triflate groups. The sulfur centers in ZrOTf-BTC displayed significant edge-step, with the K-edge energy of at 2479.8 eV.

This energy is much higher than that of sodium thiosulfate ($Na_2S_2O_3$) standard and matched well to the edge energy of $Sc(OTf)_3$, indicating the presence of triflate groups in ZrOTf-BTC (**Figure 5-3b**).

The next question we attempted to address was how triflate groups were coordinated to Zr centers. We envisioned two possible modes of triflate coordination (**Figure 5-3a**): OTf bridging two proximal Zr centers (the μ_2-model) or OTf chelation to a single Zr center (the η^2-model). Both coordination modes are commonly observed in the crystal structures of molecular metal-OTf complexes. Both structures were optimized using DFT at the B3LYP level of theory, and their free energies were calculated to compare their relative stability. The optimized structure for the μ_2-model showed an average Zr-O^{OTf} bond distance of 2.269 Å, which is similar to reported Zr-O^{OTf} bond distances in molecular Zr_2(OTf) complexes.[23-24] The optimized structure for the η^2-model showed an average Zr-O^{OTf} bond distance of 2.299 Å, which is longer than that of the μ_2 model by 0.030 Å. Bond distance analysis thus showed stronger bonding between μ_2-triflates and Zr centers. Free energy calculations also indicated the μ_2 model is thermodynamically more stable, with 24.85 kcal·mol^{-1} lower free energy than the η^2-model per six Zr centers. The DFT optimized μ_2 model fitted well to the Zr k-edge EXAFS spectrum of ZrOTf-BTC, with an R-factor of 0.007 (**Figure 5-3c**). The fitted Zr-OTf bond distances have an average value of 2.20 Å, similar to that calculated by DFT (2.269 Å).

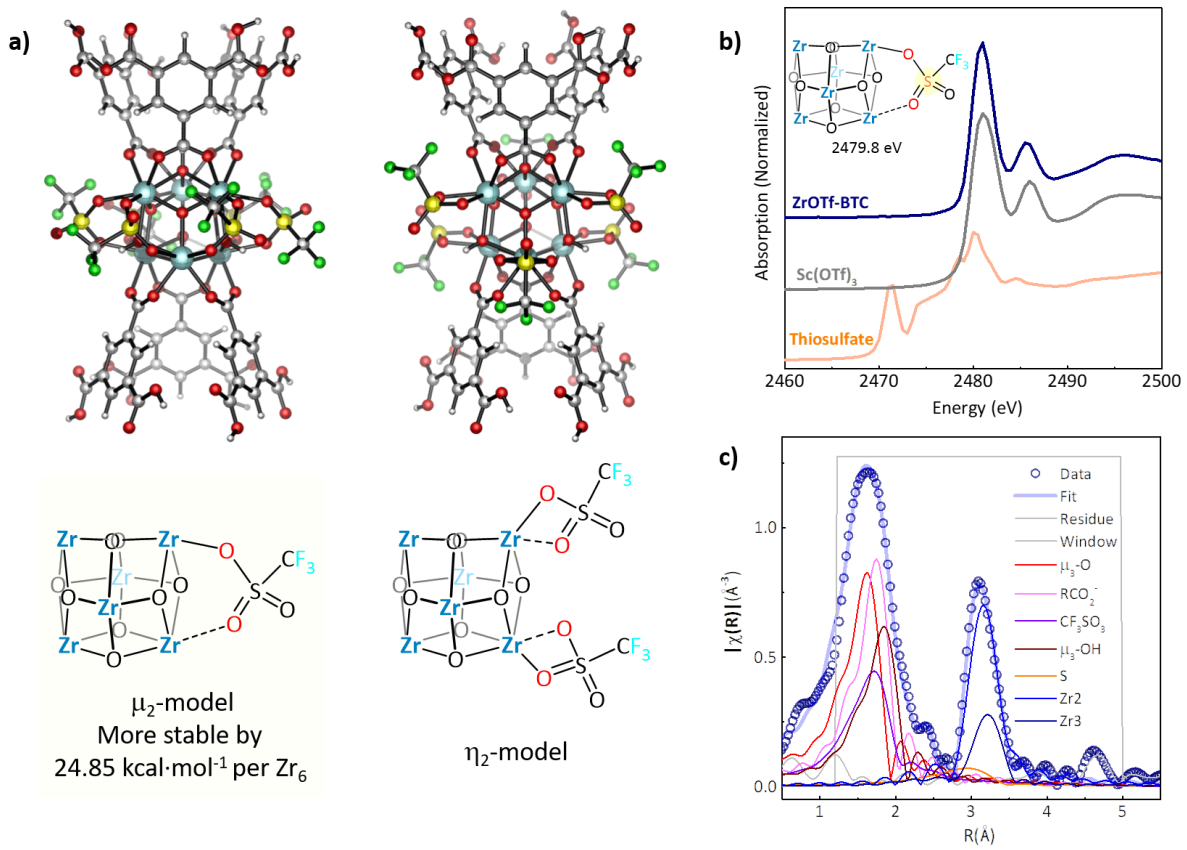

Figure 5-3. Determination of local coordination environment of ZrOTf-BTC. (a) DFT optimized structures of ZrOTf-BTC with $Zr_2(\mu_2$-OTf) and $Zr(\eta_2$-OTf) coordination modes. The μ_2-model is more stable than the η_2-model by 24.85 kcal·mol^{-1} per $Zr_6O_4(OH)_4(OTf)_6$ node. (b) The sulfur XANES spectra of ZrOTf-BTC, sodium thiosulfate, and $Sc(OTf)_3$ indicate the presence of triflate groups in ZrOTf-BTC. (c) Fitting of ZrOTf-BTC EXAFS data using the μ_2-model; the R-factor for the fitting is 0.007. Copyright 2019 American Chemical Society.

5.2.3 Quantification of ZrOTf-BTC Lewis acidity by spectroscopic methods

We then quantified the Lewis acidity of ZrOTf-BTC using two spectroscopic methods that were recently developed, EPR spectroscopy of MOF-bound superoxides ($O_2^{\bullet-}$) and fluorescence spectroscopy of MOF-bound NMA.[15] ZrOTf-BTC was shown to be more Lewis acidic than ZrOH-BTC based on the Lewis acidity measurement using both techniques.

$O_2^{\bullet-}$ probe was generated *in situ* by the 1 e^- photo-reduction of O_2, which readily binds to Lewis acidic Zr-centers by displacing weakly coordinating triflates to form EPR-active $Zr(O_2^{\bullet-})$ species.[25] Coordination to Lewis acids significantly shifts the EPR signature of $O_2^{\bullet-}$, especially the

g_{zz}-tensor that is determined by the energy splitting (ΔE) between the π_x^* and π_y^* orbitals.[26] ZrOTf-BTC bound $O_2^{\bullet-}$ exhibited a g_{zz} of 2.0310, which corresponds to a ΔE of 0.99 eV (**Figure 5-4a**), comparable with the benchmark homogeneous Lewis acid catalyst $Sc(OTf)_3$, which displays a ΔE of 1.00 eV as reported.[27] The non-triflated ZrOH-BTC has much lower Lewis acidity than ZrOTf-BTC, with a measured ΔE of 0.90 eV.

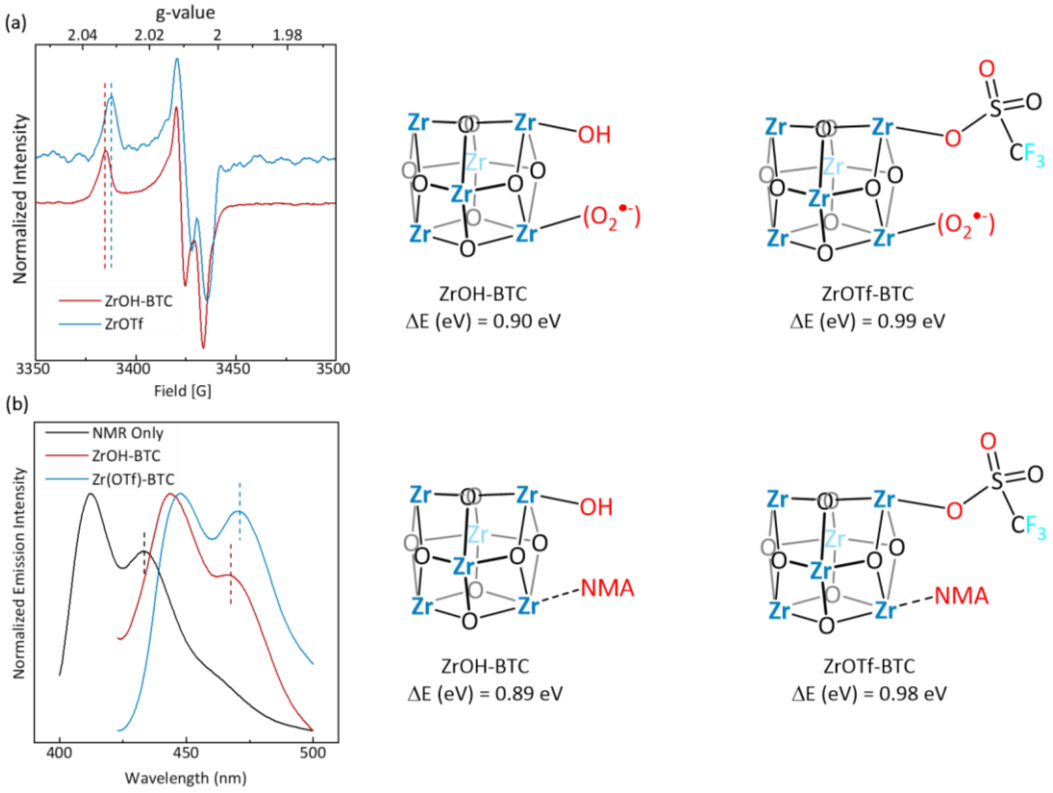

Figure 5-4. Lewis acidity measurements of ZrOTf-BTC and ZrOH-BTC. (a) EPR spectrum (100 K) of superoxide bond to ZrOTf-BTC measured in MeCN/toluene mixed solvents. (b) The fluorescence spectra of NMA in MeCN (black) and NMA bound to ZrOH-BTC (red) and ZrOTf-BTC (blue).

We also used NMA fluorescence to probe the Lewis acidity of ZrOTf-BTC. Free NMA has an emission maximum (λ_{max}) at 433.0 nm. Upon coordination to ZrOTf-BTC, the Zr(NMA)-BTC complex displayed a λ_{max} at 471.0 nm. The energy shift of NMA emission is established to be linearly correlated to the Lewis acidity of metal centers.[15, 27] We calculated the ΔE of ZrOTf-BTC to be 0.98 eV, which is almost identical to the value measured from superoxide EPR (**Figure**

5-4b). In comparison, ZrOH-BTC only shifted the NMA emission λ_{max} to 467.0 nm, with a calculated ΔE of 0.89 eV. Identical NMA fluorescence test with homogeneous $Sc(OTf)_3$ also gave a ΔE of 0.98 eV. Triflation of metal-hydroxides thus provides an effective strategy to enhance MOF Lewis acidity and to generate porous solid acids with Lewis acidity comparable to $Sc(OTf)_3$.

5.2.4 Synthesis and characterization of ZrOTf-BTC@SiO_2

Although Lewis acids have broad applications in organic synthesis, little progress has been made in immobilizing Lewis acids for flow synthesis.[28-29] BF_3 and $Sc(OTf)_3$ are commonly used to catalyze organic transformations, but they are difficult to incorporate into heterogeneous supports without sacrificing acidity.[30-31] As a result, most flow processes used Lewis acids in stoichiometry, causing significant waste of catalysts and quenching reagents and corrosion of reaction vessels. Owing to their tunable structures and high porosity, MOFs and related organic-inorganic hybrid materials represent an attractive class of solid catalysts for flow catalysis.[32-34] We sought to utilize ZrOTf-BTC as an effective fixed-bed Lewis acid catalyst to achieve flow catalysis of a broad scope of reactions.

Due to the tight packing of MOF particles and the slow substrate diffusion rate through the nano-sized MOF channels, packing pure MOFs into a column can lead to very high column pressure. Growing MOFs into much larger sizes or simply mix the MOF with inert filler can reduce the column pressure, but organic substrates cannot easily access the interiors of such MOF particles due to the increased diffusion barrier. To overcome this limitation, we directly grew ZrOTf-BTC on silica to afford the ZrOTf-BTC@SiO_2 composite material.[35-36] Zr-BTC@SiO_2 was first prepared analogously to Zr-BTC except with the addition of 30 weight equiv. of SiO_2. Surface silanol groups on SiO_2 served as the nucleation sites for the formation of octahedron-shaped Zr-

BTC particles. Due to enhanced nucleation on silica surface, the MOF particles in the composite material are smaller than pure MOF particles and are densely packed on silica.

Zr-BTC@SiO_2 was treated with 1M HCl to remove formate capping groups and then triflated with Me_3SiOTf to form ZrOTf-BTC@SiO_2 as an off-white powder. TEM imaging showed that ZrOTf-BTC@SiO_2 possessed core-shell structures with the MOF particles displaying high crystallinity and octahedral morphology (**Figures 5-5c**, **5-5d**). ZrOTf-BTC@SiO_2 exhibited the same PXRD pattern as Zr-BTC, indicating that the MOF in the composite maintained the identical structure as the pristine MOF (**Figure 5-5b**). N_2 sorption isotherms of ZrOTf-BTC@SiO_2 gave a BET surface area of 321 m^2/g. The composite material showed a sharp N_2 sorption at $P/P_o < 0.2$, which can be attributed to micropore filling of ZrOTf-BTC, and a broad adsorption with hysteresis at P/P_o =0.2 - 0.9, which is attributable to mesopore sorption by silica particles. Pore size analysis by NL-DFT indicated the presence of a uniform micropore at 1.6 nm and a broad range of larger pores at 2-10 nm (**Figures 5-5e**, **5-5f**). The Zr coordination environment was studied by EXAFS. By using the μ_2-triflate and Zr coordination sphere of $Zr(OTf)_2(\mu_3\text{-}O)_2(\mu_3\text{-}OH)_2(RCO_2)_2$, the Zr K-edge EXAFS data of ZrOTf-BTC-SiO_2 was well fitted with an average Zr-OTf bond distance of 2.217 Å (**Figure 5-5g**). The Zr active sites in ZrOTf-BTC@SiO_2 thus adopted an identical coordination environment as those in ZrOTf-BTC. The ZrOTf-BTC@SiO_2 powder was slurry-packed with CH_2Cl_2 into a stainless-steel column for flow catalysis studies. The amount of ZrOTf-BTC was quantified to be 40 μmol Zr per gram by ^1H NMR analysis of the digested material.

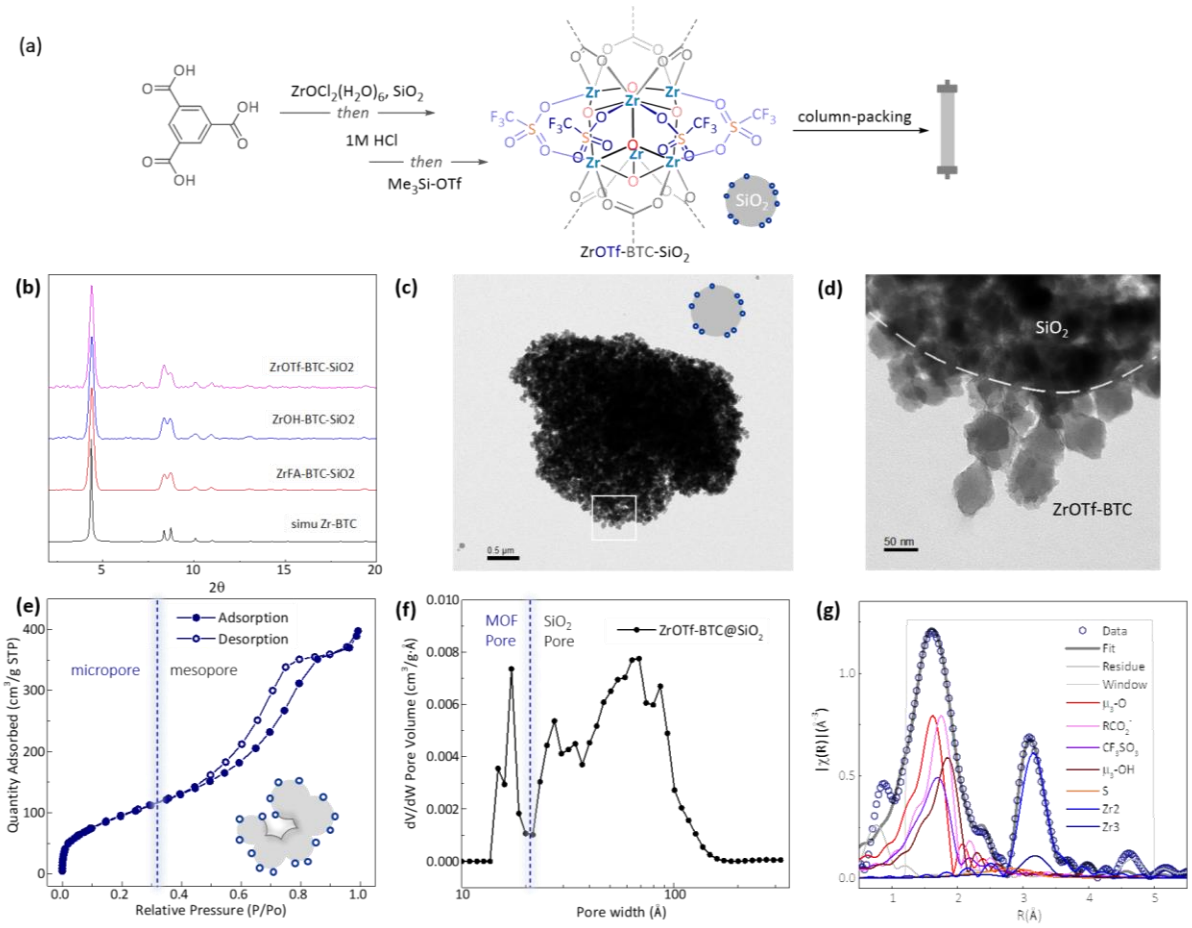

Figure 5-5. Synthesis and characterization of MOF-silica composite ZrOTf-BTC@SiO_2. (a) Schematic depiction of the synthesis of ZrOTf-BTC@SiO_2 and its packing into a column reactor. (b) PXRD patterns of ZrOTf-BTC@SiO_2 (magenta), ZrOH-BTC@SiO_2 (blue) and ZrFA-BTC@SiO_2 (red) compared to the simulated one for Zr-BTC. (c-d) TEM image of ZrOTf-BTC@SiO_2 particle. (e) N_2 sorption isotherms of ZrOTf-BTC@SiO_2. The calculated BET surface area is 321 m^2/g for the ZrOTf-BTC@SiO_2 composite. (f) Pore size distributions of ZrOTf-BTC@SiO_2. (g) Fitting of ZrOTf-BTC@SiO_2 EXAFS data using the μ_2-model structure of ZrOTf-BTC; the R-factor for the fitting is 0.009. Copyright 2019 American Chemical Society.

5.2.5 ZrOTf-BTC catalyzed Diels-Alder reactions

The Diels-Alder reaction is a very efficient strategy for constructing six-membered ring structures with regioselectivity and stereoselectivity.[4] This reaction generally requires the addition of an acid catalyst to reduce reaction temperature and time. Unlike homogeneous Lewis acidic metal complexes, MOF-based Lewis acids offer significant advantages including easy separation from reaction mixtures and catalyst recovery/reuse. Moreover, uniform active sites of MOF

catalysts generally afford higher reaction selectivity. For the reaction of 1,4-benzoquinone with cyclohexa-1,3-diene, the cyclization product was obtained in quantitative yield within 1 h at only 1.0 mol% ZrOTf-BTC loading under room temperature (**Table 5-1**). No obvious change was observed in MOF crystallinity by PXRD, whereas only minimum Zr (0.13%) leached into the supernatant after each reaction run by ICP-MS analysis. When the catalyst loading was reduced to 0.1 mol%, the cyclization product was obtained in 76% yield in 10 h, affording a turnover number (TON) of 760. The Diel-Alder reaction is significantly more challenging with electron-rich dienophiles such as α,β-unsaturated ketones and aldehydes due to their much higher LUMO energy. Impressively, at 5.0 mol% catalyst loading, ZrOTf-BTC catalyzed the cyclization of a series of challenging dienophiles, including 3-buten-2-one, methacrolein and crotonaldehyde, with both cyclohexa-1,3-diene and 2,3-dimethylbuta-1,3-diene in high yields.

Table 5-1. Catalyst evaluation and substrate scope of ZrOTf-BTC catalyzed Diels-Alder reactions.

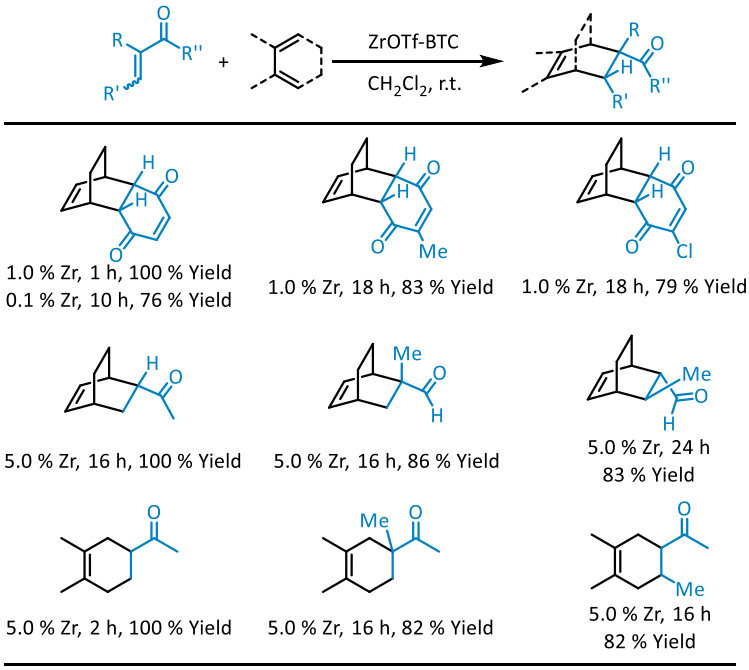

Reaction conditions: dienophile (1 equiv., 1 mmol), diene (1.2 equiv.), ZrOTf-BTC (0.1-5.0 mol%), CH_2Cl_2 (4.0 mL), 25 °C. Reaction yields were determined by ^1H NMR using mesitylene as internal standard.

The heterogeneity of ZrOTf-BTC in the Diels-Alder reaction was confirmed by the "hot filtration" test. After a reaction run, the MOF and supernatant were separated and separately used as catalyst for another reaction run. While the catalytic activity was maintained in the solid MOF, no activity was observed for the supernatant. This "hot filtration" test rules out the possibility of leached Zr salts or soluble Brönsted acids contributing to the catalytic reactivity (**Figure 5-6**).

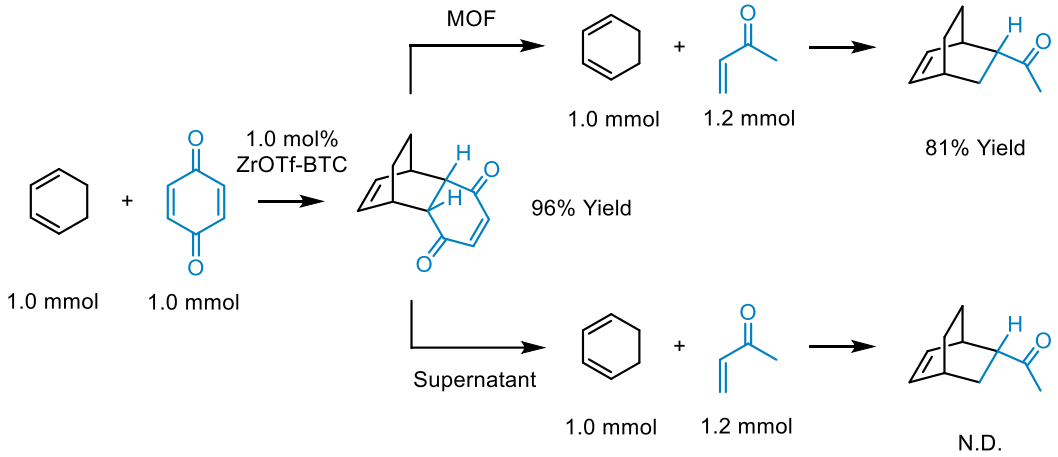

Figure 5-6. The "hot filtration" test of ZrOTf-BTC catalyzed Diels-Alder reaction.

We then tested the Diels-Alder reaction using the ZrOTf-BTC@SiO_2 packed column as a continuous flow catalyst. A CH_2Cl_2 solution of benzoquinone (limiting reagent) and cyclohexa-1,3-diene (0.5 M) in a molar ratio of 1:1.6 was flowed through the column at a rate of 10 $mL \cdot h^{-1}$ to achieve complete conversion of benzoquinone and to produce the cyclization product in quantitative yield. The turnover frequency (TOF) of the flow process was calculated to be 100 h^{-1}. The flow reaction was run for a TON of 1,700 in 17 h without a drop in the reaction yield (**Figure 5-7**).

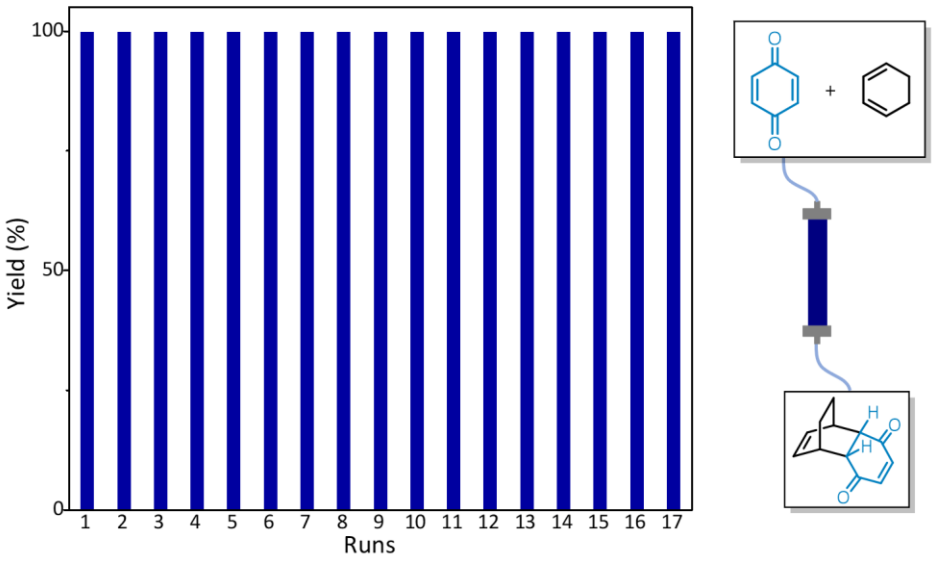

Figure 5-7. ZrOTf-BTC@SiO_2 catalyzed Diels-Alder reaction in a continuous flow mode.

5.2.6 ZrOTf-BTC catalyzed epoxide ring-opening amination

Epoxides are an important class of industrial chemicals for conversion to a broad range of commodity and fine chemicals. [37] For instance, the nucleophilic ring-opening with amines affords β-amino alcohols, which are useful intermediates for organic synthesis.[38] Several homogeneous catalysts, including metal triflates and metal halides have been used for this reaction.[39-41] However, very few heterogeneous catalysts have been tested for this reaction to achieve catalyst reuse and flow catalysis. ZrOTf-BTC is a very active catalyst for epoxide ring-opening with anilines. At 5.0 mol% ZrOTf-BTC loading, many different epoxides, including styrene oxide, cyclohexene oxide and cyclopentene oxide, reacted with aniline to form corresponding amino alcohols (**Table 5-2**) without heating. A broad range of aniline derivatives, including electron-deficient aniline (4-chloroaniline) and electron-rich aniline (2,4,6-trimethylaniline), and sterically hindered secondary anilines (*N*-methylaniline) could all be used for the ring-opening of epoxides to afford amino alcohols in high yields.

Table 5-2. Catalyst evaluation and substrate scope of ZrOTf-BTC catalyzed epoxide ring-opening reactions.[a]

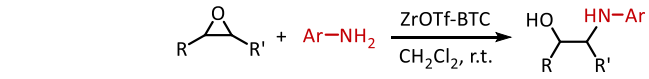

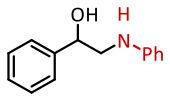 1% ZrOTf-BTC, 2h, 64% 5% ZrOTf-BTC, 2h, 100%	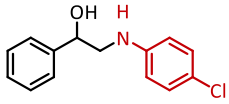 1% ZrOTf-BTC, 18h, 100%	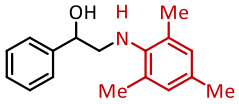 1% ZrOTf-BTC, 18h, 63%
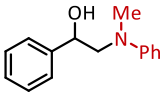 1% ZrOTf-BTC, 18h, 73%	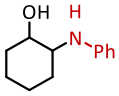 1% ZrOTf-BTC, 2h, 75% 5% ZrOTf-BTC, 2h, 100%	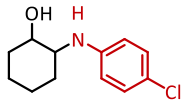 1% ZrOTf-BTC, 6h, 100%
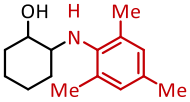 1% ZrOTf-BTC, 18h, 67%	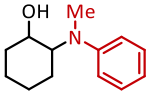 1% ZrOTf-BTC, 18h, 81%	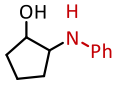 1% ZrOTf-BTC, 2h, 63% 5% ZrOTf-BTC, 2h, 93%

[a]Reaction conditions: epoxides (1 equiv., 1.0 mmol), anilines (1.2 equiv., 1.2 mmol), ZrOTf-BTC (1.0-5.0 mol%), CH_2Cl_2 (4.0 mL), 25 °C. Reaction yields were determined by ^1H NMR using mesitylene as internal standard.

The epoxide ring-opening reaction also worked well under flow conditions. Styrene oxide (limiting reagent) and aniline solution in CH_2Cl_2 (0.5 M) were flowed through ZrOTf-BTC@SiO_2 column at a rate of 60 mL·h^{-1} to form the amino alcohol product in 93% yield. High yields (83 - 93%) of the product were consistently obtained in 30 runs to afford a total TON of >2,700 in 30 h (**Figure 5-8**).

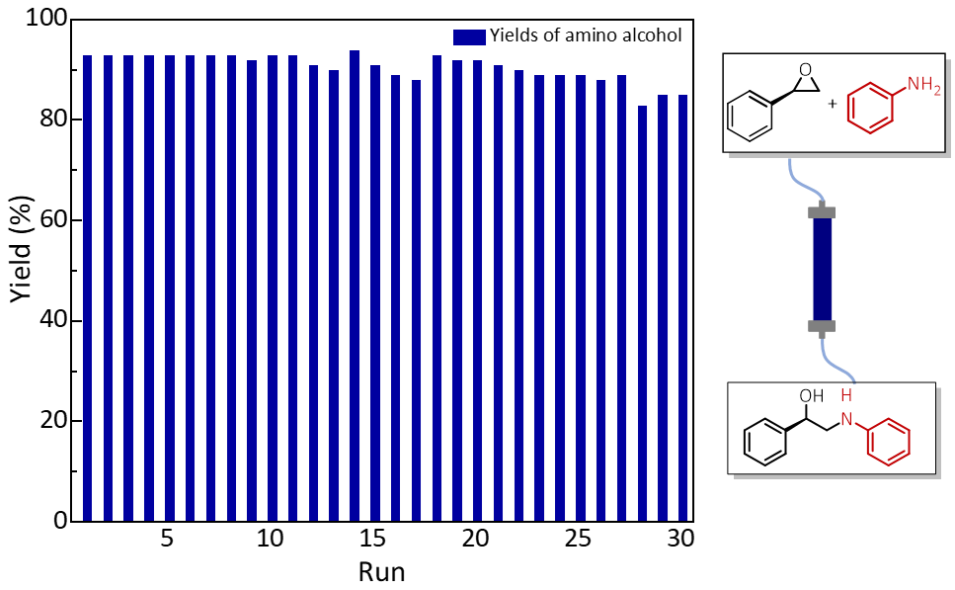

Figure 5-8. ZrOTf-BTC@SiO_2 catalyzed epoxide ring-opening reaction with aniline in a continuous flow mode.

5.2.7 ZrOTf-BTC catalyzed Friedel-Crafts acylation reactions

As one of the most convenient and useful strategies for the construction of aryl ketone moieties in a wide range of pharmaceuticals and agricultural chemicals, Friedel-Crafts acylation has drawn continuous research interests.[42] Conventional Lewis acids for Friedel-Crafts acylation include traditional metal halides (e.g., $ZnCl_2$, $AlCl_3$, $TiCl_4$) and metal triflates (e.g., $Sc(OTf)_3$, $Hf(OTf)_4$).[43-44] However, due to coordination between the Lewis acid and the produced aromatic ketone, stoichiometric amount of metal halides are usually required in these reactions. Furthermore, the recovery of these homogeneous Lewis acidic metal salts and the generation of large amounts of wastes are long-standing challenges. As a result, significant efforts have been devoted to the development of heterogenous Lewis acid catalyst for Friedel-Crafts acylation. Modified zeolites,[45-46] metal oxides,[47] heteropoly acids,[48] and hybrid materials[49] have displayed moderate to good activity in Friedel-Crafts acylation.

Table 5-3. ZrOTf-BTC catalyzed Friedel-Crafts acylation reactions.[a]

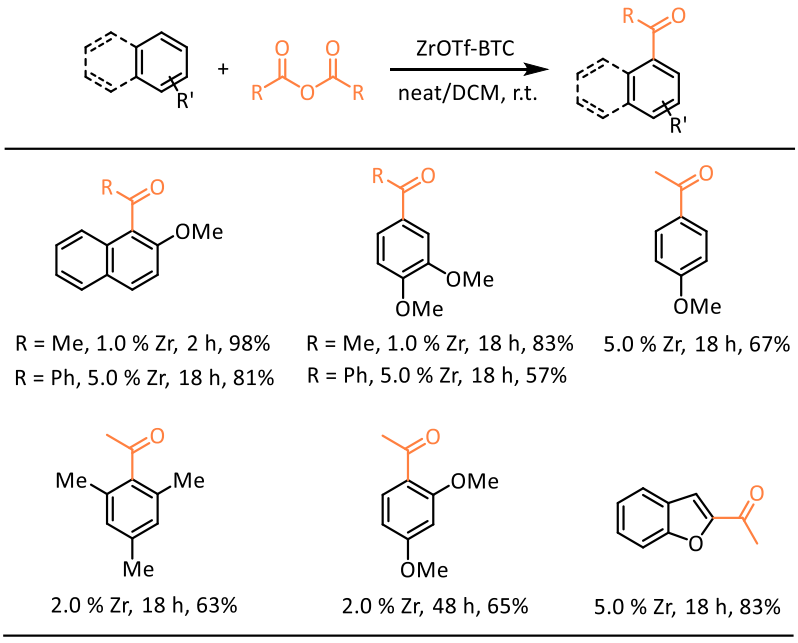

[a]Reaction conditions: arene (1 equiv., 1.0 mmol), acetic anhydride (1.0 mL, excess) or benzoic anhydride (3 equiv., 3.0 mmol, in 2.0 mL CH_2Cl_2), ZrOTf-BTC (1.0 – 5.0 mol%), 25 °C. Isolated yields are listed.

At 1.0 mol% of loading, ZrOTf-BTC catalyzed Friedel-Crafts acylation between 2-methoxynaphthalene and neat acetic anhydride in 2 h at room temperature to afford 1-acetyl-2-methoxynaphthalene in 98% isolated yield (**Table 5-3**). This level of activity is much higher than those of most Lewis acid catalysts including homogeneous metal triflates and solid acid catalysts. Several substituted arenes, including anisole, dimethoxybenzene, mesitylene, and benzofuran, underwent acylation in the presence of 1-5 mol% of ZrOTf-BTC at room temperature to afford desired products in 63-83% yields. Furthermore, 5.0 mol% ZrOTf-BTC catalyzed Friedel-Crafts acylation with benzoic anhydride in CH_2Cl_2 to afford 1-benzoyl-2-methoxynaphthalene in 81% yield.

The catalytic performance of Friedel-Crafts acylation was also tested in the continuous flow mode. When a solution of 2-methoxynaphthalene (0.05 M) in Ac_2O/CH_2Cl_2 (1:4, v/v) was

flowed through ZrOTf-BTC@SiO_2 column at a rate of 30 $mL \cdot h^{-1}$, 1-acetyl-2-methoxynaphthalene was formed as the desired product in excellent yields (85-99%) in the first 5 runs (5 mL solution per run). The yield dropped to 65% in the sixth run, but the catalytic performance was restored by simply washing the column with a CH_3CN/CH_2Cl_2 (1:9, v/v) solution. 15 consecutive runs afforded a total TON of 326 and a TOF of 130 h^{-1} (the column was washed after the 6thand 11th run). The catalyst performance in the flow mode significantly outperformed that of the batch mode (**Figure 5-9**).

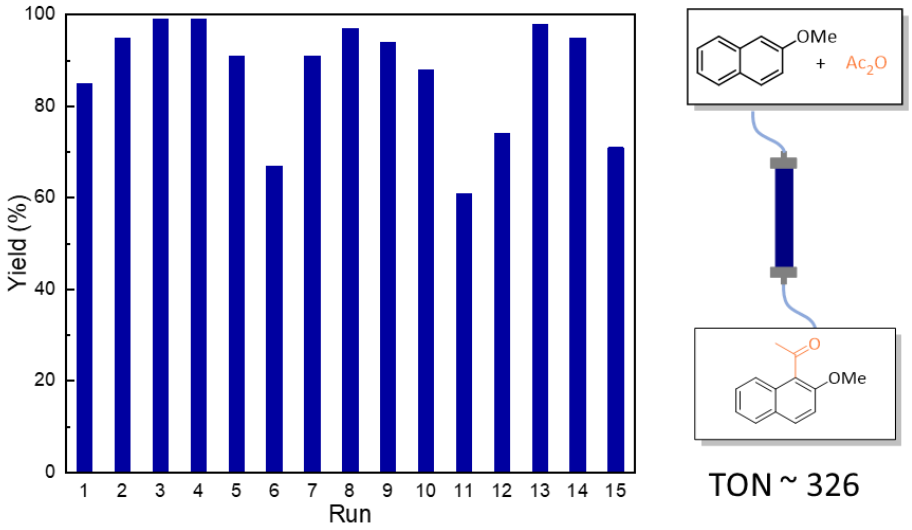

Figure 5-9. ZrOTf-BTC@SiO_2 catalyzed Friedel-Crafts acylation between 2-methoxynaphthalene and acetic anhydride in the continuous flow mode.

5.2.8 ZrOTf-BTC catalyzed alkene hydroalkoxylation reactions

ZrOTf-BTC is also a highly active catalyst for alkene hydroalkoxylation reactions. Oxygen-containing cyclic compounds are abundant in polyether antibiotics and other biologically active natural products as well as in chemical feedstocks.[50-51] The addition of alcohols across C=C bonds is the most straightforward synthetic route to cyclic ethers.[52-53] This reaction pathway is widely adopted by biological systems to synthesize cyclic ether-containing natural products.[54-55] Some homogeneous catalysts are effective for this reaction, but many of them require activated

alkenes (e.g. alkenes, dienes, and Michael acceptors).[56-58] We report the first example of MOF-catalyzed alkene hydroalkoxylation using highly acidic ZrOTf-BTC.

Table 5-4. ZrOTf-BTC catalyzed intramolecular alkene hydroalkoxylation.

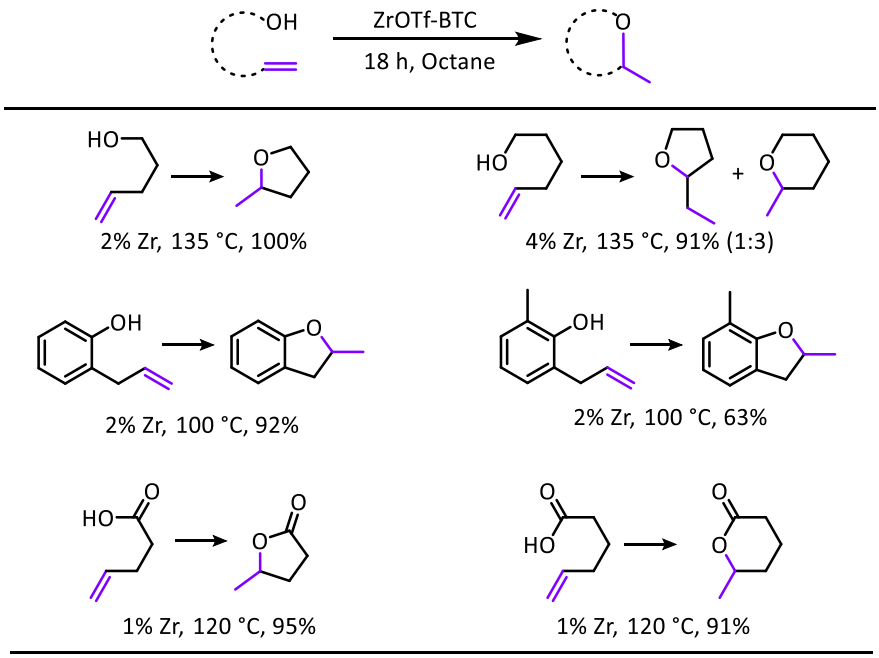

Reaction conditions: substrate (1.0 mmol), ZrOTf-BTC (1.0-4.0 mol%), octane (2.0 mL), 100-135 °C, 18 h, inert atmosphere. Reaction yields were determined by ^{1}H NMR using mesitylene as internal standard.

For the cyclization of 4-penten-1-ol, 2.0 mol% of ZrOTf-BTC afforded 2-methyltetrahydrofuran in quantitative yield after heating at 135 °C under inert atmosphere for 18 h (**Table 5-4**). 5-hexen-1-ol was also hydroalkoxylated in 91% yield at 4.0 mol% ZrOTf-BTC to afford 2-methyltetrahydropyran and 2-ethyltetrahydrofuran in a 3:1 ratio. Besides aliphatic alcohols, alkene substrates containing phenol groups such as 2-allylphenol and 2-allyl-6-methylphenol were also catalytically cyclized with ZrOTf-BTC at a lower temperature of 100 °C. Alkene-containing carboxylic acids such as pent-4-enoic acid and hex-5-enoic acid were also hydroalkoxylated to form corresponding lactones in excellent yields (91-95%) at 1.0 mol% catalyst loading.

To further demonstrate the advantage of ZrOTf-BTC over conventional $Sc(OTf)_3$ in catalyzing alkene hydroalkoxylation reactions, we conducted catalytic hydroalkoxylation of pent-4-enoic acid at 0.2 mol% loading of ZrOTf-BTC and $Sc(OTf)_3$. As shown in **Figure 5-10**, ZrOTf-BTC catalyzed the hydroalkoxylation of pent-4-enoic acid in octane to afford 90% of γ-valerolactone in 72 h, while very little product was detected in the presence of $Sc(OTf)_3$ under the same condition. The lack of catalytic activity of $Sc(OTf)_3$ is likely due to its poor solubility in non-polar octane. Changing the solvent to polar $MeNO_2$ afforded 2-methyltetrahydrofuran in 20% yield at 0.2 mol% $Sc(OTf)_3$ in 5 h. However, no further substrate conversion was observed beyond 5 h, suggesting deactivation of $Sc(OTf)_3$ in polar solvent at elevated temperature. ZrOTf-BTC thus shows much longer lifetime than $Sc(OTf)_3$ in alkene hydroalkoxylation.

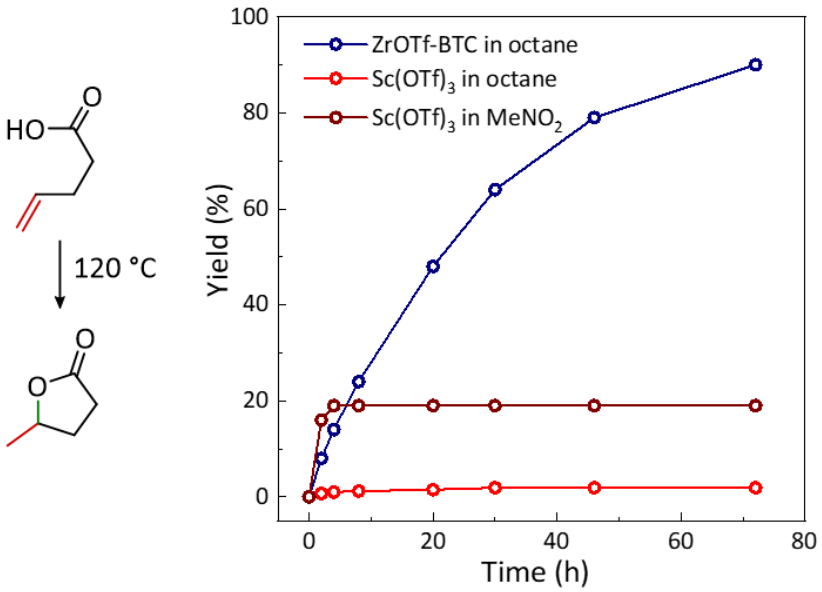

Figure 5-10. Catalytic performance of ZrOTf-BTC and $Sc(OTf)_3$ for alkene hydroalkoxylation. The catalyst loadings are both 0.2 mol%.

5.3 Conclusion

We have designed a strongly Lewis acidic MOF, ZrOTf-BTC, through two-step SBU transformations of MOF-808. The Lewis acidity of the Zr-triflate active site was quantified

through spectroscopic methods to be comparable to the homogeneous benchmark $Sc(OTf)_3$. ZrOTf-BTC was shown to be a highly active solid Lewis acid catalyst for a broad range of organic transformations, including Diels-Alder reaction, epoxide ring-opening, Friedel-Crafts acylation, and alkene hydroalkoxylation reactions. The catalytic performance of ZrOTf-BTC is superior over $Sc(OTf)_3$ in terms of catalyst activity, lifetime, and reusability. We have further developed the ZrOTf-BTC@SiO_2 composite for continuous flow catalysis. ZrOTf-BTC@SiO_2 displayed exceptionally high TONs of 1,600 for Diels-Alder reaction, 2,700 for epoxide ring-opening reaction, and 326 for Friedel-Crafts acylation under flow conditions. We have thus demonstrated the creation of strongly Lewis acidic sites in MOFs via triflation and utility of the MOF@SiO_2 composite in continuous flow catalysis of important organic transformations.

5.4 Experimental Section

5.4.1 Materials and methods

All the reactions and manipulations were carried out under ambient atmosphere unless otherwise indicated. Tetrahydrofuran and toluene were purified by passing through a neutral alumina column under N_2. The substrates for catalytic reactions, including dienes, dienophiles, epoxides, anilines, alkenyl alcohols, imines and diazo compounds were purchased from Sigma-Aldrich or Fisher and used as received. Powder X-ray diffraction (PXRD) data were collected on a Bruker D8 Venture diffractometer using a Cu Kα radiation source (l = 1.54178 Å). N_2 sorption experiments were performed on a Micromeritics TriStar II 3020 instrument. Thermogravimetric analysis (TGA) was performed in air using a Shimazu TGA-50 equipped with a platinum pan and heated at a rate of 1.5 $^{\circ}$C per min up to 800 °C. Electron paramagnetic resonance (EPR) spectra were collected with a Bruker Elexsys 500 X-band EPR spectrometer at 100 K. Fluorescence data were measured using an RF-5301PC spectrofluorophotometer (Shimadzu, Japan). ICP-MS data

were obtained with an Agilent 7700x ICP-MS and analyzed using an ICP-MS MassHunter version B01.03. Samples were diluted in a 2% HNO_3 matrix and analyzed with a ^{159}Tb internal standard against a 12-point standard curve over a range from 0.1 ppb to 500 ppb. The correlation was > 0.9997 for all analyses of interest. Data collection was performed in Spectrum Mode with five replicates per sample and 100 sweeps per replicate.

^1H NMR spectra were recorded on a Bruker NMR 500 DRX spectrometer at 500 MHz and referenced against the proton resonance resulting from incomplete deuteration of $CDCl_3$ (δ 7.26) or benzene-d_6 (δ 7.16). The following abbreviations are used: s: singlet, d: doublet, t: triplet, q: quartet, m: multiplet, br: broad, app: apparent. High-resolution mass spectra were obtained using an Agilent 6224 Accurate-Mass TOF spectrometer.

5.4.2 Synthetic procedures of MOF catalysts

Synthesis of ZrOTf-BTC: ZrOH-BTC was synthesized from Zr-BTC (formate capped) by HCl/H_2O activation as reported previously.[59] In a N_2-filled glove box, ZrOH-BTC (6.4 mmol of Zr) was weighed out in a 75 mL glass vessel and dispersed in 40 mL of toluene. Trimethylsilyl trifluoromethanesulfonate (Me_3SiOTf, 11.6 mL, 64 mmol) was then added to the suspension. The vessel was sealed with a Teflon cap and kept at 80 °C. After 6 h, the suspension was cooled to room temperature, transferred into a glove box, and washed with dry toluene 5 times. The MOF was then Soxhlet extracted with hexane to remove the trapped HOTf species inside the MOF channel. 10 equiv. of $LiCH_2SiMe_3$ was added to the round-bottom receiving flask to quench extracted HOTf during Soxhlet extraction. After solvent exchange with dry benzene, ZrOTf-BTC was freeze-dried under vacuum overnight and stored inside the glovebox for further use.

Synthesis of Zr-BTC@SiO_2 composite: $ZrOCl_2(H_2O)_8$ (1.61 g, 5.0 mmol) and trimesic acid (H_3BTC, 1.10 g, 5.25 mmol) were dissolved in DMF (50 mL) and H_2O (50 mL), and then mixed

with SiO_2 (6.0 g, 20 equiv.) in a 250 mL round-bottom flask. The mixture was heated to 100 °C on an oil bath for 2 days to afford Zr-BTC@SiO_2 as a white solid. The material was centrifuged out of suspension and then washed with DMF, THF, and benzene three times each to remove residual precursors and solvents before freeze-drying under vacuum.

Synthesis of ZrOH-BTC@SiO_2 composite: Zr-BTC@SiO_2 (6.2 g) was suspended in 400 mL of HCl (1M in H_2O) and heated in a 90 °C oven for 12 h. The mixture was centrifuged and sequentially washed with deionized H_2O, acetone, and THF three times each, and then freeze-dried in benzene to yield ZrOH-BTC@SiO_2 as a white powder (6.1 g). To ensure the successful activation of formate group, a small amount of the material was digested to quantify the amount of formate. ^{1}H NMR analysis detected only 0.18 equiv. of HCO_2H w.r.t. BTC, corresponding to only 0.06 HCO_2^- per Zr center. To quantify the ratio of MOF to SiO_2 in ZrOH-BTC@SiO_2, 5 μmol of mesitylene standard was added to 5 mg of the composite. The material was digested with D_3PO_4/DMSO-d_6 (0.3 mL/0.5 mL) and analyzed by ^{1}H NMR. In three repetitive runs, 0.066±0.006 μmol of BTC was detected per 5 mg of composite material, corresponding to 0.20 μmol of Zr centers per 5.0 mg of ZrOH-BTC@SiO_2.

Synthesis of ZrOTf-BTC@SiO_2 composite: In a N_2-filled glove box, 2.5 g of ZrOH-BTC (0.1 mmol of Zr) was weighed out in a 75 mL glass vessel and dispersed in 40 mL of toluene. Me_3SiOTf (906 μL, 5.0 mmol) was then added to the suspension. The vessel was sealed with Teflon cap and kept at 80 °C for 6 h before cooling to room temperature and washing with dry toluene for 5 times. After solvent exchange with dry benzene, ZrOTf-BTC@SiO_2 was freeze-dried under vacuum overnight and stored inside the glovebox for further use.

Packing of ZrOTf-BTC@SiO_2 into a stainless-steel column: The column for packing MOF@SiO_2 catalyst was purchased from Sigma-Aldrich. In a typical procedure, 1.25 g of ZrOTf-

BTC@SiO_2 composite was slurry-packed between two metal filter plates in a stainless-steel tubing (ID 4.16 mm, length 15 cm, Sigma-Aldrich, **Figure 5-11**). ZrOTf-BTC@SiO_2 was dispersed in CH_2Cl_2, transferred into the one-end sealed tubing, then pressurized with N_2 to compact the composite and remove the trapped air bubbles. This transfer-compress process was repeated until the tubing was filled-up with the composite material. The end of the tube was then sealed, and the column was stored for flow catalysis.

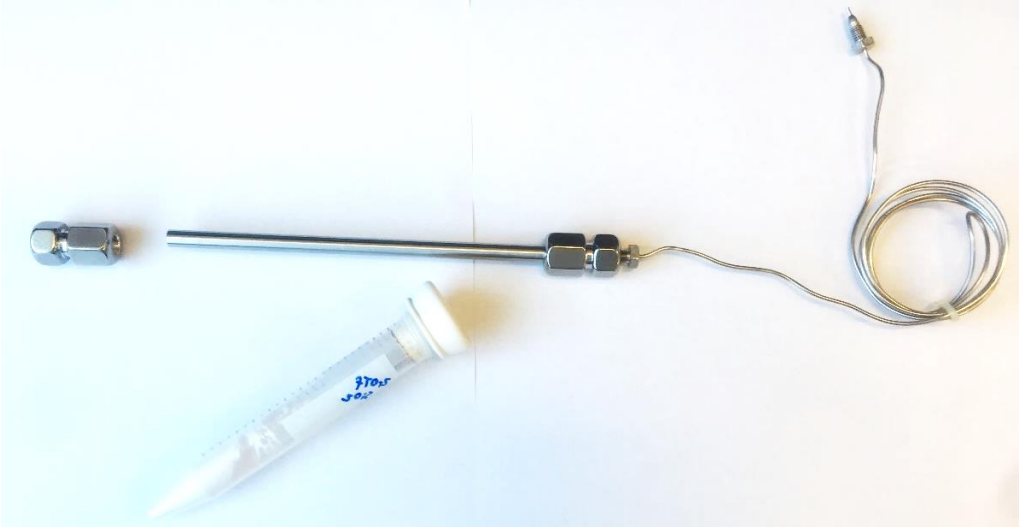

Figure 5-11. Stainless-steel column used for packing ZrOTf-BTC@SiO_2.

5.4.3 Catalytic reaction setup and product characterization

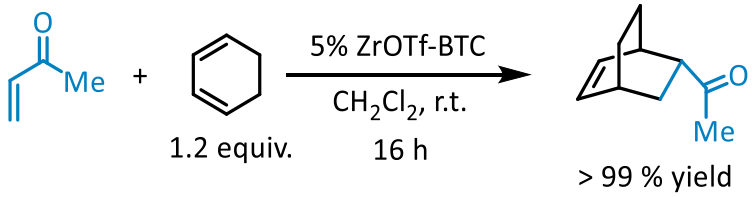

Typical procedure of ZrOTf-BTC catalyzed Diels-Alder reactions in batch mode: Under ambient atmosphere, but-3-en-2-one (81 μL, 1.0 mmol), cyclohexadiene (120 μL, 1.2 mmol), ZrOTf-BTC (50 μmol Zr), and CH_2Cl_2 (4.0 mL) was charged to a 2-dram vial. The reaction mixture was stirred at room temperature for 16 h, then the MOF catalyst was removed by

centrifugation. The supernatant was evaporated on a rotavap to give the crude product bicyclo[2.2.2]oct-5-en-2-ylethanone in a quantitative yield (> 99%, mesitylene added as internal standard). The residue was further purified by silica gel chromatography eluting with hexane/CH_2Cl_2 to afford the target molecule as a colorless oil (90% of isolated yield). The MOF crystallinity was maintained after the reaction run and minimum metal leaching with 0.13% of Zr per run was detected by ICP-MS analysis.

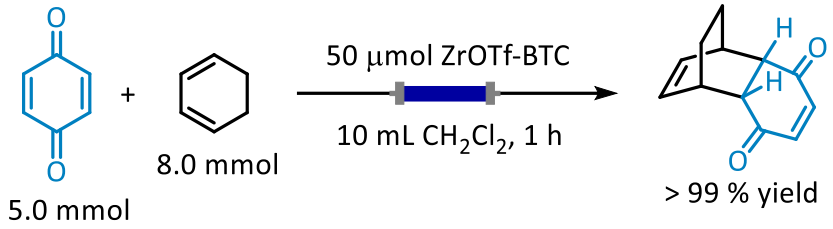

Typical procedure of ZrOTf-BTC catalyzed Diels-Alder reactions in flow mode: The Cole-Palmer peristaltic pump (Masterflex®) was used to deliver the solution of reaction substrates to the column reactor. The substrate solution sequentially flowed through the substrate stock bottle, pump head, a short guard column (silica), and then the column reactor. The product solution was received in a glass bottle. The concentration and the flow rate of the substrate solution were optimized to maximize the turnover number. The yield of the reaction product was monitored periodically with ^1H NMR using the mesitylene as internal standard. For a one-hour flow catalysis of Diels-Alder reaction, a mixture of 1,4-benzoquinone (540 mg, 5.0 mmol) and cyclohexa-1,3-diene (800 μL, 8.0 mmol) was dissolved in CH_2Cl_2 (8.0 mL), and flowed through the ZrOTf-BTC@SiO_2 column at a rate of 10 mL·h^{-1} at room temperature. After the flow, 2 mL of CH_2Cl_2 was used to wash the column to recover the remaining product. The collected solution was evaporated under rotovap to remove the solvent and excess cyclohexa-1,3-diene to obtain the cycloaddition product as an off-white solid in a quantitative yield.

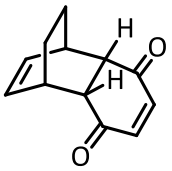

endo-tricyclo[6.2.2.0^{2,7}]dodeca-4,9-diene-3,6-dione. (CAS: 76035-69-3) ^{1}H NMR (500 MHz, Chloroform-*d*) δ 6.64 (s, 2H), 6.21 (dd, *J* = 4.5, 3.1 Hz, 2H), 3.21 (dq, *J* = 4.6, 1.6 Hz, 2H), 2.98 (t, *J* = 1.2 Hz, 2H), 1.70 (dt, *J* = 8.8, 1.5 Hz, 2H), 1.40 – 1.34 (m, 2H). ^{13}C NMR (126 MHz, Chloroform-*d*) δ 199.40, 142.02, 133.50, 49.37, 35.38, 24.77. HR-MS (ESI, positive mode): *m/z* calc'd for $C_{12}H_{13}O_2$ $[M+H]^+$:189.0916, found 189.0913.

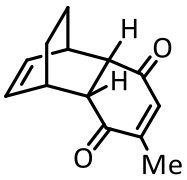

endo-4-methyl-tricyclo[6.2.2.0^{2,7}]dodeca-4,9-diene-3,6-dione. (CAS: 93139-46-9) ^{1}H NMR (500 MHz, Chloroform-*d*) δ 6.53 (q, J = 1.5 Hz, 1H), 6.22 – 6.12 (m, 2H), 3.20 – 3.15 (m, 2H), 2.98 – 2.92 (m, 2H), 1.92 (d, J = 1.4 Hz, 3H), 1.70 – 1.66 (m, 2H), 1.38 – 1.30 (m, 2H). ^{13}C NMR (126 MHz, Chloroform-*d*) δ 199.70, 199.03, 151.61, 139.61, 133.64, 133.14, 49.89, 49.24, 35.56, 35.31, 24.77, 24.72, 16.67. HR-MS (APCI, positive mode): *m/z* calc'd for $C_{13}H_{15}O_2$ $[M+H]^+$:203.1072, found 203.1071.

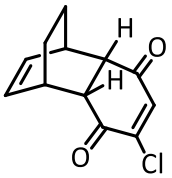

endo-4-chloro -tricyclo[6.2.2.0^{2,7}]dodeca-4,9-diene-3,6-dione.^{1}H NMR (500 MHz, Chloroform-*d*) δ 6.95 (s, 1H), 6.24 (dq, J = 8.2, 6.4 Hz, 2H), 3.24 (ddt, J = 19.7, 5.3, 2.6 Hz, 2H), 3.08 (ddd, J = 36.7, 9.2, 2.6 Hz, 2H), 1.81 – 1.65 (m, 2H), 1.39 (tq, J = 10.0, 3.2 Hz, 2H). ^{13}C NMR (126 MHz,

Chloroform-*d*) δ 196.60, 191.76, 149.61, 139.96, 133.86, 133.16, 50.19, 49.23, 35.99, 35.52, 24.74, 24.59. HR-MS (APCI, positive mode): *m/z* calc'd for $C_{12}H_{12}O_2Cl$ $[M+H]^+$:223.0526, found 223.0521.

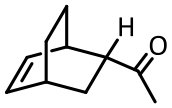

1-bicyclo[2.2.2]oct-5-en-2-yl-ethanone. (CAS: 93139-46-9) ^{1}H NMR (500 MHz, Chloroform-*d*) δ 6.27 (ddd, J = 8.1, 6.6, 1.3 Hz, 1H), 6.10 (ddd, J = 8.0, 6.4, 1.3 Hz, 1H), 2.89 (ddtd, J = 6.6, 3.4, 2.3, 1.3 Hz, 1H), 2.66 (ddd, J = 8.8, 6.5, 2.2 Hz, 1H), 2.60 (dtt, J = 5.6, 4.2, 3.0 Hz, 1H), 2.11 (s, 3H), 1.65 (ddt, J = 7.9, 2.6, 1.4 Hz, 2H), 1.60 (ddt, J = 14.1, 9.3, 2.7 Hz, 1H), 1.50 (dddd, J = 12.5, 10.2, 3.8, 2.3 Hz, 1H), 1.32 (tt, J = 11.5, 3.5 Hz, 1H), 1.28 – 1.23 (m, 1H). ^{13}C NMR (126 MHz, Chloroform-*d*) δ 209.88, 135.21, 131.05, 51.56, 32.09, 29.56, 28.65, 28.34, 25.87, 24.52. HR-MS (APCI, positive mode): *m/z* calc'd for $C_{10}H_{15}O$ $[M+H]^+$:151.1123, found 151.1121.

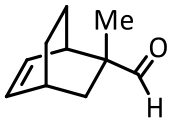

2-formyl-2-methyl-bicyclo(2.2.2)octen-(5). (CAS: 60838-99-5) ^{1}H NMR (500 MHz, Chloroform-*d*) δ 9.32 (s, 1H), 6.32 – 6.19 (m, 2H), 2.60 (dp, J = 5.8, 2.2, 1.6 Hz, 1H), 2.48 (dq, J = 5.4, 2.6 Hz, 1H), 2.01 (dt, J = 12.9, 3.3 Hz, 1H), 1.90 (ddt, J = 13.0, 10.1, 2.9 Hz, 1H), 1.53 (dddd, J = 11.5, 9.1, 4.5, 2.2 Hz, 1H), 1.32 – 1.19 (m, 3H), 1.15 (s, 3H). ^{13}C NMR (126 MHz, Chloroform-*d*) δ 205.71, 135.14, 133.55, 49.97, 36.08, 35.55, 30.53, 25.09, 21.22, 20.20. HR-MS (APCI, positive mode): *m/z* calc'd for $C_{10}H_{15}O$ $[M+H]^+$:151.1123, found 151.1118.

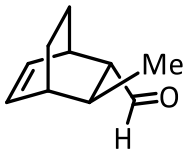

endo-trans-3-methylbicyclo(2.2.2)oct-5-ene-2-carbaldehyde. (CAS: 2958-78-3) ^{1}H NMR (500 MHz, Chloroform-*d*) δ 9.41 (d, J = 2.0 Hz, 1H), 6.44 (ddd, J = 8.1, 6.7, 1.3 Hz, 1H), 6.10 (ddd, J = 7.9, 6.3, 1.2 Hz, 1H), 2.83 (ddt, J = 4.4, 2.9, 1.7 Hz, 1H), 2.33 (ddd, J = 6.8, 3.3, 1.1 Hz, 1H), 1.94 (dt, J = 6.1, 2.0 Hz, 1H), 1.91 – 1.84 (m, 1H), 1.84 – 1.76 (m, 1H), 1.55 (tdd, J = 9.8, 4.4, 2.6 Hz, 1H), 1.38 – 1.29 (m, 1H), 1.14 (dddt, J = 10.1, 4.4, 3.0, 1.5 Hz, 1H), 1.10 (d, J = 6.9 Hz, 3H). ^{13}C NMR (126 MHz, Chloroform-*d*) δ 203.79, 137.78, 130.22, 59.73, 35.60, 32.29, 31.35, 25.64, 19.67, 18.42. HR-MS (APCI, positive mode): *m/z* calc'd for $C_{10}H_{15}O$ $[M+H]^+$:151.1123, found 151.1119.

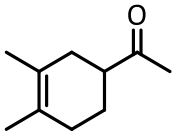

1-(3,4-dimethylcyclohex-3-enyl)ethanone. (CAS: 41723-54-0) ^{1}H NMR (500 MHz, Chloroform-*d*) δ 2.60 – 2.50 (m, 1H), 2.16 (s, 3H), 2.13 – 2.08 (m, 1H), 2.06 – 1.97 (m, 3H), 1.93 (m, 1H), 1.63 (s, 3H), 1.60 (s, 3H), 1.57 – 1.46 (m, 1H). ^{13}C NMR (126 MHz, Chloroform-*d*) δ 212.08, 125.56, 124.10, 48.44, 33.24, 31.38, 28.12, 25.47, 19.18, 18.97. HR-MS (APCI, positive mode): *m/z* calc'd for $C_{10}H_{15}O$ $[M+H]^+$:153.1279, found 153.1277.

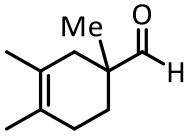

1,3,4-trimethyl-3-cyclohexene-1-carboxaldehyde. (CAS: 40702-26-9) ^{1}H NMR (500 MHz, Chloroform-*d*) δ 9.45 (s, 1H), 2.28 – 2.21 (m, 1H), 2.02 – 1.91 (m, 2H), 1.84 – 1.79 (m, 1H), 1.78 – 1.73 (m, 1H), 1.64 (dq, J = 1.9, 1.0 Hz, 3H), 1.59 (dq, J = 1.9, 0.9 Hz, 3H), 1.46 (dt, J = 13.6, 7.0 Hz, 1H), 1.02 (s, 3H). ^{13}C NMR (126 MHz, Chloroform-*d*) δ 206.40, 125.26, 123.17, 45.42, 38.01,

29.39, 28.59, 20.88, 19.36, 18.95. HR-MS (APCI, positive mode): *m/z* calc'd for $C_{10}H_{15}O$ $[M+H]^+$:153.1279, found 153.1275.

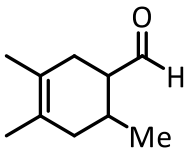

3,4,6-trimethyl-3-cyclohexene-1-carbaldehyde. (CAS: 13702-58-4) ^{1}H NMR (500 MHz, Chloroform-*d*) δ 9.61 (d, J = 3.2 Hz, 1H), 2.20 – 2.16 (m, 2H), 2.03 – 1.98 (m, 3H), 1.69 – 1.66 (m, 1H), 1.67 – 1.62 (m, 3H), 1.62 – 1.59 (m, 3H), 1.00 (d, J = 6.5 Hz, 3H). ^{13}C NMR (126 MHz, Chloroform-*d*) δ 205.54, 125.27, 122.75, 53.68, 39.06, 30.49, 28.94, 19.73, 19.03, 18.83. HR-MS (APCI, positive mode): *m/z* calc'd for $C_{10}H_{15}O$ $[M+H]^+$:153.1279, found 153.1272.

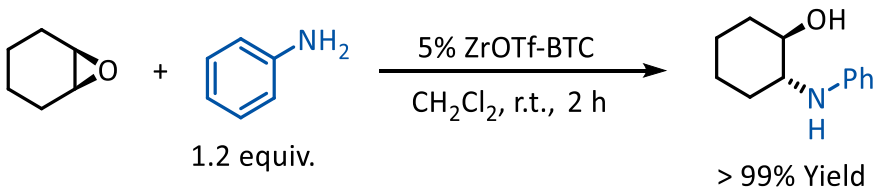

Typical procedure of ZrOTf-BTC catalyzed epoxide ring opening reactions in batch mode: Under ambient atmosphere, cyclohexene oxide (100 μL, 1.0 mmol), aniline (110 μL, 1.2 mmol), ZrOTf-BTC (50 μmol Zr), and CH_2Cl_2 (4.0 mL) were charged to a 2-dram vial. The reaction mixture was stirred at room temperature for 2 h, then the MOF catalyst was removed by centrifugation. The supernatant was evaporated on a rotavap to give the crude product 2-(phenylamino)cyclohexzan-1-ol in a quantitative yield (> 99%, mesitylene added as internal standard). The residue was further purified by silica gel chromatography eluting with hexane/CH_2Cl_2 to afford the target molecule as a colorless oil (86% of isolated yield). The MOF

crystallinity was maintained after the reaction run and minimum metal leaching with 0.14% of Zr per run was detected by ICP-MS analysis.

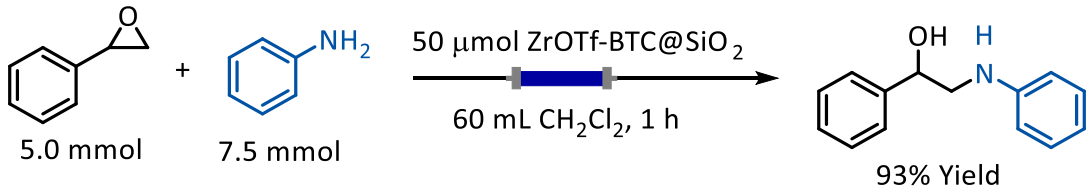

Typical procedure of ZrOTf-BTC catalyzed epoxide ring opening reactions in flow mode: For a one-hour flow catalysis of epoxide ring-opening reaction, styrene oxide (570 μL, 5.0 mmol) and aniline (690 μL, 7.5 mmol) were dissolved in CH_2Cl_2 (50 mL). The solution was flowed through the ZrOTf-BTC@SiO_2 column at a rate of 60 mL·h^{-1} at room temperature. After the flow, 10 mL of CH_2Cl_2 was used to wash the column to recover the remaining product. The collected solution was evaporated on a rotovap to remove the solvent, then 1 equiv. of mesitylene was added as an internal standard. The mixture was analyzed with ^{1}H NMR to give 1-phenyl-2-(phenylamino)ethanol in a quantitative yield.

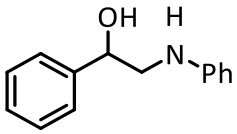

1-phenyl-2-phenylaminoethanol. (CAS: 99342-73-1) ^{1}H NMR (500 MHz, Chloroform-*d*) δ 7.40 – 7.33 (m, 4H), 7.30 – 7.25 (m, 1H), 7.14 – 7.09 (m, 2H), 6.69 (tt, J = 7.3, 1.2 Hz, 1H), 6.61 – 6.56 (m, 2H), 4.52 (dd, J = 7.0, 4.2 Hz, 1H), 3.95 (dd, J = 11.1, 4.2 Hz, 1H), 3.76 (dd, J = 11.2, 7.0 Hz, 1H), 1.79 (br, 1H). ^{13}C NMR (126 MHz, Chloroform-*d*) δ 147.24, 140.12, 129.19, 128.87, 127.65, 126.75, 117.91, 113.87, 67.40, 59.86. HR-MS (APCI, positive mode): *m/z* calc'd for $C_{14}H_{16}NO$ $[M+H]^+$:214.1232, found 214.1225.

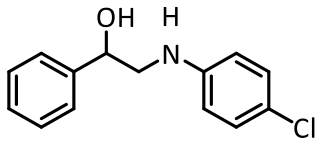

2-((4-chlorophenyl)amino)-1-phenylethan-1-ol. (CAS: 91851-16-0) ^{1}H NMR (500 MHz, Chloroform-*d*) δ 7.42 – 7.32 (m, 4H), 7.31 – 7.27 (m, 1H), 7.03 (dd, J = 9.1, 2.6 Hz, 2H), 6.47 (dd, J = 9.1, 2.7 Hz, 2H), 4.58 (br, 1H), 4.46 (dd, J = 6.8, 4.0 Hz, 1H), 3.96 (d, J = 9.9 Hz, 1H), 3.76 (dd, J = 11.1, 6.9 Hz, 1H), 1.66 (br, 1H). ^{13}C NMR (126 MHz, Chloroform-*d*) δ 145.79, 139.62, 129.00, 128.96, 127.82, 126.70, 122.49, 114.94, 67.35, 59.94. HR-MS (APCI, positive mode): *m/z* calc'd for $C_{14}H_{15}ClNO$ $[M+H]^+$:248.0842, found 248.0831.

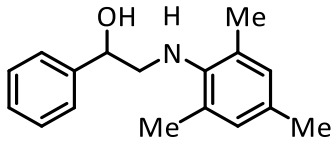

1-phenyl-2-(2,4,6-trimethylanilino)ethanol. ^{1}H NMR (500 MHz, Chloroform-*d*) δ 7.32 (m, 2H), 7.29 – 7.25 (m, 3H), 6.77 (s, 2H), 4.22 (dd, J = 6.4, 4.8 Hz, 1H), 3.96 (dd, J = 11.1, 6.4 Hz, 1H), 3.89 (dd, J = 11.1, 4.9 Hz, 1H), 2.21 (s, 3H), 2.13 (s, 6H). ^{13}C NMR (126 MHz, Chloroform-*d*) δ 141.79, 141.15, 131.28, 129.66, 129.55, 128.64, 127.59, 126.98, 65.85, 63.20, 20.54, 18.81. HR-MS (APCI, positive mode): *m/z* calc'd for $C_{17}H_{22}NO$ $[M+H]^+$:256.1701, found 256.1712.

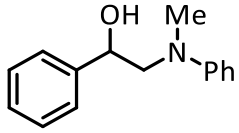

2-(*N*-methyl-*N*-phenylamino)-1-phenylethanol. (CAS: 5455-72-1) ^{1}H NMR (500 MHz, Chloroform-*d*) δ 7.34 – 7.23 (m, 5H), 7.19 – 7.11 (m, 2H), 7.01 – 6.92 (m, 2H), 6.88 – 6.79 (m, 1H), 5.10 (dd, J = 9.1, 5.7 Hz, 1H), 4.22 – 4.06 (m, 2H), 2.72 (s, 3H), 2.23 – 2.11 (m, 1H). ^{13}C NMR (126 MHz, Chloroform-*d*) δ 151.15, 137.44, 129.28, 128.59, 127.62, 127.16, 118.38, 114.81,

64.56, 61.63, 32.01. HR-MS (APCI, positive mode): *m/z* calc'd for $C_{15}H_{18}NO$ $[M+H]^+$:228.1388, found 228.1399.

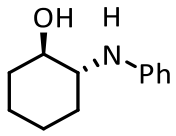

2-(phenylamino)cyclohexan-1-ol. (CAS: 75907-11-8) ^{1}H NMR (500 MHz, Chloroform-*d*) δ 7.23 – 7.12 (m, 2H), 6.85 – 6.67 (m, 3H), 3.35 (td, J = 9.7, 4.4 Hz, 1H), 3.15 (ddd, J = 11.1, 9.1, 4.2 Hz, 1H), 2.78 (br, 1H), 2.28 – 2.06 (m, 2H), 1.86 – 1.68 (m, 2H), 1.48 – 1.23 (m, 3H), 1.19 – 1.00 (m, 1H). ^{13}C NMR (126 MHz, Chloroform-*d*) δ 147.83, 129.36, 118.38, 114.39, 74.56, 60.16, 33.14, 31.63, 25.05, 24.29. HR-MS (APCI, positive mode): *m/z* calc'd for $C_{12}H_{18}NO$ $[M+H]^+$:192.1388, found 192.1393.

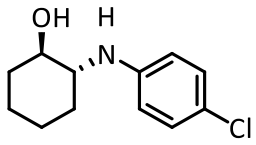

2-(4-chlorophenylamino)cyclohexanol. (CAS: 210408-09-6) ^{1}H NMR (500 MHz, Chloroform-*d*) δ 7.12 (d, J = 8.8 Hz, 2H), 6.63 (d, J = 8.9 Hz, 2H), 3.47 – 3.29 (m, 2H), 3.19 – 3.03 (m, 1H), 2.61 (br, 1H), 2.20 – 2.05 (m, 2H), 1.87 – 1.67 (m, 2H), 1.50 – 1.23 (m, 3H), 1.14 – 0.98 (m, 1H). ^{13}C NMR (126 MHz, Chloroform-*d*) δ 146.45, 129.16, 122.84, 115.42, 74.55, 60.37, 33.24, 31.54, 24.97, 24.25. HR-MS (APCI, positive mode): *m/z* calc'd for $C_{12}H_{17}ClNO$ $[M+H]^+$:226.0999, found 226.1008.

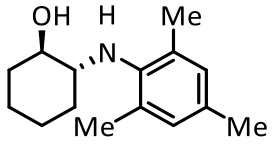

2-(mesitylamino)cyclohexanol. ^{1}H NMR (500 MHz, Chloroform-*d*) δ 6.83 (s, 2H), 3.63 (s, 1H), 3.40 (td, J = 9.9, 4.4 Hz, 1H), 2.80 (ddd, J = 10.9, 9.3, 3.9 Hz, 1H), 2.68 (br, 1H), 2.27 (s, 6H), 2.23 (s, 3H), 2.16 – 2.11 (m, 1H), 1.85 – 1.81 (m, 1H), 1.76 – 1.70 (m, 1H), 1.68 – 1.62 (m, 1H), 1.39 – 1.24 (m, 2H), 1.16 – 1.03 (m, 2H). ^{13}C NMR (126 MHz, Chloroform-*d*) δ 141.32, 131.65, 129.93, 129.76, 75.08, 63.64, 33.06, 32.36, 25.32, 24.32, 20.56, 19.09. HR-MS (APCI, positive mode): *m/z* calc'd for $C_{15}H_{24}NO$ $[M+H]^+$:234.1858, found 234.1877.

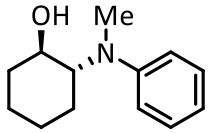

2-(*N*-methyl-*N*-phenylamino)cyclohexanol. (CAS: 109128-84-9) ^{1}H NMR (500 MHz, Chloroform-*d*) δ 7.28 (tt, J = 7.3, 6.5, 2.1 Hz, 2H), 7.02 – 6.94 (m, 2H), 6.84 (td, J = 7.2, 1.1 Hz, 1H), 3.69 (td, J = 10.1, 4.5 Hz, 1H), 3.43 (ddd, J = 11.8, 9.7, 3.7 Hz, 1H), 2.79 (s, 3H), 2.29 – 2.18 (m, 1H), 1.83 – 1.70 (m, 3H), 1.50 – 1.38 (m, 2H), 1.36 – 1.24 (m, 3H). ^{13}C NMR (126 MHz, Chloroform-*d*) δ 151.42, 129.08, 118.53, 115.61, 70.01, 67.02, 33.35, 31.10, 26.04, 25.48, 24.34. HR-MS (APCI, positive mode): *m/z* calc'd for $C_{13}H_{20}NO$ $[M+H]^+$:206.1545, found 206.1566.

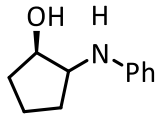

2-(phenylamino)cyclopentanol. (CAS: 109128-84-9) ^{1}H NMR (500 MHz, Chloroform-*d*) δ 7.22 – 7.16 (m, 2H), 6.72 (tt, J = 7.3, 1.1 Hz, 1H), 6.69 – 6.65 (m, 2H), 4.06 (dt, J = 6.1, 4.4 Hz, 1H), 3.61 (td, J = 6.7, 4.1 Hz, 1H), 2.32 – 2.24 (m, 1H), 1.99 (ddt, J = 13.1, 8.7, 6.5 Hz, 1H), 1.88 – 1.70 (m, 2H), 1.64 (ddt, J = 13.6, 8.6, 5.1 Hz, 1H), 1.41 (dddd, J = 13.2, 8.7, 7.1, 6.0 Hz, 1H). ^{13}C NMR (126 MHz, Chloroform-*d*) δ 147.72, 129.30, 117.53, 113.34, 78.21, 62.07, 32.85, 31.17, 21.01. HR-MS (APCI, positive mode): *m/z* calc'd for $C_{11}H_{16}NO$ $[M+H]^+$:178.1232, found 178.1247.

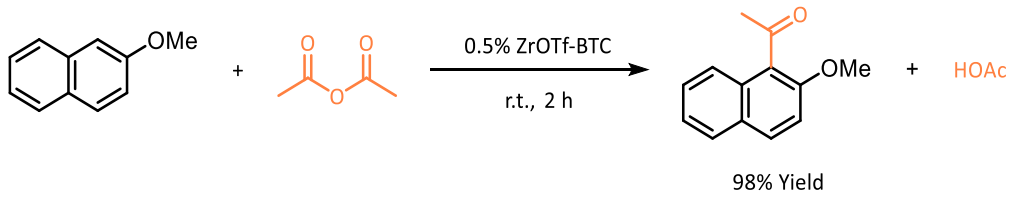

Typical procedure of ZrOTf-BTC catalyzed Friedel-Crafts acylation in batch mode: Under ambient atmosphere, 2-methoxynapthalene (158 mg, 1.0 mmol), acetic anhydride (1.0 mL, neat), and ZrOTf-BTC (5 μmol Zr) were charged to a 2-dram vial. The reaction mixture was stirred at room temperature for 2 h, then the MOF catalyst was removed by centrifugation. The residue was further washed several times with $NaHCO_3$ (aq) to remove the excess acetic anhydride and HOAc, before purified by silica gel chromatography (hexane/CH_2Cl_2). Target molecule was achieved as a white solid with 98% isolated yield. The MOF crystallinity was maintained after the reaction run and minimum metal leaching with 0.23% of Zr per run was detected by ICP-MS analysis.

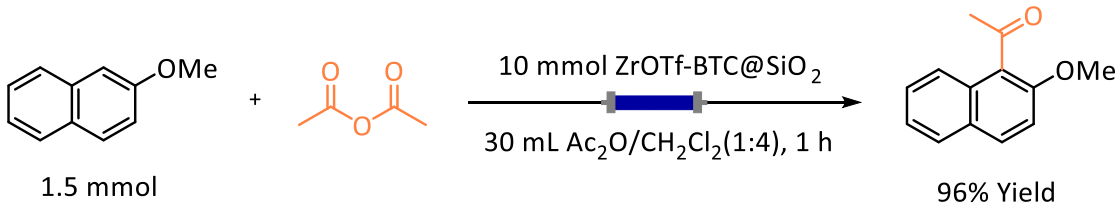

Typical procedure of ZrOTf-BTC catalyzed Friedel-Crafts acylation in flow mode: For a one-hour flow catalysis of Friedel-Crafts acylation, 2-methoxynaphthlene (237 mg, 1.5 mmol) was dissolved in a mixed solution of Ac_2O/CH_2Cl_2 (1:4, 30 mL). The solution was flowed through the ZrOTf-BTC@SiO_2 column at a rate of 30 mL·h^{-1} at room temperature. The product-containing solution was collected in several 5 mL vials and was evaporated on a rotovap to remove the solvent, then 1 equiv. of mesitylene was added as an internal standard. The mixture was analyzed with ^1H NMR to give 1-acetyl-2-methoxynaphthalene in a quantitative yield.

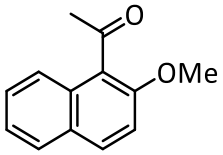

1-acetyl-2-methoxynaphthalene. (CAS: 5672-94-6) ^{1}H NMR (500 MHz, Chloroform-*d*) δ 7.89 (d, J = 8.8 Hz, 1H), 7.81 – 7.78 (m, 1H), 7.76 (dd, J = 8.6, 1.0 Hz, 1H), 7.48 (ddd, J = 8.5, 6.8, 1.4 Hz, 1H), 7.37 (ddd, J = 8.0, 6.8, 1.1 Hz, 1H), 7.28 (d, J = 9.1 Hz, 1H), 3.97 (s, 3H), 2.65 (s, 3H). ^{13}C NMR (126 MHz, Chloroform-*d*) δ 205.22, 153.96, 131.48, 130.31, 128.85, 128.17, 127.69, 125.09, 124.10, 123.64, 112.77, 56.41, 32.73. HR-MS (APCI, positive mode): *m/z* calc'd for $C_{13}H_{13}O_2$ $[M+H]^+$:201.0916, found 201.0920.

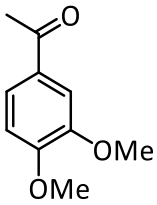

1-(3,4-dimethoxyphenyl)ethanone. (CAS: 1131-62-0) ^{1}H NMR (500 MHz, Chloroform-*d*) δ 7.56 (dd, J = 8.3, 2.0 Hz, 1H), 7.51 (d, J = 2.1 Hz, 1H), 6.87 (d, J = 8.4 Hz, 1H), 3.93 (s, 3H), 3.92 (s, 3H), 2.56 (s, 3H). ^{13}C NMR (126 MHz, Chloroform-*d*) δ 196.85, 153.27, 148.96, 130.46, 123.29, 110.01, 109.91, 56.06, 55.96, 26.21. HR-MS (APCI, positive mode): *m/z* calc'd for $C_{10}H_{13}O_3$ $[M+H]^+$:181.0865, found 181.0876.

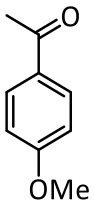

1-(4-methoxyphenyl)ethanone. (CAS: 100-06-1) ^{1}H NMR (500 MHz, Chloroform-*d*) δ 7.96 – 7.92 (m, 2H), 6.95 – 6.91 (m, 2H), 3.87 (s, 3H), 2.55 (s, 3H). ^{13}C NMR (126 MHz, Chloroform-*d*)

δ 196.83, 163.49, 130.61, 130.34, 113.69, 55.49, 26.38. HR-MS (APCI, positive mode): *m/z* calc'd for $C_9H_{11}O_2$ $[M+H]^+$:151.0759, found 151.0760.

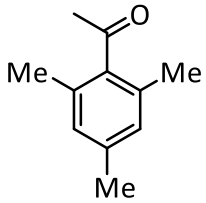

2,4,6-Trimethylacetophenone. (CAS: 1667-01-2) ^{1}H NMR (500 MHz, Chloroform-*d*) δ 6.87 – 6.81 (m, 2H), 2.46 (s, 3H), 2.28 (s, 3H), 2.22 (s, 6H). ^{13}C NMR (126 MHz, Chloroform-*d*) δ 208.69, 139.90, 138.35, 132.33, 128.52, 32.27, 21.05, 19.15. HR-MS (APCI, positive mode): *m/z* calc'd for $C_{11}H_{15}O$ $[M+H]^+$:163.1123, found 163.1126.

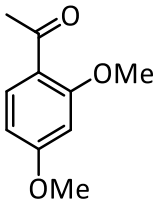

1-(2,4-dimethoxyphenyl)ethanone. (CAS: 829-20-9) ^{1}H NMR (500 MHz, Chloroform-*d*) δ 7.83 (d, J = 8.8 Hz, 1H), 6.52 (dd, J = 8.7, 2.3 Hz, 1H), 6.45 (d, J = 2.3 Hz, 1H), 3.89 (s, 3H), 3.85 (s, 3H), 2.57 (s, 3H). ^{13}C NMR (126 MHz, Chloroform-*d*) δ 197.80, 164.54, 161.10, 132.72, 121.16, 105.01, 98.32, 55.55, 55.46, 31.88. HR-MS (APCI, positive mode): *m/z* calc'd for $C_{10}H_{13}O_3$ $[M+H]^+$:181.0865, found 181.0858.

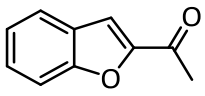

1-(benzo[b]furan-2-yl)ethanone. (CAS: 1646-26-0) ^{1}H NMR (500 MHz, Chloroform-*d*) δ 7.71 (ddd, J = 7.9, 1.3, 0.8 Hz, 1H), 7.58 (dq, J = 8.4, 0.9 Hz, 1H), 7.50 (d, J = 1.0 Hz, 1H), 7.48 (ddd, J = 8.5, 7.2, 1.3 Hz, 1H), 7.31 (ddd, J = 8.0, 7.2, 1.0 Hz, 1H), 2.61 (s, 3H). ^{13}C NMR (126 MHz,

Chloroform-*d*) δ 188.69, 155.70, 152.68, 128.30, 127.08, 123.94, 123.32, 113.07, 112.50, 26.49. HR-MS (APCI, positive mode): *m/z* calc'd for $C_{10}H_9O_2$ $[M+H]^+$:161.0603, found 161.0600.

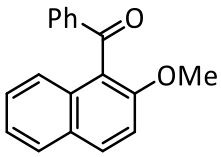

1-benzoyl-2-methoxynaphthalene. (CAS: 14344-14-0) ^{1}H NMR (500 MHz, Chloroform-*d*) δ 7.99 – 7.95 (m, 1H), 7.85 (td, J = 7.9, 1.7 Hz, 3H), 7.59 – 7.54 (m, 1H), 7.53 – 7.50 (m, 1H), 7.45 – 7.41 (m, 2H), 7.40 – 7.33 (m, 3H), 3.83 (s, 3H). ^{13}C NMR (126 MHz, Chloroform-*d*) δ 197.82, 154.09, 137.93, 133.50, 131.72, 131.20, 129.65, 128.80, 128.60, 128.14, 127.42, 124.12, 124.09, 113.11, 56.56. HR-MS (APCI, positive mode): *m/z* calc'd for $C_{18}H_{15}O_2$ $[M+H]^+$:263.1072, found 263.1068.

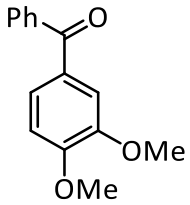

3,4-dimethoxybenzophenone. (CAS: 4038-14-6) ^{1}H NMR (500 MHz, Chloroform-*d*) δ 7.82 – 7.75 (m, 2H), 7.59 (ddq, J = 7.4, 6.6, 1.2 Hz, 1H), 7.52 (d, J = 2.0 Hz, 1H), 7.51 – 7.48 (m, 3H), 7.40 (ddd, J = 8.3, 2.0, 0.7 Hz, 1H), 6.91 (d, J = 8.3 Hz, 1H), 3.98 (d, J = 0.7 Hz, 3H), 3.96 (d, J = 0.7 Hz, 3H). ^{13}C NMR (126 MHz, Chloroform-*d*) δ 195.63, 153.02, 149.01, 138.28, 131.91, 130.21, 129.74, 128.19, 125.55, 112.09, 109.71, 56.11, 56.06. HR-MS (APCI, positive mode): *m/z* calc'd for $C_{15}H_{15}O_3$ $[M+H]^+$:243.1021, found 243.1019.

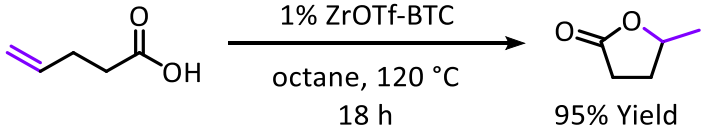

Typical procedure of ZrOTf-BTC catalyzed intramolecular hydroalkoxidation reactions in batch mode: ZrOTf-BTC (10 μmol Zr), pent-4-enoic acid (100 mg, 1.0 mmol), and octane (2.0 mL) were charged to a pressure resistant vial and sealed under ambient atmosphere. The reaction mixture was stirred at 120 °C for 18 h. After cooling down, the reaction slurry was then centrifugated to remove MOF catalyst. The supernatant was analyzed by ^{1}H NMR to give the 4-methylbutyrolactone product in 95% yield. The crude product was further purified by silica gel chromatography eluting with pentane/Et_2O to afford the target molecule as a colorless oil (87% isolated yield). The MOF crystallinity was maintained after the reaction run and minimum metal leaching with 0.20% of Zr per run was detected by ICP-MS analysis.

Recycle of ZrOTf-BTC catalyst in intramolecular hydroalkoxidation reaction: ZrOTf-BTC (50 μmol Zr), 4-penten-1-ol (103 μL, 1.0 mmol), and decane (2.0 mL) were added to a 2-dram vial under ambient atmosphere. The reaction mixture was stirred at 120 °C for 18 h for the reaction. The reaction slurry was then centrifugated to recover the MOF catalyst. The supernatant was analyzed by ^{1}H NMR to give the 2-methyltetrahydrofuran product in quantitative yield. The recovered MOF was washed with decane 3 times before being used for another round of catalysis, then added to a new solution of 4-penten-1-ol (103 μL, 1.0 mmol) in decane (2.0 mL). The reaction mixture was stirred at 120 °C for 18 h for the reaction to complete, and then recycled and monitored using the same procedure. The catalyst was recycled and reused for at least 5 times without a significant drop in catalytic activity (**Figure 5-12**).

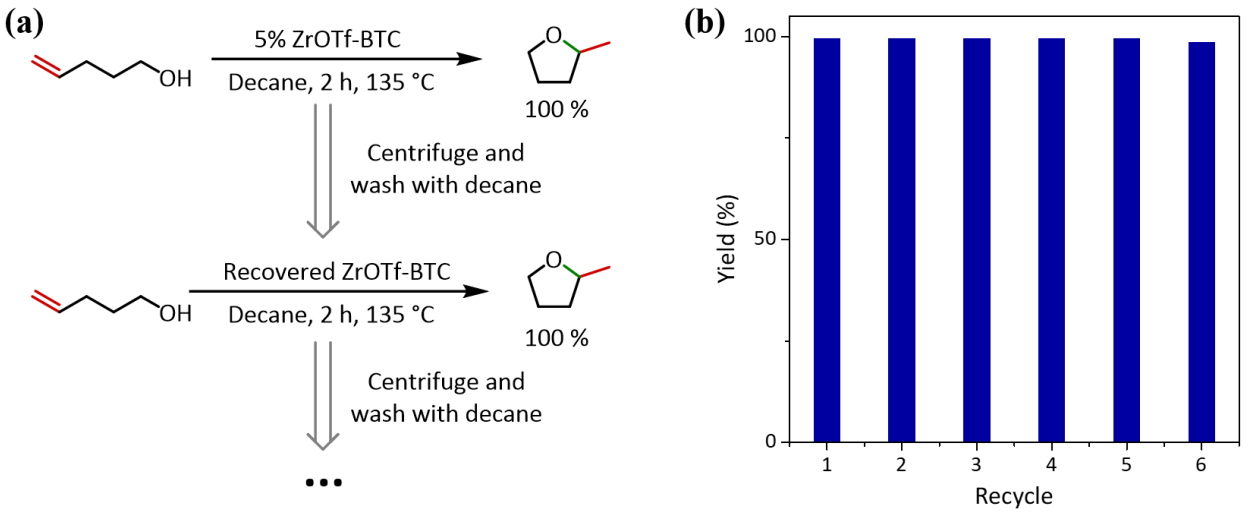

Figure 5-12. (a) Experimental procedure for the recycling experiment of ZrOTf-BTC catalyzed hydroalkoxidation reaction. (b) Plots of yields (%) for the 2-methyltetrahydrofuran products in six consecutive runs.

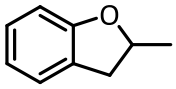

2-methyl-2,3-dihydro-1-benzofuran. (CAS: 1746-11-8) ^{1}H NMR (500 MHz, Chloroform-*d*) δ 7.18 – 7.14 (m, 1H), 7.11 (dddt, J = 8.2, 7.5, 1.5, 0.8 Hz, 1H), 6.83 (td, J = 7.4, 1.0 Hz, 1H), 6.76 (dq, J = 8.0, 0.5 Hz, 1H), 4.92 (ddq, J = 8.8, 7.7, 6.3 Hz, 1H), 3.31 (dd, J = 15.4, 8.8, 1H), 2.82 (dd, J = 15.3, 7.6, 1H), 1.47 (d, J = 6.2 Hz, 3H). ^{13}C NMR (126 MHz, Chloroform-*d*) δ 159.50, 127.96, 124.98, 120.17, 109.34, 79.50, 37.14, 21.78. HR-MS (APCI, positive mode): *m/z* calc'd for $C_9H_{11}O$ $[M+H]^+$:135.0810, found 135.0802.

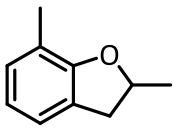

2,7-dimethyl-2,3-dihydrobenzofuran. (CAS: 3199-41-5) ^{1}H NMR (500 MHz, Chloroform-*d*) δ 7.00 (d, J = 7.3 Hz, 1H), 6.94 (ddq, J = 7.4, 1.5, 0.7 Hz, 1H), 6.75 (t, J = 7.4 Hz, 1H), 4.91 (ddq, J = 8.8, 7.8, 6.3 Hz, 1H), 3.31 (ddt, J = 15.3, 8.8, 0.9 Hz, 1H), 2.82 (ddt, J = 15.3, 7.8, 1.0 Hz, 1H), 2.21 (s, 3H), 1.48 (d, J = 6.3 Hz, 3H). ^{13}C NMR (126 MHz, Chloroform-*d*) δ 158.00, 129.15,

126.27, 122.29, 120.00, 119.48, 79.13, 37.49, 21.90, 15.32. HR-MS (APCI, positive mode): *m/z* calc'd for $C_{10}H_{13}O$ $[M+H]^+$:149.0966, found 149.0956.

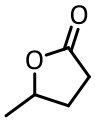

γ-valerolactone. (CAS: 108-29-2) ^{1}H NMR (500 MHz, Chloroform-*d*) δ 4.63 (dp, J = 7.9, 6.3 Hz, 1H), 2.53 (ddd, J = 9.3, 6.9, 2.4 Hz, 2H), 2.39 – 2.30 (m, 1H), 1.81 (dtd, J = 12.7, 9.4, 7.9 Hz, 1H), 1.40 (d, J = 6.2 Hz, 3H). ^{13}C NMR (126 MHz, Chloroform-*d*) δ 177.27, 77.27, 29.69, 29.09, 21.06. HR-MS (APCI, positive mode): *m/z* calc'd for $C_5H_9O_2$ $[M+H]^+$:101.0603, found 101.0600.

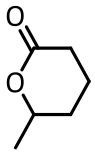

δ-hexalactone. (CAS: 823-22-3) ^{1}H NMR (500 MHz, Chloroform-*d*) δ 4.41 (dtd, J = 7.9, 6.8, 5.8 Hz, 1H), 2.51 (dd, J = 9.6, 7.0 Hz, 2H), 2.30 (dq, J = 12.7, 6.8 Hz, 1H), 1.84 (dtd, J = 12.8, 9.5, 7.9 Hz, 1H), 1.74 (dq, J = 14.6, 7.3 Hz, 1H), 1.62 (dqd, J = 13.5, 7.5, 5.8 Hz, 1H), 1.02 – 0.94 (m, 3H). ^{13}C NMR (126 MHz, Chloroform-*d*) δ 177.31, 82.18, 28.83, 28.45, 27.45, 9.40. HR-MS (APCI, positive mode): *m/z* calc'd for $C_6H_{11}O_2$ $[M+H]^+$:115.0759, found 115.0759.

5.5 References

1. Yamamoto, H., *Lewis acids in organic synthesis*. Wiley-VCH Verlag GmbH: 2000; Vol. 1.

2. Corma, A.; García, H., Lewis Acids: From Conventional Homogeneous to Green Homogeneous and Heterogeneous Catalysis. *Chemical Reviews* **2003,** *103* (11), 4307-4366.

3. Houk, K. N.; Strozier, R. W., Lewis acid catalysis of Diels-Alder reactions. *Journal of the American Chemical Society* **1973,** *95* (12), 4094-4096.

4. Nicolaou, K. C.; Snyder, S. A.; Montagnon, T.; Vassilikogiannakis, G., The Diels–Alder Reaction in Total Synthesis. *Angew. Chem. Int. Ed.* **2002,** *41* (10), 1668-1698.

5. Kobayashi, S.; Sugiura, M.; Kitagawa, H.; Lam, W. W. L., Rare-Earth Metal Triflates in Organic Synthesis. *Chemical Reviews* **2002,** *102* (6), 2227-2302.

6. Antoniotti, S.; Dalla, V.; Duñach, E., Metal Triflimidates: Better than Metal Triflates as Catalysts in Organic Synthesis—The Effect of a Highly Delocalized Counteranion. *Angewandte Chemie International Edition* **2010,** *49* (43), 7860-7888.

7. Mori, K.; Hara, T.; Mizugaki, T.; Ebitani, K.; Kaneda, K., Hydroxyapatite-Bound Cationic Ruthenium Complexes as Novel Heterogeneous Lewis Acid Catalysts for Diels−Alder and Aldol Reactions. *Journal of the American Chemical Society* **2003,** *125* (38), 11460-11461.

8. Nakajima, K.; Baba, Y.; Noma, R.; Kitano, M.; N. Kondo, J.; Hayashi, S.; Hara, M., Nb2O5·nH2O as a Heterogeneous Catalyst with Water-Tolerant Lewis Acid Sites. *Journal of the American Chemical Society* **2011,** *133* (12), 4224-4227.

9. Blackwell, J. A.; Carr, P. W., A Chromatographic Study of the Lewis Acid-Base Chemistry of Zirconia Surfaces. *Journal of Liquid Chromatography* **1991,** *14* (15), 2875-2889.

10. Lunsford, J. H.; Sang, H.; Campbell, S. M.; Liang, C.-H.; Anthony, R. G., An NMR study of acid sites on sulfated-zirconia catalysts using trimethylphosphine as a probe. *Catalysis Letters* **1994,** *27* (3), 305-314.

11. Comito, R. J.; Fritzsching, K. J.; Sundell, B. J.; Schmidt-Rohr, K.; Dincă, M., Single-Site Heterogeneous Catalysts for Olefin Polymerization Enabled by Cation Exchange in a Metal-Organic Framework. *Journal of the American Chemical Society* **2016,** *138* (32), 10232-10237.

12. Drake, T.; Ji, P.; Lin, W., Site Isolation in Metal–Organic Frameworks Enables Novel Transition Metal Catalysis. *Accounts of Chemical Research* **2018,** *51* (9), 2129-2138.

13. Feng, X.; Song, Y.; Li, Z.; Kaufmann, M.; Pi, Y.; Chen, J. S.; Xu, Z.; Li, Z.; Wang, C.; Lin, W., Metal–Organic Framework Stabilizes a Low-Coordinate Iridium Complex for Catalytic Methane Borylation. *Journal of the American Chemical Society* **2019,** *141* (28), 11196-11203.

14. Vermoortele, F.; Vandichel, M.; Van de Voorde, B.; Ameloot, R.; Waroquier, M.; Van Speybroeck, V.; De Vos, D. E., Electronic Effects of Linker Substitution on Lewis Acid Catalysis with Metal–Organic Frameworks. *Angewandte Chemie International Edition* **2012,** *51* (20), 4887-4890.

15. Ji, P.; Drake, T.; Murakami, A.; Oliveres, P.; Skone, J. H.; Lin, W., Tuning Lewis Acidity of Metal–Organic Frameworks via Perfluorination of Bridging Ligands: Spectroscopic, Theoretical, and Catalytic Studies. *Journal of the American Chemical Society* **2018,** *140* (33), 10553-10561.

16. Moon, S.-Y.; Liu, Y.; Hupp, J. T.; Farha, O. K., Instantaneous Hydrolysis of Nerve-Agent Simulants with a Six-Connected Zirconium-Based Metal–Organic Framework. *Angewandte Chemie International Edition* **2015,** *54* (23), 6795-6799.

17. Yang, D.; Ortuño, M. A.; Bernales, V.; Cramer, C. J.; Gagliardi, L.; Gates, B. C., Structure and Dynamics of Zr6O8 Metal–Organic Framework Node Surfaces Probed with Ethanol Dehydration as a Catalytic Test Reaction. *Journal of the American Chemical Society* **2018,** *140* (10), 3751-3759.

18. Horike, S.; Dincă, M.; Tamaki, K.; Long, J. R., Size-Selective Lewis Acid Catalysis in a Microporous Metal-Organic Framework with Exposed Mn2+ Coordination Sites. *Journal of the American Chemical Society* **2008,** *130* (18), 5854-5855.

19. Jiang, J.; Gándara, F.; Zhang, Y.-B.; Na, K.; Yaghi, O. M.; Klemperer, W. G., Superacidity in Sulfated Metal–Organic Framework-808. *Journal of the American Chemical Society* **2014,** *136* (37), 12844-12847.

20. Mautschke, H. H.; Drache, F.; Senkovska, I.; Kaskel, S.; Llabrés i Xamena, F. X., Catalytic properties of pristine and defect-engineered Zr-MOF-808 metal organic frameworks. *Catalysis Science & Technology* **2018,** *8* (14), 3610-3616.

21. Trickett, C. A.; Osborn Popp, T. M.; Su, J.; Yan, C.; Weisberg, J.; Huq, A.; Urban, P.; Jiang, J.; Kalmutzki, M. J.; Liu, Q.; Baek, J.; Head-Gordon, M. P.; Somorjai, G. A.; Reimer, J. A.; Yaghi, O. M., Identification of the strong Brønsted acid site in a metal–organic framework solid acid catalyst. *Nature Chemistry* **2019,** *11* (2), 170-176.

22. Furukawa, H.; Gándara, F.; Zhang, Y.-B.; Jiang, J.; Queen, W. L.; Hudson, M. R.; Yaghi, O. M., Water Adsorption in Porous Metal–Organic Frameworks and Related Materials. *Journal of the American Chemical Society* **2014,** *136* (11), 4369-4381.

23. Herrmann, H.; Gehrmann, T.; Wadepohl, H.; Gade, L. H., Zirconium and hafnium (1-pyridinio)imido complexes: functionalized terminal hydrazinediido analogues. *Dalton Transactions* **2008,** (44), 6231-6241.

24. Kristian, K. E.; Iimura, M.; Cummings, S. A.; Norton, J. R.; Janak, K. E.; Pang, K., Mechanism of the Reaction of Alkynes with a "Constrained Geometry" Zirconaaziridine. PMe3 Dissociates More Rapidly from the Constrained Geometry Complex than from its Cp2 Analogue. *Organometallics* **2009,** *28* (2), 493-498.

25. Fukuzumi, S.; Patz, M.; Suenobu, T.; Kuwahara, Y.; Itoh, S., ESR Spectra of Superoxide Anion−Scandium Complexes Detectable in Fluid Solution. *Journal of the American Chemical Society* **1999,** *121* (7), 1605-1606.

26. Sobańska, K.; Krasowska, A.; Mazur, T.; Podolska-Serafin, K.; Pietrzyk, P.; Sojka, Z., Diagnostic Features of EPR Spectra of Superoxide Intermediates on Catalytic Surfaces and Molecular Interpretation of Their g and A Tensors. *Topics in Catalysis* **2015,** *58* (12), 796-810.

27. Ohkubo, K.; Menon, S. C.; Orita, A.; Otera, J.; Fukuzumi, S., Quantitative Evaluation of Lewis Acidity of Metal Ions with Different Ligands and Counterions in Relation to the Promoting Effects of Lewis Acids on Electron Transfer Reduction of Oxygen. *The Journal of Organic Chemistry* **2003,** *68* (12), 4720-4726.

28. Román-Leshkov, Y.; Davis, M. E., Activation of Carbonyl-Containing Molecules with Solid Lewis Acids in Aqueous Media. *ACS catalysis* **2011,** *1* (11), 1566-1580.

29. Tang, B.; Song, W.-C.; Li, S.-Y.; Yang, E.-C.; Zhao, X.-J., Post-synthesis of Zr-MOR as a robust solid acid catalyst for the ring-opening aminolysis of epoxides. *New Journal of Chemistry* **2018,** *42* (16), 13503-13511.

30. Kobayashi, S.; Nagayama, S., A Microencapsulated Lewis Acid. A New Type of Polymer-Supported Lewis Acid Catalyst of Wide Utility in Organic Synthesis. *Journal of the American Chemical Society* **1998,** *120* (12), 2985-2986.

31. Tanaka, K.; Fukase, K., Acid-mediated reactions under microfluidic conditions: A new strategy for practical synthesis of biofunctional natural products. *Beilstein Journal of Organic Chemistry* **2009,** *5*, 40.

32. Zeng, L.; Liao, P.; Liu, H.; Liu, L.; Liang, Z.; Zhang, J.; Chen, L.; Su, C.-Y., Impregnation of metal ions into porphyrin-based imine gels to modulate guest uptake and to assemble a catalytic microfluidic reactor. *Journal of Materials Chemistry A* **2016,** *4* (21), 8328-8336.

33. Chen, X.; Jiang, H.; Hou, B.; Gong, W.; Liu, Y.; Cui, Y., Boosting Chemical Stability, Catalytic Activity, and Enantioselectivity of Metal–Organic Frameworks for Batch and Flow Reactions. *Journal of the American Chemical Society* **2017,** *139* (38), 13476-13482.

34. Park, H. D.; Dincă, M.; Román-Leshkov, Y., Continuous-Flow Production of Succinic Anhydrides via Catalytic β-Lactone Carbonylation by Co(CO)4⊂Cr-MIL-101. *Journal of the American Chemical Society* **2018,** *140* (34), 10669-10672.

35. Fu, Y. Y.; Yang, C. X.; Yan, X. P., Fabrication of ZIF‐8@SiO2 Core–Shell Microspheres as the Stationary Phase for High‐Performance Liquid Chromatography. *Chemistry- A European Journal* **2013,** *19* (40), 13484-13491.

36. Ehrling, S.; Kutzscher, C.; Freund, P.; Müller, P.; Senkovska, I.; Kaskel, S., MOF@SiO2 core-shell composites as stationary phase in high performance liquid chromatography. *Microporous and Mesoporous Materials* **2018,** *263*, 268-274.

37. Gorzynski Smith, J., Synthetically Useful Reactions of Epoxides. *Synthesis* **1984,** *1984* (08), 629-656.

38. Ager, D. J.; Prakash, I.; Schaad, D. R., 1,2-Amino Alcohols and Their Heterocyclic Derivatives as Chiral Auxiliaries in Asymmetric Synthesis. *Chemical Reviews* **1996,** *96* (2), 835-876.

39. Chakraborti, A. K.; Kondaskar, A., ZrCl4 as a new and efficient catalyst for the opening of epoxide rings by amines. *Tetrahedron Letters* **2003,** *44* (45), 8315-8319.

40. Procopio, A.; Gaspari, M.; Nardi, M.; Oliverio, M.; Rosati, O., Highly efficient and versatile chemoselective addition of amines to epoxides in water catalyzed by erbium(III) triflate. *Tetrahedron Letters* **2008,** *49* (14), 2289-2293.

41. Shinde, S. S.; Said, M. S.; Surwase, T. B.; Kumar, P., Mild regiospecific alcoholysis and aminolysis of epoxides catalyzed by zirconium(IV) oxynitrate. *Tetrahedron Letters* **2015,** *56* (43), 5916-5919.

42. Sartori, G.; Maggi, R., *Advances in Friedel-Crafts acylation reactions: catalytic and green processes*. CRC Press: 2009.

43. Iwao, H.; Mitsuhiro, M.; Shu, K., Hafnium(IV) Trifluoromethanesulfonate, An Efficient Catalyst for the Friedel–Crafts Acylation and Alkylation Reactions. *Bulletin of the Chemical Society of Japan* **1995,** *68* (7), 2053-2060.

44. Atsushi, K.; Shuichi, M.; Jun-ichi, M.; Takehiro, T.; Shu, K., Friedel-Crafts Reactions Catalyzed by Rare Earth Metal Trifluoromethanesulfonates. *Bulletin of the Chemical Society of Japan* **2000,** *73* (10), 2325-2333.

45. Kantam, M. L.; Ranganath, K. V. S.; Sateesh, M.; Kumar, K. B. S.; Choudary, B. M., Friedel–Crafts acylation of aromatics and heteroaromatics by beta zeolite. *Journal of Molecular Catalysis A: Chemical* **2005,** *225* (1), 15-20.

46. Gaare, K.; Akporiaye, D., Modified zeolites as catalysts in the Friedel-Crafts acylation. *Journal of Molecular Catalysis A: Chemical* **1996,** *109* (2), 177-187.

47. Quaschning, V.; Deutsch, J.; Druska, P.; Niclas, H. J.; Kemnitz, E., Properties of modified zirconia used as friedel-crafts-acylation catalysts. *Journal of Catalysis* **1998,** *177* (2), 164-174.

48. Kozhevnikov, I. V., Friedel–Crafts acylation and related reactions catalysed by heteropoly acids. *Applied Catalysis A* **2003,** *256* (1), 3-18.

49. Nguyen, L. T. L.; Nguyen, C. V.; Dang, G. H.; Le, K. K. A.; Phan, N. T. S., Towards applications of metal–organic frameworks in catalysis: Friedel–Crafts acylation reaction over IRMOF-8 as an efficient heterogeneous catalyst. *Journal of Molecular Catalysis A: Chemical* **2011,** *349* (1), 28-35.

50. Elliott, M. C., Saturated oxygen heterocycles. *Journal of the Chemical Society, Perkin Transactions 1* **2002,** (21), 2301-2323.

51. Blunt, J. W.; Carroll, A. R.; Copp, B. R.; Davis, R. A.; Keyzers, R. A.; Prinsep, M. R., Marine natural products. *Natural Products Reports* **2018,** *35* (1), 8-53.

52. Wolfe, J. P.; Rossi, M. A., Stereoselective Synthesis of Tetrahydrofurans via the Palladium-Catalyzed Reaction of Aryl Bromides with γ-Hydroxy Alkenes: Evidence for an

Unusual Intramolecular Olefin Insertion into a Pd(Ar)(OR) Intermediate. *Journal of the American Chemical Society* **2004,** *126* (6), 1620-1621.

53. Miller, Y.; Miao, L.; Hosseini, A. S.; Chemler, S. R., Copper-Catalyzed Intramolecular Alkene Carboetherification: Synthesis of Fused-Ring and Bridged-Ring Tetrahydrofurans. *Journal of the American Chemical Society* **2012,** *134* (29), 12149-12156.

54. Gao, S.-S.; Garcia-Borràs, M.; Barber, J. S.; Hai, Y.; Duan, A.; Garg, N. K.; Houk, K. N.; Tang, Y., Enzyme-Catalyzed Intramolecular Enantioselective Hydroalkoxylation. *Journal of the American Chemical Society* **2017,** *139* (10), 3639-3642.

55. Walsh, C. T.; Tang, Y., Recent Advances in Enzymatic Complexity Generation: Cyclization Reactions. *Biochemistry* **2018,** *57* (22), 3087-3104.

56. Boiteau, J.-G.; Van de Weghe, P.; Eustache, J., A New, Ring Closing Metathesis-Based Synthesis of (−)-Fumagillol. *Organic Letters* **2001,** *3* (17), 2737-2740.

57. Utsunomiya, M.; Kawatsura, M.; Hartwig, J. F., Palladium-Catalyzed Equilibrium Addition of Acidic OH Groups across Dienes. *Angewandte Chemie* **2003,** *115* (47), 6045-6048.

58. Barluenga, J.; Diéguez, A.; Rodríguez, F.; Fañanás, F. J.; Sordo, T.; Campomanes, P., [W(CO)5]-Catalyzed endo- or exo-Cycloisomerization Reactions of 1,1-Disubstituted 4-Pentyn-1-ols: Experimental and Theoretical Studies. *Chemistry- A European Journal* **2005,** *11* (19), 5735-5741.

59. Ji, P.; Solomon, J. B.; Lin, Z.; Johnson, A.; Jordan, R. F.; Lin, W., Transformation of Metal–Organic Framework Secondary Building Units into Hexanuclear Zr-Alkyl Catalysts for Ethylene Polymerization. *Journal of the American Chemical Society* **2017,** *139* (33), 11325-11328.

Chapter 6. Dimensional Reduction of Lewis Acidic MOFs for Multicomponent Reactions

6.1 Introduction

Multicomponent reactions (MCRs) combine three or more reaction partners in one pot to construct organic products containing most of the atoms in the reactants.[1-2] With excellent atom- and step-economy, MCRs provide an efficient and environmentally friendly synthetic approach toward complex molecules with good scaffold diversity and have played an important role in drug discovery and medicinal chemistry.[3-5] Brönsted and Lewis acids have been used to accelerate many MCRs under mild conditions.[6] However, high loadings of homogeneous acid catalysts (5-20 mol%) are needed to catalyze MCRs due to short catalyst lifetimes in these one-pot processes.[3-4] Meanwhile, relatively low acidity and few accessible active sites in solid acid catalysts, such as metal oxides, resins, and zeolites, have severely limited their applications in MCRs.[7-9]

Constructed from inorganic metal ions or clusters and organic linkers, metal-organic frameworks (MOFs) have emerged as an important class of crystalline porous materials for designing highly efficient single-site solid catalysts.[10-13] In particular, a series of robust MOFs with acidic sites have been developed based on electron-deficient high-valent metals (e.g., Zr^{IV}, Hf^{IV}, *etc*.) and used to catalyze important organic transformations.[14-17] The Brönsted or Lewis acidity of these high-valent MOFs was further enhanced by transforming pristine Zr-formate or other Zr-capping moieties into Zr-SO_4 or Zr-OTf (OTf = triflate) groups.[14, 18] However, increasing and stabilizing active sites in these porous materials have limited their accessibility to sterically demanding substrates. As a result, acidic MOFs performed poorly with bulky substrates or in complicated reactions as the substrates cannot readily access internal Lewis acid sites.[19-20]

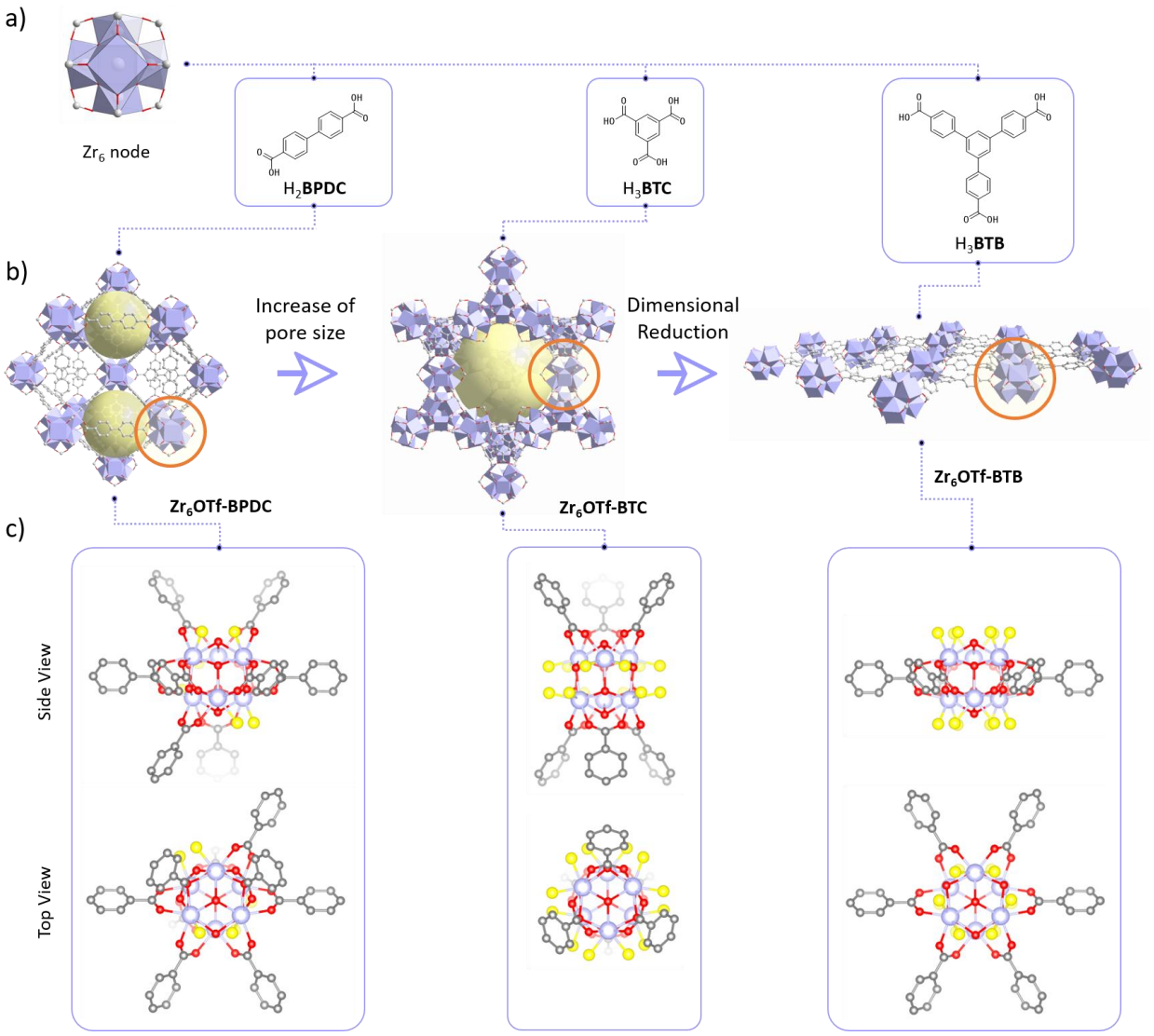

Figure 6-1. Illustration and comparison of (a) MOF node and ligands, (b) structures and pore distributions, (c) coordination defects or capping residues (highlighted in yellow) for the generation of strongly Lewis acidic Zr-OTf sites in **Zr_6OTf-BPDC**, **Zr_6OTf-BTC**, and **Zr_6OTf-BTB** (purple: Zr, red: O, grey: C, yellow: Lewis acidic site. H atoms are omitted for clarity). Copyright 2021 American Chemical Society.

To explore the application of MOF-based catalysts in synthetically useful reactions, we systematically studied in this chapter topology effects of strongly Lewis acidic MOFs on the reactivity of MCRs and uncovered a dimensional reduction approach to improve MCR activity by allowing free access to Lewis acidic sites in two-dimensional (2D) MOFs. We constructed three strongly Lewis acidic MOFs, **Zr_6OTf-BPDC**, **Zr_6OTf-BTC**, and **Zr_6OTf-BTB**, with distinct

topologies and porosities (**Figure 6-1**). **Zr_6OTf-BTB**, a 2D MOF featuring self-supporting monolayer morphology with freely accessible Lewis acidic Zr-OTf sites, outperformed two three-dimensional (3D) MOFs in MCRs for the construction of a broad range of synthetically useful tetrahydroquinoline and aziridine-carboxylate derivatives with high turnover numbers (TONs) of up to 270 and a high *cis*-selectivity of up to 100%. The topology-activity relationships in these Zr-based Lewis acidic MOFs were rationalized by comparing their Lewis acidity, numbers of Lewis acidic sites, and sterically accessible Lewis acidic sites. **Zr_6OTf-BTB** also outperformed the homogeneous benchmark $Sc(OTf)_3$ with 14 times higher TONs and 9 times longer catalyst lifetime. Lastly, **Zr_6OTf-BTB** was successfully used to construct several bio-active drug candidates via MCRs with excellent efficiency.

Scheme 6-1. Dimensional reduction of Lewis acidic MOFs for multicomponent reactions. Copyright 2021 American Chemical Society.

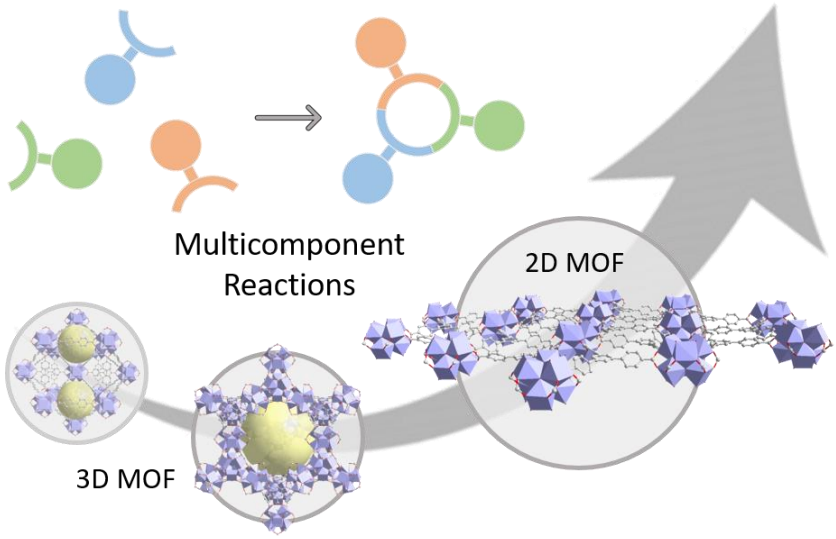

6.2 Results and Discussion

6.2.1 Synthesis and characterization of strongly Lewis acidic MOFs

Zr-based MOFs have distinguished themselves among the large families of MOFs with their isoreticular nature and outstanding stability.[21-22] With electron-deficient Zr^{IV} centers, MOFs

with Zr-oxo secondary building units (SBUs) have been extensively explored as Lewis acidic catalysts.[15, 23] Furthermore, the conservation of hexanuclear SBUs in a wide range of distinct Zr MOFs allows in-depth studies of the topology-reactivity relationships in these MOFs with Zr-oxo SBUs as catalytic sites.

Three Zr-based MOFs of different topologies, **Zr_6-BPDC**,[24] **Zr_6-BTC**,[25] and **Zr_6-BTB**,[26] were synthesized through solvothermal reactions between Zr^{IV} salts and H_2BPDC, H_3BTC, and 4-[3,5-bis(4-carboxyphenyl)phenyl]benzoic acid (H_3BTB) bridging ligands, respectively. These MOFs are built from the same $Zr_6(\mu_3\text{-}O)_4(\mu_3\text{-}OH)_4$ SBUs with different carboxylate connectivities and framework topologies. **Zr_6-BPDC** adopts an **fcu** topology with the Zr_6 SBUs coordinating with carboxylates from bidentate BPDC and ~25% defect sites that are terminated by water/hydroxide groups. The defect site content was determined by the ratio of BPDC to Zr as quantified by ^{1}H NMR and inductively coupled plasma-mass spectrometry (ICP-MS), respectively. The Zr_6 SBUs in both **Zr_6-BTC** and **Zr_6-BTB** coordinate to six carboxylates from tridentate BTC or BTB ligands and six carboxylates from capping formate groups (**Figure 6-1**). Due to the different carboxylate connectivity, **Zr_6-BTC** adopts a 3D **spn** topology while **Zr_6-BTB** adopts a 2D **kgd** topology. The three MOFs showed good crystallinity with an excellent agreement between their experimental powder X-ray diffraction (PXRD) patterns and the simulated ones based on their structure models (**Figures 6-2b**, **6-4a**, **6-5a**). **Zr_6-BPDC** displayed a nearly spherical morphology of~200 nm in size (**Figure 6-4b**) and **Zr_6-BTC** displayed a block-like morphology of 100-200 nm in size (**Figure 6-5b**) by transmission electron microscopy (TEM). In contrast, a slightly wrinkle single-layer morphology was observed for **Zr_6-BTB** (**Figure 6-3**) by TEM with clear lattice fringes by high resolution TEM (HR-TEM).

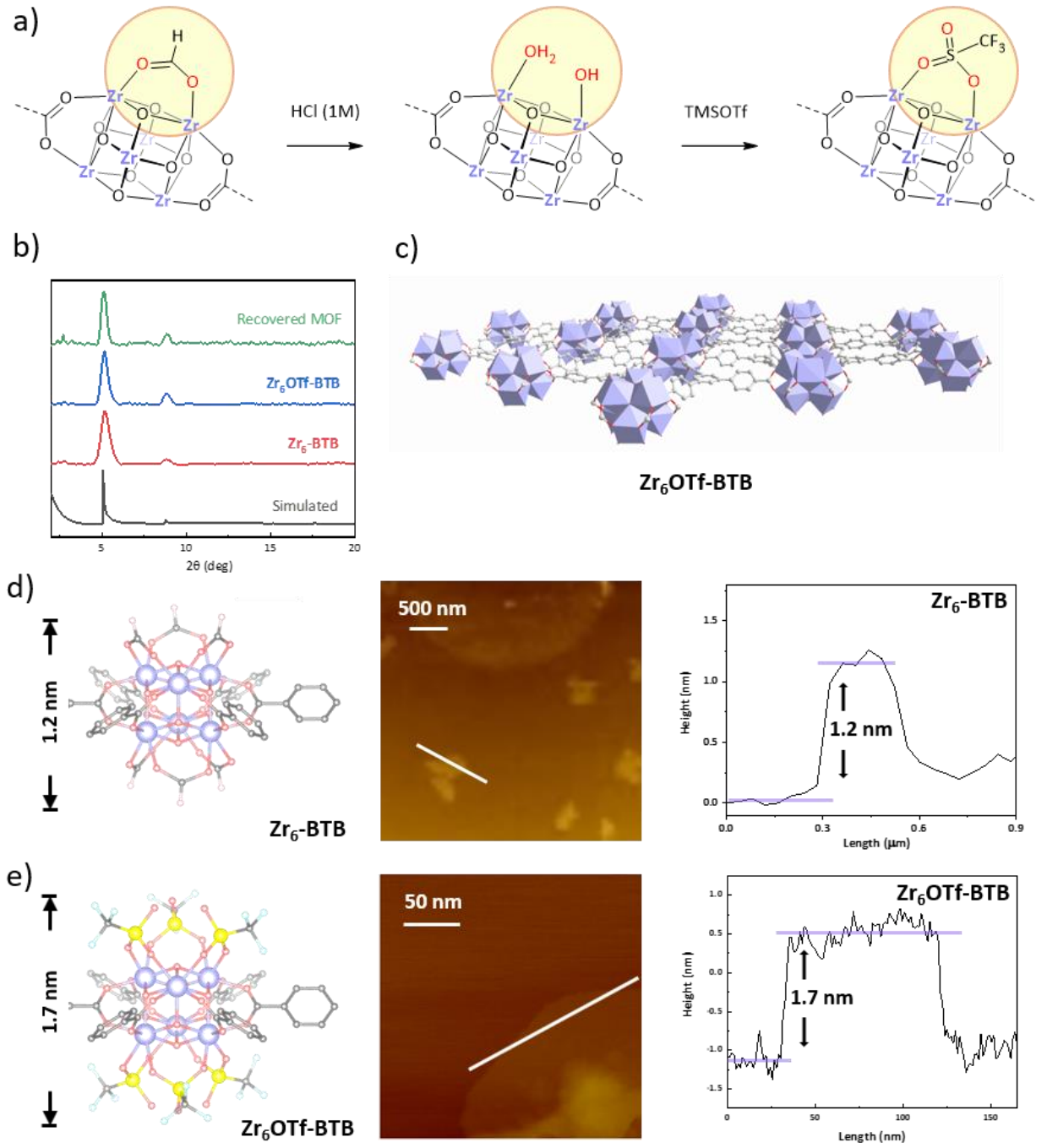

Figure 6-2. Synthesis and characterization of strongly Lewis acidic 2D MOF **Zr_6OTf-BTB**. (**a**) Post-synthetic activation of **Zr_6-BTB** through formate exchange and triflation to strongly Lewis acidic **Zr_6OTf-BTB**. (**b**) PXRD patterns of **Zr_6-BTB** (red), **Zr_6OTf-BTB** (blue), and the recovered MOF after MCR (green) compared with the simulated PXRD pattern (black). (**c**) Schematic illustration of **Zr_6-BTB** adopting a 2D **kgd** topology. **(d, e**) AFM topographies and height profiles of **Zr_6-BTB** and **Zr_6OTf-BTB**. Copyright 2021 American Chemical Society.

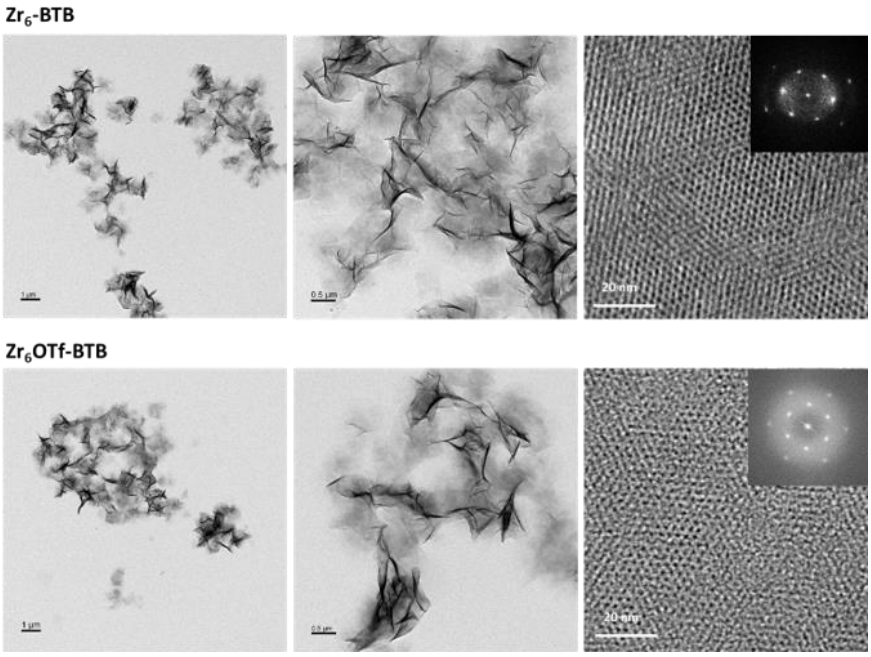

Figure 6-3. TEM images and HRTEM images of **Zr_6-BTB** (top) and **Zr_6OTf-BTB** (bottom).

Lewis acidic MOF catalysts **Zr_6OTf-BPDC**, **Zr_6OTf-BTC**, and **Zr_6OTf-BTB** were generated by transforming Zr-formate and Zr-OH/OH_2 sites in the pristine MOFs to strongly Lewis acidic Zr-OTf sites through capping formate removal by treatment with 1M HCl and triflation with trimethylsilyl trifluoromethanesulfonate (TMSOTf) (**Figure 6-2a**). The MOF structures and morphologies were maintained throughout the post-synthetic activation processes as evidenced by the unchanged PXRD patterns and TEM images (**Figures 6-2b**, **6-3**). **Zr_6OTf-BPDC** and **Zr_6OTf-BTC** displayed 3D porous structures with pore sizes of 1.2 nm and 1.6 nm, respectively, as revealed by nitrogen sorption analysis (**Figure 6-4c**). The pore sizes and volumes were slightly reduced after triflation owing to the introduction of large OTf groups. **Zr_6OTf-BTB** showed a monolayer morphology of 1.7 nm in thickness based on atomic force microscopy (AFM) analysis, which is slightly thicker than that of the pristine **Zr_6-BTB** (1.2 nm) due to OTf coordination (**Figures 6-2e**, **6-2f**). This change of MOF thickness matches well with the Van der Waals sizes

of the optimized SBUs in **Zr$_6$-BTB** and **Zr$_6$OTf-BTB** based on density functional theory (DFT) calculations.

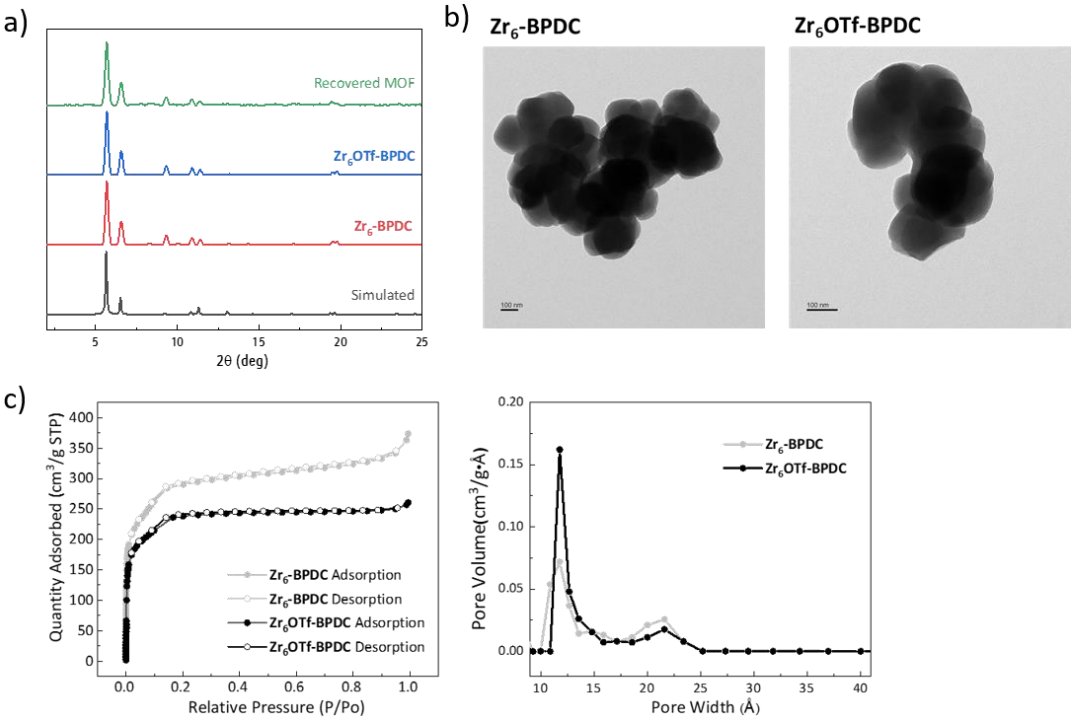

Figure 6-4. Structural characterization of **Zr$_6$OTf-BPDC**. (a) PXRD pattern of as-synthesized **Zr$_6$-BPDC** (red), **Zr$_6$OTf-BPDC** (blue), the MOF recovered from the catalytic MCR (green), and simulated UiO-67 MOF (black). (b) TEM images of **Zr$_6$-BPDC** (left) and **Zr$_6$OTf-BPDC** (right). (c) N_2 sorption isotherms of **Zr$_6$-BPDC** (grey) and **Zr$_6$OTf-BPDC** (black) with a BET surface area of 1011 m^2/g and 839 m^2/g, respectively, and pore size distribution calculated by DFT showing the pores of ~12 Å for both MOFs.

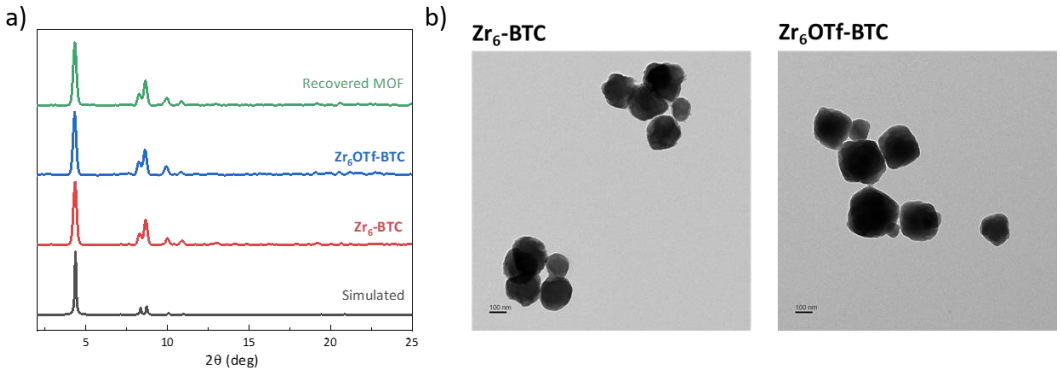

Figure 6-5. Structural characterization of **Zr$_6$OTf-BTC**. (a) PXRD pattern of as-synthesized **Zr$_6$-BTC** (red), **Zr$_6$OTf-BTC** (blue), the MOF recovered from catalytic MCR (green), and simulated for MOF-808 (black). (b) TEM images of **Zr$_6$-BTC** (left) and **Zr$_6$OTf-BTC** (right).

The enhancement of Lewis acidity in triflated MOFs was quantified by fluorescence spectra of MOF-bound *N*-methylacridone (NMA) (**Figure 6-6**). Free NMA has an emission maximum (λ_{max}) at 433 nm when excited at 413 nm. Upon binding to Lewis acidic Zr sites, this fluorescence redshifts linearly depend on the Lewis acidity of Zr centers.[27] Accordingly, the energy splitting (ΔE) between the π_x^* and π_y^* orbitals of Zr-bound NMA in **Zr$_6$-BPDC**, **Zr$_6$-BTC**, and **Zr$_6$-BTB** were determined to be 0.87, 0.88, and 0.88 eV, respectively. These values increased to 0.95, 0.97, and 0.97 eV for **Zr$_6$OTf-BPDC**, **Zr$_6$OTf-BTC**, and **Zr$_6$OTf-BTB**, respectively, indicating the generation of strongly Lewis acidic sites in these MOFs. The acidity in these MOFs is comparable to the homogeneous benchmark Sc(OTf)$_3$.[18] The extended X-ray absorption fine structure (EXAFS) feature of **Zr$_6$OTf-BTB** at the Zr K edge was well fitted to Zr$_6$ SBUs with an additional μ_2-OTf group at a Zr-O^{OTf} distance of 2.29 Å and Zr-S^{OTf} distance of 3.63 Å. In contrast, the fitting model of **Zr$_6$-BTB** lacks Zr-S^{OTf} interaction and features a shorter Zr-OH distance (2.13 Å). This result supports the conversion of Zr$_2$(OH)(OH$_2$) to Zr$_2$(μ_2-OTf) after triflation (**Figure 6-7**).

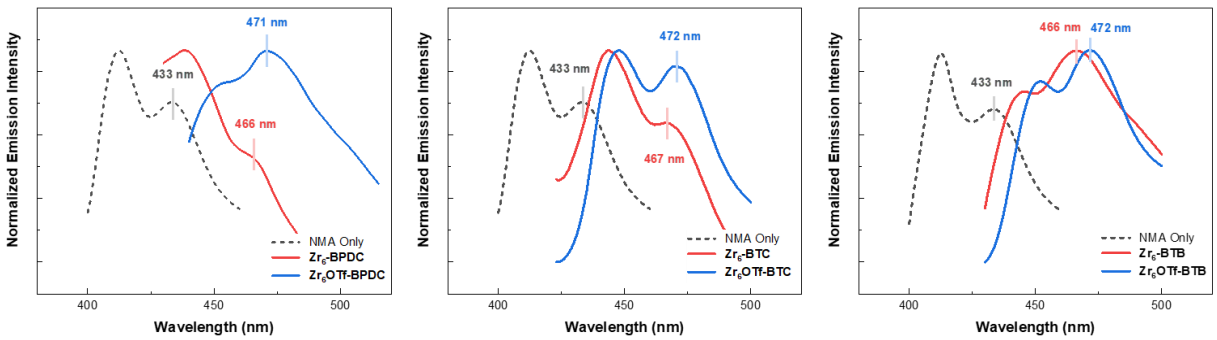

Figure 6-6. The fluorescence spectra of NMA in MeCN (black) and NMA bound to Lewis acidic MOFs before and after the triflation of **Zr$_6$-BPDC** (left), **Zr$_6$-BTC** (middle), and **Zr$_6$-BTB** (right). The red shifts of NMA fluorescence indicate stronger Lewis acidity after TMSOTf treatment of all three MOFs.

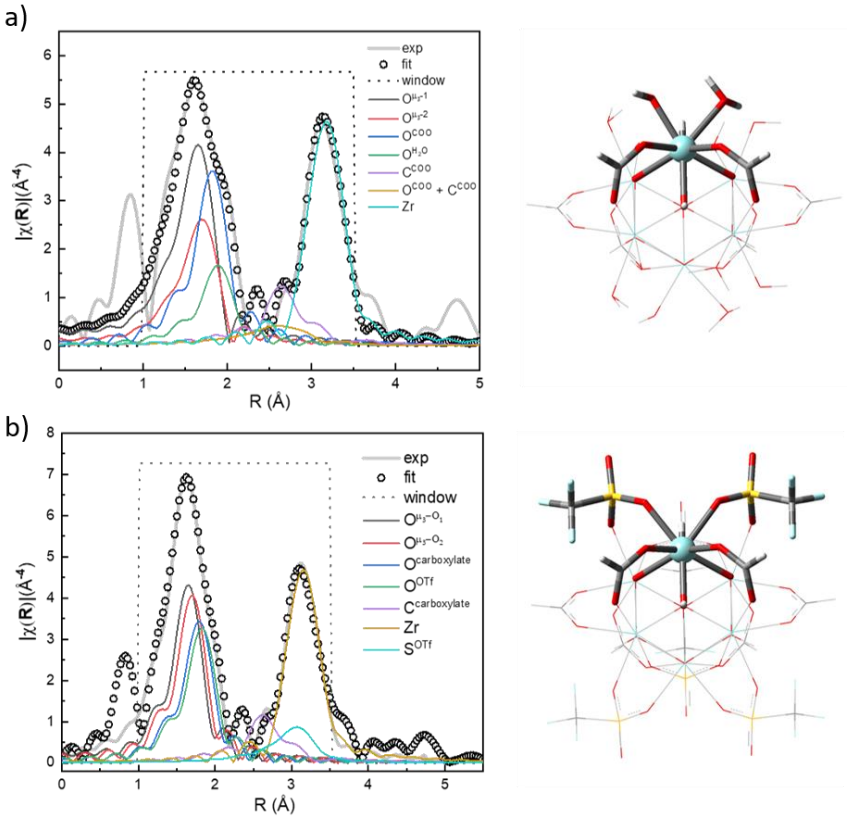

Figure 6-7. EXAFS spectra (grey solid line) and fits (black circles) in R-space at the Zr K-edge for (a) **Zr_6-BTB** and (b) **Zr_6OTf-BTB**. The EXAFS fitting structure is shown on the right (azure: Zr, red: O, grey: C, white: H).

6.2.2 Catalytic activities of Lewis acidic MOFs in multicomponent reactions

All three MOFs displayed excellent catalytic activities in Diels-Alder reactions between 1,4-benzoquinone and cyclohexa-1,3-diene (**Table 6-1**), supporting the presence of strongly Lewis acid acidic $Zr_2(\mu_2$-OTf) groups in these MOFs. We then examined the performance of these MOFs in Lewis acid catalyzed MCRs. By condensing an aniline, an aldehyde, and an activated olefin in one step to efficiently afford a 1,2,3,4-tetrahydroquinoline derivative, Povarov reaction is of great importance in constructing heterocyclic scaffolds as pharmaceutical ingredients.[28-29] Povarov reaction can be viewed as a less reactive variant of Diels-Alder cycloaddition between an alkene and an imine that is generated in situ from an aniline and an aldehyde. Strong Lewis acid catalysts, such as $Sc(OTf)_3$ and $Yb(OTf)_3$, are typically used to promote the Povarov reactions. However,

due to rapid catalyst deactivation, relatively high loadings (5-20 mol%) of catalysts or elevated temperatures are required to afford high yields of target products with satisfactory *cis*/*trans* selectivity.[30-31]

Table 6-1. MOF catalyzed Diels-Alder reaction between 1,4-benzoquinone and cyclohexadiene.

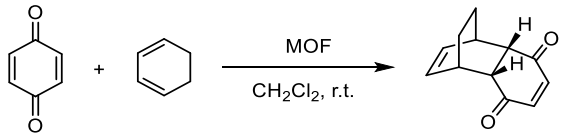

Entry	Catalyst	Yield (%)
1	1.0 mol% **Zr_6OTf-BPDC**	>99
2	1.0 mol% **Zr_6OTf-BTC**	>99
3	1.0 mol% **Zr_6OTf-BTB**	>99

Reaction condition: 1,4-benzoquinone (108 mg, 1.0 mmol), cyclohexadiene (120 μL, 1.2 mmol), MOF catalyst (10 μmol Zr-OTf), and CH_2Cl_2 (4.0 mL) at room temperature for 16 h. Yields determined by ^{1}H NMR with mesitylene as internal standard.

At 1.0 mol% catalyst loading, **Zr_6OTf-BTB** quantitatively transformed aniline, benzaldehyde, and ethyl vinyl ether into 4-ethoxy-2-phenyl-1,2,3,4-tetrahydroquinoline (**1**) with excellent *cis* selectivity (*cis*:*trans* = 15:1) in acetonitrile at room temperature (Entry 3, **Table 6-2**). A TON of 270 was achieved when the catalyst loading was lowered to 0.2 mol% (Entry 4, **Table 6-2**). PXRD patterns indicated no obvious change of MOF crystallinity (**Figure 6-2b**) and ICP-MS analysis showed a minimal amount of Zr (<0.1%) leached into the supernatant after reaction. **Zr_6OTf-BTC** and **Zr_6OTf-BPDC** afforded **1** in 79% and 23%, respectively, under the same conditions (Entries 1-2, **Table 6-2**). The MOF topology thus has a large influence on the MCR activity. With non-triflated MOFs, the MCR yields dropped to 0%, 9%, and 12% for **Zr_6-BPDC**, **Zr_6-BTC**, and **Zr_6-BTB**, respectively (Entries 4-6, **Table 6-2**). This result confirms the crucial role of strongly Lewis acidic Zr-OTf sites in catalyzing the MCR.

Table 6-2. Three-component Povarov reactions catalyzed by MOF and homogeneous catalysts.

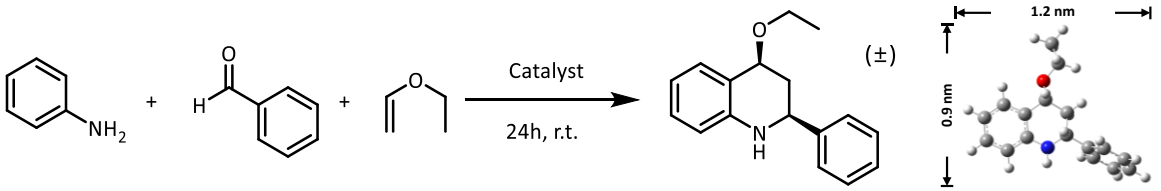

Entry	Catalyst	Yield (%)	TON
1	1.0 mol% **Zr_6OTf-BPDC**	23	23
2	1.0 mol% **Zr_6OTf-BTC**	79	79
3	1.0 mol% **Zr_6OTf-BTB**	>99	>99
4	0.2 mol% **Zr_6OTf-BTB**	54	270
5	1.0 mol% **Zr_6-BPDC**	0	0
6	1.0 mol% **Zr_6-BTC**	9	9
7	1.0 mol% **Zr_6-BTB**	12	12
8	-	0	-
9	1.0 mol% $Sc(OTf)_3$	20	20
10	1.0 mol% HOTf	0	0

Reaction condition: aniline (45 μL, 0.5 mmol), benzaldehyde (46 μL, 0.5 mmol), ethyl vinyl ether (40 μL, 0.5 mmol), MOF or homogeneous catalysts (5.0 or 1.0 μmol), and acetonitrile (2.0 mL) at room temperature. Yields include both *cis* and *trans* isomers, as determined by ^{1}H NMR with mesitylene as internal standard.

In comparison, a time-dependent study showed that 1.0 mol% $Sc(OTf)_3$ gave 20% yield of **1** with no increase of yield after the first 3h, likely due to rapid deactivation of homogenous Lewis acids (**Figure 6-8**). At 1.0 mol% loading, strong Brønsted acid HOTf failed to catalyze Povarov reaction (Entry 10, **Table 6-2**), which rules out the possibility that leached HOTf might have contributed to the MCR activity. Furthermore, **Zr_6OTf-BTB** was recycled via simple filtration and used in nine runs of Povarov reactions. The catalytic activity of **Zr_6OTf-BTB** dropped slightly in the first three runs but was completely restored in the fourth and seven runs through re-activation

with TMSOTf (**Figure 6-9**). **Zr_6OTf-BTB** significantly outperformed homogeneous acid catalyst with 14 times higher TON and at least 9 times longer lifetime.

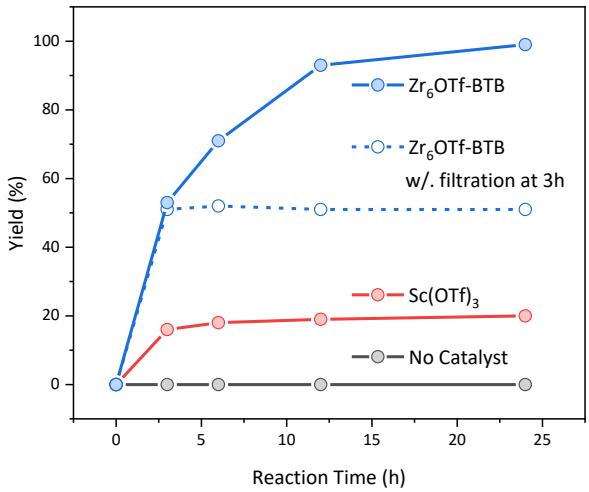

Figure 6-8. Time-dependent curves of multi-component Povarov reactions of anline, benzaldehyde, and ethyl vinyl ether catalyzed by 1.0 mol% of **Zr_6OTf-BTB** (blue), 1.0 mol% of $Sc(OTf)_3$, or without catalyst (grey). The blue dashed line indicates the reaction result of 1.0 mol% of **Zr_6OTf-BTB** with filtration to remove the MOF solid at 3h. Reaction condition: anline (45 μL, 0.5 mmol), benzaldehyde (46 μL, 0.5 mmol), ethyl vinyl ether (40 μL, 0.5 mmol), Lewis acid catalyst (5.0 μmol), and anhydrous CH_3CN (2.0 mL) at room temperature. The yields refer to a combination of both isomers, as determined by ^{1}H NMR with mesitylene as internal standard.

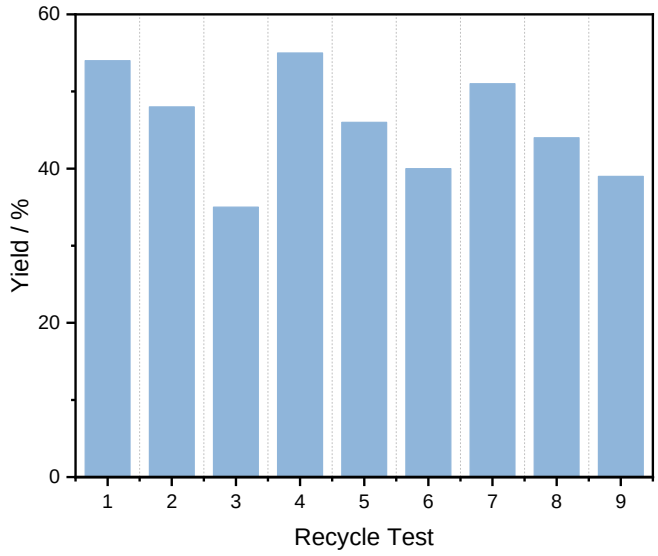

Figure 6-9. Recycle test of multi-component Povarov reaction of aniline, benzaldehyde, and ethyl vinyl ether catalyzed by 1.0 mol% of **Zr_6OTf-BTB**. Each reaction run lasted 3 h. The MOF catalyst was re-activated by TMSOTf after the 3rd, and 6th run. Reaction condition: anline (45 μL, 0.5 mmol), benzaldehyde (46 μL, 0.5 mmol), ethyl vinyl ether (40 μL, 0.5 mmol), **Zr_6OTf-BTB** (5.0 μmol), and anhydrous CH_3CN (2.0 mL) at room temperature. The yields refer to a combination of both isomers, as determined by ^1H NMR with mesitylene as internal standard.

MOF-catalyzed Povarov Reactions showed a broad substrate scope without further optimization of reaction conditions. As shown in **Table 6-3**, 1.0 mol% **Zr_6OTf-BTB** efficiently catalyzed the construction of a large variety of tetrahydroquinoline derivatives at room temperature by varying the substrate components. Distinct functional groups, including chloride, bromide, methyl, methoxy, amide, siloxy, and trifluoromethyl groups, were well tolerated to afford a wide range of 1,2,3,4-tetrahydroquinoline derivatives in good to excellent yields (43-96%) with dominantly *cis* selectivity. For the anilines, electron-withdrawing substituents (-Cl, -Br, $-CF_3$) decreased the MCR activity but enhanced *cis* selectivity when compared to electron-donating substituents ($-CH_3$, $-OCH_3$). A similar electronic effect was also observed for aldehydes, with higher activity but lower *cis* selectivity for **8** ($-OCH_3$) than **7** (-Cl). These results indicate the influence of electronic effects in imine formation which impacts the construction of cyclization

products. Several other alkenes, including cyclic (**13**, **14**) and acyclic ones (**15**, **16**), also worked well for MOF-catalyzed Povarov reactions with satisfactory yields and *cis* selectivity.

Table 6-3. Zr_6OTf-BTB catalyzed multicomponent Povarov reaction.

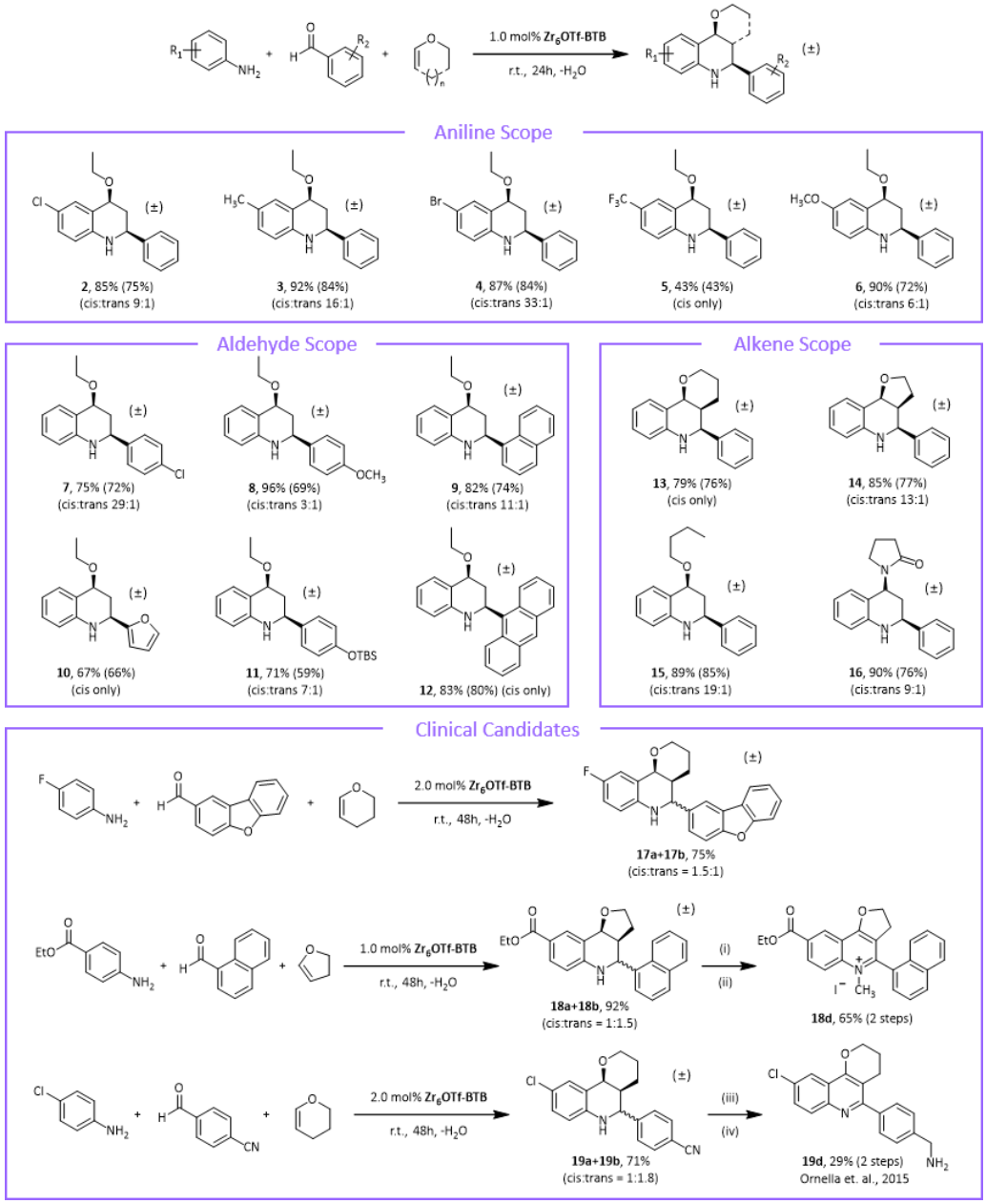

Reaction condition: anilines (0.5 mmol), aldehydes (0.5 mmol), alkenes (0.5 mmol), **Zr_6OTf-BTB** (5.0 μmol), in acetonitrile (2.0 mL), r.t.. Synthesis of **18d**: (i) 2,3-dichloro-5,6-dicyano-1,4-benzoquinone (DDQ), in CH_2Cl_2, r.t.; (ii) CH_3I, in EtOH, reflux. Synthesis of **19d**[32]: (iii)DDQ, in $CHCl_3$, r.t.; (iv) $LiAlH_4$, in THF, reflux. Yields (*cis* + *trans* isomers) determined by ^1H NMR with mesitylene added as internal standard. Isolated yields of *cis* isomers are shown in parenthesis.

Zr_6OTf-BTB was successfully used for the construction of several bioactive drug candidates (**Table 6-3**). The pyranoquinoline analogues **17** (**17a**: *cis*, **17b**: *trans*) were efficiently constructed though **Zr_6OTf-BTB**-catalyzed Povarov reaction between 4-fluoroaniline, dibenzo[*b,d*]furan-2-carbaldehyde, and 3,4-dihydro-2*H*-pyran in 75% total yield. **17a** and **17b** were reported to display comparable activity to the first line drug ethambutol against *Mycobaterium tuberculosis* H37Rv *in vitro*.[33] The furanoquinolinium salt **18d** is an inhibitor of prolyl-oligopeptidase, a key target for psychiatric diseases. **18d** was readily synthesized in 3 steps and 60% combined yield starting from **Zr_6OTf-BTB**-catalyzed Povarov reaction between ethyl 4-aminobenzoate, 1-naphthaldehyde, and 2,3-dihydrofuran.[34] The pyranoquinoline **19d** is a potent multi-trypanosomatid lead for several tropical diseases. The tricyclic heterofused scaffold of **19d** was synthesized in one step by **Zr_6OTf-BTB**-catalyzed Povarov reaction between 4-chloroaniline, 4-formylbenzonitrile, and 3,4-dihydro-2*H*-pyran in 71% yield.[32] **Zr_6OTf-BTB** is thus a versatile catalyst for Povarov reactions to afford fused heterocyclic frameworks bearing multi-functional substituents with high efficiency and step economy.

Zr_6OTf-BTB also competently catalyzed other MCRs. At 1.0 mol% loading of **Zr_6OTf-BTB**, a mixture of aniline, benzaldehyde, and ethyl diazoacetate was quantitively converted to *cis*-ethyl 1,3-diphenylaziridine-2-carboxylate (**20**) at room temperature in 6 hours (**Table 6-4**). Such aziridine derivatives can be further elaborated into useful nitrogen-containing molecules. **Zr_6OTf-BTB** also significantly outperformed traditional homogeneous Lewis acidic catalysts, which typically required much higher catalyst loadings (10-20 mol%), in this MCR.[35-36] More importantly, by varying the substrate components with different anilines, aldehydes, and diazo reagents, we successfully synthesized a series of aziridine carboxylates in good to outstanding yields (66-94%) with excellent *cis* selectivity and good functional group tolerance.

Table 6-4. Zr_6OTf-BTB catalyzed multicomponent aziridine carboxylate synthesis.

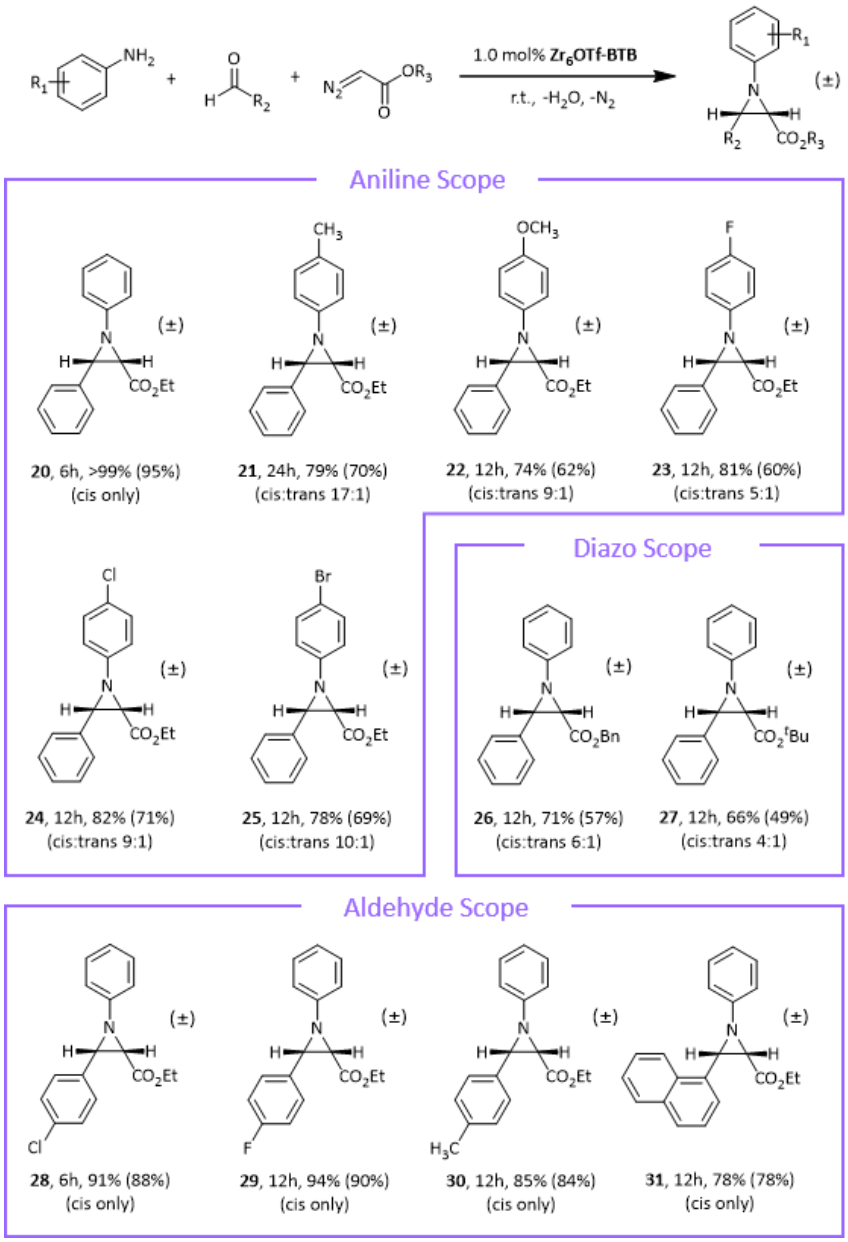

Reaction condition: anilines (0.5 mmol), aldehydes (0.5 mmol), diazo compounds (0.5 mmol), **Zr_6OTf-BTB** (5.0 μmol), in acetonitrile (2.0 mL), r.t. Yields include both *cis* and *trans* isomers, as determined by ^{1}H NMR with mesitylene added as internal standard. Isolated yields of *cis* isomers are shown in parenthesis.

6.2.3 Topology-activity relationships in and proposed mechanisms for MOF-catalyzed MCRs

The different MOF topologies lead to significantly different catalytic performances in MCRs. To gain a deeper insight into MOF topology-activity relationships, we first compared the activities of **Zr_6OTf-BPDC**, **Zr_6OTf-BTC**, and **Zr_6OTf-BTB** catalysts in Povarov reactions with different substrate sizes (**Figure 6-10**). Several aldehydes of increasing sizes, benzaldehyde (**A**), 4-methoxyl benzaldehyde (**B**), 1-naphthaldehyde (**C**), 4-((tert-butyldimethylsilyl)oxy)benzaldehyde (**D**), and anthracene-9-carbaldehyde (**E**), were selected to test their product yields. **Zr_6OTf-BTB** showed excellent activity with Povarov product yields of 99%, 96%, 82%, 71%, and 83% for aldehydes **A** through **E**, indicating minimal influence of substrate size on the catalytic activity for **Zr_6OTf-BTB**. With **Zr_6OTf-BTC** as catalyst, the yields of Povarov products decreased in the order of 79%, 43%, 36%, 16%, and 13% for aldehydes **A** through **E**. **Zr_6OTf-BPDC** performed poorly in Povarov reactions and showed negligible catalytic activity for large aldehydes (23%, 7%, 6%, <1%, and <1% for aldehydes **A** through **E**). As the different topologies of the three MOF catalysts lead to distinct porosity and pore sizes, we propose that their different catalytic activities may be caused by different substrate accessibility to the catalytic sites.

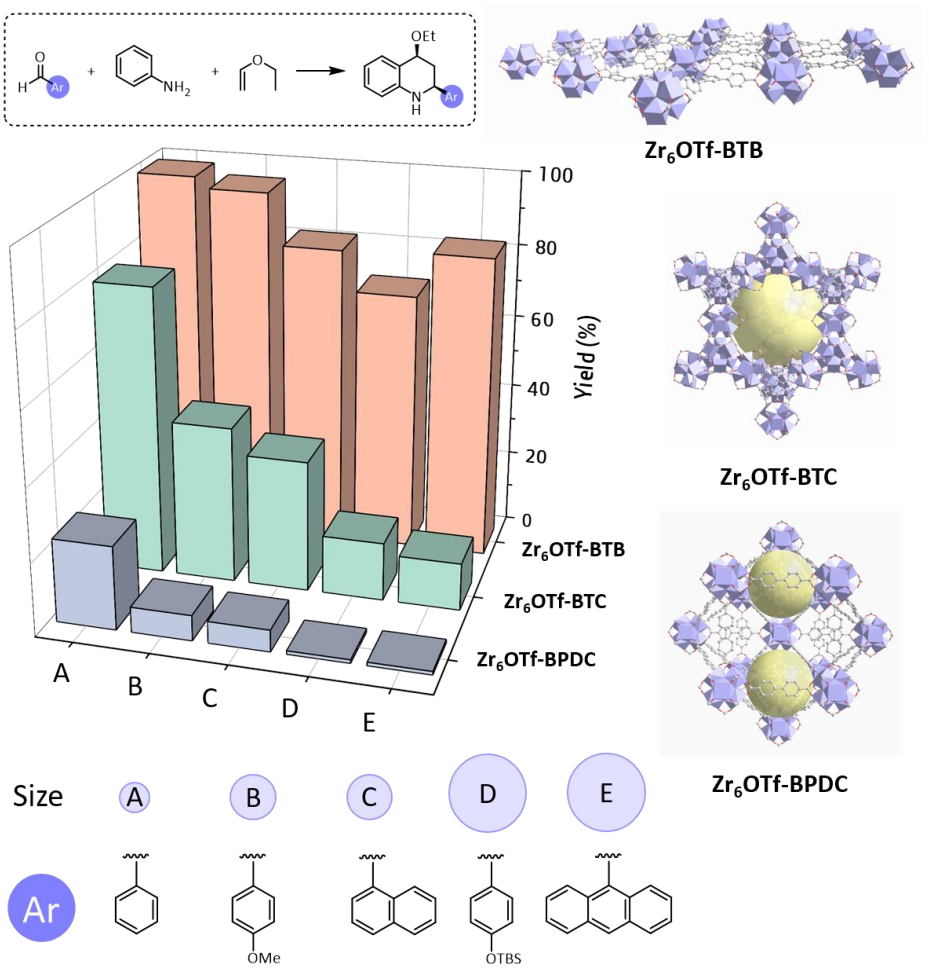

Figure 6-10. Povarov reactions with different sizes of aldehyde substrates catalyzed by **Zr_6OTf-BPDC**, **Zr_6OTf-BTC**, and **Zr_6OTf-BTB**. Copyright 2021 American Chemical Society.

Accordingly, ^{1}H and ^{19}F NMR studies were performed to quantify the percentage of Lewis acidic sites accessible to the large base probe pivalonitrile. The integration of OTf peaks in ^{19}F NMR spectra of digested MOFs showed the amounts of Lewis acidic Zr-OTf sites as 86% and 98% with respect to total Zr amounts for **Zr_6OTf-BTC** and **Zr_6OTf-BTB**, respectively (**Figure 6-11**). After treating with pivalonitrile as a bulky Lewis base probe, ^{1}H NMR analysis of digested MOFs showed the accessible Lewis acidic sites were 22% and 94% with respect to total Zr amounts for **Zr_6OTf-BTC**, and **Zr_6OTf-BTB**, respectively (**Figure 6-12**). Thus, 96% (= 94%/98%) of Lewis acidic Zr-OTf sites in **Zr_6OTf-BTB** are accessible to pivalonitrile while only 26% (= 22%/86%)

of Lewis acidic Zr-OTf sites in **Zr_6OTf-BTC** are accessible to pivalonitrile. Such a difference in Lewis acid site accessibility explains the catalytic activity trends observed for MOF catalyzed Povarov reactions with aldehydes of different sizes. Although **Zr_6OTf-BTC** and **Zr_6OTf-BTB** display similar Lewis acidity and similar activity in MCRs with less sterically hindered substrates, almost all Lewis acid sites in **Zr_6OTf-BTB** are accessible to sterically demanding substrates while only one-fourth of Lewis acid sites in **Zr_6OTf-BTC** are accessible to large substrates. The dimensional reduction from 3D **Zr_6OTf-BTC** to 2D **Zr_6OTf-BTB** thus makes almost all Lewis acid sites accessible to sterically demanding substrates, leading to superior catalytic activity for **Zr_6OTf-BTB** in sterically hindered MCRs.

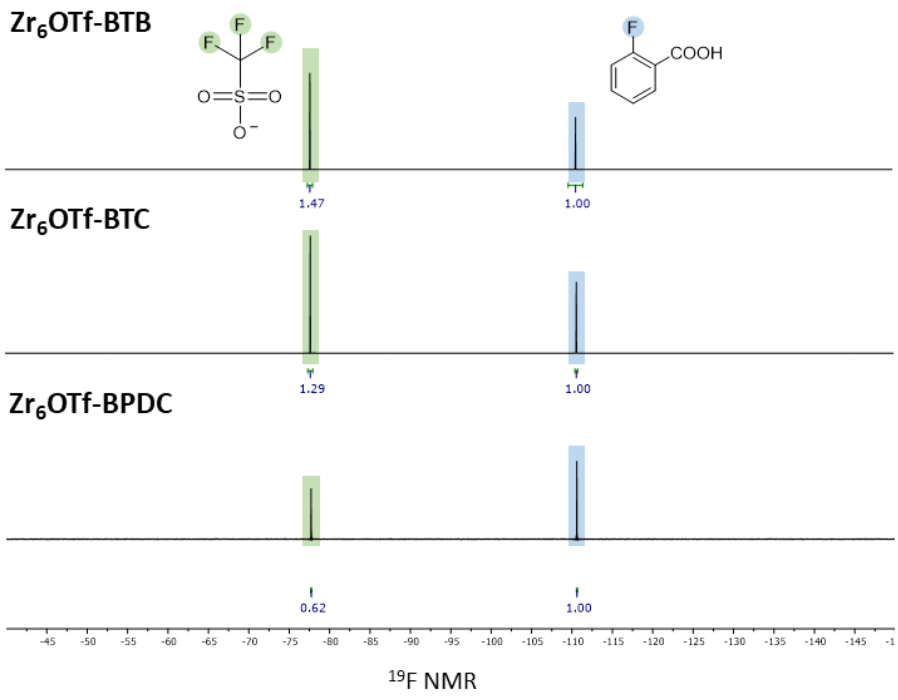

Figure 6-11. ^{19}F NMR integral of triflate capping groups in **Zr_6OTf-BTB**, **Zr_6OTf-BTC**, and **Zr_6OTf-BPDC**.

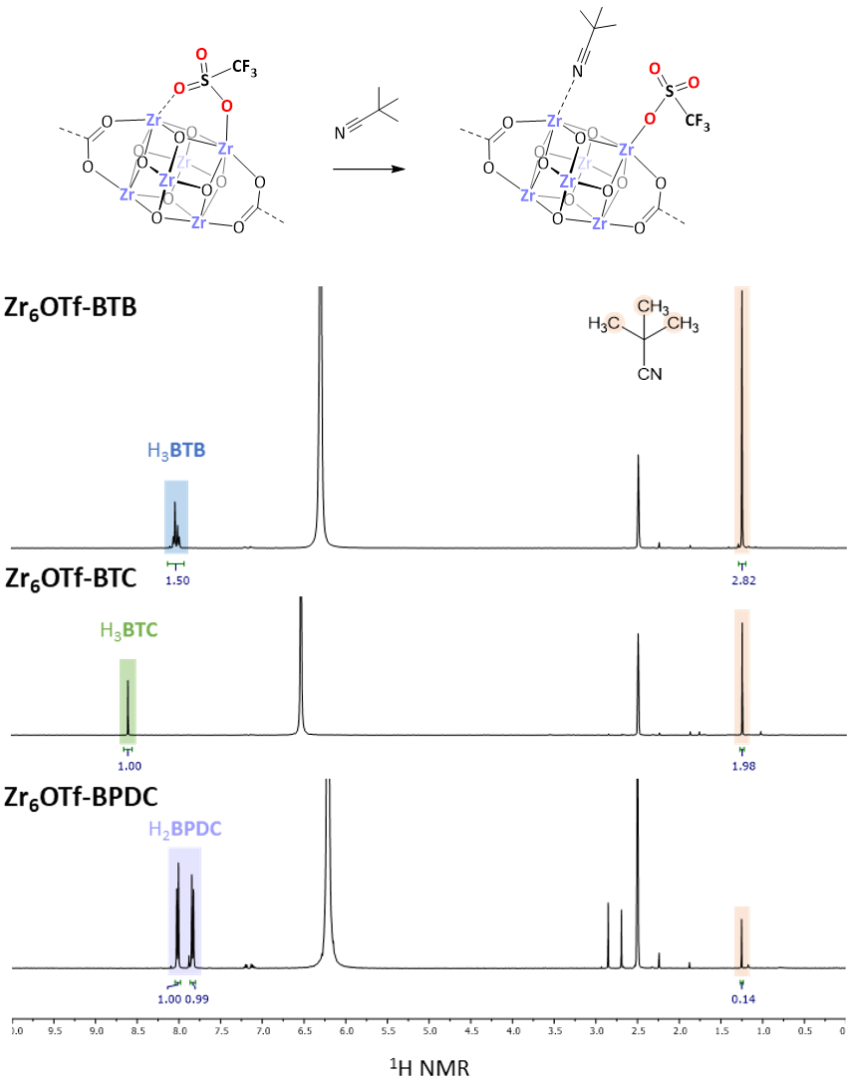

Figure 6-12. ^{1}H NMR integrals of coordinated pivalonitrile in **Zr$_6$OTf-BTB**, **Zr$_6$OTf-BTC**, and **Zr$_6$OTf-BPDC**.

The mechanisms of Lewis acidic MOF catalyzed MCRs were studied by conducting several control experiments (**Figure 6-13**). For Povarov reactions, in the absence of alkenes, **Zr$_6$OTf-BTB** efficiently accelerated condensation between an aldehyde and aniline to form N-benzylideneaniline at room temperature. On the other hand, the cycloaddition between N-benzylideneaniline and ethyl vinyl ether proceeded smoothly in the presence of 1.0 mol% **Zr$_6$OTf-BTB** at room temperature. Thus, we propose that MOFs catalyze Povarov reactions via a similar reaction pathway as homogeneous Lewis acids,[31, 37] in which anilines and aldehydes first condense

to generate imines which are further converted to the target heterocycles through cycloaddition with activated alkenes in a one-pot process (**Figure 6-14**). Both steps are catalyzed by strongly Lewis acidic catalysts. A similar reaction pathway is also proposed for MOF-catalyzed aziridine carboxylate synthesis (**Figure 6-15**).

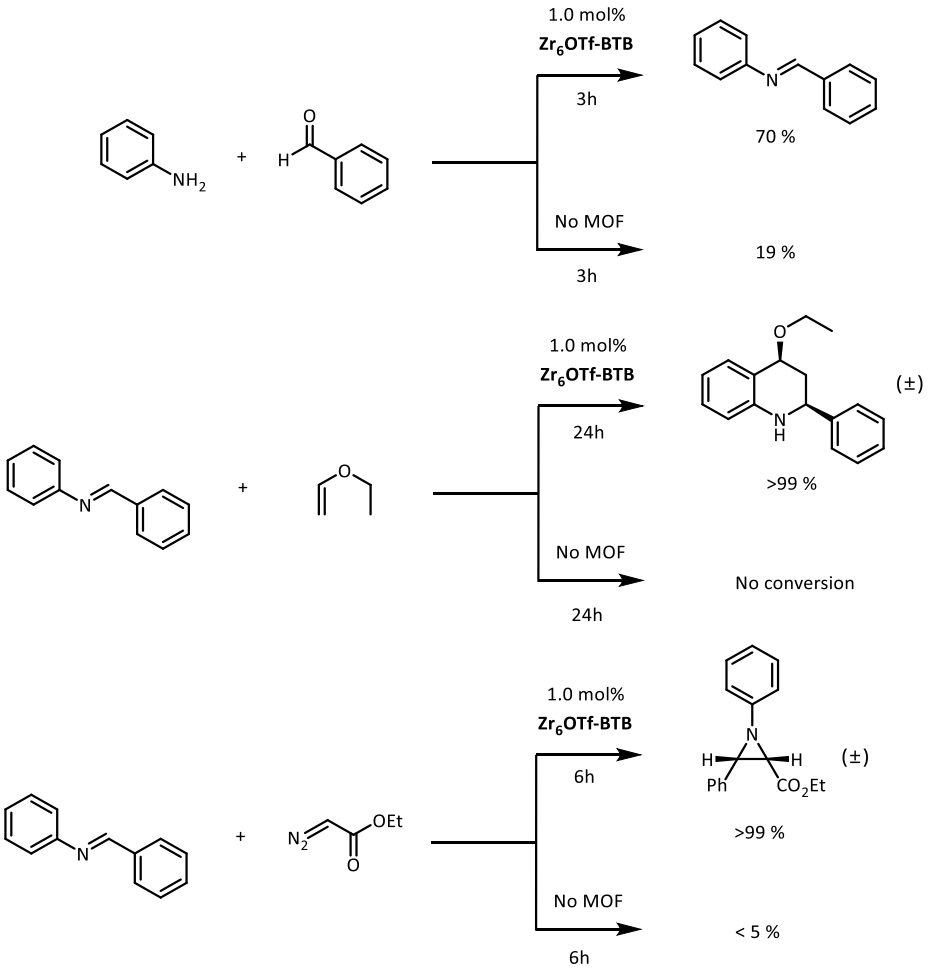

Figure 6-13. Control experiments in MOF-catalyzed MCRs for mechanistic elucidations.

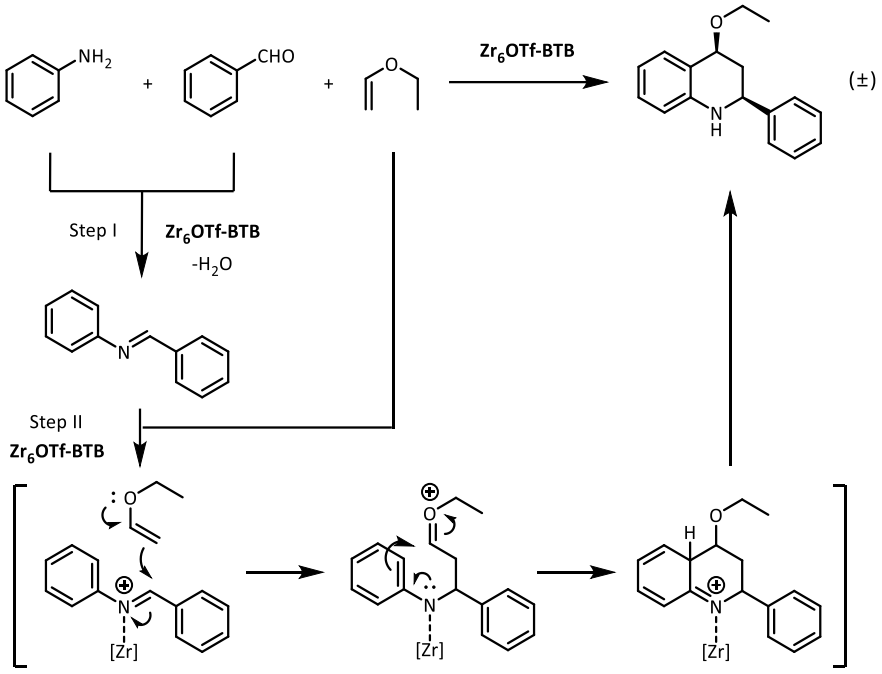

Figure 6-14. Proposed two step transformation pathways in MOF-catalyzed Povarov reaction.

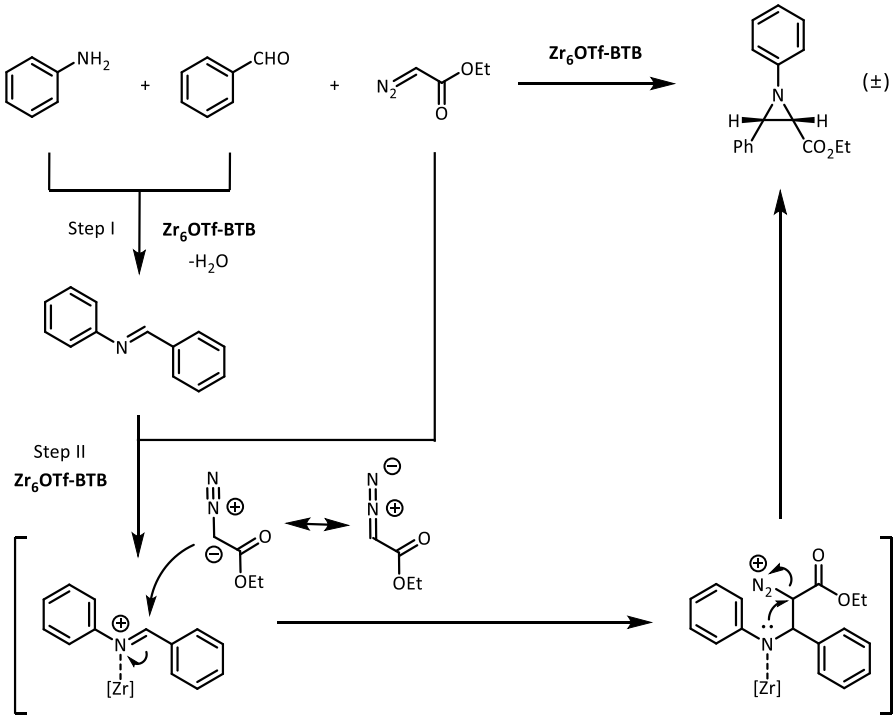

Figure 6-15. Proposed two step transformation pathways in MOF-catalyzed aziridine carboxylate synthesis.

6.3 Conclusion

We developed three strongly Lewis acidic MOFs and systematically studied the influence of their topologies on the catalytic activities of synthetically useful but sterically hindered MCRs. A 2D MOF catalyst, **Zr_6OTf-BTB**, exhibits 96% accessible Lewis acid sites and shows superb catalytic activity in MCRs to afford a broad scope of tetrahydroquinoline derivatives and aziridine carboxylate derivatives with high TONs of up to 270 and high *cis*-selectivity of up to 100%. Via dimensional reduction, **Zr_6OTf-BTB** significantly outperforms two 3D MOF counterparts in MCRs and exhibits 14 times higher TON and 9 times longer catalyst lifetime than a homogeneous benchmark. **Zr_6OTf-BTB** was also successfully used to construct several bioactive clinical candidates via MCRs with excellent efficiency. We envision this dimensional reduction strategy may allow the development of MOF catalysts towards more synthetically useful and complicated organic transformations.

6.4 Experimental Section

6.4.1 Materials and methods

All the reactions and manipulations were carried out under ambient atmosphere unless otherwise indicated. Tetrahydrofuran and toluene were purified by passing through a neutral alumina column under N_2. The substrates for catalytic reactions were purchased from Sigma-Aldrich or Fisher and used as received. The fluorescence indicator NMA was purchased from Sigma-Aldrich. Transmission electron microscopy (TEM) was carried out on TECNAI Spirit and F30 HRTEM. Atomic force microscopy (AFM) images were taken on a Bruker V /Multimode 8 instrument. Powder X-ray diffraction (PXRD) data were collected on a Bruker D8 Venture diffractometer using a Cu Kα radiation source (l = 1.54178 Å). N_2 sorption experiments were performed on a Micromeritics TriStar II 3020 instrument. Thermogravimetric analysis (TGA) was

performed in air using a Shimazu TGA-50 equipped with a platinum pan and heated at a rate of 1.5 ˚C per min up to 800 °C. Fluorescence data were measured using an RF-5301PC spectrofluorophotometer (Shimadzu, Japan). ICP-MS data were obtained with an Agilent 7700x ICP-MS and analyzed using an ICP-MS MassHunter version B01.03. Samples were diluted in a 2% HNO_3 matrix and analyzed with a ^{159}Tb internal standard against a 12-point standard curve over a range from 0.1 ppb to 500 ppb. The correlation was > 0.9997 for all analyses of interest. Data collection was performed in Spectrum Mode with five replicates per sample and 100 sweeps per replicate.

^1H NMR spectra were recorded on a Bruker NMR 500 DRX spectrometer at 500 MHz and referenced against the proton resonance resulting from incomplete deuteration of $CDCl_3$ (δ 7.26) or benzene-d_6 (δ 7.16). The following abbreviations are used: s: singlet, d: doublet, t: triplet, q: quartet, m: multiplet, br: broad, app: apparent. High-resolution mass spectra were obtained using an Agilent 6224 Accurate-Mass TOF spectrometer.

6.4.2 Synthetic procedure of MOF catalysts

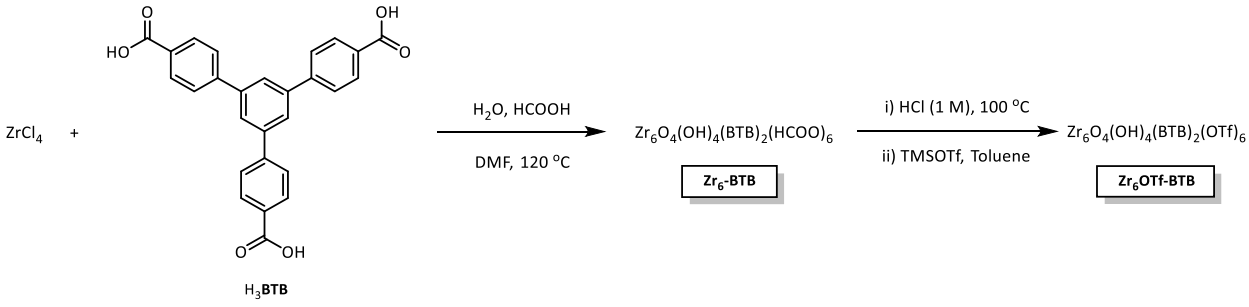

Synthesis of **Zr_6-BTB**: To a 20 mL glass vial was added 2.5 mL of $ZrCl_4$ solution (43.7 μmol in N,N-dimethylformamide, DMF), 2.5 mL of 1,3,5-tris(4-carboxyphenyl)benzene (**H_3BTB**) solution (28.5 μmol in DMF), followed by the addition of 0.15 mL H_2O and 0.85 mL HCOOH (99%). The mixture was sonicated for 5 min and kept at 120 °C oven for 2 days. The white precipitate was collected by centrifugation and washed with DMF three times. **Zr_6-BTB** with a

formula of ($Zr_6O_4(OH)_4(BTB)_2(HCOO)_6$) was obtained in 62% yield and dispersed in DMF for further use.

Synthesis of **Zr_6OTf-BTB**: **Zr_6-BTB** (5.0 μmol) was first treated with 10 mL of HCl (1 M) at 100 °C under stirring for 24 h to exchange the capping formate with water and hydroxide to afford $Zr_6O_4(OH)_4(BTB)_2(OH)_6(OH_2)_6$. The resultant white solid was centrifugated, and washed with DMF three times, and then soaked in fresh dry acetonitrile every twelve hours for a total of 3 days to remove free H_2O residue. In a N_2-filled glovebox, the above MOF (5.0 μmol) was suspended in 3 mL of toluene and TMSOTf (54.0 μL, 0.3 mmol) was then added slowly to the suspension to transform the Zr-OH/OH_2 sites into strongly Lewis acidic Zr-OTf sites. The mixture was stirred at room temperature for 12 h. The suspension was then washed with dry toluene 5 times to remove the soluble species to quantitatively afford **Zr_6OTf-BTB** with a formula of $Zr_6O_4(OH)_4(BTB)_2(OTf)_6$.

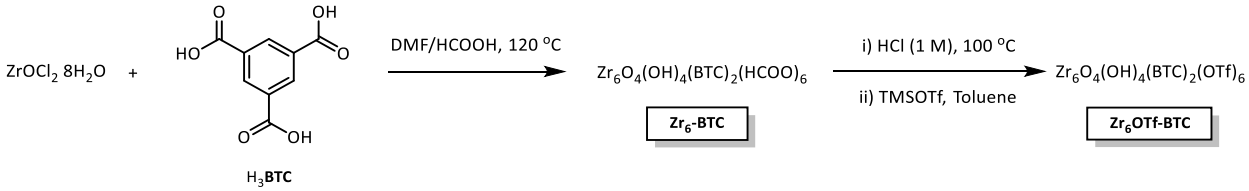

Synthesis of **Zr_6-BTC**: $ZrOCl_2 \cdot 8H_2O$ (680 mg, 2.1 mmol) and trimesic acid (H_3**BTC**, 440mg, 2.1 mmol) were dissolved in a mixed solvent of 40 mL DMF and 40 mL HCOOH (88%), and transferred to a thick-walled glass tube. The tube was sealed with a Teflon cap and heated in a 100 °C oven for 2 days to afford **Zr_6-BTC** as a white solid. The MOF was centrifuged, washed with DMF three times to remove soluble residues and then with THF three times before being dried under vacuum at 120 °C. 350 mg of white powdery **Zr_6-BTC** with a formula of $Zr_6O_4(OH)_4(BTC)_2(HCOO)_6$ was obtained (73% yield).

Synthesis of **Zr_6OTf-BTC**: **Zr_6-BTC** (5.0 μmol) was first treated with 10 mL of HCl (1 M) at 100 °C under stirring for 24 h to exchange the capping formate with water and hydroxide to afford $Zr_6O_4(OH)_4(BTC)_2(OH)_6(OH_2)_6$. The resultant white solid was centrifugated, washed with DMF three times, and then soaked in fresh dry acetonitrile every twelve hours for a total of 3 days to remove free H_2O residue. In a N_2-filled glovebox, the above MOF (5.0 μmol) was suspended in 3 mL of toluene and TMSOTf (54.0 μL, 0.3 mmol) was then added slowly to the suspension to transform the Zr-OH/OH_2 sites into strongly Lewis acidic Zr-OTf sites. The mixture was stirred at room temperature for 12 h. The suspension was washed with dry toluene 5 times to remove soluble residues to quantitatively afford **Zr_6OTf-BTC** with a formula of $Zr_6O_4(OH)_4(BTC)_2(OTf)_6$.

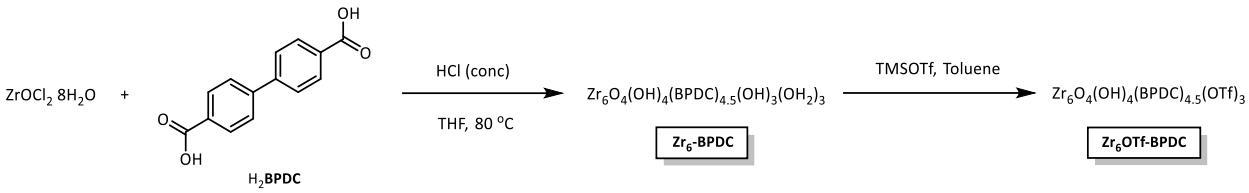

Synthesis of **Zr_6-BPDC**: $ZrOCl_2 \cdot 8H_2O$ (322 mg, 1 mmol), H_2**BPDC** (242 mg, 1 mmol), concentrated hydrochloric acid (12 M, 83 μL), and THF (8 mL, 0.1 M to Zr) were added to a 30 mL heavy-walled glass tube. The mixture was sonicated for about 5 min until all solids were well dispersed, then the tube was sealed with a Teflon cap and stirred in an 80 °C oil bath for 24 h. After cooling to room temperature, the MOF was washed with DMF three times and then with THF three times before being dried under vacuum at 120 °C. 185 mg of powdery **Zr_6-BPDC** with a formula of $Zr_6O_4(OH)_4(BPDC)_{4.5}(OH)_3(OH_2)_3$ was obtained (60% yield).

Synthesis of **Zr_6OTf-BPDC**: In a N_2-filled glovebox, **Zr_6-BPDC** (5.0 μmol) was suspended in 3 mL of toluene and TMSOTf (54.0 μL, 0.3 mmol) was then added slowly to the suspension to transform the Zr-OH/OH_2 sites into strongly Lewis acidic Zr-OTf sites. The mixture was stirred at room temperature for 12 h. The suspension was then washed with dry toluene five times to remove

soluble residues to quantitatively afford **Zr_6OTf-BPDC** with a formula of $Zr_6O_4(OH)_4(BPDC)_{4.5}(OTf)_3$.

6.4.3 Quantification of Lewis acidity

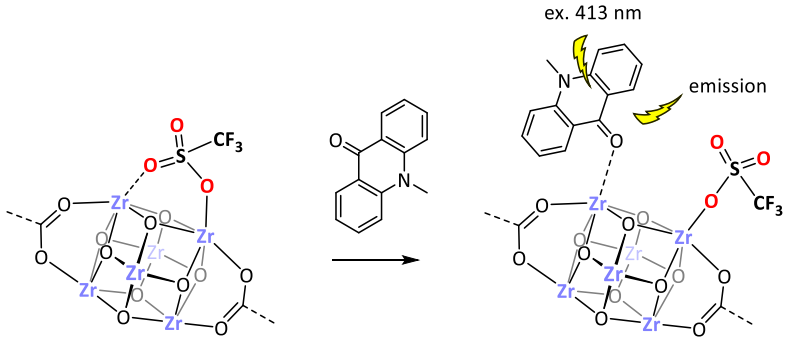

Quantification of MOF Lewis acidity by *N*-methylacridone (NMA) fluorescence: NMA was first dissolved in MeCN to form an NMA solution with a concentration of 10 μM, which gave a reference emission wavelength at 433 nm. 0.1 mmol of Lewis acidic MOF (based on Zr) was added to a 2-dram vial in an N_2-filled glovebox. 4 mL of NMA solution (10 μM in MeCN) was then added to the vial. The resulting mixture was sonicated for 2 min until the MOF was well suspended, and then the suspension was transferred to a fluorescence cuvette for measurement using an excitation wavelength of 413 nm. The emission maxima (λ_{max}) for NMA-bound Lewis acidic MOFs are shown below.

Quantification of total MOF Lewis acidic sites by ^{19}F NMR: To quantify the content of Zr-OTf sites, Lewis acidic MOFs (5 μmol of Zr) were digested in D_3PO_4/DMSO-d_6, followed by the addition of 10 μmol 2-fluorobenzoic acid as internal standard. The mixture was then analyzed by ^{19}F NMR. The chemical shifts of authentic DOTf and 2-fluorobenzoic acid are δ = 77.8, and -110.7 ppm, respectively. The amount of -OTf groups were determined to be 4.90 μmol in **Zr_6OTf-BTB**, indicating 98% of Zr sites have been triflated. Similarly, the amount of -OTf groups were determined to be 4.30 μmol in **Zr_6OTf-BTC**, indicating 86% of Zr sites have been triflated; and

2.07 μmol in **Zr_6OTf-BPDC**, indicating 41% of Zr sites have been triflated. These results indicate nearly 1:1 ratio of Zr and OTf sites in **Zr_6OTf-BTB** and **Zr_6OTf-BTC**, and nearly 2:1 ratio of Zr and OTf sites in **Zr_6OTf-BPDC**, as described by the corresponding formula. The slightly lower triflation percentage in **Zr_6OTf-BTC** and **Zr_6OTf-BPDC** was attributed to its 3D structure which hinders diffusion to cause incomplete triflation. The Zr:OTf ratio in **Zr_6OTf-BPDC** is even lower due to the triflation of defect sites only.

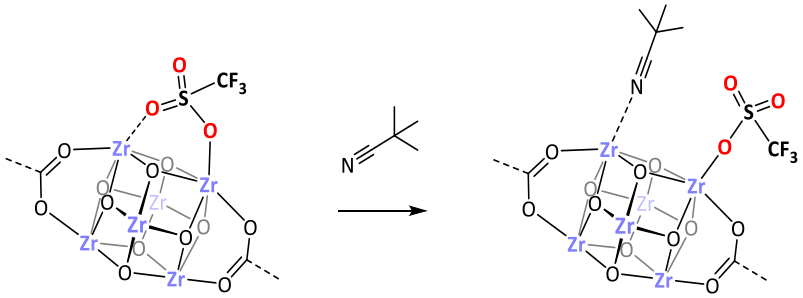

Quantification of accessible MOF Lewis acidic sites by ^{1}H NMR: To quantify accessible Zr-OTf sites, Lewis acidic MOFs (5 μmol of Zr) were treated with 20 equiv. of pivalonitrile as a steric bulky Lewis base probe in toluene for 6 h. The resultant solid was centrifugated and washed with toluene thoroughly to remove excess pivalonitrile. The resultant material was dried and digested in D_3PO_4/DMSO-*d_6*. The mixture was then analyzed by ^{1}H NMR. The chemical shifts of authentic **BTB**, **BTC**, or **BPDC**, and pivalonitrile *tert*-butyl groups are δ = 7.99-8.06, 8.60, 7.80-8.04, and 1.26 ppm, respectively. The coordinated pivalonitrile amount with respect to Zr_6 was determined to be ~5.64 equiv. in **Zr_6OTf-BTB** (94%), ~1.32 equiv. in **Zr_6OTf-BTC** (22%) and ~0.29 equiv. in **Zr_6OTf-BPDC** (10%).

6.4.4 Catalytic reaction setup and product characterization

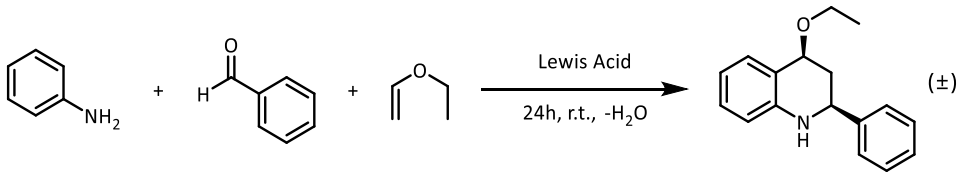

Typical procedure of **Zr_6OTf-BTB** catalyzed multi-component Povarov reaction: Anline (45 μL, 0.5 mmol), benzaldehyde (46 μL, 0.5 mmol), ethyl vinyl ether (40 μL, 0.5 mmol), **Zr_6OTf-BTB** (5.0 μmol Zr in CH_3CN suspension, 1.0 mol%), and anhydrous CH_3CN (2.0 mL) were charged to a 2-dram vial under N_2 atmosphere. The reacrion vial was capped and the mixture was stirred at room temperature. After the reaction was complete as indicated by TLC, the MOF was recovered by centrifugation and the supernatant was evaporated on a rotavap to give the crude product in a quantitative yield (> 99%, mesitylene added as internal standard). The crude product was purified by silica gel chromatography with hexane/ethyl acetate as eluent to afford the target molecule, (+/-)-cis-4-ethoxy-2-phenyl-1,2,3,4-tetrahydroquinoline, as a colorless oil (92% isolated yield). The ratio between cis and trans isomers was determined by integration of cooresponding ^1H peaks in ^1H NMR in the crude product to be cis:trans = 15:1. After one reaction run, ICP-MS analysis showed minimal leaching of <0.1% Zr into the solution.

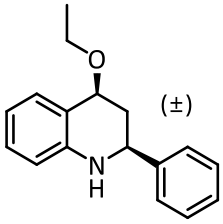

(+/-)-cis-4-ethoxy-2-phenyl-1,2,3,4-tetrahydroquinoline. (CAS: 5278-41-1) ^1H NMR (500 MHz, Chloroform-*d*) δ 7.46 – 7.44 (m, 2H), 7.42 – 7.36 (m, 3H), 7.34 – 7.30 (m, 1H), 7.06 (dddd, *J* = 8.0, 7.2, 1.6, 0.7 Hz, 1H), 6.75 (td, *J* = 7.5, 1.2 Hz, 1H), 6.53 (dd, *J* = 8.0, 1.2 Hz, 1H), 4.83 (ddt, *J* = 10.6, 5.7, 0.9 Hz, 1H), 4.54 (dd, *J* = 11.6, 2.7 Hz, 1H), 3.97 (s, 1H), 3.64 (ddq, *J* = 63.4, 9.1, 7.0 Hz, 2H), 2.42 (ddd, *J* = 12.3, 5.7, 2.7 Hz, 1H), 2.14 – 2.04 (m, 1H), 1.27 (t, *J* = 7.0 Hz, 3H). ^{13}C NMR (126 MHz, Chloroform-*d*) δ 144.58, 143.67, 128.73, 128.27, 127.84, 127.29, 126.66, 122.64, 117.87, 114.10, 74.00, 63.54, 55.96, 37.09, 15.68. HR-MS (ESI, positive mode): *m/z* calc'd for $C_{17}H_{20}NO$ $[M+H]^+$:254.1545, found 254.1539.

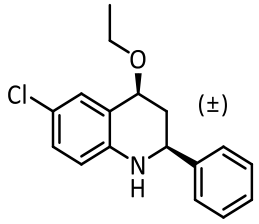

(+/-)-cis-6-chloro-4-ethoxy-2-phenyl-1,2,3,4-tetrahydroquinoline. ^{1}H NMR (500 MHz, Chloroform-*d*) δ 7.43 (d, *J* = 2.0 Hz, 1H), 7.42 – 7.39 (m, 2H), 7.37 (dt, *J* = 5.9, 2.2 Hz, 2H), 7.35 – 7.29 (m, 1H), 6.99 (ddd, *J* = 8.5, 2.5, 0.7 Hz, 1H), 6.44 (d, *J* = 8.5 Hz, 1H), 4.78 – 4.71 (m, 1H), 4.52 (dd, *J* = 11.7, 2.8 Hz, 1H), 3.95 (s, 1H), 3.72 (dq, *J* = 9.0, 7.0 Hz, 1H), 3.58 (dq, *J* = 9.1, 7.0 Hz, 1H), 2.42 (dddd, *J* = 12.4, 5.6, 2.8, 1.7 Hz, 1H), 2.02 (td, *J* = 12.1, 10.7 Hz, 1H), 1.28 (t, *J* = 7.0 Hz, 3H). ^{13}C NMR (126 MHz, Chloroform-*d*) δ 143.26, 143.06, 128.81, 128.13, 128.00, 127.02, 126.62, 124.15, 122.47, 115.14, 73.70, 63.98, 55.87, 36.71, 15.64. HR-MS (ESI, positive mode): *m/z* calc'd for $C_{17}H_{19}ClNO$ $[M+H]^+$:288.1155, found 288.1138.

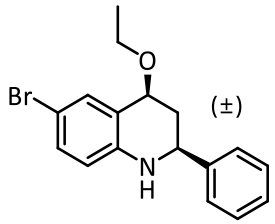

(+/-)-cis-6-bromo-4-ethoxy-2-phenyl-1,2,3,4-tetrahydroquinoline. ^{1}H NMR (500 MHz, Chloroform-*d*) δ 7.50 (dd, *J* = 2.4, 1.1 Hz, 1H), 7.44 – 7.40 (m, 2H), 7.37 (ddd, *J* = 7.7, 6.7, 1.3 Hz, 2H), 7.34 – 7.30 (m, 1H), 7.12 (ddd, *J* = 8.5, 2.4, 0.7 Hz, 1H), 6.39 (d, *J* = 8.5 Hz, 1H), 4.74 (ddt, *J* = 10.6, 5.6, 0.9 Hz, 1H), 4.51 (dd, *J* = 11.7, 2.7 Hz, 1H), 3.96 (s, 1H), 3.71 (dq, *J* = 9.0, 7.0 Hz, 1H), 3.57 (dq, *J* = 9.0, 7.0 Hz, 1H), 2.41 (ddd, *J* = 12.4, 5.5, 2.8 Hz, 1H), 2.01 (ddd, *J* = 12.5, 11.6, 10.6 Hz, 1H), 1.27 (t, *J* = 7.0 Hz, 3H). ^{13}C NMR (126 MHz, Chloroform-*d*) δ 143.46, 143.19, 130.96, 129.85, 128.80, 128.00, 126.60, 124.57, 115.55, 109.51, 73.61, 63.99, 55.78, 36.62, 15.63.

HR-MS (ESI, positive mode): *m/z* calc'd for $C_{17}H_{19}BrNO$ $[M+H]^+$:332.0650/334.0630, found 332.0623/332.0618.

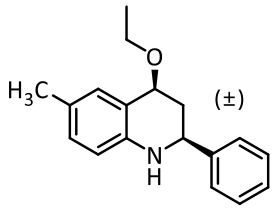

(+/-)-cis-4-ethoxy-6-methyl-2-phenyl-1,2,3,4-tetrahydroquinoline. ^{1}H NMR (500 MHz, Chloroform-*d*) δ 7.47 – 7.43 (m, 2H), 7.41 – 7.34 (m, 2H), 7.34 – 7.28 (m, 1H), 7.23 (d, *J* = 2.0 Hz, 1H), 6.88 (dd, *J* = 8.1, 2.1 Hz, 1H), 6.46 (d, *J* = 8.0 Hz, 1H), 4.81 (dd, *J* = 10.5, 5.7 Hz, 1H), 4.50 (dd, *J* = 11.6, 2.7 Hz, 1H), 3.87 (br, 1H), 3.76 – 3.65 (m, 1H), 3.58 (dq, *J* = 9.2, 7.0 Hz, 1H), 2.42 (ddd, *J* = 12.4, 5.8, 2.6 Hz, 1H), 2.27 (s, 4H), 2.07 (ddd, *J* = 12.4, 11.6, 10.5 Hz, 1H), 1.28 (t, *J* = 7.0 Hz, 3H). ^{13}C NMR (126 MHz, Chloroform-*d*) δ 143.86, 142.32, 129.89, 128.91, 128.68, 127.75, 127.66, 126.66, 122.60, 114.28, 74.08, 63.58, 56.10, 37.32, 20.64, 15.69. HR-MS (ESI, positive mode): *m/z* calc'd for $C_{18}H_{22}NO$ $[M+H]^+$:268.1701, found 268.1692.

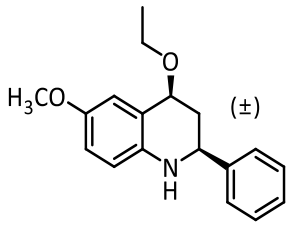

(+/-)-cis-4-ethoxy-6-methoxy-2-phenyl-1,2,3,4-tetrahydroquinoline. ^{1}H NMR (500 MHz, Chloroform-*d*) δ 7.47 – 7.43 (m, 2H), 7.37 (t, *J* = 7.3 Hz, 2H), 7.34 – 7.29 (m, 1H), 7.01 (dd, *J* = 2.9, 0.9 Hz, 1H), 6.68 (ddd, *J* = 8.6, 2.9, 0.7 Hz, 1H), 6.50 (d, *J* = 8.6 Hz, 1H), 4.82 (dd, *J* = 10.6, 5.8 Hz, 1H), 4.47 (dd, *J* = 11.7, 2.5 Hz, 1H), 3.78 (s, 3H), 3.73 – 3.52 (m, 2H), 2.41 (ddd, *J* = 12.3, 5.8, 2.5 Hz, 1H), 2.08 (td, *J* = 12.1, 10.6 Hz, 1H), 1.27 (t, *J* = 7.0 Hz, 3H). ^{13}C NMR (126 MHz, Chloroform-*d*) δ 152.49, 143.76, 128.68, 128.60, 127.79, 126.96, 126.68, 114.95, 112.30, 74.17,

63.40, 56.31, 55.88, 37.20, 15.70. HR-MS (ESI, positive mode): *m/z* calc'd for $C_{18}H_{22}NO_2$ $[M+H]^+$:284.1651, found 284.1644.

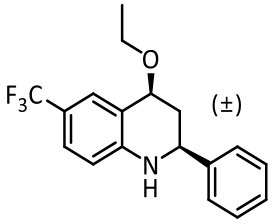

(+/-)-cis-4-ethoxy-2-phenyl-6-(trifluoromethyl)-1,2,3,4-tetrahydroquinoline. ^{1}H NMR (500 MHz, Chloroform-*d*) δ 7.66 – 7.61 (m, 1H), 7.45 – 7.30 (m, 5H), 7.31 – 7.24 (m, 1H), 6.52 (d, *J* = 8.4 Hz, 1H), 4.75 (dd, *J* = 10.6, 5.3 Hz, 1H), 4.59 (dd, *J* = 11.5, 3.0 Hz, 1H), 4.25 (s, 1H), 3.73 (dq, *J* = 9.0, 7.0 Hz, 1H), 3.60 (dq, *J* = 9.0, 7.0 Hz, 1H), 2.46 (dddd, *J* = 12.4, 5.1, 3.0, 1.6 Hz, 1H), 2.04 (ddd, *J* = 12.2, 11.5, 10.7 Hz, 1H), 1.28 (t, *J* = 7.0 Hz, 3H). ^{13}C NMR (126 MHz, Chloroform-*d*) δ 146.93, 142.90, 128.91, 128.84, 128.16, 126.92, 126.59, 125.48 (q, *J* = 3.9 Hz), 124.54 (q, *J* = 3.8 Hz), 122.19, 113.30, 73.45, 64.12, 55.64, 36.41, 15.60. HR-MS (ESI, positive mode): *m/z* calc'd for $C_{18}H_{19}F_3NO$ $[M+H]^+$:322.1419, found 322.1360.

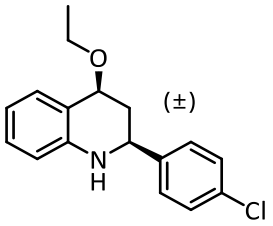

(+/-)-cis-2-(4-chlorophenyl)-4-ethoxy-1,2,3,4-tetrahydroquinoline. ^{1}H NMR (500 MHz, Chloroform-*d*) δ 7.41 – 7.36 (m, 3H), 7.36 – 7.31 (m, 2H), 7.06 (tdd, J = 7.2, 1.6, 0.7 Hz, 1H), 6.76 (td, J = 7.5, 1.2 Hz, 1H), 6.53 (dd, J = 8.0, 1.2 Hz, 1H), 4.79 (ddt, J = 10.3, 5.6, 0.9 Hz, 1H), 4.52 (dd, J = 11.3, 2.8 Hz, 1H), 3.95 (s, 1H), 3.68 (dq, J = 9.0, 7.0 Hz, 1H), 3.56 (dq, J = 9.1, 7.0 Hz, 1H), 2.38 (ddd, J = 12.5, 5.6, 2.9 Hz, 1H), 2.05 (ddd, J = 12.4, 11.3, 10.3 Hz, 1H), 1.25 (t, J = 7.0 Hz, 3H). ^{13}C NMR (126 MHz, Chloroform-*d*) δ 144.26, 142.25, 133.34, 128.82, 128.37, 128.04,

127.44, 122.59, 118.13, 114.22, 73.80, 63.60, 55.28, 37.02, 15.64. HR-MS (ESI, positive mode): *m/z* calc'd for $C_{17}H_{18}ClNO$ $[M]^+$:287.1077, found 287.1023.

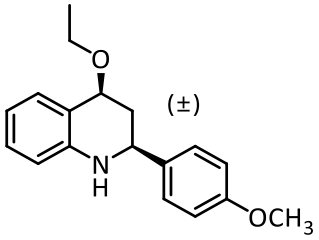

(+/-)-cis-4-ethoxy-2-(4-methoxyphenyl)-1,2,3,4-tetrahydroquinoline. ^{1}H NMR (500 MHz, Chloroform-*d*) δ 7.42 – 7.38 (m, 1H), 7.37 – 7.34 (m, 2H), 7.04 (dddd, *J* = 7.9, 7.2, 1.6, 0.7 Hz, 1H), 6.94 – 6.87 (m, 2H), 6.74 (td, *J* = 7.4, 1.2 Hz, 1H), 6.50 (dd, *J* = 8.0, 1.2 Hz, 1H), 4.81 (ddt, *J* = 10.7, 5.7, 0.9 Hz, 1H), 4.48 (dd, *J* = 11.8, 2.6 Hz, 1H), 3.88 (s, 1H), 3.82 (s, 3H), 3.75 – 3.52 (m, 2H), 2.38 (ddd, *J* = 12.3, 5.7, 2.6 Hz, 1H), 2.10 – 2.01 (m, 1H), 1.27 (t, *J* = 7.0 Hz, 3H). ^{13}C NMR (126 MHz, Chloroform-*d*) δ 159.23, 144.69, 135.74, 128.22, 127.78, 127.24, 122.63, 117.79, 114.05, 114.02, 74.07, 63.53, 55.37, 37.18, 15.71. HR-MS (ESI, positive mode): *m/z* calc'd for $C_{18}H_{22}NO_2$ $[M+H]^+$:284.1651, found 284.1588.

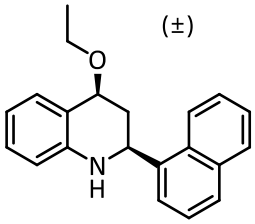

(+/-)-cis-4-ethoxy-2-(naphthalen-1-yl)-1,2,3,4-tetrahydroquinoline. ^{1}H NMR (500 MHz, Chloroform-*d*) δ 8.17 (d, *J* = 8.0 Hz, 1H), 7.91 (dd, *J* = 7.0, 2.6 Hz, 1H), 7.81 (t, *J* = 8.0 Hz, 2H), 7.58 – 7.44 (m, 4H), 7.09 (td, *J* = 7.7, 1.6 Hz, 1H), 6.81 (t, *J* = 7.4 Hz, 1H), 6.61 (d, *J* = 8.0 Hz, 1H), 5.36 (dd, 1H), 4.95 (dd, *J* = 10.4, 5.6 Hz, 1H), 3.75 – 3.54 (m, 3H), 2.63 (ddd, *J* = 12.5, 5.7, 2.7 Hz, 1H), 2.29 (q, *J* = 11.4 Hz, 1H), 1.24 (t, *J* = 7.0 Hz, 3H). ^{13}C NMR (126 MHz, Chloroform-*d*) δ 144.82, 138.81, 134.02, 130.68, 129.18, 128.34, 128.19, 127.51, 126.28, 125.74, 125.69,

123.67, 122.82, 122.67, 117.96, 114.33, 77.25, 74.23, 63.55, 35.53, 15.68. HR-MS (ESI, positive mode): *m/z* calc'd for $C_{21}H_{22}NO$ $[M+H]^+$:304.1701, found 304.1699.

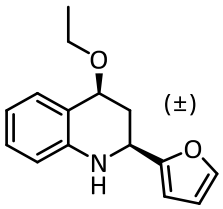

(+/-)-cis-4-ethoxy-2-(furan-2-yl)-1,2,3,4-tetrahydroquinoline. ^{1}H NMR (500 MHz, Chloroform-*d*) δ 7.40 – 7.34 (m, 2H), 7.05 (dddd, *J* = 8.0, 7.2, 1.6, 0.7 Hz, 1H), 6.75 (td, *J* = 7.5, 1.2 Hz, 1H), 6.55 (dd, *J* = 8.1, 1.2 Hz, 1H), 6.35 (dd, *J* = 3.3, 1.8 Hz, 1H), 6.26 (dt, *J* = 3.2, 0.9 Hz, 1H), 4.79 – 4.71 (m, 1H), 4.63 (ddd, *J* = 10.9, 3.0, 0.8 Hz, 1H), 4.14 (br, 1H), 3.73 (dq, *J* = 9.1, 7.0 Hz, 1H), 3.58 (dq, *J* = 9.1, 7.0 Hz, 1H), 2.52 (ddd, *J* = 12.4, 5.5, 3.0 Hz, 1H), 2.22 (ddd, *J* = 12.5, 10.9, 9.9 Hz, 1H), 1.27 (t, *J* = 7.0 Hz, 3H). ^{13}C NMR (126 MHz, Chloroform-*d*) δ 155.98, 143.67, 141.76, 128.37, 127.60, 122.66, 118.24, 114.48, 110.33, 105.21, 73.31, 63.58, 48.96, 32.79, 15.65. HR-MS (ESI, positive mode): *m/z* calc'd for $C_{15}H_{18}NO_2$ $[M+H]^+$:244.1338, found 244.1330.

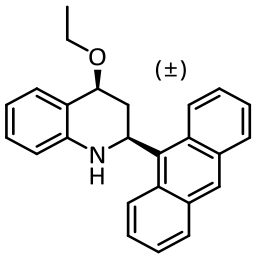

(+/-)-cis-2-(anthracen-9-yl)-4-ethoxy-1,2,3,4-tetrahydroquinoline. ^{1}H NMR (500 MHz, Chloroform-*d*) δ 9.21 – 9.03 (m, 1H), 8.45 (s, 1H), 8.38 – 8.26 (m, 1H), 8.03 (d, J = 9.5 Hz, 2H), 7.84 – 7.78 (m, 0H), 7.56 (dt, J = 7.6, 1.3 Hz, 1H), 7.53 – 7.40 (m, 3H), 7.12 (tdd, J = 7.2, 1.6, 0.7 Hz, 1H), 6.82 (td, J = 7.5, 1.2 Hz, 1H), 6.54 (dd, J = 8.0, 1.2 Hz, 1H), 6.14 (dd, J = 12.5, 3.0 Hz, 1H), 5.03 (dd, J = 10.5, 6.1 Hz, 1H), 4.18 (s, 1H), 3.70 (ddq, J = 45.8, 9.1, 7.0 Hz, 2H), 2.92 (td, J

= 12.6, 10.5 Hz, 1H), 2.55 (dddd, J = 12.7, 6.0, 3.0, 1.7 Hz, 1H), 1.30 (t, J = 7.0 Hz, 3H). ^{13}C NMR (126 MHz, Chloroform-*d*) δ 144.64, 132.66, 129.60, 129.42, 128.49, 128.39, 127.46, 126.85, 126.43, 124.96, 117.82, 114.19, 74.40, 64.03, 51.00, 33.76, 15.73. HR-MS (ESI, positive mode): *m/z* calc'd for $C_{25}H_{24}NO$ $[M+H]^+$:354.1858, found 354.1791.

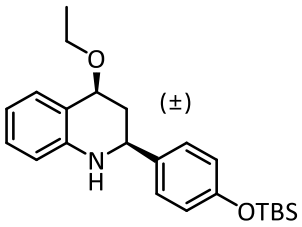

(+/-)-cis-4-ethoxy-2-(4-((tert-butyldimethylsilyl)oxy)phenyl)-1,2,3,4-tetrahydroquinoline. ^{1}H NMR (500 MHz, Chloroform-*d*) δ 7.40 (d, *J* = 7.7 Hz, 1H), 7.32 – 7.27 (m, 2H), 7.08 – 7.02 (m, 1H), 6.85 – 6.80 (m, 2H), 6.75 (t, *J* = 7.5 Hz, 1H), 6.50 (d, *J* = 8.0 Hz, 1H), 4.80 (dd, *J* = 10.6, 5.7 Hz, 1H), 4.46 (dd, *J* = 11.7, 2.6 Hz, 1H), 3.77 – 3.52 (m, 2H), 2.39 (ddd, *J* = 12.3, 5.7, 2.7 Hz, 1H), 2.06 (q, *J* = 11.6 Hz, 1H), 1.27 (t, *J* = 6.9 Hz, 3H), 0.99 (s, 9H), 0.21 (s, 6H). ^{13}C NMR (126 MHz, Chloroform-*d*) δ 155.28, 144.73, 136.31, 128.22, 127.70, 127.26, 122.65, 120.19, 117.75, 114.02, 74.11, 63.54, 55.43, 37.12, 25.72, 18.25, 15.71. HR-MS (ESI, positive mode): *m/z* calc'd for $C_{23}H_{34}NO_2Si$ $[M+H]^+$:384.2359, found 384.2346.

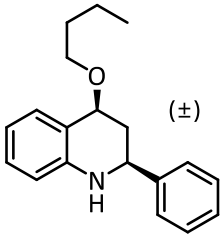

(+/-)-cis-4-butoxy-2-phenyl-1,2,3,4-tetrahydroquinoline. ^{1}H NMR (500 MHz, Chloroform-*d*) δ 7.47 – 7.44 (m, 2H), 7.42 – 7.36 (m, 3H), 7.34 – 7.30 (m, 1H), 7.06 (dddd, *J* = 7.9, 7.2, 1.6, 0.7 Hz, 1H), 6.75 (td, *J* = 7.5, 1.2 Hz, 1H), 6.52 (dd, *J* = 8.0, 1.1 Hz, 1H), 4.81 (ddt, *J* = 10.5, 5.6, 0.9 Hz, 1H), 4.54 (dd, *J* = 11.7, 2.7 Hz, 1H), 3.95 (s, 1H), 3.66 (dt, *J* = 9.0, 6.4 Hz, 1H), 3.51 (dt, *J* =

9.0, 6.7 Hz, 1H), 2.43 (ddd, *J* = 12.3, 5.7, 2.7 Hz, 1H), 2.12 – 2.02 (m, 1H), 1.68 – 1.54 (m, 2H), 1.43 (dddt, *J* = 14.8, 13.0, 9.6, 7.3 Hz, 2H), 0.94 (t, *J* = 7.4 Hz, 3H). ^{13}C NMR (126 MHz, Chloroform-*d*) δ 144.56, 143.70, 128.73, 128.24, 127.84, 127.26, 126.66, 122.74, 117.84, 114.07, 74.13, 68.07, 55.98, 37.10, 32.31, 19.51, 13.99. HR-MS (ESI, positive mode): *m/z* calc'd for $C_{19}H_{24}NO$ $[M+H]^+$:282.1858, found 282.1852.

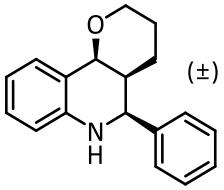

(+/-)-cis-5-phenyl-3,4,4a,5,6,10b-hexahydro-2H-pyrano[3,2-c]quinoline. ^{1}H NMR (500 MHz, Chloroform-*d*) δ 7.47 – 7.36 (m, 5H), 7.31 (t, *J* = 7.2 Hz, 1H), 7.10 (t, *J* = 7.6 Hz, 1H), 6.80 (t, *J* = 7.4 Hz, 1H), 6.61 (d, *J* = 8.0 Hz, 1H), 5.34 (d, *J* = 5.6 Hz, 1H), 4.70 (d, *J* = 2.6 Hz, 1H), 3.88 (s, 1H), 3.60 (dd, *J* = 12.5, 3.1 Hz, 1H), 3.44 (td, *J* = 11.6, 2.7 Hz, 1H), 2.18 (ddd, *J* = 9.0, 5.6, 2.8 Hz, 1H), 1.60 – 1.31 (m, 4H). ^{13}C NMR (126 MHz, Chloroform-*d*) δ 145.20, 141.15, 128.41, 128.11, 127.68, 127.55, 126.85, 119.95, 118.33, 114.43, 72.80, 60.68, 59.37, 38.97, 25.45, 18.05. HR-MS (ESI, positive mode): *m/z* calc'd for $C_{18}H_{20}NO$ $[M+H]^+$:266.1545, found 266.1538.

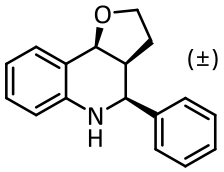

(+/-)-cis-4-phenyl-2,3,3a,4,5,9b-hexahydrofuro[3,2-c]quinoline. ^{1}H NMR (500 MHz, Chloroform-*d*) δ 7.48 (d, *J* = 7.3 Hz, 2H), 7.42 – 7.35 (m, 3H), 7.35 – 7.29 (m, 1H), 7.11 – 7.03 (m, 1H), 6.84 (t, *J* = 7.4 Hz, 1H), 6.63 (d, *J* = 8.0 Hz, 1H), 5.28 (d, *J* = 7.9 Hz, 1H), 4.71 (d, *J* = 3.1 Hz, 1H), 3.83 (td, *J* = 8.6, 3.4 Hz, 1H), 3.72 (td, *J* = 8.5, 6.8 Hz, 1H), 2.81 (dtd, *J* = 10.9, 8.0, 3.1 Hz, 1H), 2.28 – 2.15 (m, 1H), 1.60 – 1.50 (m, 1H). ^{13}C NMR (126 MHz, Chloroform-*d*) δ

144.91, 142.15, 130.16, 128.69, 128.39, 127.70, 126.57, 122.79, 119.27, 115.02, 75.98, 66.85, 57.57, 45.78, 24.70. HR-MS (ESI, positive mode): *m/z* calc'd for $C_{17}H_{18}NO$ $[M+H]^+$:252.1388, found 252.1407.

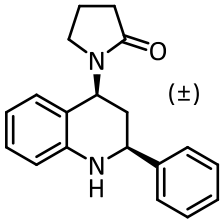

(+/-)-cis-1-2-phenyl-1,2,3,4-tetrahydroquinolin-4-yl)pyrrolidin-2-one. ^{1}H NMR (500 MHz, Chloroform-*d*) δ 7.46 – 7.41 (m, 2H), 7.40 – 7.35 (m, 2H), 7.34 – 7.29 (m, 1H), 7.10 – 7.03 (m, 1H), 6.91 – 6.84 (m, 1H), 6.72 (td, *J* = 7.5, 1.2 Hz, 1H), 6.59 (dd, *J* = 8.0, 1.1 Hz, 1H), 5.77 – 5.68 (m, 1H), 4.68 – 4.54 (m, 1H), 3.22 (q, *J* = 6.7, 6.1 Hz, 2H), 2.60 – 2.40 (m, 2H), 2.18 – 2.07 (m, 2H), 2.05 – 1.96 (m, 2H). ^{13}C NMR (126 MHz, Chloroform-*d*) δ 175.84, 145.88, 143.03, 128.80, 128.28, 128.00, 126.83, 126.49, 118.95, 118.24, 115.00, 56.43, 48.48, 42.34, 35.27, 31.43, 18.26. HR-MS (ESI, positive mode): *m/z* calc'd for $C_{19}H_{21}N_2O$ $[M+H]^+$:293.1654, found 293.1676.

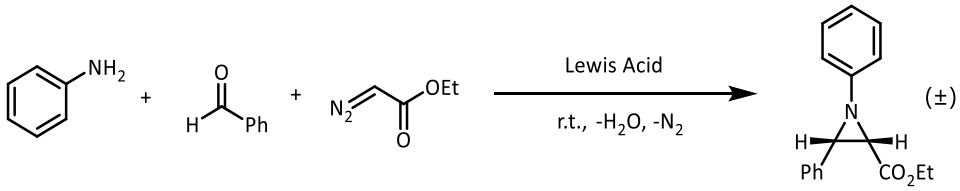

Typical procedure of **Zr_6OTf-BTB** catalyzed multi-component aziridine carboxylate synthesis: Anline (45 μL, 0.5 mmol), benzaldehyde (46 μL, 0.5 mmol), diazo acetate (75 μL, 0.6 mmol, 13 wt.% in DCM), **Zr_6OTf-BTB** (5.0 μmol Zr in a CH_3CN suspension, 1.0 mol%), and anhydrous CH_3CN (2.0 mL) were charged to a 2-dram vial under N_2 atmosphere. The reacrion vial was capped and the mixture was stirred under room temperature. After the reaction was complete as indicated by TLC, the MOF was recovered by centrifugation and the supernatant was evaporated on a rotavap to give the crude product in a quantitative yield (> 99%, mesitylene added as internal

standard). The crude product was purified by silica gel chromatography eluting with hexane/ethyl acetate to afford the target molecule, (+/-)-cis-ethyl 1,3-diphenylaziridine-2-carboxylate, as a colorless oil (95% isolated yield). The ratio between cis and trans isomers was determined by integration of cooresponding ^{1}H peaks in ^{1}H NMR spectrum of the crude product, and in this case no peaks corresponding to the trans product were detected. After one reaction run, ICP-MS analysis showed minimal leaching of <0.1% Zr into the solution.

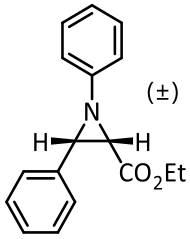

(+/-)-cis-ethyl 1,3-diphenylaziridine-2-carboxylate. ^{1}H NMR (500 MHz, Chloroform-*d*) δ 7.54 – 7.50 (m, 2H), 7.38 – 7.25 (m, 5H), 7.10 – 7.02 (m, 3H), 4.12 – 3.93 (m, 2H), 3.60 (d, *J* = 6.8 Hz, 1H), 3.20 (d, *J* = 6.8 Hz, 1H), 0.99 (t, *J* = 7.1 Hz, 3H). ^{13}C NMR (126 MHz, Chloroform-*d*) δ 167.75, 152.42, 134.67, 129.23, 128.13, 127.92, 127.72, 123.49, 120.01, 61.08, 47.18, 45.59, 13.96. HR-MS (ESI, positive mode): *m/z* calc'd for $C_{17}H_{18}NO_2$ $[M+H]^+$:268.1338, found 268.1314.

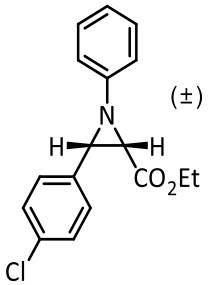

(+/-)-cis-ethyl 3-(4-chlorophenyl)-1-phenylaziridine-2-carboxylate. ^{1}H NMR (500 MHz, Chloroform-*d*) δ 7.49 – 7.44 (m, 2H), 7.34 – 7.26 (m, 4H), 7.08 – 7.02 (m, 3H), 4.14 – 3.94 (m, 2H), 3.54 (d, J = 6.7 Hz, 1H), 3.20 (dd, J = 6.7, 0.8 Hz, 1H), 1.05 (td, J = 7.1, 0.7 Hz, 3H). ^{13}C NMR (126 MHz, Chloroform-*d*) δ 167.47, 152.09, 133.81, 133.20, 129.29, 129.14, 128.33, 123.66,

119.93, 61.23, 46.50, 45.60, 14.05. HR-MS (ESI, positive mode): *m/z* calc'd for $C_{17}H_{17}ClNO_2$ $[M+H]^+$:302.0948, found 302.0950.

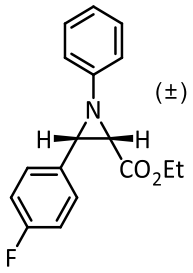

(+/-)-cis-ethyl 3-(4-fluorophenyl)-1-phenylaziridine-2-carboxylate. ^{1}H NMR (500 MHz, Chloroform-*d*) δ 7.53 – 7.46 (m, 2H), 7.30 – 7.26 (m, 2H), 7.08 – 7.00 (m, 5H), 4.13 – 3.95 (m, 2H), 3.56 (d, J = 6.7 Hz, 1H), 3.18 (d, J = 6.7 Hz, 1H), 1.04 (t, J = 7.1 Hz, 3H). ^{13}C NMR (126 MHz, Chloroform-*d*) δ 167.59, 162.57 (d, J = 246.2 Hz), 152.21, 130.39 (d, J = 3.1 Hz), 129.40 (d, J = 8.1 Hz), 129.27, 123.60, 119.93, 115.07 (d, J = 21.6 Hz), 61.16, 46.48, 45.56, 14.03. HR-MS (ESI, positive mode): *m/z* calc'd for $C_{17}H_{17}FNO_2$ $[M+H]^+$:286.1243, found 286.1249.

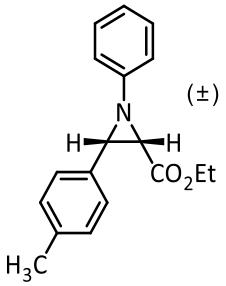

(+/-)-cis-ethyl 1-phenyl-3-(p-tolyl)aziridine-2-carboxylate. ^{1}H NMR (500 MHz, Chloroform-*d*) δ 7.40 (d, *J* = 8.0 Hz, 2H), 7.32 – 7.23 (m, 2H), 7.16 (d, *J* = 7.8 Hz, 2H), 7.09 – 7.02 (m, 3H), 4.15 – 3.94 (m, 2H), 3.56 (d, *J* = 6.7 Hz, 1H), 3.18 (d, *J* = 6.7 Hz, 1H), 2.35 (s, 3H), 1.04 (t, *J* = 7.1 Hz, 3H). ^{13}C NMR (126 MHz, Chloroform-*d*) δ 167.82, 152.54, 137.63, 131.62, 129.20, 128.83, 127.60, 123.40, 120.00, 61.05, 47.15, 45.60, 21.23, 14.02. HR-MS (ESI, positive mode): *m/z* calc'd for $C_{18}H_{20}NO_2$ $[M+H]^+$:282.1494, found 282.1496.

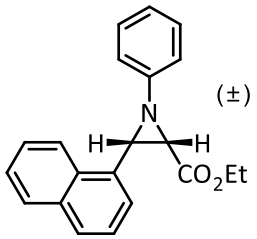

(+/-)-cis-ethyl 3-(naphthalen-1-yl)-1-phenylaziridine-2-carboxylate. ^{1}H NMR (500 MHz, Chloroform-*d*) δ 8.15 – 8.05 (m, 1H), 7.95 – 7.80 (m, 3H), 7.57 – 7.47 (m, 3H), 7.32 (tt, *J* = 7.4, 1.1 Hz, 2H), 7.17 (dq, *J* = 7.0, 1.2 Hz, 2H), 7.09 (td, *J* = 7.4, 1.2 Hz, 1H), 4.07 (d, *J* = 6.7 Hz, 1H), 3.93 – 3.69 (m, 2H), 3.47 (dd, *J* = 6.7, 1.1 Hz, 1H), 0.63 (t, *J* = 7.1 Hz, 3H). ^{13}C NMR (126 MHz, Chloroform-*d*) δ 165.93, 150.82, 131.43, 129.54, 128.66, 127.46, 126.85, 126.44, 124.61, 124.43, 123.96, 123.60, 121.72, 121.11, 118.24, 59.02, 44.01, 43.36, 11.74. HR-MS (ESI, positive mode): *m/z* calc'd for $C_{21}H_{20}NO_2$ $[M+H]^+$:318.1494, found 318.1497.

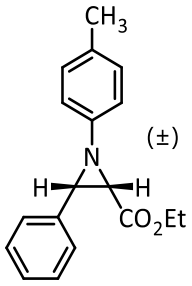

(+/-)-cis-ethyl 3-phenyl-1-(p-tolyl)aziridine-2-carboxylate. ^{1}H NMR (500 MHz, Chloroform-*d*) δ 7.51 (d, J = 7.3 Hz, 2H), 7.38 – 7.28 (m, 3H), 7.08 (d, J = 8.0 Hz, 2H), 6.99 – 6.94 (m, 2H), 4.12 – 3.93 (m, 2H), 3.55 (d, J = 6.8 Hz, 1H), 3.16 (dd, J = 6.8, 1.0 Hz, 1H), 2.30 (s, 3H), 0.99 (td, J = 7.1, 1.0 Hz, 3H). ^{13}C NMR (126 MHz, Chloroform-*d*) δ 167.87, 150.03, 134.80, 132.91, 129.73, 128.10, 127.86, 127.73, 119.85, 61.03, 47.30, 45.66, 20.77, 13.96. HR-MS (ESI, positive mode): *m/z* calc'd for $C_{18}H_{20}NO_2$ $[M+H]^+$:282.1494, found 282.1469.

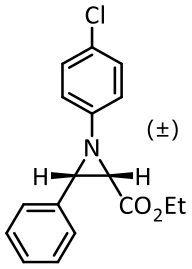

(+/-)-cis-ethyl 1-(4-chlorophenyl)-3-phenylaziridine-2-carboxylate. ^{1}H NMR (500 MHz, Chloroform-*d*) δ 7.52 – 7.46 (m, 2H), 7.38 – 7.28 (m, 3H), 7.25 – 7.21 (m, 2H), 7.03 – 6.97 (m, 2H), 4.12 – 3.93 (m, 2H), 3.56 (d, *J* = 6.8 Hz, 1H), 3.17 (dd, *J* = 6.8, 0.6 Hz, 1H), 0.99 (t, *J* = 7.1 Hz, 3H). ^{13}C NMR (126 MHz, Chloroform-*d*) δ 167.38, 151.07, 134.22, 129.24, 128.59, 128.20, 128.08, 127.65, 121.32, 61.20, 47.33, 45.76, 13.95. HR-MS (ESI, positive mode): *m/z* calc'd for $C_{17}H_{17}ClNO_2$ $[M+H]^+$:302.0948, found 302.0922.

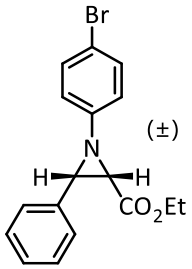

(+/-)-cis-ethyl 1-(4-bromophenyl)-3-phenylaziridine-2-carboxylate. ^{1}H NMR (500 MHz, Chloroform-*d*) δ 7.48 (d, *J* = 7.0 Hz, 2H), 7.41 – 7.28 (m, 5H), 6.98 – 6.92 (m, 2H), 4.11 – 3.92 (m, 2H), 3.56 (d, *J* = 6.8 Hz, 1H), 3.17 (d, *J* = 6.8 Hz, 1H), 0.99 (t, *J* = 7.1 Hz, 3H). ^{13}C NMR (126 MHz, Chloroform-*d*) δ 167.36, 151.59, 134.19, 132.17, 128.20, 128.09, 127.64, 121.77, 116.12, 61.21, 47.28, 45.71, 13.95. HR-MS (ESI, positive mode): *m/z* calc'd for $C_{17}H_{17}BrNO_2$ $[M+H]^+$:346.0443/348.0422, found 346.0406/348.0389.

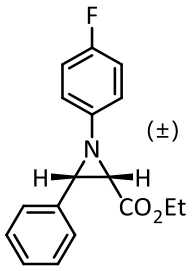

(+/-)-cis-ethyl 1-(4-fluorophenyl)-3-phenylaziridine-2-carboxylate. ^{1}H NMR (500 MHz, Chloroform-*d*) δ 7.52 – 7.47 (m, 2H), 7.38 – 7.28 (m, 3H), 7.04 – 6.93 (m, 4H), 4.11 – 3.93 (m, 2H), 3.56 (d, *J* = 6.8 Hz, 1H), 3.17 (d, *J* = 6.8 Hz, 1H), 0.99 (t, *J* = 7.1 Hz, 3H). ^{13}C NMR (126 MHz, Chloroform-*d*) δ 167.54, 148.48 (d, J = 2.5 Hz), 134.39, 128.18, 128.02, 127.66, 121.15 (d, J = 8.1 Hz), 115.88 (d, J = 22.6 Hz), 61.16, 47.46, 45.88, 13.96. HR-MS (ESI, positive mode): *m/z* calc'd for $C_{17}H_{17}FNO_2$ $[M+H]^+$:286.1243, found 286.1235.

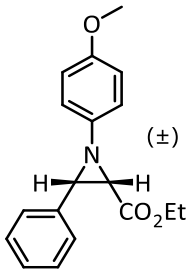

(+/-)-cis-ethyl 1-(4-methoxyphenyl)-3-phenylaziridine-2-carboxylate. ^{1}H NMR (500 MHz, Chloroform-*d*) δ 7.53 – 7.47 (m, 2H), 7.37 – 7.27 (m, 3H), 7.02 – 6.96 (m, 2H), 6.85 – 6.78 (m, 2H), 4.12 – 3.91 (m, 2H), 3.78 (s, 3H), 3.53 (d, J = 6.8 Hz, 1H), 3.14 (d, J = 6.8 Hz, 1H), 0.99 (t, J = 7.1 Hz, 3H). ^{13}C NMR (126 MHz, Chloroform-*d*) δ 167.88, 155.91, 145.81, 134.79, 128.11, 127.86, 127.73, 120.85, 114.48, 61.04, 55.59, 47.51, 45.87, 13.96. HR-MS (ESI, positive mode): *m/z* calc'd for $C_{18}H_{20}NO_3$ $[M+H]^+$:298.1443, found 298.1431.

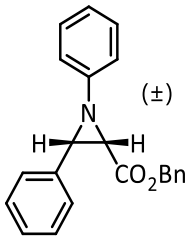

(+/-)-cis-benzyl 1,3-diphenylaziridine-2-carboxylate. ^{1}H NMR (500 MHz, Chloroform-*d*) δ 7.53 – 7.46 (m, 2H), 7.36 – 7.26 (m, 8H), 7.10 – 7.01 (m, 5H), 5.01 (d, *J* = 1.7 Hz, 2H), 3.61 (d, *J* = 6.7 Hz, 1H), 3.26 (d, *J* = 6.8 Hz, 1H). ^{13}C NMR (126 MHz, Chloroform-*d*) δ 167.59, 152.38, 135.39, 134.52, 129.25, 128.47, 128.24, 128.18, 128.00, 127.71, 123.52, 120.00, 66.82, 47.33, 45.65. HR-MS (ESI, positive mode): *m/z* calc'd for $C_{22}H_{20}NO_2$ $[M+H]^+$:330.1494, found 330.1487.

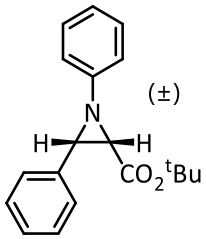

(+/-)-cis-*tert*-butyl 1,3-diphenylaziridine-2-carboxylate. ^{1}H NMR (500 MHz, Chloroform-*d*) δ 7.56 – 7.46 (m, 2H), 7.39 – 7.23 (m, 5H), 7.11 – 7.00 (m, 3H), 3.54 (d, *J* = 6.8 Hz, 1H), 3.10 (dd, *J* = 6.8, 0.9 Hz, 1H), 1.19 (s, 9H). ^{13}C NMR (126 MHz, Chloroform-*d*) δ 166.89, 152.75, 135.00, 129.17, 127.99, 127.83, 127.72, 123.25, 120.03, 81.67, 46.88, 46.27, 27.77. HR-MS (ESI, positive mode): *m/z* calc'd for $C_{19}H_{22}NO_2$ $[M+H]^+$:296.1651, found 296.1653.

Synthesis of bioactive clinical candidates:

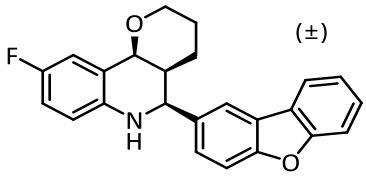

(+/-)-cis-5-(dibenzo[b,d]furan-2-yl)-9-fluoro-3,4,4a,5,6,10b-hexahydro-2H-pyrano[3,2-c]quinoline, 17a. ^{1}H NMR (500 MHz, Chloroform-*d*) δ 8.03 (d, *J* = 1.8 Hz, 1H), 7.96 (dd, *J* = 7.9, 1.3 Hz, 1H), 7.61 – 7.55 (m, 2H), 7.54 – 7.45 (m, 2H), 7.36 (td, *J* = 7.5, 1.0 Hz, 1H), 6.99 (dd, *J* = 8.9, 3.0 Hz, 1H), 6.87 – 6.80 (m, 1H), 6.52 (dd, *J* = 8.8, 4.6 Hz, 1H), 4.85 (d, *J* = 10.9 Hz, 1H), 4.40 (d, *J* = 2.8 Hz, 1H), 4.18 – 4.09 (m, 1H), 3.74 (td, *J* = 11.6, 2.5 Hz, 1H), 2.19 (d, *J* = 10.1 Hz, 1H), 1.97 – 1.80 (m, 1H), 1.67 (tt, *J* = 13.4, 4.7 Hz, 1H), 1.49 (d, *J* = 14.4 Hz, 1H), 1.36 (dt, *J* = 15.1, 3.1 Hz, 1H). ^{13}C NMR (126 MHz, Chloroform-*d*) δ 156.65, 155.96, 140.85, 136.40, 127.45, 126.99, 124.65, 124.00, 122.88, 120.79, 119.90, 116.91, 116.70, 116.59, 116.37, 115.42, 111.82, 111.75, 74.27, 68.83, 55.15, 39.16, 24.05, 22.00. HR-MS (ESI, positive mode): *m/z* calc'd for $C_{24}H_{21}FNO_2$ $[M+H]^+$:374.1556, found 374.1566.

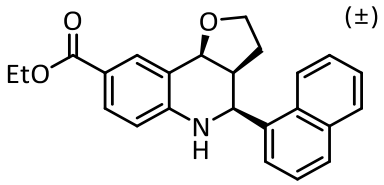

(+/-)-ethyl cis-4-(naphthalen-1-yl)-2,3,3a,4,5,9b-hexahydrofuro[3,2-c]quinoline-8-carboxylate, 18a. ^{1}H NMR (500 MHz, Chloroform-*d*) δ 8.13 (d, *J* = 2.0 Hz, 1H), 8.10 – 8.04 (m, 1H), 7.93 (dd, *J* = 7.6, 1.8 Hz, 1H), 7.87 – 7.79 (m, 3H), 7.62 – 7.50 (m, 3H), 6.66 (d, *J* = 8.5 Hz, 1H), 5.62 (d, *J* = 3.0 Hz, 1H), 5.40 (d, *J* = 7.8 Hz, 1H), 4.34 (qd, *J* = 7.1, 0.9 Hz, 2H), 3.82 (td, *J* = 8.7, 3.3 Hz, 1H), 3.69 (td, *J* = 8.5, 6.9 Hz, 1H), 3.10 (dtd, *J* = 10.9, 8.0, 3.1 Hz, 1H), 2.14 (ddt, *J* = 12.2, 10.7, 8.9 Hz, 1H), 1.38 (t, *J* = 7.1 Hz, 4H). ^{13}C NMR (126 MHz, Chloroform-*d*) δ 166.69, 149.03, 136.82, 133.90, 132.37, 130.28, 130.21, 129.27, 128.36, 126.58, 125.95, 125.51, 122.87, 122.03, 121.96, 121.02, 114.55, 75.25, 66.77, 60.43, 52.48, 43.22, 25.15, 14.50. HR-MS (ESI, positive mode): *m/z* calc'd for $C_{24}H_{24}NO_3$ $[M+H]^+$:374.1756, found 374.1759.

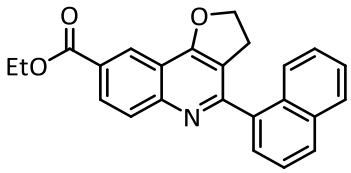

ethyl 4-(naphthalen-1-yl)-2,3-dihydrofuro[3,2-c]quinoline-8-carboxylate, 18c. ^{1}H NMR (500 MHz, Chloroform-*d*) δ 8.81 (d, *J* = 2.3 Hz, 1H), 8.30 (dd, *J* = 8.9, 2.0 Hz, 1H), 8.16 (s, 1H), 7.95 (td, *J* = 8.9, 1.6 Hz, 2H), 7.74 (d, *J* = 8.3 Hz, 1H), 7.64 – 7.57 (m, 2H), 7.52 (ddd, *J* = 8.2, 6.7, 1.3 Hz, 1H), 7.45 (ddd, *J* = 8.3, 6.8, 1.4 Hz, 1H), 4.91 (t, *J* = 9.0 Hz, 2H), 4.47 (q, *J* = 7.1 Hz, 2H), 3.20 (t, *J* = 9.0 Hz, 2H), 1.47 (t, *J* = 7.1 Hz, 3H). ^{13}C NMR (126 MHz, Chloroform-*d*) δ 166.24, 164.97, 158.69, 150.85, 137.16, 133.90, 130.74, 129.52, 129.35, 129.22, 128.52, 127.39, 126.69, 126.57, 126.10, 125.48, 125.36, 124.90, 118.34, 115.39, 73.73, 61.31, 29.03, 14.43. HR-MS (ESI, positive mode): *m/z* calc'd for $C_{24}H_{20}NO_3$ $[M+H]^+$:370.1443, found 370.1450.

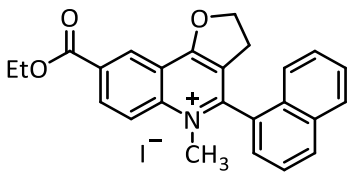

8-(ethoxycarbonyl)-5-methyl-4-(naphthalen-1-yl)-2,3-dihydrofuro[3,2-c]quinolin-5-ium iodide, 18d. ^{1}H NMR (400 MHz, DMSO-d_6) δ 8.81 (d, *J* = 2.0 Hz, 1H), 8.66 (dd, *J* = 9.3, 2.0 Hz, 1H), 8.60 (d, *J* = 9.4 Hz, 1H), 8.35 – 8.29 (m, 1H), 8.19 (d, *J* = 8.2 Hz, 1H), 7.85 – 7.81 (m, 2H), 7.71 (ddd, *J* = 8.2, 5.8, 2.2 Hz, 1H), 7.65 – 7.59 (m, 2H), 5.27 – 5.18 (m, 2H), 4.47 (q, *J* = 7.1 Hz, 2H), 4.02 (s, 3H), 3.24 – 3.13 (m, 1H), 3.01 – 2.89 (m, 1H), 1.43 (t, *J* = 7.1 Hz, 3H).^{13}C NMR (101 MHz, DMSO-d_6) δ 170.41, 163.98, 155.38, 143.32, 134.23, 133.13, 131.67, 129.28, 129.00, 128.77, 128.39, 128.32, 127.47, 127.38, 125.85, 125.13, 124.27, 123.42, 121.24, 114.99, 78.22, 61.98, 40.46, 27.70, 14.10. HR-MS (ESI, positive mode): *m/z* calc'd for $C_{25}H_{22}NO_3$ $[M-I]^+$:384.1594, found 384.1610.

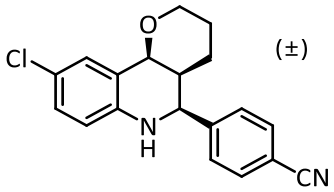

(+/-)-cis-4-(9-chloro-3,4,4a,5,6,10b-hexahydro-2H-pyrano[3,2-c]quinolin-5-yl)benzonitrile,

19a. ^{1}H NMR (500 MHz, Chloroform-*d*) δ 7.68 (d, J = 8.3 Hz, 2H), 7.53 (d, J = 8.3 Hz, 2H), 7.40 (dd, J = 2.6, 1.1 Hz, 1H), 7.06 (dd, J = 8.7, 2.3 Hz, 1H), 6.57 (d, J = 8.5 Hz, 1H), 5.27 (d, J = 5.6 Hz, 1H), 4.72 (d, J = 2.6 Hz, 1H), 3.90 (br, 1H), 3.67 – 3.57 (m, 1H), 3.41 (td, J = 11.6, 2.5 Hz, 1H), 2.25 – 2.08 (m, 1H), 1.62 – 1.39 (m, 3H), 1.24 – 1.16 (m, 1H). ^{13}C NMR (126 MHz, Chloroform-*d*) δ 146.29, 143.00, 132.35, 128.30, 127.60, 127.37, 123.99, 121.78, 118.64, 116.11, 111.65, 72.17, 60.84, 59.21, 38.53, 25.15, 18.03. HR-MS (ESI, positive mode): *m/z* calc'd for $C_{19}H_{18}ClN_2O$ $[M+H]^+$:325.1108, found 325.1093.

6.5 References

1. Slobbe, P.; Ruijter, E.; Orru, R. V. A., Recent applications of multicomponent reactions in medicinal chemistry. *MedChemComm* **2012,** *3* (10), 1189-1218.

2. Ruijter, E.; Orru, R. V. A., Multicomponent reactions – opportunities for the pharmaceutical industry. *Drug Discovery Today: Technologies* **2013,** *10* (1), e15-e20.

3. Touré, B. B.; Hall, D. G., Natural Product Synthesis Using Multicomponent Reaction Strategies. *Chemical Reviews* **2009,** *109* (9), 4439-4486.

4. Sunderhaus, J. D.; Martin, S. F., Applications of Multicomponent Reactions to the Synthesis of Diverse Heterocyclic Scaffolds. *Chemistry – A European Journal* **2009,** *15* (6), 1300-1308.

5. Cioc, R. C.; Ruijter, E.; Orru, R. V. A., Multicomponent reactions: advanced tools for sustainable organic synthesis. *Green Chemistry* **2014,** *16* (6), 2958-2975.

6. José Climent, M.; Corma, A.; Iborra, S., Homogeneous and heterogeneous catalysts for multicomponent reactions. *RSC Advances* **2012,** *2* (1), 16-58.

7. Hosseini, M. M.; Kolvari, E., Nano-magnetic Zirconia Sulfuric Acid (Fe3O4@ZrO2-SO3H): Magnetically Separable and Reusable Heterogeneous Catalyst for Multicomponent Reactions. *Chemistry Letters* **2016,** *46* (1), 53-55.

8. Lima, C. G. S.; Moreira, N. M.; Paixão, M. W.; Corrêa, A. G., Heterogenous green catalysis: Application of zeolites on multicomponent reactions. *Current Opinion in Green and Sustainable Chemistry* **2019,** *15*, 7-12.

9. Bhaskaruni, S. V. H. S.; Maddila, S.; Gangu, K. K.; Jonnalagadda, S. B., A review on multi-component green synthesis of N-containing heterocycles using mixed oxides as heterogeneous catalysts. *Arabian Journal of Chemistry* **2020,** *13* (1), 1142-1178.

10. Zhao, M.; Ou, S.; Wu, C.-D., Porous Metal–Organic Frameworks for Heterogeneous Biomimetic Catalysis. *Accounts of Chemical Research* **2014,** *47* (4), 1199-1207.

11. Rogge, S. M. J.; Bavykina, A.; Hajek, J.; Garcia, H.; Olivos-Suarez, A. I.; Sepúlveda-Escribano, A.; Vimont, A.; Clet, G.; Bazin, P.; Kapteijn, F.; Daturi, M.; Ramos-Fernandez, E. V.; Llabrés i Xamena, F. X.; Van Speybroeck, V.; Gascon, J., Metal–organic and covalent organic frameworks as single-site catalysts. *Chemical Society Reviews* **2017,** *46* (11), 3134-3184.

12. Yang, D.; Gates, B. C., Catalysis by Metal Organic Frameworks: Perspective and Suggestions for Future Research. *ACS Catalysis* **2019,** *9* (3), 1779-1798.

13. Wei, Y.-S.; Zhang, M.; Zou, R.; Xu, Q., Metal–Organic Framework-Based Catalysts with Single Metal Sites. *Chem. Rev.* **2020,** *120* (21), 12089-12174.

14. Jiang, J.; Gándara, F.; Zhang, Y.-B.; Na, K.; Yaghi, O. M.; Klemperer, W. G., Superacidity in Sulfated Metal–Organic Framework-808. *Journal of the American Chemical Society* **2014,** *136* (37), 12844-12847.

15. Hu, Z.; Zhao, D., Metal–organic frameworks with Lewis acidity: synthesis, characterization, and catalytic applications. *CrystEngComm* **2017,** *19* (29), 4066-4081.

16. Ly, H. G. T.; Fu, G.; Kondinski, A.; Bueken, B.; De Vos, D.; Parac-Vogt, T. N., Superactivity of MOF-808 toward Peptide Bond Hydrolysis. *Journal of the American Chemical Society* **2018,** *140* (20), 6325-6335.

17. Trickett, C. A.; Osborn Popp, T. M.; Su, J.; Yan, C.; Weisberg, J.; Huq, A.; Urban, P.; Jiang, J.; Kalmutzki, M. J.; Liu, Q.; Baek, J.; Head-Gordon, M. P.; Somorjai, G. A.; Reimer, J. A.; Yaghi, O. M., Identification of the strong Brønsted acid site in a metal–organic framework solid acid catalyst. *Nature Chemistry* **2019,** *11* (2), 170-176.

18. Ji, P.; Feng, X.; Oliveres, P.; Li, Z.; Murakami, A.; Wang, C.; Lin, W., Strongly Lewis Acidic Metal–Organic Frameworks for Continuous Flow Catalysis. *Journal of the American Chemical Society* **2019,** *141* (37), 14878-14888.

19. Horike, S.; Dincă, M.; Tamaki, K.; Long, J. R., Size-Selective Lewis Acid Catalysis in a Microporous Metal-Organic Framework with Exposed Mn2+ Coordination Sites. *Journal of the American Chemical Society* **2008,** *130* (18), 5854-5855.

20. Yadav, A.; Kanoo, P., Metal-Organic Frameworks as Platform for Lewis-Acid-Catalyzed Organic Transformations. *Chemistry- An Asian Journal* **2019,** *14* (20), 3531-3551.

21. Bai, Y.; Dou, Y.; Xie, L.-H.; Rutledge, W.; Li, J.-R.; Zhou, H.-C., Zr-based metal–organic frameworks: design, synthesis, structure, and applications. *Chemical Society Reviews* **2016,** *45* (8), 2327-2367.

22. Chen, Z.; Hanna, S. L.; Redfern, L. R.; Alezi, D.; Islamoglu, T.; Farha, O. K., Reticular chemistry in the rational synthesis of functional zirconium cluster-based MOFs. *Coordination Chemistry Reviews* **2019,** *386*, 32-49.

23. Taddei, M., When defects turn into virtues: The curious case of zirconium-based metal-organic frameworks. *Coordination Chemistry Reviews* **2017,** *343*, 1-24.

24. Cavka, J. H.; Jakobsen, S.; Olsbye, U.; Guillou, N.; Lamberti, C.; Bordiga, S.; Lillerud, K. P., A New Zirconium Inorganic Building Brick Forming Metal Organic Frameworks with Exceptional Stability. *Journal of the American Chemical Society* **2008,** *130* (42), 13850-13851.

25. Furukawa, H.; Gándara, F.; Zhang, Y.-B.; Jiang, J.; Queen, W. L.; Hudson, M. R.; Yaghi, O. M., Water Adsorption in Porous Metal–Organic Frameworks and Related Materials. *Journal of the American Chemical Society* **2014,** *136* (11), 4369-4381.

26. Cao, L.; Lin, Z.; Peng, F.; Wang, W.; Huang, R.; Wang, C.; Yan, J.; Liang, J.; Zhang, Z.; Zhang, T.; Long, L.; Sun, J.; Lin, W., Self-Supporting Metal–Organic Layers as Single-Site Solid Catalysts. *Angewandte Chemie International Edition* **2016,** *55* (16), 4962-4966.

27. Ohkubo, K.; Menon, S. C.; Orita, A.; Otera, J.; Fukuzumi, S., Quantitative Evaluation of Lewis Acidity of Metal Ions with Different Ligands and Counterions in Relation to the Promoting Effects of Lewis Acids on Electron Transfer Reduction of Oxygen. *The Journal of Organic Chemistry* **2003,** *68* (12), 4720-4726.

28. S. Bello Forero, J.; Jones Junior, J.; M. da Silva, F., The Povarov Reaction as a Versatile Strategy for the Preparation of 1, 2, 3, 4-Tetrahydroquinoline Derivatives: An Overview. *Current Organic Synthesis* **2016,** *13* (2), 157-175.

29. Ghashghaei, O.; Masdeu, C.; Alonso, C.; Palacios, F.; Lavilla, R., Recent advances of the Povarov reaction in medicinal chemistry. *Drug Discovery Today: Technologies* **2018,** *29*, 71-79.

30. Kobayashi, S.; Ishitani, H.; Nagayama, S., Lanthanide Triflate Catalyzed Imino Diels-Alder Reactions; Convenient Syntheses of Pyridine and Quinoline Derivatives. *Synthesis* **1995,** *1995* (09), 1195-1202.

31. Smith, C. D.; Gavrilyuk, J. I.; Lough, A. J.; Batey, R. A., Lewis Acid Catalyzed Three-Component Hetero-Diels−Alder (Povarov) Reaction of N-Arylimines with Strained Norbornene-Derived Dienophiles. *The Journal of Organic Chemistry* **2010,** *75* (3), 702-715.

32. Di Pietro, O.; Vicente-García, E.; Taylor, M. C.; Berenguer, D.; Viayna, E.; Lanzoni, A.; Sola, I.; Sayago, H.; Riera, C.; Fisa, R.; Clos, M. V.; Pérez, B.; Kelly, J. M.; Lavilla, R.; Muñoz-Torrero, D., Multicomponent reaction-based synthesis and biological evaluation of tricyclic heterofused quinolines with multi-trypanosomatid activity. *European Journal of Medicinal Chemistry* **2015,** *105*, 120-137.

33. Kantevari, S.; Yempala, T.; Surineni, G.; Sridhar, B.; Yogeeswari, P.; Sriram, D., Synthesis and antitubercular evaluation of novel dibenzo[b,d]furan and 9-methyl-9H-carbazole derived hexahydro-2H-pyrano[3,2-c]quinolines via Povarov reaction. *European Journal of Medicinal Chemistry* **2011,** *46* (10), 4827-4833.

34. Tarragó, T.; Masdeu, C.; Gómez, E.; Isambert, N.; Lavilla, R.; Giralt, E., Benzimidazolium Salts as Small, Nonpeptidic and BBB-Permeable Human Prolyl Oligopeptidase Inhibitors. *ChemMedChem* **2008,** *3* (10), 1558-1565.

35. Yadav, J. S.; Reddy, B. V. S.; Reddy, P. N.; Rao, M. S., Bi(OTf)3-[Bmim]PF6: A novel and Reusable Catalytic System for the Synthesis of cis-Aziridine Carboxylates. *Synthesis* **2003,** *2003* (09), 1387-1390.

36. Bew, S. P.; Liddle, J.; Hughes, D. L.; Pesce, P.; Thurston, S. M., Chiral Brønsted Acid-Catalyzed Asymmetric Synthesis of N-Aryl-cis-aziridine Carboxylate Esters. *Angewandte Chemie International Edition* **2017,** *56* (19), 5322-5326.

37. Domingo, L. R.; Aurell, M. J.; Sáez, J. A.; Mekelleche, S. M., Understanding the mechanism of the Povarov reaction. A DFT study. *RSC Advances* **2014,** *4* (48), 25268-25278.

Chapter 7. Multistep Engineering of Synergistic Lewis Acid and Pd Catalysts in MOF for Tandem C–O Bond Cleavage

7.1 Introduction

The conversion of abundant and renewable biomass into value-added hydrocarbon feedstocks provides a potential sustainable solution to an ever-increasing global need for commodity chemicals and fuels.[1-2] The key step of biomass conversion involves reducing the oxygen content (~40%) without breaking C-C/C-H bonds.[3-5] In the presence of hydrogen, strong C-O bonds of alcohols, ethers, and esters in abundant lignocellulosic biomass can be selectively cleaved in a hydrodeoxygenation process.[6-8] Development of novel catalytic technologies for efficient hydrodeoxygenation of C-O bonds in biomass offers a viable pathway towards green, efficient, and economic biomass utilization and establishing the bio-renewable industry.[9]

Among many strategies for the catalytic hydrodeoxygenation of lignocellulosic biomass[10-14], one-pot tandem catalysis offers an efficient method to break the strong C-O bonds and transform biomass into valuable hydrocarbon fuels.[15-17] In particular, Marks and coworkers coupled tandem catalytic cycles of C-O dehydroalkoxylation and olefin hydrogenation to drive hydrogenolysis of ethers, alcohols, and esters with a combination of homogeneous Lewis acid catalysts and Pd nanoparticles (NPs).[18-20] Thermodynamic analysis revealed that exothermic Pd NP-catalyzed hydrogenation cycle could compensate endothermic acid-catalyzed C-O dehydroalkoxylation cycle to render the overall tandem reaction exothermic.[18, 21] However, the effectiveness of this tandem catalytic hydrodeoxygenation process is limited by the reliance on non-reusable homogenous Lewis acid catalysts $M(OTf)_n$ (M =Hf, Al, Zr, *etc*) and the deactivation of metallic Pd NPs at elevated reaction temperatures. The propensity for interference between homogeneous

Lewis acidic $M(OTf)_n$ sites and Pd NPs adds another challenge to achieving long-term catalytic activities with truly orthogonal active sites, which is a common problem for other multi-catalytic systems involving homogeneous catalysts.[22-23]

Metal-organic frameworks (MOFs) have emerged as a versatile and tunable porous material platform for the design of structurally and functionally uniform solid catalysts over the past two decades.[24-26] As catalytic functionalities can be incorporated into MOFs via organic linker functionalization,[27-28] entrapment of catalytically active species in pores/channels,[29-30] and more recently, transformation of metal-hydroxo/oxo nodes,[31-33] it is feasible to install multiple catalytic functionalities in MOFs via judicious combination of metal/metal-oxo nodes and functional organic ligand linkers followed by appropriate post-synthetic tranfromations.[34-36] The rigid, periodic and porous structures of MOFs isolate disparate catalysts from each other, preventing their potential interference to afford truly orthogonal catalytic sites. However, due to the difficulty in characterizing MOFs after multistep functionalization, sequential engineering of multiple catalytic sites into MOFs has not been realized. Herein we report the first attempt at multi-step synthetic manipulations of an aluminum MOF to generate Lewis acid catalysts and Pd NPs for tandem catalytic hydrodeoxygenation of ethers, alcohols, and esters.

In this chapter, we targeted a mixed-ligand MOF (**1**) built from $(Al\text{-}OH)_n$ secondary building units (SBUs) and a mixture of 2,2'-bipyridine-5,5'-dicarboxylate(dcbpy) and 1,4-benzenediacrylate (pdac) ligands to install both Lewis acid and Pd NP active sites via multi-step synthetic manipulations (**Scheme 7-1**). The pdac ligands in **1** were selectively removed via post-synthetic ozonolysis to generate $Al_2(OH)(OH_2)$ sites. Subsequent triflation of $Al_2(OH)(OH_2)$ sites with trimethyl triflate (Me_3SiOTf) afforded strongly Lewis acidic sites for dehydroalkoxylation. Finally, coordination of $Pd(MeCN)_2Cl_2$ to dcbpy ligand followed by *in situ* reduction by hydrogen

produced orthogonal Pd NP sites as the hydrogenation catalyst. In-depth characterization of the MOFs after each post-synthetic manipulation supported selective and precise transformations to install orthogonal active sites in **1**-OTf-Pd^{NP}. The presence of both Lewis acid and Pd NP active sites in **1**-OTf-Pd^{NP} led to outstanding catalytic performance in apparent hydrogenolysis of etheric, alcoholic, and esteric C-O bonds to generate alkanes via a tandem dehydroalkoxylation-hydrogenation process under relatively mild conditions. The reactivity of C-O bonds followed the trend of tertiary carbon > secondary carbon > primary carbon. Control experiments confirmed the heterogeneous nature and recyclability of **1**-OTf-Pd^{NP} and its superior catalytic activity over the homogeneous counterparts.

Scheme 7-1. Multistep engineering of synergistic Lewis acid and Pd catalysts in MOF for tandem C–O bond cleavage. Copyright 2020 American Chemical Society.

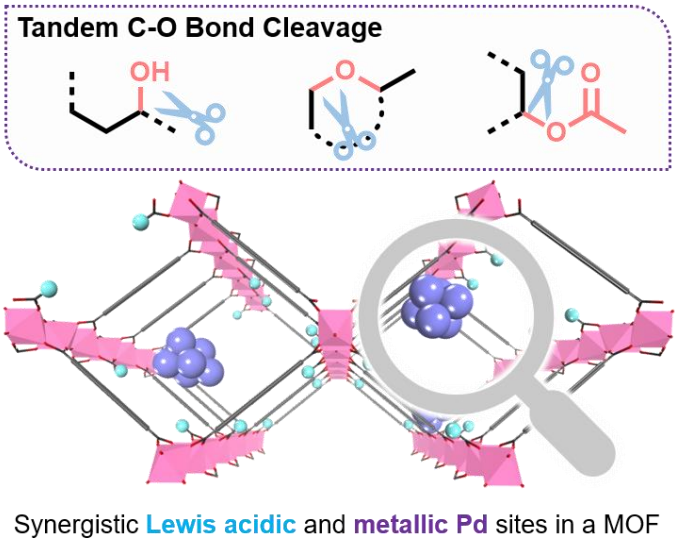

7.2 Results and Discussion

7.2.1 Synthesis of mixed-ligand MOF 1 and removal of pdac ligands via ozonolysis

The new MOF **1** with mixed dcbpy and pdac ligands based on DUT-5 structure was synthesized solvothermally by heating a mixture of $Al(NO_3)_3 \cdot 9H_2O$, dcbpy, pdac, and *N*,*N*-dimethylformamide (DMF) at 120 °C (**Figure 7-1**).[37-38] Powder X-ray diffraction (PXRD) studies

revealed that **1** was isostructural to DUT-5 of the formula Al(OH)(bpdc) (bpdc = biphenyl-4,4'-dicarboxylate) and MOF-253 of the formula Al(OH)(dcbpy) (**Figure 7-2c**). The formula of **1** was determined as $Al(OH)(dcbpy)_{0.81}(pdac)_{0.19}$ based on ^1H NMR spectra of digested **1** and confirmed by thermogravimetric analysis (TGA) of **1**. Scanning electron microscopy (SEM) and transmission electron microscopy (TEM) imaging showed a plate-like morphology for **1** (**Figures 7-2b**, **7-2e**), similar to that of DUT-5.[37] N_2 sorption measurements of **1** showed type I isotherms with a Brunauer-Emmett-Teller (BET) surface area of 1499 m^2/g, comparable to that of DUT-5 (1613 m^2/g, **Figure 7-2d**).

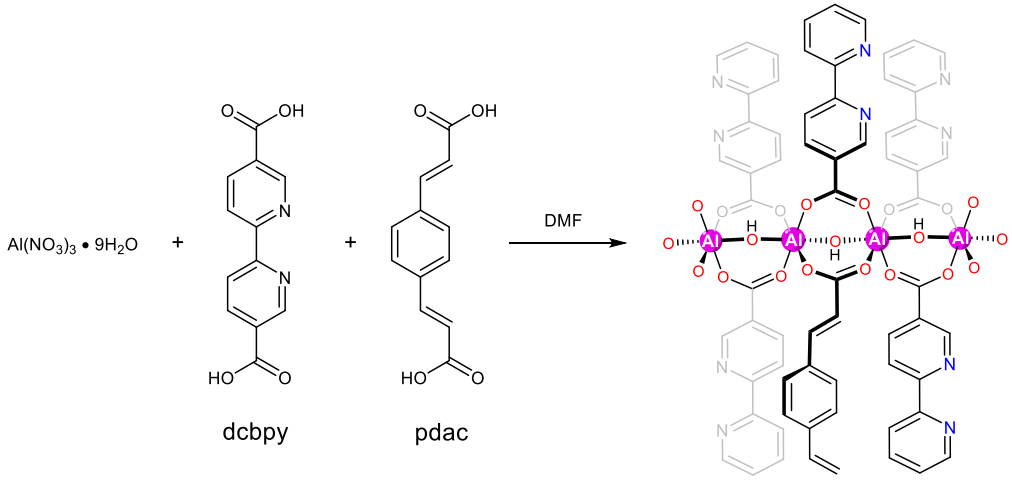

Figure 7-1. Synthetic procedure of MOF **1**.

Post-synthetic transformations have recently been used to fine-tune micro- and meso-porosity of MOFs.[39-41] In particular, Maspoch and coworkers used ozonolysis to remove olefin-containing ligands from a mixed-ligand UiO-type MOF to afford both micro- and meso-porosity.[41] This ozonolysis process also removes some carboxylate ligands to generate $Al_2(OH)(OH_2)$ defect sites on the $(Al\text{-}OH)_n$ SBUs. We treated **1** with gaseous O_3 (0.42 mol/h at 6 L/min O_2 flowing rate) to selectively remove the pdac ligands by cleaving the olefinic groups (**Figure 7-2a**). Further washing with DMF/HCl (1M) (10:1, *v*:*v*) removed the residual organic fragments trapped in the

pores to afford **1**-OH with $Al_2(OH)(OH_2)$ defect sites as a white solid. NMR and TGA analyses afforded a formula of $Al(OH)(dcbpy)_{0.81}(OH)_{0.38}(H_2O)_{0.38}$ for **1**-OH. The crystallinity of **1** was maintained after ozonolysis as demonstrated by the similarity of PXRD patterns between **1** and **1**-OH (**Figure 7-2c**). TEM imaging showed that **1**-OH maintained the plate-like morphology of **1**, with evenly distributed spongy cleavages (**Figure 7-2f**). **1**-OH showed a BET surface area of 1190 m^2/g with the hysteresis characteristic of mesoporosity (**Figure 7-2d**). The removal of pdac ligands slightly reduced the BET surface area but increased pore sizes in the 13 - 32 Å range. Ozonolysis of **1** thus generated mesopores which should facilitate substrate and product transport in catalytic reactions.

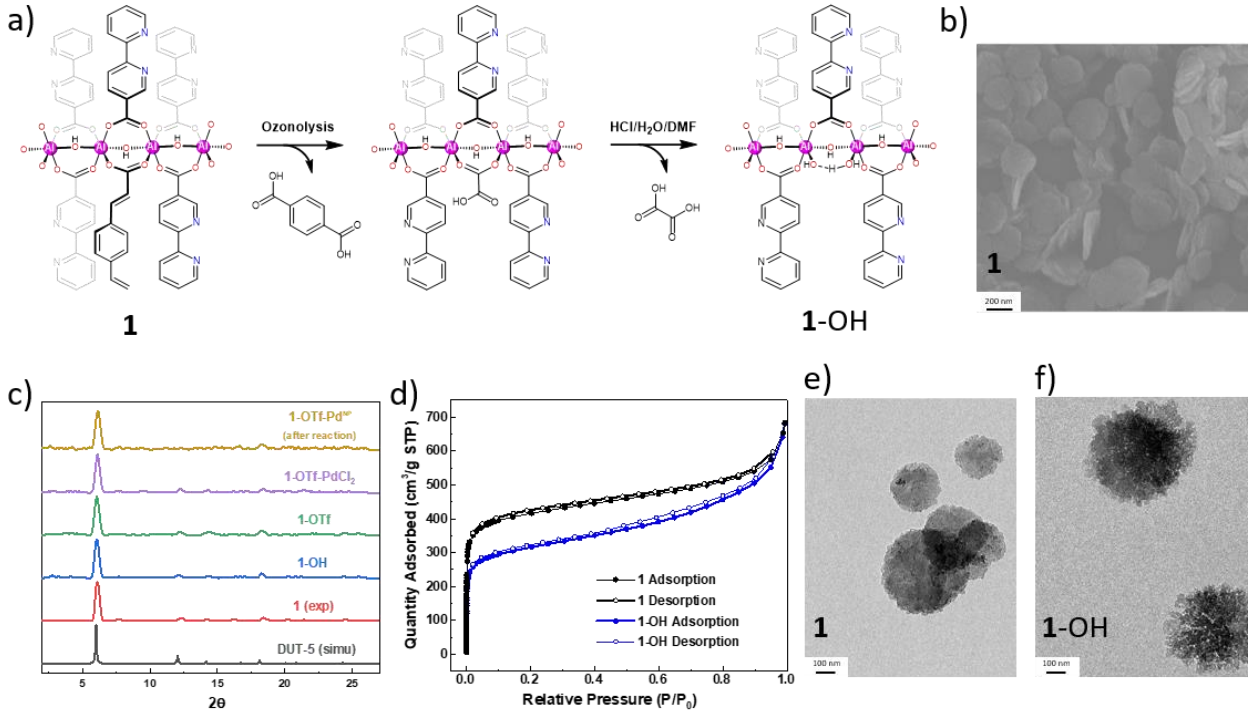

Figure 7-2. Ozonolysis of MOF **1** and characterization on MOF **1** and **1**-OH. (a) Chemical equation showing ozonolysis of **1** followed by washing with DMF/HCl (1 M) to afford **1**-OH with $Al_2(OH)(OH_2)$ defect sites. (b) SEM image of as-synthesized **1**. (c) The similarity of PXRD patterns of **1** (red), **1**-OH (blue), **1**-OTf (green), **1**-OTf-$PdCl_2$ (purple), and **1**-OTf-Pd^{NP} (khaki) to the simulated pattern of DUT-5 (black) indicates the crystallinity of the MOF was maintained after multi-step post-synthetic manipulations. (d) N_2 sorption isotherms of **1** (black) and **1**-OH (blue). (e, f) TEM images of **1** (e) and **1**-OH (f). Copyright 2020 American Chemical Society.

7.2.2 Triflation of 1-OH and Lewis acidity determination for 1-OTf

Although MOF nodes have been widely used as Lewis acidic sites to catalyze organic transformations,[42-43] their Lewis acidity is significantly lower than the homogeneous benchmark $Sc(OTf)_3$. In chapter 5, we developed a triflation strategy to significantly enhance Lewis acidity of MOF nodes.[44] **1**-OH was activated with Me_3SiOTf in benzene at room temperature for 12 h to afford **1**-OTf as a pale-yellow solid (**Figure 7-3a**). Me_3SiOTf (TMSOTf) quantitatively transformed $Al_2(OH)(OH_2)$ moieties to $Al_2(\mu_2\text{-OTf})$ sites due to the oxophilic nature of Me_3Si groups. ^1H NMR spectroscopy showed the generation of 1.93 equiv. of $(Me_3Si)_2O$ w.r.t. the $Al_2(OH)(OH_2)$ sites, agreeing well with the expected value of 2 for the proposed activation process. Diffuse reflectance infrared Fourier transform spectroscopy (DRIFTS) supported the removal of $Al_2(OH)(OH_2)$ moieties. The increased absorption at 1231 – 1266 cm^{-1} in **1**-OTf corresponded to the $\nu(S{=}O^{OTf})$ band (**Figure 7-3b**). The sharp stretching band at 3708 cm^{-1} was observed for bridging μ_2-OH groups in both **1** and **1**-OH, [45] but this band shifted significantly to 3687 cm^{-1} for **1**-OTf (**Figure 7-3b**). Electron-withdrawing OTf groups weaken the O-H bonds of μ_2-OH groups in **1**-OTf, leading to the shift to lower energy. The broad peak centered at 3689 cm^{-1} in **1**-OH was attributed to hydrogen bonding interactions between neighboring Al-OH and $Al\text{-}OH_2$ moieties.[46]

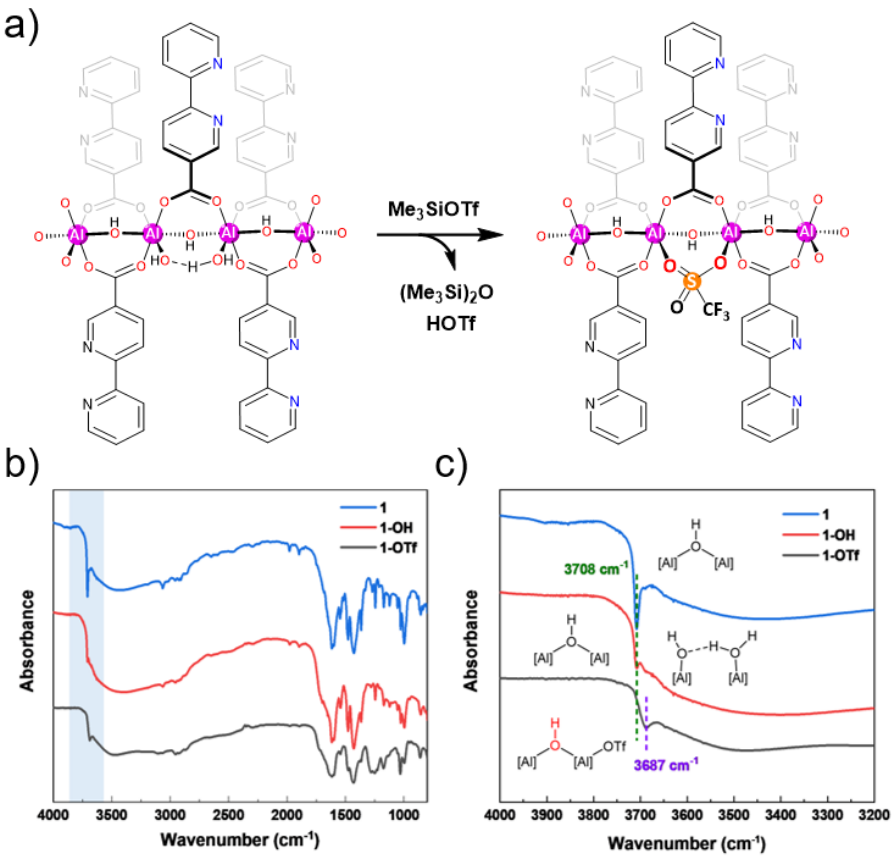

Figure 7-3. Triflation of **1**-OH to afford **1**-OTf and DRIFT characterization. (a) Chemical equation showing triflation of **1**-OH to afford **1**-OTf. (b) DRIFT spectra of **1** (blue), **1**-OH (red), and **1**-OTf (black). (c) Zoomed-in view of the DRIFT spectra show a significant red shift of $\nu(\mu_2\text{-OH})$ from 3708 cm^{-1} in **1** (blue) and **1**-OH (red) to 3687 cm^{-1} in **1**-OTf (black). Copyright 2020 American Chemical Society.

We quantified Lewis acidity enhancement in **1**-OTf by electron paramagnetic resonance (EPR) spectroscopy of MOF-bound superoxide ($O_2^{\bullet-}$) and fluorescence spectroscopy of MOF-bound *N*-methylacridone (NMA).[44, 47] Superoxide radical ions ($O_2^{\bullet-}$) can be generated *in situ* by the $1e^-$ reduction of O_2, which readily bind to Lewis acidic Al centers by displacing the weakly coordinating triflate groups to form EPR-active Al($O_2^{\bullet-}$) species (**Figure 7-4b**). Coordination to Lewis acids significantly shifted the EPR signal of $O_2^{\bullet-}$, especially the g_{zz} tensor that is determined by energy splitting (ΔE) between the π_x^* and π_y^* orbitals.[48] **1**-OTf bound $O_2^{\bullet-}$ exhibited a g_{zz} of 2.032, which corresponds to a ΔE of 0.94 eV (**Figure 7-4a).** In comparison, **1**-OH displayed a g_{zz}

of 2.0352 with a corresponding ΔE of 0.85 eV. The 0.09 eV increase in ΔE makes **1**-OTf a much stronger Lewis acid and affords a more effective catalyst for C-O bond cleavage.

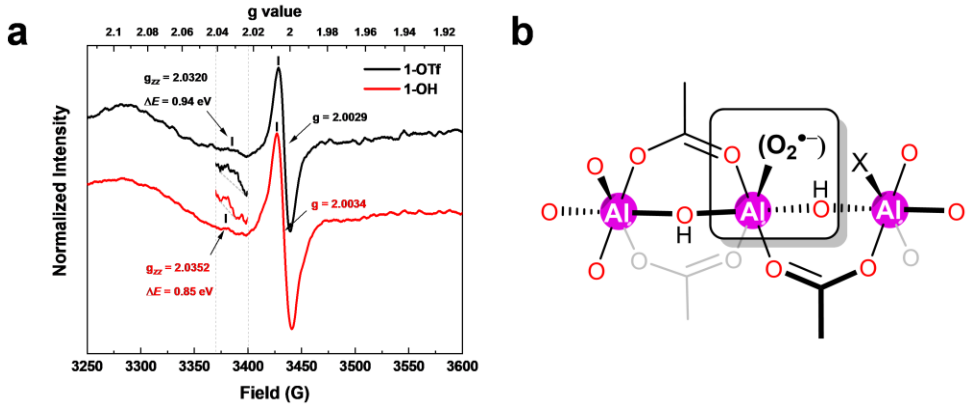

Figure 7-4. (a) EPR spectra of **1**-OTf-($O_2^{\bullet-}$) (black) and **1**-OH-$O_2^{\bullet-}$ (red). (b) Proposed structures for superoxide-coordinated **1**-X (X = -OH or -OTf). Copyright 2020 American Chemical Society.

Free NMA has an emission maximum (λ_{max}) at 433 nm when excited at 413 nm. Upon coordination to **1**-OTf, the Lewis acid adduct of NMA displayed a λ_{max} at 470 nm (**Figure 7-5b**). The energy shift of NMA emission was previously established to be linearly related to the Lewis acidity of metal centers.[47, 49] Using the reported empirical equation, we calculated the ΔE value of **1**-OTf to be 0.93 eV, which is almost identical to the value measured by superoxide EPR spectroscopy. In comparison, **1**-OH only shifted the λ_{max} of NMA emission to 463 nm, with a calculated ΔE of 0.84 eV (**Figure 7-5a**). Triflation of $Al_2(OH)(OH_2)$ moieties thus significantly enhanced Lewis acidity of **1**-OTf for catalytic applications.

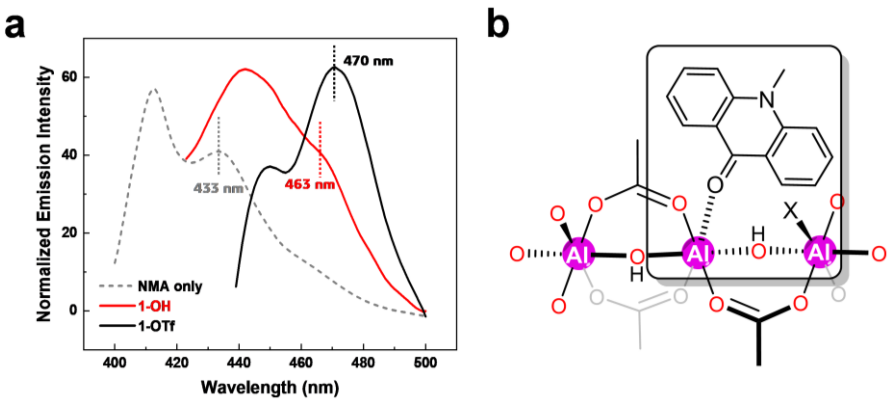

Figure 7-5. (a) Fluorescence spectra of **1**-OTf (black), **1**-OH (red), and free NMA (dashed). (b) Proposed structures for NMA-coordinated **1**-X (X = -OH or -OTf). Copyright 2020 American Chemical Society.

7.2.3 Synthesis and characterization of 1-OTf-$PdCl_2$ and 1-OTf-Pd^{NP}

1-OTf was further metalated with $Pd(MeCN)_2Cl_2$ in THF to afford the pre-catalyst **1**-OTf-$PdCl_2$ (**Figure 7-6a**). Inductively coupled plasma-mass spectrometry (ICP-MS) indicated an Al/Pd ratio of 2.10, corresponding to a formula of $Al(OH)(dcbpy)_{0.81}(PdCl_2)_{0.48}(OTf)_{0.38}$ for **1**-OTf-$PdCl_2$. This formula was supported by TGA analysis, which gave a residual weight of 27.8% (expected 28.6%) after ramping the temperature to 800 °C. PXRD studies indicated that **1**-OTf-$PdCl_2$ maintained crystalline structure of **1** (**Figure 7-2c**). Pd coordination environment of **1**-OTf-$PdCl_2$ was studied by extended X-ray absorption fine structure (EXAFS) spectroscopy. The EXAFS data was collected at Pd K-edge and fitted with reported crystal structure of $(bpy)PdCl_2$.[50] The EXAFS feature of Pd centers in **1**-OTf-$PdCl_2$ was well fit with the structure to afford nearly identical coordination geometry and bond lengths (**Figures 7-6b**, **7-6d**). Specifically, the Pd centers in **1**-OTf-$PdCl_2$ coordinate to two chlorides and one bpy ligand in a near square planar geometry with an average Pd-N bond length of 2.04 ± 0.01 Å and an average Pd-Cl bond length of 2.30 ± 0.02 Å.

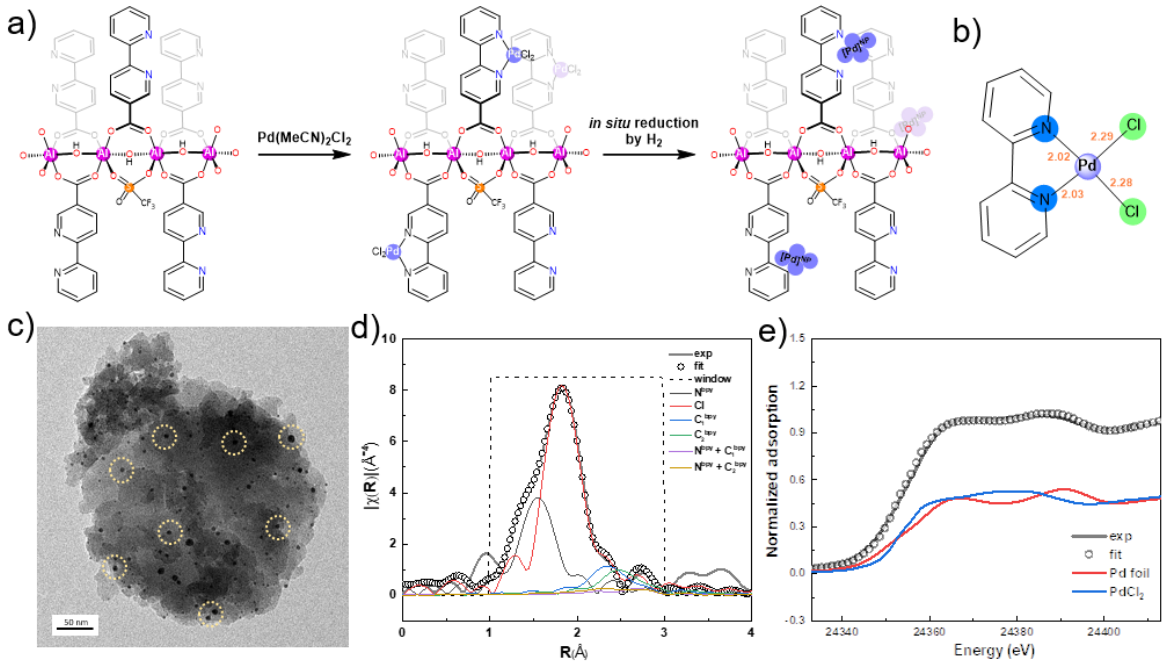

Figure 7-6. Synthesis and characterization of **1**-OTf-$PdCl_2$ and **1**-OTf-Pd^{NP}. (a) Chemical equation showing metalation of **1**-OTf with $Pd(MeCN)_2Cl_2$ to afford **1**-OTf-$PdCl_2$ and *in situ* reduction of **1**-OTf-$PdCl_2$ to generate **1**-OTf-Pd^{NP}. (b) Fragment structure of (bpy)$PdCl_2$ for EXAFS fitting of the Pd coordination environment in **1**-OTf-$PdCl_2$. H atoms were omitted for clarity. (c) TEM image of **1**-OTf-Pd^{NP} shows evenly distributed Pd NPs in the MOF matrix after *in situ* reduction in catalytic reactions. (d) EXAFS spectrum (gray solid line) and fit (black circles) in R-space at the Pd K-edge adsorption of **1**-OTf-$PdCl_2$. (e) Linear combination fitting of **1**-OTf-Pd^{NP} XANES feature using those of Pd foil and $PdCl_2$ as the basis functions. Copyright 2020 American Chemical Society.

Upon treatment with H_2 in the catalytic reaction, the Pd^{II} centers in **1**-OTf-$PdCl_2$ were readily reduced to form metallic Pd NPs in **1**-OTf-Pd^{NP}. To investigate the true catalytic active species during the reaction process, we characterized the MOF materials recovered from catalytic C-O cleavage reactions by PXRD, TEM, and XANES. PXRD studies showed that the MOF after catalysis remained crystalline (**Figure 7-2c**), whereas TEM imaging indicated the formation of Pd NPs which were dispersed evenly in the MOF matrix (**Figure 7-6c**). We further characterized the Pd^0 species in the recovered MOF by XANES. The recovered MOF showed XANES features corresponding to both Pd^0 and Pd^{II} species. We fitted the XANES spectra of **1**-OTf-Pd^{NP} with a linear combination of XANES spectra of $PdCl_2$ and Pd foil. The fitting gave ~48% Pd^0 species in

the recovered MOF (**Figure 7-6e**); it is likely that surface Pd centers of **1**-OTf-Pd^{NP} were oxidized by air to afford Pd^{II} species when the samples were processed for XANES studies.

7.2.4 1-OTf-$PdCl_2$ catalyzed tandem ether/alcohol C-O bond cleavage

Etheric and alcoholic C-O linkages widely exist in biomass-based feedstocks. Their strong bonds present a major challenge for converting biomass into chemicals and hydrocarbon fuels with low oxygen contents.[51-53] Acids are shown to catalyze the C-O bond formation from hydroalkoxylation between alcohols and alkenes[54] as well as its reversible process, dehydroalkoxylation to cleave an alkyl ether to form an olefin and an alcohol.[18-19] As the dehydroalkoxylation process is endothermic with $\Delta H \approx 10\sim20$ kcal/mol, its coupling with an exothermic alkene hydrogenation reaction makes the overall C-O bond cleavage reaction exothermic and produces a saturated alkane and an alcohol as the products.[18] Multiple catalyst systems containing acid catalysts, such as homogeneous mineral acids and Lewis acids or heterogeneous acidic materials, and hydrogenation catalysts have been used to effect such a tandem process.[55-56] In particular, metal triflate salts and supported Pd catalysts effectively catalyzed ether and alcohol C-O bond hydrogenolysis to generate saturated hydrocarbons in a tandem manner.[18-19] These catalyst systems tend to rapidly deactivate, require harsh conditions with elevated reaction temperatures and high H_2 pressures, and produce undesirable dimerized or aromatized byproducts. With isolated catalytic sites confined by the MOF framework, *in situ* generated **1**-OTf-Pd^{NP} catalyst is expected to significantly stabilize strongly Lewis acidic $Al_2(\mu_2$-OTf) sites and evenly distributed Pd NPs to realize highly effective tandem catalysis. At the same time, the pore restriction in the 1D channels of **1**-OTf-Pd^{NP} can prevent undesired dimerization and aromatization to improve product selectivity.

1,8-cinole was used as a model compound to optimize the reaction conditions for tandem C-O bond cleavage (**Table 7-1**). Initial screening of solvents revealed that 1,8-cinole could be quantitatively converted to menthane in 1,2-dichloroethane at 0.2 mol% loading of **1**-OTf-$PdCl_2$ [*w.r.t.* Lewis acidic $Al_2(\mu_2$-OTf) sites] and 100 °C under 20 bar of H_2 for 24 h. Nonpolar solvents such as octane and coordinating solvents such as THF gave lower catalytic performance, likely due to poor substrate solubility and poisoning of Lewis acidic metal sites, respectively. The highest TON of 800 was obtained when the catalyst loading was lowered to 0.1 mol%; this level of catalytic activity significantly outperformed previously reported catalytic systems. **1**-OTf-$PdCl_2$ is also advantageous to the well-studied homogeneous metal triflate plus supported Pd NP system by avoiding the use of substoichiometric amounts of expensive metal triflates such as $Hf(OTf)_4$, $Sc(OTf)_3$, and $Yb(OTf)_3$.

Table 7-1. Screening of reaction conditions for **1**-OTf-$PdCl_2$ catalyzed tandem etheric/alcohol C-O bond cleavage[a]

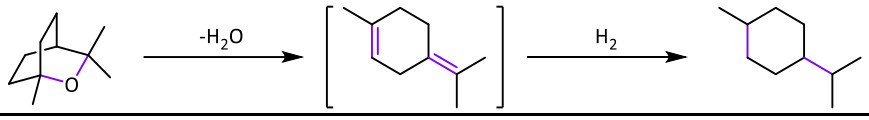

Entry	Catalyst (mol % Loading)	Solvent	Temp./ °C	Yield of menthane / %	TON
1	**1**-OTf-$PdCl_2$ (0.5%)	Octane	130	74	148
2	**1**-OTf-$PdCl_2$ (0.5%)	THF	130	31	62
3	**1**-OTf-$PdCl_2$ (0.1%)	neat	130	40	400
4	**1**-OTf-$PdCl_2$ (0.2%)	DCE	100	>99	>500
5	**1**-OTf-$PdCl_2$ (0.1%)	DCE	100	80	800
6	-	DCE	100	N.D.	-
7[b]	**1**-OTf (0.2 %)	DCE	100	<1	-
8[c]	**1**-OH-$PdCl_2$ (0.2 %)	DCE	100	22	110
9[d]	$Al(OTf)_3$ + Pd (0.2 %)	DCE	100	9	45
10[e]	HOTf + Pd (0.2 %)	DCE	100	3	15

[a]Reaction conditions: **1**-OTf-$PdCl_2$ (loading w.r.t. $Al_2(\mu_2$-OTf), 0.6 mmol 1,8-cineole, 20 bar H_2, 1 mL solvent or neat condition, 24 h; Yield of menthane was determined by GC-MS analysis. [b]Catalysts: 0.2 mol% of **1**-OTf. [c]Catalysts: 0.2 mol% of **1**-OH-$PdCl_2$ (w.r.t. $Al_2(OH)(OH_2)$). [d]Catalysts: 0.2 mol% of $Al(OTf)_3$ + 0.25 mol% $Pd(MeCN)_2Cl_2$. [e]Catalysts: 0.2 mol% of HOTf + 0.25 mol% $Pd(MeCN)_2Cl_2$.

Several control experiments were conducted to gain insights into the tandem catalytic pathway of **1**-OTf-$PdCl_2$ mediated C-O bond cleavage. In the absence of the MOF catalyst, 1,8-cinole was totally unreactive under the reaction condition (Entry 6, **Table 7-1**). At a loading of 0.2 mol% **1**-OTf, a negligible amount of menthane was detected (Entry 7, **Table 7-1**). The lack of activity of **1**-OTf is likely due to the unfavorable thermodynamics of the dehydroalkoxylation reaction. 0.2 mol% loading of **1**-OH-$PdCl_2$ gave a much lower menthane yield of 22% (Entry 8, **Table 7-1**), consistent with the much lower Lewis acidity of the $Al_2(OH)(OH_2)$ sites than the $Al_2(\mu_2\text{-OTf})$ sites. Under identical conditions, homogenous controls with $Al(OTf)_3$ plus $Pd(MeCN)_2Cl_2$ and HOTf plus $Pd(MeCN)_2Cl_2$ gave very low menthane yields of 9% and 3%, respectvely (Entries 9 and 10, **Table 7-1**). These results suggest that the C-O bond cleavage by **1**-OTf-$PdCl_2$ occurs in a tandem manner, where strong Lewis acidic $Al_2(\mu_2\text{-OTf})$ sites on the SBUs catalyze the dehydroalkoxylation of etheric/alcoholic C-O bonds to afford C=C bonds which are hydrogenated by nearby Pd NPs confined in the MOF channels. The hydrogenation reaction pushes the equilibrium to the right to form saturated hydrocarbons (**Figure 7-7a**).

We next examined the substrate scope of **1**-OTf-$PdCl_2$ catalyzed tandem etheric/alcoholic C-O bond cleavage. A broad scope of substrates including tertiary (3°), secondary (2°), and primary (1°) alcohols/ethers were readily converted to alkanes by **1**-OTf-$PdCl_2$ under similar conditions (**Table 7-2**). Quantitative conversion of 3° alcohol (1-methylcyclohexanol) and 3° ether (1,8-cineole) to saturated alkanes was achieved at 0.1-0.2 mol% loading of **1**-OTf-$PdCl_2$ and at 100 °C (Entries 1 and 2, **Table 7-2**). Reaction temperatures as high as 150 °C were needed to quantitatively convert 2° alcohols and ethers (cyclohexanol, 2-octanol, dicyclohexyl ether, and cyclohexyl phenyl ether) to corresponding saturated alkanes (Entries 4-7, **Table 7-2**). 1° alcohol (1-heptanol) required even higher reaction temperatures of up to 200 °C and 0.5 mol% loading of

1-OTf-$PdCl_2$ to afford heptane in 92% yield (Entry 8, **Table 7-2**). High product selectivity was observed for different kinds of substrates with **1**-OTf-$PdCl_2$ as the catalyst without detection of any undesired dimerization or aromatization product. The outstanding product selectivity of **1**-OTf-$PdCl_2$ is attributed to the pore size exclusion by the uniform MOF channels and well-defined, site-isolated Lewis acids and Pd NPs in the MOF. Notably, 1° ethers with active β-hydrogen atoms, i.e., phenethoxybenzene and (2-methoxyethyl)benzene, underwent C-O bond cleavage at 150 °C and 130 °C, respectively, to produce ethylbenzene as the main product with a high selectivity over the over-hydrogenated product methylcyclohexane.

Table 7-2. Substrate scope for **1**-OTf-$PdCl_2$ catalyzed tandem etheric/alcoholic C-O bond cleavage[a]

Entry	Substrate	Loading / Temp.	Product	Conversion (Yield/*isolated Yield*)[b]
1		0.1 mol% / 100 °C		100% (>99%/*89%*)
2		0.2 mol% / 100 °C	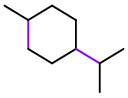	100% (>99%/*93%*)
3		0.1 mol% / 100 °C		80% (80%)
4	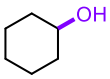	0.1 mol% / 150 °C		100% (>99%)
5	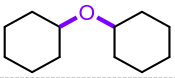	0.1 mol% / 150 °C		100% (97%)
6[c]	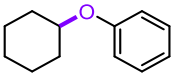	0.1 mol% / 150 °C		94% (89%)
7	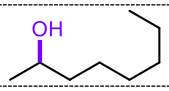	0.2 mol% / 150 °C	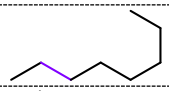	100% (>99%/*90%*)
8		0.2 mol% / 150 °C	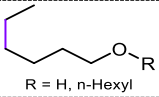 R = H, n-Hexyl	64% (55%) (alcohol : ether = 1 : 2)
9[d]	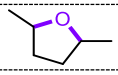	0.2 mol% / 150 °C	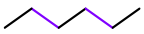	67% (67%)
10	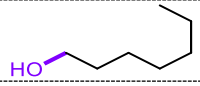	0.5 mol% / 200 °C	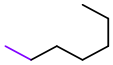	100% (92%/*78%*)
11[e,f]	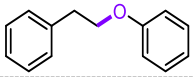	0.2 mol% / 150 °C		100% (89%)
12[e]	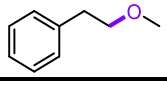	0.2 mol% / 130 °C		70% (61%/*55%*)

Table 7-2 (continued)**.** Substrate scope for **1**-OTf-$PdCl_2$ catalyzed tandem etheric/alcoholic C-O bond cleavage[a]

[a]Unless noted, all reactions performed with indicated amount of **1**-OTf- $PdCl_2$, 0.6 mmol of substrate, and 20 bar H_2 in 1.0 mL of 1,2-dichloroethane for 24 h. [b]Conversions and yields determined by GC-MS integrals with mesitylene as the internal standard. Isolated yield provided in the parenthesis if applied. [c]Phenol detected as cleavage by-product. [d]Reaction performed in 1,4-dichlorobutane. [e]Reaction performed in 1 bar H_2. [f]Phenol, cyclohexanone, and cyclohexane (1.5:1:1, mol ratio based on GC/MS) detected as cleavage by-product.

Several lines of evidence support the heterogeneity of **1**-OTf-$PdCl_2$ in tandem C-O bond cleavage reactions. The catalysts recovered from C-O bond cleavage reactions exhibited identical PXRD patterns to pristine **1**, indicating structural stability of **1**-OTf-$PdCl_2$ in catalytic reactions (**Figure 7-2c**). Lewis acidity quantification on the post-reaction MOF confirmed the maintenance of the Lewis acidity throughout the catalytic process. ICP-MS analysis showed minimal leaching of Al (0.6%) and Pd (0.02%) into the supernatant after the first reaction run, and ^{19}F NMR analysis further showed negligible amount of OTf leached into the supernatant after catalysis. "Hot filtration" test was also carried out to further exclude the possibility of soluble metal or acid species contributing to the catalytic performance. After the reaction was interrupted, the solution phase and the solid phase were separated and used, respectively, for another reaction run. The recovered solid retained the catalytic activity but the solution was totally inactive, proving the heterogeneity of **1**-OTf-$PdCl_2$. Impressively, **1**-OTf-$PdCl_2$ was readily recovered by simple centrifuged and reused for at least 5 times without significant drop in catalytic activity (**Figure 7-7b**). Moreover, ×20 times (~2 g scale) scale-up experiment was carried out for **1**-OTf-$PdCl_2$ catalyzed tandem C-O cleavage of 1,8-cinole under standard reaction conditions, which provided menthane in 75% of yield within 24 h. The excellent thermal stability and recyclability make **1**-OTf-$PdCl_2$ a potential candidate catalyst for practical tandem etheric/alcoholic C-O bond cleavage.

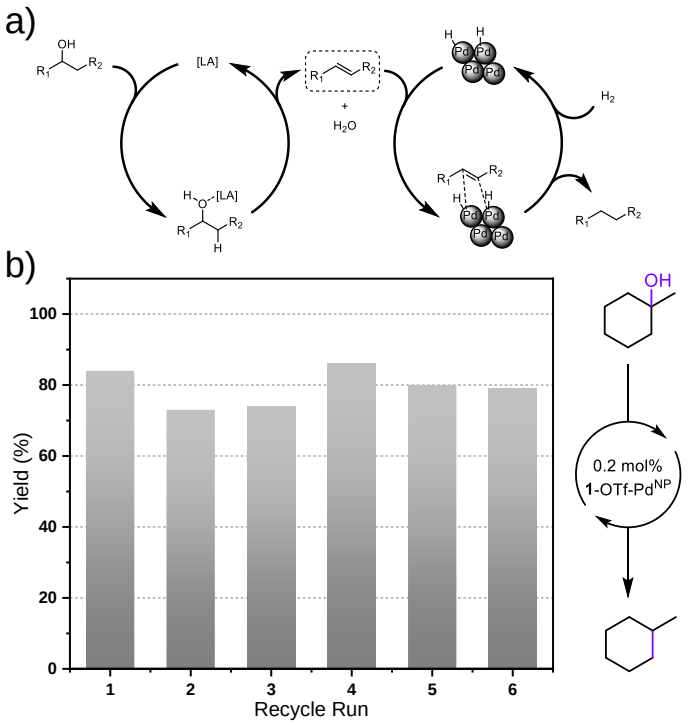

Figure 7-7. (a) Proposed tandem pathway for **1**-OTf-$PdCl_2$-mediated C-O bond cleavage. (b) Recycle experiments for **1**-OTf-$PdCl_2$ catalyzed C-O bond cleavage of 1-methylcyclohexanol. Plots of methylcyclohexane yields (%) in six consecutive runs with 3 h of reaction time. Copyright 2020 American Chemical Society.

7.2.5 1-OTf-$PdCl_2$ catalyzed tandem ester C-O bond cleavage

Ester groups also widely exist in bio-derived molecules such as triglycerides, fats, and oils, which provide a source of renewable diesel after their decarboxylation.[57-59] Traditional decarboxylation methods require high temperatures of up to 500 °C to thermally crack the C-O bond followed by CO_2 release.[60-61] Metal triflates plus Pd/C have recently been used to catalyze tandem ester C-O bond cleavage with moderate to good selectivities and yields.[20]

1-OTf-$PdCl_2$ was also proved highly active for tandem ester C-O bond cleavage with a reactivity trend of 3° carbon > 2° carbon > 1° carbon (**Table 7-3**). The 3° ester terpinyl acetate was effectively cleaved to produce menthane at 0.2 mol% loading of **1**-OTf-$PdCl_2$ at 100 °C, affording a TON of 440 (Entry 1, **Table 7-3**). The 2° ester L-menthyI acetate was decarboxylated

in the presence of 0.5 mol% **1**-OTf-$PdCl_2$ at 150 °C to afford menthane in quantitative yield (Entry 2, **Table 7-3**). Other 2° acetate or propionate esters, i.e., cyclohexyl acetate, and cyclohexyl propionate, readily underwent C-O cleavage at 0.5 mol% **1**-OTf-$PdCl_2$ at 150 °C to afford decarboxylated products in 62 to 84% yields (Entries 4 and 5, **Table 7-3**). For the 1° ester octyl acetate, a higher temperate of 200 °C was needed to afford octane in 79% yield (Entry 6, **Table 7-3**). Interestingly, 1° ester with active β-hydrogen atoms, *i.e.*, phenethyl acetate, readily underwent C-O cleavage at 0.2 mol% loading of **1**-OTf-$PdCl_2$ and 130 °C to afford ethylbenzene in 94% yield (Entry 7, **Table 7-3**). Moreover, the lactone·5-hexanolide also underwent tandem C-O cleavage to generate the saturated carboxylic acid (hexanoic acid) in 61% yield (Entry 8, **Table 7-3**). Such MOF-based tandem system thus provided a potent solution for cleavage of esteric C-O bonds.

Table 7-3. Substrate scope for **1**-OTf-$PdCl_2$ catalyzed ester C-O bond cleavage[a]

Entry	Substrate	Loading / Temp.	Product	Conversion (Yield/*isolated Yield*)[b]
1[c]	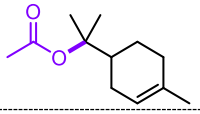	0.2 mol% / 100 °C	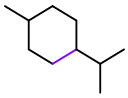	100% (88%)
2	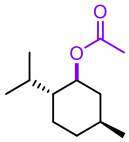	0.5 mol% / 150 °C	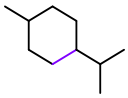	100% (>99%/*95%*)
3		0.1 mol% / 150 °C		45% (45%)
4[c]	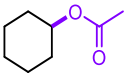	0.5 mol% / 150 °C		91% (84%)
5[c]	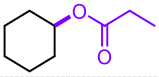	0.5 mol% / 150 °C		87% (62%)
6	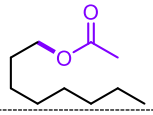	0.5 mol% / 200 °C	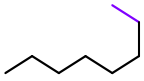	100% (79%)
7[d]	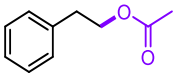	0.2 mol% / 130 °C	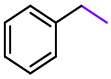	100% (94%/*90%*)
8	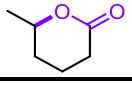	0.2 mol% / 130 °C	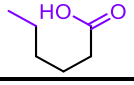	100% (61%/*55%*)

[a]Unless noted, all reactions performed with indicated amount of **1**-OTf-$PdCl_2$, 0.6 mmol of substrate, and 20 bar H_2 in 1.0 mL of 1,2-dichloroethane for 24 h. [b]Conversions and yields determined by GC-MS with mesitylene as the internal standard. Isolated yield provided in the parenthesis if applied. [c]Reaction performed for 36 h. [d]Reaction performed in 1 bar H_2 for 6 h.

7.3 Conclusion

In this work, we demonstrated hierarchical installation of orthogonal Lewis acid and Pd NP catalysts on a mixed-ligand MOF via multi-step sequential transformations. The pdac ligands in **1** were first removed via ozonolysis to generate $Al_2(OH)(OH_2)$ defect sites in the infinite chain-like $[Al(\mu_2\text{-}OH)]_n$ SBUs of **1**, which were subsequently triflated to afford the strongly Lewis acidic MOF **1**-OTf. Coordination of dcbpy ligands in **1**-OTf with $Pd(MeCN)_2Cl_2$ followed *in situ* H_2 reduction afforded multi-catalytic MOF **1**-OTf-Pd^{NP} for tandem dehydroalkoxylation-hydrogenation of etheric, alcoholic, and esteric C-O bonds to generate saturated alkanes under relatively mild conditions. **1**-OTf-Pd^{NP} exhibit C-O bond cleavage activity trend of tertiary carbon > secondary carbon > primary carbon and could be readily reused via simple solid separation. **1**-OTf-Pd^{NP} showed superior catalytic activity over the homogeneous counterparts owing to hierarchical incorporation of orthogonal Lewis acid and Pd NP active sites. Our work shows the potential of sequential engineering of multiple catalytic sites in MOFs in addressing outstanding challenges in sustainable catalysis.

7.4 Experimental Section

7.4.1 Materials and methods

All the reactions and manipulations were carried out under N_2 with the use of a glovebox or Schlenk technique, unless otherwise indicated. Tetrahydrofuran and toluene were purified by passing through a neutral alumina column under N_2. Benzene, d_6-benzene, and *n*-octane were distilled over CaH_2. Substrates including alcohols, ethers and esters were purchased from Fisher or Aldrich, and dried over freshly activated 4Å molecular sieves and degassed by freeze-pump-thaw methods before storage in a glovebox for further use.

PXRD data was collected on a Bruker D8 Venture diffractometer using Cu Kα radiation source (λ = 1.54178 Å). N_2 sorption experiments were performed on a Micrometrics TriStar II 3020 instrument. TGA was performed in air using a Shimazu TGA-50 equipped with a platinum pan and heated at a rate of 1.5 °C per min. FT-IR spectra were collected using a Nexus 870 spectrometer (Thermo Nicolet) installed with DRIFTS system. TEM images were taken on a TECNAI F30 HRTEM. SEM images were take on the Carl Zeiss Merlin, with the detectors of In-Lens, EsB, AsB, & SE2. Ozonolysis was performed on an Azcozon RMU-DG3 ozone generator, which produces up to ~0.42 mol/h ozone at a 6 L/min O_2 gas flow rate. ICP-MS data was obtained with an Agilent 7700x ICP-MS and analyzed using ICP-MS MassHunter version B01.03. Samples were diluted in a 2% HNO_3 matrix and analyzed with a ^{159}Tb internal standard against a 12-point standard curve over the range from 0.1 ppb to 500 ppb. The correlation was >0.9997 for all analyses of interest. Data collection was performed in Spectrum Mode with five replicates per sample and 100 sweeps per replicate. EPR spectra were recorded on a Bruker Elexsys 500 X-band EPR spectrometer under irradiation of a white-light lamp (Fiber-Lite MI-150) by focusing the lamp on the sample cell in the ESR cavity at 15 K. Fluorescence measurement was performed using a Shimazu RF-5301PC spectrofluorophotometer.

^{1}H NMR spectra were recorded on a Bruker NMR 500 DRX spectrometer at 500 MHz and referenced to the proton resonance resulting from incomplete deuteration of $CDCl_3$ (δ 7.26), DMSO-d_6 (δ 2.50), or C_6D_6 (δ 7.16). The following abbreviations are used herein: s: singlet, d: doublet, t: triplet, q: quartet, m: multiplet, br: broad, app: apparent. The conversions of reactions were determined by gas chromatography-mass spectrometry (GC-MS) using a Shimadzu GCMS-QP2010 Ulta equipped with SH-Rxi-5Sil MS 30 m × 0.5 mm × 0.25 μm column.

7.4.2 Synthetic procedures of MOF catalysts

Synthesis of MOF **1**: The synthetic procedure was based on literature reports for DUT-5 and MOF-253.[37-38] In a typical synthesis, 2,2'-bipyridine-5,5'-dicarboxylic acid (dcbpy, 19.5 mg, 0.08 mmol) and 1,4-benzenediacrylic acid (pdac, 4.4 mg, 0.02 mmol) were dissolved in 3 mL DMF. $Al(NO_3)_3 \cdot 9H_2O$ (52 mg, 0.14 mmol) was added. The mixture was transferred to an 8-mL vial and heated at 120 °C for 12 h under stirring. After cooling to room temperature, the white solid was recovered by centrifugation and then sequentially washed with DMF three times, THF three times, and benzene three times. This solid was then freeze-dried in benzene. After that, the white powder was further heated at 100 °C under vacuum to remove the trapped solvents in the pores.

Synthesis of MOF **1**-OH: To ensure a continuous flow of ozone through the sample, we first mixed **1** (200 mg) with 2 g Ottawa sand (20-30 mesh) to improve O_3 permeability. We then pack the solid mixture into a thin glass column, which was later connected to the ozonator with a gas flow. The excess O_3 was quenched by KI aqueous solution. The reaction was run at room temperature for 15 min to ensure complete cleavage of pdac ligands. The resulted sample was washed with DMF/HCl (1M) (10:1, *v*:*v*) three times to remove the organic and inorganic fragments trapped in the pores of ozonized **1**, and washed with THF three times and benzene three times, followed by freeze-drying in benzene, and stored in a glovebox for further use.

Synthesis of MOF **1**-OTf: In a N_2-filled glovebox, **1**-OH (0.10 mmol of -OH/OH_2) was weighed out in a 20 mL glass vial and dispersed in 10 mL of benzene. Trimethylsilyl trifluoromethanesulfonate (TMSOTf, 0.18 mL, 1.0 mmol) was then added slowly to the suspension. The vessel was sealed with a Teflon cap and stir at room temperature for 12 h. The suspension was then washed with dry toluene 5 times. The resultant MOF was further extracted with hexane in a Soxhlet extractor to remove the trapped HOTf inside the MOF channels. 10 equiv. of $LiCH_2SiMe_3$

was added to the receiving flask to quench extracted HOTf during the Soxhlet extraction.[44] After solvent exchange with dry benzene, **1**-OTf was freeze-dried under vacuum overnight and stored inside a glovebox for further use.

Synthesis of **1**-OTf-$PdCl_2$: In a N_2-filled glovebox, **1**-OTf (0.2 mmol of bpy) was weighed out in a 20 mL glass vial. 10 mL of $Pd(MeCN)_2Cl_2$ solution in THF (20 mM) was then added. The mixture was stirred at room temperature for 12 h. The brown solid was then centrifuged and washed with THF three times and benzene three times. **1**-OTf-$PdCl_2$ was then freeze-dried in benzene and stored in a glovebox for further use. ICP-MS analysis showed a Al/Pd molar ratio of 2.10, indicating ~60% of dcbpy ligands were metalated.

7.4.3 Catalytic reaction setup and product characterization

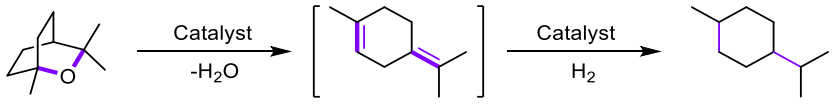

Typical procedure of **1**-OTf-$PdCl_2$ catalyzed tandem ether/alcohol C-O bond cleavage: In a nitrogen-filled glovebox, **1**-OTf-$PdCl_2$ (2.0 mg, 1.2 μmol $Al_2(\mu_2$-OTf) sites), 1,8-cineole (100 μL, 0.6 mmol), and1.0 mL of 1,2-dichloroethane were transferred to a Parr reactor to make an even suspension. The Parr reactor was then sealed under nitrogen, purged with hydrogen several times and charged with hydrogen to 20 bar. After stirring at 100 °C for 24 hours, the pressure was released, and the MOF catalyst was removed from the reaction mixture via centrifugation. The supernatant was analyzed by GC-MS to give menthane (a mixture of cis/trans isomers) in >99% yield with 100% conversion of 1,8-cineole. After one reaction run, ICP-MS analysis showed the leaching of 0.6% Al and 0.02% Pd into the solution.

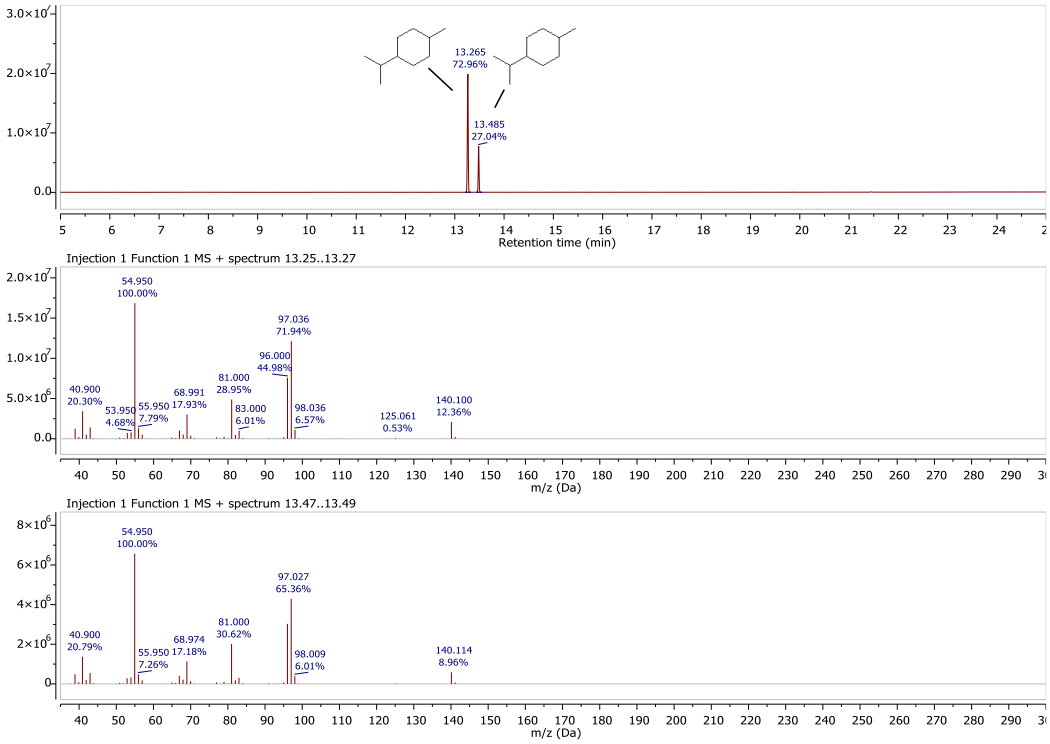

Figure 7-8. GC-MS spectrum of **1**-OTf-$PdCl_2$ catalyzed tandem ether/alcohol C-O bond cleavage of 1,8-cineole (The two MS spectra correspond to the cis/trans isomer of menthane).

Table 7-4. The retention times of GC traces for C-O cleavage products of ethers and alcohols (some compounds have multiple stereoisomers, thus showing more than one peak with the expected molecular mass).

Compound	Retention Time	Compound	Retention Time
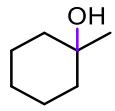	11.488 min	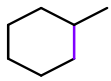	4.646 min
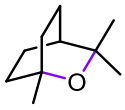	14.064 min	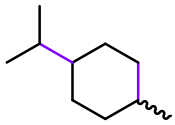	13.255 min (trans) 13.474 min (cis)
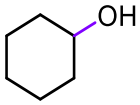	11.058 min		3.135 min
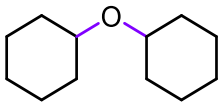	17.050 min		3.115 min

Table 7-4 (continued)**.** The retention times of GC traces for C-O cleavage products of ethers and alcohols.

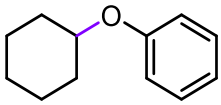	17.600 min		3.115 min
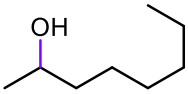	N.D.	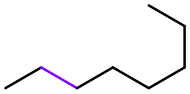	7.632 min
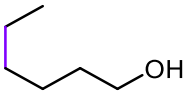	10.453 min	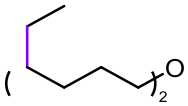	16.365 min
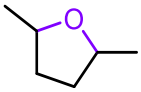	3.885 min 4.170 min		2.273 min
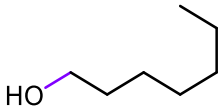	13.134 min	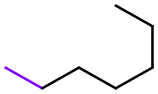	3.934 min
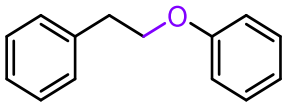	19.163 min	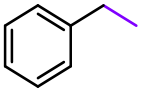	9.977 min
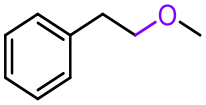	14.656 min	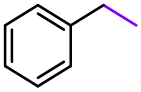	9.966 min
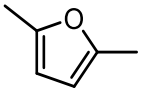	4.047 min	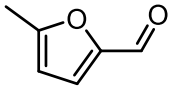	12.896 min

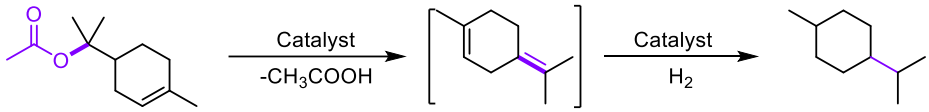

Typical procedure of **1**-OTf-$PdCl_2$ catalyzed tandem ester C-O bond cleavage: In a N_2-filled glovebox, **1**-OTf-$PdCl_2$ (5.0 mg, 3.0 μmol $Al_2(\mu_2$-OTf) sites), terpinyl acetate (123 μL, 0.6 mmol), and 1.0 mL of 1,2-dichloroethane was transferred to a Parr reactor to make an even suspension. The Parr reactor was then sealed under nitrogen, purged with hydrogen several times

and charged with hydrogen to 20 bar. After stirring at 100 °C for 24 hours, the pressure was released, and the MOF catalyst was removed from the reaction mixture via centrifugation. The supernatant was analyzed by GC-MS to give menthane (a mixture of cis/trans isomers) in 88% yield with 100% substrate conversion. After one reaction run, 0.6% of Al and 0.15% of Pd are detected in the solution by ICP-MS analysis.

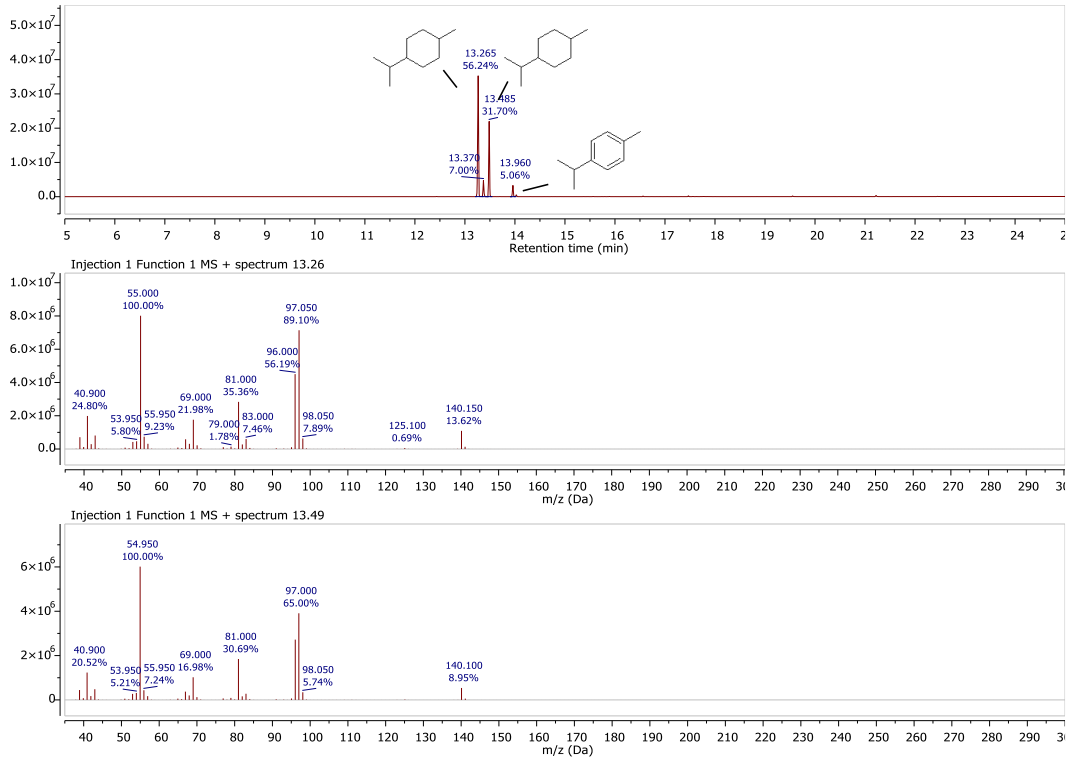

Figure 7-9. GC-MS spectra of **1**-OTf-$PdCl_2$ catalyzed tandem ester C-O bond cleavage of terpinyl acetate (The two MS spectra correspond to the cis/trans isomers of menthane).

Table 7-5. The retention times of GC traces for ester C-O cleavage products (some compounds have multiple stereoisomers, thus showing more than one peak with the expected molecular mass).

Compound	Retention Time	Compound	Retention Time
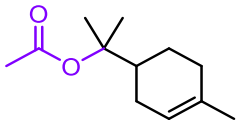	N.D.	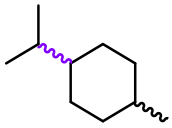	13.265 min (trans) 13.485 min (cis)
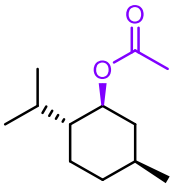	16.569 min	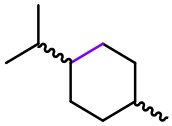	13.253 min (trans) 13.475 min (cis)
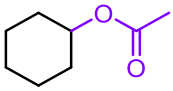	14.157 min		3.140 min
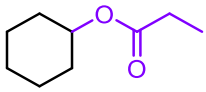	15.212 min		3.141 min
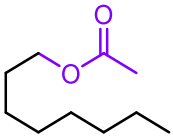	15.874 min	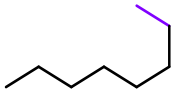	7.612 min
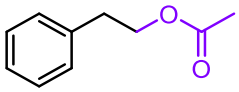	16.288 min	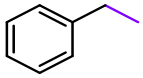	9.986 min
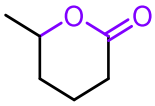	14.756 min	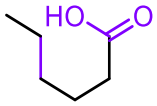	13.538 min

7.5 References

1. Azadi, P.; Inderwildi, O. R.; Farnood, R.; King, D. A., Liquid fuels, hydrogen and chemicals from lignin: A critical review. *Renewable and Sustainable Energy Reviews* **2013,** *21*, 506-523.

2. Ragauskas, A. J.; Beckham, G. T.; Biddy, M. J.; Chandra, R.; Chen, F.; Davis, M. F.; Davison, B. H.; Dixon, R. A.; Gilna, P.; Keller, M.; Langan, P.; Naskar, A. K.; Saddler, J. N.; Tschaplinski, T. J.; Tuskan, G. A.; Wyman, C. E., Lignin Valorization: Improving Lignin Processing in the Biorefinery. *Science* **2014,** *344* (6185), 1246843.

3. Corma, A.; Iborra, S.; Velty, A., Chemical Routes for the Transformation of Biomass into Chemicals. *Chemical Reviews* **2007,** *107* (6), 2411-2502.

4. Sheldon, R. A., Utilisation of biomass for sustainable fuels and chemicals: Molecules, methods and metrics. *Catalysis Today* **2011,** *167* (1), 3-13.

5. Tuck, C. O.; Pérez, E.; Horváth, I. T.; Sheldon, R. A.; Poliakoff, M., Valorization of Biomass: Deriving More Value from Waste. *Science* **2012,** *337* (6095), 695.

6. Ragauskas, A. J.; Williams, C. K.; Davison, B. H.; Britovsek, G.; Cairney, J.; Eckert, C. A.; Frederick, W. J.; Hallett, J. P.; Leak, D. J.; Liotta, C. L.; Mielenz, J. R.; Murphy, R.; Templer, R.; Tschaplinski, T., The Path Forward for Biofuels and Biomaterials. *Science* **2006,** *311* (5760), 484.

7. Swain, P. K.; Das, L. M.; Naik, S. N., Biomass to liquid: A prospective challenge to research and development in 21st century. *Renewable and Sustainable Energy Reviews* **2011,** *15* (9), 4917-4933.

8. Bruijnincx, P. C. A.; Weckhuysen, B. M., Lignin up for break-down. *Nature Chemistry* **2014,** *6* (12), 1035-1036.

9. Xie, H.; Gathergood, N., *The role of green chemistry in biomass processing and conversion*. Wiley Online Library: 2013.

10. Sergeev, A. G.; Hartwig, J. F., Selective, Nickel-Catalyzed Hydrogenolysis of Aryl Ethers. *Science* **2011,** *332* (6028), 439.

11. He, J.; Zhao, C.; Lercher, J. A., Ni-Catalyzed Cleavage of Aryl Ethers in the Aqueous Phase. *Journal of the American Chemical Society* **2012,** *134* (51), 20768-20775.

12. Zhang, J.; Teo, J.; Chen, X.; Asakura, H.; Tanaka, T.; Teramura, K.; Yan, N., A Series of NiM (M = Ru, Rh, and Pd) Bimetallic Catalysts for Effective Lignin Hydrogenolysis in Water. *ACS Catalysis* **2014,** *4* (5), 1574-1583.

13. Molinari, V.; Giordano, C.; Antonietti, M.; Esposito, D., Titanium Nitride-Nickel Nanocomposite as Heterogeneous Catalyst for the Hydrogenolysis of Aryl Ethers. *Journal of the American Chemical Society* **2014,** *136* (5), 1758-1761.

14. Zaheer, M.; Hermannsdörfer, J.; Kretschmer, W. P.; Motz, G.; Kempe, R., Robust Heterogeneous Nickel Catalysts with Tailored Porosity for the Selective Hydrogenolysis of Aryl Ethers. *ChemCatChem* **2014,** *6* (1), 91-95.

15. Huang, H.; Denard, C. A.; Alamillo, R.; Crisci, A. J.; Miao, Y.; Dumesic, J. A.; Scott, S. L.; Zhao, H., Tandem Catalytic Conversion of Glucose to 5-Hydroxymethylfurfural with an Immobilized Enzyme and a Solid Acid. *ACS Catalysis* **2014,** *4* (7), 2165-2168.

16. Orazov, M.; Davis, M. E., Tandem catalysis for the production of alkyl lactates from ketohexoses at moderate temperatures. *Proceedings of the National Academy of Sciences* **2015,** *112* (38), 11777.

17. Yang, X.; Li, T.; Tang, K.; Zhou, X.; Lu, M.; Ounkham, W. L.; Spain, S. M.; Frost, B. J.; Lin, H., Highly efficient conversion of terpenoid biomass to jet-fuel range cycloalkanes in a biphasic tandem catalytic process. *Green Chemistry* **2017,** *19* (15), 3566-3573.

18. Atesin, A. C.; Ray, N. A.; Stair, P. C.; Marks, T. J., Etheric C–O Bond Hydrogenolysis Using a Tandem Lanthanide Triflate/Supported Palladium Nanoparticle Catalyst System. *Journal of the American Chemical Society* **2012,** *134* (36), 14682-14685.

19. Li, Z.; Assary, R. S.; Atesin, A. C.; Curtiss, L. A.; Marks, T. J., Rapid Ether and Alcohol C–O Bond Hydrogenolysis Catalyzed by Tandem High-Valent Metal Triflate + Supported Pd Catalysts. *Journal of the American Chemical Society* **2014,** *136* (1), 104-107.

20. Lohr, T. L.; Li, Z.; Marks, T. J., Selective Ether/Ester C–O Cleavage of an Acetylated Lignin Model via Tandem Catalysis. *ACS Catalysis* **2015,** *5* (11), 7004-7007.

21. Assary, R. S.; Atesin, A. C.; Li, Z.; Curtiss, L. A.; Marks, T. J., Reaction Pathways and Energetics of Etheric C–O Bond Cleavage Catalyzed by Lanthanide Triflates. *ACS Catalysis* **2013,** *3* (9), 1908-1914.

22. Cui, M.; Qian, Q.; He, Z.; Zhang, Z.; Ma, J.; Wu, T.; Yang, G.; Han, B., Bromide promoted hydrogenation of CO2 to higher alcohols using Ru–Co homogeneous catalyst. *Chemical Science* **2016,** *7* (8), 5200-5205.

23. Li, R.; Zhou, Y.; Xu, X.; Dong, G., Direct Vicinal Difunctionalization of Thiophenes Enabled by the Palladium/Norbornene Cooperative Catalysis. *Journal of the American Chemical Society* **2019,** *141* (48), 18958-18963.

24. Lee, J.; Farha, O. K.; Roberts, J.; Scheidt, K. A.; Nguyen, S. T.; Hupp, J. T., Metal–organic framework materials as catalysts. *Chemical Society Reviews* **2009,** *38* (5), 1450-1459.

25. Yoon, M.; Srirambalaji, R.; Kim, K., Homochiral Metal–Organic Frameworks for Asymmetric Heterogeneous Catalysis. *Chemical Reviews* **2012,** *112* (2), 1196-1231.

26. Jiao, L.; Wang, Y.; Jiang, H.-L.; Xu, Q., Metal–Organic Frameworks as Platforms for Catalytic Applications. *Advanced Materials* **2018,** *30* (37), 1703663.

27. Cohen, S. M., Postsynthetic Methods for the Functionalization of Metal–Organic Frameworks. *Chemical Reviews* **2012,** *112* (2), 970-1000.

28. Zhao, M.; Ou, S.; Wu, C.-D., Porous Metal–Organic Frameworks for Heterogeneous Biomimetic Catalysis. *Accounts of Chemical Research* **2014,** *47* (4), 1199-1207.

29. Na, K.; Choi, K. M.; Yaghi, O. M.; Somorjai, G. A., Metal Nanocrystals Embedded in Single Nanocrystals of MOFs Give Unusual Selectivity as Heterogeneous Catalysts. *Nano Letters* **2014,** *14* (10), 5979-5983.

30. Li, X.; Goh, T. W.; Li, L.; Xiao, C.; Guo, Z.; Zeng, X. C.; Huang, W., Controlling Catalytic Properties of Pd Nanoclusters through Their Chemical Environment at the Atomic Level Using Isoreticular Metal–Organic Frameworks. *ACS Catalysis* **2016,** *6* (6), 3461-3468.

31. Nguyen, H. G. T.; Schweitzer, N. M.; Chang, C.-Y.; Drake, T. L.; So, M. C.; Stair, P. C.; Farha, O. K.; Hupp, J. T.; Nguyen, S. T., Vanadium-Node-Functionalized UiO-66: A Thermally Stable MOF-Supported Catalyst for the Gas-Phase Oxidative Dehydrogenation of Cyclohexene. *ACS Catalysis* **2014,** *4* (8), 2496-2500.

32. Comito, R. J.; Fritzsching, K. J.; Sundell, B. J.; Schmidt-Rohr, K.; Dincă, M., Single-Site Heterogeneous Catalysts for Olefin Polymerization Enabled by Cation Exchange in a Metal-Organic Framework. *Journal of the American Chemical Society* **2016,** *138* (32), 10232-10237.

33. Manna, K.; Ji, P.; Lin, Z.; Greene, F. X.; Urban, A.; Thacker, N. C.; Lin, W., Chemoselective single-site Earth-abundant metal catalysts at metal–organic framework nodes. *Nature Communications* **2016,** *7*, 12610.

34. Pan, Y.; Yuan, B.; Li, Y.; He, D., Multifunctional catalysis by Pd@MIL-101: one-step synthesis of methyl isobutyl ketone over palladium nanoparticles deposited on a metal–organic framework. *Chemical Communications* **2010,** *46* (13), 2280-2282.

35. Park, J.; Li, J.-R.; Chen, Y.-P.; Yu, J.; Yakovenko, A. A.; Wang, Z. U.; Sun, L.-B.; Balbuena, P. B.; Zhou, H.-C., A versatile metal–organic framework for carbon dioxide capture and cooperative catalysis. *Chemical Communications* **2012,** *48* (80), 9995-9997.

36. Huang, Y.-B.; Liang, J.; Wang, X.-S.; Cao, R., Multifunctional metal–organic framework catalysts: synergistic catalysis and tandem reactions. *Chemical Society Reviews* **2017,** *46* (1), 126-157.

37. Senkovska, I.; Hoffmann, F.; Fröba, M.; Getzschmann, J.; Böhlmann, W.; Kaskel, S., New highly porous aluminium based metal-organic frameworks: Al(OH)(ndc) (ndc=2,6-naphthalene dicarboxylate) and Al(OH)(bpdc) (bpdc=4,4 ′ -biphenyl dicarboxylate). *Microporous and Mesoporous Materials* **2009,** *122* (1), 93-98.

38. Bloch, E. D.; Britt, D.; Lee, C.; Doonan, C. J.; Uribe-Romo, F. J.; Furukawa, H.; Long, J. R.; Yaghi, O. M., Metal Insertion in a Microporous Metal−Organic Framework Lined with 2,2′-Bipyridine. *Journal of the American Chemical Society* **2010,** *132* (41), 14382-14384.

39. Kim, Y.; Yang, T.; Yun, G.; Ghasemian, M. B.; Koo, J.; Lee, E.; Cho, S. J.; Kim, K., Hydrolytic Transformation of Microporous Metal–Organic Frameworks to Hierarchical Micro- and Mesoporous MOFs. *Angewandte Chemie International Edition* **2015,** *54* (45), 13273-13278.

40. Feng, L.; Yuan, S.; Zhang, L.-L.; Tan, K.; Li, J.-L.; Kirchon, A.; Liu, L.-M.; Zhang, P.; Han, Y.; Chabal, Y. J.; Zhou, H.-C., Creating Hierarchical Pores by Controlled Linker Thermolysis

in Multivariate Metal–Organic Frameworks. *Journal of the American Chemical Society* **2018,** *140* (6), 2363-2372.

41. Guillerm, V.; Xu, H.; Albalad, J.; Imaz, I.; Maspoch, D., Postsynthetic Selective Ligand Cleavage by Solid–Gas Phase Ozonolysis Fuses Micropores into Mesopores in Metal–Organic Frameworks. *Journal of the American Chemical Society* **2018,** *140* (44), 15022-15030.

42. Horike, S.; Dincă, M.; Tamaki, K.; Long, J. R., Size-Selective Lewis Acid Catalysis in a Microporous Metal-Organic Framework with Exposed Mn2+ Coordination Sites. *Journal of the American Chemical Society* **2008,** *130* (18), 5854-5855.

43. Vermoortele, F.; Vandichel, M.; Van de Voorde, B.; Ameloot, R.; Waroquier, M.; Van Speybroeck, V.; De Vos, D. E., Electronic Effects of Linker Substitution on Lewis Acid Catalysis with Metal–Organic Frameworks. *Angewandte Chemie International Edition* **2012,** *51* (20), 4887-4890.

44. Ji, P.; Feng, X.; Oliveres, P.; Li, Z.; Murakami, A.; Wang, C.; Lin, W., Strongly Lewis Acidic Metal–Organic Frameworks for Continuous Flow Catalysis. *Journal of the American Chemical Society* **2019,** *141* (37), 14878-14888.

45. Copéret, C., Surface and Interfacial Chemistry. *CHIMIA International Journal for Chemistry* **2012,** *66* (3), 125-129.

46. Feng, X.; Ji, P.; Li, Z.; Drake, T.; Oliveres, P.; Chen, E. Y.; Song, Y.; Wang, C.; Lin, W., Aluminum Hydroxide Secondary Building Units in a Metal–Organic Framework Support Earth-Abundant Metal Catalysts for Broad-Scope Organic Transformations. *ACS Catalysis* **2019,** *9* (4), 3327-3337.

47. Ji, P.; Drake, T.; Murakami, A.; Oliveres, P.; Skone, J. H.; Lin, W., Tuning Lewis Acidity of Metal–Organic Frameworks via Perfluorination of Bridging Ligands: Spectroscopic, Theoretical, and Catalytic Studies. *Journal of the American Chemical Society* **2018,** *140* (33), 10553-10561.

48. Sobańska, K.; Krasowska, A.; Mazur, T.; Podolska-Serafin, K.; Pietrzyk, P.; Sojka, Z., Diagnostic Features of EPR Spectra of Superoxide Intermediates on Catalytic Surfaces and Molecular Interpretation of Their g and A Tensors. *Topics in Catalysis* **2015,** *58* (12), 796-810.

49. Ohkubo, K.; Menon, S. C.; Orita, A.; Otera, J.; Fukuzumi, S., Quantitative Evaluation of Lewis Acidity of Metal Ions with Different Ligands and Counterions in Relation to the Promoting Effects of Lewis Acids on Electron Transfer Reduction of Oxygen. *The Journal of Organic Chemistry* **2003,** *68* (12), 4720-4726.

50. Jack, L.; Yellowlees, L. J.; Parsons, S., CCDC 660772: Experimental Crystal Structure Determination. Cambridge Crystallographic Data Centre: 2008.

51. Gallezot, P., Conversion of biomass to selected chemical products. *Chemical Society Reviews* **2012,** *41* (4), 1538-1558.

52. Ruppert, A. M.; Weinberg, K.; Palkovits, R., Hydrogenolysis Goes Bio: From Carbohydrates and Sugar Alcohols to Platform Chemicals. *Angewandte Chemie International Edition* **2012,** *51* (11), 2564-2601.

53. Lohr, T. L.; Li, Z.; Marks, T. J., Thermodynamic Strategies for C–O Bond Formation and Cleavage via Tandem Catalysis. *Accounts of Chemical Research* **2016,** *49* (5), 824-834.

54. Dzudza, A.; Marks, T. J., Efficient Intramolecular Hydroalkoxylation/Cyclization of Unactivated Alkenols Mediated by Lanthanide Triflate Ionic Liquids. *Organic Letters* **2009,** *11* (7), 1523-1526.

55. Zhao, C.; Kou, Y.; Lemonidou, A. A.; Li, X.; Lercher, J. A., Highly Selective Catalytic Conversion of Phenolic Bio-Oil to Alkanes. *Angewandte Chemie International Edition* **2009,** *48* (22), 3987-3990.

56. Alonso, D. M.; Wettstein, S. G.; Dumesic, J. A., Bimetallic catalysts for upgrading of biomass to fuels and chemicals. *Chemical Society Reviews* **2012,** *41* (24), 8075-8098.

57. Olson, E. S.; Aulich, T. R.; Sharma, R. K.; Timpe, R. C., Ester fuels and chemicals from biomass. *Applied Biochemistry and Biotechnology* **2003,** *108* (1), 843-851.

58. Shahid, E. M.; Jamal, Y., Production of biodiesel: A technical review. *Renewable and Sustainable Energy Reviews* **2011,** *15* (9), 4732-4745.

59. Borugadda, V. B.; Goud, V. V., Biodiesel production from renewable feedstocks: Status and opportunities. *Renewable and Sustainable Energy Reviews* **2012,** *16* (7), 4763-4784.

60. Lestari , S.; Mäki-Arvela, P.; Beltramini, J.; Lu, G. Q. M.; Murzin, D. Y., Transforming Triglycerides and Fatty Acids into Biofuels. *ChemSusChem* **2009,** *2* (12), 1109-1119.

61. Gosselink, R. W.; Hollak, S. A. W.; Chang, S.-W.; van Haveren, J.; de Jong, K. P.; Bitter, J. H.; van Es, D. S., Reaction Pathways for the Deoxygenation of Vegetable Oils and Related Model Compounds. *ChemSusChem* **2013,** *6* (9), 1576-1594.

Chapter 8. MOFs Significantly Enhance Photocatalytic Hydrogen Evolution and Carbon Dioxide Reduction with Cu Photosensitizers

8.1 Introduction

Transition metal complexes have been used as effective light-harvesting components for the conversion of solar energy to electricity or chemical fuels by forming long-lived charge-separated excited states.[1-2] In particular, Ru- and Ir-polypyridyl complexes have served as excellent photosensitizers (PSs),[3-4] but their practical applications are limited by the extremely low crust abundance, steep costs, and high toxicity of Ru and Ir (**Figure 8-1a**). In the past decade, alternative PSs based on Earth-abundant elements (such as Cu^{I} complexes, **Figure 8-1a**) have been developed[5-7] and exhibit photosensitizing potential in hydrogen evolution reaction (HER),[8-9] dye sensitized solar cells,[10] and organic photocatalysis.[11-12] However, the performance of cuprous PSs (Cu-PSs) is suboptimal and inferior to Ru and Ir PSs owing to the relatively labile Cu^{I}-ligand bonds and the undesirable solvent-assisted quenching of the flattened excited state.[7, 13] It is thus of fundamental interest to develop novel strategies to enhance the photosensitizing performance of Cu-PSs.

As a novel class of structurally-defined porous molecular materials, MOFs have recently been shown to stabilize solution-inaccessible metal active sites for catalytic reactions.[14-15] Synthetic tunability of MOFs has also allowed hierarchical incorporation of multiple functionalities for synergistic reactions[16-18] or to facilitate energy and electron transfers.[19-22] In particular, MOFs built from Ru and Ir PSs have afforded outstanding performance in solar energy conversions.[23-26] We surmise that MOFs can be used to enhance the performance of Cu-PSs in

solar energy conversion by stabilizing the PSs and promoting electron transfer between PSs and active catalysts.

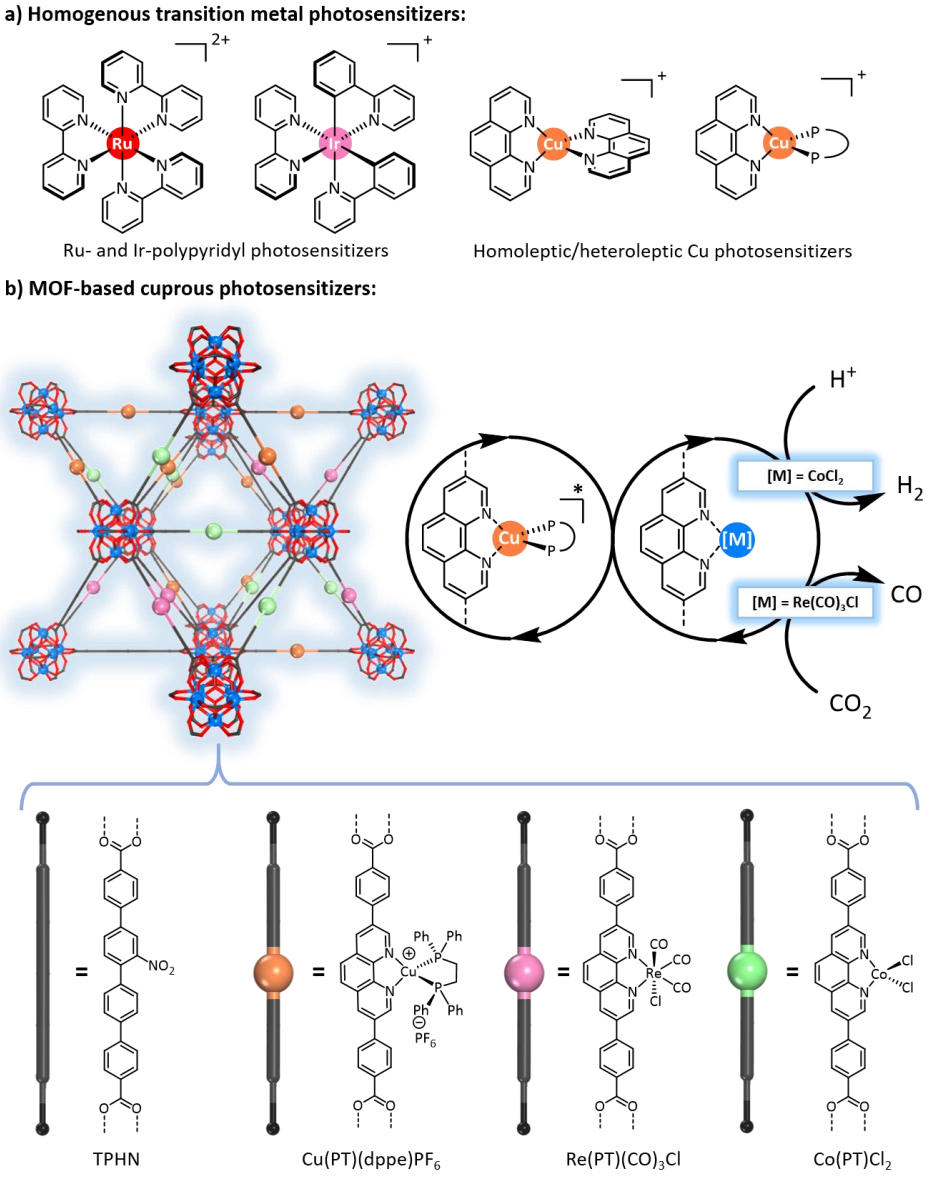

Figure 8-1. (a) Molecular structures of transition metal photosensitizers. (b) Framework structures and bridging ligands of **mPT-Cu/Co** and **mPT-Cu/Re** MOFs. The proximity between Cu-PSs and molecular Co/Re catalysts in the MOFs enhances electron transfer and photocatalytic activities. Copyright 2020 American Chemical Society.

In this chapter, we report the synthesis of multifunctional MOFs comprising of Cu-PSs and Co-based HER catalysts (**mPT-Cu/Co**) or Re-based CO_2 reduction reaction (CO_2RR) catalysts

(**mPT-Cu/Re**, **Scheme 8-1**). Hierarchical integration of Cu-PSs and Co/Re catalysts in these MOFs facilitates multielectron transfer to drive photocatalytic HER and CO_2RR under visible light with a HER turnover number (TON) of 18,700 for **mPT-Cu/Co** and a CO_2RR TON of 1328 for **mPT-Cu/Re** (**Figure 8-1b**). These TONs are nearly two orders of magnitude higher than those of their homogenous controls.

Scheme 8-1. MOFs significantly enhance photocatalytic H_2 evolution and CO_2 reduction with Cu photosensitizers. Copyright 2020 American Chemical Society.

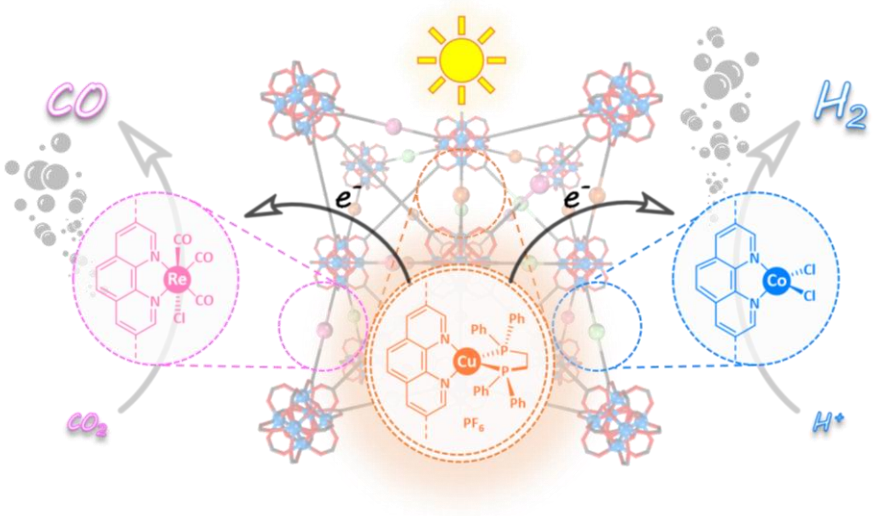

8.2 Results and Discussion

8.2.1 Synthesis and characterization of Cu-PS containing MOFs

Photocatalytic MOFs **mPT-Cu/Co** and **mPT-Cu/Re** were synthesized via multi-step postsynthetic modifications (PSMs) of previously reported mPT-MOF with mixed phenanthroline dibenzoate (PT) and 2"-nitro-[1,1':4',1":4",1"'-quaterphenyl]-4,4"'-dicarboxylate (TPHN) ligands.[27] **mPT-Cu/Co** was prepared from mPT-MOF by stepwise PT metalation with $Cu(CH_3CN)_4PF_6$, coordination of 1,2-bis(diphenylphosphino)ethane (dppe) to the Cu centers, and metalation of remaining PT sites with $CoCl_2$. **mPT-Cu/Re** was synthesized from mPT-MOF by sequential metalation of PT sites with $Re(CO)_5Cl$ and $Cu(CH_3CN)_4PF_6$ followed by coordination

of dppe to the Cu centers (**Figure 8-2a**). Transmission electron microscopy (TEM) imaging of **mPT-Cu/M** (M = Co and Re) revealed a similar octahedral morphology to the pristine mPT-MOF (**Figure 8-2d**). **mPT-Cu/M** showed similar powder X-ray diffraction (PXRD) patterns as mPT-MOF, supporting the maintenance of MOF crystallinity during PSMs (**Figure 8-2b**). N_2 sorption measurements indicated porous structures of **mPT-Cu/M** with Brunauer-Emmett-Teller (BET) surface areas of 1022 m^2/g for **mPT-Cu/Co** and 855 m^2/g for **mPT-Cu/Re**, respectively (**Figure 8-2c**). Inductively coupled plasma-mass spectrometry (ICP-MS) studies revealed 70% Cu loading and 30% Co loading in **mPT-Cu/Co** and 85% Cu loading and 14% Re loading in **mPT-Cu/Re**, which is further supported by thermogravimetric analysis results.

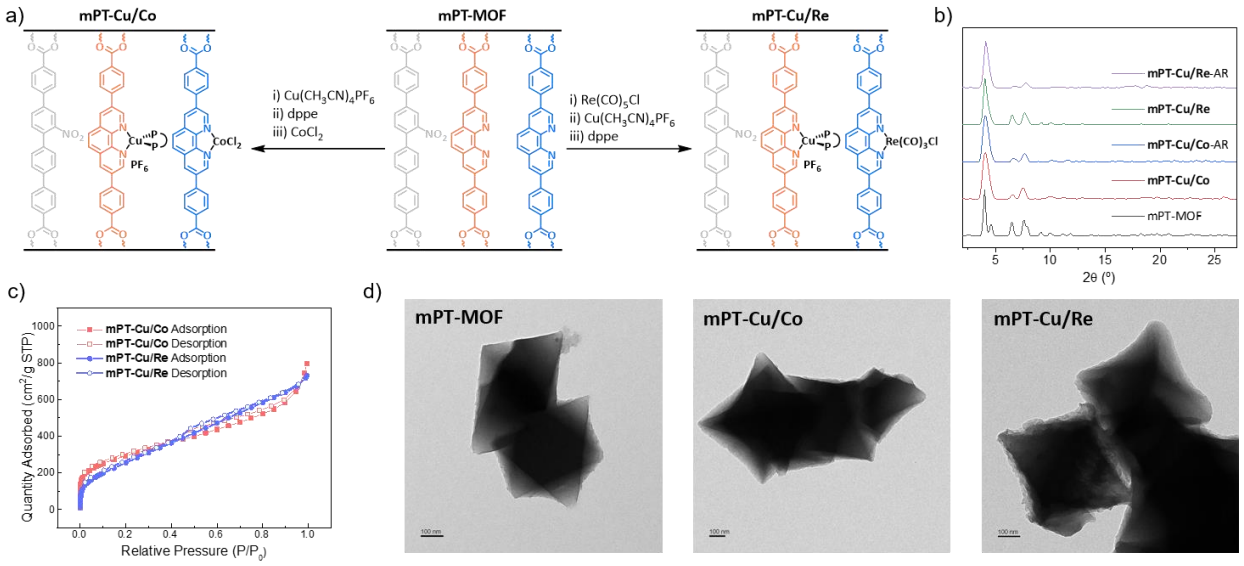

Figure 8-2. Synthesis and structural characterization of **mPT-Cu/Co** and **mPT-Cu/Re**. (a) Post-synthetic modifications of mPT-MOF to afford **mPT-Cu/Co** and **mPT-Cu/Re**. (b) PXRD patterns of **mPT-MOF** (black), **mPT-Cu/Co** (red), **mPT-Cu/Re** (blue), and recovered **mPT-Cu/Co** after HER (green) and recovered **mPT-Cu/Re** after CO_2RR (purple). (c) N_2 sorption isotherms of **mPT-Cu/Co** (red) and **mPT-Cu/Re** (blue). (d) TEM images of mPT-MOF, **mPT-Cu/Co**, and **mPT-Cu/Re** with similar octahedral morphologies and ~500 nm in sizes. Copyright 2020 American Chemical Society.

X-ray absorption spectroscopy was performed to determine metal coordination and electronic environments in **mPT-Cu/M**. EXAFS data of **mPT-Cu/M** collected at Cu K-edge, Co

K-edge, and Re L_{III}-edge were well fit with reported crystal structures of Cu, Co, and Re complexes with identical coordination environments.[28-30] In **mPT-Cu/Co**, the Cu^{I} centers coordinate to PT and dppe in a distorted tetrahedral geometry while the Co^{II} centers coordinate to PT and two chloride groups in a tetrahedral geometry (**Figures 8-3a**, **8-4a**). No EXAFS features corresponding to metallic nanoparticles were observed.[31] XANES spectroscopy showed Cu^{I} and Co^{II} oxidation states for **mPT-Cu/Co** (**Figure 8-3c**). In **mPT-Cu/Re**, the Cu^{I} centers adopt a distorted tetrahedral geometry whereas the Re centers coordinate to PT, three carbonyls and one chloride in an octahedral geometry (**Figures 8-3b**, **8-4c**). X-ray photoelectron spectroscopy (XPS) also showed binding energies consistent to Cu^{I}, Co^{II}, and Re^{I} in **mPT-Cu/M** (**Figures 8-3d**, **8-4b**, **8-4d**).

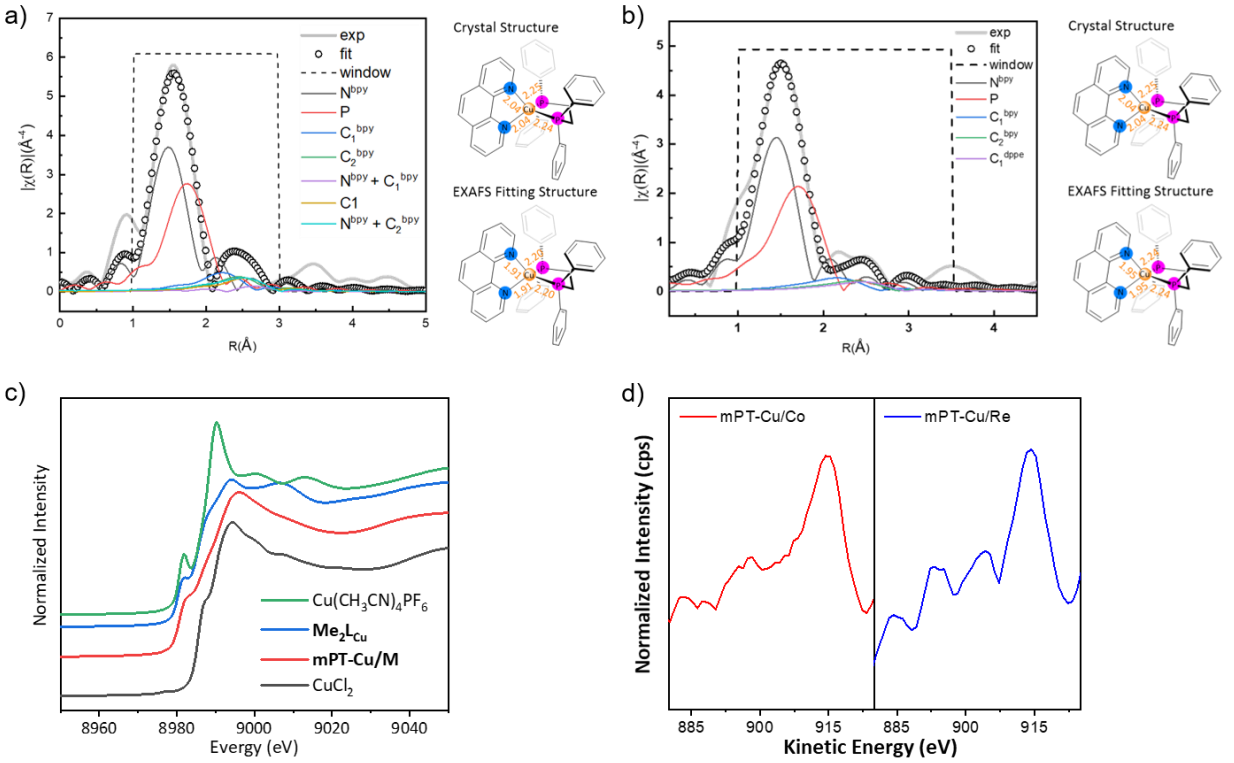

Figure 8-3. Local coordination and electronic structure characterization of Cu centers in **mPT-Cu/Co** and **mPT-Cu/Re**. (a, b) EXAFS spectra (grey solid line) and fits (black circles) of **mPT-Cu/Co** (a) and **mPT-Cu/Re** (b) in R-space at Cu K-edges. (c) Normalized XANES features of **mPT-Cu/M** (red), and $\mathbf{Me_2L_{Cu}}$ (blue), $CuCl_2$ (black), and $Cu(CH_3CN)_4PF_6$ (green). (d) Cu $L_3M_{45}M_{45}$ Auger spectra of **mPT-Cu/Co** (red) and **mPT-Cu/Re** (blue) showed Cu LMM peaks at 915.0 eV and 914.6 eV, respectively. Copyright 2020 American Chemical Society.

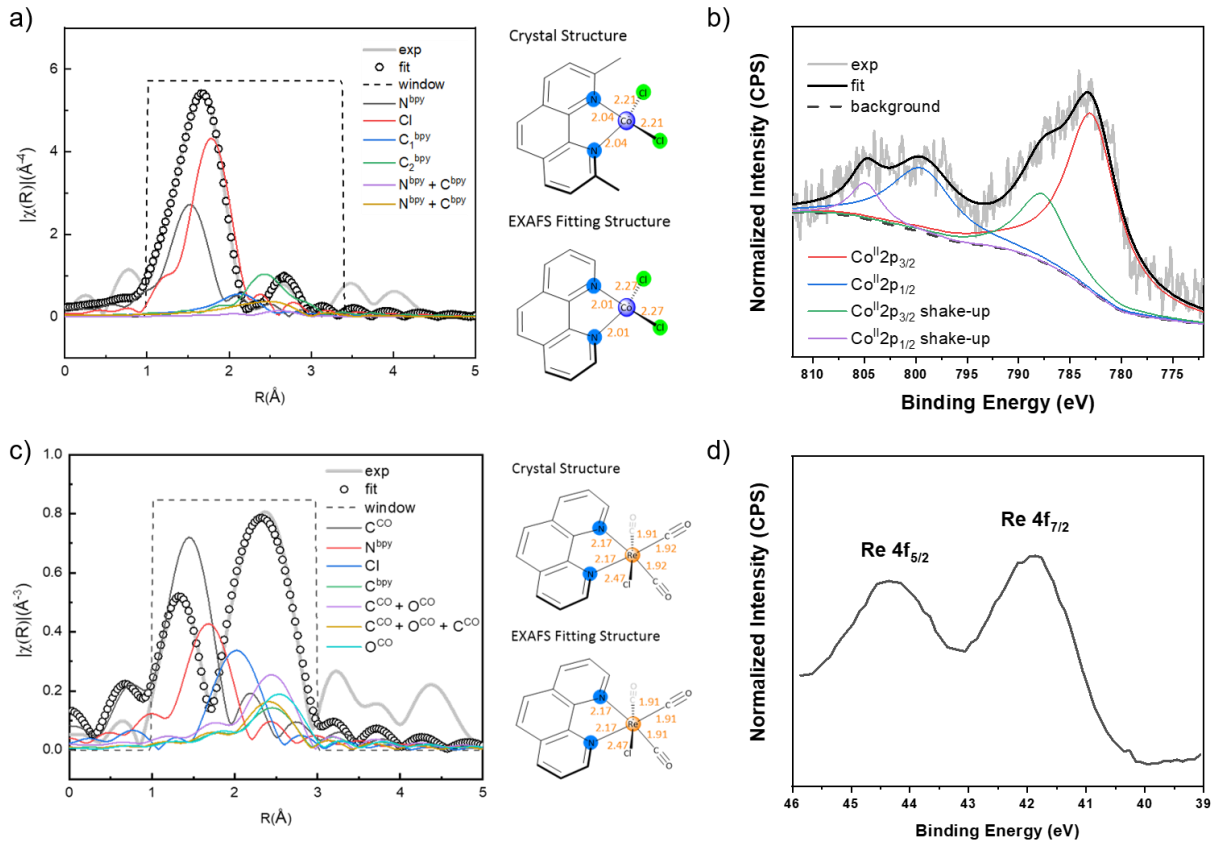

Figure 8-4. Local coordination and electronic structure characterization of Co and Re centers in **mPT-Cu/Co** and **mPT-Cu/Re**. (a) EXAFS spectra (grey solid line) and fits (black circles) of **mPT-Cu/Co** in R-space at Co K-edges. (b) Co 2p XPS spectra of **mPT-Cu/Co** indicated a Co^{II} oxidation state with $2p_{3/2}$ peak at 783.0 eV and $2p_{1/2}$ peak at 799.4 eV. (c) EXAFS spectra (grey solid line) and fits (black circles) of **mPT-Cu/Re** in R-space at Re L_{III}-edges. (d) Re 4f XPS spectra of **mPT-Cu/Re** indicated a Re^{I} oxidation state with $4f_{7/2}$ peak at 41.9 eV and $4f_{5/2}$ peak at 44.3 eV. Copyright 2020 American Chemical Society.

8.2.2 Photocatalytic hydrogenation evolution reaction catalyzed by mPT-Cu/Co

As a half-reaction of visible-light driven water splitting, photocatalytic HER has been widely studied with molecular PSs and catalysts.[32-34] Visible light-driven HER activity of **mPT-Cu/Co** was studied in CH_3CN with acetic acid as proton source and 1,3-dimethyl-2-phenyl-2,3-dihydro-1*H*-benzo[*d*]imidazole (BIH) as sacrificial agent (see **Table 8-1** for condition screening). The photocatalytic reaction was conducted under a N_2 atmosphere and irradiated with a 13.9 W 350-700 nm solid-state plasma light source equipped with a cooling fan. The amount of H_2

generated was quantified by gas chromatography (GC) analysis of the headspace gas. H_2 production increased nearly linearly in 72 h and the TON, defined as n(1/2H_2), reached 18700 based on the catalytic Co sites (**Figure 8-5a**). Such a photocatalytic HER activity outperformed not only reported Cu-PSs but also most Ir or Ru-based PSs. In comparison, the homogeneous control using molecular [Cu(Me_2PT)(dppe)]PF_6 and Co(phen)Cl_2 (prepared *in situ* as a mixture $CoCl_2$ and phen in 1:1 molar ratio) in a 2.3:1 ratio catalyzed HER with a TON of 196 in 48 h under identical conditions (**Figure 8-5a**). As a solid catalyst, **mPT-Cu/Co** was recycled and reused in at least three consecutive runs without a significant decrease in activity (**Figure 8-5b**). PXRD studies showed that the crystallinity of **mPT-Cu/Co** was maintained after HER (**Figure 8-2c**) whereas ICP-MS studies revealed <1.4% Cu and <0.1% Co leached into the supernatant during HER. The integration of [Cu(PT)(dppe)]$^+$ PS and Co(PT)Cl_2 catalyst into the mPT-MOF framework enhanced photocatalytic HER by ~95 times.

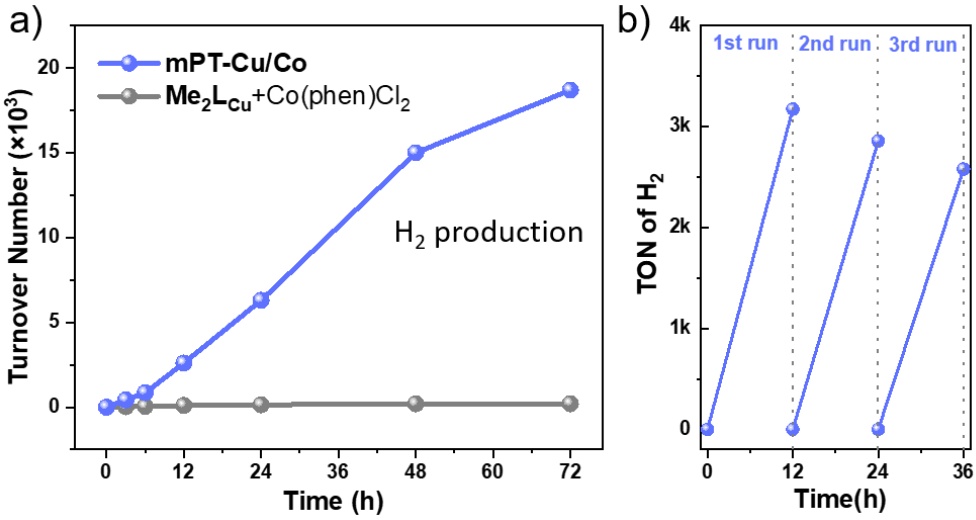

Figure 8-5. (a) Time-dependent HER TONs of **mPT-Cu/Co** and the homogeneous control. (b) Recycle test of **mPT-Cu/Co** catalyzed photocatalytic HER in three consecutive runs.

Table 8-1. Condition optimization of **mPT-Cu/Co** catalyzed visible light driven HER[a]

Entry	Catalyst	Solvent Conditions	H_2 in 200 uL headspace	TON
1	**mPT-Cu/Co**	30 μL AcOH + 1.97 mL ACN	23.98	6298
2	**mPT-Cu/Co**	30 μL AcOH + 1.97 mL DMA	5.73	1508
3	**mPT-Cu/Co**	15 μL AcOH + 1.97 mL ACN	20.62	5415
4	**mPT-Cu/Co**	45 μL AcOH + 1.97 mL ACN	3.93	1032
5[b]	**mPT-Cu/Co**	6 μL AcOH + 1.994 mL ACN	13.89	18238
6[c]	**mPT-Cu/Co**	30 μL AcOH + 1.97 mL ACN	1.68	441
7[d]	**mPT-Cu/Co**	30 μL AcOH + 1.97 mL ACN	4.83	1268

[a]Unless noted, HER reactions were conducted with **mPT-Cu/Co** catalyst (0.0078 μmol Cu site, 0.0034 μmol Co site), and 64 mg BIH under 350-700 nm solid state plasma light source for 24 h. [b] Catalyst: **mPT-Cu/Co** (0.0016 μmol Cu site, 0.0007 μmol Co site). [c]Light source: sunlight (6h, experiment conduct during 07/11/2019 13-19 pm CST). [d]Light source: 15 W Blue LED stripe light.

Table 8-2. Control experiments of photocatalytic HER[a]

Entry	Catalyst	H_2 in 200 uL headspace	TON
1	**mPT-Cu/Co**	23.98	6298
2	**mPT-Cu**+Co(phen)Cl_2	1.06	278
3[b]	**mPT-Cu**	1.25	328
4[c]	mPT-MOF+**Me_2L_{Cu}**+Co(phen)Cl_2	0.93	244
5	**Me_2L_{Cu}**+Co(phen)Cl_2	0.38	100
6[c]	mPT-MOF	0.24	63

[a]Unless noted, HER reactions were conducted with MOF or homogeneous catalysts (containing 0.0078 μmol Cu site and 0.0034 μmol Co site), and 64 mg BIH, in 30 μL AcOH + 1.97 mL ACN, under 350-700 nm solid state plasma light source for 24 h. [b]Catalyst: **mPT-Cu** (0.0078 μmol Cu site). [c]mPT-MOF (with 0.011 μmol PT site) was added.

8.2.3 Photocatalytic CO_2 reduction reaction catalyzed by mPT-Cu/Re

As Re(diimine)$(CO)_3Cl$ has been widely studied in photocatalytic CO_2RR,[35-37] we examined visible light-driven CO_2RR with **mPT-Cu/Re**. Under 350-700 nm light irradiation,

mPT-Cu/Re catalyzed CO_2RR to produce CO continuously in 48 h in a mixed solution of *N*,*N*-dimethylacetamide (DMA) and H_2O (*v*/*v* = 0.96:0.04) with BIH as sacrificial agent (see **Table 8-3** for condition screening). The CO production as quantified by GC analysis reached a TON of 1328 based on catalytic Re sites, with a CO/H_2 selectivity of 9:1 (**Figure 8-6a**). Control experiment conducted under N_2 atmosphere showed negligible CO production, excluding the possibility of CO generation from catalyst or solvent decomposition (Entry 2, **Table 8-4**). We did not detect other potential CO_2 reduction products, including HCOOH, CH_4, and MeOH, by ^{1}H NMR, GC, and GC-MS, respectively. In contrast, the homogeneous control with [Cu(Me_2PT)(dppe)]PF_6 and Re(phen)$(CO)_3$Cl in a 6:1 ratio produced CO only in the first 12 h to afford a TON of 14, indicating rapid PS and/or catalyst deactivation in solution (**Figure 8-6b**). **mPT-Cu/Re** outperformed the homogeneous control by 95 times. Impressively, CO_2RR carried out under sunlight in 6 h produced CO with a TON of 150 and a CO/H_2 selectivity of 96% (Entry 7, **Table 8-3**). Hierarchical integration of Earth-abundant Cu-based PS with catalytically active metal sites in MOFs have thus enhanced their HER and CO_2RR activities by nearly two orders of magnitude over their homogeneous controls.

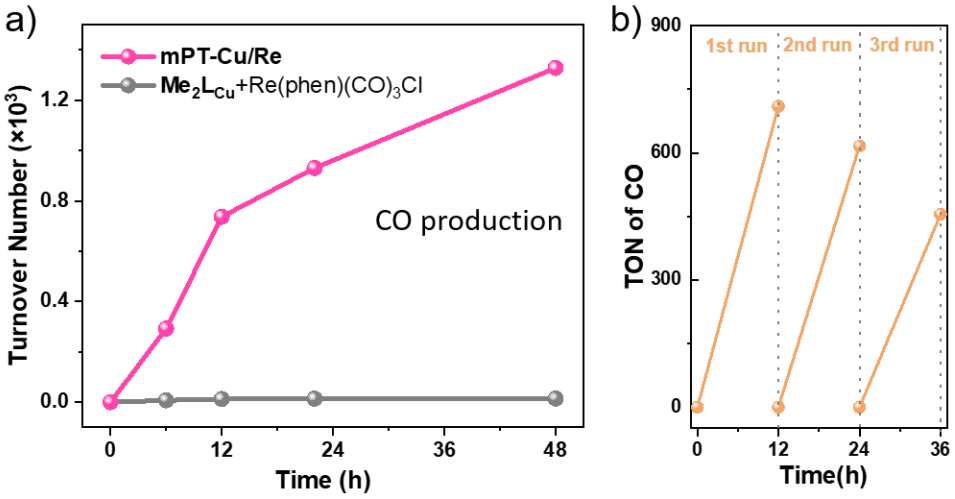

Figure 8-6. (a) Time-dependent CO_2RR TONs of **mPT-Cu/Re** and the homogeneous control. (b) Recycle Test of **mPT-Cu/Re** catalyzed photocatalytic CO_2RR in three consecutive runs.

Table 8-3. Condition optimization of **mPT-Cu/Re** catalyzed visible light driven CO_2RR[a]

Entry	Catalyst	Solvent Conditions	CO in 200 uL headspace	TON	CO/H_2 Selectivity
1	**mPT-Cu/Re**	0.1 mL H_2O + 1.90 mL DMA	5.81	1277	87%
2	**mPT-Cu/Re**	0.1 mL TEOA + 1.90 mL DMA	4.85	1065	34%
3	**mPT-Cu/Re**	0.05 mL H_2O + 1.95 mL DMA	2.29	504	88%
4	**mPT-Cu/Re**	0.075 mL H_2O + 1.925 mL DMA	4.23	930	89%
5	**mPT-Cu/Re**	0.15 mL H_2O + 1.85 mL DMA	5.83	1282	68%
6	**mPT-Cu/Re**	0.075 mL H_2O + 1.925 mL ACN	0.895	197	11%
7[b]	**mPT-Cu/Re**	0.075 mL H_2O + 1.925 mL DMA	0.68	150	96%
8[c]	**mPT-Cu/Re**	0.075 mL H_2O + 1.925 mL DMA	3.10	682	93%

[a]Unless noted, CO_2RR reactions were conduct with **mPT-Cu/Re** catalyst (0.012 μmol Cu site, 0.002 μmol Re site), and 45 mg BIH under 350-700 nm solid state plasma light source for 24 h. [b]Light source: sunlight (6h, experiment conduct during 07/11/2019 13-19 pm CST) [c]Light source: 15 W Blue LED stripe light.

Table 8-4. Control experiments of photocatalytic CO_2RR[a]

Entry	Catalyst	Atmosphere	CO in 200 uL headspace	TON	CO/H_2 Selectivity
1	**mPT-Cu/Re**	CO_2	4.23	930	89%
2	**mPT-Cu/Re**	N_2	0.010	2	9%
3	**mPT-Cu+** $Re(phen)(CO)_3Cl$	CO_2	0.084	18	31%
4[b]	**mPT-Cu**	CO_2	0.058	13	6%
5[c]	mPT-MOF+**Me_2L_{Cu}**+ $Re(phen)(CO)_3Cl$	CO_2	0.058	13	23%
6	**Me_2L_{Cu}**+$Re(phen)(CO)_3Cl$	CO_2	0.067	15	16%
7	**Me_2L_{Cu}**+$Re(phen)(CO)_3Cl$	N_2	0.026	6	40%
8[c]	mPT-MOF	CO_2	0.018	4	27%

[a]Unless noted, CO_2RR reactions were conduct with MOF or homogeneous catalysts (containing 0.012 μmol Cu site and 0.002 μmol Re site), and 45 mg BIH, in 0.075 mL H_2O + 1.925 mL DMA, under 350-700 nm solid state plasma light source for 24 h. [b]Catalyst: **mPT-Cu** (0.012 μmol Cu site). [c]mPT-MOF (with 0.014 μmol PT site) was added.

8.2.4 Studies on photocatalytic cycles

We conducted photophysical and electrochemical experiments to understand the mechanisms of **mPT-Cu/M** catalyzed HER and CO_2RR processes. First, **mPT-Cu** displayed identical absorption and luminescence spectra as the homogenous PS [Cu(Me_2PT)(dppe)]PF_6, (**Me_2L_{Cu}**) with the characteristic MLCT absorption λ_{max} at 445 nm and emission λ_{max} at 570 nm (**Figure 8-7a**). This emission λ_{max} corresponds to an energy gap of 2.18 eV between the PS excited state and the ground state. We next examined whether the photoexcited Cu-PS underwent reductive quenching or oxidative quenching to initiate photocatalytic HER and CO_2RR cycles. Luminescence measurements showed that the emission of **Me_2L_{Cu}** was effectively quenched by BIH but not by Co(phen)Cl_2 or Re(phen)$(CO)_3$Cl (**Figures 8-7b**, **8-7d**, **8-7e**). Luminescence quenching of **Me_2L_{Cu}** by BIH was well fitted with the Stern-Volmer equation to afford a quenching constant (K_{SV}) of 5.81 ± 0.13 mM^{-1} (**Figure 8-7c**). A similar quenching trend was observed for **mPT-Cu** (**Figure 8-8**). These results indicate that photocatalytic HER and CO_2RR are following a reductive quenching cycle, initiating by the electron transfer from BIH to the photoexcited [Cu-PS]* to generate the reduced [Cu-PS]$^-$, which inject electrons to Co catalytic sites for HER and to Re catalytic sites for CO_2RR (**Figure 8-7f**).

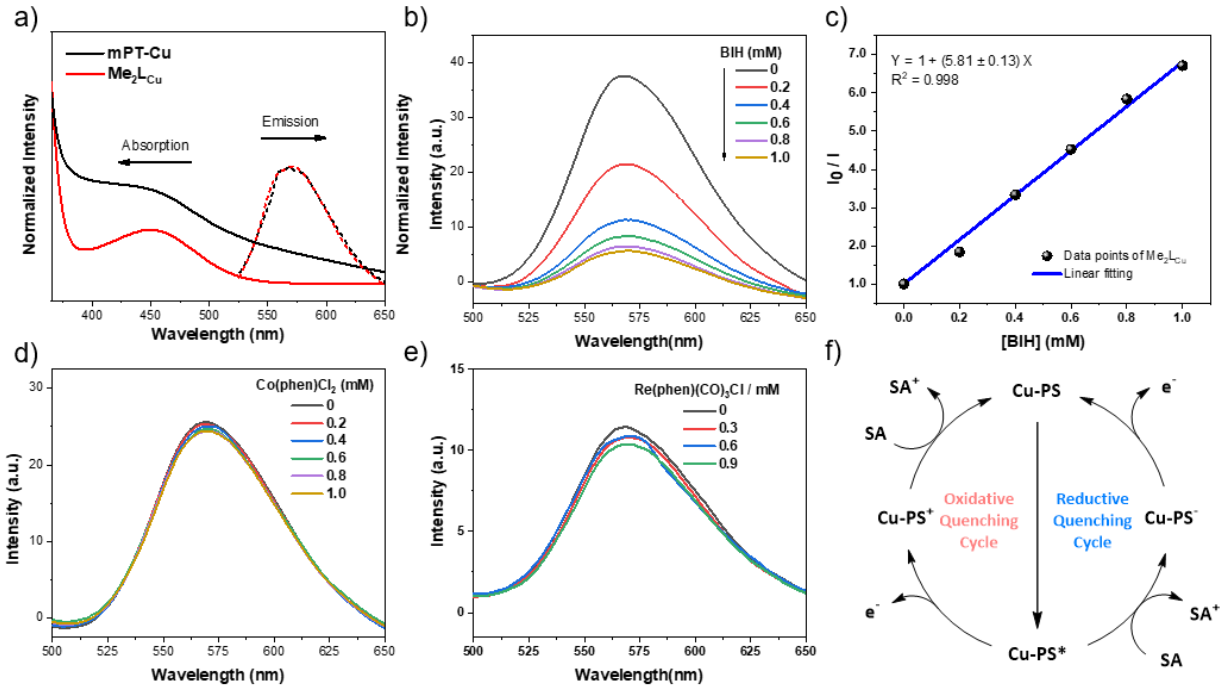

Figure 8-7. Mechanism studies on the photocatalytic cycles of photosensitizing **mPT-Cu**. (a) Normalized absorption and emission spectra of **Me_2L_{Cu}** (black) and **mPT-Cu** (red) in DMA with a concentration of 20 μM Cu. (b, d, e) Emission spectra of **Me_2L_{Cu}** (10 μM) after the addition of different amounts of (b) BIH, (d) $Co(phen)Cl_2$, or (e) $Re(phen)(CO)_3Cl$ in 2 mL of MeCN. (c) Plots of I_0/I of **Me_2L_{Cu}** as a function of the concentration of BIH (mM). (f) Reductive or oxidative quenching pathway of Cu-PS. Copyright 2020 American Chemical Society.

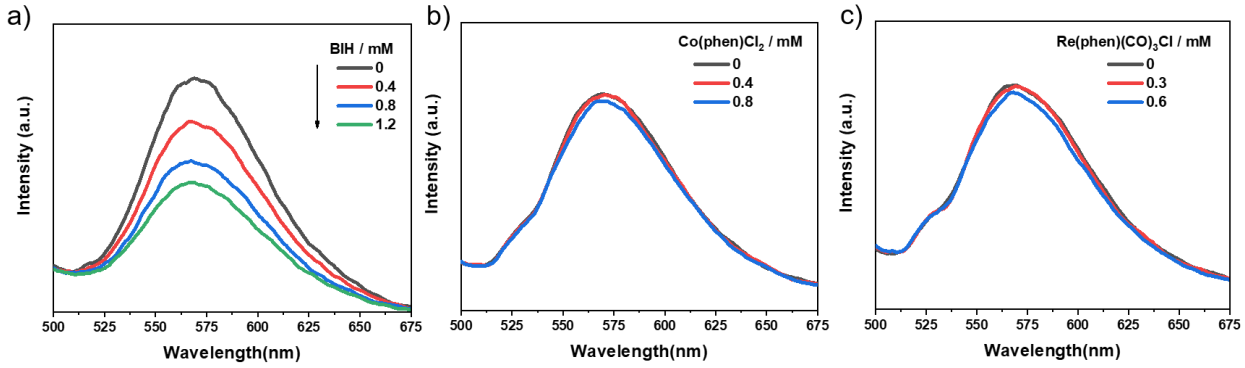

Figure 8-8. Emission spectra of **mPT-Cu** (~50 μmol Cu sites) after the addition of different amounts of (a) BIH, (b) $Co(phen)Cl_2$, or (c) $Re(phen)(CO)_3Cl$ in 2 mL of DMA with 455 nm excitation. Copyright 2020 American Chemical Society.

Cyclic voltammograms (CVs) of Cu-PS and catalysts were examined to provide additional insight into the photocatalytic mechanisms. For HER systems, CV scans were carried out on both

mPT-Co[31] and $Co(phen)Cl_2$ (**Figure 8-9a**). Under catalytic HER conditions, **mPT-Co** showed a reversible reduction peak at -0.40 V vs. NHE and an irreversible catalytic HER peak with an onset potential of -0.69 V vs. NHE, suggesting that H_2 production commences upon the injection of two electrons. In contrast, $Co(phen)Cl_2$ displayed only an irreversible catalytic HER peak with an onset potential at -0.77 V vs. NHE. This difference can be explained by the ease of forming metallic Co nanoparticles in homogeneous $Co(phen)Cl_2$ under catalytic HER conditions. Co nanoparticles exhibited higher catalytic HER onset potential than MOF-stabilized PT-Co molecular catalysts due to active site isolation. The stabilization of molecular Co HER catalyst by mPT-MOF is at least partly responsible for its enhanced photocatalytic HER activity over the homogeneous control.

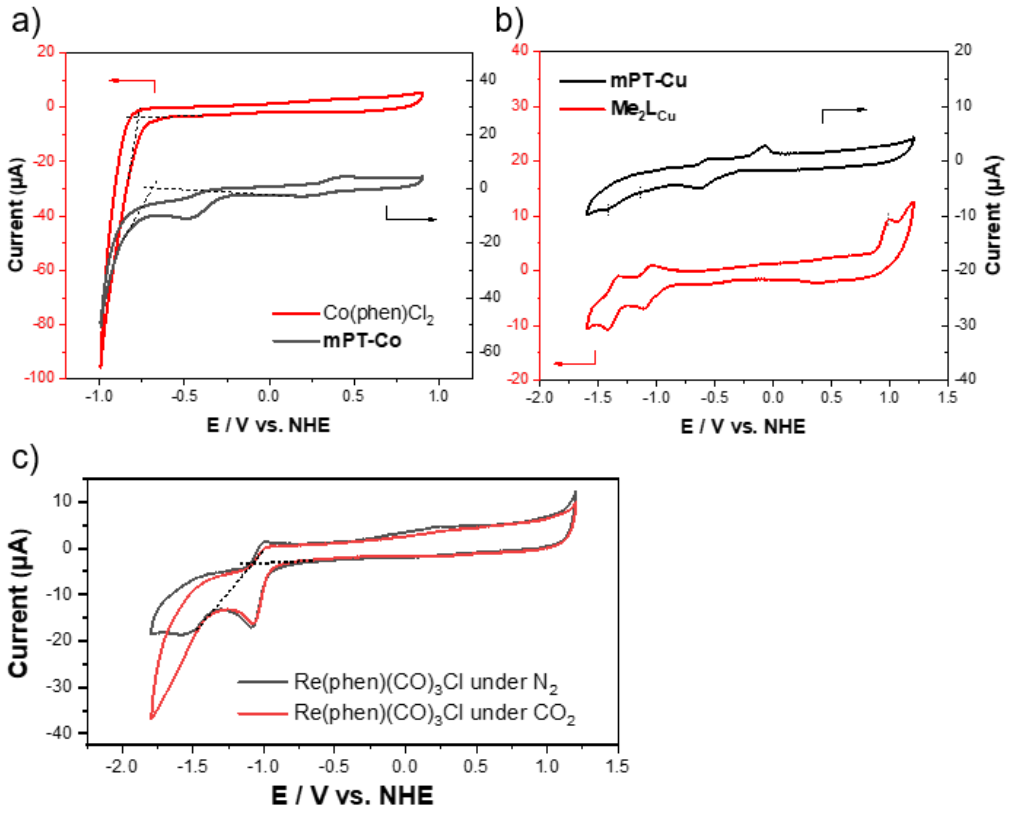

Figure 8-9. Cyclic voltammograms studies of Cu-PS and catalysts systems. (a) CVs of **mPT-Co** (black) coated on electrode surface and $Co(phen)Cl_2$ (red) under photocatalytic HER conditions (10 mL 0.1 M TBAH/CH_3CN solution with 150 μL AcOH, TBAH = tetrabutylammonium hexafluorophosphate). (b) CVs of **mPT-Cu** (black) coated on electrode surface and $\mathbf{Me_2L_{Cu}}$ (red) in 10 mL 0.1 M TBAH solution in CH_3CN. (c) CVs of $Re(phen)(CO)_3Cl$ under N_2 atmosphere (black) and CO_2 atmosphere (red) (10 mL 0.1 M TBAH/DMA solution with 1 mL H_2O).

As shown in **Figure 8-9b**, **Me_2L_{Cu}** displayed two reversible reduction peaks at -1.08 V and -1.38 V vs. NHE, which are assigned to the successive one electron reduction of the Cu^I center and the PT group, respectively. Similar reduction peaks were observed in **mPT-Cu**. The first reduction potential of Cu-PS (-1.08 V vs. NHE) provides adequate driving force for HER with the Co catalyst in **mPT-Cu/Co** (-0.69 V vs. NHE). Based on the photophysical and electrochemical results, we propose the HER photocatalytic cycle in **Figure 8-10a**. Upon visible light irradiation, the Cu-PS is excited to the [Cu-PS]* state (ΔE_1 = 2.18 eV), which is subsequently reduced by BIH to generate $[Cu\text{-}PS]^-$. Photoreduced $[Cu\text{-}PS]^-$ inject electrons to the Co sites to catalyze HER and return to the Cu-PS ground state. The corresponding energy diagram is summarized in **Figure 8-11**. Finally, CV studies showed that photoreduced $[Cu\text{-}PS]^-$ could reduce $Re(PT)(CO)_3Cl$ for CO_2RR (**Figures 8-9c**, **8-10b**).

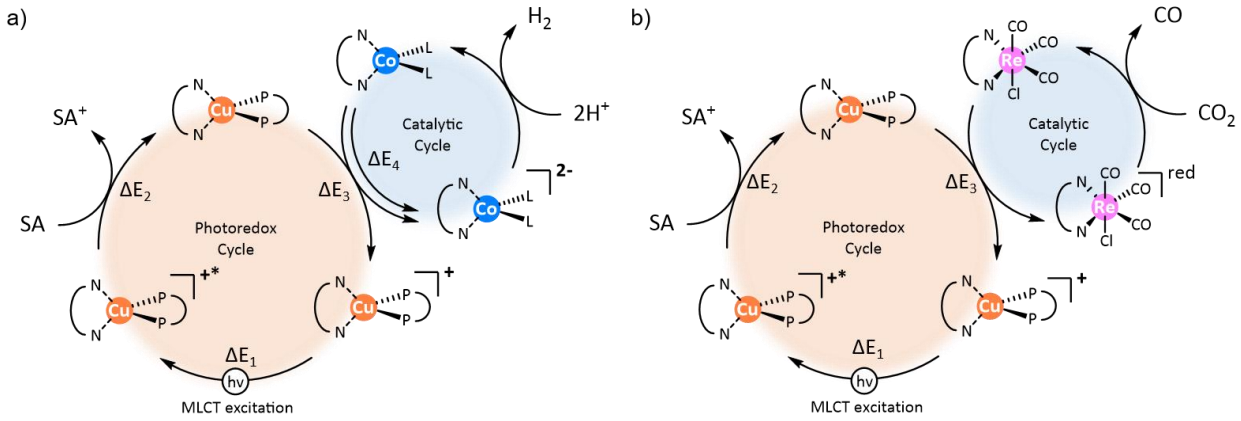

Figure 8-10. Proposed catalytic cycle for (a) **mPT-Cu/Co** catalyzed visible light-driven HER and (b) **mPT-Cu/Re** catalyzed visible light-driven CO_2RR. Copyright 2020 American Chemical Society.

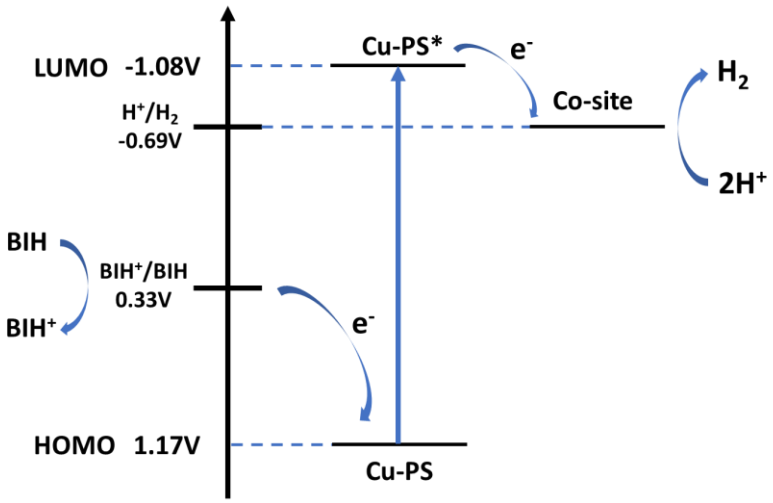

Figure 8-11. Potential energy diagrams of **mPT-Cu/Co** catalyzed photocatalytic HER. Copyright 2020 American Chemical Society.

8.3 Conclusion

In summary, we prepared multifunctional MOFs comprising of Cu-PSs and molecular Co/Re catalysts for photocatalytic HER and CO_2RR. The integration of Cu-PSs and Co/Re catalysts in MOFs significantly enhanced their photocatalytic activities to afford a HER TON of 18,700 for **mPT-Cu/Co** and a CO_2RR TON of 1328 for **mPT-Cu/Re**. The photocatalytic performances of **mPT-Cu/Co** and **mPT-Cu/Re** are nearly two orders of magnitude higher than their homogenous controls as a result of increased stability of Cu-PSs and molecular catalysts and enhanced electron transfer between Cu-PSs and Co/Re catalysts in MOFs. Photophysical and electrochemical studies further established a reductive quenching pathway in which the photoreduced $[Cu\text{-}PS]^-$ generated by BIH quenching of the photoexcited [Cu-PS]* transfers electrons to the catalytic sites to drive HER and CO_2RR. MOFs thus provide a promising platform to enhance the performance of Earth abundant Cu-PSs and molecular catalysts in solar energy conversion.

8.4 Experimental Section

8.4.1 Materials and methods

All the reactions and manipulations were carried out under N_2 with the use of a glovebox or Schlenk technique, unless otherwise indicated. Tetrahydrofuran and toluene were purified by passing through a neutral alumina column under N_2. All starting materials were purchased from Sigma-Aldrich and Fisher (USA) unless otherwise noted and used without further purification. Powder X-ray diffraction (PXRD) data was collected on a Bruker D8 Venture diffractometer using Cu Kα radiation source (l = 1.54178 Å). N_2 sorption experiments were performed on a Micrometrics TriStar II 3020 instrument. Thermogravimetric analysis (TGA) was performed in air using a Shimazu TGA-50 equipped with a platinum pan and heated at a rate of 1.5 $^{\circ}$C per min. ICP-MS data was obtained with an Agilent 7700x ICP-MS and analyzed using ICP-MS MassHunter version B01.03. Samples were diluted in a 2% HNO_3 matrix and analyzed with a ^{159}Tb internal standard against a 12-point standard curve over the range from 0.1 ppb to 500 ppb. The correlation was >0.9997 for all analyses of interest. Data collection was performed in Spectrum Mode with five replicates per sample and 100 sweeps per replicate. Cyclic voltammograms (CVs) were recorded on a CHI420 electrochemistry workstation with regular 3 electrode systems. Measurements were recorded using a glassy carbon disk working electrode (S = 0.07 cm^2) and a platinum wire as the counter electrode. The Ag/AgCl/1 M KCl electrode was used as the reference electrode in all experiments. X-ray photoelectron spectroscopy (XPS) data was collected using an AXIS Nova spectrometer (Kratos Analytical) with monochromatic Al Kα X-ray source; Al anode was powered at 10 mA and 15 kV, and the instrument work function was calibrated to give an Au $4f_{7/2}$ metallic gold binding energy (BE) of 83.95 eV. Instrument base pressure was ca. 1×10^{-9} Torr. The analysis area size was 0.3 × 0.7 mm^2. For calibration purposes,

the binding energies were referenced to the C 1s peak at 284.8 eV. Survey spectra were collected with a step size of 1 eV and 160 eV pass energy.

^{1}H and ^{13}C NMR spectra were recorded on a Bruker NMR 500 DRX spectrometer at 500 MHz and referenced to the proton resonance resulting from incomplete deuteration of $CDCl_3$ (δ 7.26) or DMSO-d_6 (δ 2.50). The following abbreviations are used herein: s: singlet, d: doublet, t: triplet, q: quartet, m: multiplet, br: broad, app: apparent. Amounts of H_2 and CO generated in the photocatalytic experiments were determined by gas chromatography (GC) using an SRI 8610C Gas Chromatograph with the nitrogen carrier gas and a TCD or FID detector. Gas chromatography-mass spectrometry (GC-MS) was conduct using a Shimadzu GCMS-QP2010 Ulta equipped with SH-Rxi-5Sil MS 30 m × 0.5 mm × 0.25 μm column.

8.4.2 Synthesis and characterization of ligands and complexes

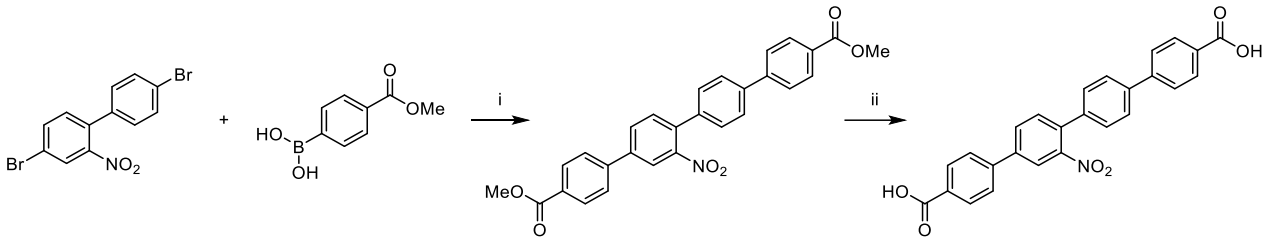

Figure 8-12. Synthesis of H_2TPHN. i) $Pd(PPh_3)_4$, K_2CO_3, THF/H_2O, 90 °C, 3 d; ii) KOH, THF/MeOH, 40 °C, 15 h.

Dimethyl 2''-nitro-[1,1':4',1'':4'',1'''-quaterphenyl]-4,4'''-dicarboxylate (**Me$_2$TPHN**): A mixture of $Pd(PPh_3)_4$ (231.0 mg, 0.200 mmol) and K_2CO_3 (1.38 g, 10.0 mmol) was dissolved in degassed THF/H_2O (40 mL/10 mL) followed by the addition of 4,4'-dibromo-2-nitro-1,1'-biphenyl (714.0 mg, 2.00 mmol) and 4-methoxycarbonylphenylboronic acid (1.08 g, 6.0 mmol). The resulting mixture was stirred under inert atmosphere at 90 °C for 3 days to afford yellow needle crystals. The solution was then cooled to room temperature, followed by filtration and washing with THF (3 times) and ether to afford **Me$_2$TPHN** as a yellow solid (0.85 g, 91% yield). ^{1}H NMR

(500 MHz, Chloroform-*d*) δ 8.21 – 8.16 (m, 2H), 8.16 – 8.13 (m, 3H), 7.90 (dd, J = 8.0, 1.9 Hz, 1H), 7.76 – 7.69 (m, 6H), 7.60 (d, J = 8.0 Hz, 1H), 7.51 – 7.43 (m, 2H), 3.97 (s, 3H), 3.96 (s, 3H). ^{13}C NMR (126 MHz, Chloroform-*d*) δ 167.08, 149.81, 144.83, 142.61, 140.73, 140.25, 136.84, 135.32, 132.69, 130.98, 130.65, 130.36, 129.41, 128.67, 127.83, 127.41, 127.22, 127.21, 123.01, 52.48, 52.34. HR-MS (ESI, positive mode): *m/z* calc'd for $C_{28}H_{22}NO_6$ $[M+H]^+$:468.1447, found 468.1440.

2"-Nitro-[1,1':4',1":4",1"'-quaterphenyl]-4,4"'-dicarboxylic acid (**H_2TPHN**): **Me_2TPHN** (0.23 g, 0.50 mmol) was suspended in 20 mL THF in a 50 mL round-bottom flask followed by dropwise addition of a KOH/MeOH solution (2.8 g KOH in 10 mL MeOH). After the mixture was stirred at 40 °C overnight, 1 M HCl (aq) was slowly added until the pH was below 7. The solid was collected and washed with water, THF, and ether before being dried under vacuum to give pure 2"-nitro-[1,1':4',1":4",1"'-quaterphenyl]-4,4"'-dicarboxylic acid (**H_2TPHN**) (0.22 g, 93% yield). ^{1}H NMR (500 MHz, DMSO-d_6) δ 13.08 (s, 2H), 8.39 (d, J = 1.9 Hz, 1H), 8.18 (dd, J = 8.1, 2.0 Hz, 1H), 8.11 – 8.03 (m, 4H), 8.01 – 7.96 (m, 2H), 7.92 – 7.84 (m, 4H), 7.76 (d, J = 8.1 Hz, 1H), 7.56 – 7.51 (m, 2H). ^{13}C NMR (126 MHz, DMSO-d_6) δ 167.13, 166.99, 149.53, 143.42, 141.38, 139.57, 138.99, 136.30, 133.86, 132.50, 130.97, 130.73, 130.15, 130.06, 129.95, 128.56, 127.44, 127.20, 126.90, 122.40. HR-MS (ESI, positive mode): *m/z* calc'd for $C_{26}H_{17}NO_6Na$ $[M+Na]^+$:462.0954, found 462.0969.

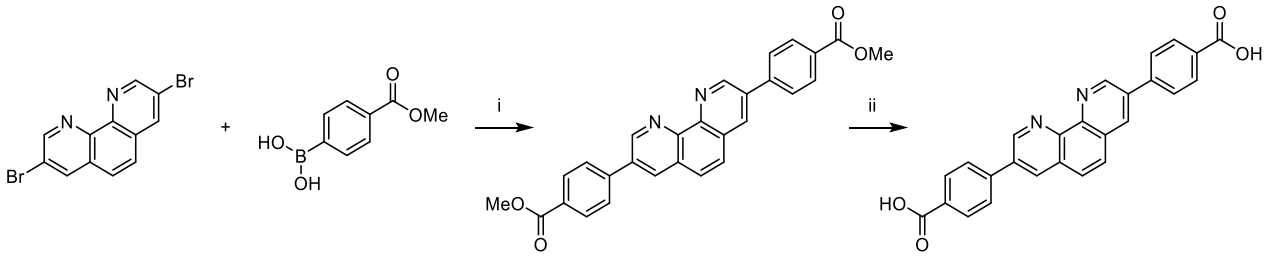

Figure 8-13. Synthesis of **H_2PT**. i) $Pd(PPh_3)_4$, CsF, 1,2-dimethoxyethane, 110 °C, 4 d; ii) NaOH, EtOH, reflux, 15 h.

Dimethyl 4,4'-(1,10-phenanthroline-3,8-diyl)dibenzoate (**Me_2PT**): 3,8-Dibromophenanthroline (0.58 g, 1.7 mmol) and 4-methoxycarbonylphenylboronic acid (0.81 g, 4.5 mmol) were suspended in 30 mL of 1,2-dimethoxyethane and degassed. Tetrakis(triphenylphosphine) palladium(0) (177 mg) and cesium fluoride (1.10 g) were then added. The resulting mixture was sealed in a pressure vessel under nitrogen and heated to 110 ºC for 7 days. After cooling to r.t., the crude product was filtered and further purified by column chromatography (SiO_2, chloroform) to give the pure product dimethyl 4,4'-(1,10-phenanthroline-3,8-diyl)dibenzoate (**Me_2PT**) as a off-white solid (0.53 g, 70% yield). ^{1}H NMR (500 MHz, Chloroform-*d*) δ 9.77 (s, 2H), 8.75 (s, 2H), 8.27 (d, J = 8.4 Hz, 4H), 8.12 (s, 2H), 7.91 (d, J = 8.4 Hz, 4H), 4.00 (s, 6H). ^{13}C NMR (126 MHz, Chloroform-*d*) δ 166.76, 149.39, 141.85, 134.94, 134.00, 133.98, 130.58, 130.10, 128.67, 127.57, 127.40, 52.38. HR-MS (ESI, positive mode): *m/z* calc'd for $C_{28}H_{21}N_2O_4$ $[M+H]^+$:449.1501, found 449.1503.

4,4'-(1,10-Phenanthroline-3,8-diyl)dibenzoic acid (**H_2PT**): **Me_2PT** (0.17 g, 0.38 mmol) was suspended in 10 mL EtOH in a 50 mL round-bottom flask followed by dropwise addition of 10 mL of 6 M NaOH (aq). After the mixture was stirred under reflux overnight, 1 M HCl (aq) was slowly added until the pH was below 7. The solid was collected and washed with water, THF, and ether before dried under vacuum to give pure 4,4'-(1,10-phenanthroline-3,8-diyl)dibenzoic acid (**H_2PT**) (0.155 g, 97% yield). ^{1}H NMR (500 MHz, DMSO-d_6) δ 13.17 (s, 2H), 9.52 (s, 2H), 8.99 (s, 2H), 8.23 – 8.07 (m, 12H). ^{13}C NMR (126 MHz, DMSO-d_6) δ 167.04, 148.30, 143.55, 140.56, 134.71, 133.90, 130.68, 130.20, 128.75, 127.67, 127.56. HR-MS (ESI, positive mode): *m/z* calc'd for $C_{26}H_{17}N_2O_4$ $[M+H]^+$:421.1188, found 421.1221.

8.4.3 Synthetic procedures of MOF catalysts

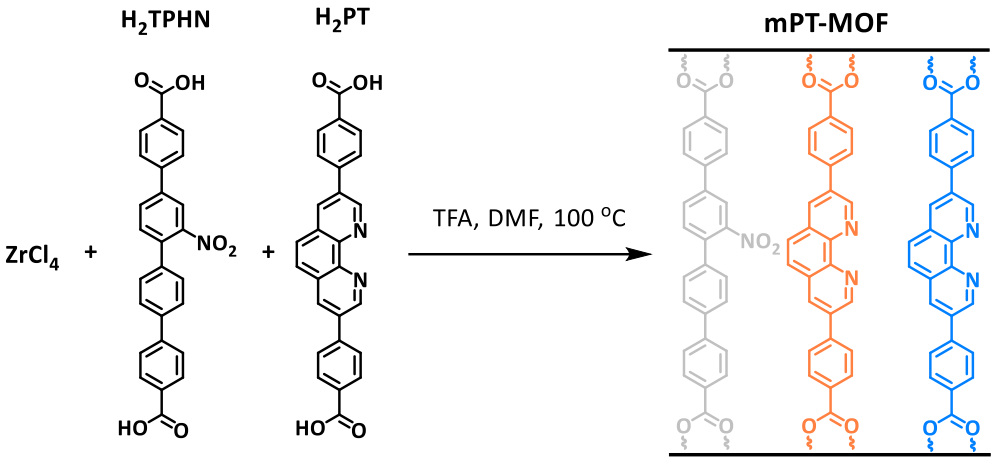

Synthesis of mPT-MOF: **H_2PT** (6.0 mg), **H_2TPHN** (14 mg) and $ZrCl_4$ (10 mg) were dissolved in DMF (5.0 mL) and trifluoroacetic acid (0.05 mL) was added. The solution was then heated in a 100 °C oven for 3 days to afford the pale-yellow powder solid mPT-MOF. The MOF was collected by centrifugation and washed thoroughly with DMF, THF three times and benzene three times and then freeze-dried to remove residual solvents under vacuum. Yield: 20 mg (53%). The integration from ^{1}H NMR spectrum of mPT-MOF digested in D_3PO_4/DMSO-d_6 indicated a **PT**/**TPHN** ratio of 1:4.

Synthesis of **mPT-Cu/Co**: In a glovebox, mPT-MOF (10.0 mg, ~ 2 μmol PT) was weighed and charged into a 2-dram vial. $Cu(CH_3CN)_4PF_6$ (10 μmol) dissolved in 2.0 mL of CH_2Cl_2 was added to the vial and the mixture was stirred inside the glovebox for 24 h. The resultant yellow solid was centrifuged out of suspension and washed with CH_2Cl_2 several times to remove excess Cu salt. 1,2-bis(diphenylphosphino)ethane (2.5 μmol) dissolved in 2.0 mL of CH_2Cl_2 was then added to the MOF and the mixture was stirred for another 24 h before being washed with CH_2Cl_2 to afford **mPT-Cu**. The Cu loading was determined by ICP-MS to be around 70% (w.r.t. PT), which can be controlled by the equivalents of the Cu salt added and the reaction time. The above yellow-orange solid **mPT-Cu** was further stirred with $CoCl_2$ (1 μmol) in 10 mL THF at room

temperature for 18 h and then thoroughly washed with THF to afford **mPT-Cu/Co** nearly quantitatively. ICP-MS analysis of **mPT-Cu/Co** revealed a Zr: Cu: Co ratio of 27: 2.3: 1, with a nearly complete metal (Cu+Co) loading based on **PT** sites. **mPT-Co** (mPT-MOF-$CoCl_2$) was also prepared for CV test based on reported method.[31]

Synthesis of **mPT-Cu/Re**: The metalation of Re is performed before the Cu installation to prevent Cu leaching at elevated temperatures. In a glovebox, mPT-MOF (10.0 mg, ~ 2 μmol PT) was weighed and charged into a tube, followed by the addition of $Re(CO)_5Cl$ (0.6 μmol) in 3 mL of tolene. The mixture was stirred at 80 ˚C for 18 h. The yellow Re-metalated MOF **mPT-Re** was thoroughly washed with toluene. The resulting MOF was transferred into a 2-dram vial, and then $Cu(CH_3CN)_4PF_6$ (10 μmol) in 2.0 mL of CH_2Cl_2 was added to the vial. The mixture was stirred in the glovebox for 24 h. The resultant solid was centrifuged and washed with CH_2Cl_2 to remove excess Cu salt, followed by the addition of 1,2-bis(diphenylphosphino)ethane (2.5 μmol) in 2.0 mL of CH_2Cl_2. The resulting mixture was stirred for 24 h before being washed with CH_2Cl_2 to afford **mPT-Cu/Re** nearly quantitatively. ICP-MS analysis of **mPT-Cu/Re** revealed a Zr: Cu: Re ratio of 59: 6.0: 1, with a nearly complete metal (Cu+Re) loading based on **PT** sites.

8.4.4 Photocatalytic reaction setup

Typical procedure and condition optimization for visible light-driven hydrogen evolution reaction (HER): Photocatalytic HER was carried out in an external illumination type reaction vessel with a magnetic stirrer. Samples were prepared in 4.0 mL septum-sealed glass vials. In a standard reaction, each sample was made up to a volume of 2.00 mL including 1.97 mL CH_3CN, 0.03 mL AcOH, and 64 mg BIH (0.3 mmol) in addition to a certain amount of MOF catalyst. Sample vials were capped and sealed and deoxygenated by bubbling nitrogen through for 10 min to ensure complete air removal. The solution was irradiated by a 13.9 W 350-700 nm solid state

plasma light source equipped with a cooling fan (HPLS-30-04 from Thorlabs Inc.) for 24 h. The reaction temperature was kept below 30 °C during the irradiation. After the hydrogen evolution reaction, the gas in the headspace of the vial was analyzed by GC to determine the amount of hydrogen generated. TON of HER was calculated based on the amount of catalytic Co sites.

Typical procedure and condition optimization for visible light-driven CO_2 reduction reaction (CO_2RR): Photocatalytic CO_2RR was carried out in an external illumination type reaction vessel with a magnetic stirrer. Samples were prepared in 4.0 mL septum-sealed glass vials. Each sample was made up to a volume of 2.00 mL including 1.90 mL DMA, 0.10 mL H_2O, and 45 mg BIH (0.21 mmol) in addition to a certain amount of MOF catalyst. Sample vials were capped and sealed and deoxygenated by bubbling CO_2 through for 10 min to ensure complete air removal. The solution was irradiated by a 13.9 W 350-700 nm solid state plasma light source (HPLS-30-04 from Thorlabs Inc.) equipped with a cooling fan for 24 h. The reaction temperature was kept under 30 °C during the irradiation. After the CO_2RR, the gas in the headspace of the vial was analyzed by GC to determine the amount of CO generated. TON of CO_2RR was calculated based on the amount of catalytic Re sites.

8.5 References

1. Balzani, V.; Juris, A.; Venturi, M.; Campagna, S.; Serroni, S., Luminescent and Redox-Active Polynuclear Transition Metal Complexes. *Chemical Reviews* **1996,** *96* (2), 759-834.

2. Frischmann, P. D.; Mahata, K.; Würthner, F., Powering the future of molecular artificial photosynthesis with light-harvesting metallosupramolecular dye assemblies. *Chemical Society Reviews* **2013,** *42* (4), 1847-1870.

3. Baranoff, E.; Collin, J.-P.; Flamigni, L.; Sauvage, J.-P., From ruthenium(ii) to iridium(iii): 15 years of triads based on bis-terpyridine complexes. *Chemical Society Reviews* **2004,** *33* (3), 147-155.

4. You, Y.; Nam, W., Photofunctional triplet excited states of cyclometalated Ir(iii) complexes: beyond electroluminescence. *Chemical Society Reviews* **2012,** *41* (21), 7061-7084.

5. Sandroni, M.; Pellegrin, Y.; Odobel, F., Heteroleptic bis-diimine copper(I) complexes for applications in solar energy conversion. *Comptes Rendus Chimie* **2016,** *19* (1), 79-93.

6. Wenger, O. S., Photoactive Complexes with Earth-Abundant Metals. *Journal of the American Chemical Society* **2018,** *140* (42), 13522-13533.

7. Zhang, Y.; Schulz, M.; Wächtler, M.; Karnahl, M.; Dietzek, B., Heteroleptic diimine–diphosphine Cu(I) complexes as an alternative towards noble-metal based photosensitizers: Design strategies, photophysical properties and perspective applications. *Coordination Chemistry Reviews* **2018,** *356*, 127-146.

8. Luo, S.-P.; Mejía, E.; Friedrich, A.; Pazidis, A.; Junge, H.; Surkus, A.-E.; Jackstell, R.; Denurra, S.; Gladiali, S.; Lochbrunner, S.; Beller, M., Photocatalytic Water Reduction with Copper-Based Photosensitizers: A Noble-Metal-Free System. *Angewandte Chemie International Edition* **2013,** *52* (1), 419-423.

9. Khnayzer, R. S.; McCusker, C. E.; Olaiya, B. S.; Castellano, F. N., Robust Cuprous Phenanthroline Sensitizer for Solar Hydrogen Photocatalysis. *Journal of the American Chemical Society* **2013,** *135* (38), 14068-14070.

10. Robertson, N., CuI versus RuII: Dye-Sensitized Solar Cells and Beyond. *ChemSusChem* **2008,** *1* (12), 977-979.

11. Reiser, O., Shining Light on Copper: Unique Opportunities for Visible-Light-Catalyzed Atom Transfer Radical Addition Reactions and Related Processes. *Accounts of Chemical Research* **2016,** *49* (9), 1990-1996.

12. Hernandez-Perez, A. C.; Collins, S. K., Heteroleptic Cu-Based Sensitizers in Photoredox Catalysis. *Accounts of Chemical Research* **2016,** *49* (8), 1557-1565.

13. Holler, M.; Delavaux-Nicot, B.; Nierengarten, J.-F., Topological and Steric Constraints to Stabilize Heteroleptic Copper(I) Complexes Combining Phenanthroline Ligands and Phosphines. *Chemistry- A European Journal* **2019,** *25* (18), 4543-4550.

14. Furukawa, H.; Cordova, K. E.; O'Keeffe, M.; Yaghi, O. M., The Chemistry and Applications of Metal-Organic Frameworks. *Science* **2013,** *341* (6149), 1230444.

15. Drake, T.; Ji, P.; Lin, W., Site Isolation in Metal–Organic Frameworks Enables Novel Transition Metal Catalysis. *Accounts of Chemical Research* **2018,** *51* (9), 2129-2138.

16. Li, B.; Wen, H.-M.; Cui, Y.; Zhou, W.; Qian, G.; Chen, B., Emerging Multifunctional Metal–Organic Framework Materials. *Advanced Materials* **2016,** *28* (40), 8819-8860.

17. Huang, Y.-B.; Liang, J.; Wang, X.-S.; Cao, R., Multifunctional metal–organic framework catalysts: synergistic catalysis and tandem reactions. *Chemical Society Reviews* **2017,** *46* (1), 126-157.

18. Kirchon, A.; Feng, L.; Drake, H. F.; Joseph, E. A.; Zhou, H.-C., From fundamentals to applications: a toolbox for robust and multifunctional MOF materials. *Chemical Society Reviews* **2018,** *47* (23), 8611-8638.

19. Wang, C.; deKrafft, K. E.; Lin, W., Pt Nanoparticles@Photoactive Metal–Organic Frameworks: Efficient Hydrogen Evolution via Synergistic Photoexcitation and Electron Injection. *Journal of the American Chemical Society* **2012,** *134* (17), 7211-7214.

20. Xiao, J.-D.; Shang, Q.; Xiong, Y.; Zhang, Q.; Luo, Y.; Yu, S.-H.; Jiang, H.-L., Boosting Photocatalytic Hydrogen Production of a Metal–Organic Framework Decorated with Platinum Nanoparticles: The Platinum Location Matters. *Angewandte Chemie International Edition* **2016,** *55* (32), 9389-9393.

21. Wang, S.; Wang, X., Multifunctional Metal–Organic Frameworks for Photocatalysis. *Small* **2015,** *11* (26), 3097-3112.

22. Dhakshinamoorthy, A.; Asiri, A. M.; García, H., Metal–Organic Framework (MOF) Compounds: Photocatalysts for Redox Reactions and Solar Fuel Production. *Angewandte Chemie International Edition* **2016,** *55* (18), 5414-5445.

23. Wang, C.; Xie, Z.; deKrafft, K. E.; Lin, W., Doping Metal–Organic Frameworks for Water Oxidation, Carbon Dioxide Reduction, and Organic Photocatalysis. *Journal of the American Chemical Society* **2011,** *133* (34), 13445-13454.

24. Kim, D.; Whang, D. R.; Park, S. Y., Self-Healing of Molecular Catalyst and Photosensitizer on Metal–Organic Framework: Robust Molecular System for Photocatalytic H2 Evolution from Water. *Journal of the American Chemical Society* **2016,** *138* (28), 8698-8701.

25. Wang, W.; Song, X.-W.; Hong, Z.; Li, B.; Si, Y.; Ji, C.; Su, K.; Tan, Y.; Ju, Z.; Huang, Y.; Chen, C.-N.; Yuan, D., Incorporation of iron hydrogenase active sites into a stable photosensitizing metal-organic framework for enhanced hydrogen production. *Applied Catalysis B: Environmental* **2019,** *258*, 117979.

26. Song, Y.; Li, Z.; Zhu, Y.; Feng, X.; Chen, J. S.; Kaufmann, M.; Wang, C.; Lin, W., Titanium Hydroxide Secondary Building Units in Metal–Organic Frameworks Catalyze Hydrogen Evolution under Visible Light. *Journal of the American Chemical Society* **2019,** *141* (31), 12219-12223.

27. Manna, K.; Zhang, T.; Greene, F. X.; Lin, W., Bipyridine- and Phenanthroline-Based Metal–Organic Frameworks for Highly Efficient and Tandem Catalytic Organic Transformations via Directed C–H Activation. *Journal of the American Chemical Society* **2015,** *137* (7), 2665-2673.

28. Constable, E. C.; Housecroft, C. E.; Kopecky, P.; Schönhofer, E.; Zampese, J. A., Restricting the geometrical relaxation in four-coordinate copper(i) complexes using face-to-face and edge-to-face π-interactions. *CrystEngComm* **2011,** *13* (7), 2742-2752.

29. Smolko, L.; Černák, J.; Kuchár, J.; Rajnák, C.; Titiš, J.; Boča, R., Field-Induced Slow Magnetic Relaxation in Mononuclear Tetracoordinate Cobalt(II) Complexes Containing a Neocuproine Ligand. *European Journal of Inorganic Chemistry* **2017,** *2017* (24), 3080-3086.

30. Chakraborty, I.; Jimenez, J.; Sameera, W. M. C.; Kato, M.; Mascharak, P. K., Luminescent Re(I) Carbonyl Complexes as Trackable PhotoCORMs for CO delivery to Cellular Targets. *Inorganic Chemistry* **2017,** *56* (5), 2863-2873.

31. Zhang, T.; Manna, K.; Lin, W., Metal–Organic Frameworks Stabilize Solution-Inaccessible Cobalt Catalysts for Highly Efficient Broad-Scope Organic Transformations. *Journal of the American Chemical Society* **2016,** *138* (9), 3241-3249.

32. Meyer, T. J., The art of splitting water. *Nature* **2008,** *451* (7180), 778-779.

33. Martin, D. J.; Reardon, P. J. T.; Moniz, S. J. A.; Tang, J., Visible Light-Driven Pure Water Splitting by a Nature-Inspired Organic Semiconductor-Based System. *Journal of the American Chemical Society* **2014,** *136* (36), 12568-12571.

34. Li, F.; Fan, K.; Xu, B.; Gabrielsson, E.; Daniel, Q.; Li, L.; Sun, L., Organic Dye-Sensitized Tandem Photoelectrochemical Cell for Light Driven Total Water Splitting. *Journal of the American Chemical Society* **2015,** *137* (28), 9153-9159.

35. Hawecker, J.; Lehn, J.-M.; Ziessel, R., Efficient photochemical reduction of CO2 to CO by visible light irradiation of systems containing Re(bipy)(CO)3X or Ru(bipy)32+–Co2+ combinations as homogeneous catalysts. *Journal of the Chemical Society, Chemical Communications* **1983,** (9), 536-538.

36. Takeda, H.; Koike, K.; Inoue, H.; Ishitani, O., Development of an Efficient Photocatalytic System for CO2 Reduction Using Rhenium(I) Complexes Based on Mechanistic Studies. *Journal of the American Chemical Society* **2008,** *130* (6), 2023-2031.

37. Choi, K. M.; Kim, D.; Rungtaweevoranit, B.; Trickett, C. A.; Barmanbek, J. T. D.; Alshammari, A. S.; Yang, P.; Yaghi, O. M., Plasmon-Enhanced Photocatalytic CO2 Conversion within Metal–Organic Frameworks under Visible Light. *Journal of the American Chemical Society* **2017,** *139* (1), 356-362.

Chapter 9. MOFs Integrate Cu Photosensitizers and SBU-Supported Fe Catalysts for Highly Efficient Photocatalytic H_2 Evolution

9.1 Introduction

Photocatalytic water splitting into H_2 using abundant and renewable sunlight is one of the most promising strategies for sustainable energy production.[1-4] Although significant progress has been made in developing catalytic materials for photocatalytic H_2 evolution,[5-8] large-scale adoption of photocatalytic water splitting still faces several challenges including: 1) the balance between catalytic site isolation to ensure stability and its proximity to photosensitizer (PS) for electron transfer;[4] 2) the balance between tight metal binding to minimize leaching and open coordination environment to facilitate H_2 formation;[9] and 3) the balance between catalytic efficiency and its Earth abundance and cost.[10-11] Thus, there is a strong need for low-cost, Earth-abundant systems containing a high density of light-harvesting units and proton reduction units in close proximity for efficient and steady H_2 production.

In the past decade, metal-organic frameworks (MOFs) have been extensively studied for solar energy utilization with the goal of addressing the above challenges.[12-17] The rigid framework built from secondary building units (SBUs) and organic linkers accommodates the hierarchical assembly of multiple functionalities in high density without active site aggregation.[18-21] As illustrated in Chapters 2-4, recent works have established metal-oxo/hydroxo SBUs as excellent ligands to support novel single-site Earth-abundant metal (EAM) catalysts for organic transformations.[22-24] We surmised that photosensitizing linkers and SBU-supported EAM catalysts could be hierarchically integrated into crystalline MOF structures to provide exceptional photocatalytic H_2 evolution performance.

In this chapter, we report a novel strategy to construct bifunctional **FeX@Zr$_6$-Cu** MOFs (X=Br$^-$, Cl$^-$, AcO$^-$, and BF$_4^-$) by combining cuprous photosensitizing linkers (Cu-PSs) and catalytically active Fe^{II} centers on the μ$_3$-OH sites of Zr$_6$(μ$_3$-O)$_4$(μ$_3$-OH)$_4$ SBUs ([Fe]) for highly effective visible light-driven H$_2$ evolution (**Scheme 9-1**). Due to the proximity (~1 nm) between Cu-PS and [Fe] moieties and stabilization of photoreduced [Fe] sites by periodically ordered SBUs, **FeX@Zr$_6$-Cu** were highly active for photocatalytic H$_2$ evolution with turnover numbers (TONs) of up to 33,700 and turnover frequencies (TOF) of up to 880 h^{-1}. H$_2$ evolution activities of **FeX@Zr$_6$-Cu** correlate with the lability of X counter anions, likely due to the generation of open coordination environments of [Fe] sites by labile X groups to facilitate the formation of Fe-hydride intermediates.

Scheme 9-1. MOFs integrate Cu photosensitizers and SBU-supported Fe catalysts for highly efficient photocatalytic H$_2$ evolution. Copyright 2020 American Chemical Society.

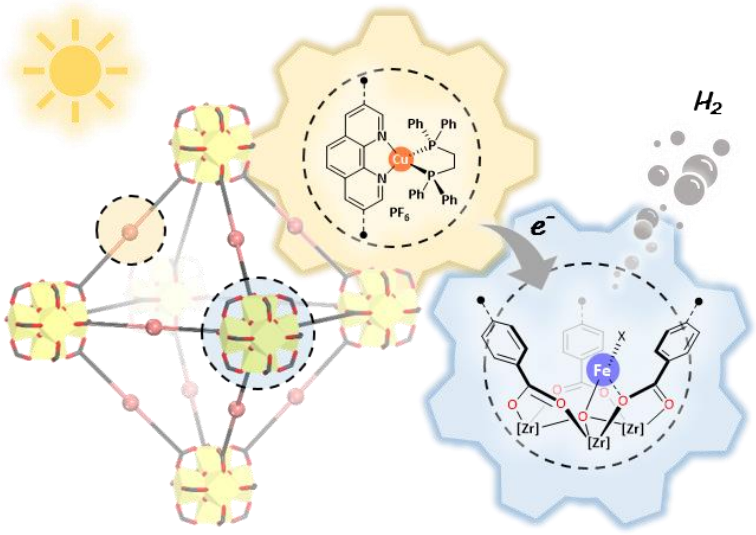

9.2 Results and Discussion

9.2.1 Synthesis and characterization of FeBr@Zr$_6$-Cu

FeBr@Zr$_6$-Cu was synthesized in multi-steps from previously reported **Zr$_6$-mPT** MOF built from Zr$_6$O$_4$(OH)$_4$ SBUs and mixed nitro-quaterphenyl dicarboxylate (**TPHN**) and *p*-

phenanthroline dibenzoate (**PT**) ligands with a **PT**/**TPHN** ratio of 1:4 (**Figure 9-1**).[25] Cu^{I} metalation to the **PT** groups in **Zr_6-mPT** followed by coordination of 1,2-diphenylphosphinoethane (dppe) to the Cu^{I} centers afforded the **Zr_6-Cu** MOF with $[Cu(\mathbf{PT})(dppe)]^{+}$ PSs as an orange solid.[26] **Zr_6-Cu** displayed absorption and emission spectra characteristic of the homogeneous analogue $[Cu(Me_2\mathbf{PT})(dppe)]PF_6$ (**L-Cu**). The μ_3-OH sites of the $Zr_6O_4(OH)_4$ SBUs in **Zr_6-Cu** were then metalated with $FeBr_2$ in the presence of the organic base $^{i}Pr_2NEt$ to generate **FeBr@Zr_6-Cu** (**Figure 9-1**).

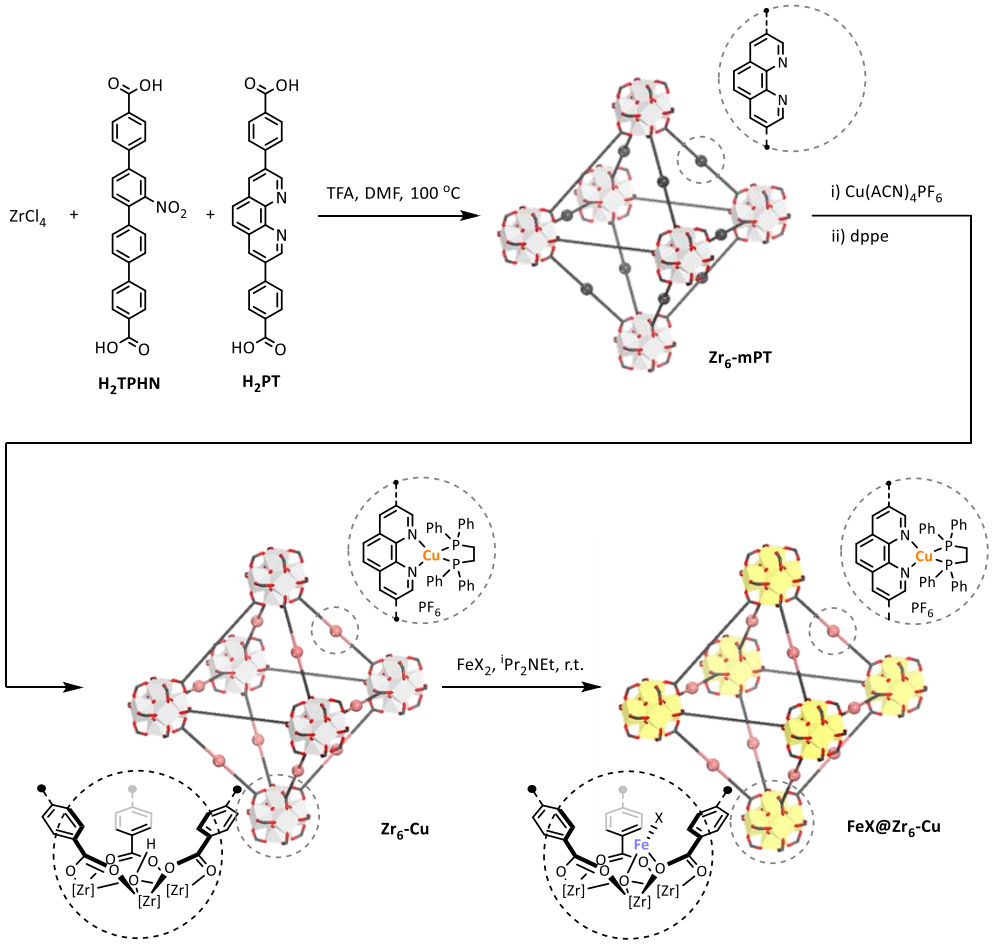

Figure 9-1. Synthesis route to **FeX@Zr_6-Cu** (X = Br^{-}, Cl^{-}, AcO^{-}, and BF_4^{-}).

The morphology and crystallinity of **Zr_6-mPT** were maintained throughout the post-synthetic functionalization steps as indicated by the similarity of transmission electron microscopy

(TEM) images (**Figure 9-2e**) and powder X-ray diffraction (PXRD) patterns (**Figure 9-2a**) between **Zr_6-mPT**, **Zr_6-Cu**, and **FeBr@Zr_6-Cu**. N_2 sorption measurements showed that **FeBr@Zr_6-Cu** exhibited a Brunauer-Emmett-Teller surface area of 922 m^2/g (**Figure 9-2b**), which is significantly lower than that of **Zr_6-mPT** (3021 m^2/g) due to the installation of Cu-PSs and [Fe] catalytic centers. Inductively coupled plasma-mass spectrometry (ICP-MS) studies revealed 92% Cu loading on **PT** ligands and 56% Fe loading on SBUs in **FeBr@Zr_6-Cu** to afford an empirical formula of $Zr_6O_4(OH)_{3.44}$ $(OFeBr)_{0.56}${**TPHN**$_{4.8}$[**PT**(Cu(dppe))$_{0.92}$]$_{1.2}$}$_{0.6}$, which was supported by thermogravimetric analysis (TGA) results (**Figure 9-2d**).

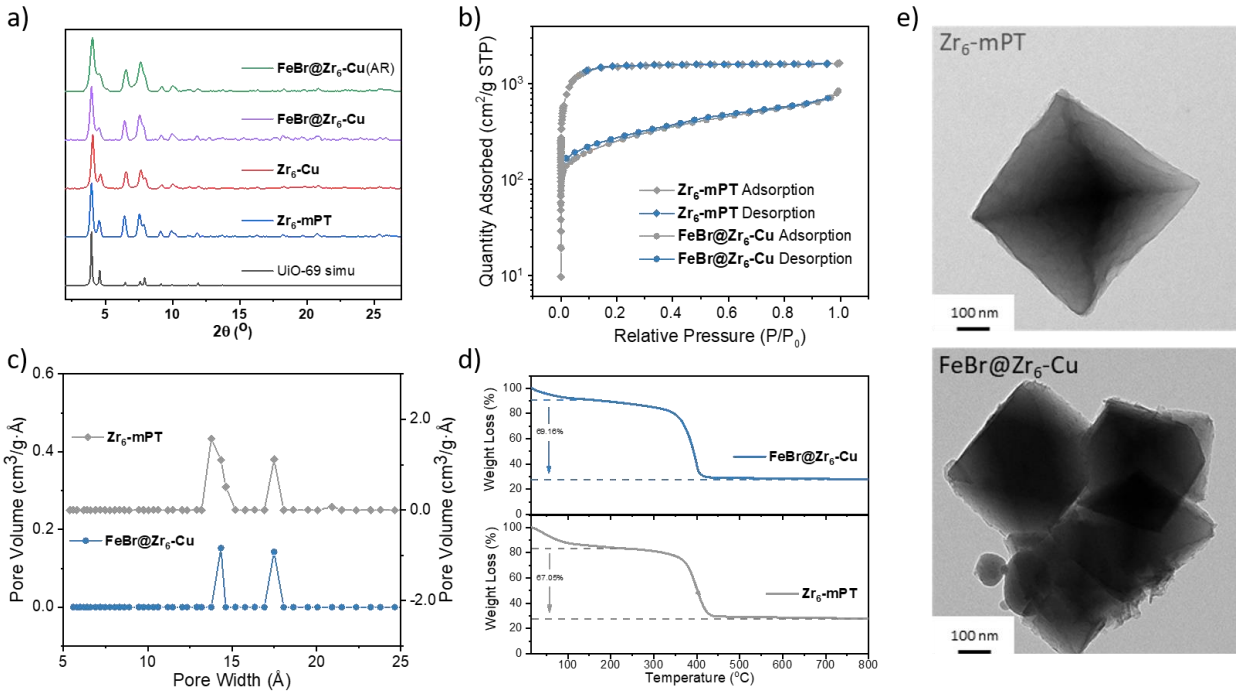

Figure 9-2. Structural characterization of **Zr_6-mPT** and **FeBr@Zr_6-Cu**. (a) PXRD patterns of **Zr_6-mPT** (navy), **Zr_6-Cu** (red), **FeBr@Zr_6-Cu** (violet), and recovered **FeBr@Zr_6-Cu**(AR) (green) from reaction, along with the simulated pattern for UiO-69 (black). (b) N_2 sorption isotherms of **FeBr@Zr_6-Cu** in comparison with the pristine MOF **Zr_6-mPT**. (c) BET Pore size distributions of **FeBr@Zr_6-Cu** and **Zr_6-mPT** calculated with non-local density functional theory (NLDFT). (d) TGA curve of **FeBr@Zr_6-Cu** and **Zr_6-mPT** (~40% ligand defect content) in the 25-800 °C range. (e) TEM image of **FeBr@Zr_6-Cu** and **Zr_6-mPT**. Copyright 2020 American Chemical Society.

X-ray absorption spectroscopy was used to characterize the Fe^{II} catalytic centers and Cu-PSs in **FeBr@Zr$_6$-Cu**. X-ray absorption near edge structure (XANES) spectroscopy indicated Fe^{II} oxidation states in **FeBr@Zr$_6$-Cu** (**Figure 9-3a**). The Fe^{II} oxidation state in **FeBr@Zr$_6$-Cu** was supported by X-ray photoelectron spectroscopic (XPS) studies (**Figure 9-3b**). Fitting of the extended X-ray absorption fine structure (EXAFS) regions of **FeBr@Zr$_6$-Cu** at the Fe K-edge revealed the coordination of each Fe^{II} center to one μ_3-O^- and two carboxylate oxygen atoms and one bromide in a near-tetrahedral geometry (**Figure 9-3c**).[27] Fitting of EXAFS spectrum of **FeBr@Zr$_6$-Cu** at the Cu K-edge afforded a distorted tetrahedral geometry of Cu^I by chelating to a **PT** ligand and a dppe ligand (**Figure 9-3d**).

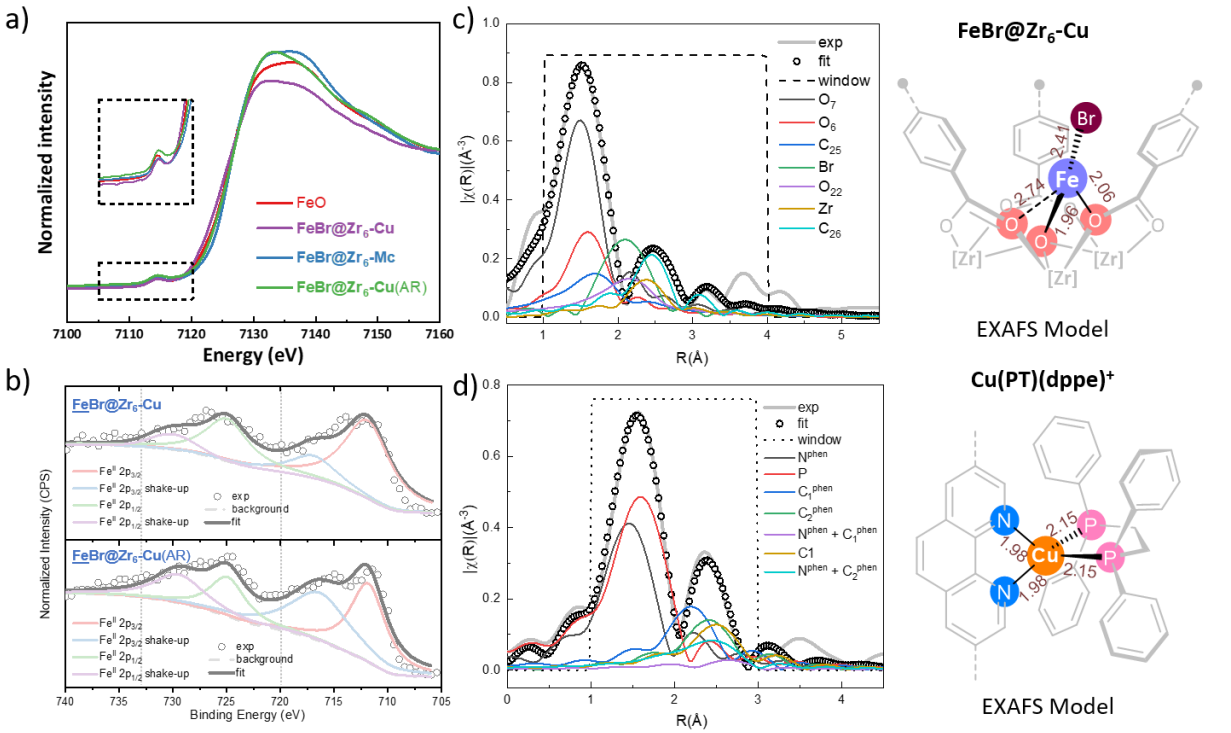

Figure 9-3. Electronic structures and local coordination environments of Fe and Cu in **FeBr@Zr$_6$-Cu**. (a) Normalized XANES features of **FeBr@Zr$_6$-Cu** (violet), **FeBr@Zr$_6$-Cu**(AR) (green), **FeBr@Zr$_6$-Mc** (navy), and FeO (red). (b) Fe 2p XPS spectra of **FeBr@Zr$_6$-Cu** (top) and **FeBr@Zr$_6$-Cu**(AR) (bottom) indicate an Fe^{II} oxidation state in both samples. (c) EXAFS spectra (grey solid line) and fits (black circles) in R-space at the Fe K-edge adsorption of **FeBr@Zr$_6$-Cu**. (d) EXAFS spectra (grey solid line) and fits (black circles) in R-space at the Cu K-edge adsorption of **FeBr@Zr$_6$-Cu**. Copyright 2020 American Chemical Society.

9.2.2 Photocatalytic HER activity of FeBr@Zr_6-Cu

With acetic acid (HOAc) as proton source and 1,3-dimethyl-2-phenyl-2,3-dihydro-1*H*-benzo[*d*]imidazole (BIH) as sacrificial electron donor, the performance of **FeBr@Zr_6-Cu** in photocatalytic H_2 evolution was evaluated in inert atmosphere with a 13.9 W 350-700 nm solid-state plasma light source. The H_2 generated was quantified by gas chromatography (GC) analysis of the headspace gas. As shown in **Figure 9-4**, H_2 evolution increased almost linearly in the presence of **FeBr@Zr_6-Cu** in the first 48 h of irradiation, with an overall TON, defined as n(1/2H_2)/n(Fe), of 24,700 and an average TOF of 650 h^{-1} in the first 6 h. Negligible amount of H_2 was detected in the absence of either light or Cu-PS (**Table 9-1**). A combination of **Zr_6-Cu** and $FeBr_2$ afforded a TON of 2440 in 48 h, approximately 10 times lower than the activity of **FeBr@Zr_6-Cu** (**Figure 9-4**). Moreover, a combination of homogeneous **L-Cu** and $FeBr_2$ produced much less H_2 with a TON of 910, which is approximately 27 times lower than that of **FeBr@Zr_6-Cu** (**Figure 9-4**).

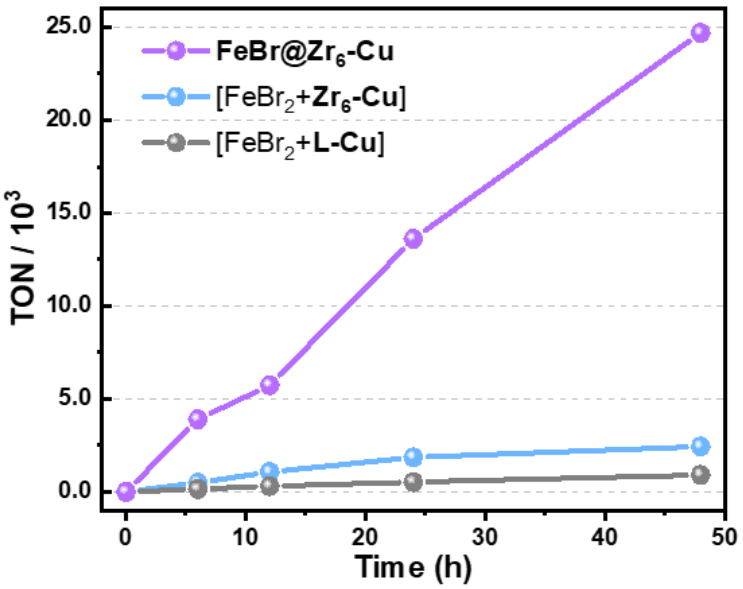

Figure 9-4. Time-dependent photocatalytic H_2 evolution TONs of **FeBr@Zr_6-Cu** along with **Zr_6-Cu** plus $FeBr_2$ and **L-Cu** plus $FeBr_2$ controls. Copyright 2020 American Chemical Society.

Table 9-1. Control experiments of photocatalytic H_2 evolution in 24 h[a]

Entry	Catalyst	H_2 in 200 uL headspace	TON
1	**FeBr@Zr$_6$-Cu**	38.13	13,617
2[b]	**FeBr@Zr$_6$-Cu** (w/o. light)	0	-
3[c]	**FeBr@Zr$_6$-TPHN**	0.54	193
4[d]	**Zr$_6$-Cu**	0.97	347
5[e]	**FeBr@Zr$_6$-Mc** + **L-Cu**	4.20	1,500
6[f]	$FeBr_2$ + **Zr$_6$-Cu**	5.21	1,860
7[g]	$FeBr_2$ + **L-Cu**	1.47	525
8[h]	-	0.007	-

[a]Unless noted, reactions were conducted with MOF or homogeneous catalysts (containing 0.0030 μmol Cu site and 0.0025 μmol Fe site), and 45 mg BIH, in 50 μL AcOH + 1.75 mL DMA + 0.2 mL H_2O, under 350-700 nm solid state plasma light source for 24 h. [b]Reaction conducted in the dark. [c]MOF catalyst without Cu-PS sites, **FeBr@Zr$_6$-TPHN** (0.0025 μmol Fe site), was used. [d]MOF catalyst without catalytic Fe sites, **Zr$_6$-Cu** (0.0030 μmol Cu site), was used. [e]Combination of **FeBr@Zr$_6$-Mc** + **L-Cu** (0.0030 μmol Cu site and 0.0025 μmol $FeBr_2$) was used. [f]Combination of [$FeBr_2$ + **Zr$_6$-Cu**] catalyst (0.0030 μmol Cu site and 0.0025 μmol $FeBr_2$) was used. [g]Combination of [$FeBr_2$ + **L-Cu**] catalyst (0.0030 μmol Cu site and 0.0025 μmol $FeBr_2$) was used. [h]Background reaction without adding catalyst.

Photocatalytic H_2 evolution activity of other Earth-abundant metal complexes supported on the MOF SBU was also tested using identical conditions as **FeBr@Zr$_6$-Cu**. **CoBr@Zr$_6$-Cu** and **NiBr@Zr$_6$-Cu** were similarly synthesized as **FeBr@Zr$_6$-Cu** using $CoBr_2$ and $NiBr_2$ in place of $FeBr_2$ (**Figure 9-5**). As shown in **Table 9-2**, both Co and Ni catalysts displayed moderate H_2 evolution activity over 24 h, with a TON of 2946 for **CoBr@Zr$_6$-Cu** and TON of 1500 for **NiBr@Zr$_6$-Cu**. These TONs are significantly lower than that of **FeBr@Zr$_6$-Cu** (13,617). These differences can be attributed to different electronic properties of metal centers. Based on this result, **FeBr@Zr$_6$-Cu** and related Fe-based catalytic systems were examined for photocatalytic H_2 evolution in details.

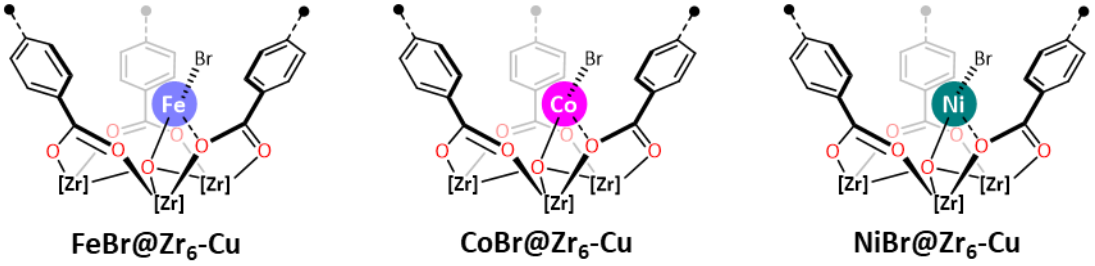

Figure 9-5. Structural depictions of SBU-supported Fe, Co, and Ni catalysts for photocatalytic H_2 evolution.

Table 9-2. Photocatalytic activities of SBU supported Fe, Co, and Ni catalysts.[a]

Entry	Catalyst	H_2 in 200 uL headspace	TON in 24 h
1	**FeBr@Zr$_6$-Cu**	38.13	13617
2	**CoBr@Zr$_6$-Cu**	8.25	2946
3	**NiBr@Zr$_6$-Cu**	4.20	1500

[a] Reactions were conducted with MOF catalysts (containing 0.0030 μmol Cu site and 0.0025 μmol Fe/Co/Ni site), and 45 mg BIH, in 50 μL HOAc + 1.75 mL DMA + 0.2 mL H_2O, under 350-700 nm solid state plasma light source for 24 h.

PXRD studies showed that the crystallinity of **FeBr@Zr$_6$-Cu** was maintained after reaction (**Figure 9-2a**). ICP-MS revealed the leaching of <1.2% Cu and <0.9% Fe into the supernatant during photocatalytic H_2 evolution. XANES and XPS studies revealed that the MOF recovered from reactions, **FeBr@Zr$_6$-Cu(**AR), exhibited the same Fe^{II} oxidation state as **FeBr@Zr$_6$-Cu** (**Figure 9-3b**). EXAFS studies further showed that the Fe coordination environment of **FeBr@Zr$_6$-Cu** was maintained in **FeBr@Zr$_6$-Cu**(AR) with no evidence for the aggregation of reduced Fe centers to form metallic particles (**Figure 9-6**). These results indicate that SBU-supported Fe catalytic centers are highly stable during photocatalytic H_2 evolution due to site isolation by the MOF framework.

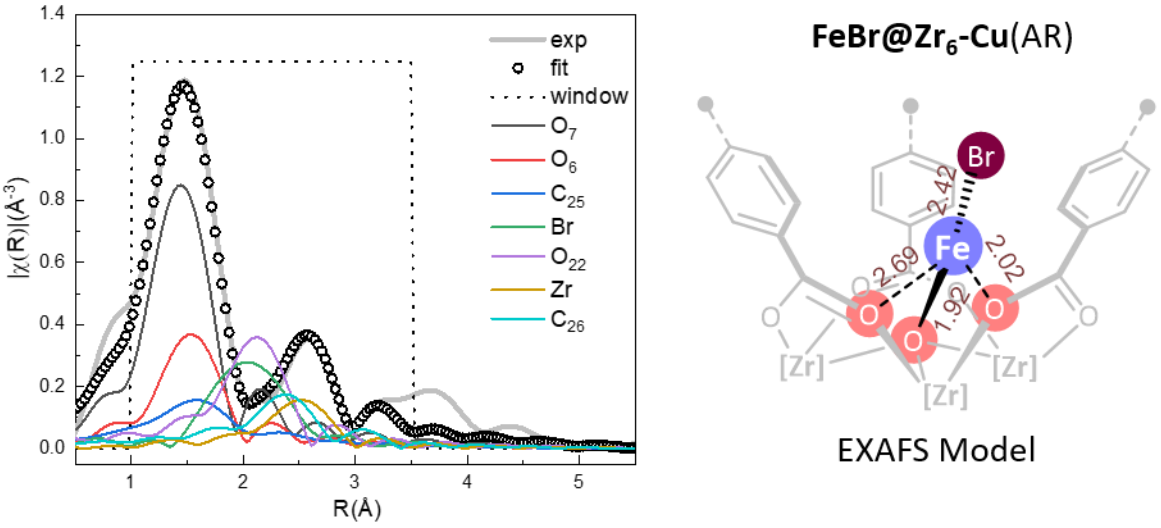

Figure 9-6. EXAFS spectra (grey solid line) and fits (black circles) in R-space at the Fe K-edge adsorption of post-reaction **FeBr@Zr$_6$-Cu** (AR). Copyright 2020 American Chemical Society.

9.2.3 Studies on photocatalytic cycles

FeBr@Zr$_6$-Mc, a homogeneous analogue of SBU-supported Fe^{II} centers, was used to reveal the electrochemical behaviors of Fe centers in **FeBr@Zr$_6$-Cu**. **FeBr@Zr$_6$-Mc** was synthesized by metalating ($Zr_6O_4(OH)_4(McO)_{12}$ clusters (**Zr$_6$-Mc**, Mc = methacrylate) with $FeBr_2$ in the presence of $^iPr_2NEt$.[28] ICP-MS and TGA studies showed of **FeBr@Zr$_6$-Mc** had nearly complete Fe loadings on the Zr_6-Mc clusters whereas XAFS studies revealed Fe^{II} oxidation state and identical Fe coordination environment to **FeBr@Zr$_6$-Cu** (**Figure 9-7**). Cyclic voltammetry (CV) was performed on **FeBr@Zr$_6$-Mc** in different solvents (**Figure 9-8**). While no obvious peak was observed for **FeBr@Zr$_6$-Mc** in *N*,*N*-dimethylacetamide (DMA), a small catalytic H_2 evolution peak appeared when H_2O was added to the solvent (H_2O/DMA = 0.2:1.75, *v*/*v*). When HOAc was added as the proton source (HOAc/H_2O/DMA = 0.05:0.2:1.75, *v*/*v*/*v*), this catalytic H_2 evolution peak became more intense with an onset potential of -0.91 V vs NHE. A reduction peak was also observed at -0.60 V vs NHE in HOAc/H_2O/DMA, indicating a one-electron pre-reduction on the catalytic Fe center before the onset of H_2 evolution.

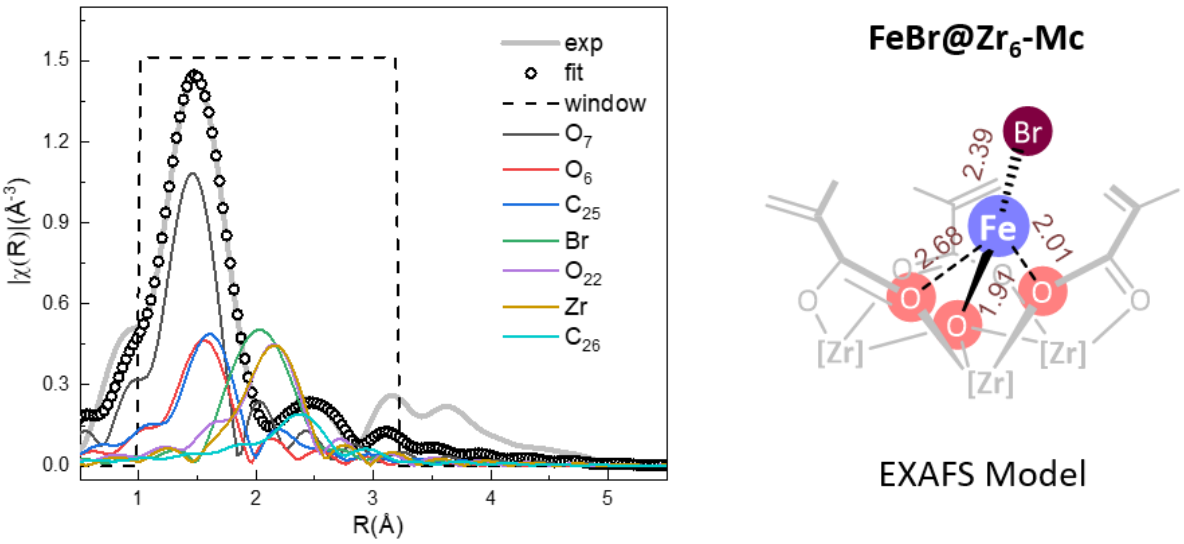

Figure 9-7. EXAFS spectra (grey solid line) and fits (black circles) in R-space at the Fe K-edge adsorption of **FeBr@Zr$_6$-Mc**. Copyright 2020 American Chemical Society.

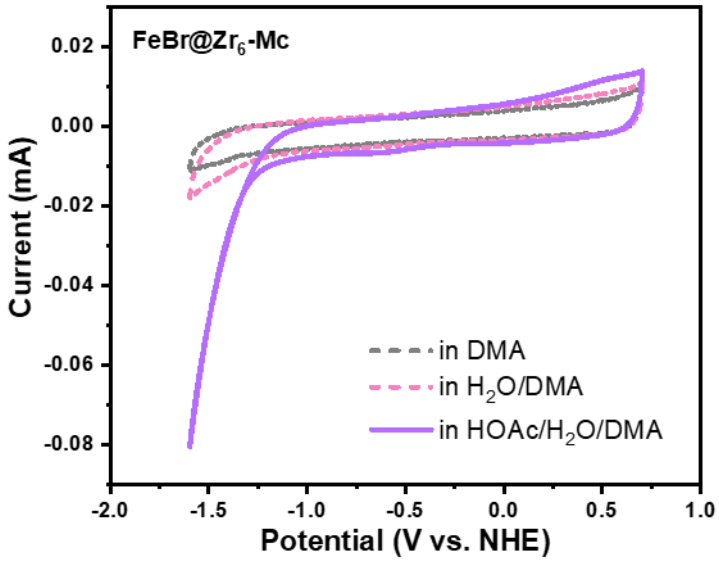

Figure 9-8. CVs of **FeBr@Zr$_6$-Mc** in different solvents with 0.1 M tetrabutylammonium hexafluorophosphate (TBAH).

The photoluminescence of **Zr$_6$-Cu** was studied to reveal the electron transfer pathway in the photocatalytic cycle. The emission of photoexcited **Zr$_6$-Cu** at 570 nm was effectively quenched by sacrificial agent BIH but not by **FeBr@Zr$_6$-Mc** (**Figures 9-9a**, **9-9c**). This

establishes a reductive quenching pathway: photocatalytic H_2 evolution is initiated by electron transfer from BIH to the photoexcited [Cu-PS]* to generate the reduced $[Cu\text{-}PS]^-$, which injects an electron to Fe^{II} centers to start the proton reduction process. CV curves of **L-Cu** and **Zr_6-Cu** showed a common reversible peak at -1.08 V vs NHE for the [Cu-PS]/$[Cu\text{-}PS]^-$ couple (**Figure 9-9d**), suggesting that $[Cu\text{-}PS]^-$ species is reductive enough to drive the proton reduction on SBU-supported Fe centers (-0.91 V vs NHE).

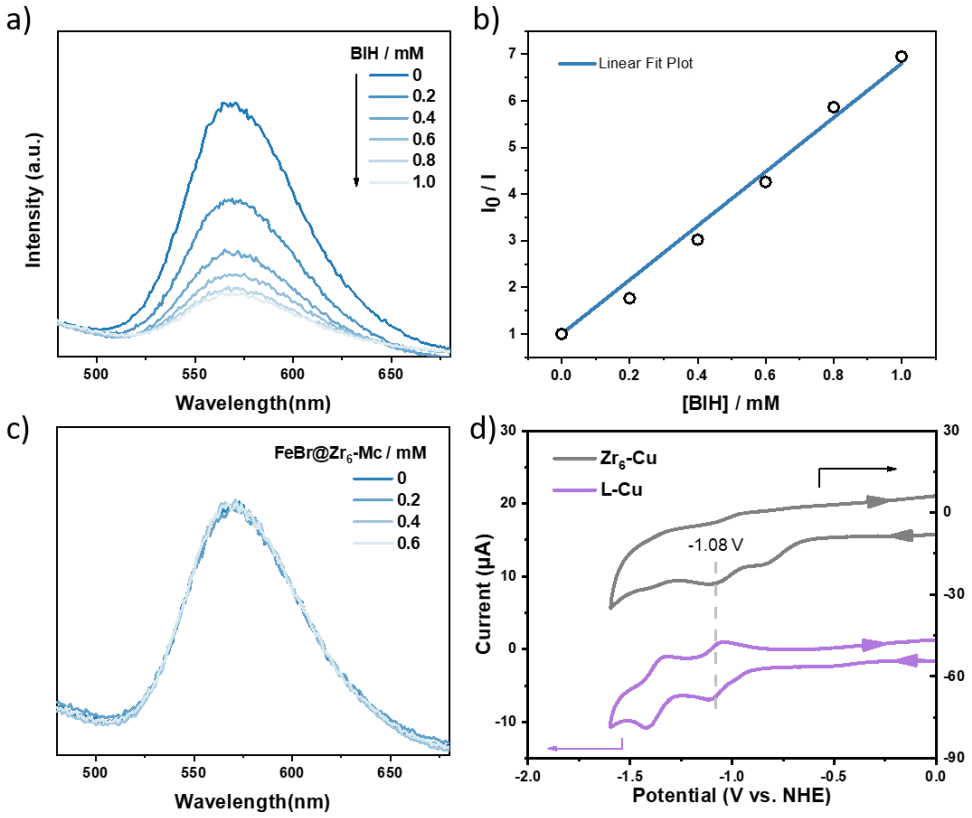

Figure 9-9. Mechanism studies on photocatalytic cycle. (a) Emission spectra of **Zr_6-Cu** (10 μM) after the addition of different amounts of BIH in 2 mL of DMA with 455 nm excitation. (b) Plots of I_0/I of **Zr_6-Cu** as a function of the concentration of BIH (mM). (c) Emission spectra of **Zr_6-Cu** (10 μM) after the addition of different amounts of **FeBr@Zr_6-Mc** in 2 mL of DMA with 455 nm excitation. (d) CVs of **Zr_6-Cu** (grey) coated on the electrode surface and **L-Cu** (violet) in 10 mL 0.1 M TBAH/CH_3CN.

Based on these electrochemical and photophysical results, we propose a catalytic cycle for **FeBr@Zr_6-Cu** catalyzed photocatalytic H_2 evolution in **Figure 9-10**. Upon irradiation, the [Cu-

PS]* is reduced by BIH to form [Cu-PS]$^-$ which transfer an electron to [Fe^{II}] to form [Fe^{I}]. Protonation of [Fe^{I}] generates [Fe^{III}]-H, which is reduced by another [Cu-PS]$^-$ to form [Fe^{II}]-H. Subsequent protonation of [Fe^{II}]-H evolves H_2 and regenerates the [Fe^{II}] site. The tridentate oxo ligand provided by the SBU ensures tight binding to the Fe center during the catalytic cycle and prevents aggregation/deactivation during the photoreduction process while the low-coordinate Fe center provides open sites to accommodate Fe-hydride formation.

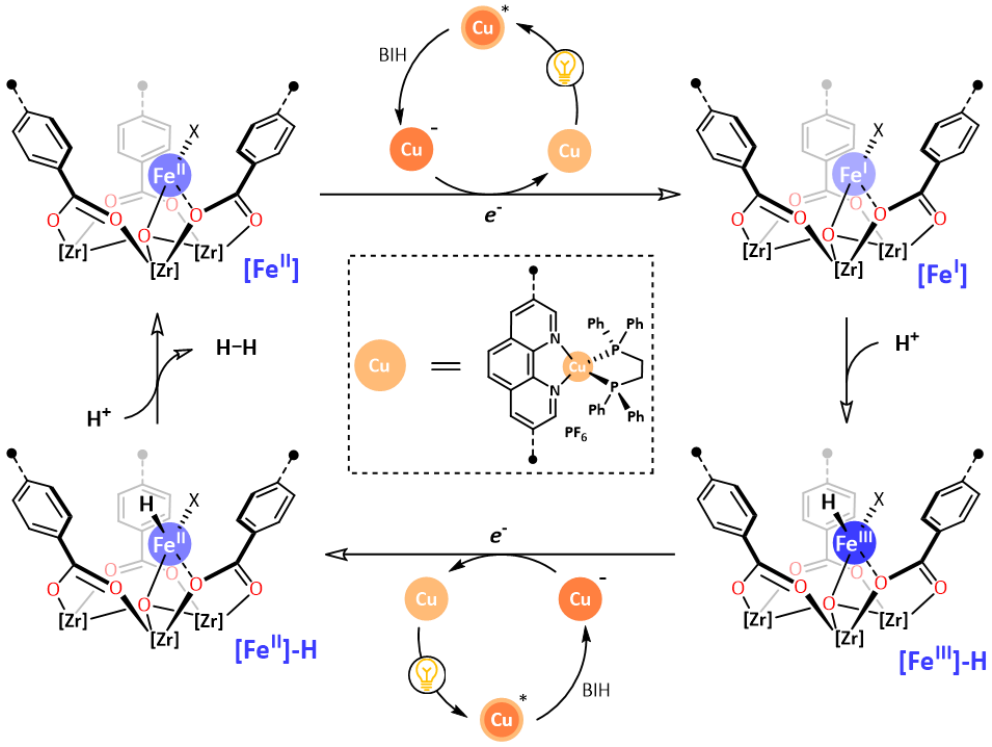

Figure 9-10. Proposed photocatalytic cycle for H_2 evolution. Copyright 2020 American Chemical Society.

9.2.4 Counter anion effect on photocatalytic HER reactivity

We next examined the influence of counter anions in **FeX@Zr$_6$-Cu** MOFs (X = AcO$^-$, Cl$^-$, Br$^-$, and BF$_4^-$) on the photocatalytic H_2 evolution performance. **FeOAc@Zr$_6$-Cu**, **FeCl@Zr$_6$-Cu**, and **FeBF$_4$@Zr$_6$-Cu** were similarly synthesized as **FeBr@Zr$_6$-Cu** with Fe(OAc)$_2$, FeCl$_2$, and Fe(BF$_4$)$_2$·6H$_2$O in place of FeBr$_2$ (**Figure 9-11a**). The similarity in PXRD patterns among

FeX@Zr$_6$-Cu MOFs (**Figure 9-11b**) and ICP-MS results confirmed the generality of this SBU metalation protocol: **FeOAc@Zr$_6$-Cu**, **FeCl@Zr$_6$-Cu**, and **FeBF$_4$@Zr$_6$-Cu** had similar Fe loadings of 59%, 64%, and 57%, respectively. **FeX@Zr$_6$-Cu** MOFs all displayed excellent photocatalytic H_2 evolution activities (**Figure 9-11c**) with an obvious reactivity trend that is inversely dependent on the coordinating strength of the counter anions. The TONs in 48 hours were 33,700, 24,700, 18,300, and 14,500 for **FeX@Zr$_6$-Cu** MOFs with BF_4^-, Br^-, Cl^-, and AcO^-, respectively. **FeBF$_4$@Zr$_6$-Cu** achieved an impressive average TOF of 880 h^{-1} in the first 6 h with an apparent quantum yields of 7.9%. **FeBF$_4$@Zr$_6$-Cu** exhibited 2.3 times higher photocatalytic H_2 evolution activity than **FeOAc@Zr$_6$-Cu**. Furthermore, **FeBF$_4$@Zr$_6$-Cu** was used in four consecutive runs without a significant loss of activity (**Figure 9-12**).

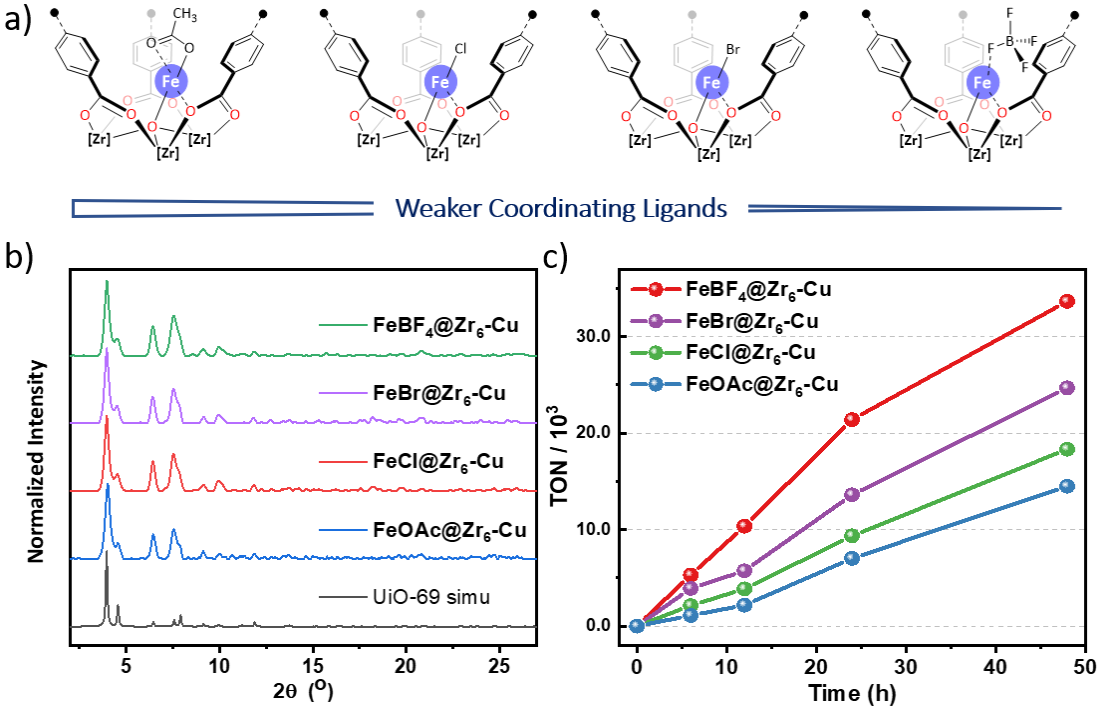

Figure 9-11. Counter anion effect on photocatalytic HER reactivity. (a) Proposed Fe^{II} coordination environments in **FeX@Zr$_6$-Cu** (X = AcO^-, Cl^-, Br^-, and BF_4^-). (b) PXRD patterns of **FeOAc@Zr$_6$-Cu** (navy), **FeCl@Zr$_6$-Cu** (red), **FeBr@Zr$_6$-Cu** (violet), and **FeBF$_4$@Zr$_6$-Cu** (green), compared with the simulated PXRD pattern for UiO-69 (black). (c) Time-dependent H_2 evolution TONs of **FeX@Zr$_6$-Cu** [X = AcO^- (navy), Cl^- (green), Br^- (violet), BF_4^- (red)). Copyright 2020 American Chemical Society.

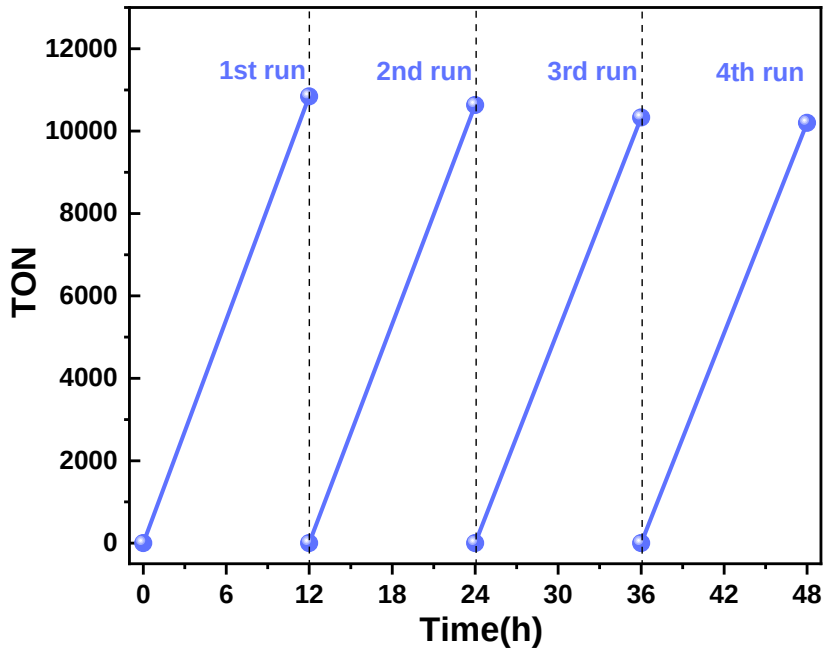

Figure 9-12. Recycle test of **FeBr@Zr$_6$-Cu** catalyzed photocatalytic H_2 evolution in four consecutive runs.

CV curves under catalytic conditions were also obtained for the homogeneous controls **FeX@Zr$_6$-Mc** (X = AcO^-, Cl^-, Br^-, and BF_4^-). Higher current densities were observed in the catalytic H_2 evolution regions for less coordinating anions, with a trend of $AcO^- < Cl^- < Br^- < BF_4^-$ (**Figure 9-13a**). A reverse trend was observed for the corresponding Tafel slopes with the values of 498, 409, 372, and 335 mV/dec for AcO^-, Cl^-, Br^-, and BF_4^-, respectively (**Figure 9-13b**). These results indicate that labile counter anions on the SBU-supported Fe^{II} centers generate open coordinating environments to facilitate the formation of key Fe-hydride intermediates in the proton reduction process, leading to higher activities.

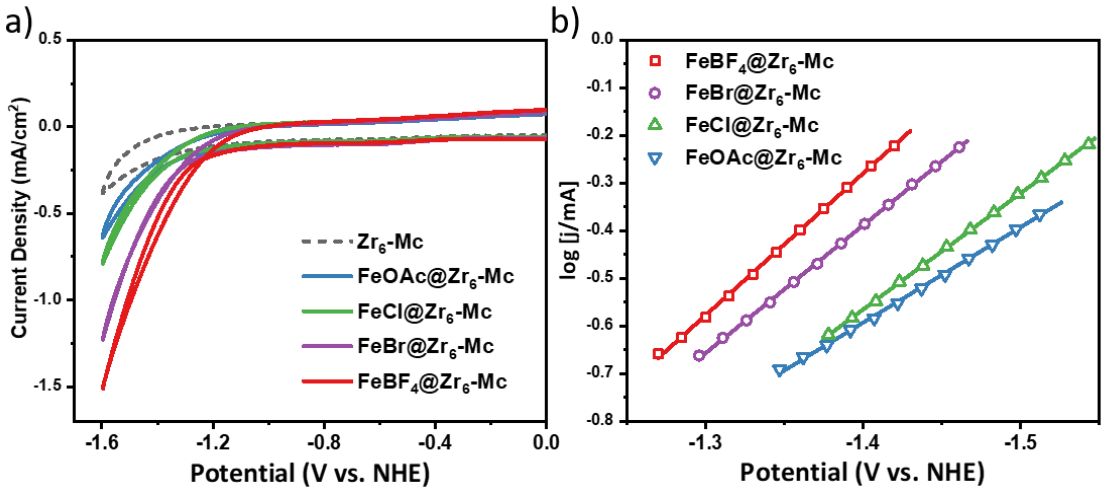

Figure 9-13. (a) CVs of **FeX@Zr$_6$-Mc** [X = AcO$^-$ (navy), Cl$^-$ (green), Br$^-$ (violet), BF$_4^-$ (red)) under reaction conditions (HOAc/H$_2$O/DMA = 0.05:0.2:1.75, *v*/*v*/*v*, with 0.1 M TBAH). (b) Tafel slops for the catalytic H$_2$ evolution regions in (a). Copyright 2020 American Chemical Society.

9.3 Conclusion

In summary, we developed a novel strategy to integrate cuprous photosensitizing linkers and SBU-supported Fe^{II} centers into bifunctional **FeX@Zr$_6$-Cu** MOFs for visible light-driven H$_2$ evolution. Owing to the proximity between Cu-PS and SBU-supported Fe sites and stabilization of Fe sites by periodically ordered SBUs, **FeX@Zr$_6$-Cu** MOFs were highly active for photocatalytic H$_2$ evolution with turnover numbers of up to 33,700 and turnover frequencies of up to 880 h^{-1}. The proton reduction occurs via reductive quenching of Cu-PS excited states by BIH to afford [Cu-PS]$^-$ species which sequentially inject two electrons to Fe^{II} site to generate the Fe^{II}-H intermediate for H$_2$ evolution. As open coordination environments of Fe sites facilitate the formation of Fe-hydride intermediates, H$_2$ evolution activities of **FeX@Zr$_6$-Cu** correlate with the lability of X counter anions. This work establishes MOFs as a powerful platform to integrate Earth-abundant components for solar energy utilization.

9.4 Experimental Section

9.4.1 Materials and methods

All the reactions and manipulations were carried out under N_2 with the use of a glovebox or Schlenk technique, unless otherwise indicated. Tetrahydrofuran and toluene were purified by passing through a neutral alumina column under N_2. All starting materials were purchased from Sigma-Aldrich and Fisher (USA) unless otherwise noted and used without further purification. PXRD data was collected on a Bruker D8 Venture diffractometer using Cu Kα radiation source (l = 1.54178 Å). N_2 sorption experiments were performed on a Micrometrics TriStar II 3020 instrument. TGA was performed in air using a Shimazu TGA-50 equipped with a platinum pan and heated at a rate of 1.5 °C per min. ICP-MS data was obtained with an Agilent 7700x ICP-MS and analyzed using ICP-MS MassHunter version B01.03. Samples were diluted in a 2% HNO_3 matrix and analyzed with a ^{159}Tb internal standard against a 12-point standard curve over the range from 0.1 ppb to 500 ppb. The correlation was >0.9997 for all analyses of interest. Data collection was performed in Spectrum Mode with five replicates per sample and 100 sweeps per replicate. CVs were recorded on a CHI420 electrochemistry workstation with regular 3 electrode systems. Measurements were recorded using a glassy carbon disk working electrode (S = 0.07 cm^2) and a platinum wire as the counter electrode. The Ag/AgCl/1 M KCl electrode was used as the reference electrode in all experiments. X-ray absorption (XAFS) data was collected at Beamline 10-BM, Advanced Photon Source (APS), Argonne National Laboratory. Spectra were collected at the K-edge of Cu or Fe in transmission mode.

^1H and ^{13}C NMR spectra were recorded on a Bruker NMR 500 DRX spectrometer at 500 MHz and referenced to the proton resonance resulting from incomplete deuteration of $CDCl_3$ (δ 7.26) or DMSO-d_6 (δ 2.50). The following abbreviations are used herein: s: singlet, d: doublet, t:

triplet, q: quartet, m: multiplet, br: broad, app: apparent. Amounts of H_2 generated in the photocatalytic experiments were determined by GC using an SRI 8610C Gas Chromatograph with the nitrogen carrier gas and a TCD detector.

9.4.2 Synthesis and characterization of complexes

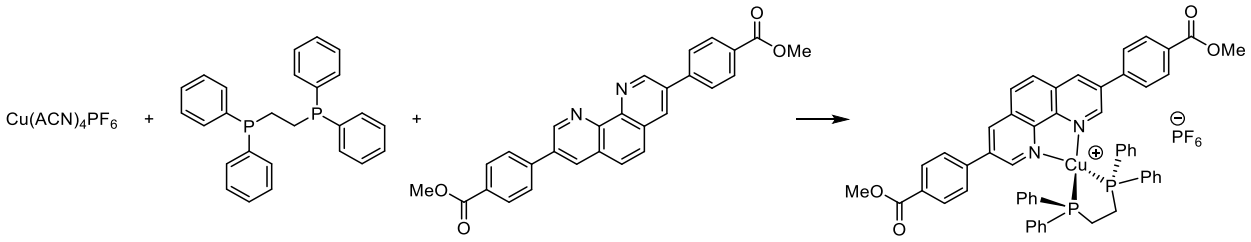

Synthesis of [Cu(Me$_2$**PT**)(dppe)]PF$_6$ (**L-Cu**): As a homogeneous analogue of the photosensitizing **Zr$_6$-Cu**, [Cu(Me$_2$**PT**)(dppe)]PF$_6$ (**L-Cu**) was prepared through a reported method.[26] In a pre-dried 100 mL 3-neck round-bottom flask, Cu(CH$_3$CN)$_4$PF$_6$ (37 mg, 0.1 mmol) and 1,2-bis(diphenylphosphaneyl)ethane (40 mg, 0.1 mmol) were dissolved in 10 mL CH_2Cl_2 and stirred for 1 h under nitrogen atmosphere. A suspension of Me$_2$PT (45 mg, 0.1 mmol) in 15 mL CH_2Cl_2 was added dropwise as the solution turned orange gradually. After stirring under nitrogen for another 3 h, the mixture was concentrated to 1 mL under reduced pressure and a large amount of Et_2O was added. The solid was collected and washed with Et_2O several times before being dried under vacuum to afford an orange powdery **L-Cu** (86 mg, 82% yield). ^{1}H NMR (500 MHz, Chloroform-*d*) δ 8.89 (s, 2H), 8.78 (s, 2H), 8.34 (s, 2H), 8.21 (d, J = 8.0 Hz, 4H), 7.61 (d, J = 8.1 Hz, 4H), 7.49 – 7.31 (m, 20H), 3.99 (s, 6H), 2.81 (t, J = 5.9 Hz, 4H). HR-MS (ESI, positive mode): *m/z* calc'd for $C_{54}H_{44}CuN_2O_4P_2$ $[M\text{-}PF_6]^+$: 909.2067, found 909.2080.

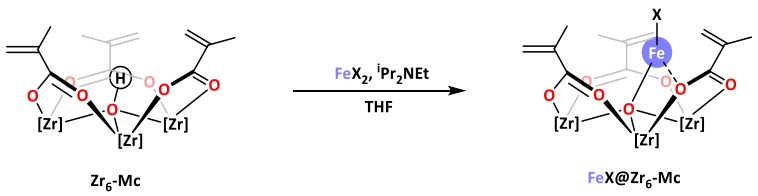

Synthesis of **FeX@Zr$_6$-Mc**: Homogeneous Zr_6-Mc clusters were metalated with FeX_2 to afford **FeX@Zr$_6$-Mc** (X= AcO^-, Cl^-, Br^-, and BF_4^-; Mc = methyl acrylate) to model the catalytic H_2 evolution centers in **FeX@Zr$_6$-Cu**. In a glovebox, 150 mg (0.35 mmol) of **Zr$_6$-Mc** ($Zr_6O_4(OH)_4(MCO)_{12}$[28] was first dissolved in 20 mL THF followed by the addition of 600 μL *N*,*N*-Diisopropylethylamine ($^iPr_2NEt$). The mixture mixed thoroughly before the addition of $FeBr_2$ (75 mg, 3.5 mmol) and the resultant mixture was stirred at room temperature overnight, and then concentrated to ~ 5 mL and filtered through Celite to remove solid impurities. Excess amount of pentane was then added to precipitate a light-brown powdery product. The solid product obtained after filtration was washed with ether and dried under vacuum to afford pure **FeBr@Zr$_6$-Mc** (139 mg, 71% of yield). ICP-MS analysis of **FeBr@Zr$_6$-Mc** revealed a Zr:Fe ratio of 6:3.92, which is close to the expected ratio of 6:4, with Fe occupying all the 4 μ_3-OH sites. TGA curve of **FeBr@Zr$_6$-Mc** displayed a weight loss of 53.5% in the 250-600 °C temperature range, which corresponds to the decomposition of the metalated cluster $Zr_6O_4(OFeBr)_4(C_4H_5O_2)_{12}$ to corresponding metal oxides $(ZrO_2)_6(FeO_{1.5})_4$, with an expected weight loss of 52.8%. HR-MS (ESI-TOF, positive mode) of **FeBr@Zr$_6$-Mc**: *m/z* calc'd for $C_{48}H_{60}Br_4Fe_4O_{32}Zr_6Na_3$ $[M+3Na]^{3+}$:769.3710, found 769.3830.

FeX@Zr$_6$-Mc (X = AcO^-, Cl^-, and BF_4^-) were synthesized similarly as **FeBr@Zr$_6$-Mc** with the exception that $FeBr_2$ was replaced by $Fe(OAc)_2$, $FeCl_2$, or $Fe(BF_4)_2{\cdot}6H_2O$. TGA curve of **FeOAc@Zr$_6$-Mc** displayed a weight loss of 52.5% in the 250-600 °C temperature range, corresponding to the decomposition of $Zr_6O_4(OFeOAc)_4(C_4H_5O_2)_{12}$ to $(ZrO_2)_6(FeO_{1.5})_4$ (expected weight loss: 51.0%). HR-MS (ESI-TOF, positive mode) of **FeOAc@Zr$_6$-Mc**: *m/z* calc'd for $C_{56}H_{72}Fe_4O_{40}Zr_6$ $[M]^{3+}$:718.5101, found 718.5316. TGA curve of **FeCl@Zr$_6$-Mc** displayed a weight loss of 49.9% in the 250-600 °C temperature range corresponding to the decomposition of

$Zr_6O_4(OFeCl)_4(C_4H_5O_2)_{12}$ to $(ZrO_2)_6(FeO_{1.5})_4$ with an expected weight loss of 48.8%. HR-MS (ESI-TOF, positive mode) of **FeCl@Zr$_6$-Mc**: *m/z* calc'd for $C_{48}H_{60}Cl_4Fe_4O_{32}Zr_6Na_3$ $[M+Na]^+$:2084.3393, found 2084.2954. TGA curve of **FeBF$_4$@Zr$_6$-Mc** displayed a weight loss of 60.8% in the 250-600 °C temperature range, corresponding to the decomposition of $Zr_6O_4(OFe(THF)BF_4)_4(C_4H_5O_2)_{12}$ to $(ZrO_2)_6(FeO_{1.5})_4$, with an expected weight loss of 61.5%. HR-MS (ESI-TOF, positive mode) of **FeBF$_4$@Zr$_6$-Mc**: *m/z* calc'd for $C_{40}H_{60}B_4F_{16}Fe_4O_{32}Zr_6K_3$ $[M+3K]^{3+}$:793.7944, found 793.7941.

9.4.3 Synthetic procedures of MOF Catalysts

Synthesis of **Zr$_6$-mPT**: **FeX@Zr$_6$-Cu** (X = AcO^-, Cl^-, Br^-, BF_4^-) was synthesized through multi-step post-synthetic installation of photosensitizer Cu(**PT**)$(dppe)^+$ on the **PT** ligand of previously reported **Zr$_6$-mPT** MOF followed by SBU metalation with Fe^{II} salts. **Zr$_6$-mPT** was synthesized as a pale-yellow powder in 53% yield through a solvothermal reaction of H_2**PT** (6.0 mg), H_2**TPHN** (14 mg), and $ZrCl_4$ (10 mg) in DMF (5.0 mL) with trifluoroacetic acid (0.05 mL) as modulator in a 100 °C oven for 3 days.[25] A **PT**/**TPHN** ratio of 1:4 was determined by ^{1}H NMR integration of the digested MOF samples.

Synthesis of **FeBr@Zr$_6$-Cu**: **FeBr@Zr$_6$-Cu** was synthesized as follows: in a glovebox, a mixture of **Zr$_6$-mPT** (10.0 mg, ~ 2 μmol PT) and $Cu(CH_3CN)_4PF_6$ (10 μmol) in CH_2Cl_2 (5 mL) was stirred at room temperature for 24 h. The resultant yellow solid was centrifuged out of suspension and washed with CH_2Cl_2 several times to remove excess Cu salt. 1,2-Bis(diphenylphosphino)ethane (dppe, 2.5 μmol) was then added to the MOF in CH_2Cl_2 and stirred for another 24 h before being washed with CH_2Cl_2 to afford **Zr$_6$-Cu**. The above yellow-orange solid **Zr$_6$-Cu** was further metalated with $FeBr_2$ (2 μmol) in 10 mL THF at room temperature in the presence of ^{i}Pr$_2$NEt (10 μmol) for 18 h and then thoroughly washed with THF to afford

FeBr@Zr$_6$-Cu as a yellow-orange solid (11 mg, 90% yield). ICP-MS analysis of **FeBr@Zr$_6$-Cu** revealed a Zr: Cu: Fe ratio of 6:0.67:0.56, with 92% Cu loading on **PT** sites and 56% Fe loading on SBU (w.r.t. Zr_6).

Synthesis of **FeX@Zr$_6$-Cu** (X = AcO^-, Cl^-, BF_4^-): **FeX@Zr$_6$-Cu** (X = AcO^-, Cl^-, BF_4^-) samples were similarly synthesized with the exception that $FeBr_2$ was replaced by $Fe(OAc)_2$, $FeCl_2$, and $Fe(BF_4)_2 \cdot 6H_2O$. Regardless the identity of X, the **FeX@Zr$_6$-Cu** samples showed comparable Fe and Cu loading as revealed by ICP-MS. **FeOAc@Zr$_6$-Cu** had a Zr: Cu: Fe ratio of 6:0.66:0.59, with 91% Cu loading on **PT** sites and 59% Fe loading on SBU (w.r.t. Zr_6). **FeCl@Zr$_6$-Cu** had a Zr: Cu: Fe ratio of 6:0.67:0.64, with 92% Cu loading on **PT** sites and 64% Fe loading on SBU (w.r.t. Zr_6). **FeBF$_4$@Zr$_6$-Cu** had a Zr: Cu: Fe ratio of 6:0.67:0.57, with 92% Cu loading on **PT** sites and 57% Fe loading on SBU (w.r.t. Zr_6).

9.4.4 Photocatalytic reaction setup

Typical photocatalytic H_2 evolution procedure: Photocatalytic H_2 evolution was carried out in an external illumination type reaction vessel with a magnetic stirrer. Samples were prepared in 4.0 mL septum-sealed glass vials. In a standard reaction, each sample was made up to a volume of 2.0 mL including 1.75 mL DMA, 0.05 mL HOAc, 0.20 mL H_2O and 45 mg BIH (0.2 mmol) in addition to a certain amount of MOF catalyst. Sample vials were capped and sealed and deoxygenated by bubbling nitrogen through for 10 min to ensure complete air removal. At room temperature, the solution was irradiated by a 13.9 W 350-700 nm solid state plasma light source equipped with cooling fans (HPLS-30-04 from Thorlabs Inc.) for 24 h. After the hydrogen evolution reaction, the gas in the headspace of the vial was analyzed by GC to determine the amount of hydrogen generated. TON of H_2 evolution was calculated based on the amount of catalytic Fe sites.

9.4.5 Quantum yield determination

A 13.9 W 350-700 nm solid state light source was used as the light source and the apparent quantum yield was measured using band-pass optical filters by a standard ferrioxalate actinometry.[29-30] 1 mL of ferrioxalate (0.15 M, prepared by dissolving 736.9 mg of potassium ferrioxalate hydrate in 10 mL of 0.05 M H_2SO_4) was added to a quartz cuvette (l = 1.0 cm). The actinometry solution was irradiated (with a 380 nm ± 2 nm wavelength band-pass optical filter) for 90 seconds. After irradiation, 175 μL of phenanthroline solution (50 mg of 1,10-phenanthroline and 11.25 g of sodium acetate dissolving in 10 mL of 0.05 M H_2SO_4) was added to the cuvette. The solution was kept in the dark for 30 min to ensure complete coordination. The absorbance of the actinometry solution was monitored at 510 nm. The absorbance of a non-irradiated (in dark) sample was also measured at 510 nm. Conversion was calculated using eq. S1:

$$mol\ Fe^{2+} = \frac{V \cdot \Delta A}{l \cdot \varepsilon} \ (\mathbf{eq.\ S1})$$

Where V is the final volume (0.001175 L) after complexation with phenanthroline, ΔA is the difference in absorbance at 510 nm between the irradiated and non-irradiated solutions, l is the path length (1.0 cm) and ε is the molar absorptivity at 510 nm (11,100 $L \cdot mol^{-1} \cdot cm^{-1}$).[30] Therefore, the photon flux can be calculated using eq. S2:

$$photo\ flux = \frac{mol\ Fe^{2+}}{\Phi \cdot t \cdot f} \ (\mathbf{eq.\ S2})$$

Where Φ is the quantum yield for the ferrioxalate actinometer,[31-32] t is the time (90 s), and f is the fraction of light absorbed at certain wavelength of band-pass optical filter (~1).

After quantifying the amount of H_2 under the irradiation of certain wavelength using band-pass optical filter, the apparent quantum yield was calculated according to **eq. S3**:

$$\Phi = \frac{mol\ of\ evolved\ H_2 \times 2}{photo\ fulx \cdot t \cdot f} \ (\mathbf{eq.\ S3})$$

The apparent quantum yield for **$FeBF_4$@Zr_6-Cu** was calculated to be 7.9%.

9.4.6 Recycle test of FeX@Zr_6-Cu catalyzed photocatalytic H_2 evolution

$FeBF_4$@Zr_6-Cu was chosen for photocatalytic H_2 evolution recycle test to demonstrate the stability and reusability of the present catalytic MOF system. Under photocatalytic H_2 evolution conditions, **$FeBF_4$@Zr_6-Cu** was recycled and reused without significant drop in activity for at least 4 consecutive runs, by simply degassing the MOF-containing catalytic solution with N_2 and adding more sacrificial agent (10 mg BIH) after each run. Specifically, H_2 evolution recycles were conducted with **$FeBF_4$@Zr_6-Cu** catalyst (0.0030 μmol Cu site, 0.0025 μmol Fe site), and 45 mg BIH, in 50 μL HOAc + 1.75 mL DMA + 0.2 mL H_2O, under 350-700 nm solid state plasma light source for 12 h. The solution was degassed with N_2 for 10 min before each run and 10 mg of BIH was added to the solution after each run.

9.5 References

1. Matsuoka, M.; Kitano, M.; Takeuchi, M.; Tsujimaru, K.; Anpo, M.; Thomas, J. M., Photocatalysis for new energy production: Recent advances in photocatalytic water splitting reactions for hydrogen production. *Catalysis Today* **2007,** *122* (1), 51-61.

2. Maeda, K.; Domen, K., Photocatalytic Water Splitting: Recent Progress and Future Challenges. *The Journal of Physical Chemistry Letters* **2010,** *1* (18), 2655-2661.

3. Acar, C.; Dincer, I.; Naterer, G. F., Review of photocatalytic water-splitting methods for sustainable hydrogen production. *International Journal of Energy Research* **2016,** *40* (11), 1449-1473.

4. Takanabe, K., Photocatalytic Water Splitting: Quantitative Approaches toward Photocatalyst by Design. *ACS Catalysis* **2017,** *7* (11), 8006-8022.

5. Na, Y.; Wang, M.; Pan, J.; Zhang, P.; Åkermark, B.; Sun, L., Visible Light-Driven Electron Transfer and Hydrogen Generation Catalyzed by Bioinspired [2Fe2S] Complexes. *Inorganic Chemistry* **2008,** *47* (7), 2805-2810.

6. Zuo, F.; Wang, L.; Wu, T.; Zhang, Z.; Borchardt, D.; Feng, P., Self-Doped Ti3+ Enhanced Photocatalyst for Hydrogen Production under Visible Light. *Journal of the American Chemical Society* **2010,** *132* (34), 11856-11857.

7. Sprick, R. S.; Jiang, J.-X.; Bonillo, B.; Ren, S.; Ratvijitvech, T.; Guiglion, P.; Zwijnenburg, M. A.; Adams, D. J.; Cooper, A. I., Tunable Organic Photocatalysts for Visible-Light-Driven Hydrogen Evolution. *Journal of the American Chemical Society* **2015,** *137* (9), 3265-3270.

8. Wang, L.; Xiao, H.; Cheng, T.; Li, Y.; Goddard, W. A., Pb-Activated Amine-Assisted Photocatalytic Hydrogen Evolution Reaction on Organic–Inorganic Perovskites. *Journal of the American Chemical Society* **2018,** *140* (6), 1994-1997.

9. Esswein, A. J.; Nocera, D. G., Hydrogen Production by Molecular Photocatalysis. *Chemical Reviews* **2007,** *107* (10), 4022-4047.

10. Ran, J.; Zhang, J.; Yu, J.; Jaroniec, M.; Qiao, S. Z., Earth-abundant cocatalysts for semiconductor-based photocatalytic water splitting. *Chemical Society Reviews* **2014,** *43* (22), 7787-7812.

11. Wang, M.; Chen, L.; Sun, L., Recent progress in electrochemical hydrogen production with earth-abundant metal complexes as catalysts. *Energy & Environmental Science* **2012,** *5* (5), 6763-6778.

12. Fu, Y.; Sun, D.; Chen, Y.; Huang, R.; Ding, Z.; Fu, X.; Li, Z., An Amine-Functionalized Titanium Metal–Organic Framework Photocatalyst with Visible-Light-Induced Activity for CO2 Reduction. *Angewandte Chemie International Edition* **2012,** *51* (14), 3364-3367.

13. Wang, J.-L.; Wang, C.; Lin, W., Metal–Organic Frameworks for Light Harvesting and Photocatalysis. *ACS Catalysis* **2012,** *2* (12), 2630-2640.

14. Pullen, S.; Fei, H.; Orthaber, A.; Cohen, S. M.; Ott, S., Enhanced Photochemical Hydrogen Production by a Molecular Diiron Catalyst Incorporated into a Metal–Organic Framework. *Journal of the American Chemical Society* **2013,** *135* (45), 16997-17003.

15. Zhang, Z.-M.; Zhang, T.; Wang, C.; Lin, Z.; Long, L.-S.; Lin, W., Photosensitizing Metal–Organic Framework Enabling Visible-Light-Driven Proton Reduction by a Wells–Dawson-Type Polyoxometalate. *Journal of the American Chemical Society* **2015,** *137* (9), 3197-3200.

16. Kim, D.; Whang, D. R.; Park, S. Y., Self-Healing of Molecular Catalyst and Photosensitizer on Metal–Organic Framework: Robust Molecular System for Photocatalytic H2 Evolution from Water. *Journal of the American Chemical Society* **2016,** *138* (28), 8698-8701.

17. Leng, F.; Liu, H.; Ding, M.; Lin, Q.-P.; Jiang, H.-L., Boosting Photocatalytic Hydrogen Production of Porphyrinic MOFs: The Metal Location in Metalloporphyrin Matters. *ACS Catalysis* **2018,** *8* (5), 4583-4590.

18. Deng, H.; Doonan, C. J.; Furukawa, H.; Ferreira, R. B.; Towne, J.; Knobler, C. B.; Wang, B.; Yaghi, O. M., Multiple Functional Groups of Varying Ratios in Metal-Organic Frameworks. *Science* **2010,** *327* (5967), 846.

19. Huang, Y.-B.; Liang, J.; Wang, X.-S.; Cao, R., Multifunctional metal–organic framework catalysts: synergistic catalysis and tandem reactions. *Chemical Society Reviews* **2017,** *46* (1), 126-157.

20. Feng, L.; Wang, K.-Y.; Day, G. S.; Zhou, H.-C., The chemistry of multi-component and hierarchical framework compounds. *Chemical Society Reviews* **2019,** *48* (18), 4823-4853.

21. Cao, C.-C.; Chen, C.-X.; Wei, Z.-W.; Qiu, Q.-F.; Zhu, N.-X.; Xiong, Y.-Y.; Jiang, J.-J.; Wang, D.; Su, C.-Y., Catalysis through Dynamic Spacer Installation of Multivariate Functionalities in Metal–Organic Frameworks. *Journal of the American Chemical Society* **2019,** *141* (6), 2589-2593.

22. Manna, K.; Ji, P.; Greene, F. X.; Lin, W., Metal–Organic Framework Nodes Support Single-Site Magnesium–Alkyl Catalysts for Hydroboration and Hydroamination Reactions. *Journal of the American Chemical Society* **2016,** *138* (24), 7488-7491.

23. Ikuno, T.; Zheng, J.; Vjunov, A.; Sanchez-Sanchez, M.; Ortuño, M. A.; Pahls, D. R.; Fulton, J. L.; Camaioni, D. M.; Li, Z.; Ray, D.; Mehdi, B. L.; Browning, N. D.; Farha, O. K.; Hupp, J. T.; Cramer, C. J.; Gagliardi, L.; Lercher, J. A., Methane Oxidation to Methanol Catalyzed by Cu-Oxo Clusters Stabilized in NU-1000 Metal–Organic Framework. *Journal of the American Chemical Society* **2017,** *139* (30), 10294-10301.

24. Xu, C.; Pan, Y.; Wan, G.; Liu, H.; Wang, L.; Zhou, H.; Yu, S.-H.; Jiang, H.-L., Turning on Visible-Light Photocatalytic C−H Oxidation over Metal–Organic Frameworks by Introducing Metal-to-Cluster Charge Transfer. *Journal of the American Chemical Society* **2019,** *141* (48), 19110-19117.

25. Manna, K.; Zhang, T.; Greene, F. X.; Lin, W., Bipyridine- and Phenanthroline-Based Metal–Organic Frameworks for Highly Efficient and Tandem Catalytic Organic Transformations via Directed C–H Activation. *Journal of the American Chemical Society* **2015,** *137* (7), 2665-2673.

26. Feng, X.; Pi, Y.; Song, Y.; Brzezinski, C.; Xu, Z.; Li, Z.; Lin, W., Metal–Organic Frameworks Significantly Enhance Photocatalytic Hydrogen Evolution and CO2 Reduction with Earth-Abundant Copper Photosensitizers. *Journal of the American Chemical Society* **2020,** *142* (2), 690-695.

27. Manna, K.; Ji, P.; Lin, Z.; Greene, F. X.; Urban, A.; Thacker, N. C.; Lin, W., Chemoselective single-site Earth-abundant metal catalysts at metal–organic framework nodes. *Nat. Commun.* **2016,** *7* (1), 12610.

28. Kickelbick, G.; Wiede, P.; Schubert, U., Variations in capping the Zr6O4(OH)4 cluster core: X-ray structure analyses of [Zr6(OH)4O4(OOC–CH CH2)10]2(μ-OOC–CH CH2)4 and Zr6(OH)4O4(OOCR)12(PrOH) (R=Ph, CMe=CH2). *Inorganica Chimica Acta* **1999,** *284* (1), 1-7.

29. Kuhn, H.; Braslavsky, S.; Schmidt, R., Chemical actinometry (IUPAC technical report). *Pure and Applied Chemistry* **2004,** *76* (12), 2105-2146.

30. Cismesia, M. A.; Yoon, T. P., Characterizing chain processes in visible light photoredox catalysis. *Chemical Science* **2015,** *6* (10), 5426-5434.

31. Murov, S. L.; Carmichael, I.; Hug, G. L., *Handbook of photochemistry*. CRC Press: 1993.

32. Hatchard, C. G.; Parker, C. A.; Bowen, E. J., A new sensitive chemical actinometer - II. Potassium ferrioxalate as a standard chemical actinometer. *Proceedings of the Royal Society of London. Series A. Mathematical and Physical Sciences* **1956,** *235* (1203), 518-536.

Chapter 10. Integration of Earth-Abundant Photosensitizers and Catalysts in MOFs Enhances Photocatalytic Aerobic Oxidation

10.1 Introduction

With the increasing emphasis on environmental sustainability and green chemistry,[1-2] O_2 has established its irreplaceable role as a green, cheap, and abundant oxidant for the synthesis of oxygen-containing chemical feedstocks.[3] The development of efficient and cost-effective catalytic systems for aerobic oxidation processes has become an important research topic, with significant progress made in recent years.[4-7] However, in order to activate the triplet O_2 and control the radical reaction during the oxidation process, traditional transition metal-catalyzed aerobic oxidations typically rely on hash reaction conditions and (sub)stoichiometric amounts of expensive radical initiators, which limits their practical applications.[8-9] In contrast, by utilizing light to provide energy for the activation of ground state O_2 and to facilitate electron transfer between the substrates and oxidants, photocatalytic aerobic oxidations can be performed under ambient temperature and atmospheric pressure without co-catalysts, thus providing an attractive platform for the development of novel catalytic systems for environmentally benign synthetic processes.[10-12]

Despite the advantages offered by and the progress made in photocatalytic aerobic oxidation systems, significant challenges remain and limit their widespread applications. For example, the reliance on rare, expensive, and toxic noble metals, such as Ru, Ir, Os, and Pt, for efficient photosensitization presents a significant roadblock for practical photocatalytic processes.[13-15] Although semiconductor-based photocatalysts can address some of these challenges, they tend to have a distribution of active centers, which makes it difficult to study the reaction mechanism in details and tune the active sites for enhanced reactivity or selectivity.[10, 16-18] Thus,

there is a strong need of developing well-defined photocatalytic systems based on inexpensive Earth-abundant metals (EAMs).[19-22] We envisioned that MOFs could provide a tunable platform to design efficient photocatalytic aerobic oxidation systems based on EAMs. MOFs have recently been shown to stabilize homogeneously-inaccessible EAM complexes for catalytic or photocatalytic applications through active site isolation and pore confinement.[12, 23-24] In the meanwhile, high local concentrations and proximity of multiple active sites in MOFs can enhance electron and mass transfer, which is critically important in photocatalytic processes.[25-27] The well-defined active centers in MOF catalysts allow in-depth understanding of reaction mechanisms to facilitate catalyst optimization.

In Chapters 8 and 9, we showed that MOFs stabilize cuprous photosensitizers (Cu-PSs) as potent photo-reductants.[28] As Cu-PSs are also effective photo-oxidants[29-30] and Fe catalysts have been successfully used in many homogeneous oxidation reactions,[7, 31] we surmised that Earth-abundant Cu-PSs and Fe catalysts could be integrated into MOFs for photocatalytic oxidation using O_2 as the oxidant (**Scheme 10-1**). The MOF catalysts with both Cu-PSs and Fe catalysts, **Zr_6-Cu/Fe-1** and **Zr_6-Cu/Fe-2**, were highly active in photocatalytic aerobic oxidation of alcohols and benzylic compounds to selectively afford corresponding carbonyl products with turnover numbers (TONs) as high as 500. No additives were required and the aerobic process proceeded smoothly under room temperature. Due to the stabilization of both EAM complexes by the MOF framework and enhanced electron transfer between proximate Cu-PSs and Fe catalysts, **Zr_6-Cu/Fe-1** showed a nearly 10-fold enhancement in TONs over the homogeneous analogue. In-depth mechanistic studies by combining control experiments, spectroscopic data, and computational results revealed that, upon light irradiation and with O_2 as oxidant, [Cu^{II}-PS] efficiently oxidizes Fe^{III}-OH to generate hydroxyl radical as the key reactive species for substrate oxidation.

Scheme 10-1. Integration of earth-abundant photosensitizers and catalysts in MOFs enhances photocatalytic aerobic oxidation. Copyright 2021 American Chemical Society.

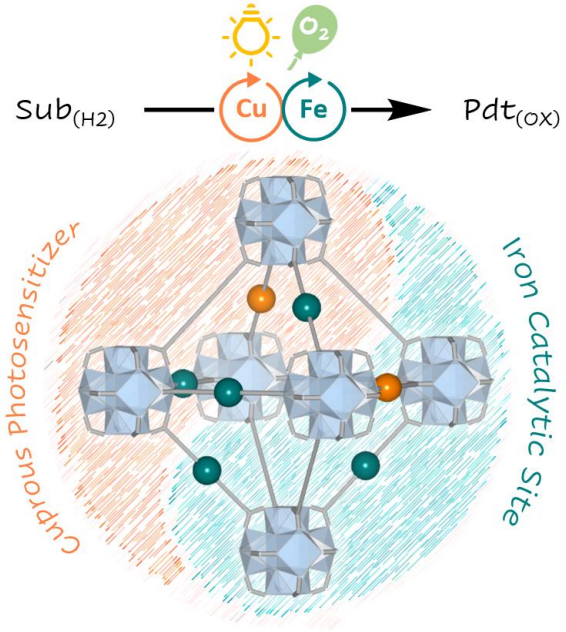

10.2 Results and Discussion

10.2.1 Synthesis and characterization of MOF catalysts

We targeted cuprous diimine-diphosphine photosensitizing complexes for the construction of visible light-responsive MOF catalysts. The initial attempt of using $ZrCl_4$ as the Zr source failed to give the targeted MOF due to the decomposition of Cu-PSs by the highly Lewis acidic $ZrCl_4$. $Zr_6O_4(OH)_4(McO)_{12}$ clusters (**Zr_6-Mc**, Mc = methacrylate)[32] , which was compatible with the cuprous complex, was applied as an alternative Zr source. After optimization, Cu-PSs [Cu(H_2bpydc)(XantP)](PF_6) (XantP = dimethyl-4,5-bis(diphenylphosphino)xanthene, H_2bpydc = 2,2'-bipyridine-5,5'-dicarboxylic acid) and [Cu(H_2bpydc)(POP)[(PF_6) (POP = bis(2-diphenylphosphino)phenyl ether) were successfully incorporated into UiO-type MOFs through solvothermal reactions of H_2bpydc, [Cu(H_2bpydc)(XantP)](PF_6) or [Cu(H_2bpydc)(POP)](PF_6), and **Zr_6-Mc** in oxygen-free *N*,*N*-dimethylformamide (DMF) to afford **Zr_6-Cu-1** and **Zr_6-Cu-2**, respectively (**Figure 10-1a**). **Zr_6-Cu/Fe-1** and **Zr_6-Cu/Fe-2** were obtained as light olive solids

through subsequent metalation of the bpy sites in **Zr_6-Cu-1** and **Zr_6-Cu-2**, respectively, with $FeCl_2$. Powder X-ray diffraction (PXRD) and transmission electron microscopy (TEM) studies showed that **Zr_6-Cu-1**, **Zr_6-Cu-2**, **Zr_6-Cu/Fe-1**, and **Zr_6-Cu/Fe-2** all adopted UiO-67-type topology with near-octahedral morphologies of ~40 nm in dimensions (**Figures 10-1b**, **10-1c**, **10-2**). Such nano size and uniform morphology are expected to facilitate light penetration and substrate diffusion as well as efficient absorption of oxygen for photocatalytic aerobic processes.

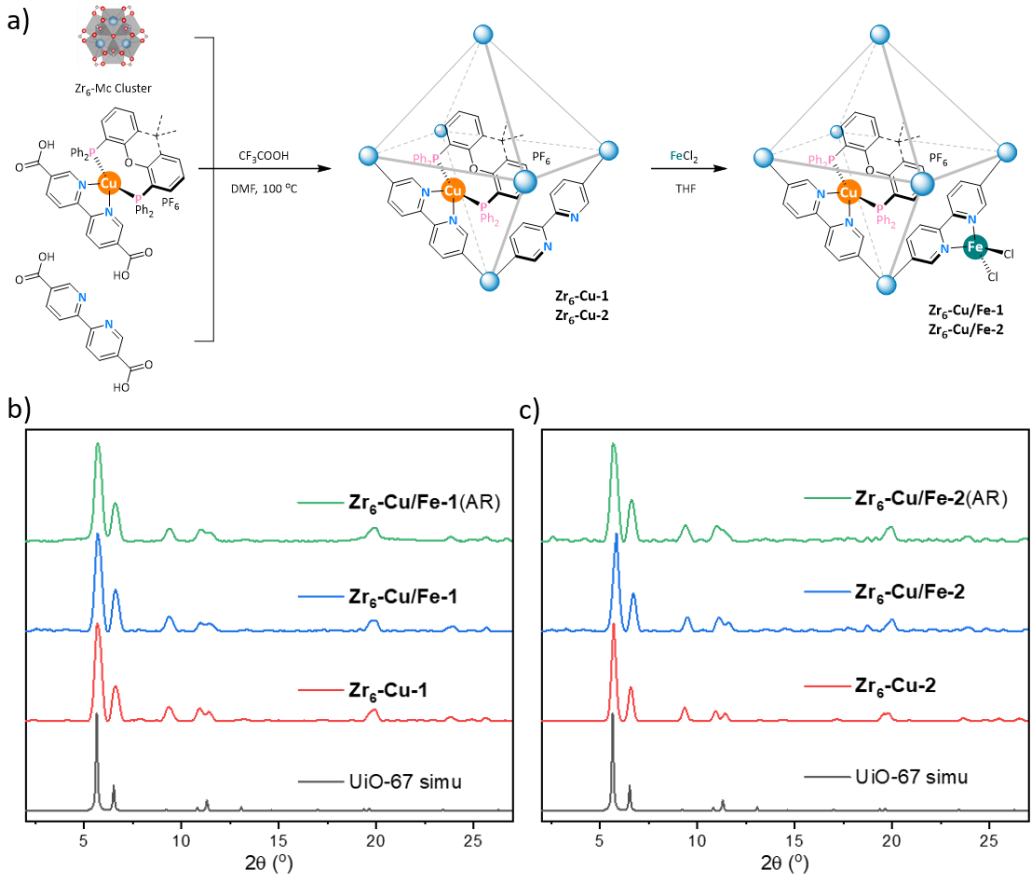

Figure 10-1. Synthesis and PXRDs of **Zr_6-Cu/Fe-1** and **Zr_6-Cu/Fe-2**. (a) Synthesis of MOF-based photocatalytic aerobic oxidation systems **Zr_6-Cu/Fe-1** and **Zr_6-Cu/Fe-2** with **Zr_6-Mc** as the Zr source. (b,c) PXRD patterns of **Zr_6-Cu-1** and **Zr_6-Cu-2** (red), **Zr_6-Cu/Fe-1** and **Zr_6-Cu/Fe-2** (navy), and **Zr_6-Cu/Fe-1** (AR) and **Zr_6-Cu/Fe-2** (AR) (green) compared to the simulated pattern of UiO-67 (black). Copyright 2021 American Chemical Society.

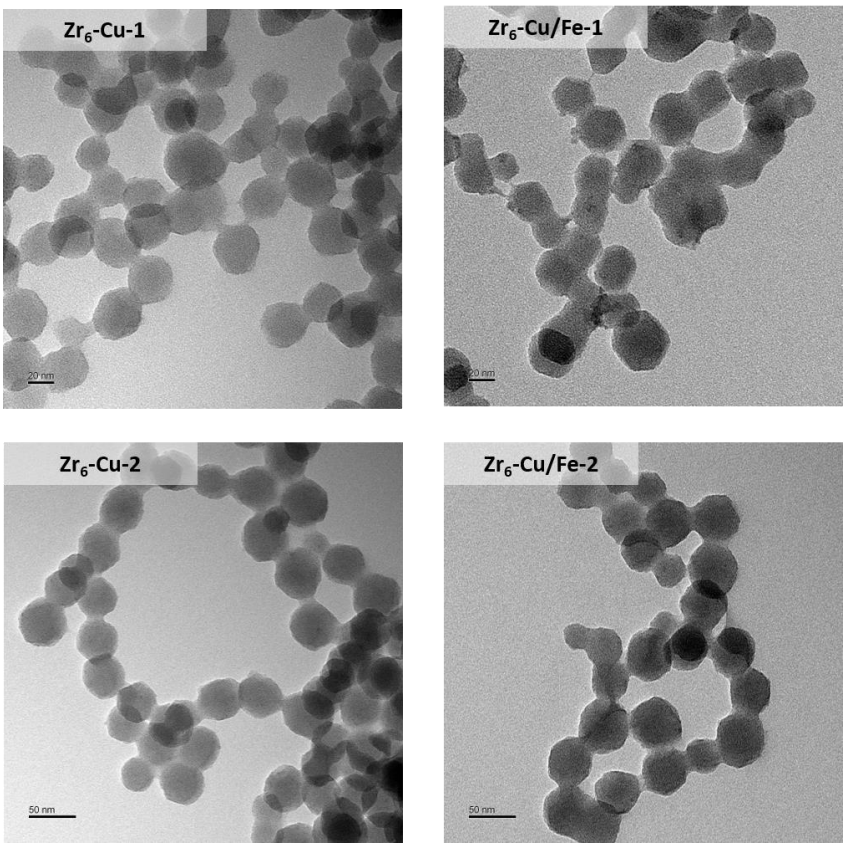

Figure 10-2. TEM images of **Zr_6-Cu-1** and **Zr_6-Cu-2** (left) and **Zr_6-Cu/Fe-1** and **Zr_6-Cu/Fe-2** (right), indicating identical morphologies before and after $FeCl_2$ metalation.

N_2 sorption measurements showed Brunauer-Emmett-Teller surface areas of 930 m^2/g, 1192 m^2/g, and 2563 m^2/g for **Zr_6-Cu/Fe-1**, **Zr_6-Cu/Fe-2**, and UiO-67-bpy,[33] respectively (**Figure 10-4**). ^1H NMR spectra of digested MOFs revealed a 1:5 $[Cu(H_2bpydc)(XantP)]^+$ to H_2bpydc ratio in **Zr_6-Cu-1** (17% Cu loading) and a 1:4 $[Cu(H_2bpydc)(POP)]^+$ to H_2bpydc ratio in **Zr_6-Cu-2** (20% Cu loading, **Figure 10-3**). Inductively coupled plasma-mass spectrometry (ICP-MS) measurements showed Fe loadings of 63% and 60% in **Zr_6-Cu/Fe-1** and **Zr_6-Cu/Fe-2** (relative to bpy), respectively.

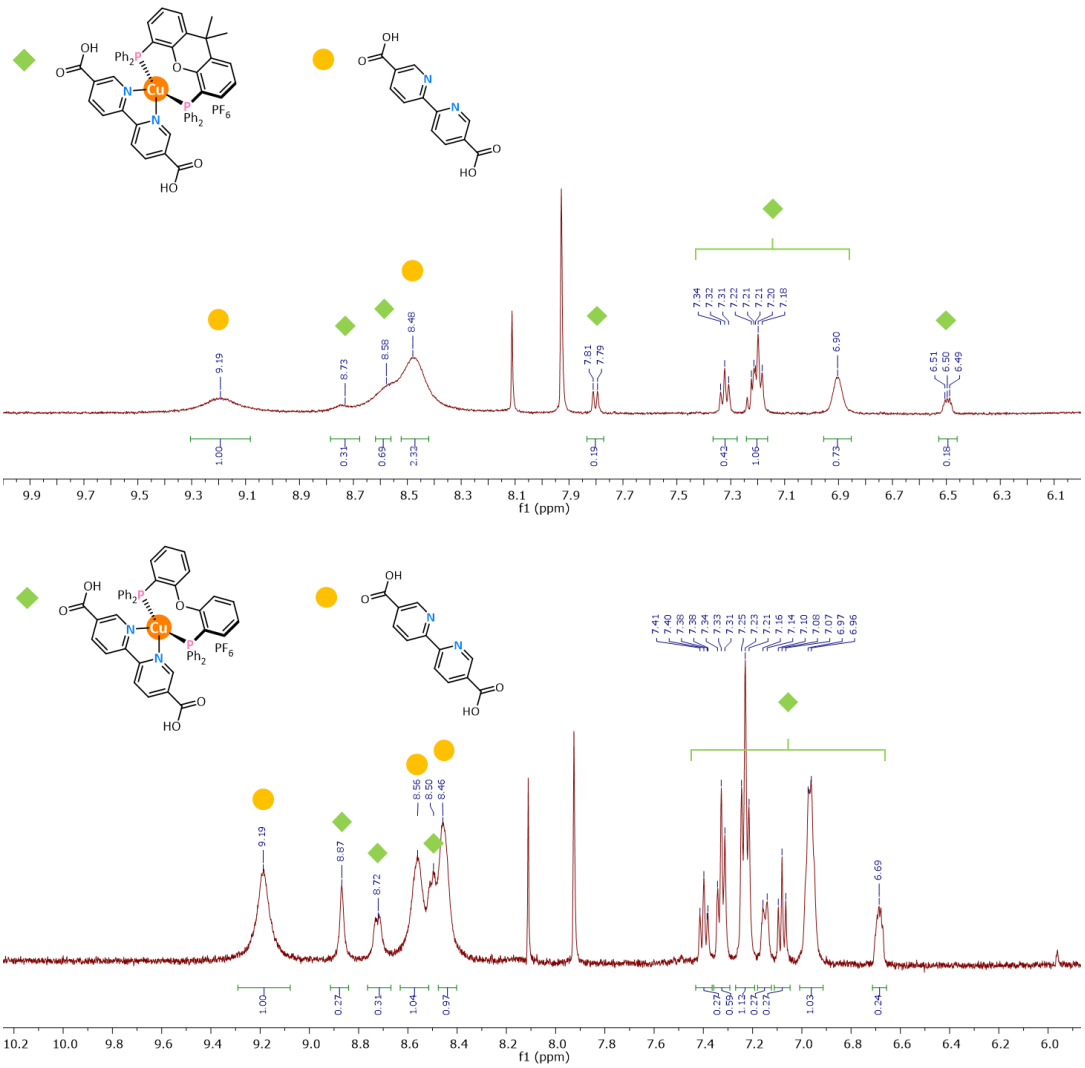

Figure 10-3. ^{1}H NMR spectra of **Zr$_6$-Cu-1** (top) and **Zr$_6$-Cu-2** (bottom) digested in conc. HF/DMSO-*d*$_6$. Peaks are assigned to Cu-PS ligands [Cu(H$_2$bpydc)(XantP)]$^+$ or [Cu(H$_2$bpydc)(POP)]$^+$ (◆) and **H$_2$bpydc** (●). ^{1}H NMR integration indicated a [Cu(H$_2$bpydc)(XantP)]$^+$/bpydc ratio of 1:5 in **Zr$_6$-Cu-1** and a [Cu(H$_2$bpydc)(XantP)]$^+$/bpydc ratio of 1:4 in **Zr$_6$-Cu-2**.

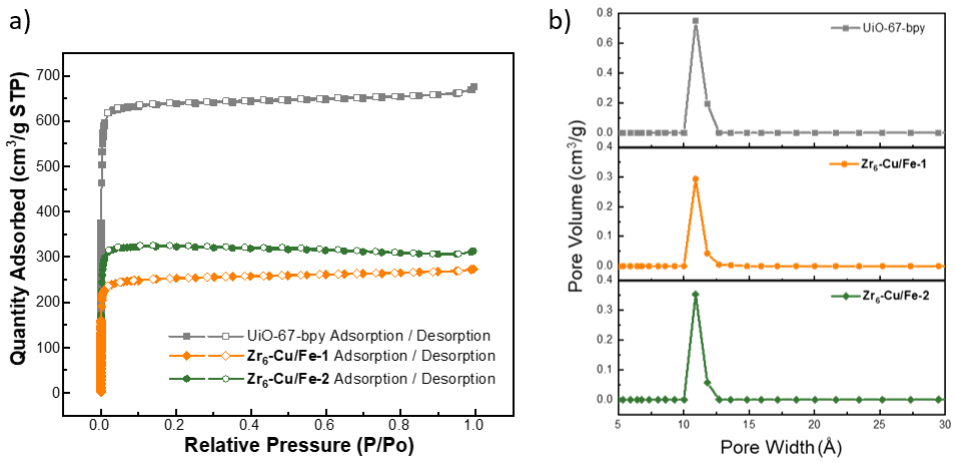

Figure 10-4. N_2 sorption isotherms and Pore size distributions of **Zr_6-Cu/Fe-1** and **Zr_6-Cu/Fe-2**. (a) N_2 sorption isotherms of **Zr_6-Cu/Fe-1** and **Zr_6-Cu/Fe-2** afford BET surface areas of 930 m^2/g for **Zr_6-Cu/Fe-1** and 1192 m^2/g for **Zr_6-Cu/Fe-2**, compared with 2563 m^2/g for UiO-67-bpy. (b) Pore size distributions of **Zr_6-Cu/Fe-1** and **Zr_6-Cu/Fe-2** calculated with non-local density functional theory (NLDFT), compared with that of UiO-67-bpy.

X-ray absorption spectroscopy was used to determine the electronic properties and coordination environments of Cu and Fe centers in **Zr_6-Cu/Fe-1** and **Zr_6-Cu/Fe-2**. X-ray absorption near edge structure (XANES) spectroscopy indicated Cu^I oxidation state in both **Zr_6-Cu/Fe-1** and **Zr_6-Cu/Fe-2** by comparing the pre-edge features with corresponding Cu salts (**Figure 10-5**). Extended X-ray absorption fine structure (EXAFS) features of **Zr_6-Cu/Fe-1** and **Zr_6-Cu/Fe-2** at both Cu K-edge and Fe K-edge were well fit with reported crystal structures of corresponding Cu^I and Fe^{II} complexes with nearly identical coordination environments: tetrahedral Cu^I centers coordinate to one bidentate bpy and one bidentate XantP or POP (**Figures 10-6a**, **10-6c**) while tetrahedral Fe^{II} centers coordinate to one bidentate bpy and two chloride groups (**Figures 10-6b**, **10-6d**). No EXAFS features corresponding to metallic nanoparticles were detected at either Cu K-edge or Fe K-edge. These results confirm successful integration of Cu-PSs and Fe catalysts with well-defined electronic and local coordination structures into the UiO frameworks.

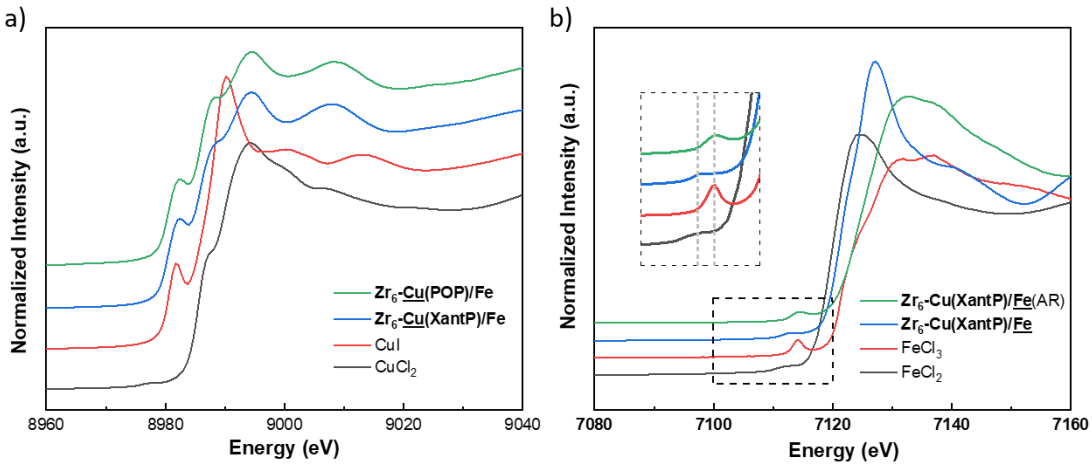

Figure 10-5. XANES spectrum of Cu and Fe centers in **Zr_6-Cu/Fe-1** and **Zr_6-Cu/Fe-2**. (a) Normalized XANES features of the Cu centers in **Zr_6-Cu/Fe-1** (navy), **Zr_6-Cu/Fe-2** (green), CuI (red), and $CuCl_2$ (black). (b) Normalized XANES features of the Fe centers in **Zr_6-Cu/Fe-1** (orange), **Zr_6-Cu/Fe-1** (AR, olive), $FeCl_2$ (black), and $FeCl_3$ (navy). Copyright 2021 American Chemical Society.

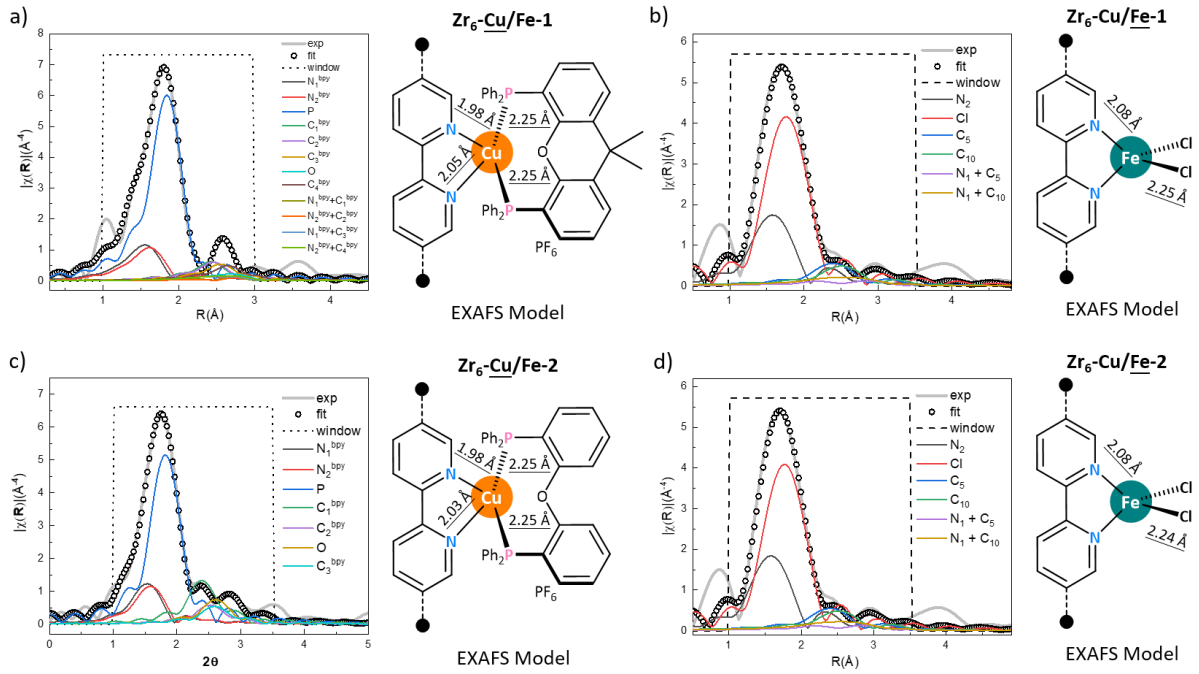

Figure 10-6. EXAFS fittings on Cu and Fe local environments in **Zr_6-Cu/Fe-1** and **Zr_6-Cu/Fe-2**. (a, b) EXAFS spectra (grey solid line) and fits (black circles) in R-space at the (a) Cu K-edge adsorption and the (b) Fe K-edge of **Zr_6-Cu/Fe-1**. (c, d) EXAFS spectra (grey solid line) and fits (black circles) in R-space at the (c) Cu K-edge adsorption and the (d) Fe K-edge of **Zr_6-Cu/Fe-2**. Copyright 2021 American Chemical Society.

10.2.2 Photocatalytic aerobic oxidation reactions

As a proof of concept, we targeted the oxidation of alcohols to aldehydes and the direct oxidation of benzylic C-H bonds to aromatic carbonyl derivatives to test the photocatalytic performance of the EAM MOF catalysts. The carbonyl products, including aldehydes, ketones, and esters, are important feedstocks for pharmaceutical synthesis and commodity chemicals.[34] Traditional synthesis protocols typically relied on elevated reaction temperature or radical initiators, which put significant burden on the environment and increased the cost.[8]

The merging of Cu-PSs and Fe catalysts in robust MOFs resulted in efficient photocatalytic aerobic oxidation of alcohols to corresponding aldehydes, under mild reaction conditions and without any additives. In the presence of 0.5 mol% of **Zr_6-Cu/Fe-1** and irradiation with a 13.9 W 350-700 nm solid-state plasma light source (equipped with a cooling fan), a solution of 4-methylbenzyl alcohol in dimethylsulfoxide (DMSO) was efficiently oxidized to 4-methylbenzaldehyde in 73% yield in 6 h and 98% yield in 24 h under ambient O_2 atmosphere and room temperature (**Table 10-1**). No significant over-oxidized products were detected. A slightly lower yield of 4-methylbenzaldehyde (82%) was obtained for **Zr_6-Cu/Fe-2** in 24 h. Further lowering the **Zr_6-Cu/Fe-1** loading to 0.2 mol% led to a TON of 340, exhibiting a 9.4-fold enhancement over the homogeneous control using [Cu(H_2bpydc)(XantP)](PF_6) and Fe(4,4'-bipyridine)Cl_2 in a 1:3 mole ratio (18% yield with a TON of 36). This enhancement of photocatalytic activity can be attributed to active center stabilization and confinement as well as the close proximity (<1 nm) between MOF-incorporated Cu-PS and Fe catalyst. As a heterogeneous catalyst, **Zr_6-Cu/Fe-1** was recovered and reused in 4 consecutive runs without a significant decrease in photocatalytic activity (**Figure 10-7**). PXRD studies indicated the maintenance of the crystallinity of both **Zr_6-Cu/Fe-1** and **Zr_6-Cu/Fe-2** after photocatalysis

(**Figures 10-1b**, **10-1c**). ICP-MS revealed minimal leaching of Cu (0.8%) and Fe (0.7%) into the supernatant after one reaction run.

Table 10-1. Photocatalytic aerobic oxidation of 4-methylbenzyl alcohol with different catalysts[a]

Entry	Catalyst	**Yield** (24h)	TON
1	0.5 mol% **Zr_6-Cu/Fe-1**	98% (73% in 6 h)	196
2	0.5 mol% **Zr_6-Cu/Fe-2**	82%	164
3	0.2 mol% **Zr_6-Cu/Fe-1**	68%	340
4[b]	0.5 mol% **Zr_6-Cu/Fe-1** (dark)	0%	-
5[c]	1.5 mol% **Zr_6-Fe**	9%	-
6	0.5 mol% **Zr_6-Cu-1**	1%	-
7	None	0%	-
8[d]	UiO-67-bpy	0%	-
9[e]	0.5 mol% [Cu(H_2bpydc)(XantP)]PF_6 + 1.5 mol% Fe(bpy)Cl_2	18%	36
10[e]	1.5 mol% Fe(bpy)Cl_2	5%	-
11	0.5 mol% [Cu(H_2bpydc)(XantP)]PF_6	0%	-

[a]Unless noted, photocatalytic aerobic oxidation reactions were conducted with certain loading of MOF or homogeneous catalysts, and 0.05 mmol 4-methylbenzyl alcohol, in 1.0 mL DMSO, under a 350-700 nm solid state plasma light source for 24 h. Temperature was monitored and maintained below 30 °C. Yield was determined by GC-MS. [b]Reaction was conducted in the dark. [c]**Zr_6-Fe** was prepared by metalation of $FeCl_2$ on UiO-67-bpy. [d]UiO-67-bpy with 1.5 μmol bpy sites was used as catalyst. [e]Fe(bpy)Cl_2 was prepared in situ with 1:1 mole ratio of $FeCl_2$ and 2,2'-bipyridine in DMSO.

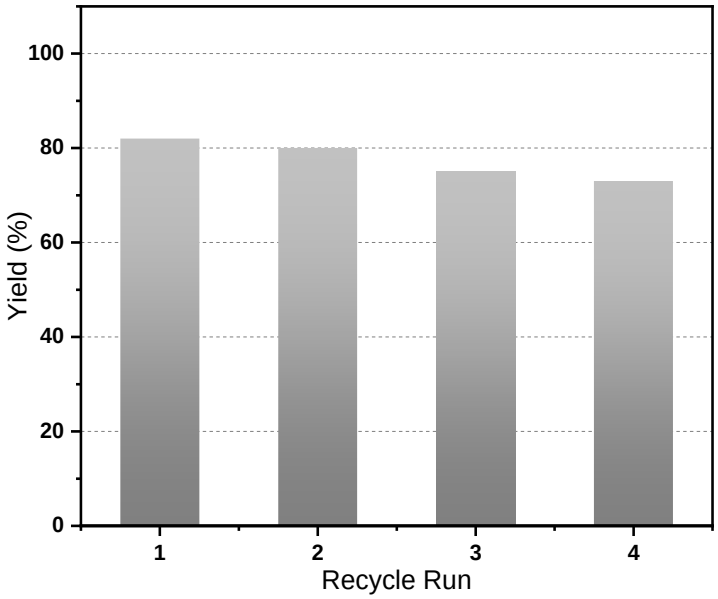

Figure 10-7. Recycle test of photocatalytic aerobic alcohol oxidation with **Zr_6-Cu/Fe-1**.

Zr_6-Cu/Fe-1 catalyzed photocatalytic aerobic oxidation of a wide scope of alcohols (**Table 10-2a**). Under standard conditions, **Zr_6-Cu/Fe-1** converted various primary and secondary benzylic alcohols to corresponding carbonyl compounds. Both electron donating groups, e.g., methyl, methoxyl, hydroxymethyl, and electron withdrawing groups, e.g., chloride, trifluoromethyl, were well tolerated during the photocatalytic processes with good to excellent yields. Moreover, aliphatic alcohols were also smoothly and selectively oxidized to corresponding aliphatic aldehydes, ketones, or α,β-unsaturated aldehydes without interference from the unsaturated bonds. All the reactions were conducted at room temperature and atmospheric pressure, suggesting potential utility of this process.

Besides the outstanding performance in photocatalytic aerobic oxidation of alcohols, **Zr_6-Cu/Fe-1** were also highly active for direct aerobic oxidation of benzylic compounds to afford aromatic carbonyl derivatives (**Table 10-2b**). Upon photo-irradiation, 4-methylanisole was quantitively oxidized to 4-methoxylbenzaldehyde in the presence of 0.5 mol% of **Zr_6-Cu/Fe-1** within 24 h. Several substrates containing benzylic C-H bonds, including 4-ethylanisole, indane,

tetralin, fluorene, and xanthene, were all successfully oxidized to afford desired ketones in 60-99% yields under similar reaction conditions. Higher photocatalytic activity was observed for substrates with adjacent oxygen atoms, e.g., phthalane, and isochromane, to afford ketones in excellent yields with lower catalyst loadings.

Table 10-2. Zr_6-Cu/Fe-1 catalyzed photocatalytic aerobic oxidation of alcohols and benzylic compounds.[a]

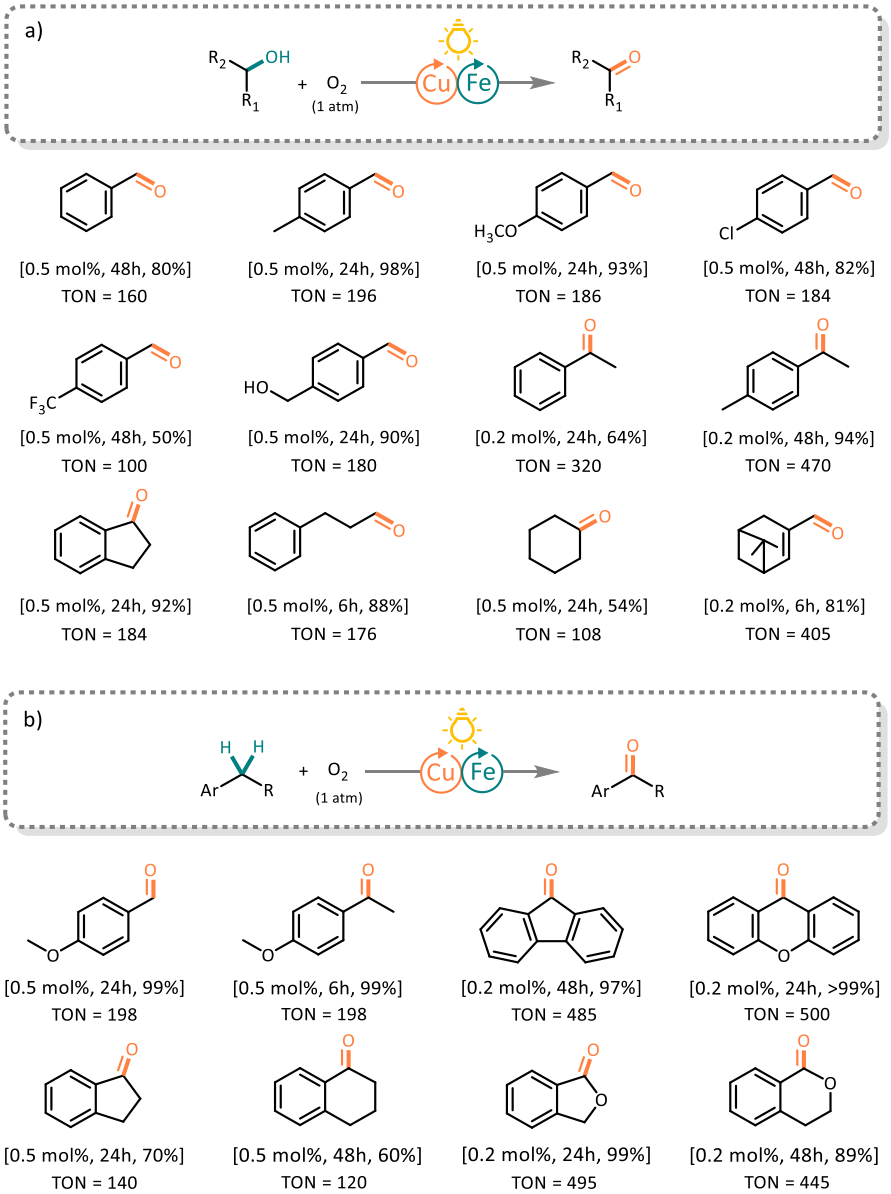

[a]Reactions were conducted with 0.05 mmol substrate in 1.0 mL DMSO and irradiated for indicated periods of time.

10.2.3 Mechanistic studies

The well-defined active site structures of the MOF catalysts provide an opportunity for in-depth mechanistic studies. To gain insights into the **Zr_6-Cu/Fe-1** catalyzed photocatalytic alcohol to aldehyde transformation, we performed several control experiments with 4-methylbenzyl alcohol. When O_2 was replaced by air and N_2, the yields of 4-methylbenzaldehyde dropped from 73% to 32% and 0%, respectively (Entries 1-3, **Table 10-3**), demonstrating the crucial role of O_2 as the oxidant. The removal of either light source, Cu-PS, or Fe catalyst significantly decreased the yields of 4-methylbenzaldehyde or completely shut down the reaction (Entries 4-6, **Table 10-1**). A significantly lower yield of 4-methylbenzaldehyde (4%) was found when 4Å molecular sieve was added as water absorbent (Entry 7, **Table 10-3**), indicating the involvement of water in the photo-oxidation process. A low yield of 7% 4-methylbenzaldehyde was obtained with H_2O_2 as the oxidant (Entry 4, **Table 10-3**), ruling out the contribution of Fenton reaction.

Table 10-3. Photocatalytic aerobic oxidation of 4-methylbenzyl alcohol under various conditions[a]

Entry	Condition Change	Yield
1	None	73% in 6 h
2	Air instead of O_2	32% in 6 h
3	N_2 instead of O_2	0% in 6 h
4[b]	H_2O_2 instead of O_2	7% in 6 h
5[b]	H_2O_2 instead of O_2 (dark)	5% in 6 h
6[c]	+ H_2O	62% in 6 h
7[d]	+ 4Å MS	4% in 6 h
8[e]	+ 1,4-Benzoquinone	79% in 6 h
9[f]	+ NaN_3	71% in 6 h
10[g]	+ TEMPO	0% in 6 h

Table 10-3 (continued)**.** Photocatalytic aerobic oxidation of 4-methylbenzyl alcohol under various conditions[a]

[a]Unless noted, photocatalytic aerobic oxidation reactions were conducted with 0.5 mol% loading of **Zr_6-Cu/Fe-1** catalysts, and 0.05 mmol 4-methylbenzyl alcohol, in 1.0 mL DMSO, under a 350-700 nm solid state plasma light source for 6 h. Temperature was monitored and maintained below 30 °C. Yield was determined by GC-MS. [b]15 μL H_2O_2 (30% solution) as oxidant. [c]10 μL H_2O was added. [d]50 mg 4A MS was used as water absorbent. [e]1,4-Benzoquinone (50 mM) was added to the reaction as O_2^- superoxide radical trapper. [f]NaN_3 (50 mM) was added to the reaction as singlet oxygen $^1O_2$ trapper. [g]TEMPO (50 mM) was added to the reaction as •OH hydroxide radical trapper.

To further identify the role of potential reactive oxygen species (ROS) in the photocatalytic oxidation process, specific ROS quenching agents were added to **Zr_6-Cu/Fe-1**-catalyzed oxidation of 4-methylbenzyl alcohol (**Figure 10-8**). In the presence of 50 mM of 1,4-benzoquinone (as a O_2^- scavenger)[35] or 50 mM of NaN_3 (as a $^1O_2$ scavenger)[36], no obvious drop of 4-methylbenzaldehyde yields was detected (Entries 8-9, **Table 10-3**). However, the addition of hydroxyl radical capturing agent TEMPO (50 mM)[37] completely shut down the reaction (Entry 10, **Table 10-3**), thus suggesting the *in situ* generated hydroxyl radical from water as the key ROS for photocatalytic oxidation. Furthermore, radical clock experiment with 4-penten-1-ol as substrate afforded 87% of cyclic products along with 13% of priminay aldehyde, confiming the alkoxyl radical as the photo-oxidation intermediate (**Figrue 10-9**).[38]

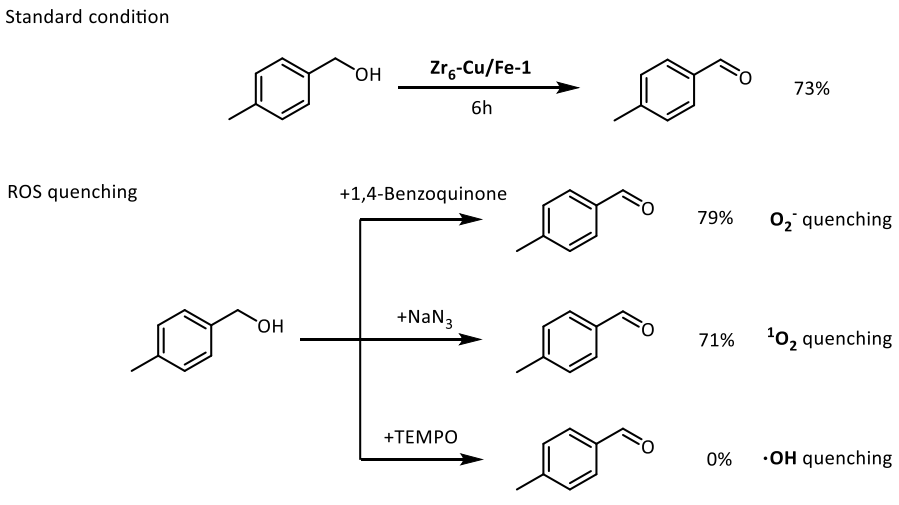

Figure 10-8. ROS quenching experiments.

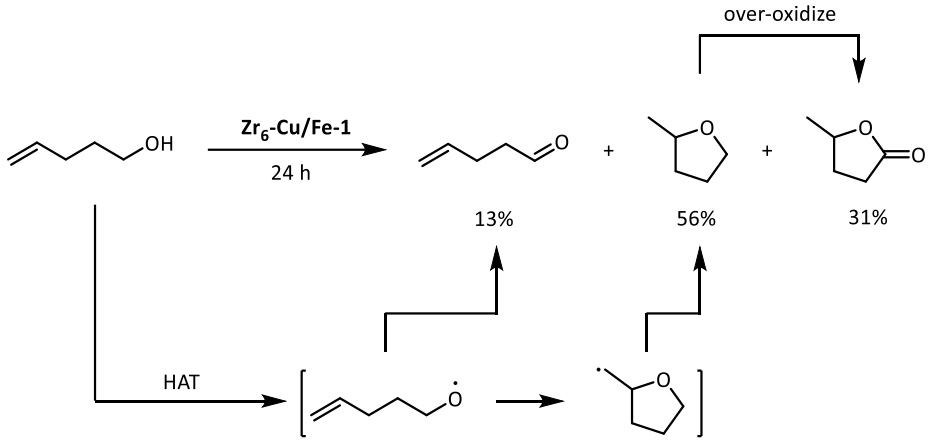

Figure 10-9. Radical clock experiment using 4-penten-1-ol as substrate. Reactions was conducted with 0.5 mol% of **Zr_6-Cu/Fe-1** and 0.05 mmol 4-penten-1-ol in 1.0 mL DMSO under a 350-700 nm solid state plasma light source for 24 h. Yields were determined by GC-MS.

Spectroscopic evidence was obtained to shed light on the electron transfer pathways across the metal centers. **Zr_6-Cu/Fe-1** and **Zr_6-Cu/Fe-2** displayed characteristic $[Cu(diimine)(diphosphine)]^+$ luminescence at 491 nm and 489 nm, respectively (**Figures 10-10a**, **10-10b**),[39] which correspond to ground state to excited state energy gaps of 2.52 eV for **Zr_6-Cu/Fe-1** and 2.54 eV for **Zr_6-Cu/Fe-2**. These emissions were effectively quenched by the increasing concentration of O_2, indicating the efficient electron transfer between [Cu-PS]* and O_2. Furthermore, CV curves of $[Cu(H_2bpydc)(XantP)]^+$ and $[Cu(H_2bpydc)(POP)]^+$ showed similar one electron oxidation peaks at +1.58 V and +1.55 V vs NHE for the $[Cu^{II}\text{-PS}]/[Cu^{I}\text{-PS}]$ couple (**Figure 10-10c**), indicating the strong oxidation power of both $[Cu^{II}\text{-PS}]$ species. XANES analysis gave the Fe^{III} oxidation state for **Zr_6-Cu/Fe-1** (AR) recovered from photocatalytic oxidation, suggesting the oxidation of Fe^{II} pre-catalyst during the photocatalytic oxidation process (**Figure 10-10e**). CV curve of the MOF-stabilized Fe catalyst, **Zr_6-Fe**, displayed a reversible one-electron oxidation peak at +0.42 V vs NHE and an irreversible one-electron oxidation peak at +1.43 V vs NHE (**Figure 10-10d**). The first peak can be assigned to the reversible Fe^{II}/Fe^{III} couple, while the second

peak can be attributed to the further irreversible oxidation of the Fe^{III} species. Both Cu-PSs in the MOFs have enough oxidation potential to drive such steps for substrate oxidation.

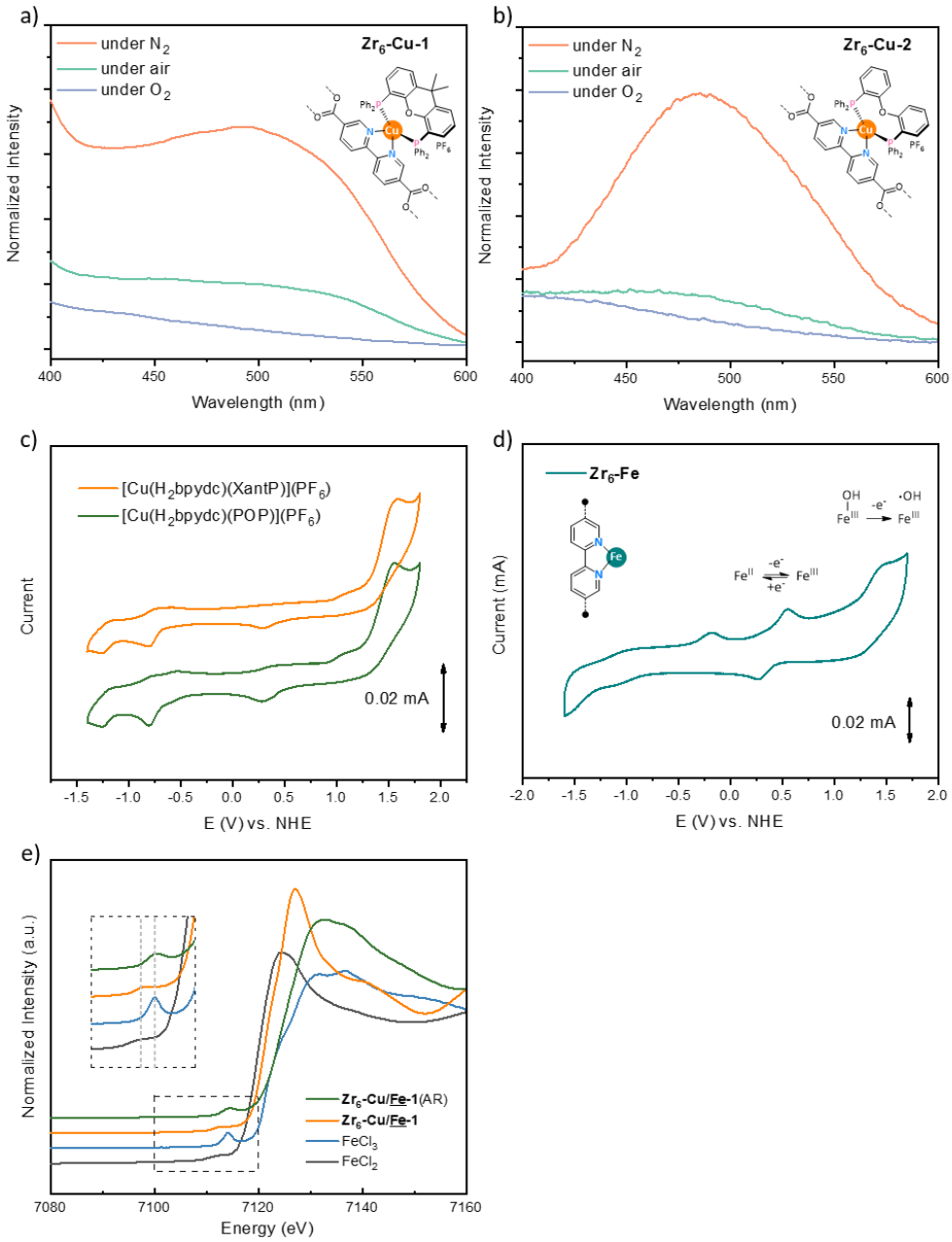

Figure 10-10. Mechanistic studies on the aerobic photocatalytic oxidations. (a, b) Photoluminescence spectra of **Zr_6-Cu-1** (a) and **Zr_6-Cu-2** (b) (10 μM) in DMF under N_2, air, or O_2 atmosphere. (c) CVs of $[Cu(H_2bpydc)(XantP)]^+$ (orange) and $[Cu(H_2bpydc)(POP)]^+$ (olive). (d) CV of **Zr_6-Fe** coated on the electrode. d) EPR signal of BMPO-•OH adduct generated by **Zr_6-Cu/Fe-1** in H_2O/toluene under N_2. (e) Normalized XANES features at Fe K-edge in **Zr_6-Cu/Fe-1** (navy), **Zr_6-Cu/Fe-1** (AR, olive), $FeCl_2$ (black), and $FeCl_3$ (red). Copyright 2021 American Chemical Society.

Density functional theory (DFT) calculations with B3LYP functional were carried out to gain insights into the second electron oxidation process on the Fe^{III} centers and the subsequent substrate oxidation. As shown in **Figure 10-11**, two possible transformation pathways were proposed: a) the metal-oxo pathway with the involvement of a key Fe^{IV}-oxo intermediate (IN-FeO) before the hydrogen atom transfer (HAT) process or b) the hydroxyl radical pathway with the generation of •OH from the oxidation of Fe^{III}-OH intermediate followed by the HAT between the highly reactive •OH and the substrate. With the energy input from the oxidant $[Cu(H_2bpydc)(XantP)]^{2+}$, the hydroxyl radical pathway from IN-FeOH to IN-Fe required ΔG of a +39.1 kcal/mol while the metal-oxo pathway required a much higher ΔG of +78.5 kcal/mol for the generation of IN-FeO. Although both processes were driven by the exothermic HAT between the active intermediates and alcoholic substrates, the hydroxyl radical pathway is favored to occur to form alkoxyl radicals.

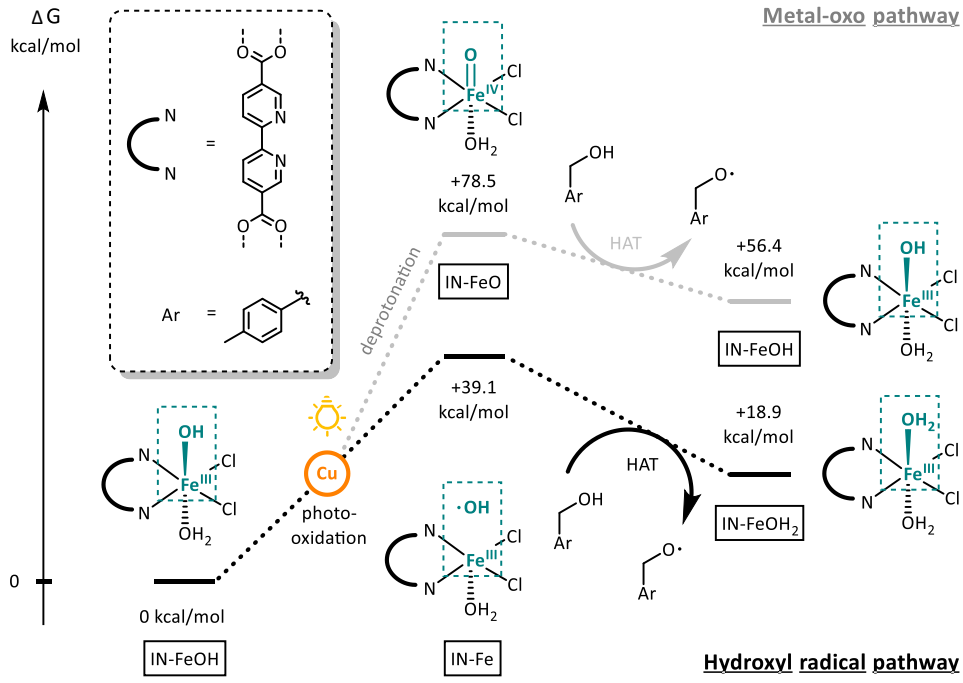

Figure 10-11. Gibbs free energy changes for the photocatalytic oxidation steps on the Fe centers via the metal-oxo pathway or the hydroxyl radical pathway as calculated by DFT. Copyright 2021 American Chemical Society.

Finally, electron paramagnetic resonance (EPR) experiments were conducted to detect the *in situ* generated ROS. The generation of $O_2^{\bullet-}$ was confirmed by detecting the characteristic EPR signal for the BMPO-$O_2^{\bullet-}$ adduct when BMPO was added to the suspension of **Zr_6-Cu-1** in anhydrous MeOH/toluene in air with irradiation (**Figure 10-12a**). We also detected the characteristic quartet EPR signal for the BMPO-•OH adduct at g = 2.006 when Ag^+ (sacrificial electron acceptor) and BMPO were added to a suspension of **Zr_6-Cu/Fe-1** in H_2O/toluene under N_2 and light irradiation (**Figure 10-12b**). EPR signals from other BMPO-radical adducts were also evident in the spectrum, which were likely generated from the reactions between highly reactive •OH and organic solvents.

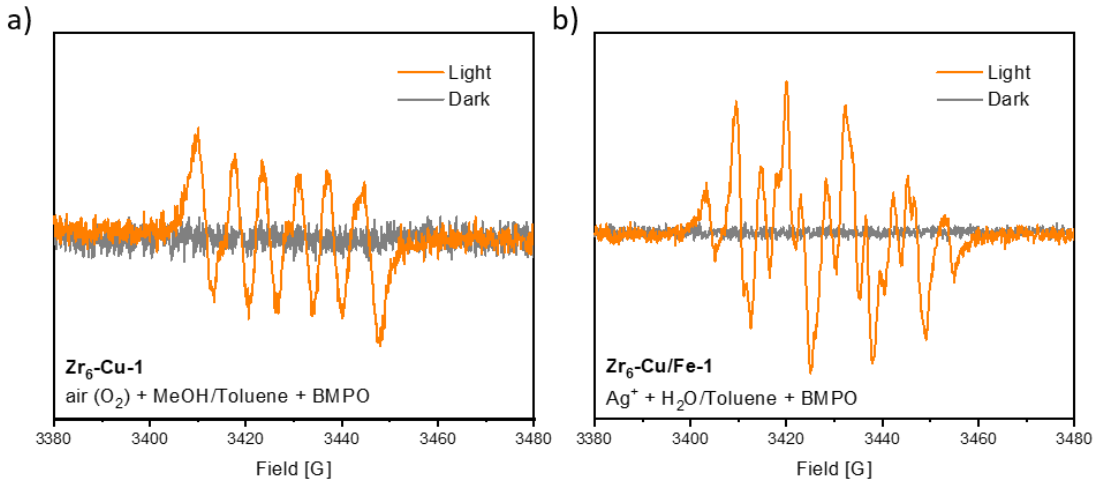

Figure 10-12. EPR signals of (a) BMPO-$O_2^{\bullet-}$ adduct generated by **Zr_6-Cu-1** under light irradiation and (b) BMPO-•OH adduct generated by **Zr_6-Cu/Fe-1** under light irradiation.

Based on these control experiments, computational results, and spectroscopic evidence, we propose a dual Cu-Fe photocatalytic cycle for **Zr_6-Cu/Fe-1** catalyzed aerobic oxidation (**Figure 10-13**). Upon photoirradiation, the [Cu^{I}-PS] in the MOF is first excited to [Cu-PS]*, which is subsequently oxidized by O_2 to generate $O_2^{\bullet-}$ and [Cu^{II}-PS]. The strongly oxidizing [Cu^{II}-PS] efficiently oxidizes [Fe^{III}-OH], which is formed by deprotonation of H_2O on the acidic Fe^{III} center, to generate highly reactive •OH. Through HAT, •OH rapidly oxidizes alcohol to generate alkoxyl

radical species as the key intermediate which subsequently transforms into the aldehyde product. In the presence of H_2O, the generated [Fe^{III}] undergoes hydrolysis to afford [Fe^{III}-OH] for the next oxidation cycle. Akin to natural enzymes, the product selectivity of the MOFs is likely controlled by the uniform and small hydrophobic channels, which facilitate substrate and product diffusion and minimize over-oxidized products. Similarly, •OH can efficiently oxidize alkanes with benzylic C-H bonds to generate benzylic radicals, which are further converted to the corresponding carbonyl products (**Figure 10-13**).

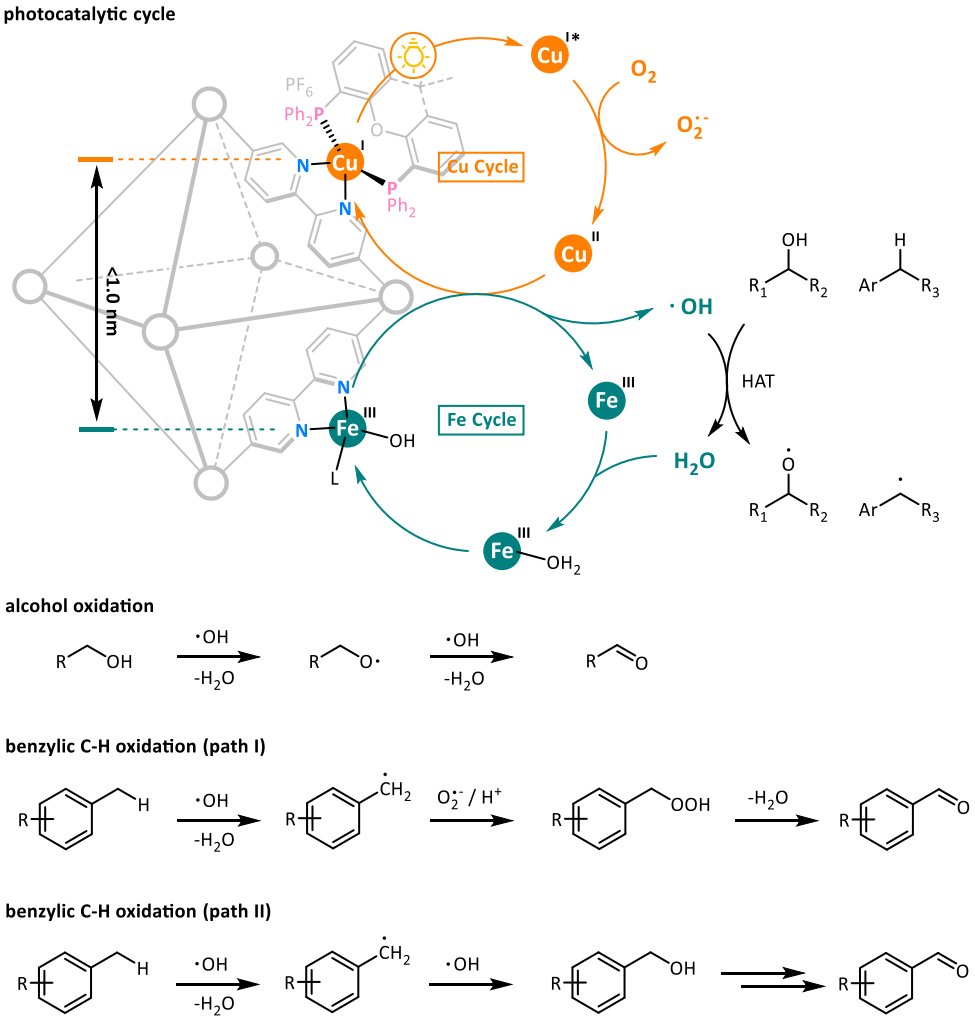

Figure 10-13. Proposed mechanism of photocatalytic aerobic oxidation of alcohol and benzylic C-H bonds. Copyright 2021 American Chemical Society.

10.3 Conclusion

In summary, we hierarchically integrated Earth-abundant cuprous photosensitizers and Fe catalysts into two robust MOF catalysts for visible-light driven aerobic oxidation. Spectroscopic evidence shows that the well-defined Cu-PSs and Fe catalysts in the MOFs are significantly stabilized by site isolation and pore confinement to afford robust and reusable heterogeneous EAM-based photocatalysts. The close proximity between Cu-PSs and Fe catalysts further enhances electron and mass transfer during the photocatalytic process to significantly increase catalytic performance. Under mild reaction condition and without additives, Zr_6-Cu/Fe-1 displays excellent activity in photocatalytic aerobic oxidation of alcohols and benzylic compounds to corresponding carbonyl products with broad substrate scopes, high TONs, which is nearly an order of magnitude higher than the homogeneous counterpart, and excellent recyclability. Benefitting from uniform active centres, a combination of control experiments, spectroscopic evidence, and computational results established the mechanism of the aerobic photo-oxidation process: [Cu^{I}-PS] is first photoexcited to [Cu-PS]* and then oxidized by O_2 to generate [Cu^{II}-PS]. As a potent oxidant, [Cu^{II}-PS] oxidizes in situ generated Fe^{III}-OH to afford highly reactive hydroxyl radical which further oxidizes alcohols and benzylic C-H bonds to corresponding carbonyl products through a radical process. To the best of our knowledge, this work reports the first example of MOF-based dual EAM catalysts for photocatalytic oxidation process, thus highlighting the great potential of MOFs in stabilizing EAM complexes for photocatalytic organic synthesis.

10.4 Experimental Section

10.4.1 Materials and methods

All the reactions and manipulations were carried out under N_2 with the use of a glovebox or Schlenk technique, unless otherwise indicated. Tetrahydrofuran and toluene were purified by

passing through a neutral alumina column under N_2. All starting materials were purchased from Sigma-Aldrich and Fisher (USA) unless otherwise noted and used without further purification. Powder X-ray diffraction (PXRD) data was collected on a Bruker D8 Venture diffractometer using Cu Kα radiation source (l = 1.54178 Å). N_2 sorption experiments were performed on a Micrometrics TriStar II 3020 instrument. TGA was performed in air using a Shimazu TGA-50 equipped with a platinum pan and heated at a rate of 1.5 °C per min. ICP-MS data was obtained with an Agilent 7700x ICP-MS and analyzed using ICP-MS MassHunter version B01.03. Samples were diluted in a 2% HNO_3 matrix and analyzed with a ^{159}Tb internal standard against a 12-point standard curve over the range from 0.1 ppb to 500 ppb. The correlation was >0.9997 for all analyses of interest. Data collection was performed in Spectrum Mode with five replicates per sample and 100 sweeps per replicate. CVs were recorded on a CHI420 electrochemistry workstation with regular 3 electrode systems. Measurements were recorded using a glassy carbon disk working electrode (S = 0.07 cm^2) and a platinum wire as the counter electrode. The Ag/AgCl/1 M KCl electrode was used as the reference electrode in all experiments. EPR spectra were recorded on a Bruker Elexsys 500 X-band EPR spectrometer under irradiation of a white-light lamp (Fiber-Lite MI-150) by focusing the lamp on the sample cell in the ESR cavity at 15 K. X-ray absorption (XAFS) data was collected at Beamline 10-BM, Advanced Photon Source (APS), Argonne National Laboratory. Spectra were collected at the K-edge of Cu or Fe in transmission mode.

^1H and ^{13}C NMR spectra were recorded on a Bruker NMR 500 DRX spectrometer at 500 MHz and referenced to the proton resonance resulting from incomplete deuteration of $CDCl_3$ (δ 7.26) or DMSO-d_6 (δ 2.50). The following abbreviations are used herein: s: singlet, d: doublet, t: triplet, q: quartet, m: multiplet, br: broad, app: apparent. The conversions of reactions were

determined by GC-MS using a Shimadzu GCMS-QP2010 Ulta equipped with SH-Rxi-5Sil MS 30 m × 0.5 mm × 0.25 μm column.

10.4.2 Synthesis and characterization of ligands and complexes

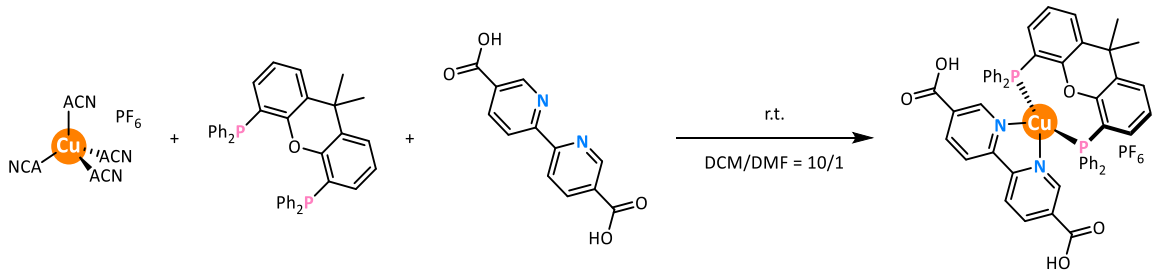

Synthesis of [Cu(H$_2$bpydc)(XantP)](PF$_6$): In a pre-dried 100 mL 3-neck round-bottom flask, [Cu(CH$_3$CN)$_4$]PF$_6$ (93 mg, 0.25 mmol) and dimethyl-4,5-bis(diphenylphosphino)xanthene (XantP, 145 mg, 0.25 mmol) were dissolved in 10 mL CH_2Cl_2 and stirred for 1 h under nitrogen. A suspension of (2,2'-bipyridine)-5,5'-dicarboxylic acid (bpydc, 61 mg, 0.25 mmol) in 20 mL CH_2Cl_2/DMF (10/1, v/v) was added dropwise as the solution turned deep-orange gradually. After stirring under nitrogen for another 6 h, the mixture was concentrated under reduced pressure and filtered. A large amount of Et_2O (50 mL) was added to the solution to precipitate the product. The solid product collected by filtration and washed with Et_2O three times before being dried under vacuum to afford orange powdery [Cu(H$_2$bpydc)(XantP)](PF$_6$) (220 mg, 86% yield). ^{1}H NMR (500 MHz, DMSO-d_6) δ 8.79 (s, 2H), 8.52 (d, J = 8.2 Hz, 4H), 7.81 (d, J = 7.9 Hz, 2H), 7.34 (d, J = 7.5 Hz, 6H), 7.28 – 7.15 (m, 10H), 6.92 (br, 6H), 6.52 (br, 2H), 1.73 (s, 6H). HR-MS (ESI, positive mode): *m/z* calc'd for $C_{51}H_{40}CuN_2O_5P_2$ $[M\text{-}PF_6]^+$: 885.1708, found 885.1693.

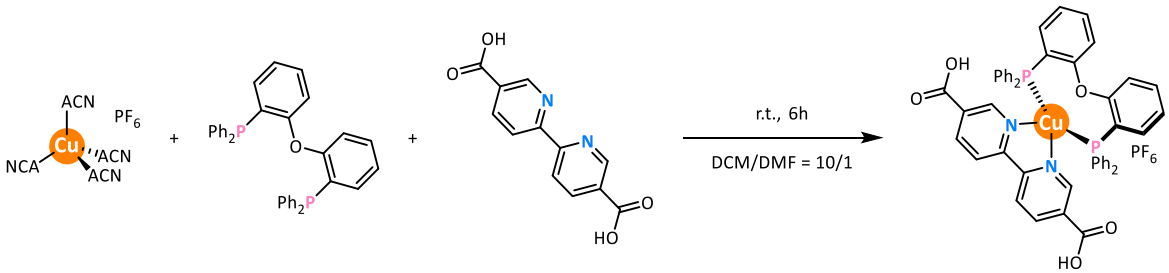

Synthesis of [Cu(H_2bpydc)(POP)](PF_6): [Cu(H_2dcbpy)(POP)](PF_6) was synthesized using a similar procedure as [Cu(H_2bpydc)(XantP)](PF_6) with POP replacing XantP. Orange-red powdery [Cu(H_2bpydc)(POP)](PF_6) was obtained in 91% yield. ^{1}H NMR (500 MHz, DMSO-d_6) δ 8.89 (s, 2H), 8.78 (d, J = 8.4 Hz, 2H), 8.52 (dd, J = 8.3, 2.0 Hz, 2H), 7.44 – 7.31 (m, 8H), 7.30 – 7.20 (m, 8H), 7.12 – 6.95 (m, 10H), 6.70 (br, 2H). HR-MS (ESI, positive mode): *m/z* calc'd for $C_{48}H_{36}CuN_2O_5P_2$ $[M\text{-}PF_6]^+$: 845.1395, found 845.1404.

10.4.3 Synthetic procedures of MOF catalysts

Synthesis of **Zr_6-Cu-1** and **Zr_6-Cu-2**: **Zr_6-Cu-1** was synthesized solvothermally by heating an oxygen-free DMF solution (1.0 mL) of [Cu(H_2bpydc)(XantP)](PF_6) ligand (0.005 mmol), bpydc ligand (0.005 mmol), and $Zr_6O_4(OH)_4(C_5H_5O_2)_{12}$ clusters (**Zr_6-Mc**, 0.01 mmol)[32] in a molar ratio of 1:1:2 at 100 °C for 24 h. Trifluoroacetic acid (10 μL) was also added as a modulator. Orange-yellow powder of **Zr_6-Cu-1** was obtained in 38% yield. **Zr_6-Cu-1** was dispersed in DCM and stored in the glovebox for further usage. **Zr_6-Cu-2** was similarly synthesized with [Cu(H_2bpydc)(POP)](PF_6) (0.005 mmol) in pace of [Cu(H_2bpydc)(XantP)](PF_6) in 46% yield. The [Cu(H_2bpydc)(XantP)](PF_6) to bpydc ratio in **Zr_6-Cu-1** was determined by ^{1}H NMR analysis of the digested solution of **Zr_6-Cu-1** (1.0 mg) in conc. HF (0.5 mL)/DMSO-d_6 (0.5 mL). A [Cu(H_2bpydc)(XantP)](PF_6) to bpydc ratio of 1:5 was determined by ^{1}H NMR integration. Similarly, a $[Cu(H_2bpydc)(POP)]^+$ to bpydc ratio of 1:4 was obtained for the digested MOF **Zr_6-Cu-2**.

Synthesis of **Zr_6-Cu/Fe-1** and **Zr_6-Cu/Fe-2**: **Zr_6-Cu-1** and **Zr_6-Cu-2** were then metalated with $FeCl_2$ to afford **Zr_6-Cu/Fe-1** and **Zr_6-Cu/Fe-2**. Specifically, in the glovebox, a mixture of **Zr_6-Cu-1** (containing 10 μmol Cu sites) and $FeCl_2$ (40 μmol) in 10 mL anhydrous THF was stirred at room temperature for 12 h. The resultant light olive solid was centrifuged out of suspension and

washed with THF 3 times to remove excess $FeCl_2$ to afford **Zr_6-Cu/Fe-1** quantitatively. **Zr_6-Cu/Fe-2** was similarly synthesized in a quantitative yield. Inductively coupled plasma-mass spectrometry (ICP-MS) was used to determine metal contents in **Zr_6-Cu/Fe-1** and **Zr_6-Cu/Fe-2**. A Cu/Fe ratio of 1:3.7 was detected in **Zr_6-Cu/Fe-1**, corresponding to 63% Fe loading and 17% Cu-PS loading in **Zr_6-Cu/Fe-1**. Similarly, a Cu/Fe ratio of 1:3.0 was detected in **Zr_6-Cu/Fe-2**, corresponding to 60% of Fe loading and 20% of Cu-PS loading in **Zr_6-Cu/Fe-2**.

10.4.4 Photocatalytic reaction setup and product characterization

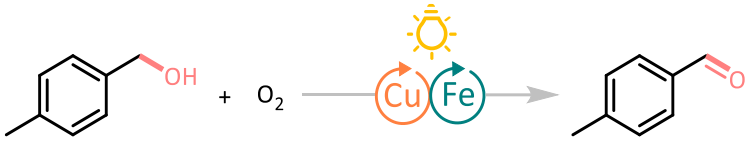

Typical procedure of photocatalytic aerobic alcohol oxidation: Photocatalytic aerobic oxidation of alcohols was carried out in an external illumination type reaction vessel with a magnetic stirrer. In a standard reaction, **Zr_6-Cu/Fe-1** (0.5 mol% w.r.t. Cu sites), 4-methylbenzyl alcohol (0.05 mmol), and 1.0 mL of DMSO were transferred to a 1-dram septum-sealed glass vial. Sample vials were capped, sealed, and bubbled with oxygen from a balloon to ensure O_2 atmosphere. At room temperature, the solution was irradiated by a 13.9 W 350-700 nm solid state plasma light source equipped with cooling fans (HPLS-30-04 from Thorlabs Inc.). The supernatant was analyzed by GC-MS to give 4-methylbenzaldehyde in 73% yield in 6 h and 98% yield in 24 h. After one reaction run, ICP-MS analysis showed the leaching of 0.8 % Cu and 0.7 % Fe into the solution.

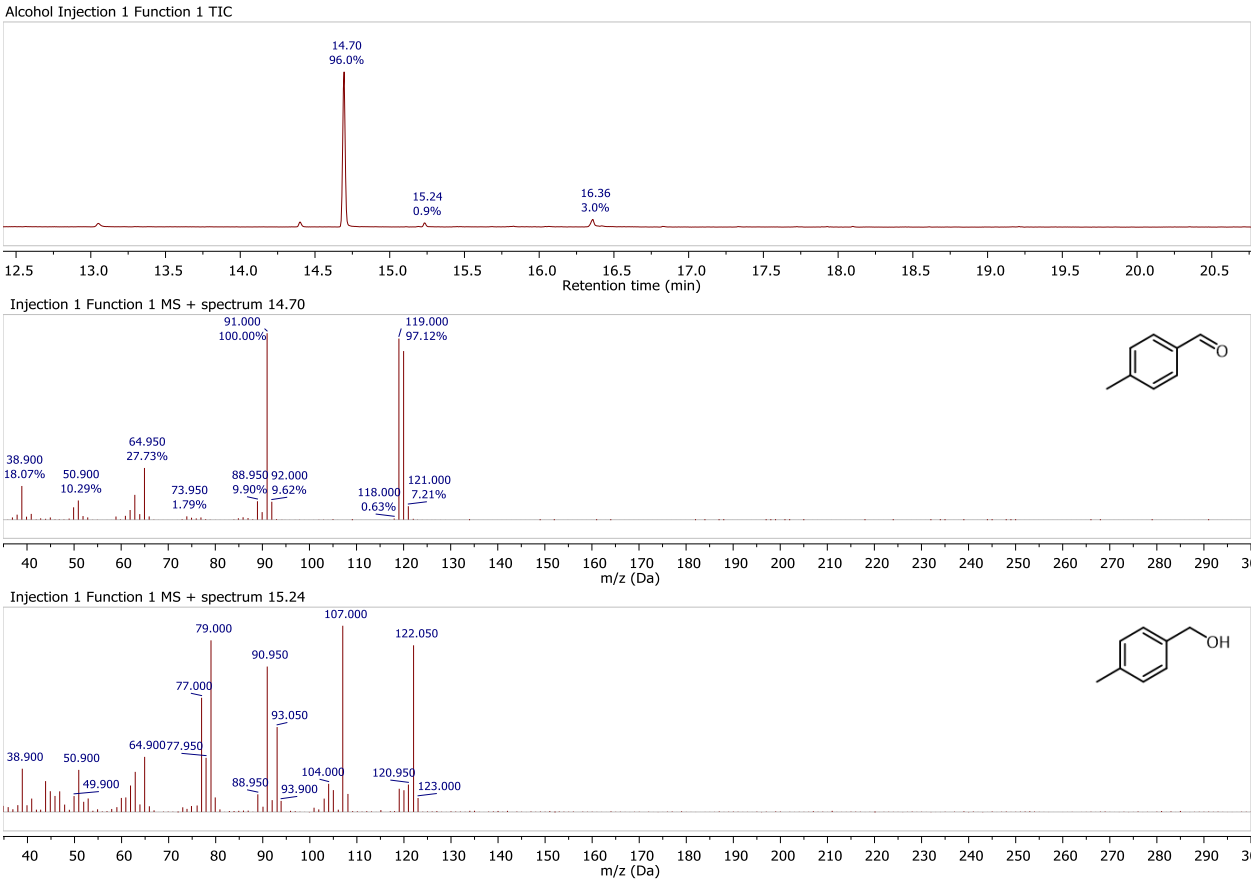

Figure 10-14. GC-MS spectra of **Zr_6-Cu/Fe-1** catalyzed photocatalytic aerobic oxidation of 4-methylbenzyl alcohol.

Table 10-4. The retention times of GC traces I.

Compound	Retention Time	Compound	Retention Time
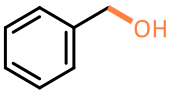	14.08 min	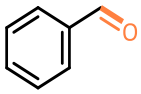	12.93 min
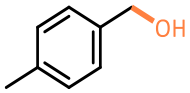	15.25 min	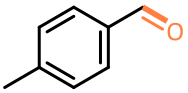	14.70 min
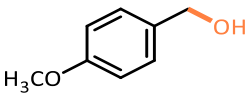	N.D.	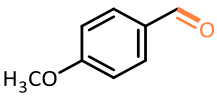	16.31 min

Table 10-4 (continued)**.** The retention times of GC traces I.

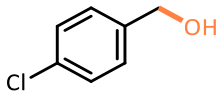	16.18 min	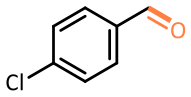	15.20 min
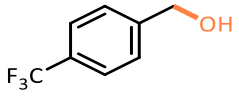	14.82 min	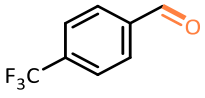	12.92 min
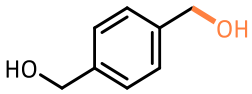	17.50 min	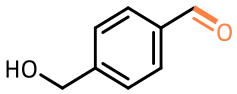	17.22 min
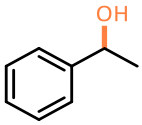	14.42 min	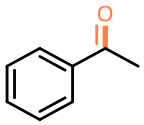	14.48 min
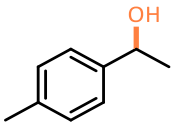	15.50 min	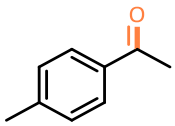	15.73 min
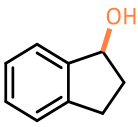	16.14 min	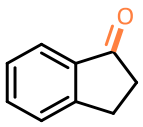	16.56 min
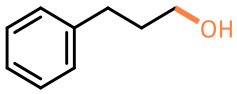	16.11 min	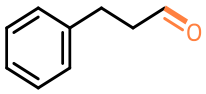	15.52 min
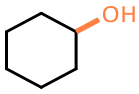	11.14 min	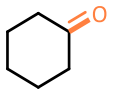	11.24 min
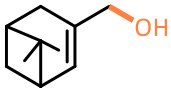	16.80 min		15.85 min

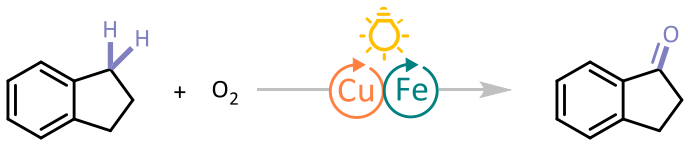

Typical procedure of photocatalytic aerobic C-H oxidation: Photocatalytic aerobic C-H oxidation was carried out in the same external illumination type reaction vessel with a magnetic stirrer. In a standard reaction, **Zr_6-Cu/Fe-1** (0.5 mol% w.r.t. Cu sites), indane (0.05 mmol), and 1.0 mL of

dimethylsulfoxide (DMSO) were transferred to a 1-dram septum-sealed glass vial. Sample vial was capped, sealed, and bubbled with oxygen from a balloon to ensure O_2 atmosphere. At room temperature, the solution was irradiated by a 13.9 W 350-700 nm solid state plasma light source equipped with cooling fans. The supernatant was analyzed by GC-MS to give 1-indanone in 70% yield in 24 h. After one reaction run, ICP-MS analysis showed the leaching of 0.7% Cu and 1.0% Fe into the solution.

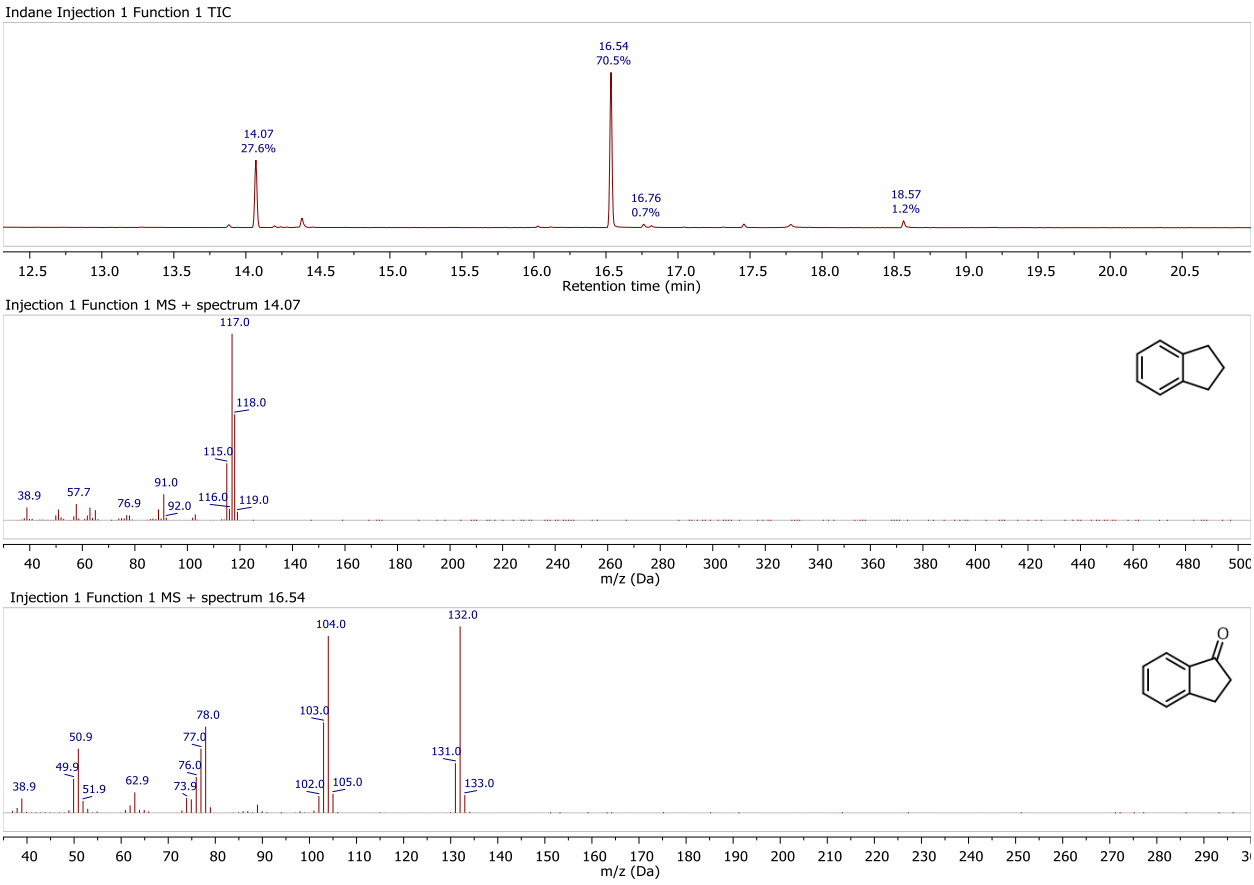

Figure 10-15. GC-MS spectrum of **Zr_6-Cu/Fe-1** catalyzed photocatalytic aerobic oxidation of indane.

Table 10-5. The retention times of GC traces II.

Compound	Retention Time	Compound	Retention Time
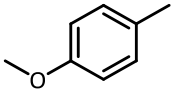	13.87 min	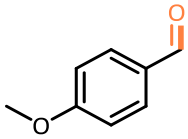	16.32 min
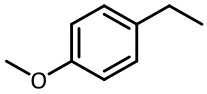	14.97 min	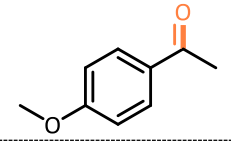	17.06 min
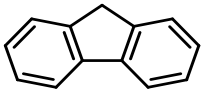	18.70 min	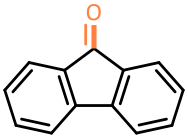	19.62 min
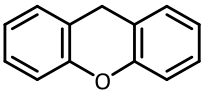	19.08 min	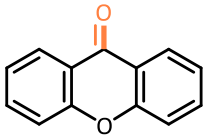	20.30 min
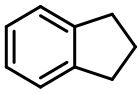	14.08 min	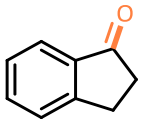	16.55 min
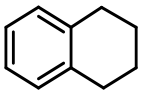	15.54 min	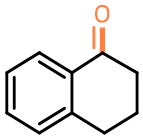	17.29 min
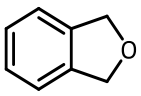	14.66 min	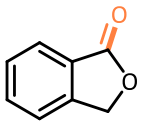	17.04 min
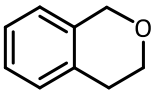	15.72 min	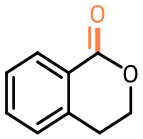	17.94 min

10.5 References

1. Anastas, P. T.; Warner, J. C., Green chemistry. *Frontiers* **1998,** *640*.

2. de Marco, B. A.; Rechelo, B. S.; Tótoli, E. G.; Kogawa, A. C.; Salgado, H. R. N., Evolution of green chemistry and its multidimensional impacts: A review. *Saudi Pharmaceutical Journal* **2019,** *27* (1), 1-8.

3. Anastas, P. T.; Kirchhoff, M. M., Origins, Current Status, and Future Challenges of Green Chemistry. *Accounts of Chemical Research* **2002,** *35* (9), 686-694.

4. Wang, Q.; Zhang, M.; Chen, C.; Ma, W.; Zhao, J., Photocatalytic Aerobic Oxidation of Alcohols on TiO2: The Acceleration Effect of a Brønsted Acid. *Angewandte Chemie International Edition* **2010,** *49* (43), 7976-7979.

5. Hoover, J. M.; Steves, J. E.; Stahl, S. S., Copper(I)/TEMPO-catalyzed aerobic oxidation of primary alcohols to aldehydes with ambient air. *Nature Protocols* **2012,** *7* (6), 1161-1166.

6. Zhang, W.; Fernández-Fueyo, E.; Ni, Y.; van Schie, M.; Gacs, J.; Renirie, R.; Wever, R.; Mutti, F. G.; Rother, D.; Alcalde, M.; Hollmann, F., Selective aerobic oxidation reactions using a combination of photocatalytic water oxidation and enzymatic oxyfunctionalizations. *Nature Catalysis* **2018,** *1* (1), 55-62.

7. Guðmundsson, A.; Schlipköter, K. E.; Bäckvall, J.-E., Iron(II)-Catalyzed Biomimetic Aerobic Oxidation of Alcohols. *Angewandte Chemie International Edition* **2020,** *59* (13), 5403-5406.

8. Parmeggiani, C.; Cardona, F., Transition metal based catalysts in the aerobic oxidation of alcohols. *Green Chemistry* **2012,** *14* (3), 547-564.

9. Cao, Q.; Dornan, L. M.; Rogan, L.; Hughes, N. L.; Muldoon, M. J., Aerobic oxidation catalysis with stable radicals. *Chemical Communications* **2014,** *50* (35), 4524-4543.

10. Lang, X.; Ma, W.; Chen, C.; Ji, H.; Zhao, J., Selective Aerobic Oxidation Mediated by TiO2 Photocatalysis. *Accounts of Chemical Research* **2014,** *47* (2), 355-363.

11. Jin, Y.; Ou, L.; Yang, H.; Fu, H., Visible-Light-Mediated Aerobic Oxidation of N-Alkylpyridinium Salts under Organic Photocatalysis. *Journal of the American Chemical Society* **2017,** *139* (40), 14237-14243.

12. Xu, C.; Pan, Y.; Wan, G.; Liu, H.; Wang, L.; Zhou, H.; Yu, S.-H.; Jiang, H.-L., Turning on Visible-Light Photocatalytic C−H Oxidation over Metal–Organic Frameworks by Introducing Metal-to-Cluster Charge Transfer. *Journal of the American Chemical Society* **2019,** *141* (48), 19110-19117.

13. Koike, T.; Akita, M., Visible-light radical reaction designed by Ru- and Ir-based photoredox catalysis. *Inorganic Chemistry Frontiers* **2014,** *1* (8), 562-576.

14. Tóth, B. L.; Tischler, O.; Novák, Z., Recent advances in dual transition metal–visible light photoredox catalysis. *Tetrahedron Letters* **2016,** *57* (41), 4505-4513.

15. Stephenson, C., Yoon, T., MacMillan, D.W.C., Prier, C.K. and MacMillan, D.W.C. (2018). Dual Photoredox Catalysis: The Merger of Photoredox Catalysis with Other Catalytic Activation Modes. In *Visible Light Photocatalysis in Organic Chemistry*, pp 299-333. doi:10.1002/9783527674145.ch10.

16. Cherevatskaya, M.; Neumann, M.; Füldner, S.; Harlander, C.; Kümmel, S.; Dankesreiter, S.; Pfitzner, A.; Zeitler, K.; König, B., Visible-Light-Promoted Stereoselective Alkylation by Combining Heterogeneous Photocatalysis with Organocatalysis. *Angewandte Chemie International Edition* **2012,** *51* (17), 4062-4066.

17. Yuan, B.; Chong, R.; Zhang, B.; Li, J.; Liu, Y.; Li, C., Photocatalytic aerobic oxidation of amines to imines on BiVO4 under visible light irradiation. *Chemical Communications* **2014,** *50* (98), 15593-15596.

18. Wang, Z.; Lang, X., Visible light photocatalysis of dye-sensitized TiO2: The selective aerobic oxidation of amines to imines. *Applied Catalysis B: Environmental* **2018,** *224*, 404-409.

19. Pirtsch, M.; Paria, S.; Matsuno, T.; Isobe, H.; Reiser, O., [Cu(dap)2Cl] As an Efficient Visible-Light-Driven Photoredox Catalyst in Carbon–Carbon Bond-Forming Reactions. *Chemistry – A European Journal* **2012,** *18* (24), 7336-7340.

20. Gualandi, A.; Marchini, M.; Mengozzi, L.; Natali, M.; Lucarini, M.; Ceroni, P.; Cozzi, P. G., Organocatalytic Enantioselective Alkylation of Aldehydes with [Fe(bpy)3]Br2 Catalyst and Visible Light. *ACS Catalysis* **2015,** *5* (10), 5927-5931.

21. Higgins, R. F.; Fatur, S. M.; Shepard, S. G.; Stevenson, S. M.; Boston, D. J.; Ferreira, E. M.; Damrauer, N. H.; Rappé, A. K.; Shores, M. P., Uncovering the Roles of Oxygen in Cr(III) Photoredox Catalysis. *Journal of the American Chemical Society* **2016,** *138* (16), 5451-5464.

22. Zhang, Y.; Petersen, J. L.; Milsmann, C., A Luminescent Zirconium(IV) Complex as a Molecular Photosensitizer for Visible Light Photoredox Catalysis. *Journal of the American Chemical Society* **2016,** *138* (40), 13115-13118.

23. Zhang, T.; Manna, K.; Lin, W., Metal–Organic Frameworks Stabilize Solution-Inaccessible Cobalt Catalysts for Highly Efficient Broad-Scope Organic Transformations. *Journal of the American Chemical Society* **2016,** *138* (9), 3241-3249.

24. Baek, J.; Rungtaweevoranit, B.; Pei, X.; Park, M.; Fakra, S. C.; Liu, Y.-S.; Matheu, R.; Alshmimri, S. A.; Alshehri, S.; Trickett, C. A.; Somorjai, G. A.; Yaghi, O. M., Bioinspired Metal–Organic Framework Catalysts for Selective Methane Oxidation to Methanol. *Journal of the American Chemical Society* **2018,** *140* (51), 18208-18216.

25. Hod, I.; Sampson, M. D.; Deria, P.; Kubiak, C. P.; Farha, O. K.; Hupp, J. T., Fe-Porphyrin-Based Metal–Organic Framework Films as High-Surface Concentration, Heterogeneous Catalysts for Electrochemical Reduction of CO2. *ACS Catalysis* **2015,** *5* (11), 6302-6309.

26. Zhu, Y.-Y.; Lan, G.; Fan, Y.; Veroneau, S. S.; Song, Y.; Micheroni, D.; Lin, W., Merging Photoredox and Organometallic Catalysts in a Metal–Organic Framework Significantly Boosts Photocatalytic Activities. *Angewandte Chemie International Edition* **2018,** *57* (43), 14090-14094.

27. Feng, L.; Wang, Y.; Yuan, S.; Wang, K.-Y.; Li, J.-L.; Day, G. S.; Qiu, D.; Cheng, L.; Chen, W.-M.; Madrahimov, S. T.; Zhou, H.-C., Porphyrinic Metal–Organic Frameworks Installed with

Brønsted Acid Sites for Efficient Tandem Semisynthesis of Artemisinin. *ACS Catalysis* **2019,** *9* (6), 5111-5118.

28. Feng, X.; Pi, Y.; Song, Y.; Brzezinski, C.; Xu, Z.; Li, Z.; Lin, W., Metal–Organic Frameworks Significantly Enhance Photocatalytic Hydrogen Evolution and CO2 Reduction with Earth-Abundant Copper Photosensitizers. *Journal of the American Chemical Society* **2020,** *142* (2), 690-695.

29. Hernandez-Perez, A. C.; Collins, S. K., A Visible-Light-Mediated Synthesis of Carbazoles. *Angewandte Chemie International Edition* **2013,** *52* (48), 12696-12700.

30. Zhou, K.; Yu, Y.; Lin, Y.-M.; Li, Y.; Gong, L., Copper-catalyzed aerobic asymmetric cross-dehydrogenative coupling of C(sp3)–H bonds driven by visible light. *Green Chemistry* **2020,** *22* (14), 4597-4603.

31. Jiang, X.; Liu, J.; Ma, S., Iron-Catalyzed Aerobic Oxidation of Alcohols: Lower Cost and Improved Selectivity. *Organic Process Research & Development* **2019,** *23* (5), 825-835.

32. Kickelbick, G.; Wiede, P.; Schubert, U., Variations in capping the Zr6O4(OH)4 cluster core: X-ray structure analyses of [Zr6(OH)4O4(OOC–CH CH2)10]2(μ-OOC–CH CH2)4 and Zr6(OH)4O4(OOCR)12(PrOH) (R=Ph, CMe=CH2). *Inorganica Chimica Acta* **1999,** *284* (1), 1-7.

33. Li, L.; Tang, S.; Wang, C.; Lv, X.; Jiang, M.; Wu, H.; Zhao, X., High gas storage capacities and stepwise adsorption in a UiO type metal–organic framework incorporating Lewis basic bipyridyl sites. *Chemical Communications* **2014,** *50* (18), 2304-2307.

34. Amslinger, S., The Tunable Functionality of α,β-Unsaturated Carbonyl Compounds Enables Their Differential Application in Biological Systems. *ChemMedChem* **2010,** *5* (3), 351-356.

35. Pelaez, M.; Falaras, P.; Likodimos, V.; O'Shea, K.; de la Cruz, A. A.; Dunlop, P. S. M.; Byrne, J. A.; Dionysiou, D. D., Use of selected scavengers for the determination of NF-TiO2 reactive oxygen species during the degradation of microcystin-LR under visible light irradiation. *Journal of Molecular Catalysis A: Chemical* **2016,** *425*, 183-189.

36. Franco, R.; Panayiotidis, M. I.; Cidlowski, J. A., Glutathione depletion is necessary for apoptosis in lymphoid cells independent of reactive oxygen species formation. *The Journal of biological chemistry* **2007,** *282* (42), 30452-65.

37. Voest, E. E.; Faassen, E. v.; Marx, J. J. M., An electron paramagnetic resonance study of the antioxidant properties of the nitroxide free radical tempo. *Free Radical Biology and Medicine* **1993,** *15* (6), 589-595.

38. Hartung, J.; Gallou, F., Ring Closure Reactions of Substituted 4-Pentenyl-1-oxy Radicals. The Stereoselective Synthesis of Functionalized Disubstituted Tetrahydrofurans. *The Journal of Organic Chemistry* **1995,** *60* (21), 6706-6716.

39. Zhang, Y.; Schulz, M.; Wächtler, M.; Karnahl, M.; Dietzek, B., Heteroleptic diimine–diphosphine Cu(I) complexes as an alternative towards noble-metal based photosensitizers: Design strategies, photophysical properties and perspective applications. *Coordination Chemistry Reviews* **2018,** *356*, 127-146.